

Synthesis of Donor-Acceptor Dyes and their Application in Organic Solar Cells

Dissertation

Zur Erlangung des Doktorgrades Dr. rer. nat.
der Fakultät für Naturwissenschaften
der Universität Ulm

vorgelegt von

Martin Weidener

Ulm, 2015

Amtierender Dekan: Prof. Dr. P. Dürre

1. Gutachter: Prof. Dr. P. Bäuerle

2. Gutachter: Prof. Dr. S. Rau

Tag der Promotionsprüfung: 12.11.2015

Universität Ulm, Fakultät für Naturwissenschaften, 2015

Contents

Contents	i
Preface	vi
List of abbreviations	vii
Introduction	1
Chapter 1	
Dyes as Sensitizers for p-Type Dye-Sensitized Solar Cells	
1.1 Introduction	8
1.2 Built-up and fundamental principles of p-type DSSCs	8
1.3 Characterization of solar cells	10
1.4 Development of sensitizers for p-type DSSCs	12
1.5 Conclusions for the design of sensitizers for p-type DSSCs	18
1.6 References	20
Chapter 2	
Investigation of the Hexyl Substitution Pattern on Peryleny-Bithiophene-Triphenylamine Triads for p-Type DSSCs	
2.1 Introduction	26
2.2 Results and discussion	28
2.2.1 Synthesis of A- π -D triad 46	28

2.2.2 Optical properties of PMI-bithiophene-TPA triads 14 and 44-46	31
2.2.3 Electrochemical properties of PMI-bithiophene-TPA triads 14 and 44-46	33
2.2.4 Quantum chemical calculations of PMI-bithiophene-TPA triads 14 and 44-46	34
2.2.5 Photovoltaic performance of PMI-bithiophene-TPA triads 14 and 44-46	36
2.2.6 Transient absorption spectroscopy of PMI-bithiophene-TPA triads 14 and 44-46	38
2.3 Summary	40
2.4 Experimental section	41
2.4.1 General procedures	41
2.4.2 Synthesis	44
2.5 References	49
 Chapter 3	
Acceptor-Functionalized Bithiophene-Triphenylamine Triads for p-Type DSSCs	
3.1 Introduction	52
3.2 Results and discussion	54
3.2.1 Synthesis of A- π -D dyes 57-60	54
3.2.2 Optical properties of A- π -D triads 57-60	69
3.2.3 Electrochemical properties of A- π -D triads 57-60	71
3.2.4 Quantum chemical calculations of A- π -D triads 57-60	73
3.2.5 Photovoltaic performance of A- π -D triads 57-60	75
3.2.6 Impedance spectroscopy of A- π -D triads 14, 58, and 59	77
3.3 Summary	78
3.4 Experimental section	79
3.4.1 General procedures	79
3.4.2 Synthesis	81

3.5 References	96
-----------------------	-----------

Chapter 4

Structurally Defined Co-Oligomers as Donor Materials for Solution-Processed Organic Solar Cells

4.1 Introduction	100
4.2 Fundamental principles of structurally defined oligomer-based BHJSCs	102
4.3 Development of structurally defined oligomers and co-oligomers for solution-processed BHJSCs	103
4.4 Conclusions for the molecular design of structurally defined oligomers and co-oligomers for solution-processed BHJSCs	122
4.5 References	124

Chapter 5

Structurally Defined Co-Oligomers Containing Dithienopyrrole for Solution-Processed Organic Solar Cells

5.1 Introduction	130
5.1.1 General introduction	130
5.1.2 Dithieno[3,2-b:2',3'-d]pyrrole-based materials	132
5.2 Results and discussion	147
5.2.1 Synthesis of DTP-based co-oligomers 129-131	147
5.2.2 Optical properties of co-oligomers 129-131	154
5.2.3 Electrochemical properties of co-oligomers 129-131	156
5.2.4 Photovoltaic performance of co-oligomers 129-131	158
5.2.5 Photoactive layer characterization and external device optimization	164
5.3 Summary	168
5.4 Experimental section	168

5.4.1 General procedures	168
5.4.2 Synthesis	171
5.5 References	179

Chapter 6

Acceptor-Substituted Bi(dithienopyrrole) Derivatives

6.1 Introduction	184
6.1.1 General introduction	184
6.1.2 Bidithienopyrroles	185
6.2 Results and discussion	188
6.2.1 Synthesis of bi(DTP)s 181-183	188
6.2.2 Optical properties of bi(DTP)s 181-183	195
6.2.3 Electrochemical properties of bi(DTP)s 181-183	197
6.2.4 Photovoltaic performance of bi(DTP)s 181-183	199
6.3 Summary	212
6.4 Experimental section	212
6.4.1 General procedures	212
6.4.2 Synthesis	214
6.5 References	226

Chapter 7

Dicyanovinylene-Substituted Oligo(dithienopyrrole)s

7.1 Introduction	230
7.2 Results and discussion	231
7.2.1 Synthesis of DCV-substituted oligo(DTP)s 202, 204, and 205	231
7.2.2 Optical properties of DCV-substituted oligo(DTP)s 202-205	242

7.2.3 Electrochemical properties of DCV-substituted oligo(DTP)s 202-205	245
7.2.4 Photovoltaic performance of DCV-substituted ter(DTP) 204	248
7.3 Summary	253
7.4 Experimental section	254
7.4.1 General procedures	254
7.4.2 Synthesis	256
7.5 References	264
 Summary	 265
 Zusammenfassung	 271
 Acknowledgement - Danksagung	 I
Curriculum vitae	II
Publications and presentations	IV

Preface

The aim of this thesis was the synthesis of donor(D)-acceptor(A) substituted oligothiophenes for organic solar cells. During the characterization and evaluation of these dyes the focus laid on gathering structure-property relationships, which should in turn enable the synthesis of new compounds with improved properties and solar cell performance. Device testing experiments and photophysical studies concerning p-type dye-sensitized solar cells (DSSCs) were performed in collaboration with Monash University, VIC, Australia and University of Wollongong, NSW, Australia (*Chapter 2 and 3*), theoretical calculations in *Chapter 3* were carried out in the EPFL, Lausanne, Switzerland; regarding solution-processed bulk heterojunction solar cells (BHJSC), devices were partly made in collaboration with Zentrum für Sonnenenergie- und Wasserstoff-Forschung Baden-Württemberg, Stuttgart, Germany (*Chapter 5*).

First a general introduction into the field of organic solar cells from the view of an organic chemist is given. Since the requirements of the two classes of dyes synthesized in this work are quite different the thesis is then divided into two parts.

Chapter 1 gives an introduction and overview of the requirements and characteristics of dyes for p-type DSSCs. In *Chapter 2* the positioning of hexyl chains on the oligothiophene part of D-A-substituted oligothiophene triads is considered. Therefore, a novel triad is synthesized to complete a series of bithiophene-containing triads. The impact on optoelectronic properties and solar cell performance is discussed in detail. Based on the results of *Chapter 2*, *Chapter 3* deals with the variation of the acceptor-unit of such triads. The synthesis of various novel triads is described and their properties are investigated and compared to the parental compound.

Chapter 4 presents an overview of molecular state-of-the-art dyes for solution-processed bulk heterojunction solar cells (BHJSC). *Chapter 5* starts with an introduction of dithieno[3,2-b:2',3'-d]pyrrole (DTP) as electron-donating unit in oligomeric dyes and continues with the synthesis of first A-D-A solution-processible dyes incorporating DTP. Again, the positioning of hexyl chains on the oligothiophene part plays a major role on differences in optoelectronic properties and device performance and will be elucidated. Additionally, the length of the oligothiophene is varied and investigated. In *Chapter 6*, the synthesis and properties of three soluble dyes with the same conjugated backbone bearing alkyl chains at different positions are reported. The effect of the alkyl chains is explored and elaborated. Finally, *Chapter 7* covers the synthesis and characterization of an acceptor-functionalized oligomeric DTP series as an expansion of *Chapter 6*.

List of abbreviations

A	acceptor
AFM	atomic force microscopy
APCE	absorbed photon conversion efficiency
BDT	benzodithiophene
BHJ	bulk heterojunction
BHJSC	bulk heterojunction solar cell
BINAP	2,2'-bis(diphenylphosphino)-1,1'-binaphthyl
<i>n</i> -BuLi	<i>n</i> -butyllithium
(<i>n</i> -Bu) ₄ NF	tetra- <i>n</i> -butylammonium fluoride
(<i>n</i> -Bu) ₄ NPF ₆	tetra- <i>n</i> -butylammonium hexafluorophosphate
CB	chlorobenzene
CN	1-chloronaphthalene
C _μ	chemical capacitance
D	donor
D-SIMS	dynamic secondary ion mass spectrometry
ODCB	<i>o</i> -dichlorobenzene
DCE	1,2-dichloroethane
DCM	dichloromethane
DCV	dicyanovinylene
DIAD	diisopropylazodicarboxylate
DIO	1,8-diiodooctane
DME	1,2-dimethoxyethane
DMF	N,N-dimethylformamide
DPP	diketopyrrolopyrrole
DPPA	diphenylphosphoryl azide
dppf	1,1'-bis(diphenylphosphino)ferrocene
dpppNiCl ₂	1,3-bis(diphenylphosphino)propanenickel(II) chloride
DPV	differential pulse voltammetry
DSSC	dye-sensitized solar cell
DTP	dithieno[3,2-b:2',3'-d]pyrrole
DTS	dithieno[3,2-b:2',3'-d]silole
Δ <i>E</i> _{cv}	electrochemically determined band gap

ΔE_{opt}	optical band gap
$\Delta E_{\text{opt, film}}$	optical band gap in thin film
EDOT	3,4-ethylenedioxythiophene
eq.	equivalent(s)
EQE	external quantum efficiency
EtOH	ethanol
Fc/Fc ⁺	ferrocene/ferrocenium
FF	fill factor
FWHM	full width at half maximum
GC	gas chromatography
Hg(OAc) ₂	mercury(II) acetate
Hg(OCp) ₂	mercury(II) caproate
HOMO	highest occupied molecular orbital
HPLC	high performance liquid chromatography
[HPtBu ₃] ⁺ BF ₄ ⁻	tri- <i>t</i> -butylphosphonium tetrafluoroborate
IPCE	incident photon-to-current conversion efficiency
IQE	internal quantum efficiency
I_{sc}	short-circuit current
ITDB	2-isopropoxy-4,4,5,5-tetramethyl-1,3,2-dioxaborolane
ITO	indium tin oxide
J_{sc}	short-circuit current density
K ₃ PO ₄	potassium phosphate
LDA	lithium diisopropylamide
LUMO	lowest unoccupied molecular orbital
m.p.	melting point
MS	mass spectroscopy
MW	microwave
NaHCO ₃	sodium bicarbonate
NBS	N-bromosuccinimide
NEt ₃	triethylamine
NiO	nickel oxide
NIR	near-infrared
NMR	nuclear magnetic resonance
OFET	organic field-effect transistor

PC ₆₁ BM	[6,6]-phenyl-C61-butyric acid methyl ester
PC ₇₁ BM	[6,6]-phenyl-C71-butyric acid methyl ester
PCE	power conversion efficiency
Pd ₂ dba ₃	tris(dibenzylideneacetone)dipalladium(0)
PDMS	polydimethylsiloxane
Pd(OAc) ₂	palladium(II) acetate
Pd(PPh ₃) ₄	tetrakis(triphenylphosphine)palladium(0)
PEDOT:PSS	poly(3,4-ethylenedioxythiophene):poly(styrenesulfonate)
PPh ₃	triphenylphosphine
<i>R</i> _{Res}	recombination resistance
r.t.	room temperature
SCE	saturated calomel electrode
SCLC	space charge limited current
SEC	size exclusion chromatography
SVA	solvent vapor annealing
TAS	transient absorption spectroscopy
TCE	1,1,2,2-tetrachloroethane
TEM	transmission electron microscopy
TCF	tricyano-substituted furane-derivative
TCV	tricyanovinylene
TFA	trifluoroacetic acid
THF	tetrahydrofuran
TLC	thin layer chromatography
TMEDA	tetramethylethylenediamine
TMS	trimethylsilyl
TPA	triphenylamine
TCO	transparent conducting oxide
V _{OC}	open-circuit voltage
XRD	X-ray diffraction

Introduction

Conventional inorganic semiconductor-based solar cell modules are a well-established technology covering 5.7% of the power generation in Germany in 2014 (total power generation: 614 TWh).^[1] Most of the operating modules use polycrystalline silicon for power generation and reach power-conversion-efficiencies (PCE) of up to 16%. Lab-sized devices (active area $\approx 1 \text{ cm}^2$) based on silicon achieve even higher PCEs in the range of 20-25%. More sophisticated technologies using other inorganic semiconductors (e.g. GaAs) and multijunction devices (e.g. InGaP/GaAs/InGaAs) convert solar energy to electricity with efficiencies of up to 29 and 38%, respectively.^[2]

Organic solar cells (OSCs) represent a novel class of solar cells consisting of organic materials, although in the majority of cases only the photoactive layer including the light-absorbing material comprises organics.^[3] The progress of this technology has been remarkable in the last 30 years and it attracts more and more scientific and economical interest. OSCs can be divided into two classes: dye-sensitized solar cells (DSSCs) and organic thin film solar cells. Today both classes achieve in lab-sized devices PCEs of 12-13%.^[4,5] Despite their lower efficiencies, OSCs offer various advantages in comparison to their inorganic counterparts, for example, the production of lightweight and portable modules, semi-transparent or colored devices, the low consumption of material needed for fabrication, or the usage of flexible substrates, just to name a few.^[5-10] With the advance in technology, the complexity of state-of-the-art OSCs rises and therefore requires interdisciplinary collaboration of physicists, engineers, theoreticians, and chemists to overcome current benchmark efficiencies. The role of chemists clearly lays on the development and synthesis of new materials.

Concerning OSCs, one of the most challenging tasks for an organic chemist is the synthesis of the photoactive semi-conducting material, facing a multi-parameter problem. A number of interconnected prerequisites have to be considered during the synthesis of such advanced materials based on π -conjugated systems. But exactly here lies also its greatest strength: their optical and electronic properties can be tuned by chemical modifications which is not the case for inorganic semiconductors. Still, they have to feature mechanical, thermal, and chemical durability as well as distinct electronical and photophysical properties. By performing subtle changes on these π -

conjugated materials, structure-property relationships can be drawn which then can lead to further improvements of the materials.

In this work, light-absorbing π -conjugated materials were developed for two kinds of OSCs: p-type DSSCs^[11,12] and bulk heterojunction solar cells (BHJSCs)^[13,14]. In both cases, structurally defined oligomers or dyes were synthesized, their optoelectronic properties characterized and investigated concerning their performance in the respective devices. Since the requirements of the two classes of dyes synthesized in this work are quite different, the thesis is divided into two parts. Introductions into the fields of p-type DSSCs and structurally defined oligomers/co-oligomers for BHJSCs are given in *Chapter 1* and *4*, respectively.

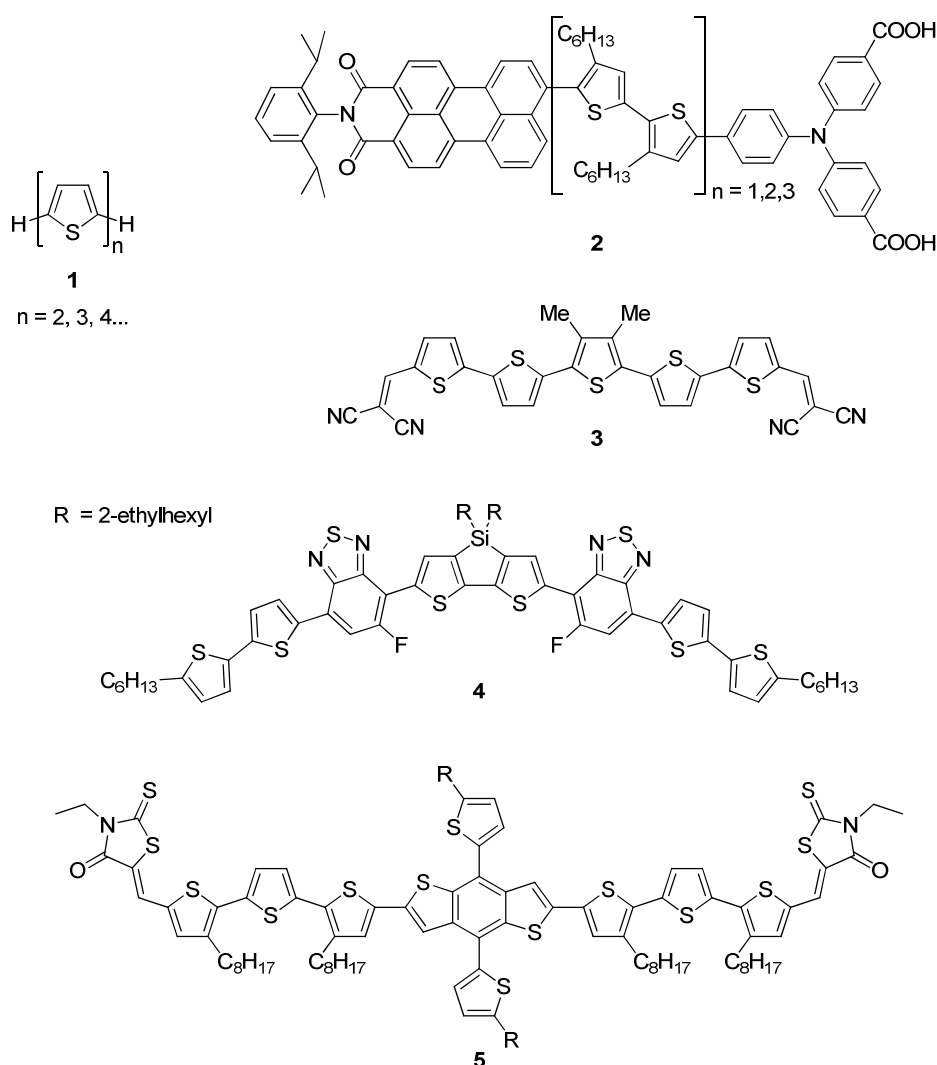


Chart 1. General structure of oligothiophenes **1** and structures of thiophene-containing light absorbers **2-5** used in OSCs.

For both projects, oligothiophenes **1** were chosen to build the major part of the conjugated backbone (general structure shown in Chart 1). Oligothiophenes are one of the most used π -conjugated materials in organic electronics due to their outstanding chemical and physical properties.^[15-23] Their unique electronic, optical, and redox properties are intriguing, as well as their unique self-assembling properties on solid surfaces or in the bulk. The high polarizability of the sulfur atoms in thiophene rings leads to a stabilization of the conjugated chain and to excellent charge transport properties which are one of the most crucial assets for applications in organic and molecular electronics.^[15,24] In Chart 1, several π -conjugated systems comprising oligothiophenes are shown, featuring record PCEs in OSCs (**2**,^[25] **3**,^[26] **4**,^[27] **5**^[28]).

Thiophene derivatives can be readily modified during their synthesis,^[29] but more important are the uncountable possibilities to connect thiophene or oligothiophenes among each other or with other conjugates via transition metal-catalyzed cross-coupling reaction, such as the Suzuki-Miyaura or Stille cross-coupling reaction.^[30,31] Recent developments concerning catalysts and ligands resulted in a wide variety of tools to couple different building blocks^[32-34] being the key method to form and tune π -conjugated light-absorbing materials.

References

- [1] Bruttostromerzeugung in Deutschland, Arbeitsgruppe Energiebilanzen (AGEB), Statistisches Bundesamt, **2014**, www.destatis.de, (retrieved on May 7, 2015)
- [2] M. A. Green, K. Emery, Y. Hishikawa, W. Warta, E. D. Dunlop, *Prog. Photovolt: Res. Appl.* **2013**, *21*, 827-837.
- [3] M. P. Ramuz, M. Vosgueritchian, P. Wei, C. Wang, Y. Gao, Y. Wu, Y. Chen, Z. Bao, *ACS Nano* **2012**, *6*, 10384-10395.
- [4] A. Yella, H.-W. Lee, H. N. Tsao, C. Yi, A. K. Chandiran, M. K. Nazeeruddin, E. W.-G. Diau, C.-Y. Yeh, S. M. Zakeeruddin, M. Grätzel, *Science* **2011**, *334*, 629-634.
- [5] http://www.heliatek.com/newscenter/latest_news; press release March 23, **2012**. (retrieved on May 7, 2015)
- [6] M. Pagliaro, R. Ciriminna, G. Palmisano, *ChemSusChem* **2008**, *1*, 880-891.
- [7] F. C. Krebs, S. A. Gevorgyan, J. Alstrup, *J. Mater. Chem.* **2009**, *19*, 5442-5451.
- [8] <http://solarmer.com/aboutus/>, **2015**. (retrieved on May 7, 2015)
- [9] <http://eight19.com/company/off-grid-opportunity>, **2014**. (retrieved on May 7, 2015)
- [10] <http://www.dyesol.com/about-dsc>, **2014**. (retrieved on May 7, 2015)

- [11] F. Odobel, L. Le Pleux, Y. Pellegrin, E. Blart, *Acc. Chem. Res.* **2010**, *43*, 1063-1071.
- [12] F. Odobel, Y. Pellegrin, E. A. Gibson, A. Hagfeldt, A. L. Smeigh, L. Hammarström, *Coord. Chem. Rev.* **2012**, *256*, 2414-2423.
- [13] A. J. Heeger, *Adv. Mater.* **2014**, *26*, 10-28.
- [14] A. Facchetti, *Mater. Today* **2013**, *16*, 123-132.
- [15] A. Mishra, C.-Q. Ma, P. Bäuerle, *Chem. Rev.* **2009**, *109*, 1141-1276.
- [16] P. Bäuerle, T. Fischer, B. Bidlingmeier, J. P. Rabe, A. Stabel, *Angew. Chem. Int. Ed.* **1995**, *34*, 303-307.
- [17] K. Takimiya, K. Sakamoto, T. Otsubo, Y. Kunugi, *Chem. Lett.* **2006**, *35*, 942-943.
- [18] T. Izumi, S. Kobashi, K. Takimiya, Y. Aso, T. Otsubo, *J. Am. Chem. Soc.* **2003**, *125*, 5286-5287.
- [19] R. Azumi, G. Götz, T. Debaerdemaeker, P. Bäuerle, *Chem. Eur. J.* **2000**, *6*, 735-744.
- [20] R. Azumi, E. Mena-Osteritz, R. Boese, J. Benet-Buchholz, P. Bauerle, *J. Mater. Chem.* **2006**, *16*, 728-735.
- [21] G. Horowitz, B. Bachet, A. Yassar, P. Lang, F. Demanze, J.-L. Fave, F. Garnier, *Chem. Mater.* **1995**, *7*, 1337-1341.
- [22] I. F. Perepichka, Perepichka Dmitrii F., *Handbook of Thiophene-Based Materials, Vol. 1*, Wiley, **2009**.
- [23] F. Denis, *Handbook of Oligo- and Polythiophenes*, Wiley-VCH, Weinheim, **1999**.
- [24] L. Zhang, N. S. Colella, B. P. Cherniawski, S. C. B. Mannsfeld, A. L. Briseno, *ACS Appl. Mater. Interfaces* **2014**, *6*, 5327-5343.
- [25] S. Powar, T. Daeneke, M. T. Ma, D. Fu, N. W. Duffy, G. Götz, M. Weidelener, A. Mishra, P. Bäuerle, L. Spiccia, U. Bach, *Angew. Chem.* **2013**, *125*, 630-633.
- [26] R. Fitzner, E. Mena-Osteritz, A. Mishra, G. Schulz, E. Reinold, M. Weil, C. Körner, H. Ziehlke, C. Elschner, K. Leo, M. Riede, M. Pfeiffer, C. Uhrich, P. Bäuerle, *J. Am. Chem. Soc.* **2012**, *134*, 11064-11067.
- [27] J. Zhou, Y. Zuo, X. Wan, G. Long, Q. Zhang, W. Ni, Y. Liu, Z. Li, G. He, C. Li, B. Kan, M. Li, Y. Chen, *J. Am. Chem. Soc.* **2013**, *135*, 8484-8487.
- [28] A. K. K. Kyaw, D. H. Wang, D. Wynands, J. Zhang, T.-Q. Nguyen, G. C. Bazan, A. J. Heeger, *Nano Lett.* **2013**, *13*, 3796-3801.
- [29] A.-B. Britta-Hörfeldt, S. Gronowitz, *Thiophenes, Vol. 1.*, Elsevier Academic Press, Oxford, **2004**.
- [30] F. Diederich, P. J. Stang, *Metal-catalyzed Cross-coupling Reactions*, Wiley-VCH, Weinheim, **1998**.
- [31] http://www.nobelprize.org/nobel_prizes/chemistry, **2010**. (retrieved on May 7, 2015)
- [32] G. C. Fu, *Acc. Chem. Res.* **2008**, *41*, 1555-1564.

- [33] M. García-Melchor, A. A. C. Braga, A. Lledós, G. Ujaque, F. Maseras, *Acc. Chem. Res.* **2013**, *46*, 2626-2634.
- [34] L. Xue, Z. Lin, *Chem. Soc. Rev.* **2010**, *39*, 1692-1705.

Chapter 1

Dyes as Sensitizers for p-Type Dye-Sensitized Solar Cells

1.1 Introduction

Grätzel cells or n-type dye-sensitized solar cells (DSSC) have attracted much research interest since the seminal paper of O'Regan and Grätzel^[1] due to their potential low-cost production and high power conversion efficiencies (PCEs) of over 13%.^[2,3] For photocurrent generation, these devices commonly use a photoactive anode consisting of a dye, also called sensitizer, which is adsorbed onto high surface area mesoporous n-type titanium dioxide.^[4-6] The elemental processes in such devices have been extensively investigated and are well understood.^[4,5] A lot of effort has also been done to develop more efficient sensitizers, mostly Ru-based or metal-free organic dyes, to increase the PCE.^[6-8]

A possibility to further improve n-type DSSCs is to exchange the counter electrode by a photoactive cathode resulting in pn-tandem DSSCs^[9] which can theoretically overcome PCE limits of single cells (Shockley-Queisser limit).^[10-12] p-Type DSSCs using a photocathode, firstly reported in 1999 by He *et al.*,^[13] attracted only little attention in comparison to n-type DSSCs.^[14] This might be due to the low performance of p-type DSSCs (PCE = 1.3%^[15]) and pn-tandem DSSCs (PCE = 2.4%^[11]). The first publications about p-type DSSCs dealt with the electronic processes and the dynamics in such devices employing photophysical studies.^[13,16-19] A lot of effort has then been put into improving p-type DSSCs by modifying the p-type semiconductor and electrolyte used.^[20-25] Only recently, elaborate synthesis of novel p-type sensitizers has been started.^[14] One way to improve sensitizers is to synthesize dye series and elucidate structure-property relationships which then will help in the development of more efficient dyes.

This chapter provides an overview of the composition of a p-type DSSC, its crucial processes, and dyes used as sensitizers. The understanding of all of them is a prerequisite for the design of efficient sensitizers.

1.2 Built-up and fundamental principles of p-type DSSCs

The device architecture of a p-type DSSC and its working principle is shown in Figure 1. The photocathode is composed of a transparent conducting oxide (TCO), e.g. fluorine-doped tin oxide, applied on a glass substrate with interconnected mesoporous particles of a p-type semiconductor, usually nickel oxide, on top of the TCO. A monolayer of the dye or sensitizer is adsorbed onto the NiO film. The counter electrode consists of a platinized TCO-coated glass. An electrolyte containing the redox mediator, mostly iodide/triiodide or $\text{Co}^{3+/2+}$ salts, completes the electrochemical cell.

Photocathodes of p-type DSSCs operate in an inverse mode compared to n-type DSSCs (Figure 1b).^[12,14] 1) Upon light excitation of the sensitizer an electron is promoted from the highest occupied molecular orbital (HOMO) to the lowest unoccupied molecular orbital (LUMO) of the dye. 2) Subsequently, an electron is transferred from the p-type wide band-gap semiconductor to the dye, often referred to as hole injection. The hole is then transported through the p-type semiconductor to the external electrical circuit. 3) The reduced sensitizer is regenerated to its ground state by the oxidized species of the redox mediator, which is in turn reduced. 4) The reduced species of the redox mediator diffuses to the counter electrode closing the electrical circuit by regeneration of the oxidized species. The maximum obtainable voltage is basically determined by the difference of the NiO valence band edge and the redox potential of the redox mediator.

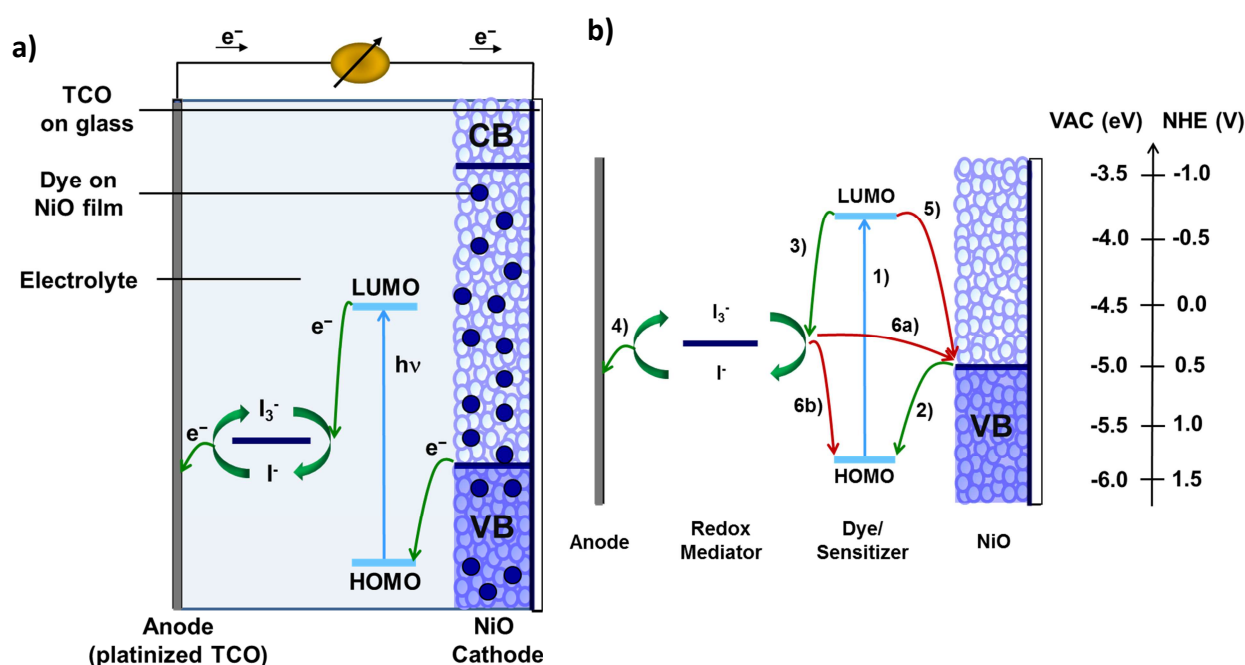


Figure 1. (a) Schematic device architecture of a p-type DSSC. (b) Working principle of a p-type DSSC (green arrows 1-4: desired electron processes, red arrows 5, 6a, and 6b: undesired competitive electron processes; CB = conduction band, VB = valence band).

The generated current is reduced by loss mechanisms, see red arrows in Figure 1b: 5) After hole injection a back electron transfer from the resulting formal dye anion to the NiO can occur which is one of the major losses in p-type DSSCs.^[16] 6a) and 6b) are electron losses due to recombination of the redox mediator's oxidized species with the NiO and the excited dye, respectively. All three of them counteract photocurrent generation and lead to a decrease in solar cell performance. How the photovoltaic properties are characterized in general is presented in the next section.

1.3 Characterization of solar cells

In order to characterize and evaluate solar cells, current(I)-voltage(V)-curves are measured which help to obtain various parameters needed to calculate the PCE of a solar cell.^[26] An example for such an I - V curve under illumination and in the dark is depicted in Figure 2.

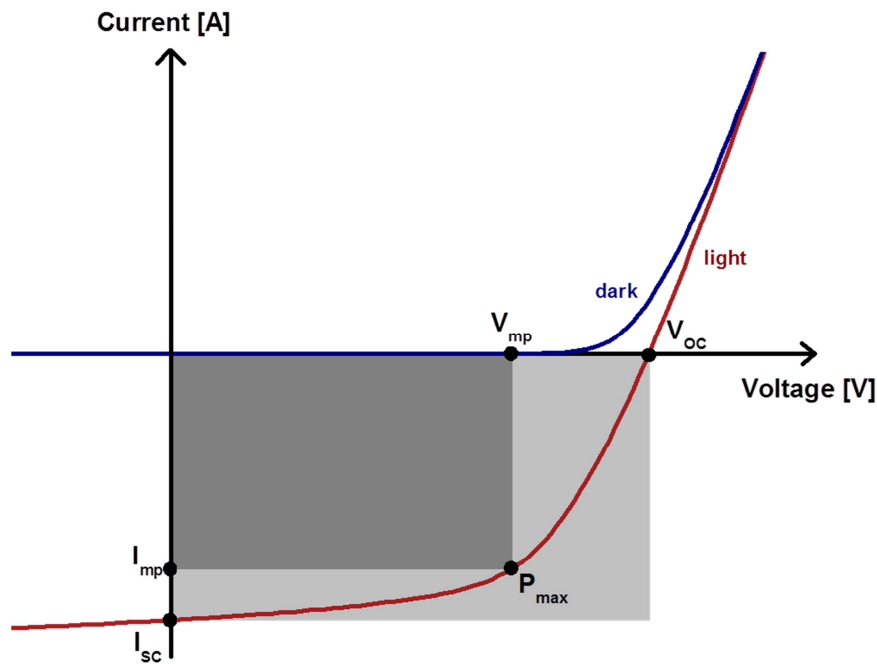


Figure 2. I - V curve of a solar cell in the dark (blue) and under illumination (red).

The most important solar cell characteristics which can be extracted from Figure 2 are defined as follows:

The open-circuit voltage (V_{oc}) is obtained when the net current through the solar cell is zero. This is achieved by applying a forward bias counteracting the bias produced by the photocurrent generation of the device. The V_{oc} describes the maximum obtainable voltage from a solar cell (Figure 2).^[26]

The short-circuit current (I_{sc}) equals the current when the solar cell is short-circuited, i.e., when $V = 0$. I_{sc} is the maximum current provided by a solar cell. As I_{sc} is dependent of the solar cell area, the short-circuit current density (J_{sc}), which is defined as I_{sc} divided by the cell area, is a more common parameter to evaluate and compare solar cells.^[26]

The fill factor (FF) is a parameter which describes the quality of a solar cell. The power of a solar cell is equal to the product of current and voltage, i.e. it corresponds to the area under the I - V curve. In the ideal case, the I - V curve would show a shape of the light grey rectangle in Figure 2 and the power

would correspond to the product of V_{OC} and I_{SC} . Due to losses, the maximum power P_{max} drawn out of a solar cell is a certain point on the I - V curve where the product of voltage and current is maximized (Figure 2). Thus, the FF can be calculated by dividing the area of the dark grey rectangle, which is defined by V_{mp} and I_{mp} , by the area of the light grey rectangle (Equation 1).^[26,27]

$$FF = \frac{V_{mp} \cdot I_{mp}}{V_{OC} \cdot I_{SC}} \quad (1)$$

Finally, the PCE is described by the quotient of the energy output from the solar cell P_{out} and the input energy from the irradiation P_{in} (Equation 2). Knowing the input energy, the PCE can be calculated by determining the V_{OC} , I_{SC} , and FF (Equation 3).^[26,27] V_{OC} , I_{SC} , and FF have to be maximized in order to obtain a high performing solar cell.

$$PCE = \frac{P_{out}}{P_{in}} = \frac{P_{max}}{P_{in}} = \frac{V_{mp} \cdot I_{mp}}{P_{in}} \quad (2)$$

$$PCE = \frac{V_{OC} \cdot I_{SC} \cdot FF}{P_{in}} \quad (3)$$

To guarantee comparability of PCEs, P_{in} and measuring conditions have to be carefully controlled. Standard testing conditions for terrestrial power-generating devices are illumination under air mass 1.5 global (AM1.5G) and a temperature of 25 °C. The air mass quantifies the reduction of the power of the sunlight by passing through the atmosphere. AM1.5G determines a solar irradiation at a zenith angle of 48.2° with a radiation intensity of 100 mW cm⁻².^[26,28,29]

The incident photon-to-current conversion efficiency (IPCE) or external quantum efficiency (EQE) denotes the ratio of collected electrons and incident photons at a specific wavelength under short-circuit conditions (Equation 4).

$$IPCE_{\lambda} = EQE_{\lambda} = \frac{\text{number of collected electrons}}{\text{number of incident photons } (\lambda)} \quad (4)$$

By measuring the reflected or unabsorbed photons coming from the device and subtracting them from the number of incident photons the absorbed photon-to-current conversion efficiency (APCE) or internal quantum yield (IQE) can be calculated giving further insight in the efficiency of the photoactive material without taking the absorbance into account (Equation 5).^[27,30]

$$APCE_{\lambda} = IQE_{\lambda} = \frac{\text{number of collected electrons}}{\text{number of absorbed photons } (\lambda)} \quad (5)$$

1.4 Development of sensitizers for p-type DSSCs

The first p-type DSSCs used commercially available dyes as sensitizers. Mainly fluorone (**6**),^[10,13,31] porphyrin (**7**),^[13,16] coumarin (**8**),^[17,19,31-34] and merocyanine derivatives (**9**)^[32,35] were applied and served rather for understanding and characterization of the mechanism of photocurrent generation than achieving high PCEs (**6-9**, Chart 1). Maximum PCEs of 0.055%^[32] and IPCEs up to 11%^[33] were achieved. Carboxylic acid groups act as anchoring groups and bind the sensitizer to the NiO surface. Derivatives without anchoring groups did not adsorb well onto the NiO particles and hence produced less photocurrent.^[19] This is in agreement with the same finding for sensitizers for n-type DSSCs.^[7,36]

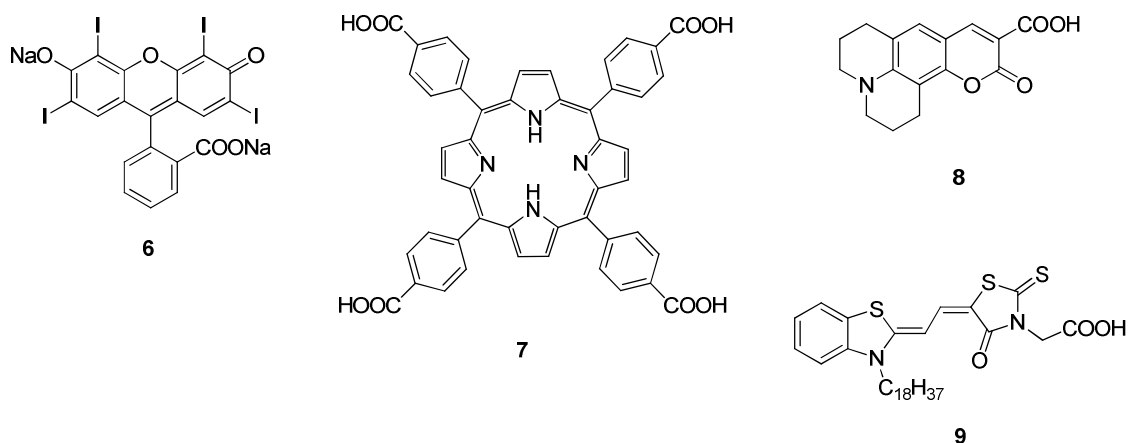


Chart 1. First sensitizers used in p-type DSSCs.

The first dyes solely synthesized as sensitizers for p-type DSSCs were reported from Morandeira *et al.*^[37] and Qin *et al.*^[38] in 2008. They followed two different approaches to slow down the fast back electron transfer by providing an electron transfer pathway from the NiO to the redox mediator

(Figure 1b, 5). Morandeira *et al.* prepared perylenemonoimide-based sensitizer **10** as well as sensitizer-acceptor dyad **11** by adding a naphthalenediimide as an electron acceptor to **10** (Chart 2).^[37] Femtosecond transient absorption spectroscopy (TAS) studies clearly showed that **11** exhibits a much longer charge-separated state in comparison to **10**. This is due to an electron cascade: after hole injection, the excess electron is transferred from the perylenemonoimide moiety to the naphthalenediimide and is therefore spatially separated from the NiO, hence recombination is retarded. IPCE and APCE measurements of p-type DSSCs exactly reflect this finding by increasing their values by a factor of three when changing the sensitizer from **10** to **11**.^[37] Qin *et al.* synthesized donor-acceptor dye **12** as sensitizer on the basis of sensitizers for n-type DSSCs,^[7] but instead of putting the anchoring group on the electron acceptor they placed it on the donor group (Chart 2). With sensitizer **12** a PCE of 0.05% and an IPCE of 18% was achieved which was the highest IPCE until then.^[38] Using thicker NiO layers and changing the π -spacer between the acceptor dicyanovinylene (DCV) and the donor triphenylamine (TPA) from thiophene (**12**) to benzene (**13**, Chart 2), record IPCE of 44% and PCE of 0.09% were obtained.^[39]

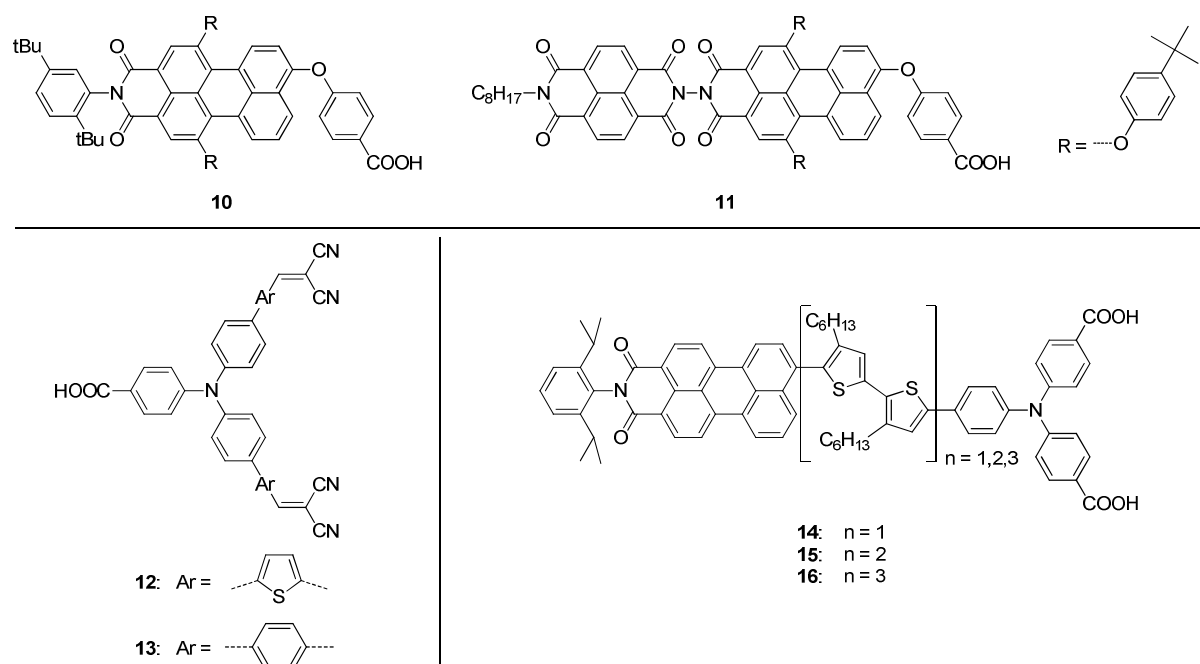


Chart 2. First dyes developed as sensitizers for p-type DSSCs.

In 2010, Nattestad *et al.* showed new record PCEs of up to 0.41% in p-type DSSCs using dyes **14-16** as sensitizers (Chart 2). This linear acceptor- π -bridge-donor (A- π -D) dye series comprised three dyes with a perylenemonoimide acceptor, a TPA donor with two anchoring groups, and a variable-length oligothiophene π -bridge which provides control over the spatial separation of the acceptor and the

NiO and thus over the photo-generated charge carriers.^[11] Elongation of the oligothiophene bridge starting from a bithiophene (**14**) to a sexithiophene (**16**) resulted in an enormous increase in APCE from 28% to 96%, respectively, which is mainly due to a slower back electron transfer process, proven by TAS. The authors also supposed that an increased hydrophobicity of the dye which comes along with an increasing amount of hexyl chains should also help to shield the NiO from the electrolyte. This was also shown to be favorable for ruthenium complexes bearing hydrophobic groups in n-type DSSCs.^[40] By optimizing the photocathode material^[25,41-43] and the electrolyte,^[15] A- π -D dye **16** recently reached a PCE of 1.3%, which is by far the best value for p-type DSSCs.

Qin *et al.* synthesized sensitizers **17**, **18**, and **19** (Chart 3) by replacing the DCV acceptors of their well performing dye **12** (Chart 2) with stronger electron-accepting groups which should lead to a better charge separation and to a longer-lived charge-separated species.^[44] In solution, A- π -D dyes **17**, **18**, and **19** showed red-shifts of the absorption maximum compared to **12** by 50, 93, and 9 nm, respectively, leading to a better light harvesting. Despite these advantages, p-type DSSCs of **17**, **18**, and **19** only reached PCEs of 0.07, 0.03, and 0.09%, respectively, compared to devices using sensitizer **12** yielding a PCE of 0.15%.^[44] Especially devices containing dye **18**, bearing tricyanovinylene (TCV) groups as acceptors, showed a huge decrease in V_{oc} and J_{sc} in comparison to solar cells using **12** as sensitizer. Photoinduced absorption spectroscopy proved an inefficient regeneration of the dye by the electrolyte (Figure 1b, 3), whose reason lies in the lowering of the LUMO energy level of **18** by changing the DCV acceptors with more strongly electron-withdrawing TCV groups. Hence, the LUMO energy level of **18** ($E = -4.14$ eV) is lying hardly below the reduction potential of $I_3^-/I_2^{\bullet-}$ ($E(I_3^-/I_2^{\bullet-}) = -4.15$ eV vs. vacuum). This resulted in an insufficient driving force for dye regeneration.^[44] Ji *et al.* synthesized TPA- π -bridge-DCV dyes **20**, **21**, and **22** (Chart 3) investigating the effect of thiophene, benzene, and 3,4-ethylenedioxythiophene (EDOT), respectively, as π -bridging units.^[45] In solution, dyes **20** and **22** featured a red-shift of the absorption maximum by 55 and 69 nm, respectively, in comparison to phenylene derivative **21**. Sensitizer **22** performed best in p-type DSSCs showing PCEs of up to 0.06%, **20** and **21** gave PCEs of 0.04 and 0.05%, respectively. The slightly reduced performance of **20** compared to **21** and **22** can be explained by the five times lower dye loading.^[45] In contrast to this finding, dye **20** featured the longest electron lifetimes measured by electrochemical impedance spectroscopy, pointing to the beneficial influence of thiophenes as π -bridging unit. Yen *et al.* reported on sensitizers **23**, **24**, and **25** bearing one or two anchoring groups on the TPA donor unit and compared them with dye **20** (Chart 3).^[46] In general, dyes **23** and **24** having one anchoring group attached to the TPA performed with PCEs of 0.06 and 0.05%, respectively, worse than **25** possessing two anchoring groups and yielding a PCE of 0.09%. The dye loading for all four dyes was very similar. This correlates with results from TiO₂-based n-type DSSCs obtained by using ruthenium complexes

with one and two anchoring groups suggesting that sensitizers with two carboxylic acid groups more effectively cover the TiO_2 and therefore prevent recombination between the electrolyte and the metal oxide (Figure 1b, 6a).^[47]

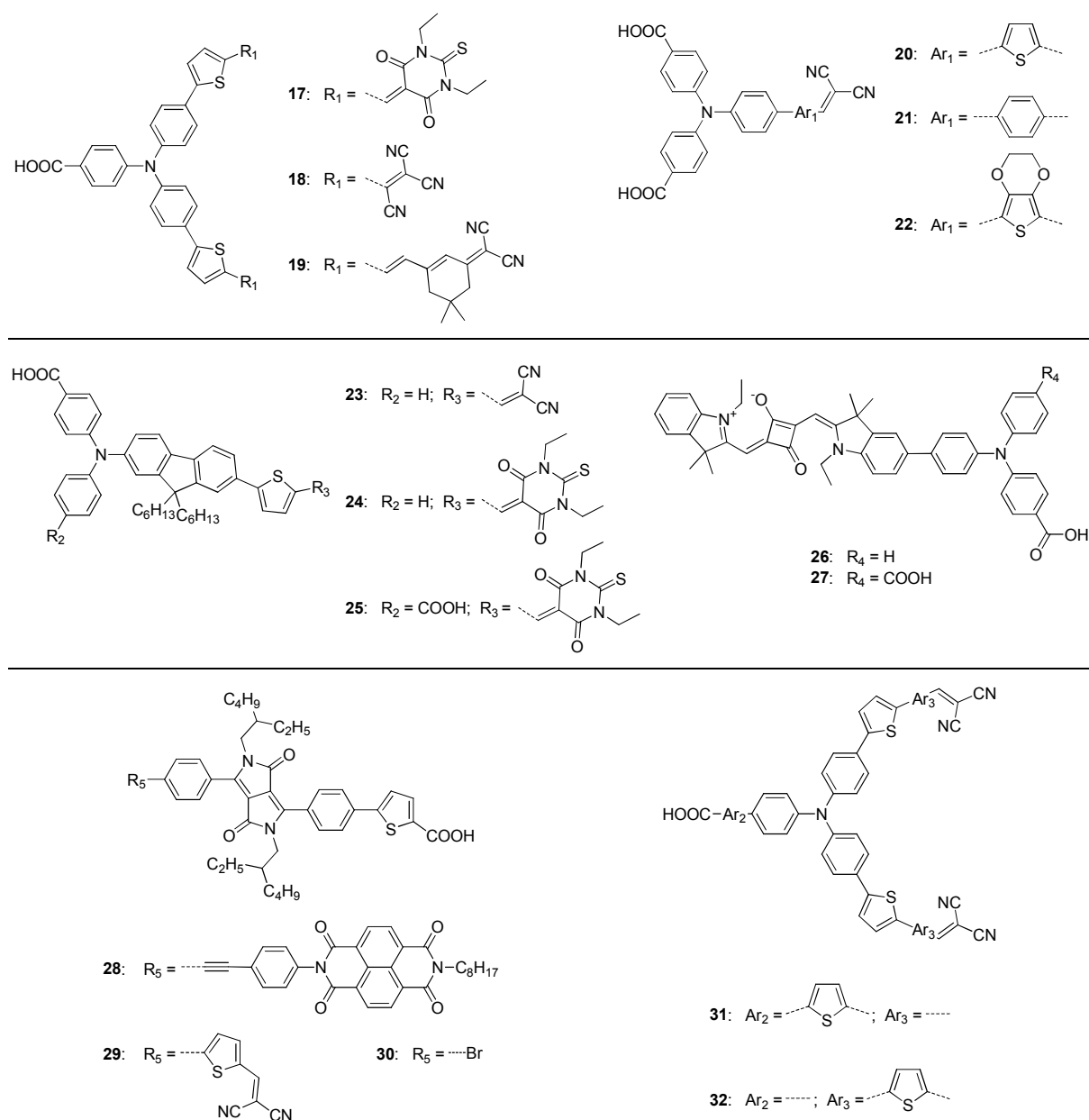


Chart 3. p-Type DSSC sensitizers reported between 2011 and 2013.

Later in 2012, the same group found a similar behaviour on TPA-substituted squaraine dyes **26** and **27** (Chart 3).^[48] Derivative **27** with two anchoring groups outperformed **26** bearing only one carboxylic acid group reaching a two times higher PCE of 0.11%. But this time, the dye loading of the sensitizer bearing two carboxylic acid groups, **27**, was with $1.98 \times 10^{-7} \text{ mol cm}^{-2}$ clearly higher in

comparison to 1.07×10^{-7} mol cm⁻² for **26**. The authors suggest that two anchoring groups may lead to a more upright anchoring and therefore to a more compact packing of the sensitizer.^[48] This leads to a more effective coverage resulting in a better blocking of the electrolyte from the NiO.^[46] Favereau *et al.* recently reported on a diketopyrrolopyrrole (DPP)-naphthalenediimide dyad **28** and two new DPP-based sensitizers **29** and **30** (Chart 3).^[49] Similar to the results obtained on sensitizers **10** and **11** (Chart 2), where acceptor cascade sensitizer **11** outperformed perylenemonoimide **10**, DPP-naphthalenediimide-based dye **28** yielded a higher PCE than **29** and **30**. Among **29** and **30**, the latter is inferior concerning solar cell characteristics because of a lack of a second electron acceptor and therefore the capability of draining the electronic density away from the NiO surface. In 2012, Zhu *et al.*^[50] modified sensitizer **12**^[38] by firstly inserting a thiophene unit between the carboxylic acid group and the TPA donor to obtain **31** and secondly by adding thiophenes between TPA and the DCV acceptors for **32** (Chart 3). In comparison to **12**, modified sensitizers **31** and **32** showed a slightly red-shifted absorption of about 20 nm and an improved extinction while maintaining appropriate HOMO and LUMO level energies (E_{HOMO} and E_{LUMO}). The increased distance of the acceptor part of the dye to the NiO semiconductor led to reduced charge recombination and superior hole injection processes of **31** and **32** compared to **12**. Nevertheless, **31** outperforms not only **12**, but also **32** with a PCE of 0.11%. This is on one hand due to the longest hole lifetime present for devices containing **31** and on the other hand a result of the fact that **32** molecules have a more stretched umbrella-like shape on the NiO in comparison to **12** and **31**. Hence, a ~10% lower dye loading is observed for **31**, which has a negative influence on charge recombination processes, light harvesting, and therefore in PCE. In n-type DSSCs sterical demanding dyes have shown to produce lower dye loadings and hence lower PCEs, too.^[51] Despite carboxylic acids have been used as efficient anchoring groups, there are also sensitizers for n-type DSSCs bearing pyridine rings.^[52] Recently, Jin *et al.* synthesized **33** and **34** containing pyridine as anchoring group and used them as sensitizers for p-type DSSCs (Chart 4).^[53] They showed that the PCE is dependent of the dye-adsorption time similar to n-type DSSC sensitizers.^[54] **34** reaches a maximum PCE of 0.14% at 1.5 h dye-adsorbing time and produces an IPCE of up to 30% emphasizing the suitability of pyridine as anchoring group in p-type DSSCs.

Many of the high efficient dyes used in n-type DSSCs are polypyridyl ruthenium (II) complexes.^[55-61] In contrast to this, only a few publications deal with ruthenium complexes sensitizing NiO.^[31,62-64] The most efficient ones are depicted in Chart 4. Pellegrin *et al.* investigated a series of bipyridine (bipy) ruthenium complexes **35-38** substituted by different anchoring groups, such as carboxylic acid (**35**), methyl phosphonic acid (**36**), dithio carboxylic acid (**37**), or catechol (**38**).^[64] They showed that **35** with two carboxylic acid groups has the highest binding constant towards NiO, followed by **36**. Within this series, **37** and **38** with two dithio carboxylic acids and catechol anchoring groups,

naphthalene unit.^[63] Therefore, the PCE of p-type DSSCs is increased when replacing sensitizer **39** by acceptor-substituted complex **40** from 0.004 to 0.006% using a iodide/triiodide-based electrolyte and further to 0.02% using a cobalt-based electrolyte. Recently, Ji *et al.* synthesized a series of ruthenium sensitizers **41**, **42**, and **43** consisting of two bipy or phenanthrolines and a cyclometalated ligand carrying TPA with two carboxylic acid groups.^[62] Comparing previously used ruthenium complexes,^[31,63,64] they showed decent PCEs of 0.07-0.10% when used as sensitizers in p-type DSSCs. This result can be explained by the increased spatial separation of the metal center of **41**, **42**, and **43** from the NiO surface in comparison to other ruthenium-based sensitizers (Chart 4). Among the three cyclometalated ruthenium complexes **41** has the highest J_{SC} , although it shows the lowest light-harvesting capability compared to **42** and **43** which possess ligands with a more extended π -conjugated system. The reason for the better performance of **41** is justified by a slower charge recombination implying that the auxiliary ligands play an important role in the electron-hole recombination kinetics and thus the device performance.^[62]

1.5 Conclusions for the design of sensitizers for p-type DSSCs

From the previous sections important design rules for the synthesis of sensitizers for p-type DSSCs can be summarized. First of all, the sensitizer should absorb in a very broad region of the solar spectrum to increase the photocurrent generation to a maximum. Additionally, it is also critical that the dyes display high extinction coefficients because the optimal thickness of the p-type semiconductor films (generally around 2-3 μm mesoporous NiO) is much lower than that of n-type DSSCs (the TiO_2 thickness of cells operating with liquid electrolyte is rarely lower than 10 μm), hence less dye is adsorbed in p-type DSSCs than in conventional n-type DSSCs.^[65] This is realized in the before mentioned sensitizers by using a strongly absorbing chromophore, e.g. perylene, squaraine, or diketopyrrolopyrrole or by combining an electron-donating and an electron-accepting group generating a charge transfer absorption band. Secondly, the HOMO and LUMO energy levels have to fit to the valence band edge of the NiO and to the reduction potential of the redox electrolyte, respectively. For electron transfer processes usually an energy gap between the involved energy levels of ~ 0.3 eV is sufficient to ensure an unhindered process. Assuming that NiO has a valence band edge at ~ -5.0 eV vs. vacuum,^[31] the HOMO energy level (E_{HOMO}) of the sensitizer should have an energy of -5.3 eV or lower to guarantee efficient hole injection into the NiO electrode. Accordingly to this, the LUMO energy level (E_{LUMO}) has to be at least ~ 0.3 eV higher in energy than the redox

potential of the redox mediator. For dye regeneration, the relevant redox couple in a triiodide/iodide based electrolyte is $I_3^-/I_2^{\bullet-}$ with a redox potential at ~ -4.15 eV vs. vacuum.^[44]

Additionally to these fundamental rules, the structure of the sensitizer can be designed in a way that loss mechanisms are retarded and beneficial ones accelerated. By studying the examples mentioned in section 1.4 it is evident that the anchoring groups have to be attached to the donor part of the sensitizer facilitating hole injection after excitation by the close spatial arrangement of the molecule part with high electron density and NiO.^[11,38,64] Clearly, an acceptor positioned at the periphery of the molecule pointing away from NiO and hence having the greatest distance to the injected holes results in longer-lived charge separated species after hole injection and significantly inhibits back electron transfer, one of the major losses in p-type DSSCs.^[16,31,38] By adding hydrophobic substituents at the sensitizer the usually polar electrolyte is blocked from the NiO resulting in a slower recombination of holes from the NiO and electrons from the redox mediator.^[31,40]

Therefore, an organic dye with a linear A- π -D structure seems to be most suitable for combining all these properties. Regarding a linear sensitizer, the use of two anchoring groups is improving the perpendicular positioning referring to the NiO surface. A perpendicular positioning of the sensitizer should lead to the most efficient p-type DSSCs.^[46] In Figure 3 a schematic structure of a linear D- π -A dye is given. Bent yellow arrows indicate electron transfer processes and straight arrows imply an electron cascade from the donor to the acceptor as desired.

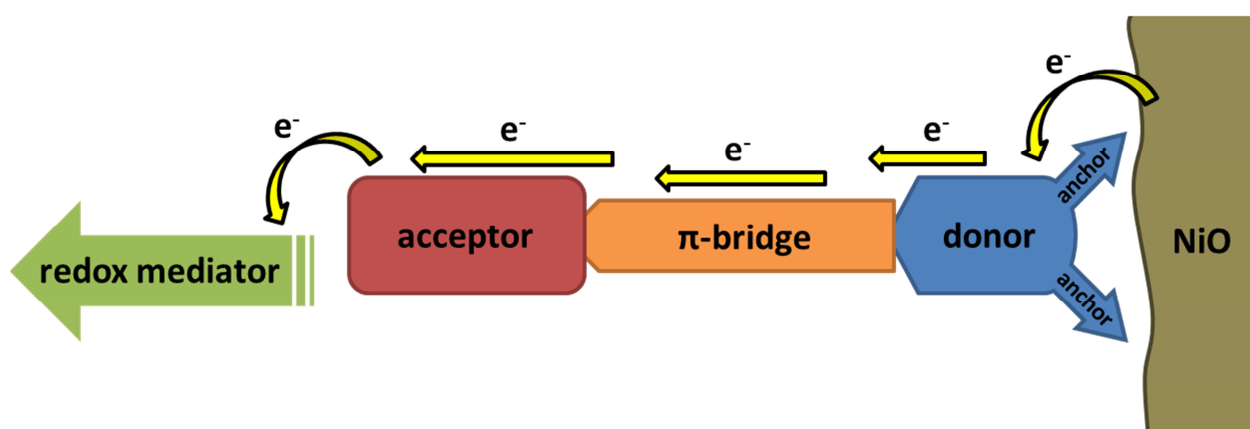


Figure 3. Schematic design of a linear acceptor- π -bridge-donor sensitizer with two anchoring groups for p-type DSSCs.

In the following two chapters the derived design rules are applied to synthesize novel sensitizers, which in turn should contribute to a further understanding concerning sensitizer design.

1.6 References

- [1] B. O'Regan, M. Grätzel, *Nature* **1991**, 353, 737-740.
- [2] S. Mathew, A. Yella, P. Gao, R. Humphry-Baker, B. Curchod, F. E., N. Ashari-Astani, I. Tavernelli, U. Rothlisberger, M. K. Nazeeruddin, M. Grätzel, *Nat. Chem.* **2014**, 6, 242-247.
- [3] A. Yella, C.-L. Mai, S. M. Zakeeruddin, S.-N. Chang, C.-H. Hsieh, C.-Y. Yeh, M. Grätzel, *Angew. Chem.* **2014**, 126, 3017-3021; *Angew. Chem. Int. Ed.* **2014**, 53, 2973-2977.
- [4] M. Grätzel, *Inorg. Chem.* **2005**, 44, 6841-6851.
- [5] A. Hagfeldt, M. Grätzel, *Acc. Chem. Res.* **2000**, 33, 269-277.
- [6] N. Robertson, *Angew. Chem.* **2006**, 118, 2398-2405; *Angew. Chem. Int. Ed.* **2006**, 45, 2338-2345.
- [7] A. Mishra, M. K. R. Fischer, P. Bäuerle, *Angew. Chem.* **2009**, 121, 2510-2536; *Angew. Chem. Int. Ed.* **2009**, 48, 2474-2499.
- [8] Y. Ooyama, Y. Harima, *ChemPhysChem* **2012**, 13, 4032-4080.
- [9] W. Shockley, H. J. Queisser, *J. Appl. Phys.* **1961**, 32, 510-519.
- [10] J. He, H. Lindstrom, A. Hagfeldt, S.-E. Lindquist, *Sol. Energy Mater. Sol. Cells* **2000**, 62, 265-273.
- [11] A. Nattestad, A. J. Mozer, M. K. R. Fischer, Y. B. Cheng, A. Mishra, P. Bäuerle, U. Bach, *Nat. Mater.* **2010**, 9, 31-35.
- [12] F. Odobel, L. Le Pleux, Y. Pellegrin, E. Blart, *Acc. Chem. Res.* **2010**, 43, 1063-1071.
- [13] J. He, H. Lindstrom, A. Hagfeldt, S.-E. Lindquist, *J. Phys. Chem. B* **1999**, 103, 8940-8943.
- [14] F. Odobel, Y. Pellegrin, E. A. Gibson, A. Hagfeldt, A. L. Smeigh, L. Hammarström, *Coord. Chem. Rev.* **2012**, 256, 2414-2423.
- [15] S. Powar, T. Daeneke, M. T. Ma, D. Fu, N. W. Duffy, G. Götz, M. Weidelener, A. Mishra, P. Bäuerle, L. Spiccia, U. Bach, *Angew. Chem.* **2013**, 125, 630-633; *Angew. Chem. Int. Ed.* **2013**, 52, 602-605.
- [16] M. Borgström, E. Blart, G. Boschloo, E. Mukhtar, A. Hagfeldt, L. Hammarström, F. Odobel, *J. Phys. Chem. B* **2005**, 109, 22928-22934.
- [17] A. Morandeira, G. Boschloo, A. Hagfeldt, L. Hammarström, *J. Phys. Chem. B* **2005**, 109, 19403-19410.
- [18] F. Vera, R. Schrebler, E. Munoz, C. Suarez, P. Cury, H. Gomez, R. Cordova, R. E. Marotti, E. A. Dalchiele, *Thin Solid Films* **2005**, 490, 182-188.
- [19] H. Zhu, A. Hagfeldt, G. Boschloo, *J. Phys. Chem. C* **2007**, 111, 17455-17458.
- [20] J. H. Rhee, Y. H. Lee, P. Bera, S. I. Seok, *Chem. Phys. Lett.* **2009**, 477, 345-348.
- [21] L. Li, E. A. Gibson, P. Qin, G. Boschloo, M. Gorlov, A. Hagfeldt, L. Sun, *Adv. Mater.* **2010**, 22, 1759-1762.

- [22] M. Awais, M. Rahman, J. M. Don MacElroy, D. Dini, J. G. Vos, D. P. Dowling, *Surf. Coat. Technol.* **2011**, *205*, S245-S249.
- [23] X.-H. Chan, J. R. Jennings, M. A. Hossain, K. Koh Zhen Yu, Q. Wang, *J. Electrochem. Soc.* **2011**, *158*, H733-H740.
- [24] A. Nattestad, X. Zhang, U. Bach, Y.-B. Cheng, *J. Photonics Energy* **2011**, *1*, 011103.
- [25] X. L. Zhang, F. Huang, A. Nattestad, K. Wang, D. Fu, A. Mishra, P. Bäuerle, U. Bach, Y.-B. Cheng, *Chem. Commun.* **2011**, *47*, 4808-4810.
- [26] R. Hull, R. M. O. Jr., J. Parisi, *Laser-Surface Interactions for New Materials Production*, Springer-Verlag, Berlin Heidelberg, **2003**.
- [27] S. Günes, H. Neugebauer, N. S. Sariciftci, *Chem. Rev.* **2007**, *107*, 1324-1338.
- [28] F. Kasten, A. T. Young, *Appl. Opt.* **1989**, *28*, 4735-4738.
- [29] R. Hulstrom, R. Bird, C. Riordan, *Solar Cells* **1985**, *15*, 365-391.
- [30] J. Rostalski, D. Meissner, *Sol. Energy Mater. Sol. Cells* **2000**, *61*, 87-95.
- [31] A. Nattestad, M. Ferguson, R. Kerr, Y.-B. Cheng, U. Bach, *Nanotechnology* **2008**, *19*, 295304-295312.
- [32] S. Mori, S. Fukuda, S. Sumikura, Y. Takeda, Y. Tamaki, E. Suzuki, T. Abe, *J. Phys. Chem. C* **2008**, *112*, 16134-16139.
- [33] A. Morandeira, G. Boschloo, A. Hagfeldt, L. Hammarström, *J. Phys. Chem. C* **2008**, *112*, 9530-9537.
- [34] H. Zhu, A. Hagfeldt, G. Boschloo, *J. Phys. Chem. C* **2007**, *111*, 17455-17458.
- [35] A. Nakasa, H. Usami, S. Sumikura, S. Hasegawa, T. Koyama, E. Suzuki, *Chem. Lett.* **2005**, *34*, 500-501.
- [36] J. N. Clifford, E. Martinez-Ferrero, A. Viterisi, E. Palomares, *Chem. Soc. Rev.* **2011**, *40*, 1635-1646.
- [37] A. Morandeira, J. Fortage, T. Edvinsson, L. Le Pleux, E. Blart, G. Boschloo, A. Hagfeldt, L. Hammarstrom, F. Odobel, *J. Phys. Chem. C* **2008**, *112*, 1721-1728.
- [38] P. Qin, H. Zhu, T. Edvinsson, G. Boschloo, A. Hagfeldt, L. Sun, *J. Am. Chem. Soc.* **2008**, *130*, 8570-8571.
- [39] P. Qin, M. Linder, T. Brinck, G. Boschloo, A. Hagfeldt, L. Sun, *Adv. Mater.* **2009**, *21*, 2993-2996.
- [40] S. M. Zakeeruddin, M. K. Nazeeruddin, R. Humphry-Baker, P. Péchy, P. Quagliotto, C. Barolo, G. Viscardi, M. Grätzel, *Langmuir* **2002**, *18*, 952-954.
- [41] X. L. Zhang, Z. Zhang, D. Chen, P. Bäuerle, U. Bach, Y.-B. Cheng, *Chem. Commun.* **2012**, *48*, 9885-9887.
- [42] S. Powar, Q. Wu, M. Weidelener, A. Nattestad, Z. Hu, A. Mishra, P. Bäuerle, L. Spiccia, Y.-B. Cheng, U. Bach, *Energy Environ. Sci.* **2012**, *5*, 8896-8900.

- [43] X. L. Zhang, Z. Zhang, F. Huang, P. Bäuerle, U. Bach, Y.-B. Cheng, *J. Mater. Chem.* **2012**, *22*, 7005-7009.
- [44] P. Qin, J. Wiberg, E. A. Gibson, M. Linder, L. Li, T. Brinck, A. Hagfeldt, B. Albinsson, L. Sun, *J. Phys. Chem. C* **2010**, *114*, 4738-4748.
- [45] Z. Ji, G. Natu, Z. Huang, Y. Wu, *Energy Environ. Sci.* **2011**, *4*, 2818-2821.
- [46] Y.-S. Yen, W.-T. Chen, C.-Y. Hsu, H.-H. Chou, J. T. Lin, M.-C. P. Yeh, *Org. Lett.* **2011**, *13*, 4930-4933.
- [47] S. N. Mori, W. Kubo, T. Kanzaki, N. Masaki, Y. Wada, S. Yanagida, *J. Phys. Chem. C* **2007**, *111*, 3522-3527.
- [48] C.-H. Chang, Y.-C. Chen, C.-Y. Hsu, H.-H. Chou, J. T. Lin, *Org. Lett.* **2012**, *14*, 4726-4729.
- [49] L. Favereau, J. Warnan, Y. Pellegrin, E. Blart, M. Boujtita, D. Jacquemin, F. Odobel, *Chem. Commun.* **2013**, *49*, 8018-8020.
- [50] L. Zhu, H. Yang, C. Zhong, C. M. Li, *Chem. Asian J.* **2012**, *7*, 2791-2795.
- [51] M. K. R. Fischer, S. Wenger, M. Wang, A. Mishra, S. M. Zakeeruddin, M. Grätzel, P. Bäuerle, *Chem. Mater.* **2010**, *22*, 1836-1845.
- [52] Y. Ooyama, S. Inoue, T. Nagano, K. Kushimoto, J. Ohshita, I. Imae, K. Komaguchi, Y. Harima, *Angew. Chem.* **2011**, *123*, 7567-7571; *Angew. Chem. Int. Ed.* **2011**, *50*, 7429-7433.
- [53] B. Jin, W. Wu, X. Zhang, F. Guo, Q. Zhang, J. Hua, *Chem. Lett.* **2013**, *42*, 1271-1272.
- [54] Y. Ooyama, T. Nagano, S. Inoue, I. Imae, K. Komaguchi, J. Ohshita, Y. Harima, *Chem. Eur. J.* **2011**, *17*, 14837-14843.
- [55] M. Grätzel, *J. Photochem. Photobiol., A* **2004**, *164*, 3-14.
- [56] M. K. Nazeeruddin, A. Kay, I. Rodicio, R. Humphry-Baker, E. Müller, P. Liska, N. Vlachopoulos, M. Grätzel, *J. Am. Chem. Soc.* **1993**, *115*, 6382-6390.
- [57] Y. Chiba, A. Islam, Y. Watanabe, R. Komiya, N. Koide, L. Han, *Jpn. J. Appl. Phys.* **2006**, *45*, L638-L640.
- [58] M. K. Nazeeruddin, P. Pechy, M. Grätzel, *Chem. Commun.* **1997**, 1705-1706.
- [59] Mohammad K. Nazeeruddin, P. Péchy, T. Renouard, S. M. Zakeeruddin, R. Humphry-Baker, P. Comte, P. Liska, L. Cevey, E. Costa, V. Shklover, L. Spiccia, G. B. Deacon, C. A. Bignozzi, M. Grätzel, *J. Am. Chem. Soc.* **2001**, *123*, 1613-1624.
- [60] M. K. Nazeeruddin, R. Splivallo, P. Liska, P. Comte, M. Grätzel, *Chem. Commun.* **2003**, 1456-1457.
- [61] M. K. Nazeeruddin, F. De Angelis, S. Fantacci, A. Selloni, G. Viscardi, P. Liska, S. Ito, B. Takeru, M. Grätzel, *J. Am. Chem. Soc.* **2005**, *127*, 16835-16847.
- [62] Z. Ji, G. Natu, Y. Wu, *ACS Appl. Mater. Interfaces* **2013**, *5*, 8641-8648.
- [63] J. C. Freys, J. M. Gardner, L. D'Amario, A. M. Brown, L. Hammarström, *Dalton Trans.* **2012**, *41*, 13105-13111.

- [64] Y. Pellegrin, L. Le Pleux, E. Blart, A. Renaud, B. Chavillon, N. Szuwarski, M. Boujtita, L. Cario, S. Jolic, D. Jacquemin, F. Odobel, *J. Photochem. Photobiol., A* **2011**, 219, 235-242.
- [65] F. Odobel, Y. Pellegrin, *J. Phys. Chem. Lett.* **2013**, 4, 2551-2564.

Chapter 2

Investigation of the Hexyl-Substitution Pattern on Perylene-Bithiophene-Triphenylamine Triads for p-Type DSSCs

Adapted from M. Weidelener et al., *J. Mater. Chem.* **2012**, 22, 7366-7379.
with permission from The Royal Society of Chemistry

2.1 Introduction

In the previous chapter, clear design rules for p-type DSSC sensitizers were compiled. Perylenyl-oligothiophene-triphenylamine series **14-16** (Chart 1), synthesized in the Institute of Organic Chemistry II and Advanced Materials, Ulm University, includes most of these design rules and hence shows to date the best photovoltaic performance in p-type DSSCs with a PCE of 1.3%.^[1,2] Within the linear acceptor- π -bridge-donor (A- π -D) series, the oligothiophene π -bridge was elongated gradually from bithiophene to quaterthiophene to sexithiophene. An important structure-property relationship was discovered upon this stretching using transient absorption spectroscopy (TAS): the bigger the spatial separation of the perylenemonoimide (PMI) acceptor and the triphenylamine (TPA) donor, the longer-lived is the charge-separated species. It is also anticipated that the hexyl chains attached to the oligothiophene π -bridge play an important role reducing unfavorable recombination between the redox mediator and the NiO electrode by avoiding close contact of the electrolyte with NiO.^[1] These results imply that the π -bridge of the sensitizer has a detrimental effect on the photovoltaic performance.

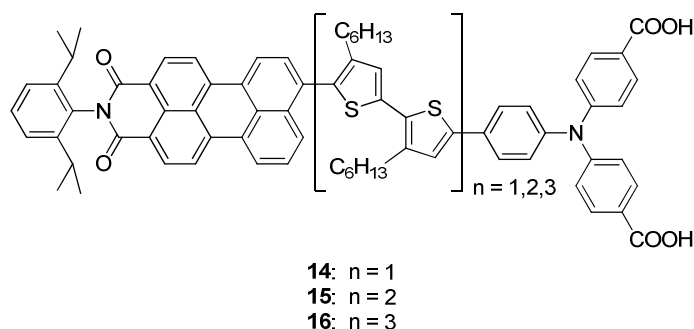


Chart 1. Chemical structure of perylenyl-oligothiophene-triphenylamine series **14-16**.^[1]

In this chapter, the influence of the positioning of the hexyl chains on the oligothiophene π -bridge on the optical, electrochemical, and photovoltaic properties is studied. The investigations are limited to the shortest bithiophene derivative **14** in order to shorten synthetic efforts assuming valid extrapolation of the changed properties to the sexithiophene-bridged triad **16**.

By shifting the hexyl chains of **14** to the free β -position of the thiophenes, constitutional isomer **44**^[3] was obtained (Chart 2). Dye **44** was synthesized during my diploma thesis in order to develop a new synthetic strategy towards A- π -D triads in which the acceptor is introduced in the penultimate step.^[3] Slight changes in absorption and electrochemical properties were observed for **44** compared to **14** (*vide infra*). These effects are most likely due to a different molecular geometry of the two isomers. It

is anticipated that due to variation in the positioning of hexyl chains **14** exhibits a stronger torsion between the PMI and bithiophene, whereas **44** features a stronger one on the other side of the π -bridge between bithiophene and TPA. For complete clarification of the origin of these changes ethynylene-containing triad **45**, synthesized by Dr. Jens Cremer,^[4] and the herein newly synthesized triad **46** are included in this study. When going from **45** to **46**, the torsion between the perylene and bithiophene unit is reduced similarly as going from **14** to **44**, but the torsion between the bithiophene and TPA remains the same due to the incorporated ethynylene spacer. This should clarify the ultimate cause of the different properties of the triads and the effect of steric hindrances within sensitizing molecules for p-type DSSCs.

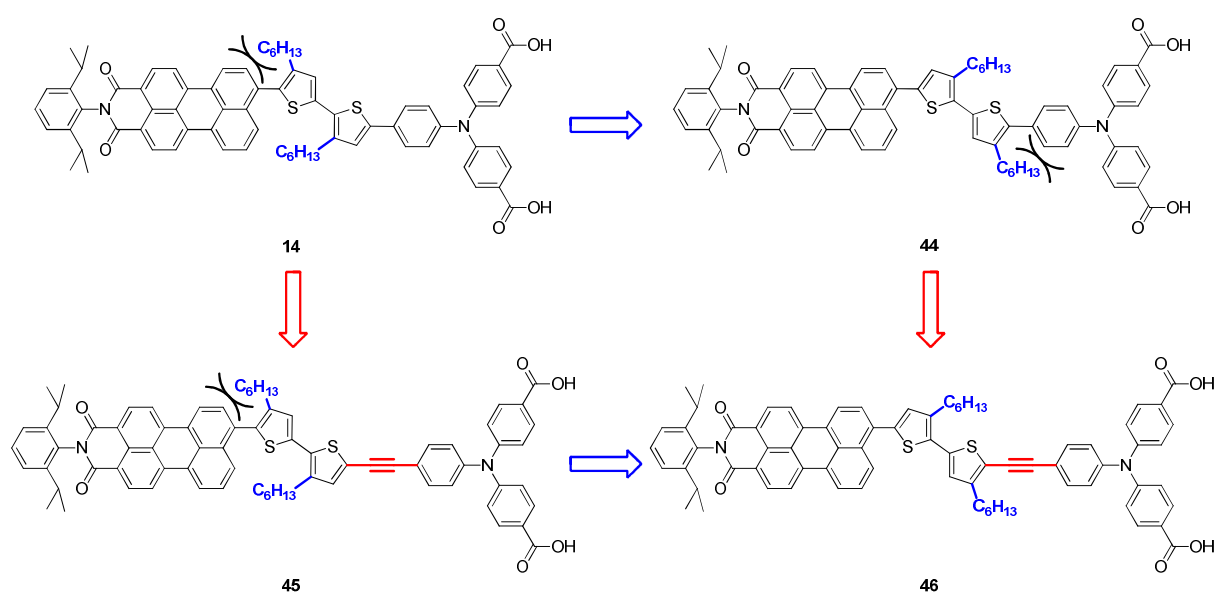



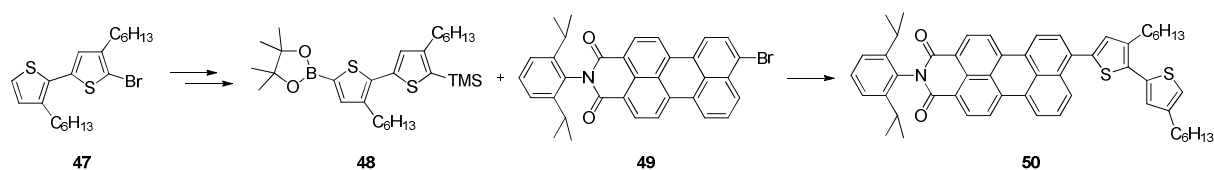
Chart 2. Structural modifications on **14** resulting in triads **44-46**. Red arrows indicate ethynylene insertion between bithiophene and TPA. Blue arrows denote change of the hexyl substitution pattern.  symbolizes steric hindrance.

In the following sections of this chapter, the synthesis and characterization of triad **46** is presented. The optical and electrochemical properties of dye **46** were investigated and compared to its constitutional isomer **45** as well as to ethynylene-free sensitizers **14** and **44**. Furthermore, quantum chemical calculations and photovoltaic performance of **44-46** were performed and compared to parental sensitizer **14**. Finally, all four derivatives were incorporated in p-type DSSCs and solar cell characteristics and transient absorption spectra were measured and interpreted.

2.2 Results and discussion

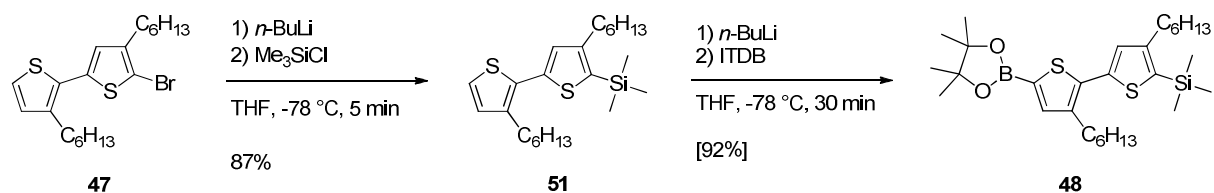
2.2.1 Synthesis of A- π -D triad **46**

For the stepwise built-up of triad **46**, first perylenyl-bithiophene dyad **50** had to be synthesized as depicted in Scheme 1. The reaction sequence started from regioregular bromo-dihexylbithiophene **47**^[5] which was converted into a boronic acid ester. Afterwards a Suzuki-Miyaura cross-coupling with bromo-PMI **49** should lead to desired dyad **50**.



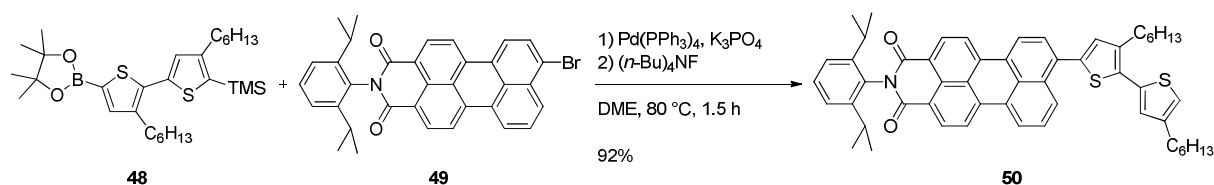
Scheme 1. Schematic synthesis of perylenyl-bithiophene dyad **50** starting from bromo-dihexylbithiophene **47**.

The boronic acid ester functionality was introduced in two reaction steps (Scheme 2). First lithiation with *n*-butyl lithium (*n*-BuLi) in tetrahydrofuran (THF) at -78 °C within 5 min and successive quenching with trimethylsilyl (TMS) chloride afforded TMS-protected bithiophene **51** in 87% yield after silica gel column chromatography. By protection of the bromo-substituted α -position, selective lithiation of the free α -position on the opposite site is now possible. Borylation of bithiophene **51** was carried out at -78 °C using *n*-BuLi and quenching with 2-isopropoxy-4,4,5,5-tetramethyl-1,3,2-dioxaborolane (ITDB). Since the deprotonation on the 5' position is slower than the lithium-halogen exchange in the previous step a six times longer lithiation time is needed. After lithiation took place, ITDB was added to the reaction mixture providing boronic ester **48** in 92% yield after aqueous work-up. The purity of the product was determined via GC showing a mixture of 95% product and 5% reactant. This mixture was used in the next step without further purification, since **51** is easily separable after the next reaction step.



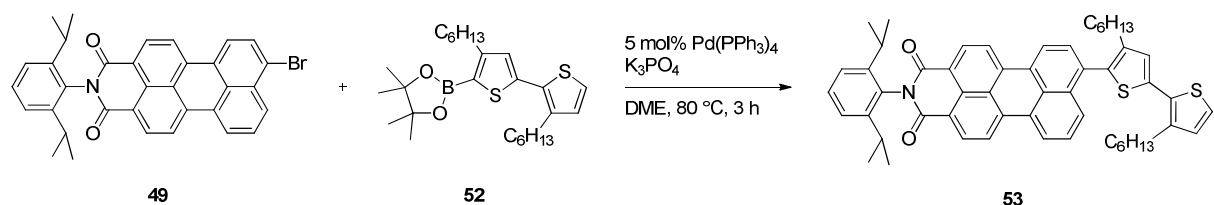
Scheme 2. Synthesis of boronic acid ester **48**.

PMI-bithiophene dyad **50** was synthesized in a one-pot reaction by Pd(0)-catalyzed Suzuki-Miyaura cross-coupling reaction of borylated bithiophene **48** and brominated PMI **49** followed by cleavage of the trimethylsilyl group with a total yield of 92% (Scheme 3).



Scheme 3. One-pot reaction synthesis: Suzuki-Miyaura cross-coupling and cleavage of the trimethylsilyl group towards perylenyl-bithiophene dyad **50**.

Similar reaction conditions for the Suzuki-Miyaura cross-coupling (K_3PO_4 as base, 1,2-dimethoxyethane (DME), 80°C , 1.5 h) and tetrakis(triphenylphosphine)palladium(0) ($\text{Pd}(\text{PPh}_3)_4$) as catalyst were reported in literature for converting boronic ester **52** and bromo-PMI **49** to dyad **53** (Scheme 4), representing a constitutional isomer of **50**.^[5]

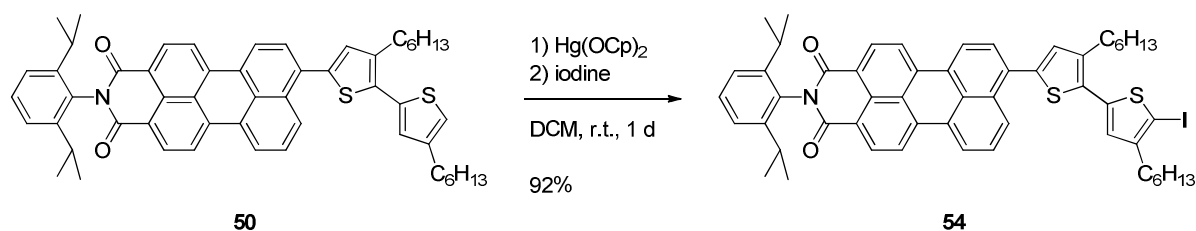


Scheme 4. Synthesis of dyad **53** bearing hexyl chains pointing towards the PMI-unit.^[5]

Since the sterical hindrance in the cross-coupling reaction towards dyad **50** bearing hexyl chains pointing away from the PMI-unit is reduced in comparison to the one towards **53**, the catalyst loading and the reaction time could be reduced to 4 mol% and 1.5 h, respectively, in comparison to 5 mol% and 3 h for the synthesis of **53**. After completion of the cross-coupling reaction, in-situ deprotection of the TMS group was carried out using 4 equivalents (eq.) tetra-*n*-butylammonium fluoride ($(n\text{-Bu})_4\text{NF}$). Stirring at 80°C for further 2.5 h finally led to dyad **50** in 92% yield after aqueous work-up and column chromatography.

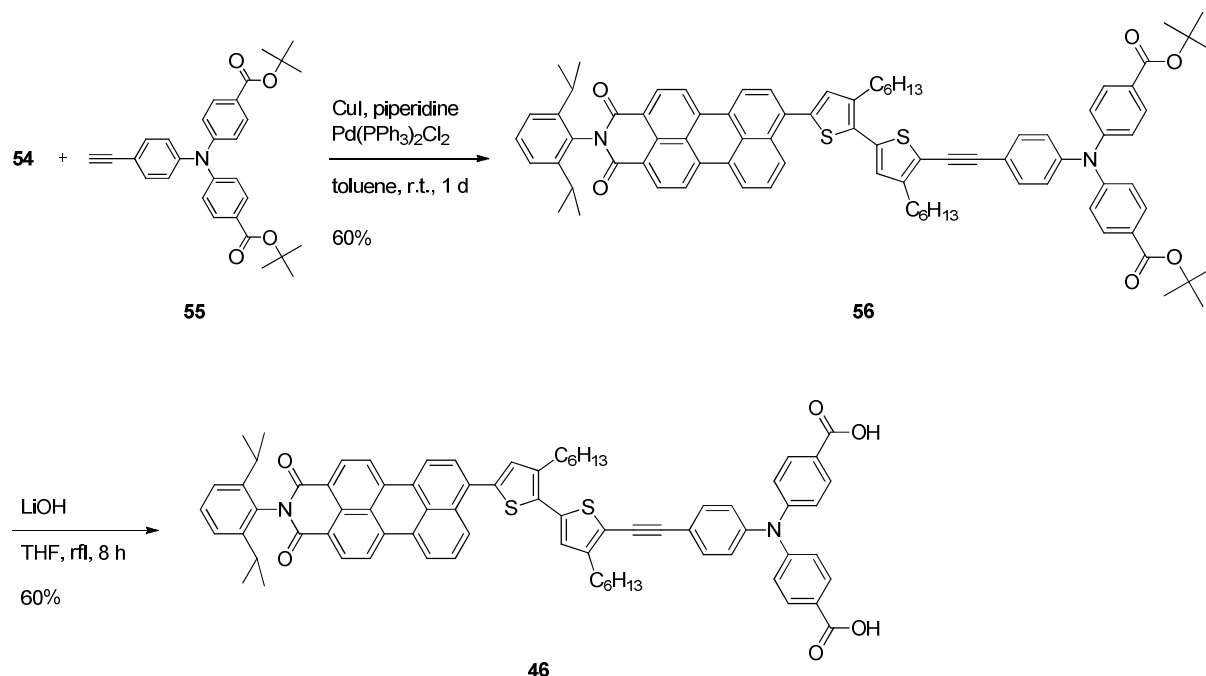
Selective iodination of the free α -position was realized stirring dyad **50** with mercury caproate overnight in dichloromethane (DCM) and subsequent addition of elemental iodine (Scheme 5). The

reaction mixture was then filtered over a short alumina column and upon addition of methanol iodinated dyad **54** precipitated purely in a yield of 92%.



Scheme 5. Synthesis of iodinated PMI-bithiophene dyad **54**.

Further conversion of iodinated dyad **54** in a Sonogashira-Hagihara-type cross-coupling reaction with TPA ethynylene **55** (freshly prepared according to reference^[4]) took place using piperidine as base, copper iodide as copper source, and bis(triphenylphosphine)palladium(II) dichloride ($\text{Pd(PPh}_3)_2\text{Cl}_2$) as catalyst (Scheme 3). Stirring at room temperature for one day afforded triad **56** in 60% yield after column chromatography.



Scheme 6. Synthesis of target triad **46**.

As final step, deprotection of the acid groups was carried out in refluxing THF using an excess of 1 N methanolic lithium hydroxide solution. After acidic aqueous work-up, the crude product was purified

via silica column chromatography to obtain target dye **46** in a moderate yield of 60%. Higher yields were reported for the deprotection of isomeric dye **45**.^[4] The reason therefore might be found in the purification method. For triad **45** the use of a silica plug was sufficient for purification whereas in the case of **46** silica column chromatography was necessary due to traces of various side-products coming along with a bigger loss of product.

2.2.2 Optical properties of PMI-bithiophene-TPA triads **14** and **44-46**

Absorption spectroscopy of triad **46** in DCM was performed and is compared to the absorption spectra of **14**,^[4] **44**,^[3] and **45**^[4] (Figure 1). The corresponding data are summarized in Table 1. All four dyes showed intense absorption bands positioned at 520 to 530 nm (λ_{abs1}) with a molar extinction coefficient ϵ of $\sim 45,000 \text{ M}^{-1}\text{cm}^{-1}$ and at $\sim 360 \text{ nm}$ (λ_{abs2}) with ϵ of $\sim 57,000 \text{ M}^{-1}\text{cm}^{-1}$.

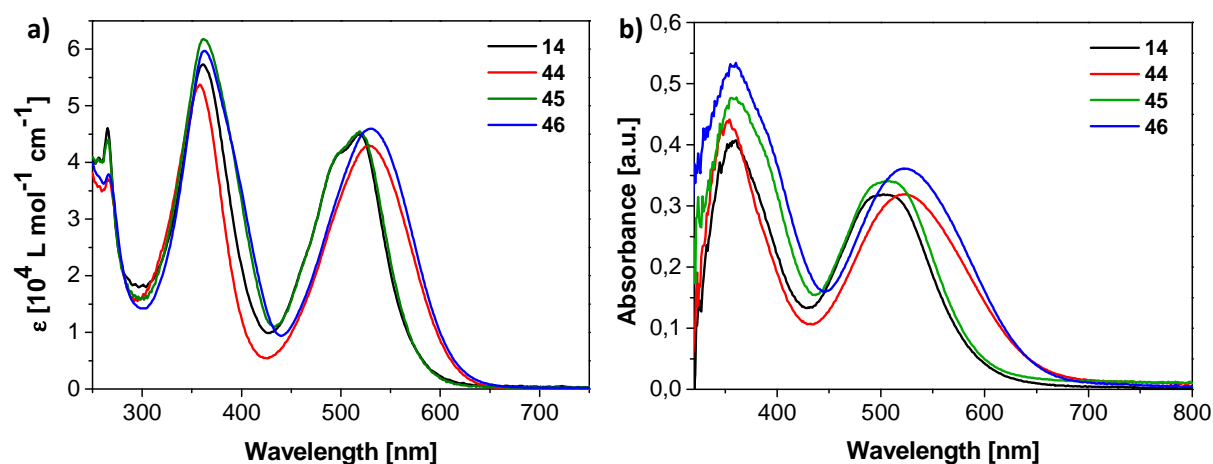


Figure 1. Absorption spectroscopy of **14** and **44-46** (a) in DCM and (b) on NiO film (NiO absorption subtracted).

The elongation of the donor part by a triple bond in **45** and **46** caused no shift of the high energy absorption band ($\lambda_{\text{abs2}} \approx 360 \text{ nm}$) compared to triads **14** and **44**.^[4,6] However, λ_{abs2} corresponding to the donor unit is slightly broadened towards the lower energy region. In comparison to triads **14** and **45**, the change of the hexyl positions in dyes **44** and **46** led to a red-shift of about 10 nm and a broadening of λ_{abs1} . This might be due to a partial decoupling of the perylene and bithiophene π -orbitals caused by a stronger torsion between the PMI-unit and bithiophene in **14** and **45**, as a result of the hexyl chain close to the PMI-unit. This assumption is supported by the observed low-energy absorption band showing only one red-shifted maximum ($\lambda_{\text{abs1}} = 528 \text{ nm}$) for **44** and **46** in comparison to a more structured absorption band in the case of **14** and **45** with a maximum absorption $\lambda_{\text{abs1}} = 520 \text{ nm}$ and an additional shoulder at $\sim 500 \text{ nm}$. This points towards a more rigid geometry with a

narrower distribution of conformers in the ground state. The optical band gaps ΔE_{opt} are 2.15 eV for **14** and **45** and 2.00 eV for **44** and **46**.

Table 1. Optical data of triads **14** and **44-46** in DCM ($c = 5 \times 10^{-5}$ M) and on NiO film (NiO absorption subtracted).

dye	λ_{abs1} [nm] (ϵ [$\text{M}^{-1}\text{cm}^{-1}$])	λ_{abs2} [nm] (ϵ [$\text{M}^{-1}\text{cm}^{-1}$])	λ_{onset} [nm]	$\Delta E_{\text{opt}}^{[a]}$ [eV]	$\lambda_{\text{abs,film}}$ [nm]	$\lambda_{\text{onset,film}}$ [nm]	$\Delta E_{\text{opt,film}}^{[a]}$ [eV]
14 ^[4]	518 (45,000)	362 (57,300)	574	2.16	358, 502	591	2.10
44 ^[3]	528 (43,100)	362 (53,800)	611	2.03	353, 521	649	1.91
45 ^[4]	519 (45,500)	361 (61,800)	577	2.15	358, 502	594	2.09
46	531 (46,000)	358 (59,700)	614	2.02	358, 521	645	1.92

[a] Calculated by the low energy onset of λ_{max} , $\Delta E = 1240 \text{ eVnm} / \lambda_{\text{onset}}$.

Absorption spectra of dyes **14** and **44-46** adsorbed onto the surface of transparent 0.9 μm thick NiO films were performed by Dr. S. Powar in collaboration with the Department of Materials Engineering at Monash University and are depicted in Figure 1b (absorption of the blank NiO film subtracted). Compared to solution spectra, dyes adsorbed on the NiO surface showed blue-shifts of 10 to 20 nm for the low energy absorption band along with a spectral broadening. As a result of this broadening, the onset of absorption on NiO film is extended to wavelengths of up to 650 nm for triad **45** and **46** and nearly 600 nm for **14** and **44** in comparison to 610 and 575 nm in solution, respectively. A spectral broadening is also commonly observed in the absorption of organic dyes adsorbed onto the surface of n-type TiO_2 , which is ascribed to the electronic interactions of the dye with the semiconductor and adjacent dye molecules.^[6,7] The shift of the low energy absorption band between the dyes in solution and attached to NiO is nearly identical for all dyes. The red-shift of dyes **44** and **46** compared to **14** and **45** is associated with the change of the hexyl chain pattern and is clearly observed in solution and on NiO film. This result promotes dyes **44** and **46**, with slightly narrower optical band gaps on NiO of 1.9 eV compared to 2.1 eV for **14** and **45**, as better light absorbers for p-type DSSCs. The similar spectral shifts for each dye, as compared to solution, suggest that there is no major difference in the orientation or packing of the dye molecules on the NiO surface. Additionally, the matching of the absolute absorbance of the four dyes points to a very similar amount of dye loading onto NiO.

2.2.3 Electrochemical properties of PMI-bithiophene-TPA triads **14** and **44-46**

Oxidation and reduction potentials of triad **46** were measured by cyclic voltammetry in DCM and compared to those of triads **14**,^[4] **44**,^[3] and **45**^[4] using tetra-*n*-butylammonium hexafluorophosphate [(*n*-Bu)₄NPF₆] as supporting electrolyte and were referenced to the redox couple ferrocene/ferrocenium (Fc/Fc⁺) (Figure 2). Redox potentials, calculated highest occupied molecular orbital (HOMO) and lowest unoccupied molecular orbital (LUMO) energy levels as well as electrochemically determined band gaps (ΔE_{CV}) are summarized in Table 2.

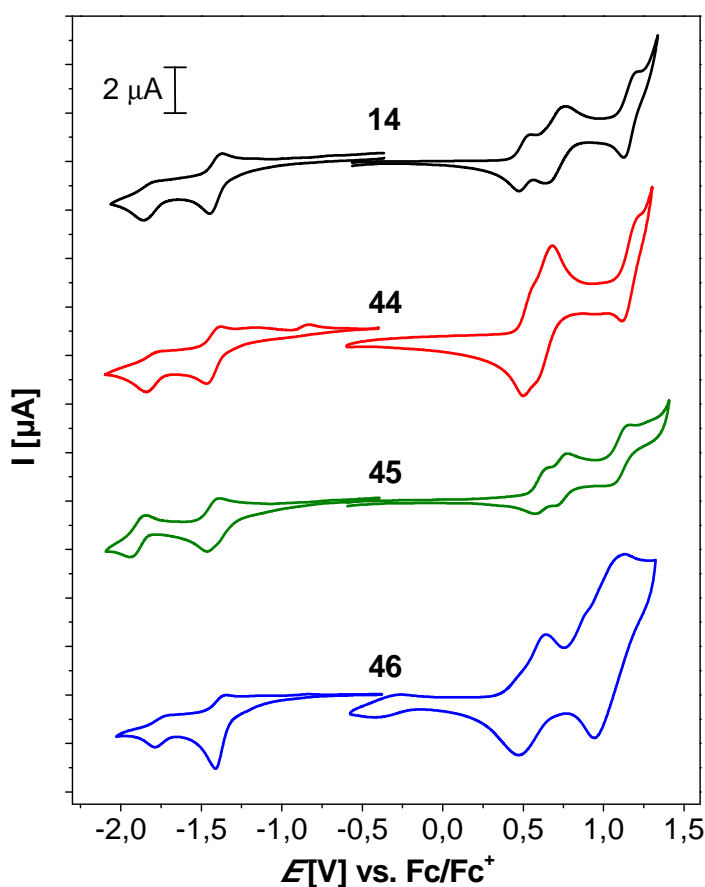


Figure 2. Cyclic voltammograms of triads **14** and **44-46** measured in DCM using (*n*-Bu)₄NPF₆ (0.1 M) as supporting electrolyte at 100 mV s⁻¹; c = 10⁻³ mol/L.

In the oxidative regime, one oxidation process can be attributed to the PMI-unit (E°_{ox3}) while the remaining ones originate from the oxidation of the combined bithiophene and TPA donor. It is interesting to note that the first and second oxidation potential (E°_{ox1} and E°_{ox2}) of the ethynyl-containing dyes **45** and **46** are positively shifted compared to non-ethynylated counterparts **14** and **44**. This can be ascribed to the presence of the electron-withdrawing ethynylene group at the

molecular backbone slightly elongating the π -conjugated system or by a conformational change of the thiophene and TPA unit along the triple bond.^[4,8] The PMI oxidation of **45** ($E^{\circ}_{\text{ox}3} = 1.10$ V) and **46** ($E^{\circ}_{\text{ox}3} = 1.04$) is favored over that of **14** ($E^{\circ}_{\text{ox}3} = 1.15$ V) and **44** ($E^{\circ}_{\text{ox}3} = 1.12$). The results demonstrate that the dications of ethynyl-containing dyes **45** and **46**, which are formed prior to the PMI oxidation, withdraw less electron density from the adjacent PMI-unit than the donor dications of ethynyl-free dyes **14** and **44**. On the other hand, all triads possess a nearly identical electrochemical behaviour in the reductive regime, which corresponds to the two step reduction of the PMI unit at around -1.41 V and -1.87 V, respectively.

Table 2. Electrochemical data of perylene-bithiophene-triphenylamine triads **14** and **44-46** ($c = 10^{-3}$ M) in DCM/ $(n\text{-Bu})_4\text{NPF}_6$ (0.1 M) vs. Fc/Fc^+ at 100 mV s^{-1} .

dye	$E^{\circ}_{\text{ox}1}$ [V]	$E^{\circ}_{\text{ox}2}$ [V]	$E^{\circ}_{\text{ox}3}$ [V]	$E^{\circ}_{\text{red}1}$ [V]	$E^{\circ}_{\text{red}2}$ [V]	$E_{\text{HOMO}}^{[a]}$ [eV]	$E_{\text{LUMO}}^{[a]}$ [eV]	$\Delta E_{\text{CV}}^{[b]}$ [eV]
14 ^[4]	0.51	0.69	1.15	-1.41	-1.88	-5.54	-3.80	1.74
44 ^[3]	0.48	0.67	1.12	-1.42	-1.86	-5.57	-3.76	1.81
45 ^[4]	0.62	0.75	1.10	-1.42	-1.87	-5.64	-3.84	1.80
46	0.60	0.77	1.04	-1.37	-1.76	-5.47	-3.82	1.65

[a] E_{HOMO} and E_{LUMO} were calculated from the onset of $E^{\circ}_{\text{ox}1}$ and $E^{\circ}_{\text{red}1}$, respectively, and related to the Fc/Fc^+ couple with an absolute energy of -5.1 eV. [b] Electrochemical band gap calculated to $\Delta E_{\text{CV}} = E_{\text{HOMO}} - E_{\text{LUMO}}$.

The HOMO levels of the triads calculated from electrochemical measurements were sufficiently lower than the valance band edge of NiO (-5.0 eV vs. vacuum or 0.5 V vs. NHE) enabling sufficient driving force for hole injection from the dye to the p-type semiconductor in DSSCs. Equally, the LUMO energy levels of **14** and **44-46** are sufficiently above the redox potential of the iodide/triiodide redox couple which should facilitate dye regeneration. The electrochemical band gaps ΔE_{CV} lie between 1.65 and 1.81 eV and are smaller than the optical band gaps determined by absorption spectroscopy (see section 2.2.2).

2.2.4 Quantum chemical calculations of PMI-bithiophene-TPA triads **14** and **44-46**

Density functional theory (DFT) calculations with a B3LYP hybrid base (6-31G⁺(d,p)) were performed by Dr. E. Mena-Osteritz in order to evaluate the distortion between the PMI-unit and the adjacent

hexylthiophene unit and to analyze the electron distribution of the frontier orbitals. The HOMO-LUMO orbital distribution of all dyes is shown in Figure 3.

The HOMO orbital distribution in dyes **44** and **46** is slightly more localized on the thiophene and TPA-unit, whereas in dyes **14** and **45** a more pronounced distribution on the PMI compared to the TPA part is observed. The differences in the HOMO orbital distribution are most probably due to a larger twist in the thiophene-PMI bond in dyes **14** and **45** that arises from the close proximity of the alkyl side chain to the PMI-unit (torsion angle = $\sim 63^\circ$) compared to **44** and **46** (torsion angle = 54°). Consequently, a better electronic delocalization between PMI and thiophene parts can be expected in dyes **14** and **45** as manifested in the HOMO electronic distribution. In contrast, the LUMO orbital distribution is very similar for all dyes and localized almost entirely on the PMI unit.

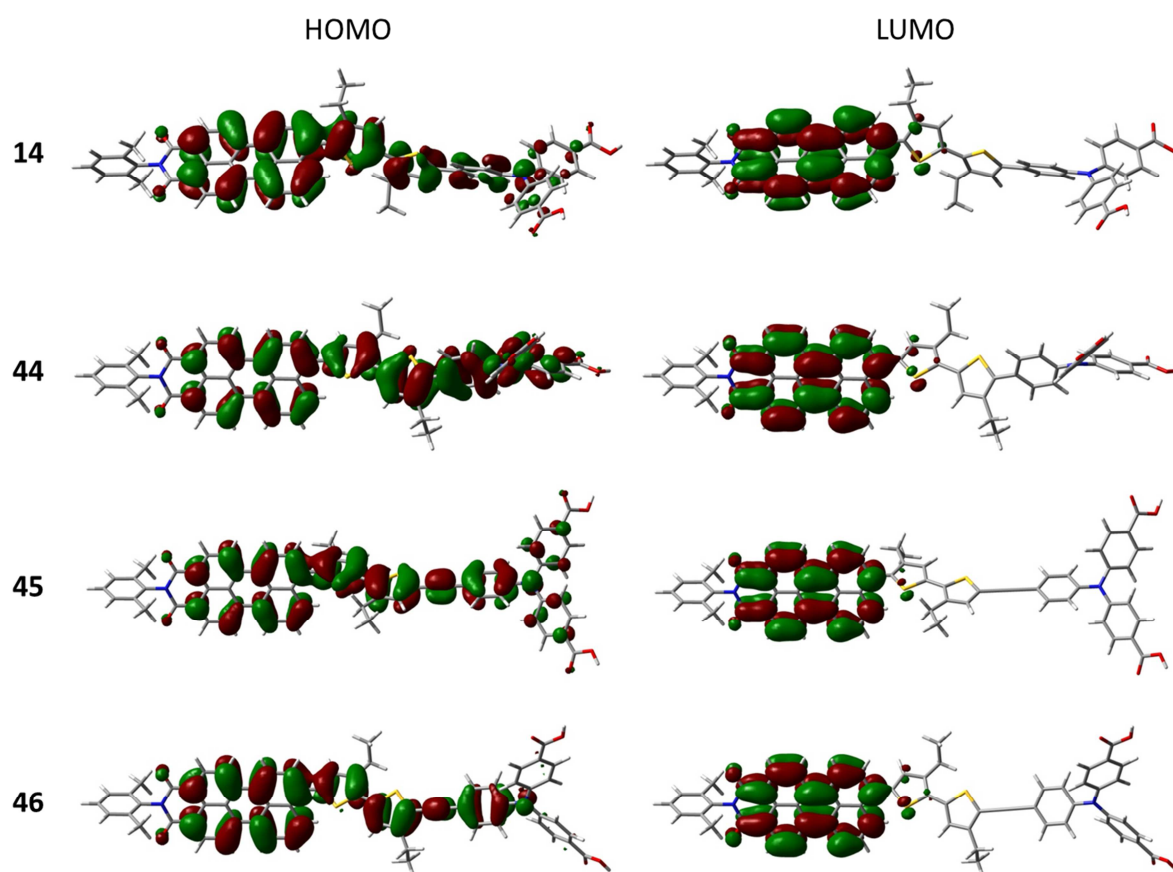


Figure 3. Frontier orbitals distribution of dyes **14** and **44-46** calculated using the B3LYP (6-31G+(dp)) DFT method (carbons in gray, nitrogens in blue, oxygens in red, sulfurs in yellow and hydrogens in white). In order to accelerate the convergence of optimizations the long hexyl chains were replaced with ethyl substituents.

In the case of dye **44**, the presence of the alkyl side chain on the TPA side resulted in a large torsion angle of about 47.4° between the thiophene and phenyl units compared to dye **14** with a torsion

angle of only 25°. The torsion between the TPA and adjacent thiophene unit was further reduced to planarity by the introduction of a triple bond (improper torsion angle = 0.9°) in dye **45** and **46**.

2.2.5 Photovoltaic performance of PMI-bithiophene-TPA triads **14** and **44-46**

In collaboration with the Department of Materials Engineering at Monash University, triads **14** and **44-46** were implemented as sensitizers in p-type DSSCs using an iodide/iodine-based electrolyte and 1.5 μm thick NiO electrodes. The experiments were carried out by Dr. S. Powar. Current density-voltage (J - V) curves of devices based on dyes **14** and **44-46** are shown in Figure 4a. The corresponding data are summarized in Table 3. The device measurements are very coherent and the data are reproducible within the given experimental accuracy. The results presented were repeated three times (different days) and are averaged over four devices each. Additionally, p-type DSSCs using **14** as sensitizer achieved already the same results in similar devices.^[1]

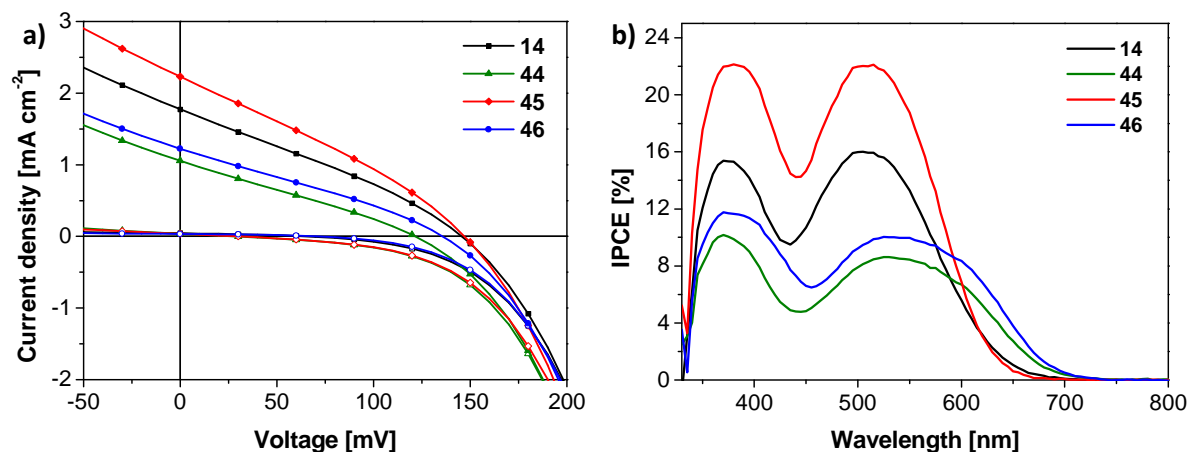


Figure 4. (a) J - V characteristics of devices under AM 1.5 simulated solar illumination (100 mW cm^{-2} ; filled symbols) and in the dark (open symbols) produced using 1.5 μm thick NiO electrodes, sensitized with dyes **14** and **44-46**. (b) IPCE responses for devices using triads **14** and **44-46** as sensitizers.

The advantage of the presence of the ethynylene-unit in triad **45** is reflected in an increased short-circuit current density (J_{sc}) value by about 30% compared to parent dye **14**, roughly half the increase seen previously by going from a bithiophene to quaterthiophene bridge.^[1] Absorption data (Figure 1), however, showed little difference in the light-harvesting properties of dyes **14** and **45**. This improvement in J_{sc} is likely to arise from the retardation of charge recombination of the photoreduced dyes with holes in the NiO-photocathode. This assumption is made based on the observation by Nattestad *et al.* that the tunnelling distance between electrons occupying the dye's

LUMO and holes located in the semiconductor electrode strongly governs the observable recombination time constants.^[1] No change was observed in the open-circuit voltage (V_{oc}) and FF values for dyes **14** and **45**. Devices based on ethynyl-containing sensitizer **45** yielded the highest power conversion efficiency (PCE) of 0.10% among the dyes studied here which is about 25% higher compared to dye **14**. In comparison to devices sensitized with triad **14**, a decrease in V_{oc} and J_{sc} values was seen by changing the hexyl chain position in regioisomeric triad **44**, thus lowering the PCE to 0.04%. This decrease in J_{sc} and V_{oc} points towards faster recombination processes for devices in which **45** is employed as sensitizer. The introduction of a triple bond in regioisomeric dye **46** slightly increases the J_{sc} compared to dye **44** and subsequently the overall PCEs for both dyes are very similar. The comparable performance of triads **44** and **46** can be ascribed to the planarization of the PMI-thiophene bond due to the different hexyl substitution pattern compared to isomeric counterparts **14** and **45**. These results further confirm that the partial decoupling between the acceptor and donor moieties appears to be essential for better device performance. Compared to dyes **14** and **44**, the J_{sc} values are increased for ethynyl-containing sensitizers, **45** and **46**, which could be ascribed to the improved injection and/or reduced recombination process.

Table 3. Photovoltaic parameters for devices with 1.5 μm thick mesoporous NiO electrodes, sensitized with dyes **14** and **44-46** under solar illumination (AM 1.5G, 100 mW cm^{-2}).

dye	J_{sc} [mA cm^{-2}]	V_{oc} [mV]	FF	PCE [%]	$\lambda_{IPCE,max}$ [nm]	IPCE [%]
14	1.77 ± 0.04	146 ± 1	30 ± 1	0.08 ± 0.01	509	16
44	1.06 ± 0.01	122 ± 8	29 ± 3	0.04 ± 0.01	529	9
45	2.24 ± 0.09	147 ± 9	30 ± 1	0.10 ± 0.01	508	22
46	1.23 ± 0.22	136 ± 4	28 ± 1	0.05 ± 0.01	531	10

The IPCE responses of devices constructed using **14** and **44-46** are shown in Figure 4b and correspond well with the measured J_{sc} values given in Table 3. Compounds **14** and **45** exhibit broad IPCE responses ranging from 350 up to 650 nm. This region is extended to nearly 700 nm for dyes **44** and **46**. The IPCE spectrum of dye **14** shows a maximum of about 16% at 380 and 509 nm. An increase in the IPCE peak maximum to 22% was observed by the insertion of an ethynylene group in dye **45**. The result is also consistent with their absorption spectra in thin films, thus, showing the contribution of absorption bands to the IPCE and J_{sc} . In contrast, regioisomeric dye **45** features an IPCE maximum of only about 9% at 529 nm which is slightly increased to 10% for ethynyl-containing

regioisomeric dye **46**. The results clearly show the influence of the ethynylene spacer on the solar cell performance. In addition to the increasing magnitude of the IPCE response, there is also an observed broadening in the absorption peak corresponding to high energy absorption (400 to 450 nm), which is in agreement with the thin film absorption spectra seen in Figure 1b.

The IPCE responses show that in spite of the improved light-harvesting and a similar magnitude of light absorption (Figure 1b) lower quantum efficiencies for either charge injection or transport are mostly responsible for the smaller J_{sc} values recorded for dyes **44** and **46**. This is most probably due to the planarization of the PMI-thiophene linkage. In Figure 1b it can be seen that all spectra of the dyes on NiO films show a peak at 350 to 360 nm which is higher than the one at 500 nm. In contrast, the peaks of the IPCE at both wavelength regions for all devices are nearly identical. In these p-type DSSC devices the IPCE response at short wavelengths is mitigated due to the light-harvesting competition from both the electrolyte and NiO.

2.2.6 Transient absorption spectroscopy of PMI-bithiophene-TPA triads **14** and **44-46**

In collaboration with the Intelligent Polymer Research Institute at University of Wollongong, TAS experiments of dyes **14** and **44-46** on NiO films in the absence of a redox mediator were performed by Dr. Attila Mozer in order to investigate the recombination kinetics of the photo-reduced dye anions with holes in the NiO-photocathode (Figure 5).

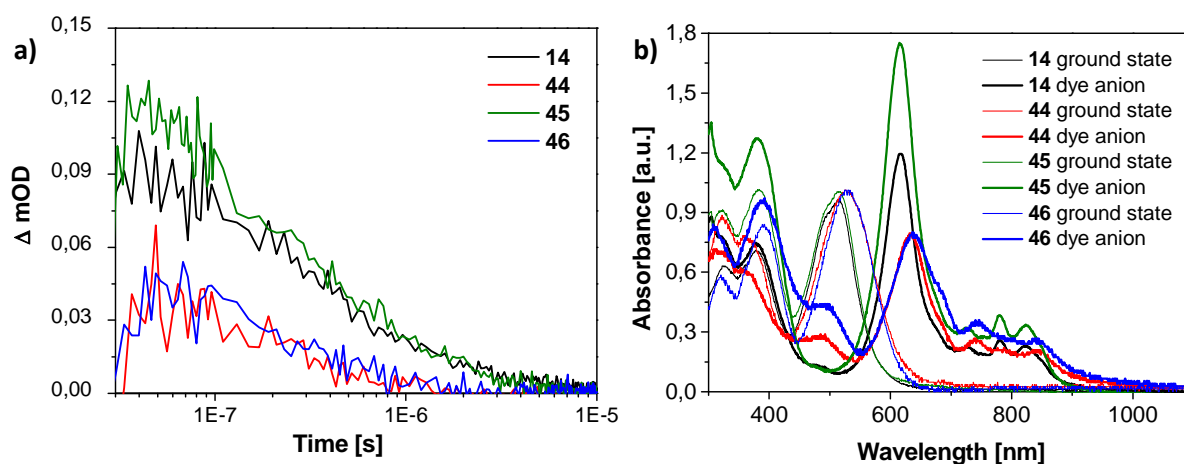


Figure 5. (a) Transient absorption decay signals of NiO films sensitized with **14** and **44-46** after laser excitation at a wavelength of 532 nm (intensity: $32 \mu J cm^{-2} pulse^{-1}$) probing at 700 nm. (b) Neutral and anion absorption spectra in DMF, normalized to most red-shifted ground state absorption peak ($\sim 500-550 nm$). The anion spectra of **14**, **45**, and **46** were recorded at -500 mV, the one for **44** at -550 mV.

Substantially higher signal magnitudes have been measured for dyes **14** and **45** compared to the regioisomeric dyes **44** and **46**, respectively. This behaviour cannot be attributed to differences in the absorbed pump beam intensity ($1-10^{-\alpha d}$, where αd is the optical density of the films) at the pump wavelength of 532 nm, since the optical densities of the films were nearly identical (see Figure 1b). Furthermore, the absorbance of the electrochemically reduced dye species in N,N-dimethylformamide (DMF) is also very similar at the probe wavelength of 700 nm (see Figure 5b). While the electrochemically reduced species of **44** and **46** absorb less light in the 600-700 nm main anion absorption band, the anions of **44** and **46** absorb slightly more due to their red-shifted absorption band at the 700 nm TA probe wavelength. Therefore, the reduced TAS signal magnitude in Figure 5a is not due to a lower absorption coefficient of the **44** and **46** anions, but rather originates from reduced hole injection yield and/or a fast component of the recombination kinetics, beyond the time resolution of the setup (50 ns).

The transient spectra of photo-reduced dyes **14** and **44** resemble those of the electrochemically generated species (Figure 6a and b as well as Figure 5b). It can be observed that the intense absorption peak of the electrochemically generated anion **44** centered at 625 nm is not evident in the TA spectrum (Figure 6b). This is attributed to the stronger overlap of the red-shifted ground state absorption of **44** and the first absorption peak of the anion, which has not shifted significantly between **14** and **44**.

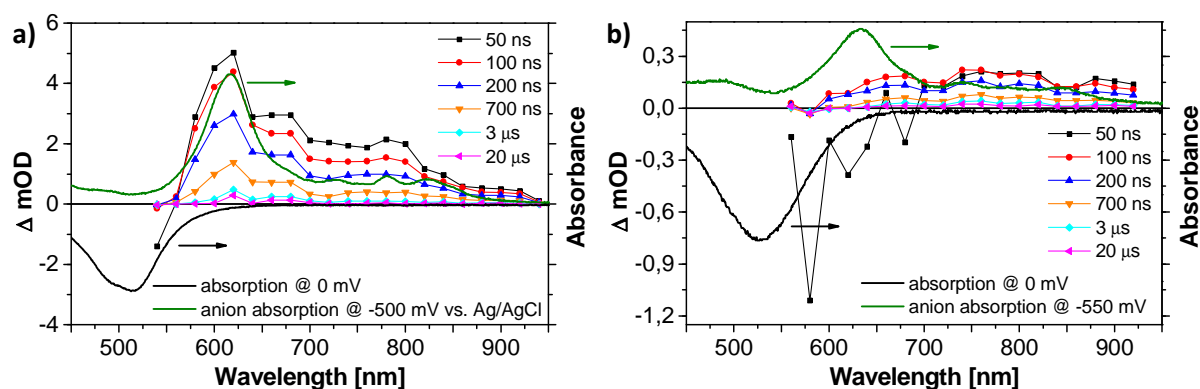


Figure 6. Transient absorption spectrum of NiO films sensitized with **14** (a) and **44** (b) after laser excitation at a wavelength of 532 nm (intensity: $90 \text{ mJ cm}^{-2} \text{ pulse}^{-1}$). The green solid line represents scaled absorption of electrochemically reduced (at -500 and -550 mV versus Ag/AgCl, respectively) dye anion in DMF. The thick black line represents scaled and inverted absorption spectrum of neutral dye in DMF at open circuit.

As a result, TAS of NiO sensitized with dye **44** showed a less significant absorption feature in the 600-650 nm wavelength range than NiO films sensitized with dye **14**. The NiO hole-dye anion

recombination kinetics for all dyes in Fig. 5a are quite similar and can be characterized with a signal decay half time of around 300 ns for **14** and **45** and around 250 ns for **44** and **46**, which is very similar to the previously reported value for dye **14**.^[1] Contrary to the expectation, the elongation of the π -bridge in dyes **45** and **46** using the ethynylene spacer did not translate into an improved dye anion lifetime compared to **14** and **44**. Nattestad *et al.* found that increasing the number of thiophene units in the π -bridge resulted in a 7-fold increase going from a bithiophene to a quaterthiophene (**15**) and a further 2 fold increase for the sexithiophene bridge (**16**).^[1] Clearly, the ethynylene linker is found to be not as effective as the bithiophene bridge. An explanation for the reduced charge generation yield in **44** and **46** is the reduction of the torsion angle between the PMI and the adjacent thiophene unit, thus resulting in a faster hole-dye anion recombination rate showing the necessity of the hexyl chain next to the PMI unit for a higher charge generation yield. Similar findings concerning geometrical twists due to subtle structural modifications and resulting recombination kinetics within sensitizers for n-type DSSCs were also found by Haid *et al.*^[9] Furthermore, photoreduced dye anion and NiO recombination is fast for all four dyes competing with dye anion regeneration occurring on a similar time scale. Extending dye-NiO anion lifetimes to the μ s to ms time range, similarly to frequently observed long photo-oxidized dye-TiO₂ lifetimes of most n-type dye-sensitized photoanodes, will be crucial for photocathodes to match the performance of photoanodes, a prerequisite for high efficiency tandem devices.

2.3 Summary

In this chapter, triad **46** was synthesized in good to excellent yields to complete the PMI-bithiophene-TPA series **14** and **44-46** where (1) the positions of the hexyl chains on the thiophenes that comprise the π -bridge were altered and/or (2) an ethynyl group was used to extend the π -bridge length and release the sterical strain between the bithiophene and TPA. Subsequently, steric hindrances within the dye series were investigated. Absorption spectroscopy showed a red-shift for triads **44** and **46** in comparison to **14** and **45**, respectively, of ~ 10 nm in solution and ~ 20 nm on NiO film meaning a greater light-harvesting ability. This is due to a stronger conjugation between the PMI-unit and the bithiophene-TPA moiety, which is in turn due to the planarization of the PMI-thiophene linkage for compounds **44** and **46** of about 10° , shown by quantum-chemical DFT calculations. Cyclic voltammetry of **14** and **44-46** proved their suitability as sensitizers in p-type DSSCs. Slight changes in the oxidations potentials are also attributed to a stronger conjugation of the PMI acceptor and the donor part of the dyes. Device characteristics of p-type DSSCs using **14** and **44-46** as sensitizers

together with an iodide/iodine-based electrolyte showed that the aforementioned beneficial red-shift of compounds **44** and **46** is outweighed by a decreased charge generation and/or collection indicating that the torsion between the acceptor and the donor is crucial for high quantum efficiencies. Using 1.5 μm thick mesoporous NiO films, PCEs in the range from 0.04 to 0.10% were obtained under full sun illumination (simulated AM 1.5G sunlight, 100 mW cm^{-2}). It should be noted that with dye **45** comprising an ethynylene spacer the PCE of the original sensitizer **14** could be increased from 0.08 to 0.10%, i.e. a 25% improvement, whereas isomeric dyes **44** and **46** showed a decreased PCE of 0.04 and 0.05%, respectively. A broad IPCE spectrum is observed for the dye series in the spectral region between 350 and 700 nm, which increases for triads **45** and **46** compared to **14** and **44**, respectively by the insertion of an ethynylene-unit leading to an increased π -conjugation length. Sensitizer **14** and **45** showed IPCEs of 16 and 22%, respectively whereas **44** and **46** feature decreased IPCEs of only up to 10% proving the structural importance of a hexyl chain pointing towards the PMI-unit as present in **14** and **45**. TAS experiments point towards a reduced hole injection yield and/or a fast component of the recombination kinetics for triads **44** and **46** giving a good explanation for the reduced PCEs and IPCEs. All together within the PMI-bithiophene-TPA series a higher sterical hindrance between the PMI and the adjacent thiophene coming along with a stronger torsion of the PMI-thiophene linkage and hence with a stronger decoupling of the acceptor and the donor seems to be crucial for efficient device performance and is an important structure-property relationship for future dye series.

2.4 Experimental section

2.4.1 General procedures

^1H NMR spectra were recorded in CDCl_3 and THF-d_8 on a Bruker AMX 400 at 400 MHz. ^{13}C NMR spectra were recorded in CDCl_3 and THF-d_8 on a Bruker AMX 400 at 100 MHz. Chemical shifts are denoted by δ (ppm) and are referenced to the residual solvent peak (CDCl_3 : ^1H δ = 7.26 ppm and ^{13}C δ = 77.0 ppm; d_8 -THF: ^1H δ = 3.57 ppm and ^{13}C δ = 67.2 ppm). The splitting patterns are designated as follows: s (singlet), d (doublet), t (triplet), and m (multiplet) and the assignments are Pery (perylene), TPA (triphenylamine), Ph (phenyl), and Th (thiophene) for ^1H NMR. Mass spectra were recorded with a Varian Saturn 2000 GC-MS and with a MALDI-TOF MS Bruker Reflex 2 (dithranol as the generally used matrix and 2,5-dihydroxybenzoic acid for the free acids). Melting points were determined with a Büchi B-545 melting point apparatus and are not corrected. Gas chromatography was carried out using a Varian CP-3800 gas chromatograph. HPLC analyses were performed on a Merck Hitachi L7000

equipped with a L7455 photodiode array detector, a L7200 autosampler and a L7100 solvent delivery system using a LiChrospher column (Nucleosil 100-5 NO₂). Thin-layer chromatography was carried out on Silica Gel 60 F254 aluminium plates (Merck). Solvents and reagents were purified and dried by usual methods prior to use and typically used under inert gas atmosphere. The following starting materials were purchased and used without further purification: iodine (Merck), magnesium (Merck), mercury acetate (Merck), β -alanine (Merck), trifluoroacetic acid (Merck), zinc (Merck), triphenylphosphine (Merck), malononitrile (Aldrich), pinacolborane (Aldrich), *n*-butyllithium (1.6 M, in *n*-hexane; Aldrich), tri-*t*-butylphosphonium tetrafluoroborate (Aldrich), tris(dibenzylideneacetone)-dipalladium(0) (Aldrich), bis(triphenylphosphine)palladium(II) dichloride (Aldrich), 1,3-bis(diphenylphosphino)propane nickel(II) chloride (Aldrich) and 1,1'-bis(diphenylphosphino)ferrocene (Aldrich). Tetrakis(triphenylphosphine)palladium(0) was synthesized according to literature.^[10]

Optical and cyclic voltammetric measurements

UV-Vis spectra in dichloromethane solution were taken on a Perkin-Elmer Lambda 19 spectrometer. Thin film spectra on NiO were taken using a Varian Cary 5000 spectrometer with integrating sphere attachment (Varian Internal DRA 2500). Cyclic voltammetry experiments were performed with a computer-controlled Autolab PGSTAT30 potentiostat in a three-electrode single compartment cell (3 mL). The platinum working electrode consisted of a platinum wire sealed in a soft glass tube with a surface of $A = 0.785 \text{ mm}^2$, which was polished down to $0.25 \text{ }\mu\text{m}$ with Buehler polishing paste prior to use in order to obtain reproducible surfaces. The counter electrode consisted of a platinum wire and the reference electrode was an Ag/AgCl reference electrode. All potentials were internally referenced to the ferrocene/ferrocenium couple. For the measurements, concentrations of $5 \times 10^{-4} \text{ mol L}^{-1}$ of the electroactive species were used in freshly distilled and deaerated dichloromethane (Lichrosolv, Merck) and 0.1 M tetra-*n*-butylammonium hexafluorophosphate ((*n*-Bu)₄NPF₆, Fluka; recrystallized twice from ethanol).

Quantum-chemical calculations

Density functional theory was employed with the hybrid functionals B3LYP and the basis set 6-31G+ including d and p diffuse functions from the Gaussian 09 package. The long hexyl chains, which have no significant impact on the frontier orbitals of the chromophores, were replaced with ethyl substituents in order to accelerate the convergence of optimizations.

Device fabrication

4 × 4 mm NiO films were screen printed onto F:SnO₂ glass (Nippon Sheet Glass) using a paste produced by grinding 15 g of NiO (Inframat) in ethanol, added in small aliquots. 50 mL of a 10 wt% ethyl cellulose solution in ethanol and 100 mL terpineol were then added and after mixing ethanol

was evaporated to leave a terpeneol based paste. These were sintered for 30 minutes at 400 °C, then 10 minutes at 550 °C, before being immersed into dye solutions (0.2 mM in DMF) for 2 hours. Films were then removed from this dye solution and rinsed subsequently in DMF and ethanol before being allowed to dry. Counter electrodes were produced by applying one drop of chloroplatinic acid solution (10 mM in ethanol) to F:SnO₂ glass and thermally decomposing by firing at 400 °C for 15 min under a gentle flow of air. Counter and working electrodes were sandwiched together with a 25 µm Surlyn (Dupont) spacer, and heated to 120 °C for 30 s in order to create a seal. The electrolyte solution (0.03 M iodine, 0.6 M 1-butyl-3-methylimidazolium iodide, 0.5 M 4-*t*-butylpyridine, and 0.1 M guanidinium thiocyanate in 85:15 acetonitrile: valeronitrile) was introduced through a pre-drilled hole in the counter electrode, which was subsequently sealed with another piece of Surlyn and a microscope cover slip.

Current-voltage characterization

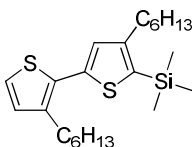
Solar cells were tested using simulated sunlight (AM1.5, 1000 W m⁻²) provided by an Oriel solar simulator with an AM1.5 filter. Current-voltage characteristics were measured using a Keithley 2400 source meter. Cells were biased from high to low, with 10 mV steps and a 250 ms settling time between the application of a bias and current measurement. IPCE was measured with the cell held under short circuit conditions and illuminated by monochromatic light. A Cornerstone 260 monochromator was used in conjunction with an optical fibre, Keithly 2400 source meter and 150 W Oriel Xe lamp. Prior to testing a 30 second 'rest' period was introduced to ensure the dark current dropped to zero when the cell was short circuited. Additionally, 200 ms settling time was applied between the monochromator switching to a wavelength and measurement commencing, which was followed by an averaged reading over a 1 second period.

Transient absorption spectroscopy

TAS experiments were performed as described reported.^[11] A 532 nm pump was used (Nd-YAG, INDI-40-10, Spectra-Physics), operating in Q-switch mode (6 ns pulse) at a 10 Hz repetition rate. A 1000W Xe lamp (Edinburgh Instruments) was used for the probe, employing a 700 nm bandpass filter with an FWHM of 40 nm. The signal was passed through a monochromator to a Si detector (Femto) and recorded by a Tektronix 4054 oscilloscope.

2.4.2 Synthesis

5-Trimethylsilyl-4,3'-dihexyl-2,2'-bithiophene (**51**)



n-BuLi (0.39 mL, 0.62 mmol) was added dropwise to a solution of 5-bromo-3',4-dihexyl-2,2'-bithiophene **47** (250 mg, 0.60 mmol) in 3 mL THF at -78 °C. After the addition the solution was stirred for 15 min at -78 °C. TMS chloride (100 μ L, 0.79 mmol) was added, subsequently. The cooling bath was removed and the reaction was stirred until it had warmed up to room temperature. Then the mixture was poured into water, the organic layer was separated and the aqueous phase was extracted with diethyl ether. The combined organic phases were washed with brine and dried over sodium sulfate and the solvent was removed by rotary evaporation. The crude product was purified by column chromatography (silica/*n*-hexane) to give 5-trimethylsilyl-bithiophene **51** (203 mg, 0.50 mmol, 83%) as a yellow oil.

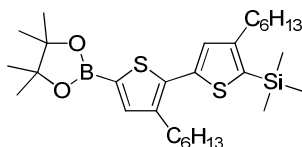
¹H NMR (400 MHz, CDCl₃): δ = 7.13 (d, ³*J* = 5.2 Hz, 1 H, 5'-H), 7.03 (s, 1 H, 3-H), 6.91 (d, ³*J* = 5.2 Hz, 1 H, 4'-H), 2.75 (t, ³*J* = 7.9 Hz, 2 H, α' -CH₂), 2.64 (t, ³*J* = 7.9 Hz, 2 H, α -CH₂), 1.66-1.57 (m, 4 H, β -CH₂, β' -CH₂), 1.41-1.26 (m, 12 H, -CH₂-), 0.90 (t, ³*J* = 6.8 Hz, 3 H, Th'-CH₃), 0.88 (t, ³*J* = 6.7, 3 H, Th-CH₃), 0.35 (s, 9 H, Si-CH₃).

¹³C NMR (100 MHz, CDCl₃): δ = 150.67, 140.04, 139.16, 132.88, 130.97, 129.92, 129.13, 123.29, 31.76, 31.72, 31.64, 31.45, 30.63, 29.40, 29.18, 22.62, 14.10, 0.40.

GC-MS (EI) *m/z*: calcd for C₂₃H₃₈S₂Si: 406, found [M]⁺: 406.

Elemental analysis: calcd (%) for C₂₃H₃₈S₂Si: C 67.91, H 9.42, S 15.77; found (%): C 68.18, H 9.40, S 15.56.

2-(4,3'-Dihexyl-5'-trimethylsilyl-2,2'-bithien-5-yl)-4,4,5,5-tetramethyl-[1,3,2]dioxaborolane (**48**)



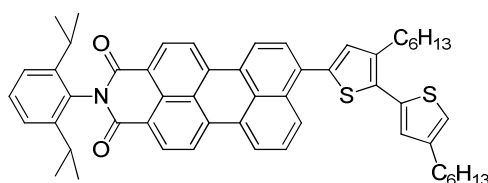
n-BuLi (0.14 mL, 0.35 mmol) was added dropwise to a solution of 5-trimethylsilyl-bithiophene **51** (130 mg, 0.32 mmol) in 1.5 mL THF at -78 °C. After the addition the solution was stirred for 30 min at -78 °C. Subsequently, ITDB (71.4 mg, 0.38 mmol) was added. The cooling bath was removed and the

reaction was stirred until it had warmed up to room temperature. Then the mixture was poured into saturated aqueous ammonium chloride solution, the organic layer was separated and the aqueous phase was extracted with diethyl ether. The combined organic phases were washed with brine and dried over sodium sulfate and the solvent was removed by rotary evaporation. 5-trimethylsilyl-bithiophene boronic ester **48** was obtained as a yellow oil (165 mg, 0.31 mmol, 92%) with a purity of 95% (GC). It was used without further purification.

¹H NMR (400 MHz, CDCl₃): δ = 7.44 (s, 1 H, 4-H), 7.10 (s, 1 H, 3'-H), 2.75 (t, ³*J* = 7.9 Hz, 2 H, α' -CH₂), 2.64 (t, ³*J* = 7.9 Hz, 2 H, α -CH₂), 1.66-1.57 (m, 4 H, β -CH₂, β' -CH₂), 1.41-1.26 (m, 24 H, C-CH₃, -CH₂-), 0.90 (t, ³*J* = 6.8 Hz, 3 H, Th-CH₃), 0.88 (t, ³*J* = 6.7, 3 H, Th-CH₃), 0.35 (s, 9 H, Si-CH₃).

MS (EI) *m/z*: calcd for C₂₉H₄₉BO₂S₂Si: 532, found [M+H]⁺: 533.

5-([N-{2,6-Diisopropylphenyl}]-9-perylenyl-3,4-dicarboximide)-3,4'-dihexyl-2,2'-bithiophene (**50**)



N-(2,6-diisopropylphenyl)-9-bromoperylene-3,4-dicarboximide **49** (187 mg, 0.32 mmol) and 5 trimethylsilyl-bithiophene boronic ester **48** (226 mg, 0.38 mmol) were dissolved in 3 mL DME. The resulting solution was carefully degassed and the catalyst (Pd(PPh₃)₄ (4 mol%)) and the base (2 M aqueous potassium phosphate solution (0.48 mL, 3 eq.)) were added. Next, the reaction mixture was carefully degassed and stirred at 80 °C for 1.5 h. Then (*n*-Bu)₄NF (400 mg, 1.27 mmol) was added and the reaction mixture was stirred for further 2.5 h. After completion of the reaction, the mixture was poured into water (15 mL), the organic layer was separated and the aqueous phase was extracted with DCM. The combined organic phases were dried over sodium sulfate and the solvent was removed by rotary evaporation. The crude product was purified by column chromatography (silica/DCM:*n*-hexane [2:1]) to give PMI-bithiophene **50** (238 mg, 0.29 mmol, 92%) as a red solid.

M.p.: 94-96 °C.

¹H NMR (400 MHz, CDCl₃): δ = 8.65-8.62 (m, 2 H, Pery-1H,6H), 8.49-8.36 (m, 5 H, Pery-2H,5H,7H,8H,12H), 7.71 (d, ³*J* = 7.9 Hz, 1 H, Pery-10H), 7.64 (t, ³*J* = 8.0 Hz, 1 H, Pery-11H), 7.49 (t, ³*J* = 7.7 Hz, 1 H, Ph-4H), 7.36 (d, ³*J* = 7.8 Hz, 2 H, Ph-3H,5H), 7.18 (s, 1 H, Th-4H), 7.07 (d, ⁴*J* = 0.9, 1 H, Th'-5H), 6.96 (d, ⁴*J* = 0.9, 1 H, Th'-3H), 2.87 (t, ³*J* = 7.7 Hz, 2 H, Th- α' -CH₂), 2.84-2.74 (m, 2 H, Ph-CH₂-).

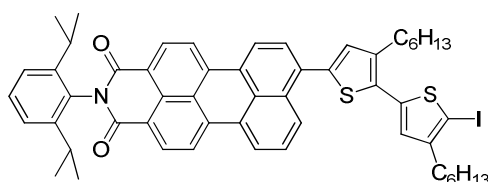
(CH₃)₂), 2.65 (t, ³J = 7.6 Hz, 2 H, Th-α'-CH₂), 1.79-1.64 (m, 4 H, Th-β-CH₂, Th-β'-CH₂), 1.49-1.29 (m, 12 H, -CH₂-), 1.20 (d, ³J = 6.8 Hz, 12 H, Ph-CH-(CH₃)₂), 0.91 (t, ³J = 7.0 Hz, 6 H, Th-CH₃, Th'-CH₃).

¹³C NMR (100 MHz, CDCl₃): δ = 163.92, 145.64, 143.80, 139.98, 138.33, 137.49, 137.18, 135.37, 135.21, 132.76, 132.36, 131.98, 131.28, 131.01, 130.43, 129.42, 129.29, 129.07, 128.80, 128.64, 128.44, 127.51, 127.26, 126.74, 124.04, 124.00, 123.36, 120.88, 120.82, 120.40, 120.28, 120.10, 31.69, 30.71, 30.51, 30.41, 29.43, 29.30, 29.14, 29.02, 24.02, 22.66, 14.11.

MS (MALDI-TOF) *m/z*: calcd for C₅₄H₅₅NO₂S₂: 813, found [M+H]⁺: 814.

Elemental analysis: calcd (%) for C₅₄H₅₅NO₂S₂: C 79.66, H 6.81, N 1.72; found (%): C 79.66, H 6.61, N 1.80.

5-([N-{2,6-Diisopropylphenyl}]-9-perylenyl-3,4-dicarboximide)-3,4'-dihexyl-5'-iodo-2,2'-bithiophene (54)



To a solution of PMI-bithiophene **50** (230 mg, 0.28 mmol) in 2.5 mL DCM was added mercury caproate (122 mg, 0.28 mmol). The resulting suspension was stirred at room temperature for 24 h until the mercury caproate was nearly completely dissolved. Next, iodine (87.9 mg, 0.31 mmol) was added and the mixture was stirred at room temperature for additional 6 h. Then the solution was filtered through a basic alumina plug and the filtrate was concentrated in vacuum. Upon addition of methanol the product was allowed to precipitate, filtered and dried in vacuum to give iodo-PMI-bithiophene **54** (245 mg, 0.26 mmol, 92%) as a red solid.

M.p.: 98-100 °C.

¹H NMR (400 MHz, CDCl₃): δ = 8.68-8.65 (m, 2 H, Pery-1H,6H), 8.53-8.44 (m, 5 H, Pery-2H,5H,7H,8H,12H), 7.73 (d, ³J = 7.8 Hz, 1 H, Pery-10H), 7.69 (t, ³J = 8.0 Hz, 1 H, Pery-11H), 7.49 (t, ³J = 7.8 Hz, 1 H, Ph-4H), 7.35 (d, ³J = 7.8 Hz, 2 H, Ph-3H,5H), 7.18 (s, 1 H, Th-4H), 6.87 (s, 1 H, Th'-3H), 2.85-2.75 (m, 4 H, Th'-α-CH₂, Ph-CH-CH₃)₂), 2.58 (t, ³J = 7.7 Hz, 2 H, Th-α-CH₂), 1.77-1.59 (m, 4 H, Th-β-CH₂, Th'-β-CH₂), 1.49-1.28 (m, 12 H, -CH₂-), 1.19 (d, ³J = 6.9 Hz, 12 H, Ph-CH-(CH₃)₂), 0.91 (t, ³J = 6.9 Hz, 6 H, Th-CH₃, Th'-CH₃).

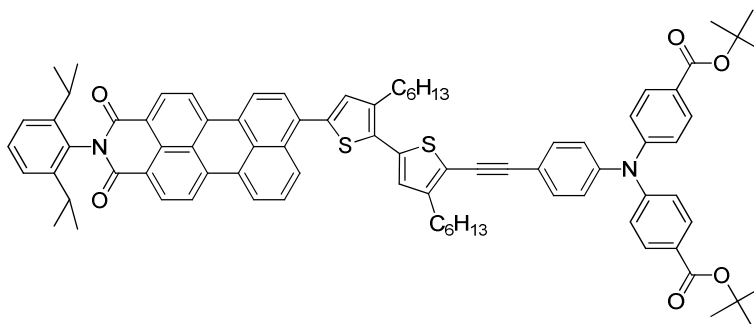
¹³C NMR (100 MHz, CDCl₃): δ = 163.96, 147.79, 145.73, 140.58, 140.23, 139.00, 137.58, 137.27, 135.20, 132.54, 132.07, 131.83, 131.25, 131.06, 130.55, 129.52, 129.42, 129.03, 129.00, 128.96,

128.60, 127.43, 126.92, 126.79, 124.15, 124.00, 123.39, 121.09, 120.47, 120.30, 74.46, 32.38, 31.66, 30.70, 29.98, 29.45, 29.26, 29.16, 28.92, 24.01, 22.65, 22.62, 14.09.

MS (MALDI-TOF) m/z : calcd for $C_{54}H_{54}INO_2S_2$: 939, found $[M+H]^+$: 940.

Elemental analysis: calcd (%) for $C_{54}H_{54}INO_2S_2$: C 69.00, H 5.74, N 1.49; found (%): C 69.18, H 5.64, N 1.63.

Di-*t*-butyl-4,4'-([4-({5'-([N-{2,6-diisopropyl}phenyl)]-9-perylenyl-3,4-dicarboximide)-3',4-dihexyl-2,2'-bithien-5-yl}ethynyl]phenyl)imino]dibenzoate (56)



Iodo-PMI-bithiophene **54** (45.0 mg, 47.9 μ mol), ethynyl-TPA **55** (27.0 mg, 57.4 μ mol), copper(I) iodide (0.9 mg, 4.79 μ mol) and 1 mL piperidine were dissolved in 1.5 mL toluene. The solution was carefully degassed and $Pd(PPh_3)_2Cl_2$ (1.3 mg, 1.91 μ mol) was added. The resulting solution was degassed carefully and stirred at room temperature for 24 h. After completion of the reaction the mixture was poured into water, the organic layer was separated and the aqueous phase was extracted with DCM. The combined organic phases were dried over sodium sulfate and the solvent was removed by rotary evaporation. The crude product was purified by column chromatography (silica/petrol ether:ethyl acetate [5:1]) to give protected acetylene-containing PMI-bithiophene-TPA triad **56** (36.8 mg, 28.7 μ mol 60%) as a dark red solid.

M.p.: 181-182 $^{\circ}C$.

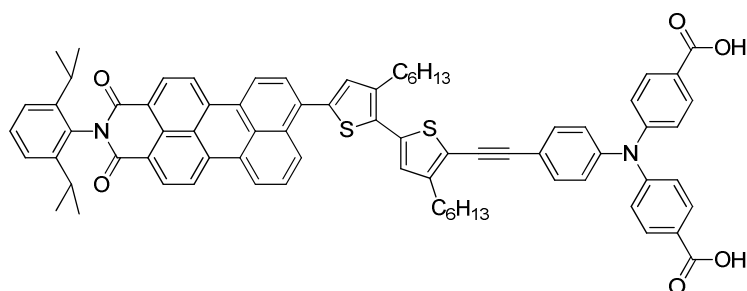
1H NMR (400 MHz, $CDCl_3$): δ = 8.67 (d, 3J = 8.1 Hz, 2 H, Pery-1H,6H), 8.52-8.46 (m, 4 H, Pery-2H,5H,7H,12H), 7.98 (d, 3J = 8.4 Hz, 1 H, Pery-8H), 7.79 (approx. d, 3J = 8.6 Hz, 4 H, (tBu)OOC-Ph-2H,6H), 7.69 (d, 3J = 7.8 Hz, 1 H, Pery-10H), 7.64 (t, 3J = 7.9 Hz, 1 H, Pery-11H), 7.49 (t, 3J = 7.7 Hz, 1 H, Ph-4H), 7.44 (d, 3J = 8.6 Hz, 2 H, TPA-Ph-3H,5H), 7.35 (d, 3J = 7.8 Hz, 2 H, Ph-3H,5H), 7.15 (m, 2 H, Th-3H,Th'-4H), 7.12-7.06 (m, 6 H, (tBu)OOC-Ph-3H,5H,TPA-Ph-2H,6H), 2.75-2.65 (m, 4 H, Th- α' -CH₂, Ph-CH-(CH₃)₂), 2.44 (t, 3J = 7.6 Hz, 2 H, Th- α -CH₂), 1.70 (m, 3J = 6.8 Hz, 2 H, Th- β' -CH₂), 1.59 (s, 18 H, C(CH₃)₃), 1.55 (m, 3J = 6.8 Hz, 2 H, Th- β -CH₂), 1.45-1.40 (m, 2 H, Th- γ -CH₂), 1.39-1.30 (m, 4 H, Th-CH₂-),

1.20-1.10 (m, 6 H, Th-CH₂-), 1.19 (d, ³J = 6.8 Hz, 12 H, Ph-CH-(CH₃)₂), 0.89 (t, ³J = 6.8 Hz, 3 H, Th'-CH₃), 0.77 (t, ³J = 6.9 Hz, 3 H, Th-CH₃).

¹³C NMR (100 MHz, CDCl₃): δ = 165.27, 163.97, 150.23, 146.42, 145.70, 142.05, 139.53, 137.53, 137.25, 135.34, 134.97, 134.71, 134.49, 133.86, 132.69, 132.43, 132.11, 132.07, 131.01, 130.51, 130.39, 129.47, 128.26, 127.66, 127.37, 126.91, 126.83, 124.89, 124.03, 123.20, 123.12, 121.15, 120.89, 120.39, 118.53, 93.72, 82.99, 80.78, 31.68, 31.47, 30.48, 30.45, 29.38, 29.20, 29.15, 28.99, 28.90, 28.23, 24.03, 22.63, 22.49, 14.12, 14.02.

High-Resolution MS (MALDI-TOF) *m/z*: calcd for C₈₄H₈₄N₂O₆S₂: 1280.577, found [M+H]⁺: 1281.578, δ*m/m* = 5.3 ppm.

4,4'-([4-([5'-[N-(2,6-Diisopropylphenyl)]-9-perylenyl-3,4-dicarboximide]-3',4-dihexyl-2,2'-bithien-5-yl)ethynyl]phenyl)imino)dibenzoic acid (46**)**



Protected acetylene-containing PMI-bithiophene-TPA triad **56** (36.8 mg, 28.7 μmol) was dissolved in 1 mL THF. To the resulting solution 1 mL of a 1 N methanolic lithium hydroxide solution (0.75 mL, 0.75 μmol) was added and the resulting solution was stirred for 8 h at 70 °C. After completion of the reaction the mixture was poured into water (5 mL) and was acidified with 1M HCl (pH = 1). The organic layer was separated and the aqueous phase was extracted with DCM. The combined organic phases were dried over sodium sulfate and the solvent was removed by rotary evaporation. The crude product was purified by column chromatography (silica/DCM:acetic acid [50:1]) and was dried in vacuum to give protected acetylene-containing PMI-bithiophene-TPA triad **46** (20.1 mg, 17.2 μmol, 60%) as a dark red solid.

M.p.: 218-219 °C.

¹H NMR (400 MHz, THF-d₈): δ = 8.72-8.66 (m, 4 H, Pery-1H,6H,2H,5H), 8.62-8.59 (m, 2 H, Pery-7H,12H), 8.47 (d, ³J = 8.5 Hz, 1 H, Pery-8H), 7.94 (d, ³J = 8.7 Hz, 4 H (tBu)OOC-Ph-2H,6H), 7.79 (d, ³J = 7.8 Hz, 1 H, Pery-10H), 7.72 (t, ³J = 8.0 Hz, 1 H, Ph-4H), 7.49 (d, ³J = 8.6 Hz, 2 H, Ph-3H,5H), 7.41-7.37 (m, 1 H, Pery-11H), 7.32-7.28 (m, 3 H, Ph-3H,5H,Th'-4H), 7.17-7.13 (m, 7 H, Th-3H, (tBu)OOC-Ph-

3H,5H, TPAPh-2H,6H), 2.93 (t, $^3J = 7.8$ Hz, 2 H, Th'- α -CH₂), 2.84-2.76 (m, 4 H, Ph-CH-(CH₃)₂, Th- α -CH₂), 1.83-1.73 (m, 4 H, Th- β -CH₂, Th- β -CH₂), 1.53-1.31 (m, 12 H, -CH₂-), 1.14 (d, $^3J = 6.8$ Hz, 12 H, Ph-CH-(CH₃)₂), 0.92 (t, $^3J = 7.3$ Hz, 3 H, Th'-CH₃), 0.91 (t, $^3J = 7.4$ Hz, 3 H, Th-CH₃).

¹³C NMR (100 MHz, THF-d₈): δ = 166.07, 163.32, 150.43, 148.19, 146.72, 145.85, 140.73, 139.23, 137.32, 136.98, 135.68, 134.77, 132.47, 132.39, 131.78, 131.71, 131.65, 131.48, 131.47, 131.08, 130.41, 129.61, 129.21, 128.91, 128.65, 128.54, 127.44, 127.08, 126.84, 125.90, 125.08, 124.45, 123.68, 123.33, 123.11, 121.39, 120.81, 120.70, 118.74, 118.48, 96.40, 81.79, 31.69, 31.67, 30.59, 30.19, 29.44, 29.28, 29.01, 28.94, 23.31, 22.59, 22.55, 13.47.

High-Resolution MS (MALDI-TOF) m/z : calcd for C₇₆H₆₈N₂O₆S₂, 1168.452; found [M+H]⁺: 1169.456, $\delta m/m = 3.3$ ppm.

2.5 References

- [1] A. Nattestad, A. J. Mozer, M. K. R. Fischer, Y. B. Cheng, A. Mishra, P. Bäuerle, U. Bach, *Nat. Mater.* **2010**, *9*, 31-35.
- [2] S. Powar, T. Daeneke, M. T. Ma, D. Fu, N. W. Duffy, G. Götz, M. Weidelener, A. Mishra, P. Bäuerle, L. Spiccia, U. Bach, *Angew. Chem.* **2013**, *125*, 630-633; *Angew. Chem. Int. Ed.* **2013**, *52*, 602-605.
- [3] M. Weidelener, diploma thesis, Ulm University, **2009**.
- [4] J. Cremer, PhD thesis, Ulm University, **2005**.
- [5] J. Cremer, E. Mena-Osteritz, N. G. Pschierer, K. Müllen, P. Bäuerle, *Org. Biomol. Chem.* **2005**, *3*, 985-995.
- [6] Z. S. Wang, Y. Cui, K. Hara, Y. Dan-oh, C. Kasada, A. Shinpo, *Adv. Mater.* **2007**, *19*, 1138-1141.
- [7] M. Xu, S. Wenger, H. Bala, D. Shi, R. Li, Y. Zhou, S. M. Zakeeruddin, M. Grätzel, P. Wang, *J. Phys. Chem. C* **2009**, *113*, 2966-2973.
- [8] A. Mishra, C.-Q. Ma, R. A. J. Janssen, P. Bäuerle, *Chem. Eur. J.* **2009**, *15*, 13521-13534.
- [9] S. Haid, M. Marszalek, A. Mishra, M. Wielopolski, J. Teuscher, J.-E. Moser, R. Humphry-Baker, S. M. Zakeeruddin, M. Grätzel, P. Bäuerle, *Adv. Funct. Mater.* **2012**, *22*, 1291-1302.
- [10] L. Malatesia, M. Angoletta, *J. Chem. Soc.* **1957**, 1186-1188.
- [11] A. J. Mozer, D. K. Panda, S. Gambhir, B. Winther-Jensen, G. G. Wallace, *J. Am. Chem. Soc.* **2010**, *132*, 9543-9545.

Chapter 3

Acceptor-Functionalized Bithienyl-Triphenylamines for p-Type DSSCs

Adapted from M. Weidelener *et al.*, *Chem. Asian J.* **2014**, 9, 3251-3263.
with permission from WILEY-VCH Verlag GmbH & Co. KGaA

3.1 Introduction

The mentioned theoretical improvement of n-type DSSCs by combining them with p-type DSSCs in *Chapter 1* is due to the possibility of harvesting more light by complementary absorption of the deployed dyes on each electrode, thus increasing J_{SC} . Furthermore, an increased V_{OC} which is for pn-tandem DSSCs equal to the energy gap between the valence band edge of the p-type semiconductor cathode and the conduction band edge of the n-type semiconductor anode enhances solar cell performance.^[1-4] However, the complexity of the device increases as well and hence there are additional prerequisites for efficient pn-tandem DSSCs.^[4] With respect to the dye development, it is very important that the sensitizers of the respective photoactive electrodes absorb light in different wavelength regimes. Otherwise, they would compete against each other for photons and this would decrease the produced photocurrent of at least one of them.

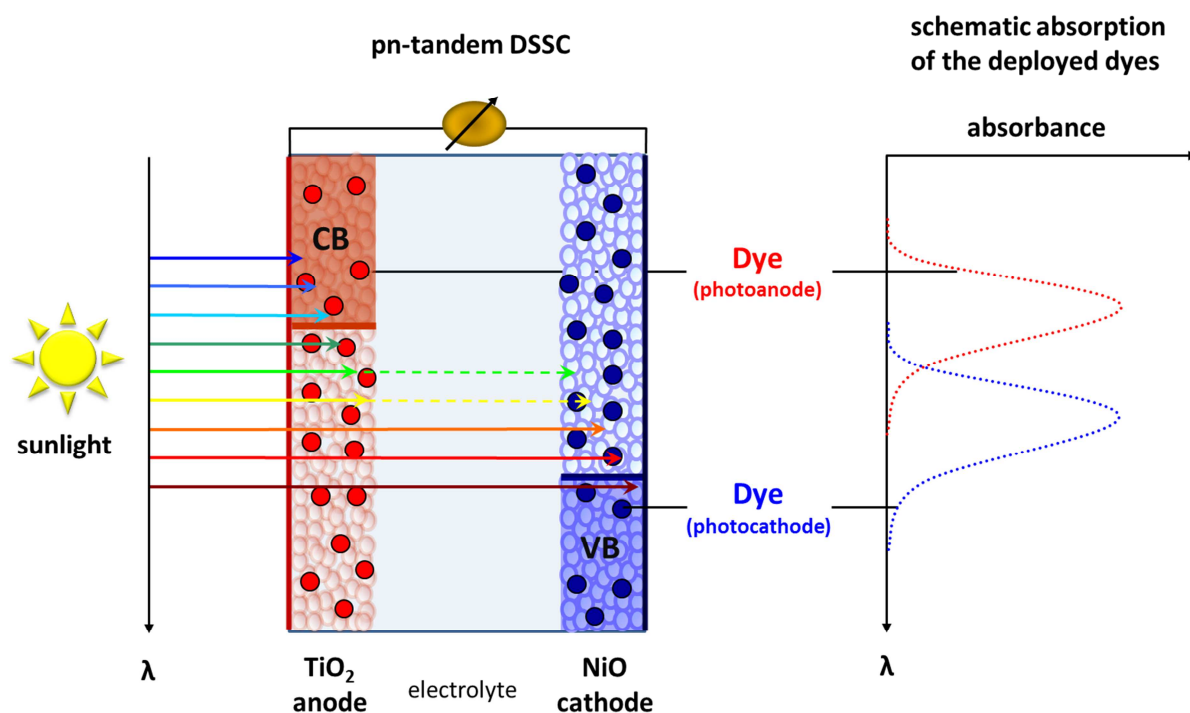


Figure 1. A pn-tandem DSSC sensitized with two complementary absorbing dyes is irradiated with sunlight (colored arrows correspond to photons of the visible light). The dye adsorbed on the photoanode absorbs low-energy photons. The passing, residual high-energy photons are then absorbed by the dye adsorbed on the photocathode. Schematic absorption spectra of the adsorbed dyes are shown at the right.

In case of pn-tandem DSSCs, where the light should encounter the TiO_2 -photoanode first due to the higher optical density of NiO up to 500 nm^[5], it is important that the dye adsorbed on the photoanode has a relatively large optical band gap and therefore absorbs only the high-energy

photons. The dye adsorbed on the photocathode has to have a low band gap so that it can absorb all the low-energy photons which are not absorbed by the dye deployed at the photoanode (Figure 1). Another important aspect is current balancing of the photoanode and the photocathode, since the total current of the tandem cell is limited by the photoelectrode with the lower J_{sc} . Up to now, all reported tandem DSSCs showed limited J_{sc} values of maximum 2.4 mA cm^{-2} (4.1 mA cm^{-2} when illuminated from the p-side) due to low performing photocathodes.^[1-2,6,7] For the development of pn-tandem DSSCs with PCEs exceeding those of highly efficient n-type DSSCs,^[8,9] it is crucial to further improve photocurrent production of photocathodes with sensitizers absorbing low-energy photons.

In this chapter, four new A- π -D triads **57-60** (Chart 1) are reported differing in their acceptor-unit. They were synthesized with the aim of shifting their absorption maxima in comparison to perylenemonoimide(PMI)-containing sensitizer **14**. Their optoelectronic properties and photovoltaic performances in p-type DSSCs were investigated and compared to reference sensitizer **14**.^[2]

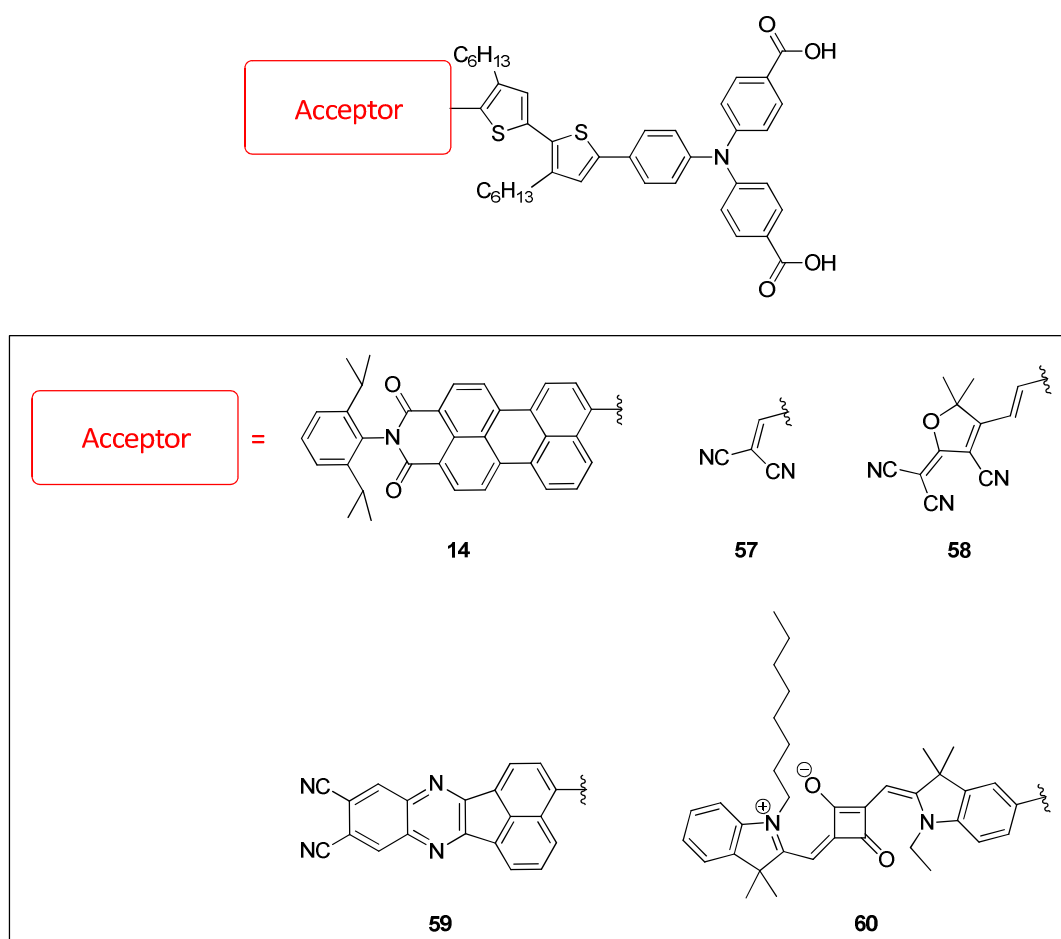


Chart 1. Chemical structures of acceptor-substituted bithiophene-triphenylamine triads **14** and **57-60**.

In *Chapter 2*, the alkyl-substitution pattern at the bithiophene π -bridge was investigated concerning its effect on the device performance. Sensitizers having alkyl chains pointing towards the PMI acceptor showed better performance compared to the ones with alkyl chains pointing away from the acceptor. This is due to a sterically induced torsion between the acceptor and the adjacent thiophene ring. The same principle is also realized in this series of dyes. Dicyanovinylene (DCV), a tricyano-substituted furane-derivative (TCF), 9,10-dicyano-acenaphtho[1,2-b]quinoxaline (DCANQ), and a squaraine-based moiety (SQ) were chosen as acceptors. DCV, TCF, and DCANQ bear electron-withdrawing cyano groups and are therefore electron-poor units. By combining them with the electron-rich bithiophene-triphenylamine (TPA) moiety it is expected that resulting triads **57-59** show CT bands absorbing in the green to red region of the solar spectrum. Triad **60** should feature an intense absorption band in the red to near-infrared (NIR) region, which is typical for SQ-based chromophores due to their rigid, planar, and zwitterionic structure.^[10-13]

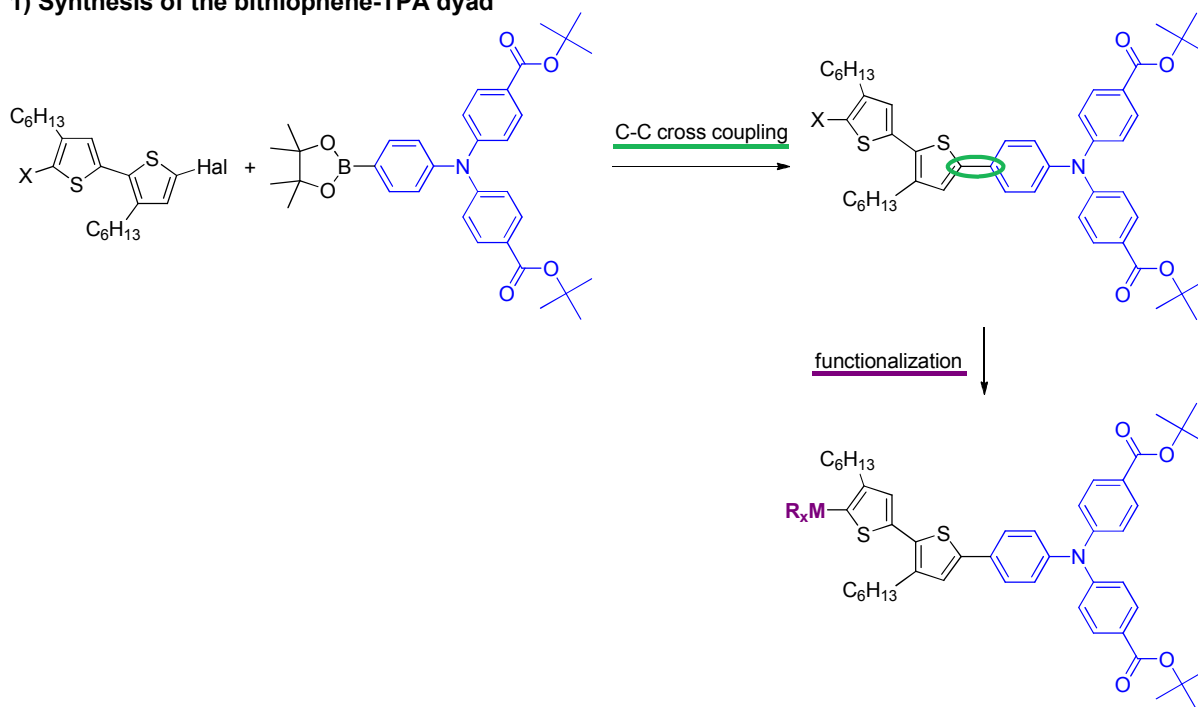
3.2 Results and discussion

3.2.1 Synthesis of A- π -D dyes 57-60

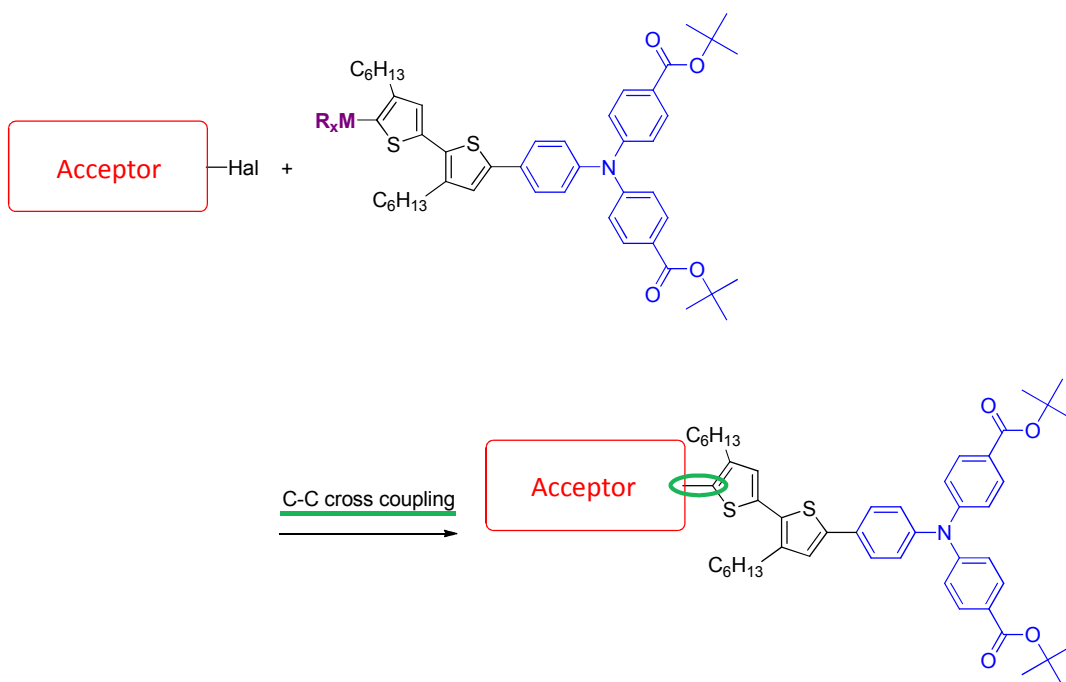
The differently acceptor-substituted sensitizers **57-60** were synthesized in a convergent way, similar to triad **46** (see *Chapter 2*). Concerning the convergent synthesis there are two plausible routes to build up D- π -A triads **57-60**. In route A (Scheme 1), the bithiophene moiety is coupled first to the TPA donor. Afterwards the formed dyad is further functionalized and then connected to the acceptor unit in order to obtain the protected triad. Route B (Scheme 2) starts with the synthesis of the acceptor-functionalized bithiophene which is then linked to the TPA donor unit resulting as well in the desired protected triad. The special feature of route A is that the acceptor is inserted at the penultimate step of the synthetic pathway. This is especially advantageous if the availability of the acceptor represents a bottleneck in the synthesis of the triads, e.g. due to complex or costly synthesis of the acceptor moiety. Halogen-functionalized dicyano-acenaphthoquinoxaline and squaraine building blocks were obtained in limited amount from the Müllen (MPI, Mainz) and Nüesch (EMPA, Dübendorf) group, respectively. Hence, route A was chosen for the synthesis of **59** and **60**.

Route A

1) Synthesis of the bithiophene-TPA dyad



2) Synthesis of the protected A- π -D triad

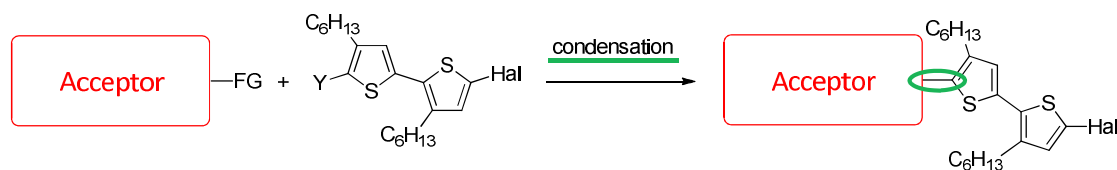
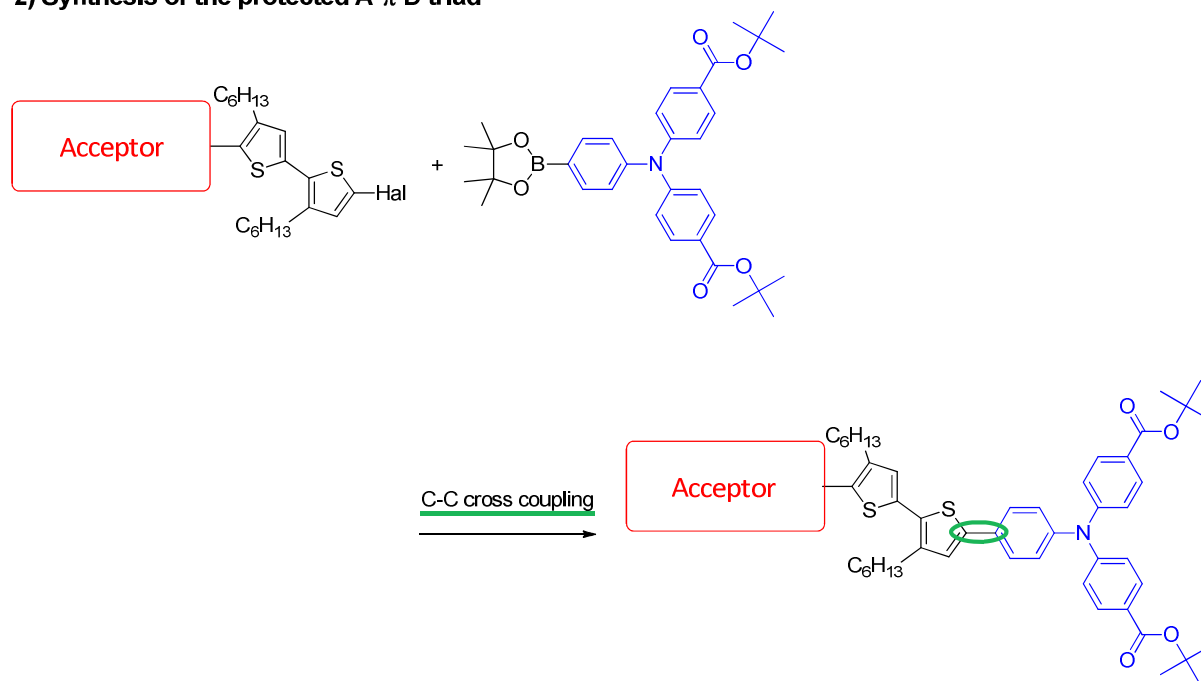


Scheme 1. Synthetic route A towards protected A- π -D triads via formation of a bithiophene-TPA dyad and subsequent coupling to the acceptor-unit.

As malononitrile and TCF are easily accessible precursors for the synthesis of acceptor-functionalized bithiophenes, route B was chosen for the synthesis of **57** and **58**, which is described in the following.

Route B

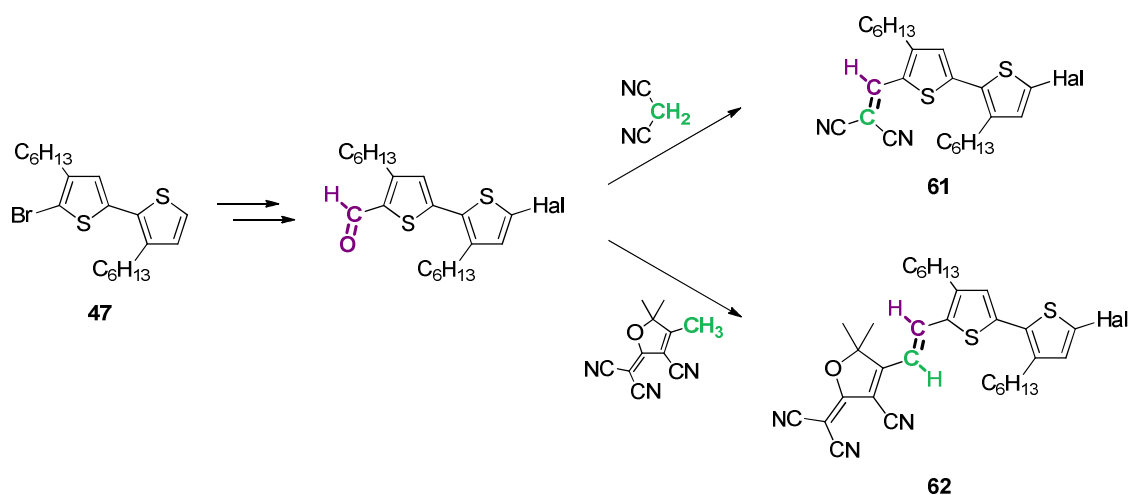
1) Synthesis of the acceptor-bithiophene dyad

2) Synthesis of the protected A- π -D triad

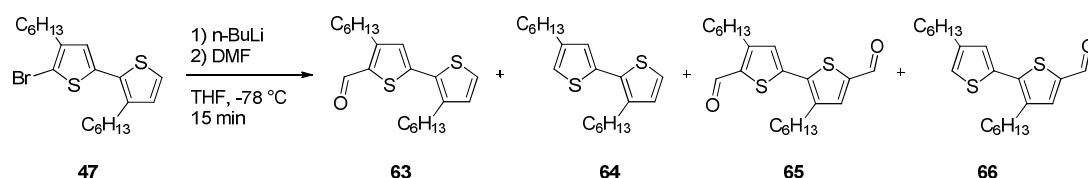
Scheme 2. Synthetic route B towards protected A- π -D triads via formation of a acceptor-bithiophene dyad and subsequent coupling to the TPA donor.

Synthesis of A- π -D triads **57** and **58**

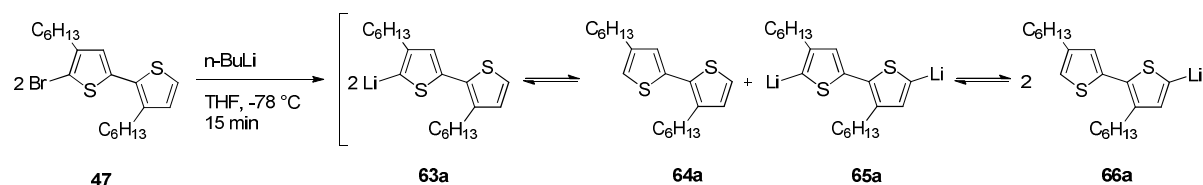
In the first reaction sequence acceptor-substituted bithiophenes **61** and **62** (Scheme 3) were synthesized starting from 5-bromo-3,4'-dihexyl-2,2'-bithiophene **47**. In order to introduce the acceptor moieties distal to the hexyl chains of the bithiophene the bromo-functionality of **47** had to be converted into an aldehyde group. This was realized via metal-bromine-exchange and further reaction of the metallated intermediate with N,N-dimethylformamide (DMF). In a first attempt, *n*-butyllithium (*n*-BuLi) was used as metalation reagent (Scheme 4). After the dropwise addition of 1 equivalent (eq.) of *n*-BuLi at -78 °C, the reaction was stirred for further 15 min at that temperature before quenching the reaction with DMF. ¹H-NMR and GC-MS of the crude product showed besides desired product **63**, an isomeric side-product **66**, as well as traces of and debrominated bithiophene **64** and dialdehyde **65**.



Scheme 3. Plan of synthesis for halogenated acceptor-functionalized bithiophenes **61** and **62**.



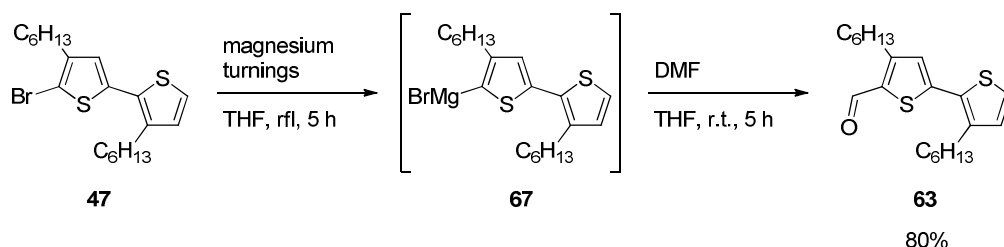
Equilibrium of the lithiated species



Scheme 4. Top: Synthesis of bithiophene aldehyde **63** using $n\text{-BuLi}$ as metalation reagent coming along with the formation of side-products **64-66**. Bottom: Resulting equilibrium upon lithiation of bromo-bithiophene **47**.

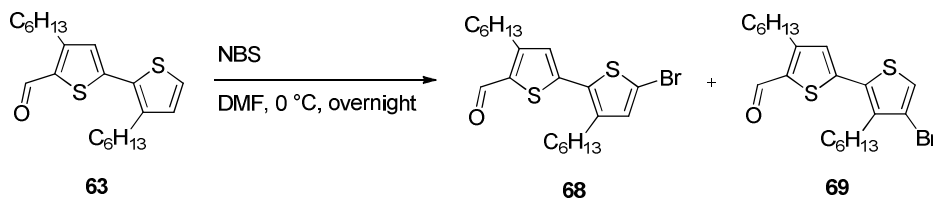
The separation of the undesired isomer **66** from product **63** was not possible due to its very similar crystallization behaviour and polarity on silica gel. The formation of side-products **64-66** can be explained by the existence of the equilibrium between mono-, di- and nonlithiated species (Scheme 4, **63a-66a**). The explanation for the formation of lithiated species **66a** and hence of side-product **66** is that the negative charge is better stabilized on the α -position distal to the alkyl chains. Thus, the equilibrium is shifted to the more thermodynamically favorable isomer **66a**. In order to suppress the formation of isomer **66** a kinetically controlled reaction would be necessary. This can be realized by reducing the reaction temperature, the reaction time by the means of shortening the stirring time after the addition of $n\text{-BuLi}$ and/or replacing DMF with a more reactive formylation reagent (e.g. ethyl formate or N -formyl-piperidine).

However, to develop an efficient synthesis with the use of *n*-BuLi leading to an isomer-free aldehyde **63** is not guaranteed by applying the proposed changes for which reason magnesium was used to build Grignard reagent **67** as intermediate which was then quenched with DMF in order to form aldehyde **63** (Scheme 5, a procedure for the synthesis of 3-hexylthiophene-2-carbaldehyde from 2-bromo-3-hexylthiophene was adopted^[15]). Bromo-bithiophene **47** was vigorously stirred with magnesium turnings in tetrahydrofuran (THF) under reflux for 5 h. Full conversion of the magnesium-bromine-exchange was confirmed via GC-MS (by quenching a sample with water upon only the mass of the debrominated species was detected). Subsequent reaction of the regioselectively formed Grignard reagent with DMF led to isomer-free aldehyde **63** in 80% yield after column chromatography.



Scheme 5. Selective synthesis of aldehyde **63** via Grignard reagent **67**.

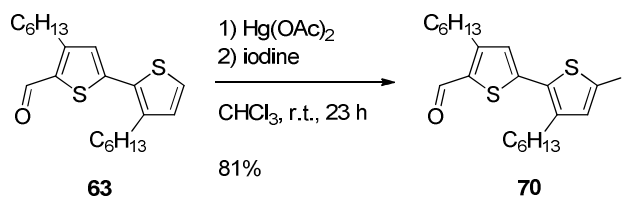
Bromination of bithiophene-carbaldehyde **63** with 1 eq. of NBS in DMF again generated a mixture of two isomers (Scheme 6, **68** and **69**) due to insufficient selectivity of the electrophilic aromatic substitution. The origin of this result lies in the hexyl chain increasing the electron density of the β -position next to the unsubstituted α -position. Reducing the temperature did not change the ratio of the mixture dramatically emphasizing the very similar reactivity of the two positions towards NBS.



Scheme 6. Formation of an isomeric mixture of bromo-aldehydes **68** and **69** using NBS as halogenation reagent.

Therefore, iodination of **63** was performed using mercury acetate and iodine resulting in isomer-free iodo-derivative **70** after chromatographic work-up in 81% yield (Scheme 7). In this case, the

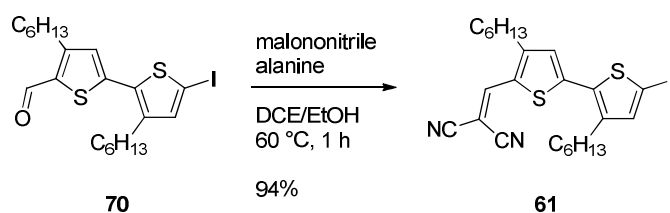
selectivity concerning the halogenation of the free α -position is given completely and no other isomers were detected.



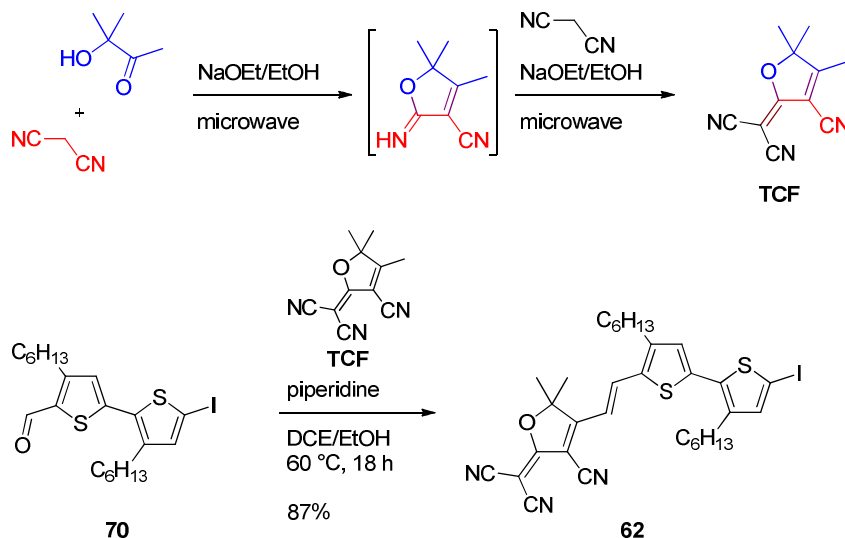
Scheme 7. Selective halogenation of carbaldehyde **63** towards iodinated key building block **70**.

Key building block **70** was then reacted with malononitrile and 2-(3-cyano-4,5,5-trimethyl-5H-furan-2-ylidene)malononitrile (**TCF**) in Knoevenagel condensation reactions to accomplish acceptor-substituted bithiophene **61** and **62** in a yield of 94% and 87%, respectively, after column chromatography and recrystallization (Scheme 8). **TCF** was synthesized according to literature in an one-pot microwave-assisted reaction with malononitrile and 3-hydroxy-3-methyl-2-butanone as starting materials.^[16]

Synthesis of DCV-substituted iodo-bithiophene **61**:



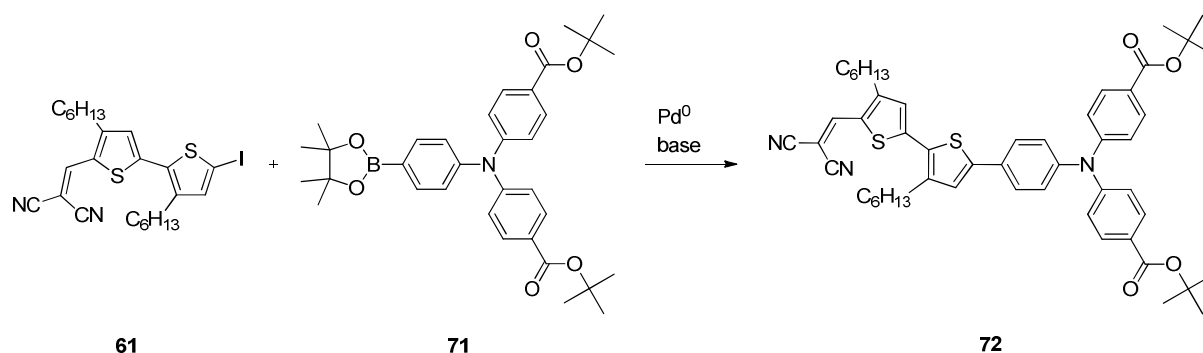
Synthesis of TCF-substituted iodo-bithiophene **62**:



Scheme 8. Synthesis of acceptor-substituted iodo-bithiophenes **61** and **62** via Knoevenagel condensation.

In the reaction of aldehyde **70** with malononitrile, β -alanine was used as catalyst and an excellent yield of 94% was achieved (Scheme 8). For the Knoevenagel condensation of **70** with TCF using β -alanine a lower yield of 76% was obtained. By applying piperidine as a stronger base, the reaction time was reduced from 5 to 2 days and the yield of **62** could be raised to 87%. The exclusive formation of the trans-isomer was confirmed via $^1\text{H-NMR}$ showing only one doublet for each olefinic proton with a coupling constant of 15.6 Hz.

Iodo-bithiophenes **61** and **62** were then further reacted in Suzuki-Miyaura cross-coupling reactions with 1.2 eq. TPA boronic ester **71**^[17] using an aqueous base and a Pd^0 catalyst system (Scheme 9 and 10).



Scheme 9. Synthesis of protected triad **72** via Suzuki-Miyaura cross-coupling reaction.

In a first attempt to obtain ester protected triad **72**, palladium(II) acetate ($\text{Pd}(\text{OAc})_2$) was used as palladium source and triphenylphosphine (PPh_3) was added as ligand (Table 1, Entry 1). 2 N aqueous K_3PO_4 solution and THF was used as base and solvent, respectively. After heating the reaction to 50°C for 5 h, iodinated bithiophene **61** was consumed completely. However, aqueous work-up and column chromatography yielded only 35% of triad **72**. In literature, similar reaction conditions were used for the coupling of bromo-bithiophene **47** and triphenylamine **71** leading to the corresponding product in 81% yield.^[18] In general, Suzuki-Miyaura cross-coupling reaction should proceed faster when using aryl halide **61** instead of **47** due to the more reactive iodo-functionality of **61** in comparison to the bromo-functionality of **47**.^[19] Additionally, DCV-substituted bithiophene **61** is more electron-deficient than bromo-bithiophene **47** and therefore oxidative addition should occur even faster. These two facts explain the shorter reaction time of 5 h in the case of **61** in comparison to 19 h using bromo-bithiophene **47**.^[18] The low yield of 35% can be explained by the formation of numerous side-products, which could not be isolated and hence identified.

Table 1. Optimization of the reaction conditions of the Suzuki-Miyaura cross-coupling reaction yielding triad **72**.

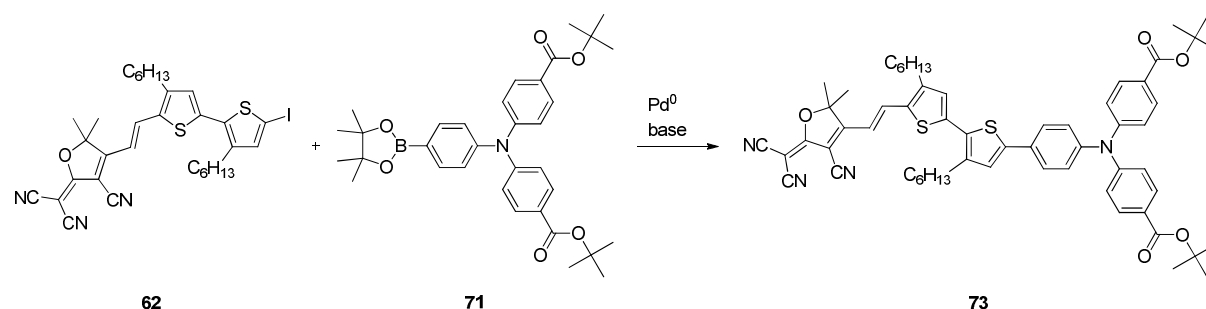
entry	catalyst system	base (eq. ^[a])	reaction conditions	yield
1	2.5 mol% Pd(OAc) ₂ , 10 mol% PPh ₃	K ₃ PO _{4(aq)} (5)	THF, 50 °C, 5 h	35
2	2.5 mol% Pd ₂ dba ₃ , 10 mol% [HPtBu ₃]BF ₄	K ₃ PO _{4(aq)} (5)	THF, 50 °C, 19 h	78
3	2.5 mol% Pd ₂ dba ₃ , 10 mol% [HPtBu ₃]BF ₄	K ₃ PO _{4(aq)} (4)	toluene, 120 °C, 2 d	59

[a] with respect to iodo-bithiophene **61**.

Changing the catalyst system to tris(dibenzylideneacetone)dipalladium(0) (Pd₂dba₃) / tri-*t*-butylphosphonium tetrafluoroborate ([HPtBu₃]BF₄) (Table 1, Entry 2) the reaction time had to be elongated to 19 h to achieve full conversion of bithiophene **61**, resulting in a good yield of 78% by reducing the number and amount of side-products. The formation of some of the side-products might be attributed to the added base or rather the formed hydroxide ions, which might attack and hydrolyze the DCV groups. Therefore, in another reaction the amount of base was reduced from 5 to 4 eq. and toluene, a less polar solvent, was used (Table 1, Entry 3). As water is less soluble in toluene than in THF, less base is present in the toluene phase resulting in a lower concentration of hydroxide ions. If there are side reactions concerning base-catalyzed hydrolysis, these should be lessened due to the lower concentration of hydroxide ions. However, with a reduced concentration of hydroxide ions the transmetallation step is also influenced. The reaction was performed in a Schlenk-tube at 120 °C. After 2 days the reaction was stopped. Aqueous work-up and column chromatography brought up 59% of dyad **72** and a considerable amount of deiodinated reactant. Deiodination is a hint that the oxidative addition is much faster than the transmetallation step in the catalytic cycle proving that toluene and reducing the amount of base is not suitable to further improve the yield compared to reaction conditions described in Table 1, Entry 2.

The synthesis of TCF-containing triad **73** (Scheme 10) starting from dyad **62** and boronic acid ester **70** was optimized as well. The catalyst system and reaction conditions from Table 1, Entry 2 were taken as starting point for the Suzuki-Miyaura cross-coupling reaction of **73**. Since no conversion took place by stirring at 50 °C the reaction temperature was increased to 80 °C (Table 2, Entry 1). After 18 h at 80 °C the reaction was stopped and purification of the crude product resulted in triad **73** in 37% yield. The low yield is due to formation of various side-products and the difficult separation of these from the product via column chromatography and high performance liquid chromatography (HPLC). The

presence of at least four side-products can be seen in the olefinic region of the ^1H -NMR-spectrum after column chromatography (Figure 2).



Scheme 10. Synthesis of protected triad **73** via Suzuki-Miyaura cross-coupling reaction.

Table 2. Optimization of the Suzuki-Miyaura cross-coupling reaction yielding triad **73**.

entry	catalyst system	base (eq. ^[a])	reaction conditions	yield
1	2.5 mol% Pd_2dba_3 , 10 mol% $[\text{HPtBu}_3]\text{BF}_4$	$\text{K}_3\text{PO}_{4(\text{aq})}$ (3)	THF, 80 °C, 18 h	37
2	2.5 mol% Pd_2dba_3 , 10 mol% $[\text{HPtBu}_3]\text{BF}_4$	$\text{K}_3\text{PO}_{4(\text{aq})}$ (2.5)	THF, MW	-
3	4 mol% $\text{Pd}(\text{PPh}_3)_4$	$\text{K}_3\text{PO}_{4(\text{aq})}$ (3)	THF, 90 °C, 6 h	45
4	4 mol% $\text{Pd}(\text{PPh}_3)_4$	$\text{NaHCO}_{3(\text{aq})}$ (3)	THF, 90 °C, 16 h	15
5	4 mol% $\text{Pd}(\text{PPh}_3)_4$	$\text{K}_3\text{PO}_{4(\text{aq})}$ (2.5)	THF, 90 °C, 3 h	26

[a] with respect to iodo-bithiophene **62**.

These are probably side-products with a similar structure than the product since they can only be seen due to additional signals right next to the peaks of the olefinic protons at ~6.5 (Figure 2). The sum of the integrals fits to triad **73**, which is a hint that the side-products have the same amount of protons. Also mass spectrometric analysis could not clarify the structure of the side-products leading to the assumption that they are triads bearing differently hydrolyzed TCF groups. Despite the formation of these side-products triad **73** could be isolated using HPLC. The aromatic and olefinic region of the ^1H -NMR spectrum of pure product **73** is shown in Figure 3. The olefinic protons are situated at 8.13 and 6.46 ppm. The aromatic protons of the thiophene and benzene rings form a singlet (7.17 ppm), two duplets (7.89 and 7.52 ppm) and a multiplet (7.14-7.10 ppm). For a more precise assignment see Figure 3 or the *Experimental section (vide infra)*.

One way to reduce the assumed hydrolysis side-reactions is to increase the rate of the cross-coupling reaction. Microwave (MW) irradiation is known to increase reaction rates remarkably.^[20] Therefore, the reaction was carried out under MW irradiation (Table 2, Entry 2). However, irradiating the reaction with a power of 300 W, at a maximum temperature of 125 °C and a maximum pressure of 4.7 bar in the vessel led to complete decomposition of the TCF-unit.

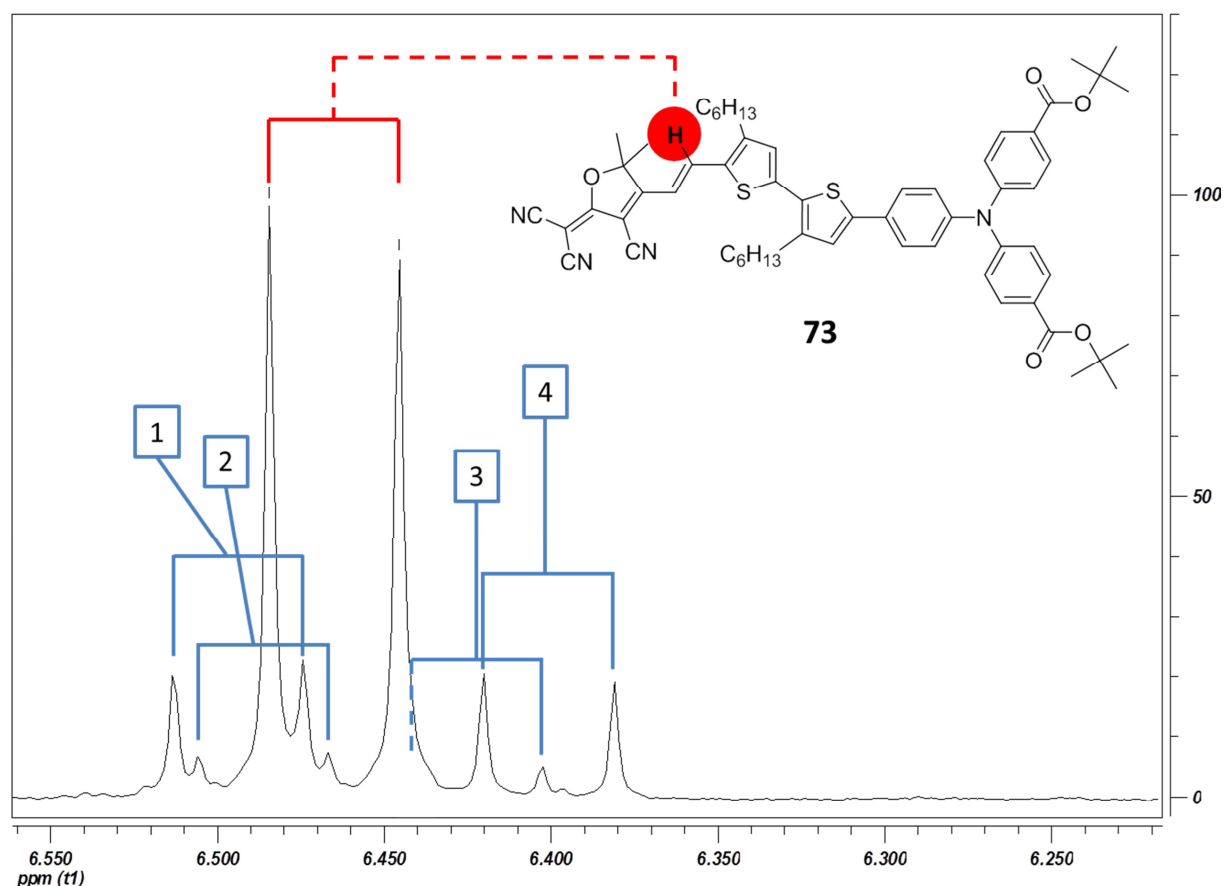


Figure 2. Olefinic region of the ^1H -NMR spectrum of **73**, showing the duplet of the red-marked proton. Blue-marked duplets 1-4 correspond to the side-products formed during the Suzuki-Miyaura cross-coupling reaction.

Changing the catalyst system from $\text{Pd}_2\text{dba}_3/[\text{HPtBu}]_3\text{BF}_4$ to $\text{Pd}(\text{PPh}_3)_4$ and stopping the reaction after 6 h at 90 °C (Table 2, Entry 3) led to an increased yield of 45% after column chromatography and HPLC. Reaction control by thin layer chromatography showed incomplete conversion of iodo-bithiophene **62**. However, the reaction was stopped in order to circumvent hydrolysis or other side reactions of the formed product. The purification process remained the same, but was eased because a lower amount of side-products were formed. Nevertheless, purification via HPLC was necessary as well. In another reaction, using NaHCO_3 as a weaker base than K_3PO_4 the reaction proceeded slower. It was stopped after 16 h and resulted in a lower yield of 15% (Table 2, Entry 4).

This indicates that the reaction rate for the formation of triad **73** is decreased more strongly than reaction rate of the side reactions of the TCF acceptor moiety. Hence, for the next reaction K_3PO_4 was again used as base. Reducing the amount of base from 3 to 2.5 equivalents and the reaction time to 3 h, the reaction yielded 26% of **73** (Table 2, Entry 5).

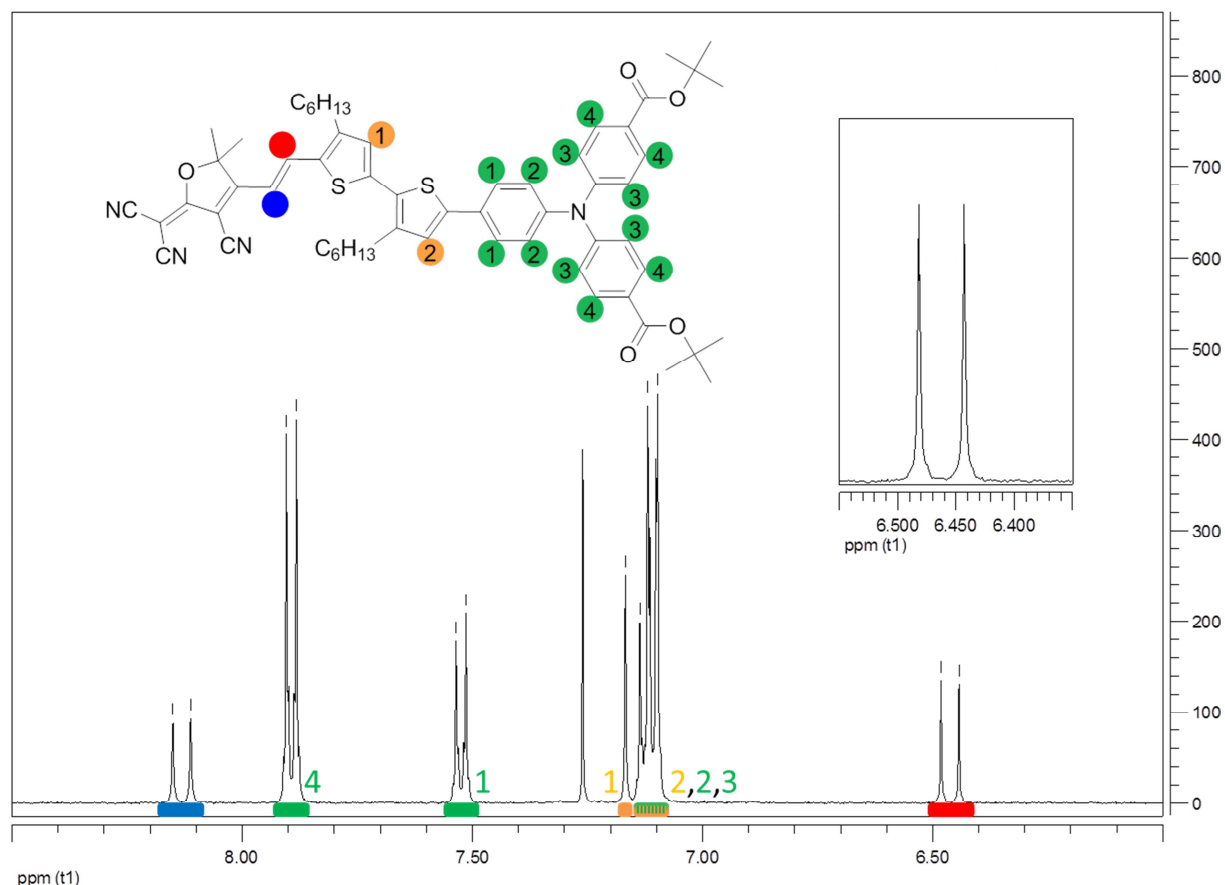
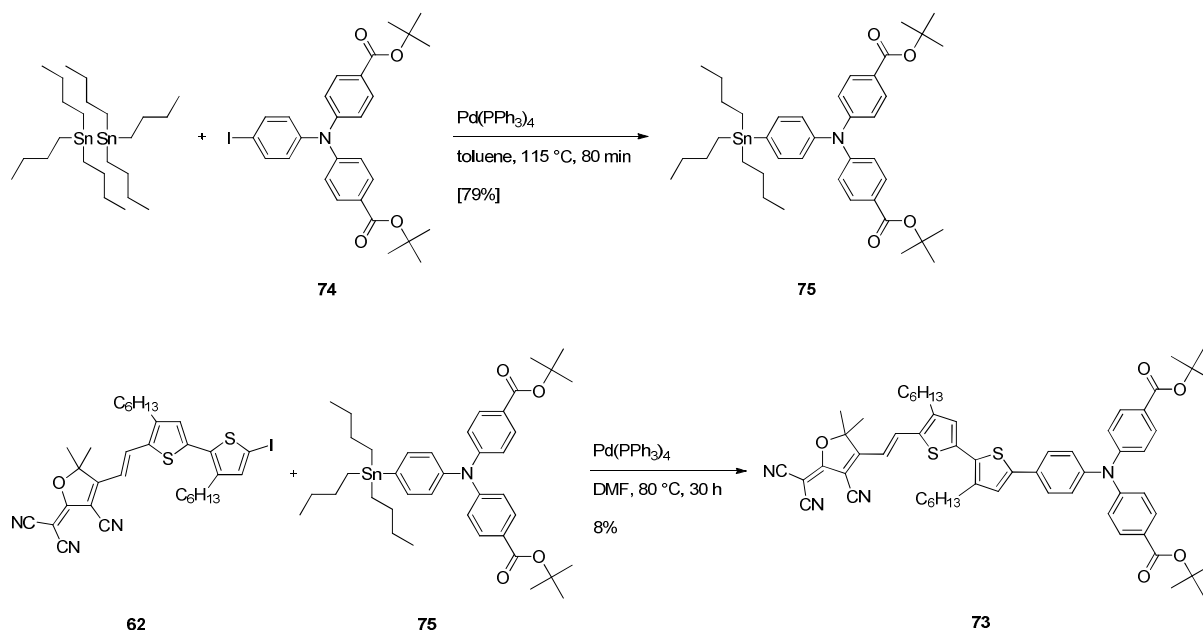


Figure 3. 1H -NMR spectrum of triad **73** after purification via HPLC, the inset shows the duplet of the red-marked olefinic proton.

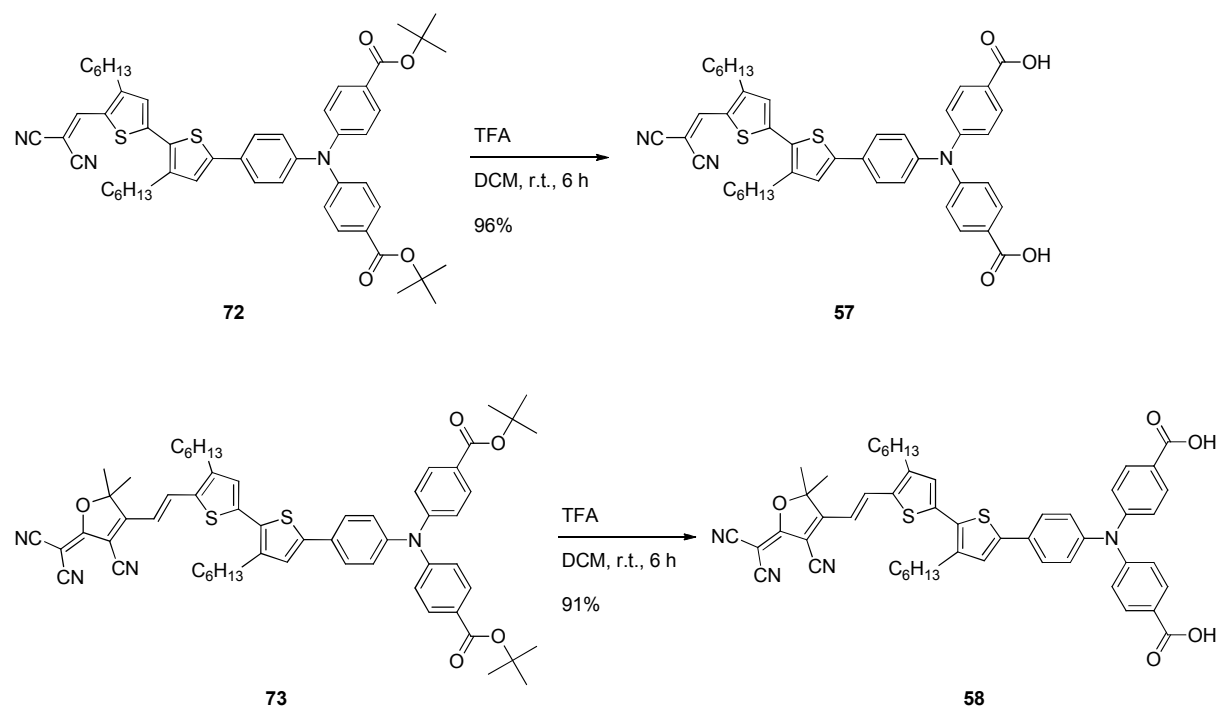
Due to the problems concerning formation of various side-products during Suzuki-Miyaura reaction, Stille cross-coupling reactions were performed in order to omit the usage of bases. First, stannylated TPA **75** was synthesized starting from iodinated TPA **74**^[17] via Pd-catalyzed coupling reaction with 2.3 eq. hexabutylditin (Scheme 11). After a short reaction time of 80 min at 115 °C, the solvent was evaporated and the crude product was purified via column chromatography. Hereupon stannylated TPA **75** was obtained in 79% yield still containing minor alkyl tin impurities. The slightly impure product was used without further purification for the next step since the stability of **75** on silica gel is critical. Subsequently, iodo-bithiophene **62** was reacted with TPA **75** in a Stille cross-coupling reaction using $Pd(PPh_3)_4$ as catalyst (Scheme 11).



Scheme 11. Formation of stannylated triarylamine **75** and the following Stille cross-coupling reaction with TCF-bithiophene **62** towards ester protected triad **73**.

The reaction was stopped after 30 h due to increasing formation of side-products detected by TLC. Column chromatography brought up ^1H -NMR-pure triad **73** in 8% yield showing no unidentified side-products. The reason for the low yield is most probably a slow transmetalation step in the catalytic cycle of the Stille cross-coupling reaction. This is indicated by the high amount of deiodination taking place during the reaction. Additionally, homocoupling of the iodinated species was observed. Optimization of the Stille cross-coupling reaction has not been pursued due to the very low yield of 8% and the sufficient amount of **73** available at that moment. Though, a different catalyst system and the addition of caesium fluoride might speed up transmetalation and thus increase the yield of the Stille cross-coupling reaction.

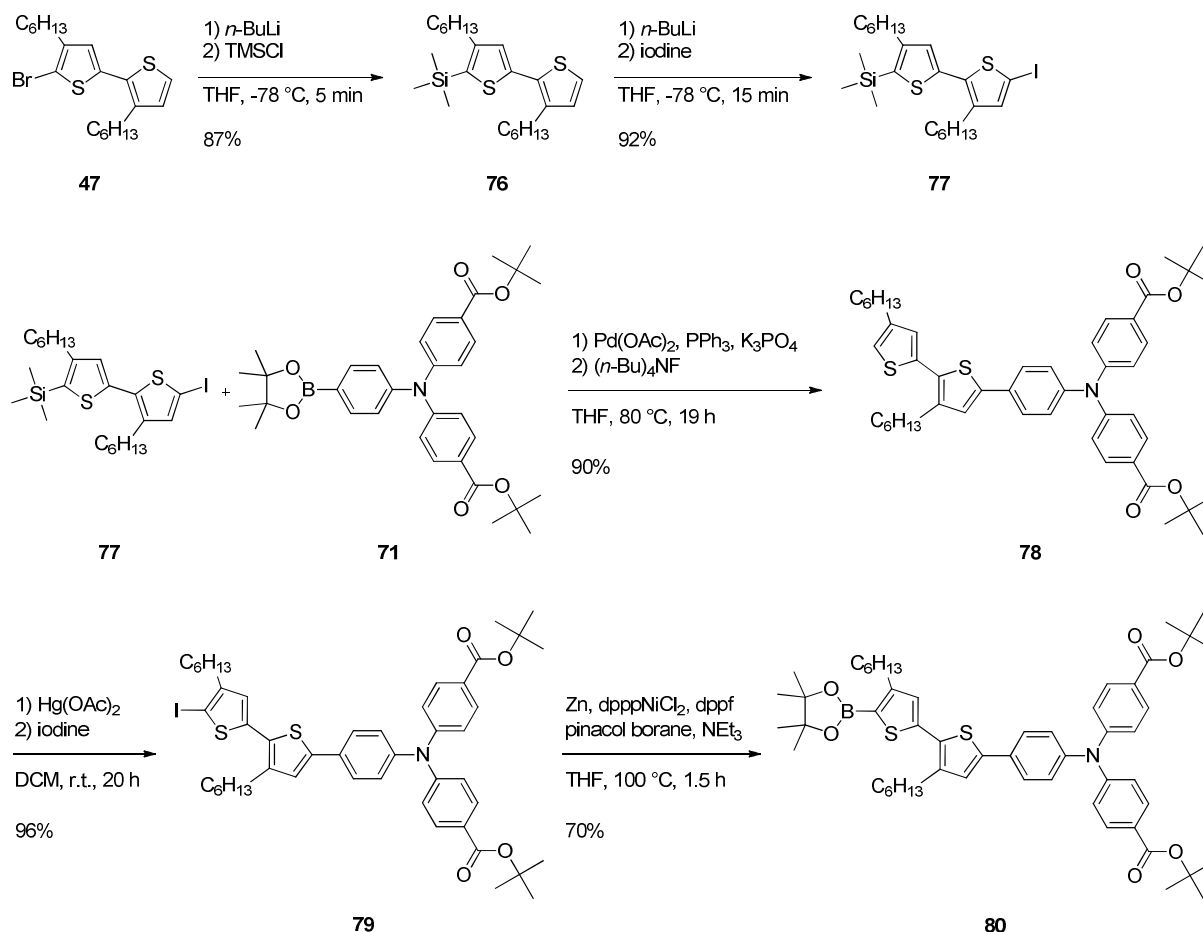
In order to obtain deprotected sensitizers DCV-bithiophene-TPA **57** and TCF-bithiophene-TPA **58**, the *t*-butyl ester groups at the TPA moiety of triads **72** and **73** were cleaved off by the use of trifluoroacetic acid (TFA). Therefore, triad **72** was stirred with 50 eq. TFA at room temperature (Scheme 8). After removal of the solvent and excessive TFA in high vacuum, pure DCV-containing dye **57** was obtained in an excellent yield of 96% by precipitation from THF/*n*-hexane. Triad **73** was deprotected using the same procedure, whereupon pure TCF-containing dye **58** was obtained in a similar yield of 91% by precipitation from THF/*n*-hexane.



Scheme 12. Cleavage of the *t*-butyl ester groups at the TPA moiety to obtain sensitizers DCV-bithiophene-TPA **57** and TCF-bithiophene-TPA **58**.

Synthesis of A- π -D triads **59** and **60**

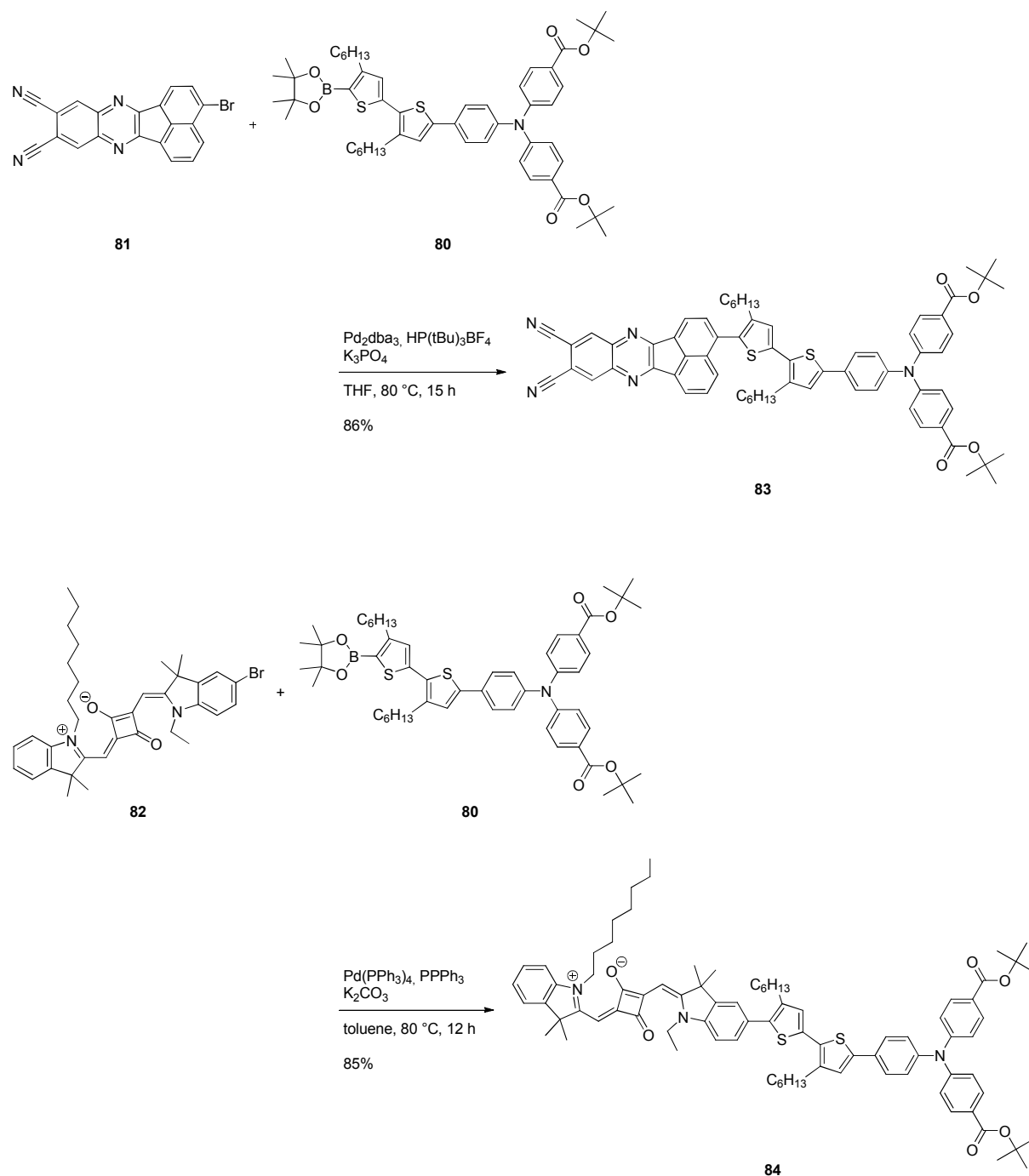
For the synthesis of triads **59** and **60** containing DCANQ and SQ as acceptor-units, boronic ester **80** was synthesized as depicted in Scheme 13. Starting from 5'-bromo-3,4'-dihexyl-2,2'-bithiophene **47**^[14] the halogen functionality had to be shifted to the other side of the bithiophene. Therefore the bromo substituent of **47** was exchanged by a trimethylsilyl (TMS) group by lithiation of bithiophene **47** with *n*-BuLi and quenching with TMS-chloride to obtain **76** in 87% yield after column chromatography. For the upcoming halogenation step, electrophilic aromatic substitution was not possible due to the risk of *ipso*-substitution of the TMS group. Further lithiation of TMS-bithiophene **76** with *n*-BuLi and quenching with iodine resulted in iodo-TMS-bithiophene **77** in a yield of 92% after purification via column chromatography. Bithiophene **77** was further reacted with TPA boronic ester **71** in a Suzuki-Miyaura cross-coupling reaction followed by in-situ cleavage of the TMS group of the bithiophene-TPA intermediate with tetra-*n*-butylammonium fluoride ((*n*-Bu)₄NF). After aqueous work-up and column chromatography, dyad **78** was obtained in a very good yield of 90%. Introduction of an iodo-functionality at the free α -position was realized using mercury acetate and iodine. Bromination was not performed, as on similar systems formation of isomers occurred.^[18] Pure iodinated bithiophenyl-triphenylamine **79** was obtained in 96% yield after filtration of the reaction mixture over a short alumina column.



Scheme 13. Synthesis of key building block boronic ester **80**.

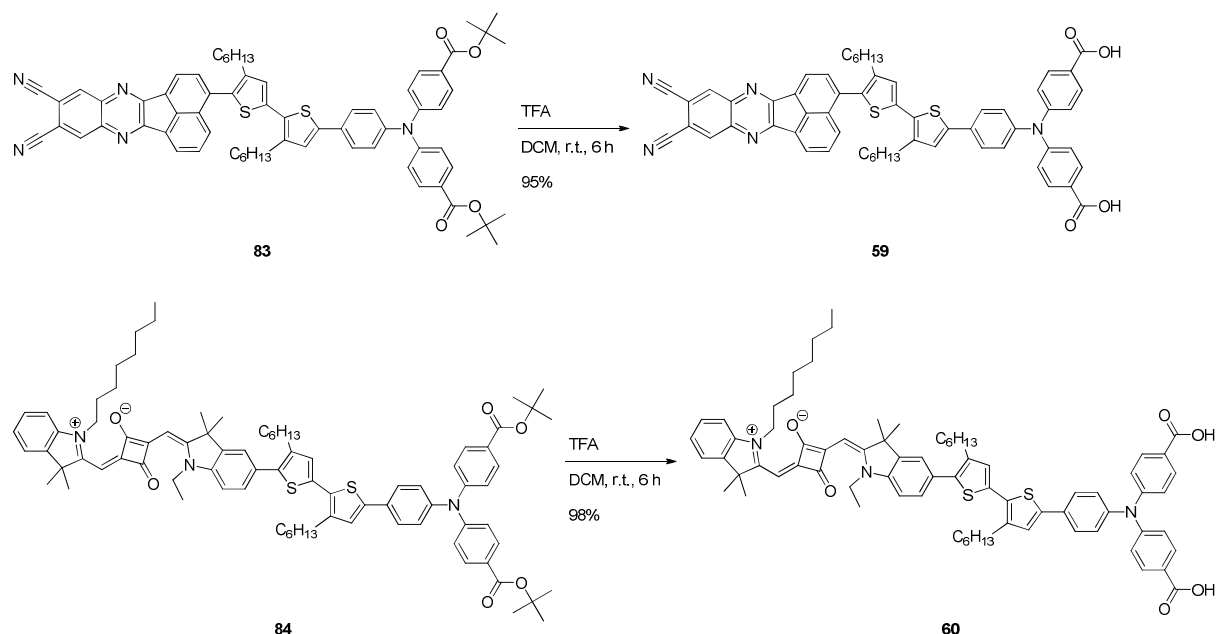
Borylation of dyad **79** took place under conditions described by Percec *et al.*^[21] Iodinated dyad **79** was reacted with pinacol borane, a Ni^0 catalyst, and triethylamine as base in the presence of zinc dust. Boronic ester **80** was obtained in 70% yield after column chromatography. It is assumed that the reaction proceeds similar to the mechanism of the palladium catalyzed Miyaura borylation reaction.^[22] Zinc usually accelerates the reaction and increases the conversion.^[22,23] However, in the case of **80** without the addition of zinc no product at all could be isolated. Boronic ester **80** represents a valuable building block giving the opportunity to introduce different acceptors.

Triads **83** and **84** were synthesized via Suzuki-Miyaura cross-coupling reaction converting boronic ester **80** with bromo-DCANQ **81** and bromo-SQ **82**, respectively (Scheme 10). As catalyst systems $\text{Pd}_2\text{dba}_3/\text{HP}(t\text{Bu}_3)\text{BF}_4$ and $\text{Pd}(\text{PPh}_3)_4/\text{PPh}_3$, respectively, were chosen as they turned out to be efficient for these kind of coupling components.^[17,18,24,25] Both protected triads **83** and **84** were obtained in good yields of 86% and 85% after column chromatography, respectively.



Scheme 14. Synthesis of protected triads **83** and **84** via Suzuki-Miyaura cross-coupling reaction.

Finally, DCANQ-containing dye **59** and SQ-containing dye **60** were obtained in 95% and 98% yield, respectively, after deprotection of the *t*-butyl ester groups using the well-established deprotection procedure: stirring with TFA at room temperature followed by precipitation from *n*-hexane (Scheme 15).



Scheme 15. Cleavage of the *t*-butyl ester groups at the TPA moiety to obtain sensitizers DCANQ-bithiophene-TPA **59** and SQ-bithiophene-TPA **60**.

All four synthesized sensitizers **57-60** were fully characterized by the means of melting points, NMR spectroscopy, and high-resolution mass spectrometry.

3.2.2 Optical properties of A- π -D triads **57-60**

Absorption spectra of triads **57**, **58**, and **60** in solution were measured in dichloromethane (DCM); DCANQ-derivative **59** was measured in DMF due to its low solubility in chlorinated solvents (Figure 4a). The corresponding data are summarized in Table 3. The acceptor-unit in triads **14** and **57-60** has a strong influence on the absorption properties in solution. PMI-substituted sensitizer **14** showed a typical absorption at 518 nm for perylene^[26] with a high molar extinction coefficient ϵ of $57,200 \text{ M}^{-1}\text{cm}^{-1}$. SQ-containing dye **60** featured a common narrow and extremely intense absorption band^[27] at 654 nm with an ϵ of $215,300 \text{ M}^{-1}\text{cm}^{-1}$. Triads **57** and **58** incorporating DCV and TCF groups as electron-accepting moieties showed charge transfer (CT) absorption bands at 489 ($\epsilon = 34,400 \text{ M}^{-1}\text{cm}^{-1}$) and 592 nm ($\epsilon = 42,100 \text{ M}^{-1}\text{cm}^{-1}$), respectively. The 103 nm red-shifted absorption band of **58** compared to **57** is due to the stronger electron-acceptor TCF in **58** in comparison to the DCV group in **57**. Triad **59** possessing a cyano-substituted acenaphthoquinoxaline as electron acceptor produced only a weak CT absorption band resulting in a shoulder at around 450 nm. Its strongest absorption is located at 331 nm and overlaps with the absorption of the bithiophene-TPA donor part of the molecule positioned at 360-365 nm. The low intensity of the CT band can be assigned to decoupling

of the acceptor- and donor-units by a strong torsion of these two parts as confirmed by molecular orbital calculations (*vide infra*). The absorption band of the donor part is not shifted within the series **57-60**. Longest wavelength absorption maxima of dyes **14** and **57-60** are distributed between 331 and 654 nm with ϵ ranging from 34,400 to 215,300 $\text{M}^{-1}\text{cm}^{-1}$ demonstrating the effect of different electron-accepting moieties on the absorption behaviour and hence light-harvesting.

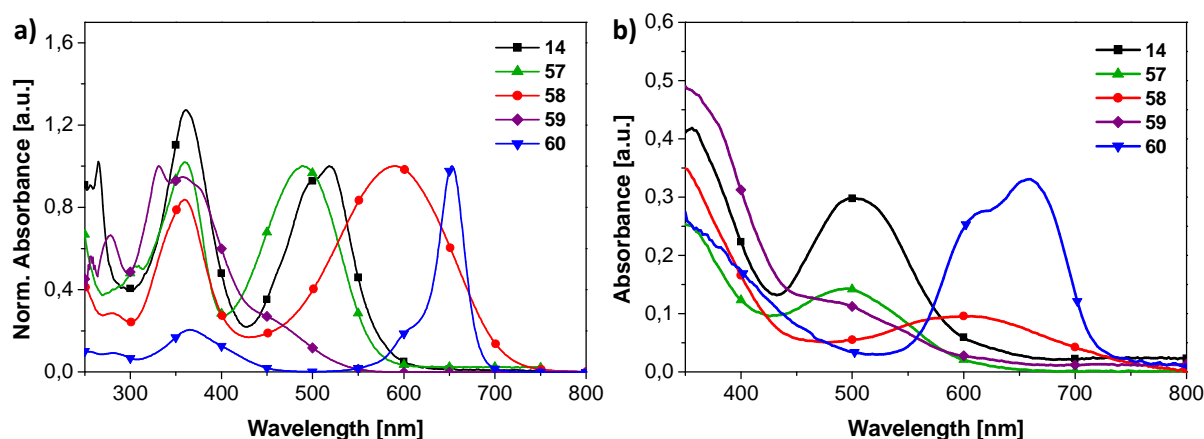


Figure 4. Absorption spectroscopy of **14** and **57-60** (a) in solution and (b) on NiO film (NiO absorption subtracted).

Table 3. Optical data of triads **14** and **57-60** in solution ($c = 5 \times 10^{-5}$ M) and on NiO film (NiO absorption subtracted).

dye	λ_{abs} [nm] (ϵ [$\text{M}^{-1}\text{cm}^{-1}$])	ΔE_{opt} [eV] ^[a]	$\lambda_{\text{abs film}}$ [nm]	$\Delta E_{\text{opt film}}$ [eV] ^[a]
14 ^[b]	361 (57,200) 518 (45,000)	2.16	500	2.07
57 ^[b]	360 (34,800) 489 (34,400)	2.19	494	2.06
58 ^[b]	358 (32,900) 592 (42,100)	1.75	608	1.63
59 ^[c]	331 (56,900)	2.32	(~460) ^[e]	2.02
60 ^[b]	365 (44,100) 653 (215,300)	1.82	659	1.73

[a] Calculated by the low energy onset of λ_{max} . [b] Measured in DCM. [c] Measured in DMF. [d] Taken from the lowest energy shoulder. [e] Shoulder.

Figure 4b shows the absorption spectra of dyes **14** and **57-60** adsorbed onto the surface of transparent 0.9 μm thick NiO films. Compared to the spectra in solution, all triads experience a spectral broadening resulting in a red-shift of the onset of the absorption by at least 25 nm for **14**

and up to 79 nm for dye **59**. The low energy absorption band of PMI-substituted triad **14** on NiO is the only one being blue-shifted (18 nm) in comparison to solution, whereas triads **57-60** showed red-shifts of 5, 16, 10, and 6 nm, respectively. Additionally, these bands are broadened which was already observed for dyes **44-46** described in *Chapter 2* and is ascribed to the electronic interactions of the dye with the semiconductor and adjacent dye molecules.^[28,29] Comparing the absorption of the triads on NiO film, it is noticeable that triads **57** and **58** showed less intense absorption probably caused by a lower degree of dye loading. Taking the high ϵ of sensitizer **60** into account its absorption on NiO is also quite low pointing towards a low dye loading as well. On the other hand, polycyclic acceptor substituted triads **14** and **59** showed the strongest absorptions on NiO films. This could be due to similarities in their conformation when adsorbed on NiO leading to a higher dye loading.

3.2.3 Electrochemical properties of A- π -D triads 57-60

Cyclic voltammograms of A- π -D sensitizers **57-60** were measured in DCM using tetra-*n*-butylammonium hexafluorophosphate (*n*-Bu)₄NPF₆ as supporting electrolyte (Figure 5). Redox potentials, the electrochemically determined band gaps as well as the highest occupied molecular orbital (HOMO) and lowest unoccupied molecular orbital (LUMO) energy levels (E_{HOMO} and E_{LUMO}) are compared to parental dye **14**^[17] and summarized in Table 4.

Table 4. Electrochemical data of triads **14** and **57-60** in DCM with (*n*-Bu)₄NPF₆ (0.1 M) as supporting electrolyte measured vs. Fc/Fc⁺ at 100 mV s⁻¹.

dye	E°_{ox1} [V]	E°_{ox2} [V]	E°_{ox3} [V]	E°_{ox4} [V]	E°_{red1} [V]	E°_{red2} [V]	E_{HOMO} [eV] ^[a]	E_{LUMO} [eV] ^[a]	ΔE_{CV} [eV] ^[b]
14	0.51	0.69	1.15	-	-1.41	-1.88	-5.54	-3.80	1.74
57	0.75	1.06	-	-	-1.31 ^[c]	-	-5.78	-3.86	1.92
58	0.50	0.78	-	-	-1.03 ^[c]	-1.47	-5.56	-4.10	1.46
59	0.43	0.70	-	-	-1.51 ^[c]	-	-5.46	-3.90	1.56
60	0.05	0.48	0.56	0.71	-1.71	-	-5.11	-3.47	1.64

[a] E_{HOMO} and E_{LUMO} calculated from the onset of E°_{ox1} and E°_{red1} , respectively; related to the Fc/Fc⁺-couple with a calculated absolute energy of -5.1 eV. [b] Band gap calculated to $\Delta E_{\text{CV}} = E_{\text{HOMO}} - E_{\text{LUMO}}$. [c] Taken from differential pulse voltammetry (DPV) measurement.

For each triad, two oxidation processes can be attributed to the oxidation of the combined bithiophene and TPA donor taking place at ~ 0.4 - 0.5 and ~ 0.7 - 0.8 V for **14** and **58-60**. The oxidation potentials are shifted to higher potentials at 0.75 and 1.06 V for **57** indicating a strong influence of the electron-accepting DCV-unit on the bithiophene donor. The additional reversible oxidation waves at 1.15 V in **14** and 0.05 and 0.48 V in **60** are ascribed to the oxidation of the PMI and SQ moieties. Due to the different acceptor-units, the electrochemical behaviour of triads **14** and **57-60** in the reductive regime is very different. The PMI-unit of **14** showed two reversible reduction waves at -1.41 and -1.88 V. Besides PMI, TCF-acceptor in **58** is the only acceptor showing also two reduction waves. In contrast to **14**, the first reduction for sensitizer **58** is irreversible and the second quasi-reversible. DCV-containing triad **57** showed an irreversible reduction at -1.31 V as well as DCANQ-substituted triad **59** at -1.51 V. SQ-derivative **60** showed one reversible reduction at -1.71 V. The differences in the redox behaviour, especially in the reductive regime, presumably influence the electron transfer processes of the sensitizers within the devices critically.

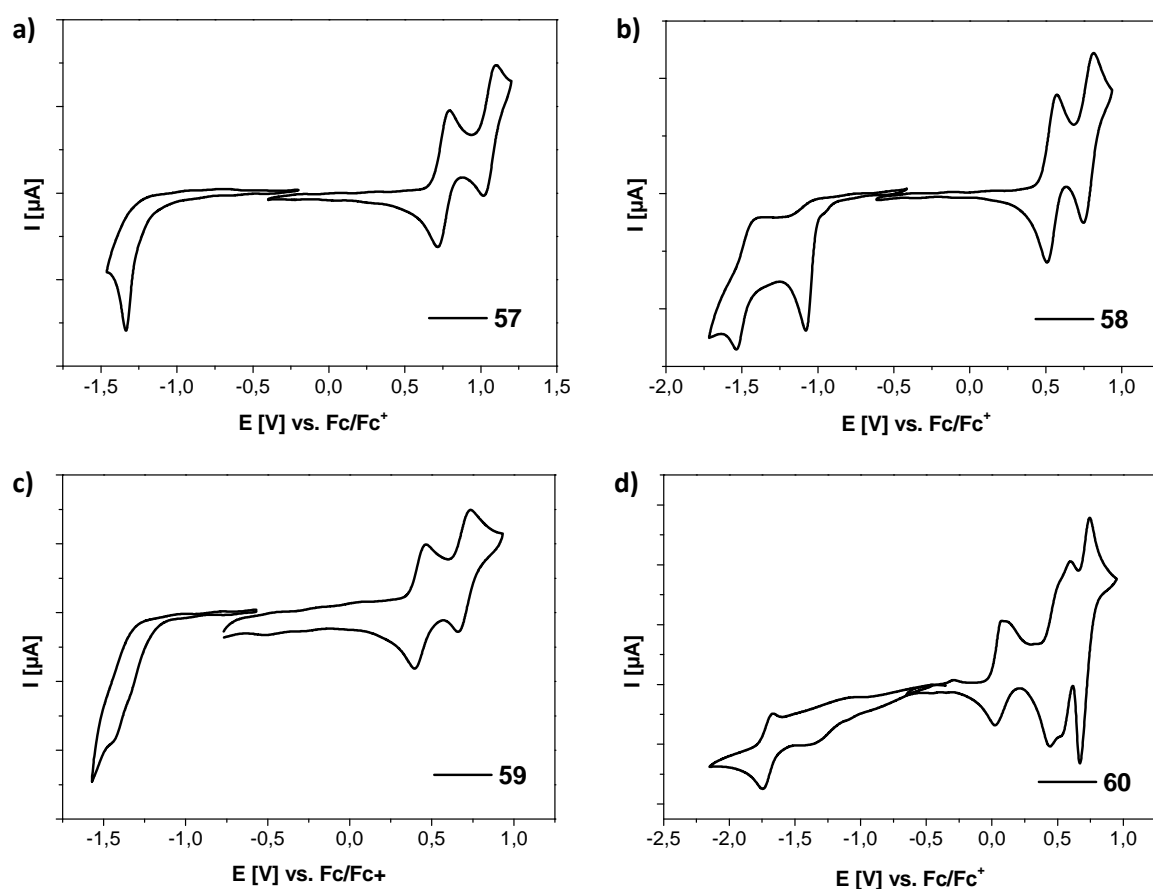


Figure 5. Cyclic voltammograms of **57-60** (a-d) measured in DCM using $(n\text{-Bu})_4\text{NPF}_6$ (0.1 M) as supporting electrolyte at 100 mV s^{-1} ; $c = 5 \times 10^{-4}\text{ mol/L}$.

The HOMO and LUMO energy levels of the triads were calculated from the onset of the first oxidation and reduction waves. The HOMO energy levels of dyes **14** and **57-59** are sufficiently lower than the valence band edge of NiO (~ -5.0 eV vs. vacuum or 0.5 V vs. NHE) enabling sufficient driving force for hole injection from the dye to the NiO. However, SQ-containing dye **60** possesses a HOMO level energy of -5.11 eV which might be a problem for efficient hole injection. Concerning the electron transfer from the dye to the redox mediator, dyes **14**, **57**, **59**, and **60** showed LUMO energy levels lying well above of the triiodide-iodine radical anion redox couple ($I_3^-/I_2^{\cdot-}$) (~ -4.15 eV vs. vacuum or -0.35 V vs. NHE^[30]) which is important for dye regeneration. Triad **58** bearing the strong electron accepting TCF unit unfortunately has a very low LUMO energy level of -4.10 eV presumably resulting in a low driving force for efficient dye regeneration. In Figure 6 a schematic view of the HOMO and LUMO energy levels is given as well as the redox potentials of the redox shuttle and the valence band edge energy of the NiO electrode.

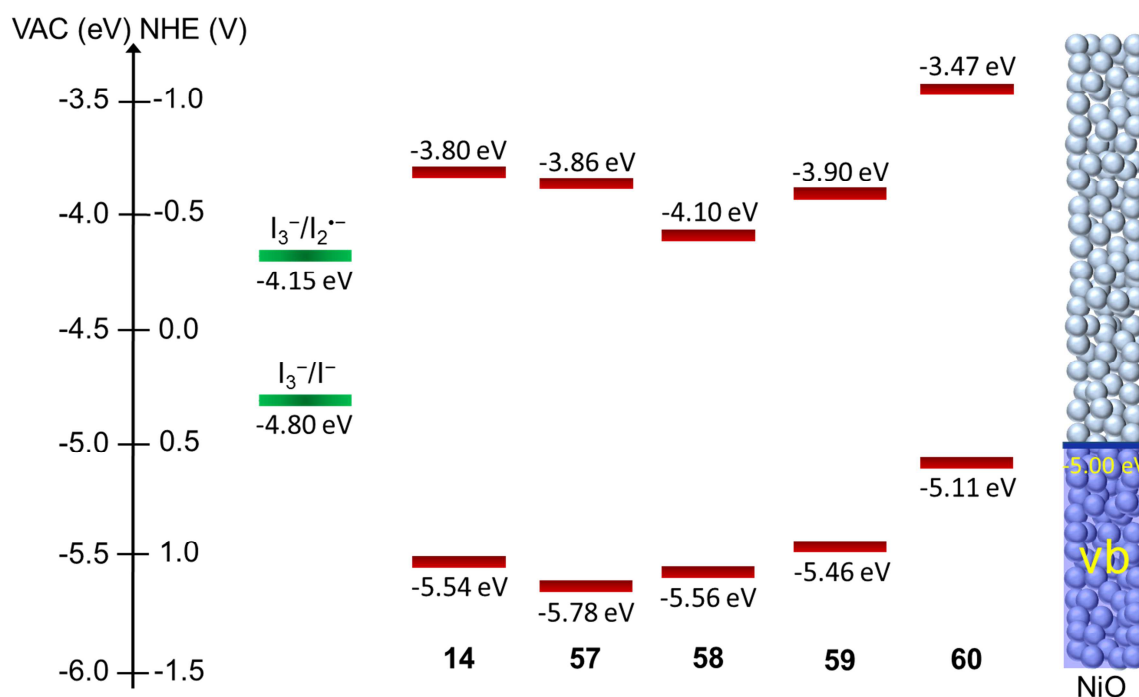


Figure 6. Position of HOMO and LUMO energy levels of discussed dyes **14** and **57-60** as well as relevant energy levels for p-type DSSCs (vb = valence band).

3.2.4 Quantum chemical calculations of A- π -D triads 57-60

Density functional theory (DFT) calculations with a B3LYP hybrid base (6-31G*) were performed in order to analyze the electron distribution of the frontier orbitals. The calculations were done by Dr.

T. Geiger from EMPA, Dübendorf. The HOMO-LUMO electron density distribution of all dyes is presented in Figure 7. The electron density distribution of the HOMO in dyes **14**, **59**, and **60** is mainly localized on the bithiophene-TPA moiety due to a twist between the acceptor-unit and the adjacent thiophene. In contrast to this, in dyes **57** and **58** the HOMO is distributed over the whole molecule.

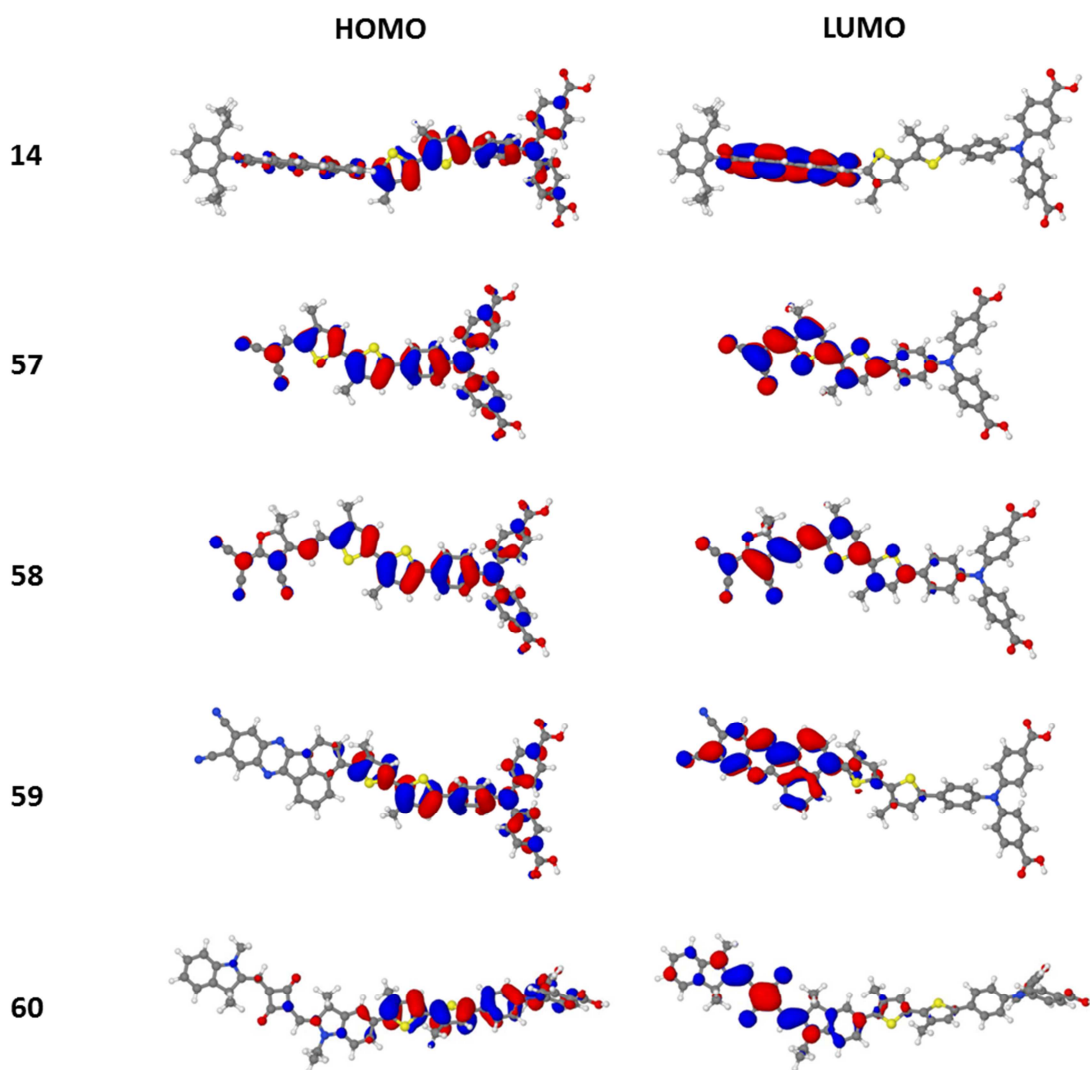


Figure 7. Frontier orbitals distribution of dyes **14** and **57-60** calculated using the B3LYP (6-31G+(dp)) DFT method (carbons in gray, nitrogens in blue, oxygens in red, sulfurs in yellow and hydrogens in white). In order to accelerate the convergence of optimizations the long hexyl chains were replaced with methyl substituents.

The electron density distribution of the LUMO is also very similar for dyes **14**, **59**, and **60** being mostly localized on the acceptor part and to a small extend on the adjacent thiophene ring. Dyes **57** and **58**, on the other hand, showed electron density distributions of the LUMO over the whole acceptor and bithiophene owing to the planarization of the acceptor and the thiophene and maybe also due to the

smaller size of the acceptor resulting in a minor delocalization of the electron density on the acceptor. Because of the less electron withdrawing DCV group in triad **57**, compared to TCF in **58** the electron density of the LUMO is further extended to the first phenyl ring of the TPA. This is less pronounced in the case of TCF-containing triad **58**.

3.2.5 Photovoltaic performance of A- π -D triads **57-60**

p-Type DSSCs with 1.5 μm thick nanostructured NiO films were fabricated using dyes **57-60** as sensitizers and iodide/triiodide (I^-/I_3^-) as redox shuttle. Cells using reference sensitizer **14** were also fabricated for the purpose of comparison. J - V curves of these devices are shown in Figure 8a and the data are summarized in Table 5. Among the new sensitizers, DCANQ-containing dye **59** showed the highest short-circuit current density (J_{SC}) of 1.66 mA cm^{-2} which is comparable to the value obtained with reference dye **14** (1.87 mA cm^{-2}). Despite this slightly lower J_{SC} and a very similar E_{HOMO} for **14** and **59**, devices based on dye **59** produced a higher open-circuit voltage (V_{OC}) of 163 mV and FF of 0.28 in comparison to **14** resulting in a similar PCE of 0.08%. This is quite remarkable since dye **59** features an inferior absorption on NiO film in comparison to **14**. The superior performance of the bulky acceptor-containing dyes **14** and **59** in comparison to **57**, **58**, and **60** is attributed to the larger torsion between the acceptor and the donor backbone which impedes back electron transfer and retards charge recombination processes in the device.

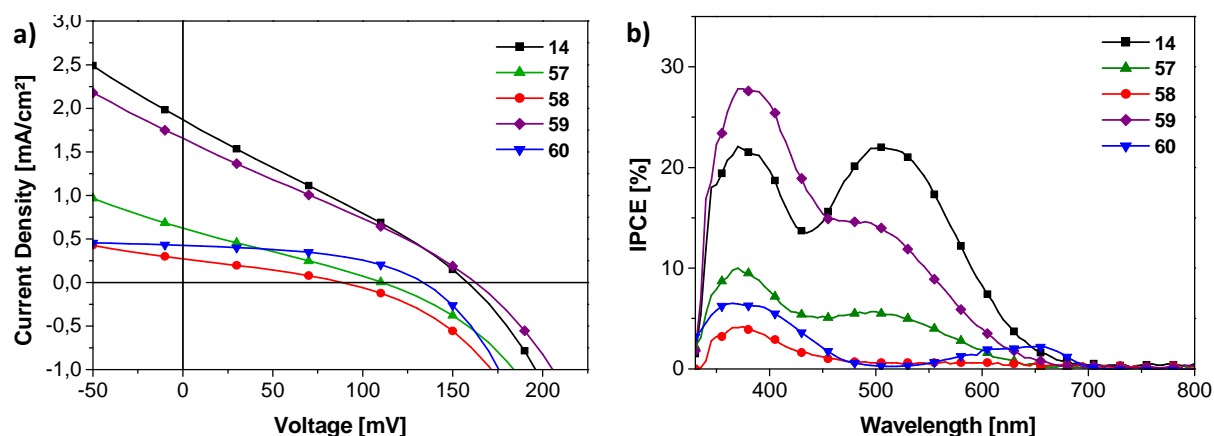


Figure 8. Current-voltage (J - V) curves (a) and IPCE spectra (b) of devices using **14** and **57-60** as sensitizers under AM 1.5 conditions (100 mW cm^{-2}) using I^-/I_3^- as redox mediator.

In comparison to the devices based on sensitizer **14** and **59**, a reduced J_{SC} of 0.62 mA cm^{-2} and a V_{OC} of 111 mV was observed for dye **57** comprising the DCV-acceptor group, thus lowering the PCE to

0.02%. The lower J_{SC} value for device **57** is attributed partly to a lower dye loading on the NiO surface (Figure 4b). The reduced V_{OC} indicates recombination losses, which might be due to a less stable charge-separated species in **57** compared to **14** and **59** as confirmed by quantum chemical calculations (*vide supra*). Sensitizer **58** containing the TCF-acceptor group performed poorly showing a very low J_{SC} of 0.27 mA cm^{-2} , V_{OC} of 88 mV, and PCE of 0.01%. As depicted in Figure 6, the LUMO level energy of triad **58** is very low lying (-4.10 eV) and is very close to the redox potential of $I_3^-/I_2^{\bullet-}$ (-4.15 eV) resulting in a weak driving force for efficient dye regeneration.^[30] Squaraine-containing triad **60** as well exhibited a moderate PCE of 0.03%. The result is explained by the very high lying HOMO energy level causing an inefficient hole injection process leading to lower J_{SC} of 0.43 mA cm^{-2} . The reduced V_{OC} of 133 mV in comparison to reference **14** and dye **59** suggests that recombination losses are more pronounced in these devices. However, triad **60** yielded the highest FF of 0.47 within this series. Triads **14** and **57-59** achieved FF values of 0.27-0.28. The lower performance of triads **57**, **58**, and **60** is attributed to a lower degree of adsorption on NiO in comparison to **14** and **59**. An incomplete surface coverage could result in close contact of electrolyte and NiO surface leading to recombination between the electrolyte and the hole.^[31]

Table 5. Photovoltaic parameters for devices made with 1.5 μm thick mesoporous NiO electrodes, sensitized with dyes **14** and **57-60**, and using an I^-/I_3^- based electrolyte.

dye	J_{SC} [mA/cm ²]	V_{OC} [mV]	Fill factor	PCE [%]	$\lambda_{IPCE,max}$ [nm]	IPCE [%]
14	1.87	158	0.27	0.08	500	22
57	0.62	111	0.27	0.02	380	10
58	0.27	88	0.27	0.01	380	6
59	1.66	163	0.28	0.08	380	28
60	0.43	133	0.47	0.03	380	5

The corresponding IPCE spectra of triads **14** and **57-60** are depicted in Figure 8b and the calculated spectral responses agree well with the measured J_{SC} values given in Table 5. Dyes **14** and **59** possessing annulated systems as acceptors showed maximum IPCE values of 22% and 28%, respectively, at 380 nm and 22% and 15% at 500 nm. Sensitizer **57** showed a moderate IPCE of 6% at the CT band at $\sim 500 \text{ nm}$, which might be due to a lower dye loading in comparison to **14** and **59** (Figure 4b). TCF containing triad **58** does not really contribute to the IPCE which is due to the above mentioned mismatch of the LUMO energy level and the redox potential of $I_3^-/I_2^{\bullet-}$. In fact, the

absorption of the electrolyte and/or the donor part of the molecule bithiophene-TPA of **58** at ~ 370 nm is responsible for the resulting photocurrent. Dye **60** revealed a very weak contribution of $\sim 2\%$ at the region of the squaraine absorption band. Similar to **58**, in devices containing **60** the electrolyte and bithiophene-TPA-unit absorption is responsible for the photocurrent generation.

3.2.6 Impedance spectroscopy of A- π -D triads **14**, **58**, and **59**

In order to further elucidate the main differences between the two best performing absorbers, impedance spectroscopy was measured for devices based on dye **14** and **59** and compared to a lower efficiency device based on dye **58**. The experiments were performed by Dr. S. Powar and Dr. P. P. Boix. The obtained spectra were fitted following a transmission line model previously developed for DSSCs which allows the determination of the parameters by means of an equivalent model fitting.^[32] The chemical capacitance (C_μ) plot (Figure 9a) showed an equivalent behavior for dye **58** and **59**, and lower values for dye **14**. This difference in the C_μ indicates a shift in the NiO valence band towards deeper positions when **14** is employed. This observation is in good agreement with the difference on the photogenerated currents for sensitizers **14** and **58**: although the former has clearly more absorbance than the latter (see Figure 4b), this difference is reduced in the IPCE (Figure 8b) because the conduction band shift hinders hole injection.

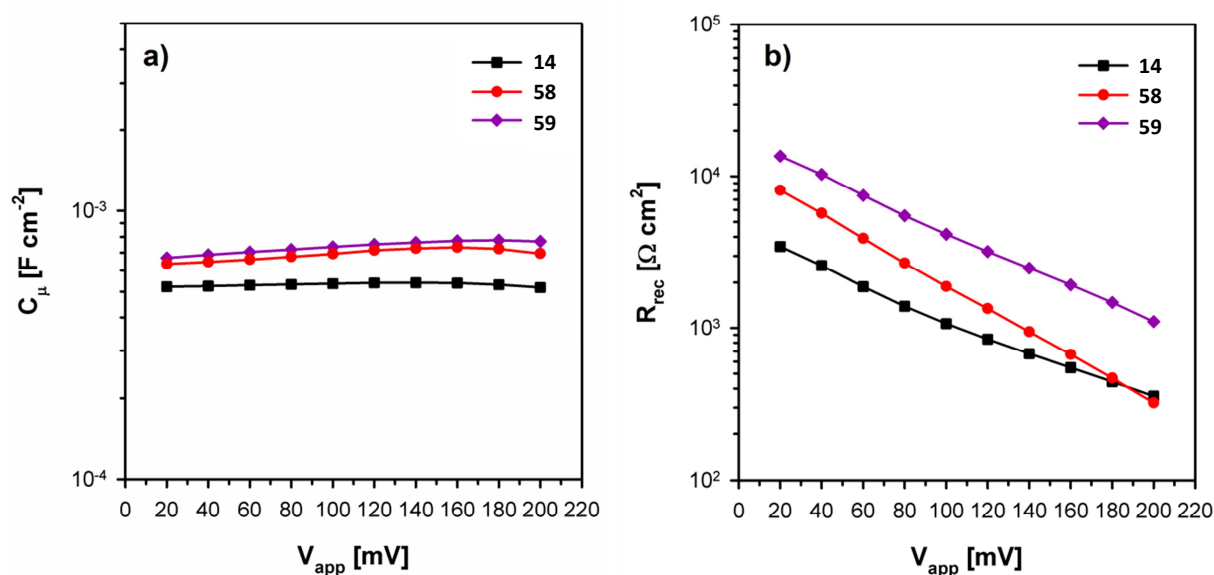


Figure 9. (a) Chemical capacitance and (b) recombination resistance extracted from the impedance spectra measured for solar cells based on sensitizer **14**, **58** and **59** in dark conditions.

The recombination resistance (R_{rec}) in Figure 9b revealed significantly higher values for devices based on dye **59** followed by dye **58** and dye **14**, which represent the lower values. A higher recombination resistance denotes lower recombination rate and therefore fewer losses of photogenerated charges. As a result, the higher R_{rec} of DCANQ derivative **59** compared to reference **14** reduces the losses allowing a better splitting of the Fermi levels for electron and holes. As a result, the solar cells using dye **59** can achieve higher V_{OC} values although the J_{SC} is lower. Sensitizer **58** presented a lower R_{rec} than **59** and a higher one than triad **14**. However, in this case the splitting of the quasi-Fermi levels and as a consequence, the lower V_{OC} , is not mainly limited by this factor, but by the lower charge generation rate which can be seen from the lower J_{SC} .

3.3 Summary

In summary, four new triads **57-60** comprising four different acceptor groups attached to a bithiophene-TPA dyad were designed. Two different synthetic approaches were used to synthesize **57-60** in good to excellent yields. In the case of triads **57** and **58**, the acceptors are introduced in an early stage of the synthesis, whereas DCANQ- and SQ-acceptor were inserted in the penultimate step to obtain **59** and **60**. Their optical and electrochemical properties were compared to the reference PMI-containing sensitizer **14**.^[2] It was shown that the absorption and the HOMO and LUMO energy levels can be easily fine-tuned by varying the electron-accepting moiety. Investigation of these dyes as sensitizers in p-type DSSCs using I^-/I_3^- as electrolyte afforded cells with PCEs in the range from 0.01 to 0.08%. Triad **14** and **58** containing the bulky PMI and DCANQ acceptors showed the highest PCEs indicating that the torsion between the acceptor and donor moieties plays a crucial role to hinder back electron transfer and retard charge recombination processes in the device. Further photophysical investigation, namely impedance spectroscopy, was performed pointing toward a lower recombination rate of injected hole and electron in devices containing **59**. This explains the similar performance of sensitizer **59** in p-type DSSCs compared to **57** despite the poor spectral matching of absorption and solar spectrum.

3.4 Experimental section

3.4.1 General procedures

^1H NMR spectra were recorded in CDCl_3 and THF-d_8 on a Bruker AMX 400 at 400 MHz. ^{13}C NMR spectra were recorded in CDCl_3 and $\text{d}_8\text{-THF}$ on a Bruker AMX 400 at 100 MHz. Chemical shifts are denoted by δ (ppm) and are referenced to the residual solvent peak (CDCl_3 : ^1H δ = 7.26 ppm and ^{13}C δ = 77.0 ppm; $\text{d}_8\text{-THF}$: ^1H δ = 3.57 ppm and ^{13}C δ = 67.2 ppm). The splitting patterns are designated as follows: s (singlet), d (doublet), t (triplet), dt (double triplet), and m (multiplet) and the assignments are DCANQ (9,10-dicyano-acenaphtho[1,2-b]quinoxalin), SQ (squaraine), Ph (phenyl), and Th (thiophene) for ^1H NMR. Mass spectra were recorded with a Varian Saturn 2000 GC-MS and with a MALDI-TOF MS Bruker Reflex 2 (dithranol as the generally used matrix and 2,5-dihydroxybenzoic acid for the free acids). Melting points were determined with a Büchi B-545 melting point apparatus and are not corrected. Gas chromatography was carried out using a Varian CP-3800 gas chromatograph. HPLC analyses were performed on a Merck Hitachi L7000 equipped with a L7455 photodiode array detector, a L7200 autosampler and a L7100 solvent delivery system using a LiChrospher column (Nucleosil 100-5 NO_2). Semi-/recycling preparative HPLC was performed on a Merck Hitachi 7000/Shimadzu CBM-20A equipped with a L7420/SPD-20A UV-vis detector and a L7150/LC-8A solvent delivery system using LiChrospher columns (Nucleosil 100-5 NO_2). Thin-layer chromatography was carried out on Silica Gel 60 F254 aluminium plates (Merck). Solvents and reagents were purified and dried by usual methods prior to use and typically used under inert gas atmosphere. The following starting materials were purchased and used without further purification: trimethylsilyl chloride (Merck), iodine (Merck), magnesium (Merck), mercury acetate (Merck), β -alanine (Merck), trifluoroacetic acid (Merck), zinc (Merck), triphenylphosphine (Merck), malononitrile (Aldrich), pinacolborane (Aldrich), *n*-butyllithium (Aldrich), tri-*t*-butylphosphonium tetrafluoroborate (Aldrich), tris(dibenzylideneacetone)dipalladium(0) (Aldrich), palladium(II)acetate (Aldrich), 1,3-bis-(diphenylphosphino)propane nickel(II) chloride (Aldrich) and 1,1'-bis(diphenylphosphino)ferrocene (Aldrich). Tetrakis(triphenylphosphine)palladium(0) was synthesized according to literature.^[33]

Optical and cyclic voltammetric measurements

UV-Vis spectra in solution were taken on a Perkin-Elmer Lambda 19 spectrometer. Thin film spectra were taken using a Varian Cary 5000 spectrometer with integrating sphere attachment (Varian Internal DRA 2500). Cyclic voltammetry experiments were performed with a computer-controlled Autolab PGSTAT30 potentiostat in a three-electrode single compartment cell (3 mL). The platinum working electrode consisted of a platinum wire sealed in a soft glass tube with a surface of $A = 0.785 \text{ mm}^2$, which was polished down to 0.25 mm with polishing paste prior to use in order to obtain

reproducible surfaces. The counter electrode consisted of a platinum wire and the reference electrode was an Ag/AgCl reference electrode. All potentials were internally referenced to the ferrocene/ferrocenium couple. For the measurements, concentrations of 5×10^{-4} mol L⁻¹ of the electroactive species were used in freshly distilled and deaerated dichloromethane/DMF (Lichrosolv, Merck) purified with an MB-SPS-800 and 0.1 M tetrabutylammonium hexafluorophosphate ((*n*-Bu)₄NPF₆, Fluka; recrystallized twice from ethanol).

Quantum chemical calculations

Density functional theory was employed with the hybrid functionals B3LYP and the basis set 6-31G* from the NWChem package.^[34] The long hexyl chains, which have no significant impact on the frontier orbitals of the chromophores, were replaced with methyl substituents in order to accelerate the convergence of optimizations.

Device fabrication

4 × 4 mm NiO films were screen printed onto F:SnO₂ glass (Nippon Sheet Glass) using a paste produced by grinding 15 g of NiO (Inframat) in ethanol, added in small aliquots. 50 mL of a 10 wt% ethyl cellulose solution in ethanol and 100 mL terpineol were then added and after mixing ethanol was evaporated to leave a terpineol based paste. These were sintered for 30 minutes at 400 °C, then 10 minutes at 550 °C, before being immersed into dye solutions (0.2 mM in DMF) for 2 hours. Films were then removed from this dye solution and rinsed subsequently in DMF and ethanol before being allowed to dry. Counter electrodes were produced by applying one drop of chloroplatinic acid solution (10 mM in ethanol) to F:SnO₂ glass and thermally decomposing by firing at 400 °C for 15 min under a gentle flow of air. Counter and working electrodes were sandwiched together with a 25 μm Surlyn (Dupont) spacer, and heated to 120 °C for 30 seconds in order to create a seal. The electrolyte solution (0.03 M iodine, 0.6 M 1-butyl-3-methylimidazolium iodide, 0.5 M 4-*t*-butylpyridine, and 0.1 M guanidinium thiocyanate in 85:15 acetonitrile: valeronitrile) was introduced through a pre-drilled hole in the counter electrode, which was subsequently sealed with another piece of Surlyn and a microscope cover slip.

Current-voltage characterization

Solar cells were tested using simulated sunlight (AM1.5, 1000 W m⁻²) provided by an Oriel solar simulator with an AM1.5 filter. Current-voltage characteristics were measured using a Keithley 2400 source meter. Cells were biased from high to low, with 10 mV steps and a 250 ms settling time between the application of a bias and current measurement. IPCE was measured with the cell held under short circuit conditions and illuminated by monochromatic light. A Cornerstone 260 monochromator was used in conjunction with an optical fibre, Keithly 2400 source meter and 150 W

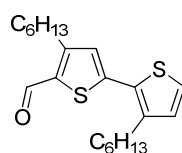
Oriel Xe lamp. Prior to testing a 30 second 'rest' period was introduced to ensure the dark current dropped to zero when the cell was short circuited. Additionally, 200 ms settling time was applied between the monochromator switching to a wavelength and measurement commencing, which was followed by an averaged reading over a 1 second period.

Impedance spectroscopy

Impedance spectroscopy was carried out with a VMP2 potentiostat (Bio-Logic-Science Instruments) using EC-lab program; under dark conditions. The DC voltage was swiped from 0 mV to 200 mV, and a AC perturbation of 10 mV was applied with a frequency varying from 500000 Hz to 0.025 Hz. The results were fitted with ZView software.

3.4.2 Synthesis

4,3'-Dihexyl-2,2'-bithiophene-5-carbaldehyde (**63**)



5-Bromo-4,3'-dihexyl-2,2'-bithiophene **47** (400 mg, 0.97 mmol), magnesium turnings (38.0 mg, 1.56 mmol), a small grain of iodine and 4.5 mL THF were refluxed for 5 h. Then the reaction mixture was cooled down to room temperature and DMF (0.15 mL, 1.93 mmol) was added dropwise. Subsequently, 1 N hydrochloric acid was used for hydrolization. The organic layer was separated and the aqueous phase was extracted with diethyl ether. The combined organic layers were washed with saturated sodium hydrogen carbonate solution and brine and dried over sodium sulfate. The solvents were removed by rotary evaporation. The crude product was purified by column chromatography (silica/DCM:*n*-hexane [1:1]) and was dried in vacuum to give bithiophene-5-carbaldehyde **63** (282 mg, 0.78 mmol, 80%) as a yellow oil.

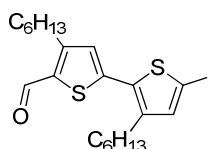
¹H NMR (400 MHz, CDCl₃): δ = 10.01 (s, 1 H, CHO), 7.24 (d, ³J = 5.2 Hz, 1 H, 5'-H), 7.02 (s, 1 H, 3-H), 6.95 (d, ³J = 5.2 Hz, 1 H, 4'-H), 2.94 (t, ³J = 7.7 Hz, 2 H, α-CH₂), 2.80 (t, ³J = 7.8 Hz, 2 H, α'-CH₂), 1.74-1.61 (m, 4 H, β-CH₂, β'-CH₂), 1.43-1.25 (m, 12 H, -CH₂-), 0.89 (t, ³J = 6.9 Hz, 3 H, -CH₃), 0.88 (t, ³J = 6.9 Hz, 3 H, -CH₃).

¹³C NMR (100 MHz, CDCl₃): δ = 181.69, 153.25, 145.53, 141.97, 136.43, 130.67, 129.86, 128.53, 125.47, 77.38, 77.06, 76.75, 31.66, 31.58, 31.41, 30.40, 29.61, 29.21, 29.00, 28.51, 22.67, 22.61, 22.56, 14.12, 14.06.

MS (CI) m/z : calcd for $C_{21}H_{30}OS_2$: 362, found $[M+H]^+$: 363.

Elemental analysis: calcd (%) for $C_{21}H_{30}OS_2$: C 69.56, H 8.34, S 17.69; found (%): C 69.73, H 8.40, S 17.95.

5'-Iodo-4,3'-dihexyl-2,2'-bithiophene-5-carbaldehyde (70)



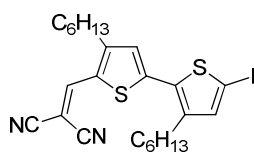
Bithiophene-5-carbaldehyde **63** (1.00 g, 2.76 mmol) was dissolved in 70 mL chloroform. Mercury acetate (0.88 g, 2.76 mmol) was added and the resulting suspension was stirred for 23 h at room temperature. Then iodine (0.70 g, 2.76 mmol) was added and the reaction mixture was stirred for further 5.5 h at room temperature. After that the mixture was poured into 1 N sodium metabisulfite solution. The organic layer was separated and the aqueous phase was extracted with DCM. The combined organic layers were washed with water and brine and dried over sodium sulfate. The solvents were removed by rotary evaporation. The crude product was purified by column chromatography (silica/DCM:*n*-hexane [2:3]) and was dried in vacuum to give 5'-iodo-bithiophene-5-carbaldehyde **70** (1.09 g, 2.23 mmol, 81%) as a yellow oil.

1H NMR (400 MHz, $CDCl_3$): δ = 10.01 (s, 1 H, CHO), 7.10 (s, 1 H, 3-H), 6.95 (s, 1 H, 4'-H), 2.93 (t, 3J = 7.7 Hz, 2 H, α -CH₂), 2.75 (t, 3J = 7.8 Hz, 2 H, α' -CH₂), 1.72-1.57 (m, 4 H, β -CH₂, β' -CH₂), 1.40-1.26 (m, 12 H, -CH₂-), 0.89 (t, 3J = 6.9 Hz, 3 H, -CH₃), 0.88 (t, 3J = 6.9 Hz, 3 H, -CH₃).

^{13}C NMR (100 MHz, $CDCl_3$): δ = 181.71, 153.12, 143.75, 143.53, 140.35, 136.78, 135.77, 128.81, 74.10, 31.57, 31.53, 31.35, 30.31, 29.23, 29.10, 28.95, 28.46, 22.54, 22.52, 14.02.

MS (CI) m/z : calcd for $C_{21}H_{29}IOS_2$: 488, found $[M+H]^+$: 489.

Elemental analysis: calcd (%) for $C_{21}H_{29}IOS_2$: C 51.63, H 5.98, S 13.13; found (%): C 51.83, H 5.87, S 12.91.

2-([3',4-Dihexyl-5'-iodo-{2,2'-bithiophen}-5-yl)methylene)malononitrile (61)


In a Schlenk-tube 5'-iodo-bithiophene-5-carbaldehyde **70** (110 mg, 0.23 mmol), malononitrile (44.6 mg, 0.68 mmol) and β -alanine (1.2 mg, 14.0 μ mol) were dissolved in 20 mL DCE:ethanol [1:1]. The reaction mixture was stirred at 60 °C for 1 d. After filtration of the hot reaction mixture the solvent was removed and the crude product was recrystallized from ethanol. Another pure fraction was obtained by column chromatography of the mother liquor (silica/DCM:*n*-hexane [1:1]). DCV iodo-bithiophene **61** (total: 113 mg, 0.21 mmol, 94%) was obtained as an orange solid.

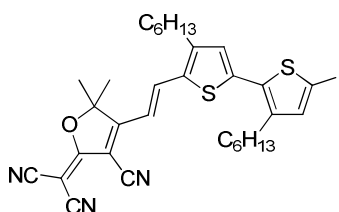
M.p.: 95 °C.

^1H NMR (400 MHz, CDCl_3): δ = 7.82 (s, 1 H, C=CH), 7.13 (s, 1 H, 3-H), 7.01 (s, 1 H, 4'-H), 2.80 (t, 3J = 7.8 Hz, 2 H, α' -CH₂), 2.74 (t, 3J = 7.8 Hz, 2 H, α -CH₂), 1.66-1.59 (m, 4 H, β -CH₂, β' -CH₂), 1.41-1.28 (m, 12 H, -CH₂-), 0.91 (t, 3J = 7.0 Hz, 3 H, -CH₃), 0.88 (t, 3J = 6.9 Hz, 3 H, -CH₃).

^{13}C NMR (100 MHz, CDCl_3): δ = 156.08, 147.53, 145.42, 144.91, 140.83, 135.09, 129.57, 127.84, 114.94, 113.64, 75.91, 74.71, 31.56, 31.49, 31.25, 30.31, 29.59, 29.09, 29.08, 29.00, 22.52, 22.51, 14.02.

MS (MALDI-TOF) m/z : calcd for $\text{C}_{24}\text{H}_{29}\text{IN}_2\text{S}_2$: 536, found $[\text{M}]^+$: 536.

Elemental analysis: calcd (%) for $\text{C}_{24}\text{H}_{29}\text{IN}_2\text{S}_2$: C 53.73, H 5.45, N 5.22, S 11.95; found (%): C 53.96, H 5.39, N 5.41, S 11.85.

(E)-2-(3-Cyano-4-[2-{3',4-dihexyl-5'-iodo-(2,2'-bithiophen)-5-yl}vinyl]-5,5-dimethylfuran-2(5H)-ylidene)malononitrile (62)


In a Schlenk-tube 5'-iodo-4,3'-dihexyl-2,2'-bithiophene-5-carbaldehyde **70** (290 mg, 0.59 mmol) and 2-(3-cyano-4,5,5-trimethyl-5H-furan-2-ylidene)malononitrile **TCF** (220 mg, 1.10 mmol) were dissolved in 14 mL DCE:ethanol [1:1]. Four drops of piperidine were added and the reaction was stirred at 60 °C for 18 h. After removal of the solvent the crude product was recrystallized from ethanol and

additionally purified via column chromatography (silica/DCM) to obtain TCF iodo bithiophene **62** (347 mg, 0.52 mmol, 87%) as a dark purple solid.

M.p.: 120-121 °C.

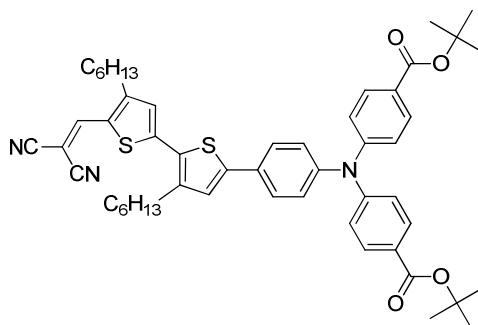
¹H NMR (400 MHz, CDCl₃): δ = 8.11 (d, ³J = 15.6 Hz, 1 H, C=CH), 7.13 (s, 1 H, 3-H), 6.99 (s, 1 H, 4'-H), 6.47 (d, ³J = 15.6 Hz, 1 H, C=CH), 2.78 (t, ³J = 7.7 Hz, 2 H, α-CH₂), 2.74 (t, ³J = 7.6 Hz, 2 H, α'-CH₂), 1.73 (s, 6 H, C-CH₃), 1.67-1.60 (m, 4 H, β-CH₂, β'-CH₂), 1.42-1.26 (m, 12 H, -CH₂-), 0.88 (t, ³J = 6.9 Hz, 3 H, -CH₃), 0.88 (t, ³J = 6.9 Hz, 3 H, -CH₃).

¹³C NMR (100 MHz, CDCl₃): δ = 175.82, 173.32, 153.37, 144.07, 142.54, 140.59, 137.58, 135.60, 134.06, 129.13, 112.09, 111.29, 111.27, 111.12, 97.09, 95.68, 75.30, 56.19, 31.51, 31.47, 31.09, 30.07, 29.35, 29.07, 29.03, 28.97, 26.32, 22.48, 22.47, 14.03, 14.00.

MS (MALDI-TOF) *m/z*: calcd for C₃₂H₃₆IN₃OS₂: 669, found [M]⁺: 669.

Elemental analysis: calcd (%) for C₃₂H₃₆IN₃OS₂: C 57.39, H 5.42, N 6.27, S 9.58; found (%): C 57.43, H 5.42, N 6.37, S 9.61.

N,N-Di(4-benzoic acid-tert-butylester)-4-(5'-[2,2-dicyanovinyl]-3,4'-dihexyl-2,2'-bithien-5-yl)-phenylamine (72)



DCV iodo-bithiophene **61** (21.4 mg, 39.9 μmol), triphenylamine boronic ester **71** (27.4 mg, 47.9 μmol), Pd₂dba₃ (1.2 mg, 1.20 μmol) and [HPtBu₃]₂BF₄ (1.2 mg, 3.99 μmol) were dissolved in 1.2 mL THF. The resulting solution was degassed and 2 molar aqueous potassium phosphate solution (0.10 mL, 200 μmol) was added. The resulting mixture was degassed and stirred at room temperature for 5 h and at 50 °C for 19 h. Then the reaction mixture was poured into water and the organic compounds were extracted with DCM. The combined organic phases were dried over sodium sulfate and the solvent was removed by rotary evaporation. The crude product was purified via column chromatography (silica/DCM:*n*-hexane [1:1]) to obtain protected DCV-bithiophene-TPA **72** (26.7 mg, 31.3 μmol, 78%) as a red solid.

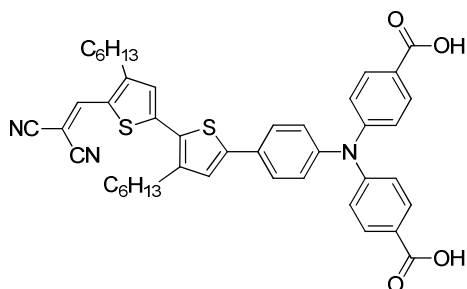
M.p.: 121-122 °C.

¹H NMR (400 MHz, CDCl₃): δ = 7.89 (d, ³J = 8.7 Hz, 4 H, (tBu)OOC-Ph-2H,6H), 7.82 (s, 1 H, C=CH), 7.52 (d, ³J = 8.6 Hz, 2 H, Ph-3H,5H), 7.16 (s, 1H, Th-3'H), 7.13-7.10 (m, 7 H, Th-4H,(tBu)OOC-Ph-3H,5H,Ph-2H,6H), 2.86 (t, ³J = 7.8 Hz, 2 H, α'-CH₂), 2.75 (t, ³J = 7.7 Hz, 2 H, α-CH₂), 1.74-1.62 (m, 4 H, β-CH₂, β'-CH₂), 1.59 (s, 18 H, tBu), 1.46-1.82 (m, 12 H, -CH₂-), 0.91 (t, ³J = 6.7 Hz, 3 H, -CH₃), 0.89 (t, ³J = 6.8 Hz, 3 H, -CH₃).

¹³C NMR (100 MHz, CDCl₃): δ = 165.25, 156.37, 150.22, 147.34, 147.27, 146.45, 144.94, 144.58, 130.89, 129.27, 129.05, 128.42, 127.13, 126.91, 126.88, 126.66, 125.66, 122.97, 115.27, 113.95, 80.87, 73.42, 31.63, 31.50, 31.30, 30.35, 30.21, 29.19, 29.10, 29.04, 28.20, 22.56, 22.52, 14.07, 14.04.

High-Resolution MS (MALDI-TOF) *m/z*: [M]⁺ calcd for C₅₂H₅₉N₃O₄S₂: 853.39470, found [M]⁺: 853.39348, δ*m/m* = 1.4 ppm.

N,N-Di(4-benzoic acid)-4-(5'-[2,2-dicyanovinyl]-3,4'-dihexyl-2,2'-bithien-5-yl)-phenylamine (57)



Protected DCV-bithiophene-TPA **72** (12.0 mg, 14.1 μmol) was dissolved in 0.25 mL DCM. After adding TFA (54 μL, 700 μmol) the reaction mixture was stirred at room temperature for 6 h. Then the mixture was poured into water and the organic compounds were extracted with chloroform. The combined organic phases were dried over sodium sulfate and the solvent was removed by rotary evaporation. The crude product was dissolved in THF and precipitated with *n*-hexane to obtain DCV-bithiophene-TPA **57** (10.0 mg, 13.5 μmol, 96%) as a red solid.

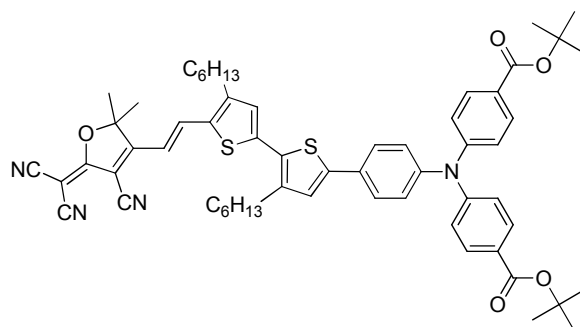
M.p.: 164-166 °C.

¹H NMR (400 MHz, THF-d₈): δ = 8.23 (s, 1 H, C=CH), 7.93 (d, ³J = 8.7 Hz, 4 H, (tBu)OOC-Ph-2H,6H), 7.66 (d, ³J = 8.6 Hz, 2 H, Ph-3H,5H), 7.38 (s, 1 H, Th-3'H), 7.29 (s, 1 H, Th-4H), 7.18 (d, ³J = 8.6 Hz, 2 H, Ph-2H,6H), 7.14 (d, ³J = 8.7 Hz, 4 H, (tBu)OOC-Ph-3H,5H), 2.93-2.86 (m, 4 H, α-CH₂, α'-CH₂), 1.71-1.63 (m, 2 H, β-CH₂), 1.50-1.29 (m, 14 H, β-CH₂, -CH₂-), 0.93-0.88 (m, 6 H, -CH₃).

^{13}C NMR (100 MHz, THF- d_8): δ = 166.93, 157.50, 151.24, 148.66, 147.38, 146.59, 145.38, 145.06, 131.82, 130.34, 130.06, 129.23, 128.16, 128.04, 127.56, 126.62, 126.51, 123.64, 115.43, 114.75, 74.66, 32.46, 32.40, 32.09, 31.06, 30.91, 30.44, 29.99, 29.77, 29.23, 23.29, 14.24, 14.23.

High-Resolution MS (MALDI-TOF) m/z : calcd for $\text{C}_{44}\text{H}_{43}\text{N}_3\text{O}_4\text{S}_2$: 741.26950, found $[\text{M}]^+$: 741.26900, $\delta m/m$ = 0.7 ppm.

(E)-N,N-Di(4-benzoic acid-tert-butylester)-4-(5'-[2-{4-cyano-5-(dicyanomethylene)-2,2-dimethyl-2,5-dihydrofuran-3-yl}vinyl]-3,4'-dihexyl-2,2'-bithien-5-yl)-phenylamine (73)



TCF iodo-bithiophene **62** (26.0 mg, 38.8 μmol), triphenylamine boronic ester **71** (28.0 mg, 50.0 μmol) and $\text{Pd}(\text{PPh}_3)_4$ (1.8 mg, 1.55 μmol) were dissolved in 1.2 mL THF. The resulting solution was degassed and 2 molar aqueous potassium phosphate solution (0.06 mL, 120 μmol) was added. The resulting mixture was degassed again and stirred at 80 $^\circ\text{C}$ for 18 h. Then the mixture was poured into saturated aqueous ammonium chloride solution and the organic compounds were extracted with DCM. The combined organic phases were dried over sodium sulfate and the solvent was removed by rotary evaporation. The crude product was purified via column chromatography (silica/*n*-hexane:ethyl acetate [8:2]) and HPLC (nucleosil/*n*-hexane:DCM [3:7]) to obtain protected TCF-bithiophene-TPA **73** (17.2 mg, 17.4 μmol , 45%) as a dark blue solid.

M.p.: 140-141 $^\circ\text{C}$.

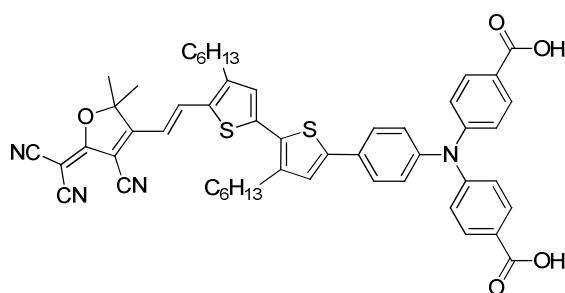
^1H NMR (400 MHz, CDCl_3): δ = 8.13 (d, 3J = 15.5 Hz, 1 H, C=CH), 7.89 (d, 3J = 8.7 Hz, 4 H, (tBu)OOC-Ph-2H,6H), 7.52 (d, 3J = 8.6 Hz, 2 H, Ph-3H,5H), 7.17 (s, 1 H, Th'-3H), 7.14-7.10 (m, 7 H, Th-4H,(tBu)OOC-Ph-3H,5H,Ph-2H,6H), 6.46 (d, 3J = 15.5 Hz, 1 H, C=CH), 2.87 (t, 3J = 7.7 Hz, 2 H, α' -CH $_2$), 2.76 (t, 3J = 7.6 Hz, 2 H, α -CH $_2$), 1.77-1.63 (m, 10 H, C-CH $_3$, α -CH $_2$), 1.59 (s, 18 H, tBu), 1.48-1.30 (m, 12 H, -CH $_2$ -), 0.92-0.87 (m, 6 H, -CH $_3$).

^{13}C NMR (100 MHz, CDCl_3): δ = 175.95, 173.22, 165.25, 153.84, 150.21, 146.42, 144.63, 144.19, 144.10, 137.62, 133.65, 130.90, 129.32, 129.06, 128.58, 126.87, 126.73, 126.68, 125.67, 122.98,

112.26, 111.49, 111.44, 110.57, 96.92, 95.07, 80.89, 55.93, 31.63, 31.54, 31.18, 30.17, 30.03, 29.20, 29.16, 29.06, 28.20, 26.44, 22.57, 22.52, 14.10, 14.05.

High-Resolution MS (MALDI-TOF) m/z : calcd for $C_{60}H_{66}N_4O_5S_2$: 986.44746, found $[M]^+$: 986.44642, $\delta m/m = 1.1$ ppm.

(E)-N,N-Di(4-benzoic acid)-4-(5'-[2-{4-cyano-5-(dicyanomethylene)-2,2-dimethyl-2,5-dihydrofuran-3-yl}vinyl]-3,4'-dihexyl-2,2'-bithien-5-yl)-phenylamine (58)



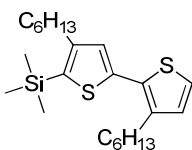
Protected TCF-bithiophene-TPA **73** (18.5 mg, 18.7 μ mol) was dissolved in 0.5 mL DCM. After adding TFA (72 μ L, 937 μ mol) the reaction mixture was stirred for 6 h at room temperature. After drying in vacuum, the crude product was dissolved in THF and precipitated with *n*-hexane to obtain TCF-bithiophene-TPA **58** (15.0 mg, 11.4 μ mol, 91%) as a dark blue solid.

M.p.: 174-176 °C.

^1H NMR (400 MHz, CDCl_3): δ = 8.13 (d, 3J = 15.5 Hz, 1 H, C=CH), 8.02 (d, 3J = 8.7 Hz, 4 H, (tBu)OOC-Ph-2H,6H), 7.58 (d, 3J = 8.6 Hz, 2 H, Ph-3H,5H), 7.19-7.17 (m, 7 H, Th'-3H,(tBu)OOC-Ph-2H,6H,Ph-3H,5H), 7.11 (s, 1 H, Th-4H), 6.48 (d, 3J = 15.5 Hz, 1 H, C=CH), 2.86 (t, 3J = 7.7 Hz, 2 H, α' -CH₂), 2.77 (t, 3J = 7.5 Hz, 2 H, α -CH₂), 1.75-1.64 (m, 10 H, C-CH₃, β -CH₂, β' -CH₂), 1.47-1.28 (m, 12 H, -CH₂-), 0.92-0.86 (m, 6 H, -CH₃).

^{13}C NMR (100 MHz, CDCl_3): δ = 175.89, 170.71, 153.72, 151.22, 145.82, 144.44, 144.13, 143.75, 137.55, 133.75, 133.09, 131.85, 130.26, 129.34, 128.68, 127.10, 126.95, 126.48, 126.47, 123.68, 122.90, 112.17, 111.43, 111.39, 110.75, 96.93, 95.35, 56.09, 31.64, 31.55, 31.19, 30.16, 30.07, 29.20, 29.17, 29.06, 26.46, 22.58, 22.53, 14.10, 14.05.

High-Resolution MS (MALDI-TOF) m/z : calcd for $C_{52}H_{50}N_4O_5S_2$: 874.32226, found $[M]^+$: 874.32184, $\delta m/m = 0.5$ ppm.

5-Trimethylsilyl-4,3'-dihexyl-2,2'-bithiophene (76)

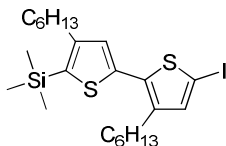
n-BuLi (0.39 mL, 0.62 mmol) was added dropwise to a solution of 5-bromo-3',4'-dihexyl-2,2'-bithiophene **47** (250 mg, 0.60 mmol) in 3 mL THF at -78 °C. After the addition the solution was stirred for 15 min at -78 °C. TMS chloride (100 μ L, 0.79 mmol) was added, subsequently. The cooling bath was removed and the reaction was stirred until it had warmed up to room temperature. Then the mixture was poured into water, the organic layer was separated and the aqueous phase was extracted with diethyl ether. The combined organic phases were washed with brine and dried over sodium sulfate and the solvent was removed by rotary evaporation. The crude product was purified by column chromatography (silica/*n*-hexane) to give 5-trimethylsilyl-bithiophene **76** (203 mg, 0.50 mmol, 83%) as a yellow oil.

^1H NMR (400 MHz, CDCl_3): δ = 7.13 (d, 3J = 5.2 Hz, 1 H, 5'-H), 7.03 (s, 1 H, 3-H), 6.91 (d, 3J = 5.2 Hz, 4'-H), 2.75 (t, 3J = 7.9 Hz, 2 H, α' -CH₂), 2.64 (t, 3J = 7.9 Hz, 2 H, α -CH₂), 1.66-1.57 (m, 4 H, β -CH₂, β' -CH₂), 1.41-1.26 (m, 12 H, -CH₂-), 0.90 (t, 3J = 6.8 Hz, 3 H, Th'-CH₃), 0.88 (t, 3J = 6.7 Hz, 3 H, Th-CH₃), 0.35 (s, 9 H, Si-CH₃).

^{13}C NMR (100 MHz, CDCl_3): δ = 150.67, 140.04, 139.16, 132.88, 130.97, 129.92, 129.13, 123.29, 31.76, 31.72, 31.64, 31.45, 30.63, 29.40, 29.18, 22.62, 14.10, 0.40.

MS (EI) *m/z*: calcd for $\text{C}_{23}\text{H}_{38}\text{S}_2\text{Si}$: 406, found $[\text{M}]^+$: 406.

Elemental analysis: calcd (%) for $\text{C}_{23}\text{H}_{38}\text{S}_2\text{Si}$: C 67.91, H 9.42, S 15.77; found (%): C 68.18, H 9.40, S 15.56.

5-Iodo-5'-trimethylsilyl-3,4'-dihexyl-2,2'-bithiophene (77)

n-Butyllithium (1.6 M, 4.36 mL, 6.97 mmol) was added dropwise to a solution of 5-trimethylsilyl-bithiophene **76** (2.70 g, 6.64 mmol) in 32 mL THF at -78 °C. After the addition the solution was stirred for 15 min at -78 °C and subsequently iodine (2.02 g, 7.97 mmol) dissolved in 21 mL THF was added in one portion. Then after stirring for 5 min at -78 °C the cooling bath was removed and the mixture

was allowed to warm up to room temperature. The reaction mixture was then poured into water. The organic layer was separated and the aqueous phase was extracted with diethyl ether. The combined organic phases were washed with 1 N sodium metabisulfite solution, water and brine, dried over sodium sulfate and the solvent was removed by rotary evaporation. The crude product was purified by column chromatography (silica/petroleum ether) to obtain 5-iodo-5'-trimethylsilyl-bithiophene **77** (3.27 g, 6.14 mmol, 92%) as a slightly yellow oil.

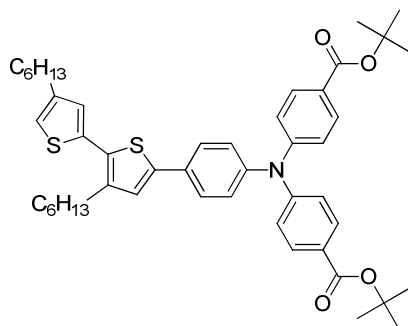
^1H NMR (400 MHz, CDCl_3): δ = 7.04 (s, 1 H, 4-H), 6.98 (s, 1 H, 3'-H), 2.70 (t, 3J = 7.9 Hz, 2 H, $\alpha\text{-CH}_2$), 2.63 (t, 3J = 7.9 Hz, 2 H, $\alpha'\text{-CH}_2$), 1.64-1.55 (m, 4 H, $\beta\text{-CH}_2$, $\beta'\text{-CH}_2$), 1.41-1.28 (m, 12 H, $-\text{CH}_2-$), 0.91-0.87 (m, 6 H, $-\text{CH}_3$), 0.35 (s, 9 H, Si-CH_3).

^{13}C NMR (100 MHz, CDCl_3): δ = 150.33, 140.66, 139.34, 138.28, 136.79, 133.38, 129.15, 70.78, 31.40, 31.32, 31.23, 31.05, 30.19, 29.01, 28.73, 28.51, 22.26, 22.23, 13.71, 0.02.

MS (EI m/z : calcd for $\text{C}_{23}\text{H}_{37}\text{IS}_2\text{Si}$: 532, found $[\text{M}+\text{H}]^+$: 533.

Elemental analysis: calcd (%) for $\text{C}_{23}\text{H}_{37}\text{IS}_2\text{Si}$: C 51.86, H 7.00, S 12.04; found (%): C 52.16, H 6.78, S 12.07.

N,N-Di(4-benzoic acid-tert-butylester)-4-(3,4'-dihexyl-2,2'-bithien-5-yl)-phenylamine (**78**)



5-Iodo-5'-trimethylsilyl-bithiophene **77** (565 mg, 1.06 mmol), triphenylamine boronic ester **71** (816 mg, 1.43 mmol), PPh_3 (31.2 mg, 119 μmol) and $\text{Pd}(\text{OAc})_2$ (8.02 mg, 35.7 μmol) were dissolved in 9 mL THF. The resulting solution was degassed and 2 molar aqueous potassium phosphate solution (1.79 mL, 3.57 mmol) was added. The resulting mixture was degassed again and stirred for 19 h at 80 $^\circ\text{C}$. $(n\text{-Bu})_4\text{NF}$ trihydrate (1.45 g, 4.60 mmol) was then added to the mixture and stirred at 80 $^\circ\text{C}$ for further 2 h. After that the mixture was poured into saturated aqueous ammonium chloride solution. The organic layer was separated and the aqueous phase was extracted with DCM. The combined organic phases were dried over sodium sulfate and the solvent was removed by rotary evaporation. The crude product was purified via column chromatography (silica/*n*-hexane:ethyl acetate [19:1]) to obtain bithiophene-TPA **78** (734 mg, 0.95 mmol, 90%) as a yellow solid.

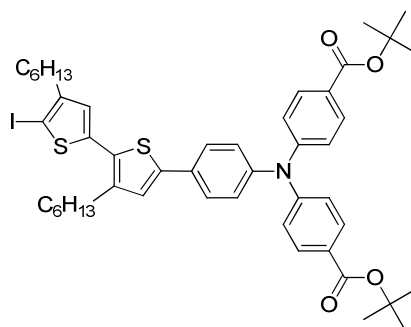
M.p.: 217-219 °C.

¹H NMR (400 MHz, CDCl₃): δ = 7.89 (d, ³J = 8.8 Hz, 4 H, (tBu)OOC-Ph-2H,6H), 7.52 (d, ³J = 8.6 Hz, 2 H, Ph-3H,5H), 7.12-7.09 (m, 7 H, Th'-5H,(tBu)OOC-Ph-3H,5H,Ph-2H,6H), 6.98 (s, 1 H, Th'-3H), 6.89 (s, 1 H, Th-4H), 2.76 (t, ³J = 7.8 Hz, 2 H, α'-CH₂), 2.62 (t, ³J = 7.7 Hz, 2 H, α-CH₂), 1.71-1.62 (m, 4 H, β-CH₂,β'-CH₂), 1.60 (s, 18 H, tBu), 1.43-1.30 (m, 12 H, -CH₂-), 0.91 (t, ³J = 6.5 Hz, 3 H, -CH₃), 0.90 (m, ³J = 6.9 Hz, 3 H, -CH₃).

¹³C NMR (100 MHz, CDCl₃): δ = 165.31, 150.45, 145.41, 143.62, 140.65, 140.30, 135.75, 130.84, 130.76, 130.62, 127.10, 126.65, 126.37, 126.08, 125.87, 122.66, 119.91, 80.73, 31.67, 31.65, 30.57, 30.49, 30.38, 29.43, 29.21, 28.99, 28.23, 22.60, 14.07.

High-Resolution MS (MALDI-TOF) *m/z*: calcd for C₆₀H₆₆N₄O₅S₂: 777.38855, found [M]⁺: 777.38758, δ*m/m* = 1.3 ppm.

N,N-Di(4-benzoic acid-tert-butylester)-4-(5'-iodo-3,4'-dihexyl-2,2'-bithien-5-yl)-phenylamine (79)



Bithiophene-TPA **78** (2.09 g, 2.69 mmol) was dissolved in 55 mL DCM. Mercury acetate (0.86 g, 2.69 mmol) was added and the resulting suspension was stirred for 20 h at room temperature. Then iodine (0.69 g, 2.71 mmol) was added and reaction mixture was stirred for further 5 h at room temperature. After that the mixture was filtered over a short column (basic alumina/DCM). After removing the solvent and drying in vacuum iodo-bithiophene-TPA **79** (2.32 g, 2.57 mmol, 96%) was obtained as a yellow solid.

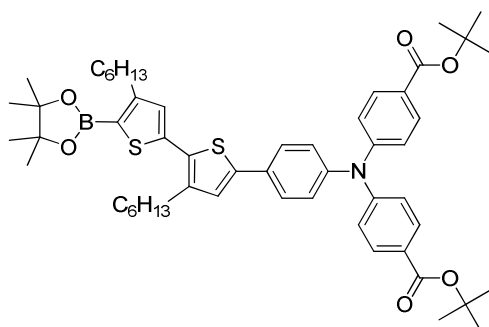
M.p.: 240-242 °C.

¹H NMR (400 MHz, CDCl₃): δ = 7.88 (d, ³J = 8.7 Hz, 4 H, (tBu)OOC-Ph-2H,6H), 7.50 (d, ³J = 8.6 Hz, 2 H, Ph-3H,5H), 7.11-7.09 (m, 7 H, Th'-3H,(tBu)OOC-Ph-3H,5H,Ph-2H,6H), 6.79 (s, 1 H, s, 1H, Th-4H), 2.72 (t, ³J = 7.8 Hz, 2 H, α'-CH₂), 2.55 (t, ³J = 7.7 Hz, 2 H, α-CH₂), 1.70-1.59 (m, 22 H, tBu, β-CH₂, β'-CH₂), 1.43-1.30 (m, 12 H, -CH₂-), 0.92-0.88 (m, 6 H, -CH₃).

^{13}C NMR (100 MHz, CDCl_3): δ = 165.30, 150.41, 147.60, 145.61, 141.26, 140.91, 140.72, 130.86, 130.47, 129.66, 126.71, 126.44, 126.32, 126.02, 125.82, 122.72, 80.76, 73.85, 32.34, 31.64, 31.63, 30.55, 29.93, 29.44, 29.18, 28.89, 28.23, 22.59, 14.07.

High-Resolution MS (MALDI-TOF) m/z : calcd for $\text{C}_{48}\text{H}_{58}\text{INO}_4\text{S}_2$: 903.28519, found $[\text{M}]^+$: 903.28438, $\delta m/m$ = 0.9 ppm.

N,N-Di(4-benzoic acid-tert-butylester)-4-(5'-[4,4,5,5-tetramethyl-[1,3,2]dioxaborolan-2-yl]-3,4'-hexyl-2,2'-bithien-5-yl)-phenylamine (80)



Iodo-bithiophene-TPA **79** (440 mg, 487 μmol), zinc powder (73.2 mg, 1.12 mmol), 1,3-bis(diphenylphosphino)propane nickel(II) chloride (13.2 mg, 24.3 μmol) and 1,1'-bis(diphenylphosphino)ferrocene (27.0 mg, 48.7 μmol) were added in a Schlenk-tube, which was then evacuated for several minutes. Then 5 mL THF and triethylamine (0.2 mL, 1.46 mmol) were added. After degassing pinacolborane (156 mg, 1.22 mmol) was added and the resulting reaction mixture was stirred for 1.5 h at 100 $^{\circ}\text{C}$. Then saturated aqueous ammonium chloride solution was added slowly and the organic compounds were extracted with DCM. After drying over sodium sulfate the solvent was removed via rotary evaporation. The crude product was purified by column chromatography (silica/*n*-hexane:ethyl acetate [92:8]) to obtain bithiophene-TPA boronic ester **80** (306 mg, 338 μmol , 70 %) as a yellow solid.

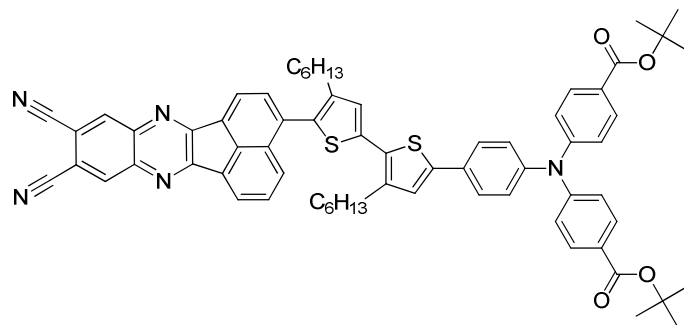
M.p.: 73-74 $^{\circ}\text{C}$.

^1H NMR (400 MHz, CDCl_3): δ = 7.88 (d, 3J = 8.7 Hz, 4 H, (tBu)OOC-Ph-2H,6H), 7.51 (d, 3J = 8.6 Hz, 2 H, Ph-3H,5H), 7.11-7.09 (m, 7 H, Th'-3H,(tBu)OOC-Ph-3H,5H,Ph-2H,6H), 7.07 (s, 1 H, Th-4H), 2.86 (t, 3J = 7.6 Hz, 2 H, α' -CH₂), 2.80 (t, 3J = 7.8 Hz, 2 H, α -CH₂), 1.71-1.61 (m, 22 H, tBu, β -CH₂, β' -CH₂), 1.42-1.28 (m, 12 H, -CH₂-), 0.89 (t, 3J = 6.5 Hz, 6 H, -CH₃).

^{13}C NMR (100 MHz, CDCl_3): δ = 165.33, 155.02, 150.42, 145.45, 141.67, 140.96, 140.79, 130.84, 130.65, 130.60, 128.88, 126.67, 126.32, 126.06, 125.98, 122.67, 83.59, 80.75, 31.69, 31.66, 30.37, 30.27, 29.51, 29.19, 28.96, 28.23, 24.78, 22.61, 14.13, 14.10.

High-Resolution MS (MALDI-TOF) m/z : calcd for $C_{48}H_{58}INO_4S_2$: 903.47376, found $[M]^+$: 903.47322, $\delta m/m = 0.6$ ppm.

N,N-Di(4-benzoic acid-tert-butylester)-4-(5'-(9,10-dicyano-acenaphtho[1,2-b]quinoxalin-3-yl)-3,4'-dihexyl-2,2'-bithien-5-yl)-phenylamine (83)



3-Bromo-9,10-dicyano-acenaphtho[1,2-b]quinoxaline **81** (15.0 mg, 39.1 μ mol), bithiophene-TPA boronic ester **80** (42.5 mg, 47.0 μ mol), Pd_2dba_3 (1.0 mg, 0.98 μ mol) and $[HPtBu_3]BF_4$ (0.6 mg, 1.96 μ mol) were added in a Schlenk-tube, which was then evacuated for several minutes. Then 2 mL tetrahydrofuran and 2 molar aqueous potassium phosphate solution (0.08 mL, 157 μ mol) was added. The resulting mixture was degassed and stirred at 80 °C for 15 h. After that the mixture was poured into water and the organic compounds were extracted with dichloromethane. The combined organic phases were dried over sodium sulfate and the solvent was removed by rotary evaporation. The crude product was purified via column chromatography (silica/ *n*-hexane:ethyl acetate [4:1] and silica/*n*-hexane:dichloromethane [1:1] to [3:1]) to obtain protected DCANQ-bithiophene-TPA **83** (36.2 mg, 33.5 μ mol, 86%) as a red solid.

M.p.: 242-243 °C.

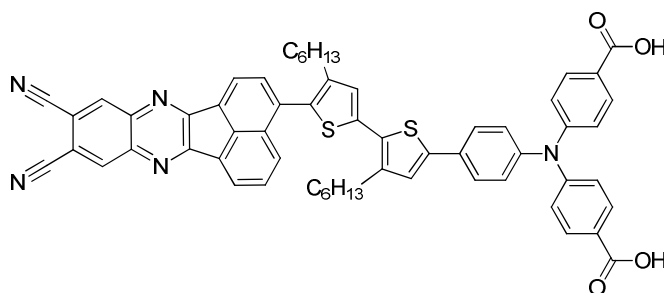
1H NMR (400 MHz, $CDCl_3$): δ = 8.68 (s, 2 H, DCANQ-8H, DCANQ-11H), 8.58-8.56 (m, 2 H, DCANQ-1H, DCANQ-6H), 8.34 (d, 3J = 8.4 Hz, 1 H, DCANQ-4H), 7.98-7.94 (m, 2 H, 2-H, DCANQ-5H), 7.89 (d, 3J = 8.7 Hz, 4 H, (tBu)OOC-Ph-2H,6H), 7.54 (d, 3J = 8.6 Hz, 2 H, Ph-3H,5H), 7.20 (s, 1 H, Th'-3H), 7.16 (s, 1 H, Th-4H), 7.14-7.10 (m, 6 H, (tBu)OOC-Ph-3H,5H,Ph-2H,6H), 2.85 (t, 3J = 7.8 Hz, 2 H, α' -CH₂), 2.55 (t, 3J = 7.6 Hz, 2 H, α CH₂), 1.77-1.69 (m, 2 H, β' -CH₂), 1.59 (s, 18 H, tBu), 1.47-1.40 (m, 2 H, β -CH₂), 1.35-1.10 (m, 12 H, CH₂-), 0.88 (t, 3J = 6.7 Hz, 3 H, -CH₃), 0.75 (t, 3J = 6.9 Hz, 3 H, -CH₃).

^{13}C NMR (100 MHz, $CDCl_3$): δ = 165.36, 157.37, 156.87, 150.42, 145.70, 142.45, 142.36, 142.31, 141.30, 140.95, 138.26, 137.22, 137.06, 136.91, 132.47, 131.80, 130.91, 130.75, 130.42, 130.23, 129.81, 129.74, 129.71, 129.43, 127.56, 126.73, 126.46, 126.15, 126.07, 124.09, 123.51, 122.79,

115.31, 113.44, 113.36, 80.87, 31.73, 31.48, 30.70, 30.63, 29.73, 29.32, 29.15, 28.93, 28.28, 22.68, 22.51, 14.17, 14.03.

High-Resolution MS (MALDI-TOF) m/z : calcd for $C_{68}H_{65}N_5O_4S_2$: 1079.44780, found $[M]^+$: 1079.44666, $\delta m/m = 1.1$ ppm.

N,N-Di(4-benzoic acid)-4-(5'-[9,10-dicyano-acenaphtho[1,2-b]quinoxalin-3-yl]-3,4'-dihexyl-2,2'-bithien-5-yl)-phenylamine (59)



Protected DCANQ-bithiophene-TPA **83** (31.0 mg, 28.7 μ mol) was dissolved in 1 mL DCM. After adding TFA (111 μ L, 1.43 mmol) the reaction mixture was stirred at room temperature for 6 h. After drying in vacuum, the crude product was dissolved in THF and precipitated with *n*-hexane to obtain DCANQ-bithiophene-TPA **59** (26.3 mg, 27.2 μ mol, 95%) as a red solid.

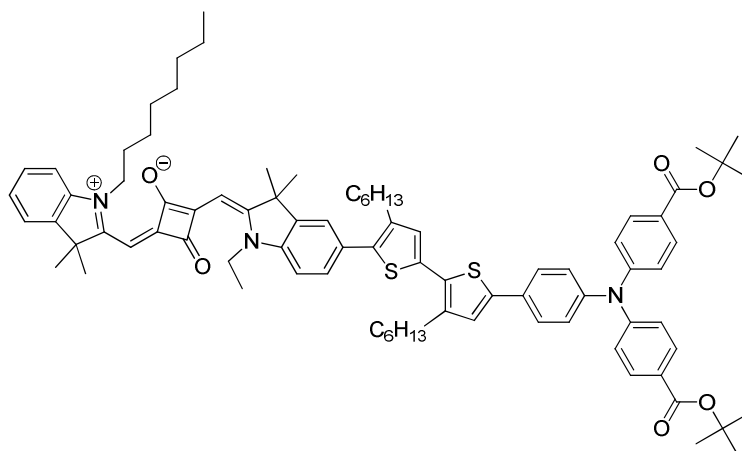
M.p.: 267-269 °C.

1H NMR (400 MHz, THF- d_8): δ = 8.85 (s, 1 H, DCANQ-8H), 8.84 (s, 1 H, DCANQ-11H), 8.61-8.57 (m, 2 H, 1-H, DCANQ-6H), 8.34 (d, $^3J = 8.2$ Hz, 1 H, DCANQ-4H), 8.03-8.01 (m, 2 H, DCANQ-2H, DCANQ-5H), 7.93 (d, $^3J = 8.8$ Hz, 4 H, (tBu)OOC-Ph-2,6), 7.66 (d, $^3J = 8.6$ Hz, 2 H, Ph-3,5), 7.36 (s, 1 H, Th'-3H), 7.32 (s, 1 H, Th-4H), 7.20-7.14 (m, 6 H, (tBu)OOC-Ph-3H,5H,Ph-2H,6H), 2.90 (t, $^3J = 7.6$ Hz, 2 H, α' -CH₂), 2.59 (t, $^3J = 7.6$ Hz, 2 H, α -CH₂), 1.79-1.73 (m, 2 H, β' -CH₂), 1.62-1.57 (m, 2 H, β -CH₂), 1.48-1.43 (m, 2 H, γ' -CH₂), 1.38-1.31 (m, 4 H, γ -CH₂, δ' -CH₂), 1.21-1.10 (m, 6 H, -CH₂-), 0.89 (t, $^3J = 7.0$ Hz, 3 H, Th-CH₃), 0.75 (t, $^3J = 7.0$ Hz, 3H, Th'-CH₃).

^{13}C NMR (100 MHz, THF- d_8): δ = 166.84, 157.93, 157.44, 151.40, 146.69, 143.36, 143.25, 143.08, 142.11, 141.59, 138.73, 137.65, 137.64, 137.63, 137.61, 137.20, 133.51, 132.61, 131.81, 131.64, 131.35, 131.28, 130.79, 130.50, 130.35, 130.28, 128.31, 127.31, 127.11, 126.97, 126.19, 124.33, 123.73, 123.44, 115.91, 114.40, 114.34, 32.50, 32.23, 31.34, 31.28, 30.28, 30.01, 29.70, 29.64, 23.35, 23.18, 14.27, 14.11.

High-Resolution MS (MALDI-TOF) m/z : calcd for $C_{60}H_{49}N_5O_4S_2$: 967.32260, found $[M]^+$: 967.32190, $\delta m/m = 0.7$ ppm.

(E)-2-((Z)-[5-{5'-(4-[Bis(4-(tert-butoxycarbonyl)phenyl)amino]phenyl)-3',4'-dihexyl-(2,2'-bithiophene)-5-yl]-1-ethyl-3,3-dimethylindolin-2-ylidene)methyl)-4-([3,3-dimethyl-1-octyl-3H-indol-1-ium-2-yl]methylene)-3-oxocyclobut-1-enolate (84)



(E)-2-((Z)- [5-bromo-1-ethyl-3,3-dimethylindolin-2-ylidene)methyl)-4-([3,3-dimethyl-1-octyl-3H-indol-1-ium-2-yl]methylene)-3-oxocyclobut-1-enolate **82** (35.0 mg, 56.9 μmol), bithiophene-TPA boronic ester **80** (56.5 mg, 62.5 μmol), potassium carbonate (15.7 mg, 114 μmol), $\text{Pd}(\text{PPh}_3)_4$ (3.3 mg, 2.84 μmol) and PPh_3 (7.46 mg, 28.43 μmol) were added in a Schlenk-tube, which was then evacuated for several minutes. Then 1.7 mL toluene and 0.33 mL ethanol were added. The resulting mixture was degassed and stirred at 80 $^\circ\text{C}$ for 12 h. After that the mixture was poured into saturated aqueous ammonium chloride solution and the organic compounds were extracted with DCM. The combined organic phases were dried over sodium sulfate and the solvent was removed by rotary evaporation. The crude product was purified via column chromatography (silica/ethyl acetate:methanol [97:3]) to obtain protected SQ-bithiophene-TPA **84** (63.7 mg, 48.5 μmol , 85%) as a green solid.

M.p.: 166-168 $^\circ\text{C}$.

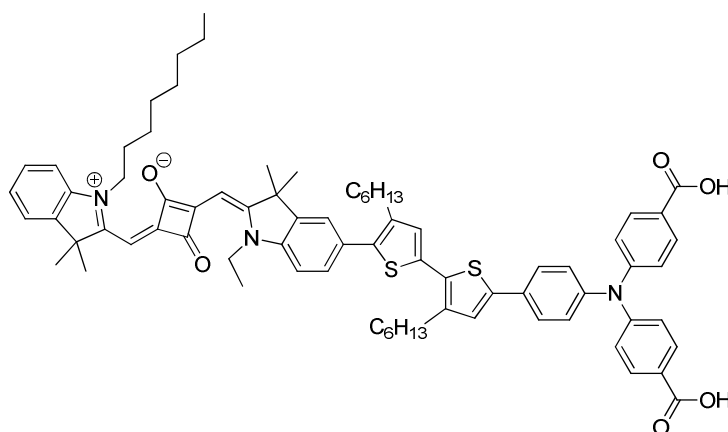
^1H NMR (400 MHz, CDCl_3): δ = 7.88 (d, 3J = 8.7 Hz, 4 H, (tBu)OOC-Ph-2H,6H), 7.53 (d, 3J = 8.6 Hz, 2 H, Ph-3H,5H), 7.42-7.36 (m, 3 H, 3x SQ-H), 7.33-7.29 (m, 1 H, SQ-H), 7.17-7.09 (m, 8 H, SQ-H, Th'-3H, (tBu)OOC-Ph-3H,5H, Ph-2H,6H), 7.04 (s, 1 H, Th-4H), 7.03-6.99 (m, 2 H, 2x SQ-H), 5.99 (br s, 2 H, C=CH), 4.14-3.90 (m, 4 H, α -CH₂-SQ), 2.81 (t, 3J = 7.8 Hz, 2 H, α' -CH₂), 2.65 (t, 3J = 7.8 Hz, 2 H, α -CH₂), 1.84-1.80 (m, 14 H, 4x indole-CH₃, N-CH₂-CH₃), 1.74-1.63 (m, 4 H, β -CH₂, β' -CH₂), 1.58 (s, 18 H, tBu), 1.44-1.25 (m, 25H, N-CH₂-CH₃, all other CH₂), 0.91-0.85 (m, 9 H, -CH₂-CH₂-CH₃).

^{13}C NMR (100 MHz, CDCl_3): δ = 170.45, 165.26, 150.36, 145.37, 142.31, 140.60, 140.32, 139.02, 137.33, 134.07, 130.80, 130.59, 130.29, 129.72, 128.80, 128.13, 127.71, 126.58, 126.27, 126.02, 125.97, 123.80, 123.09, 122.62, 122.25, 109.45, 108.85, 80.70, 49.38, 49.08, 43.76, 31.68, 31.63,

31.60, 31.53, 30.97, 30.53, 29.64, 29.51, 29.27, 29.20, 29.10, 28.81, 28.17, 27.07, 27.03, 26.92, 22.59, 22.57, 22.55, 14.08, 14.05, 14.03, 12.01.

High-Resolution MS (MALDI-TOF) m/z : calcd for $C_{84}H_{101}N_3O_6S_2$: 1311.71318, found $[M]^+$: 1311.71318, $\delta m/m = 0.0$ ppm.

(E)-2-((Z)-[5-{5'-(4-[Bis(4-carboxyphenyl)amino]phenyl)-3',4-dihexyl-(2,2'-bithiophen)-5-yl]-1-ethyl-3,3-dimethylindolin-2-ylidene)methyl)-4-([3,3-dimethyl-1-octyl-3H-indol-1-ium-2-yl]methylene)-3-oxocyclobut-1-enolate (60)



Protected SQ-bithiophene-TPA **84** (47.5 mg, 36.2 μ mol) was dissolved in 2.2 mL DCM. After adding TFA (0.83 μ L, 1.09 mmol) the reaction mixture was stirred at room temperature for 6 h. After drying in vacuum, the crude product was dissolved in DCM and precipitated with *n*-hexane to obtain SQ-bithiophene-TPA **60** (42.7 mg, 35.6 μ mol, 98%) as a red solid.

M.p.: 175-176 $^{\circ}$ C.

1H NMR (400 MHz, $CDCl_3$): δ = 8.01 (d, 3J = 8.8 Hz, 4 H, (tBu)OOC-Ph-2H,6H), 7.58 (d, 3J = 8.5 Hz, 2 H, Ph-3H,5H), 7.43-7.33 (m, 4 H, 4x SQ-H), 7.22-7.16 (m, 8 H, SQ-H, Th'-3H, (tBu)OOC-Ph-3H,5H, Ph-2H,6H), 7.08-7.04 (m, 2 H, Th-4H, SQ-H), 6.04 (s, 1 H, C=CH), 6.02 (s, 1 H, C=CH), 4.12-4.00 (m, 4 H, α -CH₂-SQ), 2.82 (t, 3J = 7.8 Hz, 2 H, α' -CH₂), 2.66 (t, 3J = 7.7 Hz, 2 H, α -CH₂), 1.81-1.78 (m, 14 H, 4x indole-CH₃, N-CH₂-CH₃), 1.73-1.63 (m, 4 H, β -CH₂, β' -CH₂), 1.44-1.25 (m, 25 H, N-CH₂-CH₃, all other CH₂), 0.91-0.80 (m, 9 H, H₂-CH₂-CH₃).

^{13}C NMR (100 MHz, $CDCl_3$): δ = 170.86, 159.73, 151.45, 144.77, 142.48, 140.58, 140.50, 139.46, 136.84, 134.48, 132.50, 131.28, 131.22, 131.08, 130.41, 127.52, 127.43, 126.25, 126.16, 123.23, 123.14, 122.42, 121.93, 116.03, 109.56, 49.75, 49.53, 44.60, 32.70, 31.69, 31.65, 31.61, 30.61, 30.19, 29.60, 29.26, 29.22, 28.88, 26.89, 26.84, 26.81, 25.89, 25.74, 22.64, 22.58, 21.61, 14.63, 14.56, 13.62.

High-Resolution MS (MALDI-TOF) m/z : calcd for $C_{76}H_{85}N_3O_6S_2$: 1199.58798, found $[M]^+$: 1199.58508, $\delta m/m = 2.4$ ppm.

3.5 References

- [1] J. He, H. Lindstrom, A. Hagfeldt, S.-E. Lindquist, *Sol. Energy Mater. Sol. Cells* **2000**, *62*, 265-273.
- [2] A. Nattestad, A. J. Mozer, M. K. R. Fischer, Y. B. Cheng, A. Mishra, P. Bäuerle, U. Bach, *Nat. Mater.* **2010**, *9*, 31-35.
- [3] F. Odobel, L. Le Pleux, Y. Pellegrin, E. Blart, *Acc. Chem. Res.* **2010**, *43*, 1063-1071.
- [4] F. Odobel, Y. Pellegrin, *J. Phys. Chem. Lett.* **2013**, *4*, 2551-2564.
- [5] H. Zhu, A. Hagfeldt, G. Boschloo, *J. Phys. Chem. C* **2007**, *111*, 17455-17458.
- [6] A. Nakasa, H. Usami, S. Sumikura, S. Hasegawa, T. Koyama, E. Suzuki, *Chem. Lett.* **2005**, *34*, 500-501.
- [7] E. A. Gibson, A. L. Smeigh, L. Le Pleux, J. Fortage, G. Boschloo, E. Blart, Y. Pellegrin, F. Odobel, A. Hagfeldt, L. Hammarström, *Angew. Chem.* **2009**, *121*, 4466; *Angew. Chem. Int. Ed.* **2009**, *48*, 4402-4405.
- [8] Q. Yu, Y. Wang, Z. Yi, N. Zu, J. Zhang, M. Zhang, P. Wang, *ACS Nano* **2010**, *4*, 6032-6038.
- [9] A. Yella, H.-W. Lee, H. N. Tsao, C. Yi, A. K. Chandiran, M. K. Nazeeruddin, E. W.-G. Diao, C.-Y. Yeh, S. M. Zakeeruddin, M. Grätzel, *Science* **2011**, *334*, 629-634.
- [10] J. Sambeth, F. Grundschober, *Angew. Chem.* **1965**, *77*, 718-719; *Angew. Chem. Int. Ed.* **1965**, *4*, 693-694.
- [11] W. Ziegenbein, H. E. Sprenger, *Angew. Chem.* **1966**, *78*, 937-937; *Angew. Chem. Int. Ed.* **1966**, *5*, 894-894.
- [12] L. Beverina, P. Salice, *Eur. J. Org. Chem.* **2010**, *2010*, 1207-1225.
- [13] L. Hu, Z. Yan, H. Xu, *RSC Adv.* **2013**, *3*, 7667-7676.
- [14] J. Cremer, E. Mena-Osteritz, N. G. Pschierer, K. Müllen, P. Bäuerle, *Org. Biomol. Chem.* **2005**, *3*, 985-995.
- [15] Naraso, F. Wudl, *Macromolecules* **2008**, *41*, 3169-3174.
- [16] D. Villemin, L. Liao, *Synth. Commun.* **2001**, *31*, 1771-1780.
- [17] J. Cremer, PhD thesis, Ulm University, **2005**.
- [18] M. Weidelenner, diploma thesis, Ulm University, **2009**.
- [19] N. Miyauchi, A. Suzuki, *Chem. Rev.* **1995**, *95*, 2457-2483.
- [20] V. P. Mehta, E. V. Van der Eycken, *Chem. Soc. Rev.* **2011**, *40*, 4925-4936.

- [21] P. Leowanawat, A.-M. Resmerita, C. Moldoveanu, C. Liu, N. Zhang, D. A. Wilson, L. M. Hoang, B. M. Rosen, V. Percec, *J. Org. Chem.* **2010**, *75*, 7822-7828.
- [22] T. Ishiyama, N. Miyaura, *The Chemical Record* **2004**, *3*, 271-280.
- [23] C. Moldoveanu, D. A. Wilson, C. J. Wilson, P. Leowanawat, A.-M. Resmerita, C. Liu, B. M. Rosen, V. Percec, *The Journal of Organic Chemistry* **2010**, *75*, 5438-5452.
- [24] M. Weidelener, A. Mishra, A. Nattestad, S. Powar, A. J. Mozer, E. Mena-Osteritz, Y.-B. Cheng, U. Bach, P. Bäuerle, *J. Mater. Chem.* **2012**, *22*, 7366-7379.
- [25] C.-H. Chang, Y.-C. Chen, C.-Y. Hsu, H.-H. Chou, J. T. Lin, *Org. Lett.* **2012**, *14*, 4726-4729.
- [26] Y. Geerts, H. Quante, H. Platz, R. Mahrt, M. Hopmeier, A. Bohm, K. Müllen, *J. Mater. Chem.* **1998**, *8*, 2357-2369.
- [27] K.-Y. Law, *J. Phys. Chem.* **1995**, *99*, 9818-9824.
- [28] Z. S. Wang, Y. Cui, K. Hara, Y. Dan-oh, C. Kasada, A. Shinpo, *Adv. Mater.* **2007**, *19*, 1138-1141.
- [29] M. Xu, S. Wenger, H. Bala, D. Shi, R. Li, Y. Zhou, S. M. Zakeeruddin, M. Grätzel, P. Wang, *J. Phys. Chem. C* **2009**, *113*, 2966-2973.
- [30] P. Qin, J. Wiberg, E. A. Gibson, M. Linder, L. Li, T. Brinck, A. Hagfeldt, B. Albinsson, L. Sun, *J. Phys. Chem. C* **2010**, *114*, 4738-4748.
- [31] S. N. Mori, W. Kubo, T. Kanzaki, N. Masaki, Y. Wada, S. Yanagida, *J. Phys. Chem. C* **2007**, *111*, 3522-3527.
- [32] F. Fabregat-Santiago, G. Garcia-Belmonte, I. Mora-Sero, J. Bisquert, *Phys. Chem. Chem. Phys.* **2011**, *13*, 9083-9118.
- [33] L. Malatesia, M. Angoletta, *J. Chem. Soc.* **1957**, 1186-1188.
- [34] M. Valiev, E. J. Bylaska, N. Govind, K. Kowalski, T. P. Straatsma, H. J. J. Van Dam, D. Wang, J. Nieplocha, E. Apra, T. L. Windus, W. A. de Jong, *Comput. Phys. Commun.* **2010**, *181*, 1477-1489.

Chapter 4

Structurally Defined Co-Oligomers as Donor Materials for Solution-Processed Organic Solar Cells

4.1 Introduction

The interest in organic photovoltaic (OPV) was awakened in the 70s and early 80s of the 20th century mainly due to scientific breakthroughs concerning thin layer organic solar cells (OSC) from IBM,^[1] Eastman Kodak,^[2,3] and Exxon Research & Engineering Company^[4,5] affording solar cells with power conversion efficiencies (PCEs) of about 1%. The photoactive layer in these devices consisted of photoactive organic semiconductors, for example squaraines or merocyanines, which were sandwiched between two electrodes (Figure 1a). In thin layer OSCs, the photocurrent is generated by creation of strongly bound electron-hole pairs (excitons) upon light absorption. These excitons have to diffuse to a heterointerface, where they can be separated. A main drawback of the first thin layer OSC was the low fill factor (FF), which was generally not higher than 0.25-0.30 due to charge recombination and decay of unseparated excitons and was overcome by Tang in 1986.^[6] By building the first bilayer device consisting of a p-type (donor, copper phthalocyanine) and n-type semiconductor (acceptor, perylene tetracarboxylic acid derivative) layer deposited by sequential thermal vacuum sublimation (Figure 1b), he obtained OSCs with FF greater than 0.65. This breakthrough was attributed to the highly efficient exciton separation at the interface between donor and acceptor.^[7] It is noteworthy to mention that the layer thicknesses of the donor and acceptor layer are limited by the corresponding exciton diffusion length L_D . If thicker layers are present, not all excitons are able to reach the donor acceptor interface anymore and recombine.

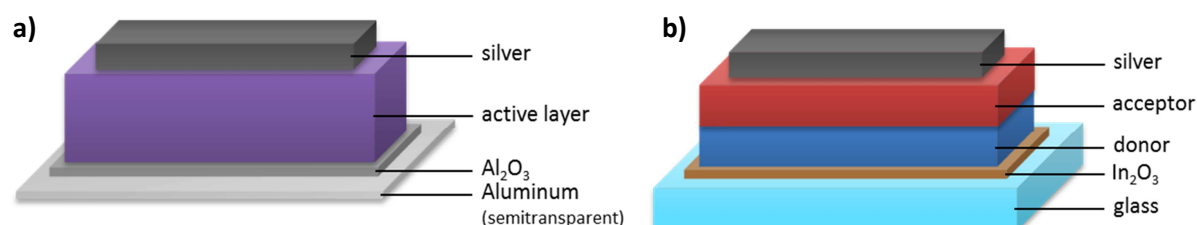


Figure 1. (a) Monolayer OSC as published in [5]. (b) Bilayer OSC incorporating a p-type (donor) and n-type semiconductor (acceptor) in the photoactive layer as reported by Tang.^[6]

By the use of soluble semiconducting polymers in OSCs, starting in 1995, it became possible to process donor (p-type semiconductor) and acceptor (n-type semiconductor) simultaneously from solution (e.g. by spin-coating, doctor-blading, or printing). This led to a novel constitution of the active layer: a bicontinuous interpenetrating network of donor and acceptor, the bulk heterojunction (BHJ) (Figure 2).^[8-10] Thus, the interface area between the donor and the acceptor is increased enormously which leads to a higher number of separated excitons, the possibility to produce thicker

active layers with efficient exciton separation, and therefore to higher photocurrents. Today, after 20 years of research, single junction bulk heterojunction solar cells (BHJSC) reach PCEs of up to 9-10% using functional semiconducting polymers as donor and soluble fullerene derivatives [6,6]-phenyl-C₆₁-butyric acid methyl ester (PC₆₁BM) or [6,6]-phenyl-C₇₁-butyric acid methyl ester (PC₇₁BM) as acceptor.^[11-14]

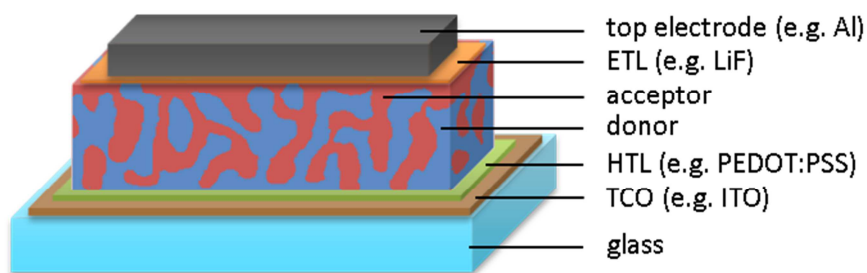


Figure 2. Typical device architecture of a BHJSC (ETL = electron transport layer; TCO = transparent conducting oxide; HTL = hole transport layer).

In contrast to conjugated polymers, structurally defined oligomers and co-oligomers offer many prominent advantages when used in organic electronic applications. They are monodisperse and possess a defined structure and molecular weight, excluding end group effects. Their synthesis is reproducible and due to established purification methods, their purity can be very high thus reducing batch-to-batch variations. Additionally, the synthesis can be kept straightforward which allows easy mass-scale production. Furthermore, the absorption and energy levels are easily tunable and the intrinsic mobility is generally quite high. Despite these advantages, for a long time structurally defined oligomers and co-oligomers lagged behind their conjugated polymer counterparts, due to bad film-forming properties when blended with PC₆₁BM or PC₇₁BM.^[15] Owing to discouraging early results of devices with PCE of 0.3-1.7% little effort was put into the field of solution-processed BHJSC using structurally defined oligomers as donor.^[16-25] At that time solar cells using conjugated polymers as donors were reaching PCEs of >5%. On the contrary, structurally defined oligomers covered a rapid development in vacuum-processed OSC together with fullerene (C₆₀) as acceptor. Because of the precise adjustment of the layer architecture devices nowadays reach PCEs of 8.3%.^[26-29] Tandem and triple junction solar cells result in even higher efficiencies of up to 12.0%.^[30] However, in the last five years the development of solution-processed BHJSCs with structurally defined oligomers and co-oligomers as donor accelerated substantially^[15,28,31] and caught up with the best performing polymer BHJSCs approaching PCEs of 9%.^[32-34]

This chapter provides an overview of fundamental principles and recent developments in structurally defined oligomers and co-oligomers for solution-processed BHJSCs. At the end of this chapter, design rules for structurally defined oligomers and co-oligomers are highlighted and summarized which should help to develop novel structures as donor materials for BHJSCs.

4.2 Fundamental principles of structurally defined oligomer-based BHJSCs

In a BHJSC (Figure 2), the photoactive layer is sandwiched between a transparent conducting oxide (TCO), typically indium tin oxide (ITO), acting as anode and a metal cathode, such as Ca or Al. The ITO is coated with an hole conducting layer, usually a mixture of poly(3,4-ethylenedioxythiophene) and poly(styrenesulfonate) (PEDOT:PSS) to ensure unidirectional hole transport. Often, an additional layer between the organic blend and the top cathode is employed, such as LiF, to enhance charge extraction and/or operate as an electron transport layer obstructing holes and excitons from the electrode.^[35] The ideal bulk heterojunction solar cell (BHJSC) features a blend layer, which is composed of a bicontinuous interpenetrating network of donor and acceptor phase-separated with percolation pathways allowing charge transport to the corresponding electrodes. The phase separation of the donor and the acceptor material should be in the nanometer scale to guarantee exciton diffusion within its lifetime to the donor/acceptor interface. The exciton diffusion length in organic materials is typically on the order of 10 nm. This nanometer scale constitution of the active layer is usually referred to as morphology and is influenced by the nature of donor and acceptor as well as the processing conditions (e.g. processing solvent, temperature, concentration, ratio of donor and acceptor material (D:A), etc.).

Photocurrent generation is initiated by the formation of excitons (Figure 3, (1)) upon excitation of electrons in the donor (or the acceptor, not shown in Figure 3) by light absorption. Diffusion of the excitons to the donor/acceptor interface (2) is crucial to enable exciton dissociation (3). Excitons which do not reach the interface, undergo recombination and are lost concerning photocurrent generation. Those reaching the interface can dissociate and form geminate electron hole pairs. It is noted that relatively high exciton dissociation energies (ca. 100 meV) have to be overcome. Once dissociated, the free charges must then be transported to (4) and collected at the corresponding electrodes (5). Losses can occur when charges from a dissociated exciton recombine (geminate recombination) or when electrons/holes travelling to the corresponding electrode recombine with their counterpart (non-geminate recombination).^[28]

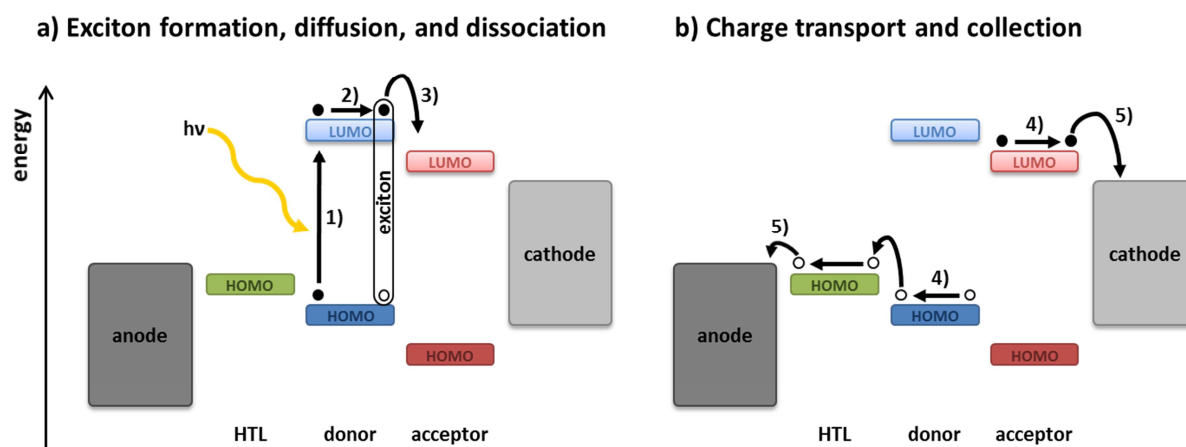


Figure 3. Working principle of charge generation in a BHJSC. 1) Excitation/formation of an exciton. 2) Exciton diffusion to the donor/acceptor interface. 3) Exciton dissociation/separation. 4) Charge (electron/hole) transport. 5) Charge collection at the electrodes.

Keeping the working principle in mind, specific criteria for the properties of the donor and acceptor material can be extracted: (1) The energy gap ΔE_{gap} between the highest occupied molecular orbital (HOMO) energy level of the donor and the lowest unoccupied molecular orbital (LUMO) energy level of the acceptor is directly related with the maximum photovoltage (=open-circuit voltage, V_{OC}) obtained from the device ($V_{\text{OC}} = (1/e)(|E_{\text{HOMO,donor}}| - |E_{\text{LUMO,acceptor}}|) - 0.3 \text{ V}$; e = elementary charge).^[36] Therefore, a low lying HOMO energy level of the donor and a high lying LUMO energy level of the acceptor material is favorable. (2) Additionally, the difference of the LUMO energy levels of donor and acceptor should be roughly $>0.3 \text{ eV}$ to ensure efficient exciton dissociation. (3) Furthermore, the energy levels of the donor and the acceptor have to fit to the energy alignment of the other used material in the device (e.g. the HOMO energy level of the HTL) to assure efficient charge extraction. (4) When processed, donor and acceptor should form a morphology which allows exciton diffusion to a donor/acceptor interface and charge transport of the generated charges to their respective electrodes. Therefore, domain sizes of donor and acceptor should be ideally in the order of $2L_D$, so that excitons generated in the center of the domains can still reach the interface.^[37]

4.3 Development of structurally defined oligomers and co-oligomers for solution-processed BHJSCs

The field of structurally defined oligomers and co-oligomers as solution-processable donor material in BHJSCs has evolved very fast in the last years. Many structures have been synthesized and recently

reviewed.^[28,38] Despite the large number of reports in literature, highly efficient BHJSCs are still countable and structural motifs are limited to surprisingly few donor (D) and acceptor (A) moieties. In this section, the development of structurally defined molecular donor materials yielding highly efficient BHJSCs with PCE >4.5% is reviewed.

Structurally defined co-oligomers containing diketopyrrolopyrrole (DPP)

In 2009, the group of T.-Q. Nguyen published structurally defined molecule **85** based on diketopyrrolopyrrole (DPP) and flanked by 2-(thien-2-yl)benzofuran on each side (Chart 1) yielding a PCE of 4.42%, with a short-circuit current (J_{SC}) of 10.0 mA cm⁻², a V_{OC} of 0.92 V, and a FF of 0.48 when mixed with PC₇₁BM (Table 1) representing a big improvement concerning the performance of solution-processed structurally defined molecule BHJSC at that time.^[31,39]

The reason lies on one hand in the high optical density of donor(D)-acceptor(A) dye **85** featuring a strong, broad, and structured absorption band at ~630 nm in solution, typical for DPP-based compounds,^[40] whereas the onset of this band is located at 660 nm and shifts to over 700 nm in thin film. On the other hand, **85**:PC₇₁BM blend films analyzed by atomic force microscopy (AFM) showed good film morphologies with domain sizes of 10-50 nm after thermal annealing and balanced charge carrier mobilities.^[39] By thermal annealing an increase in the crystallinity is induced leading to bigger domain sizes and hence higher charge mobilities. For **85**:PC₇₁BM blend films the optimal annealing temperature concerning photovoltaic performance was found to be 110 °C. Recently, the group of T.-Q. Nguyen could improve the PCE from 4.42% to 4.80%, due to an enhancement of the FF to 0.54 (Table 1).^[41]

The same group synthesized structurally defined co-oligomers **86** and **87** containing three DPP moieties in order to obtain an increase in conjugation, absorption, and charge carrier mobility and hence enhanced solar cell performance (Chart 1).^[42] Both co-oligomers showed a similar behaviour in solution possessing a strong absorption band at ~600 nm with an onset at around 670 nm. Going from solution to thin films, the absorption maximum of **86** hardly shifts in comparison to a 30 nm red-shift of the absorption maximum for **87**. This can be attributed to a different film morphology induced during spin-coating by the 2-ethylhexyl and hexyl side chains of the middle DPP-unit of **86** and **87**, respectively. However, upon thermal annealing the absorption curve of **86** adapted the one of **87**. The authors explain this behaviour by the lower tendency for crystallization of **86** due to its branched side-chains, confirmed by thin film X-ray diffraction (XRD).^[42] On the other hand, **86** features a 2.5 times higher solubility of 25 mg mL⁻¹ in chloroform at room temperature compared to **87** making it easier to handle and process.

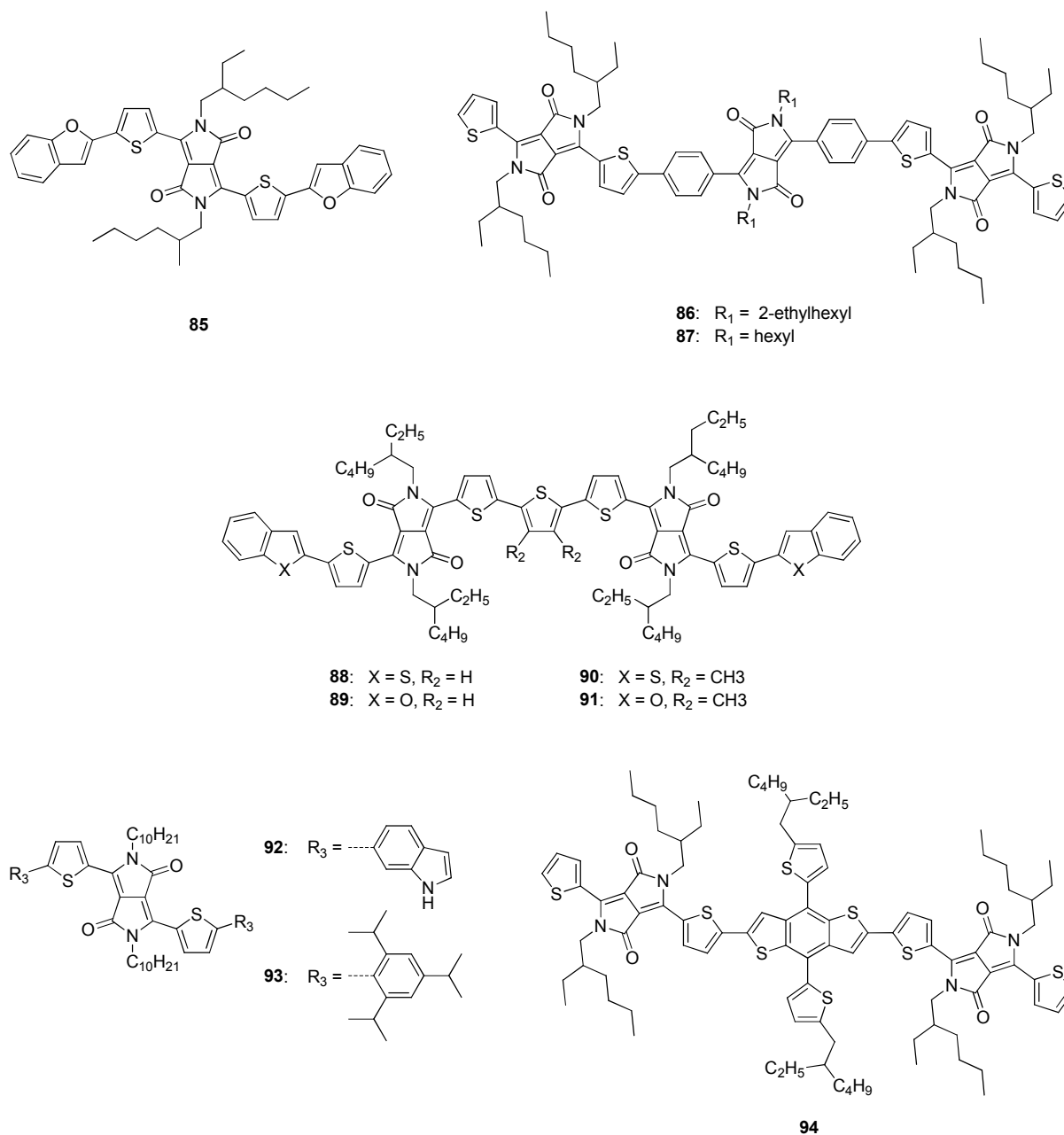


Chart 1. Chemical structures of structurally defined co-oligomers for solution-processed highly efficient BHJSCs based on DPP.

Charge carrier mobilities were determined by fabricating organic field effect transistors and applying the space charge limited current (SCLC) method onto hole-only devices. In both cases, hole mobilities were improved upon annealing at 100 °C, annealing at higher temperatures again led to decreased charge transport properties. Concerning hole mobilities, **87** was superior to **86** in each measurement reaching a maximum hole mobility of $4.3 \times 10^{-3} \text{ cm}^2 \text{ V}^{-1} \text{ s}^{-1}$ which is one order of magnitude higher than the one of **86** ($6.6 \times 10^{-4} \text{ cm}^2 \text{ V}^{-1} \text{ s}^{-1}$) and **85** ($5.3 \times 10^{-4} \text{ cm}^2 \text{ V}^{-1} \text{ s}^{-1}$).^[41,42] The reason therefore lies mainly in the formation of larger crystallites in thin films, which was shown by AFM measurements.

BHJ devices were made from **86** and **87** with PC₇₁BM as acceptor. In both cases, solvent additives were used to maximize solar cell performance, for the two co-oligomers different D:A ratios were applied (**86** D:A [50:50], **87** D:A [40:60]). For **86** 1,8-diiodooctane (DIO, 1%) was used as additive, yielding a PCE of 4.79% with a J_{sc} of 8.98 mA cm⁻², a V_{oc} of 0.89 V, and a FF of 0.61, whereas processing without DIO or with 1-chloronaphthalene (CN, 1%) afforded only low performing solar cells with PCEs <0.6% (Table 1).

Table 1. Photovoltaic parameters of DPP-based donor materials for solution-processed BHJSC (PC₇₁BM was used as acceptor material if not stated otherwise).

donor	J_{sc} [mA cm ⁻²]	V_{oc} [mV]	FF	PCE [%]
85 ^{[a][39]}	10.0	0.92	0.48	4.42
85 ^{[a][41]}	9.85	0.90	0.54	4.80
86 ^[42]	0.67	0.88	0.43	0.25
86 ^{[b][42]}	8.98	0.89	0.61	4.79
86 ^{[c][42]}	2.10	0.93	0.30	0.59
87 ^[42]	8.09	0.87	0.59	4.15
87 ^{[b][42]}	9.91	0.86	0.60	5.11
87 ^{[c][42]}	10.4	0.86	0.62	5.52
88 ^[43]	11.9	0.69	0.57	4.63
89 ^[43]	10.4	0.67	0.58	4.04
90 ^{[d][43]}	10.6	0.73	0.45	3.48
91 ^{[d][43]}	10.3	0.71	0.52	3.80
92 ^{[a][44]}	10.8	0.82	0.56	4.96
93 ^{[a][44]}	7.34	0.90	0.46	3.04
94 ^{[a][f][45]}	12.0	0.84	0.58	5.79
94 ^{[g][46]}	11.9	0.72	0.62	5.29

[a] Thermally annealed at 110 °C. [b] DIO (1%) was used as additive. [c] CN (1%) was used as additive. [d] DIO (0.2 vol%) was used as additive. [f] PC₆₁BM was used as acceptor material. [g] DIO (1%) was used as additive.

In the case of **87**, the PCE is not so strongly affected by additive addition reaching efficiencies of 4.15, 5.11, and 5.52% using no additive, DIO (1%), or CN (1%), respectively. The best cell produced a J_{SC} of 10.4 mA cm⁻², a V_{OC} of 0.86 V, and a FF of 0.62. The better overall PCE of **87** is due to a higher J_{SC} having its origin in smoother and more uniform blend films determined by AFM.^[42] Influences of thermal annealing upon solar cell performances are not discussed. The diverse behaviour of **86** and **87** concerning its film formation with PC₇₁BM is believed to be due to a different ability for crystallization or aggregation as well as a different interaction behaviour with solvent additives induced by the alkyl chain on the central DPP-unit.^[42]

In the group of R. Janssen, a series of D-A-D co-oligomers with two DPP-units were developed (Chart 1). The two DPP moieties were linked to each other by a terthiophene (**88** and **89**) or a dimethylated terthiophene (**90** and **91**) and end-capped by 2-(thien-2-yl)benzothiophene (**88** and **90**) or 2-(thiophen-2-yl)benzofuran (**89** and **91**).^[43] All four co-oligomers showed absorption bands between 645 and 665 nm. **88** and **89** bearing no methyl groups are 20 nm red-shifted in comparison to **90** and **91**. The reason therefore lies probably in slight torsions within the dimethylterthiophene backbone due to sterical hindrance leading to a small reduction of the conjugation. Going from solution to thin films the absorption onset of all co-oligomers is red-shifted from ~740 nm to 835 nm. Interestingly, the absorption maximum of **89** is exclusively blue-shifted by 30 nm in thin film compared to the solution, because of a broadening of the absorption to the high energy region suggesting major changes in film morphology upon subtle structural changes. The broad spectral coverage of the solar spectrum becomes noticeable in the solar characteristics. **88-91** were blended with PC₇₁BM and spin-coated from tetrachloroethane (**89** and **90**) or chloroform with 0.2 vol% DIO (**91** and **92**) to maximize PCE. All co-oligomers showed J_{SC} values above 10 mA cm⁻², whereas **89** has the highest J_{SC} of nearly 12 mA cm⁻² which is among the highest J_{SC} values of DPP-based structurally defined oligomers and co-oligomers. PCEs ranged from 4.6% for **89** to 3.5% for **91** and suffered from lower V_{OC} values of around 0.7 V in comparison to other DPP-based materials (0.8-0.9 V, Table 1). Dimethyl substituted **91** and **92** featured thereby slightly higher V_{OC} values in comparison to **89** and **90** due to the inductive effect of the methyl groups decreasing the HOMO energy level. However, unmethylated co-oligomers **89** and **90** achieved higher FF of ~0.6. Also this series proves that small variations on the molecular structure can have great impact on the device performance and greatly influence the processing conditions for obtaining the optimal morphology.

Sharma *et al.* synthesized **92** and **93** having the same D-A-D design as **85** (Chart 1).^[44] The difference lies in the solubility promoting decyl chain on the DPP-unit and the different end groups attached to the thiophene. D-A-D system **92** bearing indoles as end groups showed an absorption maximum similarly to **85** at 624 nm in solution. In contrast to this, **93** possessing two triisopropylphenyl end

groups featured a 58 nm blue-shifted absorption maximum compared to **85** at 566 nm. The difference can be explained by the weaker electron-donating capability of triisopropylphenyl compared to indole and by a partially interrupted conjugation induced by a stronger torsion of the C-C bond between thiophene and benzene in the case of **93** hampering the intramolecular charge transfer from the D to the A moiety. However, this torsion and the triisopropylphenyl groups lead to an increased solubility of 40 mg mL⁻¹ in chloroform for **93** in comparison to 25 mg mL⁻¹ for **92**.^[44] In thin films, the absorption is 20-25 nm red-shifted and broadened resulting in an absorption onset of about 700 and 650 nm for **92** and **93**, respectively, which is in the case of **92** again similar to **85**. BHJSCs were fabricated by spin-coating **92** or **93** with PC₇₁BM from chloroform. After optimization, a D:A ratio of 1:1 with thermal annealing of the devices was found to give the best photovoltaic performance (Table 1). DPP-derivative **92** exhibited a J_{sc} of 10.8 mA cm⁻², a V_{oc} of 0.82, a FF of 0.56, and a PCE of 4.96%. More soluble derivative **93** had a J_{sc} of 7.34 mA cm⁻², a V_{oc} of 0.90, a FF of 0.46, and a PCE of 3.04%. The lower performance of **93**, despite its higher V_{oc} which is most probably a result of the lower electron-donating ability of triisopropylphenyl compared to indole consequently leading to a lower lying HOMO energy level, can be explained by the higher J_{sc} and FF values of **92** originating from a better spectral overlap of absorption and solar irradiation and a higher hole mobility, respectively. The good spectral overlap with the solar spectrum is also expressed in the IPCE spectrum of **92**, showing an IPCE of 40-60% between 360 and 580 nm and an excellent IPCE of up to 78% in the region of the main absorption band between 580 to 700 nm.^[44] The results of Sharma *et al.* emphasize the importance of strong and broad absorption bands.

DPP-based co-oligomer **94** was synthesized at the same time by Lin *et al.*^[45] and Huang *et al.*^[46] The linear A-D-A design consists of two DPPs as acceptors and the two-dimensionally conjugated benzodithiophene (BDT) core as donor. The planar and rigid structure of BDT aimed at a better packing of the molecules in the solid state. The vertically attached thiophenes at the BDT increase conjugation orthogonal to the conjugated backbone of the molecule. Both facts possibly enhance charge transport properties and the latter one surely contributes to an increased absorption. In solution, **94** showed an intense absorption band at 620 nm with an extinction coefficient of 125,000 M⁻¹cm⁻¹. Going to the thin film, the absorption maximum is hardly shifted, but the emergence of a strong shoulder peak red-shifts the absorption onset by nearly 100 nm to 760 nm emphasizing the potential light-harvesting ability of **94**. OFET devices were fabricated to measure hole mobilities, which were determined to be 1.6×10^{-3} cm² V⁻¹s⁻¹ which is among the top values of molecular donors for BHJSC.^[28,38,45] Lin *et al.* incorporated **94** in BHJSCs using PC₆₁BM as acceptor. After thermal annealing a PCE of 5.79% was obtained featuring a J_{sc} of 12.0 mA cm⁻², a V_{oc} of 0.84 and a FF of 0.58 (Table 1). Without thermal annealing the PCE was lower (5.26%).^[45] In contrast, Huang *et al.*

prepared BHJSCs via spin-coating of **94**:PC₇₁BM mixtures from 1,2-dichlorobenzene mixed with 0.7% DIO. Thermal or solvent annealing led to deterioration of the devices.^[46] Despite the usage of PC₇₁BM possessing an improved absorption compared to PC₆₁BM, only a similar J_{SC} of 11.9 mA cm⁻² was achieved. The main reason for the lower PCE is a decrease in V_{OC} of ~0.1 V to 0.72 V, which is consistent with the lower LUMO energy level of PC₇₁BM in comparison to PC₆₁BM. The comparable FF of 0.6 suggests equivalent quality in morphology for PC₆₁BM- and PC₇₁BM-blended films. These results show that an optimized morphology is a crucial point to obtain high performance in BHJSCs. A batch-to-batch variation (trace impurities) between **94** of Lin *et al.* and Huang *et al.* cannot be excluded as the two co-oligomers were synthesized in different laboratories. However, the synthetic routes were the same and analytical data (melting point, mass analysis, elemental analysis *etc.*) fit very well.

Structurally defined oligomers and co-oligomers with A-D-A architecture incorporating oligothiophenes

The group of Y. Chen synthesized various structurally defined oligomers and co-oligomers leading to highly efficient BHJSCs.^[15] The linear A-D-A structure of these structurally defined oligomers and co-oligomers using mainly oligothiophenes as D and cyano-substituted units as end-capping A was chosen on the basis of the pioneering work on sublimable DCV-end-capped quinquethiophenes for vacuum-processed BHJSCs.^[26,27] In 2009, Liu *et al.* synthesized a first series of DCV end-capped octyl-substituted ter-, quinque-, and septithiophene: **95**, **96**, and **97**, respectively (Chart 2).^[47] The spectral coverage and the absorption coefficient in solution and in thin films improved within the series with increasing number of thiophenes which correlates with the conjugation length of the π -system. Septithiophene **97** possessing an absorption maxima of 517 nm in solution and 613 nm in thin film was used as donor together with PC₆₁BM as acceptor in BHJSCs, yielding a PCE of 3.7% with a J_{SC} of 12.4 mA/cm², V_{OC} of 0.88 V, but a low FF of 0.34 after device optimization (Table 2).^[48] The low FF and hence the limited PCE is ascribed to the low solubility of **97** causing a poor morphology of the blend layer.

By replacing the terminal DCV end groups by cyanoacrylic acid ester groups, Liu *et al.* prepared **98**, **99**, and **100** as a series with significantly raised solubility (Chart 2).^[49] A drawback of the alkyl cyanoacrylate group is the lower electron-accepting strength compared to DCV which results in a more than 25% less intense and ~20 nm blue-shifted absorption in solution for **98-100** in comparison to DCV-containing structurally defined oligomer **97**.^[47,49] It is noteworthy that depending on the bulkiness of the alkyl ester, the absorption in thin films of **98-100** is red-shifted differently. For **98** and

99 featuring linear ethyl and octyl ester, respectively, the absorption maximum in thin films shifts by 98 nm to 592 nm and by 88 nm to 580 nm, whereas for branched 2-ethylhexyl ester **100** it is only shifted by 77 nm to 569 nm. The reason is a less dense packing due to the more bulky octyl and 2-ethylhexyl alkyl ester in **99** and **100** which was proven by XRD analysis of the thin films.^[49] BHJSCs of the series using PC₆₁BM as acceptor yielded PCEs of 4.46%, 5.08%, and 4.52% for **98**, **99** and **100**, respectively (Table 2). The crucial increase in FF from 0.34 for **97** to 0.51 for **99** even compensated the drop in J_{sc} . The improved FF is explained by a better film morphology with an optimized donor-acceptor interpenetrating network suggested by AFM measurements. This leads to an improved charge carrier collection efficiency which is supported by the intense and broad IPCE curves covering 350-700 nm and reaching a maximum at 540 nm of 67% for **99**. In comparison to the DCV-substituted series,^[47] the overall absorption was reduced, however, due to higher solubilities a better device optimization was feasible which resulted in better performing solar cells.

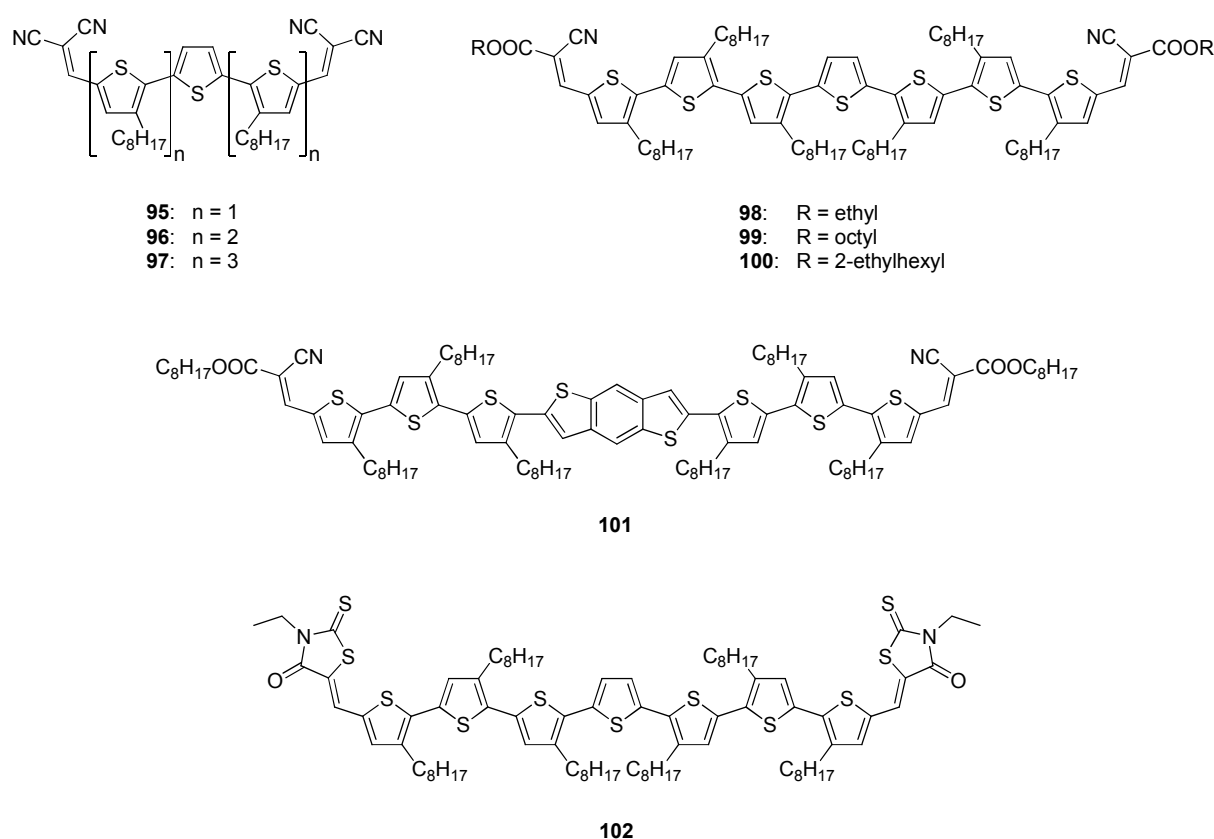


Chart 2. Chemical structures of structurally defined oligomers and co-oligomers for BHJSCs synthesized by Y. Chen and co-workers incorporating regioregular trioctylterthiophene moieties.^[47,49]

Table 2. Photovoltaic parameters of donor materials based on oligothiophenes for solution-processed BHJSCs (PC₆₁BM was used as acceptor).

donor	J_{SC} [mA cm ⁻²]	V_{OC} [mV]	FF	PCE [%]
97 ^[48]	12.4	0.88	0.34	3.71
98 ^[49]	9.94	0.88	0.51	4.46
99 ^[49]	10.74	0.86	0.55	5.08
100 ^[49]	9.91	0.93	0.49	4.52
101 ^[50]	9.77	0.93	0.60	5.44
102 ^[51]	13.98	0.92	0.47	6.10

Modification of **99** by the means of substituting the central thiophene by benzo[1,2-b:4,5-b']dithiophene or substituting the octyl cyanoacrylate groups by 3-ethylrhodanine led to co-oligomer **101**^[50] and oligomer **102**^[51], respectively (Chart 2). By introducing the BDT-system the optical properties changed slightly in comparison to parental oligomer **99**. This is expressed by a blue-shift of 14 nm and a somewhat narrower absorption band. In contrast to that, higher hole mobilities were measured for pristine **101** (4.5×10^{-4} cm² V⁻¹s⁻¹) compared to **99** (3.3×10^{-4} cm² V⁻¹s⁻¹)^[49] using the SCLC method which was attributed to the possibility of stronger intermolecular orbital overlap due to the large and rigid planar conjugated BDT-unit leading to good packing, proven by XRD measurements.^[50] Hence, BHJSCs using **101** and PC₆₁BM were fabricated reaching high FF values of up to 0.60. The J_{SC} decreased from 10.74 mA cm⁻² for **99** to 9.77 mA cm⁻² for **101** and is consistent with the lower IPCE values for **101** which is probably a result of the reduced absorbance of **101** in comparison to **99**. A high V_{OC} of 0.93 V was achieved for **101** resulting in a PCE of up to 5.44%.

102 with two 3-ethylrhodanine groups showed a broad and intense absorption band in thin film at 618 nm with an onset at about 750 nm, which means a red-shift of 38 nm compared to **99**. AFM-measurements of **102**/PC₆₁BM blend films suggested the formation of an interpenetrating network with domain sizes of 10-20 nm for the acceptor-rich and donor-rich domains.^[51] BHJSCs resulted in excellent PCEs of up to 6.10%, with a high J_{SC} of 13.98 mA cm⁻², V_{OC} of 0.92, and FF of 0.47. The high J_{SC} in comparison to the before mentioned dyes can be explained by the better spectral overlap with the solar spectrum. The lower FF in comparison to the previous oligomers bearing alkyl cyanoacrylate groups is on one hand due to the sensitivity of the materials to device optimization (obtaining an optimized morphology) and to complicated interfacial contact issues and/or on the other hand due to a lower hole mobility of the pristine film (1.50×10^{-4} cm² V⁻¹s⁻¹) in comparison to **99**.^[51-53]

Further structural changes were carried out by the group of Y. Chen in terms of combining the favorable BDT- and rhodanine-units unifying good hole transport, film forming properties, and absorbance leading to series **103-106** depicted in Chart 3.^[32,54] It is noteworthy to mention that the octyl substitution pattern on the terthiophene building blocks changed in this series from a regioregular pattern for structurally defined oligomers and co-oligomers presented above (all octyl chains pointing inward) to a symmetrical terthiophene bearing two octyl chains pointing to the middle unsubstituted thiophene. The effect of this modification on the optoelectronic properties and solar cell performance is not discussed or further investigated by Y. Chen *et al.*

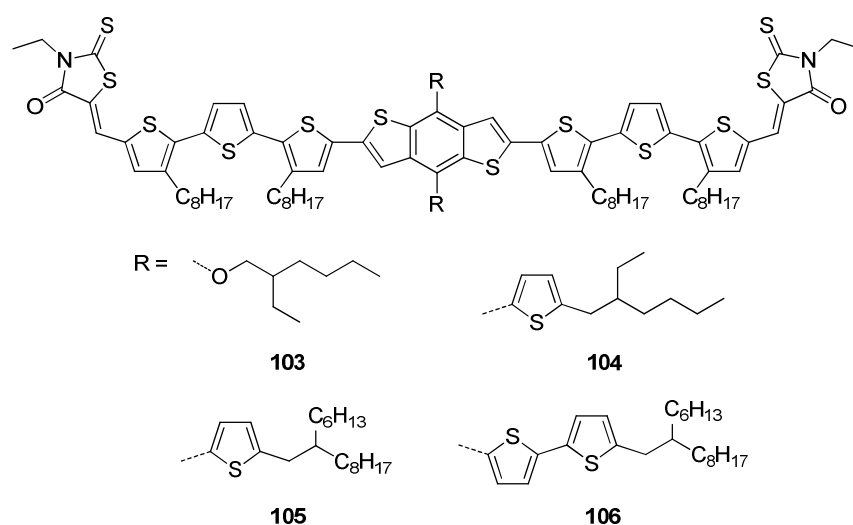


Chart 3. Rhodanine end-capped oligothiophenes incorporating differently substituted BDT center units.^[32,54]

The functionalization of the central BDT-unit with alkyl chains aimed at enhancing solubility and eventually influencing photovoltaic performance positively (e.g. due to a different morphology of the blend film). The introduction of additional thiophenes increased the conjugation and should further improve charge transport and optical properties.^[55] **103-106** showed intense absorption bands at ~510 nm in solution which is red-shifted to ~590 nm in thin films. Co-oligomers **104**, **105**, and **106** absorbed slightly more light in the region from 350 to 450 nm due to their additional thiophene and bithiophene moieties at the central BDT-unit. In thin films, **104** showed a more prominent low energy shoulder with a red-shifted onset at ~725 nm in comparison to ~715 nm for **103**, **105**, and **106** indicating a more effective π - π stacking for **104** which could be favorable for charge transport. AFM measurements of blend films of alkoxy-substituted BDT derivative **103** and PC₆₁BM or PC₇₁BM showed advantageous domain sizes of 20-30 nm. For **99** and **101** the domain sizes of blend films with PC₇₁BM were always larger than the ones in blend films with PC₆₁BM. For both compounds, the

domain sizes were generally larger in comparison to rhodanine substituted structurally defined oligomers and co-oligomers presented in Chart 2 and 3.^[49-50] The authors suggested that the miscibility of oligomers/co-oligomers with PC₆₁BM or PC₇₁BM increases with shorter terminal alkyl chains. This means that the miscibility of octyl cyanoacrylate-substituted oligomers with fullerene derivatives is lower than the one of 3-ethyl-rhodanine-substituted oligomers.^[56]

Table 3. Photovoltaic parameters of highly efficient donor materials based on rhodanine end-capped oligothiophenes incorporating differently substituted central BDT-units (PC₇₁BM was used as acceptor).

donor	J_{sc} [mA cm ⁻²]	V_{oc} [mV]	FF	PCE [%]
103 ^[54]	11.4	0.93	0.65	6.92
103 ^{[a][54]}	12.2	0.93	0.65	7.38
104 ^[32]	13.2	0.91	0.63	7.51
104 ^{[a][32]}	13.2	0.93	0.66	8.12
105 ^[32]	12.4	0.96	0.53	6.32
105 ^{[a][32]}	11.9	0.96	0.59	6.79
106 ^[32]	12.0	0.90	0.70	7.58
106 ^{[a][32]}	12.1	0.92	0.72	8.02

[a] PDMS (0.2 mg mL⁻¹) was used as additive.

Solution-processed BHJ devices with **103-106** as donor material were fabricated and optimized using PC₇₁BM as acceptor and chloroform or chloroform/polydimethylsiloxane (PDMS) as solvent system. The corresponding data are summarized in Table 3. All four donor materials yielded high PCEs between 6.3 and 7.6% without the use of PDMS, which could be improved to >8% by the addition of a small amount of PDMS (0.2 mg mL⁻¹) to the spin-coating solution causing an improved interpenetrating network of donor and acceptor-rich phases, determined by AFM.^[32,54] **104** and **106** with larger conjugation in the orthogonal direction demonstrated the highest PCEs of 8.12% and 8.02%, respectively. Cells containing **105** resulted in a lower PCE of 6.79% which corresponds well to the lower FF values compared to the other three co-oligomers. The lower FF was attributed to an unfavorable morphology in the **105**:PC₇₁BM blends supported by AFM, transmission electron microscopy (TEM), and X-ray spectroscopy. The highest FF was measured for **106** which is probably due to its high and well-balanced hole and electron mobilities (3.29×10^{-4} and 4.19×10^{-4} cm² V⁻¹s⁻¹,

respectively) of the active layer measured by hole/electron-only devices applying the SCLC method. The best J_{SC} value of 13.2 mA cm^{-2} featured **104** and corresponds well to the most red-shifted absorption of the series.^[32]

The groups of Y. Yang and Y. Li also synthesized series of linear co-oligomers employing the A-D-A design (Chart 4).^[57,58] In both cases, promising building blocks which are also present in well performing structurally defined co-oligomers of the group of Y. Chen are used.^[15] The group of Y. Yang synthesized a series of octamers end-capped with octyl cyanoacrylates. The donor part constitutes of a fourfold hexyl-substituted sexithiophene as the center which is flanked by furane, thiophene, or selenophene on each side (**107**, **108**, and **109**, respectively).^[57]

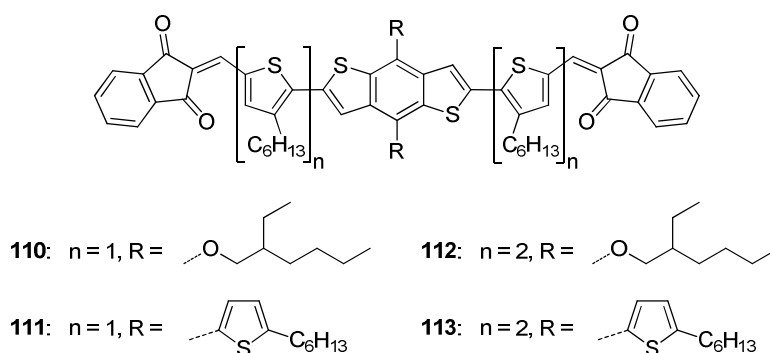
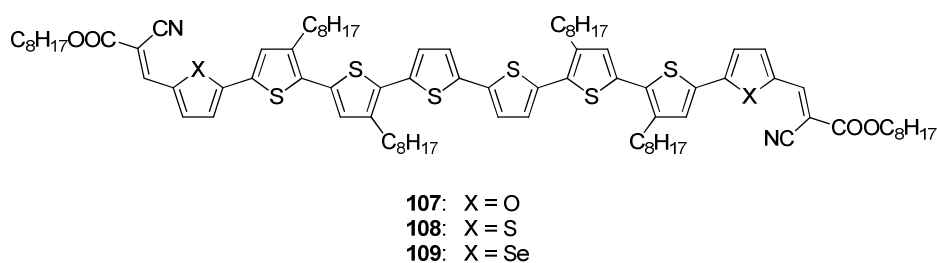


Chart 4. Chemical structures of structurally defined oligomers and co-oligomers synthesized by the groups of Y. Yang and Y. Li.^[57,58]

The absorption spectra in solution showed an absorption band at 493, 501, and 513 nm for **107**, **108**, and **109**, respectively. Oligomer **108** featuring an octithiophene as donor featured a 9 nm red-shifted absorption in comparison to septithiophene **99** caused by the longer π -conjugated system. Thin film absorption spectra of **107-109** showed obvious broadening and large red shift ($\sim 90 \text{ nm}$) compared to the absorption in solution. Selenophene-thiophene co-oligomer **109** featured the best spectral overlap with the solar spectrum in thin films due to its larger π -overlap of the larger p-orbitals of selenium atoms and the intermolecular Se-Se interactions improving molecular packing and hence

facilitating intermolecular charge transfer.^[57] BHJSCs of **107**, **108**, and **109** were fabricated and optimized utilizing PC₇₁BM as acceptor yielding PCEs of 3.18, 4.52, and 5.04%, respectively (Table 4). J_{SC} values continuously increased going from **107** to **108** and to **109**. The reasons therefore are most probably the low mobility of **107** and the improved spectral coverage for **108** and the even better one for **109**. The lower V_{OC} of 0.78 V for **107** in comparison to 0.85 V for **108** and **109** is explained by the higher lying HOMO energy level of furan-thiophene co-oligomer **107**.^[57] By further optimization, namely the addition of PDMS (0.1 mg mL⁻¹) to the spin-coating solution, the PCE of **109** could be further improved to 6.15%. While FF and V_{OC} were equal to cells, which were fabricated without the help of PDMS, J_{SC} is improved to 10.8 mA cm⁻² agreeing well with the high IPCE response of 50-55% from ~380-620 nm (42-48% for **109** without PDMS). The authors attribute this to a more efficient exciton dissociation due to an optimized interdigitated donor/acceptor network as observed from TEM and AFM images.^[57] Despite the fact that the highest PCE was obtained for devices containing **109**, BHJSCs using all-thiophene compound **108** as donor showed the best FF of 0.72 within this series, the origin hereof was not further investigated.

Structurally defined co-oligomers **110-113** bearing a central BDT-unit and 1,3-indandione acceptors were synthesized in the group of Y. Li (Chart 4).^[58] The central unit and the acceptor groups are linked with each other with a thiophene (**110**, **111**) or a bithiophene (**112**, **113**) and the BDT is substituted either with (2-ethylhexyl)oxy (**110**, **112**) or 5-hexylthien-2-yl (**111**, **113**) which results in a smaller π -conjugation length in comparison to BDT-containing structurally defined co-oligomers of the group of Y. Chen.^[32,54] All four derivatives featured an absorption band at ~500 nm in solution. The absorption maximum of thienyl-substituted derivatives **111** and **113** were slightly red-shifted in comparison to the ones of alkoxy-substituted co-oligomers **110** and **112**, respectively. Furthermore, longer co-oligomers **112** and **113** showed slightly red-shifted absorptions compared to **110** and **111**, respectively, owing to the increased conjugation length of the co-oligomers comprising more thiophenes. The biggest difference can be seen in the extinction coefficient ϵ , which is higher for **112** and **113** (~95'000 M⁻¹cm⁻¹) when compared to **110** and **111** (~75'000 M⁻¹cm⁻¹) having its origin in the increased conjugation. The absorption spectra in thin films are significantly broadened and red-shifted by ca. 90 nm due to emergence of a new vibronic peak at higher wavelengths (660 nm for **113**).^[58]

Table 4. Photovoltaic parameters of solution-processed BHJSCs (PC₇₁BM was used as acceptor) incorporating defined co-oligomers synthesized by the groups of Y. Yang and Y. Li.

donor	J_{sc} [mA cm ⁻²]	V_{oc} [mV]	FF	PCE [%]
107 ^[57]	6.34	0.78	0.64	3.18
108 ^[57]	7.43	0.85	0.72	4.52
109 ^[57]	8.99	0.85	0.66	5.04
109 ^{[a][57]}	10.8	0.85	0.67	6.15
110 ^[58]	9.47	0.91	0.48	4.15
111 ^[58]	10.1	1.03	0.55	5.67
112 ^[58]	8.58	0.92	0.65	5.11
113 ^[58]	11.1	0.92	0.66	6.75

[a] PDMS (0.1 mg mL⁻¹) was used as additive.

XRD measurements of the thin films pointed out that **110** and **112** possess a better layer by layer packing of the co-oligomers in comparison to **111** and **113** due to their less bulky side chains on the BDT-unit. In contrast to that, hole mobilities determined by SCLC method tend to be higher for **111** and **113** compared to their corresponding alkoxy analogues **110** and **112**, respectively. However, a much stronger influence is exerted by the π -bridge, **110** and **112** incorporating a bithiophene π -bridge showed with $2.63 \times 10^{-2} \text{ cm}^2 \text{ V}^{-1} \text{ s}^{-1}$ and $2.82 \times 10^{-2} \text{ cm}^2 \text{ V}^{-1} \text{ s}^{-1}$ two order of magnitude higher hole mobilities than **110** and **112** ($1.71 \times 10^{-4} \text{ cm}^2 \text{ V}^{-1} \text{ s}^{-1}$ and $2.04 \times 10^{-4} \text{ cm}^2 \text{ V}^{-1} \text{ s}^{-1}$; SCLC method). Solar cells were fabricated with **110-113** as donor and PC₇₁BM as acceptor. PCEs range from 4.15% for **110** to 6.75% for **113**. The corresponding photovoltaic characteristics are listed in Table 4. Alkoxy substituted co-oligomers **110** and **112** showed lower J_{sc} values of 9.47 and 8.58 mA cm⁻² compared to 10.1 and 11.1 mA cm⁻² of thienyl-substituted co-oligomers **111** and **113**, respectively. This is ascribed to a better miscibility of **111** and **113** with PC₇₁BM in the blend film,^[58] but could be also due to higher hole mobilities of **110** and **112** in comparison to **111** and **113**, respectively. Co-oligomer **113** incorporating the highest number of thiophenes and featuring the strongest and most red-shifted absorption as well as the highest hole mobility exhibited the highest J_{sc} and FF and hence performed best with a PCE of 6.75% and an IPCE response of 50-60% between 450 and 650 nm. Noticeably, **111** produced the highest V_{oc} of 1.03 V which the authors attribute to a hardly lower lying HOMO energy level of -5.19 eV for **111** in comparison to -5.18 eV for **110** and -5.16 eV for **112** and **113**. The series of

the group of L. Yi proved that longer conjugated backbones lead to better light-harvesting and that a better charge transport raises J_{SC} and FF values.

Structurally defined co-oligomers synthesized by the group of G. Bazan

G. Bazan and his group synthesized various linear D-A-D-A-D systems with bent shapes containing dithieno[3,2-b:2',3'-d]silole (DTS) as middle, two hexyl-bithiophenes as peripheral donor blocks, and two six-membered aromatic rings fused with thiadiazole as acceptors (Chart 5).^[59] In 2011, **114** was published as the first molecule of this series. It showed an intense charge transfer band at 625 nm in solution, which is red-shifted to 720 nm in thin films. The absorption onset is also shifted by 95 nm from 725 nm in solution to 820 nm in thin films.^[60]

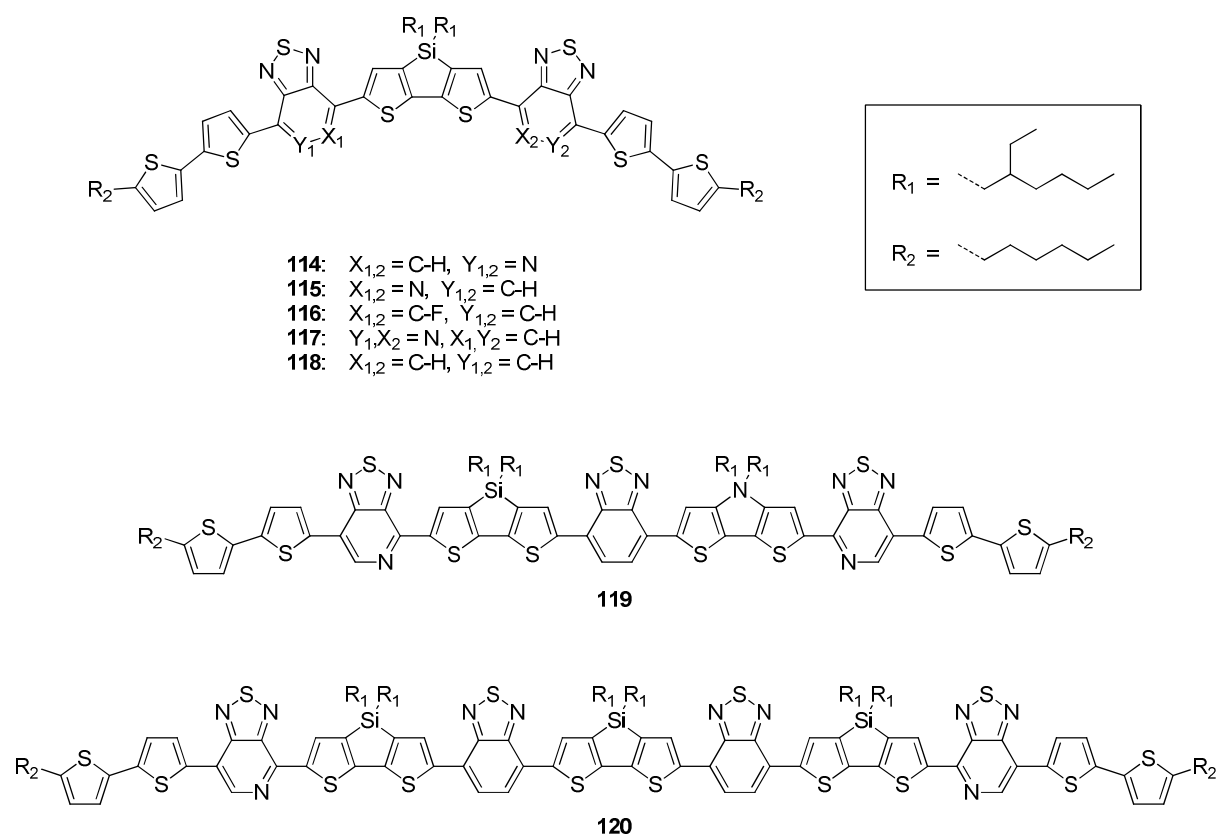


Chart 5. Structurally defined co-oligomers synthesized by the group of G. Bazan.^[60-64]

BHJSCs were fabricated blending **114** with PC₇₁BM. After device optimization including thermal annealing, which led to substantially more ordered donor domains, PCEs of up to 3.2% were reached ($J_{SC} = 10.9 \text{ mA cm}^{-2}$, $V_{OC} = 0.7 \text{ V}$, FF = 0.42, Table 5).^[60] Co-oligomer **115**, in which the nitrogen atoms of the formal pyridine rings are pointing towards the central DTS-unit, featured similar absorption

properties in thin films. Devices incorporating **115** exhibited improved PCEs of 6.7% ($J_{sc} = 14.4 \text{ mA cm}^{-2}$, $V_{oc} = 0.78 \text{ V}$, and $FF = 0.59$). The more than doubled PCE has its origin in different processing conditions (for **115** 0.25 v/v% DIO was used as additive) and a variation of the HTL layer. In reference [60] Plexcore OC AQ-1330 (Plextronics), a polythiophene bearing sulfonic acid groups, was used as HTL, on which **114**/PC₇₁BM blends were deposited. In contrast to this, MoO_x was used in the case of **115**.^[61] The improved PCE of **115** can be explained by a better interfacial contact between MoO_x and the blend layer (**115**:PC₇₁BM). Acidic HTLs, like Plexcore OC AQ-1330 or PEDOT:PSS, protonated the pyridyl nitrogens and resulted in interfacial contact issues. This was proven by replacing Plexcore OC AQ-1330 in devices using **114** as donor and employing NiO_x as HTL, whereupon a PCE of 5.1% was reached due to an increase in all solar cell characteristics (Table 5).^[65]

Table 5. Photovoltaic parameters of solution-processed BHJSCs (PC₇₁BM was used as acceptor, if not stated otherwise) incorporating structurally defined co-oligomers synthesized by the group of G. Bazan.

donor	HTL	$J_{sc} [\text{mA cm}^{-2}]$	$V_{oc} [\text{mV}]$	FF	PCE [%]
114 ^{[a][60]}	Plexcore OC AQ-1330	10.9	0.70	0.42	3.20
114 ^{[a][65]}	NiO _x	12.3	0.74	0.56	5.10
114 ^{[b][62]}	MoO _x	12.7	0.73	0.60	5.56
115 ^{[b][61]}	MoO _x	14.4	0.78	0.59	6.70
116 ^{[a,b][63]}	PEDOT:PSS	12.8	0.81	0.68	7.04
117 ^{[b][62]}	MoO _x	9.80	0.72	0.45	3.16
118 ^{[b][62]}	MoO _x	0.90	0.78	0.25	0.18
116 ^{[b,c][66]}	PEDOT:PSS	14.7	0.77	0.72	8.24
116 ^{[b,d][33]}	PEDOT:PSS	15.5	0.80	0.72	8.94
116 ^{[b,e][34]}	PEDOT:PSS	15.5	0.78	0.75	9.02
119 ^[a,e]	MoO _x	13.6	0.71	0.60	5.79
120 ^[e]	MoO _x	15.2	0.66	0.65	6.52

[a] Thermally annealed. [b] DIO was used as additive. [c] Low sheet resistance ITO used. [d] Optical spacer (ZnO) used. [e] Ba-cathode layer used. [e] PC₆₁BM was used as acceptor.

Formal replacement of the basic pyridyl nitrogens by fluoro-substituted carbons in **115** led to non-basic structurally defined molecule **116** (Chart 5).^[63] It showed a slightly blue-shifted absorption band at 590 nm with an onset at 678 nm in solution and one at 670 nm ($\lambda_{\text{onset}} = 800$ nm) in thin film in comparison to **114** and **115** (*vide supra*). The blue-shift originates from the slightly higher electron density in the fluoro substituted six-membered ring of **116** compared to **115** making it a weaker electron-accepting unit. However, the non-basic character and hence inert donor allowed to fabricate solar cells using PEDOT:PSS as HTL reaching PCEs of up to 7.0% ($J_{\text{sc}} = 12.8 \text{ mA cm}^{-2}$, $V_{\text{oc}} = 0.81 \text{ V}$, $\text{FF} = 0.68$) with PC₇₁BM as acceptor.

Since subtle molecular changes can have a dramatic effect on photovoltaic performance, the group of G. Bazan investigated the effect of the position of the pyridinyl nitrogen. Therefore, **117** and **118** were synthesized with pyridyl nitrogen atoms pointing to one side of the molecule and without any pyridyl nitrogen, respectively (Chart 5).^[62] The absorption in thin films is very similar for **114**, **115**, and **117** with a maximum at ~715 nm and the corresponding onset at ~825 nm. On the contrary, absorption spectra of **118** with its less electron-withdrawing benzothiadiazole acceptor units are around 40 nm blue-shifted. Fabrication of BHJSCs with PC₇₁BM, MoO_x as HTL, and the use of DIO as additive yielded PCEs of 5.56, 6.70, 3.16, and 0.18% for **114**, **115**, **117**, and **118**, respectively (Table 5). The lower moderate performance of **117** compared to **114** and **115** is attributed to the asymmetrical molecular structure leading to a larger degree of disorder in thin films, which is reflected in a lower hole mobility of $0.05 \text{ cm}^2 \text{ V}^{-1} \text{ s}^{-1}$ in comparison to 0.07 and $0.20 \text{ cm}^2 \text{ V}^{-1} \text{ s}^{-1}$ for **114** and **115**, respectively (determined by OFET measurement). This finding is also consistent with a lower FF observed for **117**.^[62] The highest hole mobility of $0.20 \text{ cm}^2 \text{ V}^{-1} \text{ s}^{-1}$ for **115** is explained by a intramolecular interaction of pyridyl nitrogen and DTS sulfur atoms in the bulk which enables **115** to bend more strongly than the other three co-oligomers leading to a favorable ordering in the solid state. On the contrary, **118** showing the lowest hole mobility of $0.01 \text{ cm}^2 \text{ V}^{-1} \text{ s}^{-1}$ and the lowest solar cell characteristics, has the worst ordering in the bulk in comparison to the other co-oligomers of the series, possibly due to the missing pyridyl nitrogen-sulfur interactions leading to a broader distribution of conformers and hence a lower tendency to self-assemble.^[62] These studies once again underline the importance of the morphology of the blend layer, which can be only partly controlled or modified by the processing conditions.

Recently, the group of A. Heeger could improve the PCE of **116** from 7.0% to over 8.2% by using ITO covered substrates with a lower sheet resistance of 5Ω (compared to 20 and 40Ω used before). Lower sheet resistances are obtained by thicker ITO layers, however light absorption by the HTL is increased as well.^[66] Further improvements to PCEs of around 9% were made by inserting a ZnO layer functioning as an optical spacer, for which reason more light could be harvested or using a Ba layer

to increase charge collection (Table 5).^[33] These layer optimizations show that also the architecture of the whole device plays a decisive role for the photovoltaic performance.

By synthesizing **119** and **120**, the group of G. Bazan studied the effect of elongating the conjugated backbone (Chart 5).^[64] Combining several donor and acceptor moieties as in **119** and **120**, the longest wavelength absorption in solution was ~50 nm red-shifted to 670 nm in comparison to the before mentioned series. High ϵ of 107,000 and 147,000 M⁻¹cm⁻¹ were obtained for **119** and **120**, respectively. Thin film absorption reached up to 850 nm which reflects the decreased bandgap of **119** and **120** and the better light-harvesting capability compared to the shorter series. OFETs were fabricated to measure hole mobilities of **119** and **120**.^[64] As-cast thin films of **115**, as the shortest representative of this series, featured a hole mobility of 0.02 cm² V⁻¹s⁻¹ showing complete deterioration upon thermal annealing beyond 150 °C. As-cast films of **119** and **120** possessed hole mobilities of 10⁻² and 6 × 10⁻³ cm² V⁻¹s⁻¹ and OFET devices exhibited high thermal stability up to 230 °C (3 × 10⁻³ cm² V⁻¹s⁻¹) and 250 °C (2.6 × 10⁻³ cm² V⁻¹s⁻¹) for **119** and **120**, respectively.^[64] BHJSCs were fabricated using PC₆₁BM (Table 5). Devices including **119** yielded a PCE of 5.79%, with a J_{sc} of 13.6 mA cm⁻², a V_{oc} of 0.71 V, and a FF of 0.60. **120** produced a higher J_{sc} of 15.2 mA cm⁻² due to better light-harvesting capability, but a lower V_{oc} of 0.66 V owing to the longer π -conjugated system leading to a higher lying HOMO energy level. Together with a slightly higher FF of 0.65 a PCE of 6.52% is reached for **120**. This means a more than 1.5 fold increase in PCE compared to devices containing **115** as donor material being fabricated without solvent additives or thermal annealing (PCE = 4.5%).^[61] These studies suggest that there is value in increasing molecular size within structurally well-defined organic semiconductors. Whether these advantages outweigh the additional synthetic effort has to be considered carefully.^[64]

Non-linear structurally defined co-oligomers

Besides linear molecular semiconductors also other architectures like dendritic or star-shaped structures are known.^[67] However, nearly exclusively linear architectures dominate the area of BHJSCs, this might be ascribed due to better film formation with a more favorable phase separation of the ball shaped fullerenes and rod-like linear semiconductors, since the combination of two three dimensional components may not lead to an optimal interpenetrated network.

Up to now, there is only one star-like system known yielding PCEs higher than 4.5%, tris-2-cyano-2-(4-nitrophenyl)-vinyl functionalized dithienyl carbazole **121** synthesized by Singh *et al.* (Chart 6).^[68] Due to its high polarity and missing alkyl chains in comparison to the previous presented co-oligomers, **121** is not sufficiently soluble in common solvents used for solution-processing of active

layers of BHJSCs like chloroform, chlorobenzene, dichlorobenzene, or xylene. Absorption spectroscopy was therefore performed in tetrahydrofuran (THF) solution and thin films were spin-coated from THF. The longest wavelength absorption band in solution is positioned at 580 nm and shifts by 40 nm to 620 nm and becomes broader and more structured when going to thin films. The emerging well-defined vibronic shoulder at around 656 nm indicates an effective π - π packing between the molecule backbones in the solid state and leads to a favorable absorption onset of ~ 700 nm.^[68]

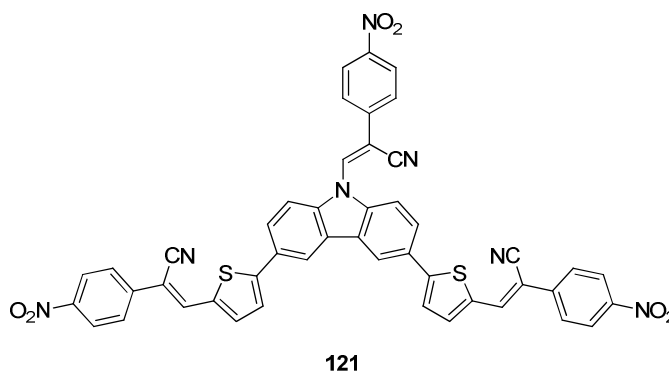


Chart 6. Star-shaped structurally defined molecule **121** for solution-processed BHJSCs.

121 was implemented in solution-processed BHJSCs. First device optimization regarding the use of PC₆₁BM and PC₇₁BM together with **121** in different weight ratios led to devices with PCEs of up to 2.65% (Table 6). High V_{OC} values of nearly 1 V were achieved, but low FF values below 0.4 limited the photovoltaic performance. The higher PCE for PC₇₁BM-based devices is claimed to be due to a more efficient charge transfer from the donor to the acceptor, probed by photoluminescence of thin films of neat **121** and **121**/PC₆₁BM and **121**/PC₇₁BM blends. This is also indicated by lower FF and J_{SC} values of devices using PC₆₁BM instead of PC₇₁BM as acceptor.^[68] The performance increase could also be due to an improved absorbance of the active layer due to the stronger absorbance of PC₇₁BM compared to PC₆₁BM. Further optimization was done by fabricating PC₆₁BM- and PC₇₁BM-based devices adding 3 v/v% CN to the spin-coating solution. By probing thin films spin-coated with and without CN as additive with XRD spectroscopy, it was found that a more organized assembly of **121** is present in thin films spin-coated from CN-THF mixture. Also, electron and hole mobilities determined by the SCLC method on electron- and hole-only devices are more balanced for **121**/PC₇₁BM blend layers spin-coated from CN-THF with a hole mobility of $2.4 \times 10^{-5} \text{ cm}^2 \text{ V}^{-1} \text{ s}^{-1}$ and an electron mobility of $9.8 \times 10^{-5} \text{ cm}^2 \text{ V}^{-1} \text{ s}^{-1}$ compared to layers fabricated without the use of CN (hole mobility: $5.87 \times 10^{-7} \text{ cm}^2 \text{ V}^{-1} \text{ s}^{-1}$ and electron mobility: $2.05 \times 10^{-4} \text{ cm}^2 \text{ V}^{-1} \text{ s}^{-1}$). The better film morphology improves J_{SC} and FF to 11.2 mA cm^{-2} and 0.48, respectively, resulting in a PCE of 4.96%. The effect of the additive is

ascribed to the low solubility of fullerenes in THF which is improved by the addition of CN being a good solvent for both PC₆₁BM and PC₇₁BM. Slowing down the nucleation and crystallization process by increasing the solubility leads to larger crystallites and better phase separation between the donor and acceptor materials in the BHJ layer, which consequently enhances PCE of the device.^[68] However, too large domains (domain sizes » 2L_D) are detrimental for device performance. One drawback of non-linear structure **121** certainly is its low solubility, which is insufficient for solution-processing in solvents which are commonly used for processing fullerene derivatives. Hence, FF does not exceed 0.5 reflecting a moderate morphology. Up to now, **121** is the only example for a non-linear molecular donor material for solution-processed BHJSCs with a PCE greater than 4.5%.

Table 6. Photovoltaic parameters of solution-processed BHJSC incorporating structurally defined molecule **121** as donor.

donor	acceptor	J_{sc} [mA cm ⁻²]	V_{oc} [mV]	FF	PCE [%]
121 ^[68]	PC ₆₁ BM	6.08	0.94	0.34	1.94
121 ^[68]	PC ₇₁ BM	7.26	0.96	0.38	2.65
121 ^{[a][68]}	PC ₆₁ BM	9.73	0.92	0.43	3.76
121 ^{[a][68]}	PC ₇₁ BM	11.2	0.92	0.48	4.96

[a] 3 v/v% CN added

4.4 Conclusions for the molecular design of structurally defined oligomers and co-oligomers for solution-processed BHJSCs

From the previous two sections rough design rules for the synthesis of solution-processable structurally defined oligomers and co-oligomers can be extracted. First of all, optoelectronic properties should be optimized with respect to light-harvesting and energy alignment of the HOMO and LUMO energy levels. Light-harvesting capability is determined by the band gap between the HOMO and LUMO energy levels. In order to be able to absorb low energy photons the band gap should be minimized. In most examples, reviewed in this chapter, this is realized by combining electron-rich donor and electron-poor acceptor moieties thus raising the HOMO energy level and lowering the LUMO energy level of the oligomer, respectively. However, two compromises have to be made: (1) E_{LUMO} of the donor has to be positioned ~0.3 eV higher than E_{LUMO} of the acceptor to

ensure efficient exciton separation at the donor acceptor interface. (2) The energy difference between E_{HOMO} of the donor and E_{LUMO} of the acceptor directly influences the V_{OC} ($V_{\text{OC}} = (1/e)(|E_{\text{HOMO,donor}}| - |E_{\text{LUMO,acceptor}}|) - 0.3 \text{ V}$; e = elementary charge).^[36] PC₆₁BM, which is commonly used as acceptor material in BHJSC, possesses an E_{LUMO} of -4.0 eV and an E_{HOMO} of -6.0 eV.^[69] A device with a desired V_{OC} of 0.8 V should therefore utilize a donor material with an E_{LUMO} of -3.7 eV and an E_{HOMO} of -5.1 eV. This would result in an optical band gap of 1.4 eV which corresponds to an absorption of up to 880 nm. For absorbing photons with energy lower than 1.4 eV, either the E_{LUMO} has to be decreased (probably leading to issues in charge separation) or the E_{HOMO} has to be raised (leading to lower V_{OC}). Secondly, solubility of the donor has to be high to guarantee solution processability and favorable film forming properties. Usually this is achieved by introducing linear or branched alkyl chains orthogonal to and/or as elongation of the conjugated backbone.^[54,60,64,70] However, alkyl chains do not contribute to charge transport, especially long alkyl chains may have an insulating bulk effect, thereby reducing charge transport.^[71] Additionally, they can cause the conjugated backbone to twist which then reduces the conjugation length and consequently increases the optical band gap.^[72] Also the packing/stacking can be influenced by the nature and size of alkyl chains.^[42,49] Therefore, also here a reasonable compromise has to be found. This leads to the next important property: high charge transport mobilities (in the case of the donor material a high hole mobility). By incorporating large, rigid, and planar fused multicyclic systems self-assembly and molecular packing can be improved which promote cofacial π - π stacking in the solid state leading to higher charge transport mobilities.^[32,58,62] Polar motifs can build up intermolecular interaction which also help the ordering of the oligomers and co-oligomers in the bulk and hence be beneficial for charge transport.^[27,73,74]

Beside these properties, which are mainly determined by the molecular structure, there are also other important factors that play a major role for the photovoltaic performance. For example the device structure (e.g. optical spacers^[33]), the materials chosen for the corresponding layers (e.g. HTL^[65]), or the until now unpredictable morphology of the photoactive layer. The morphology, generally given by the nature of donor and acceptor material, can be strongly influenced by the processing conditions, e.g. temperature, solvent, additive, concentration, or constitution (D:A ratio) of the spin-coating solution, spin-coating velocity, duration, or temperature, post treatments of the blend layer (thermal or solvent annealing) etc. This clearly shows that fabricating high performing BHJSCs is a multidisciplinary challenge.

In the following three chapters, the herein before mentioned guidelines are applied to synthesize novel soluble molecular donor materials and incorporate them in BHJSCs, which in turn should contribute to further insight and understanding concerning molecular design.

4.5 References

- [1] V. Y. Merritt, H. J. Hovel, *Appl. Phys. Lett.* **1976**, 29, 414-415.
- [2] A. P. Marchetti, C. W. Tang, R. H. Young, *US4125414 A*, Eastman Kodak, **1978**.
- [3] C. W. Tang, *CA1085947 A1*, Eastman Kodak, **1980**.
- [4] T. Feng, A. K. Ghosh, *US 4127738 A*, Exxon Research & Engineering Company, **1978**.
- [5] D. L. Morel, A. K. Ghosh, T. Feng, E. L. Stogryn, P. E. Purwin, R. F. Shaw, C. Fishman, *Appl. Phys. Lett.* **1978**, 32, 495-497.
- [6] C. W. Tang, *Appl. Phys. Lett.* **1986**, 48, 183-185.
- [7] B. A. Gregg, *MRS Bull.* **2005**, 30, 20-22.
- [8] N. S. Sariciftci, L. Smilowitz, A. J. Heeger, F. Wudl, *Science* **1992**, 258, 1474-1476.
- [9] G. Yu, J. Gao, J. C. Hummelen, F. Wudl, A. J. Heeger, *Science* **1995**, 270, 1789-1791.
- [10] J. J. M. Halls, C. A. Walsh, N. C. Greenham, E. A. Marseglia, R. H. Friend, S. C. Moratti, A. B. Holmes, *Nature* **1995**, 376, 498-500.
- [11] Z. He, C. Zhong, X. Huang, W.-Y. Wong, H. Wu, L. Chen, S. Su, Y. Cao, *Adv. Mater.* **2011**, 23, 4636-4643.
- [12] Z. He, C. Zhong, S. Su, M. Xu, H. Wu, Y. Cao, *Nat Photon* **2012**, 6, 591-595.
- [13] L. Dou, W.-H. Chang, J. Gao, C.-C. Chen, J. You, Y. Yang, *Adv. Mater.* **2013**, 25, 825-831.
- [14] L. Dou, C.-C. Chen, K. Yoshimura, K. Ohya, W.-H. Chang, J. Gao, Y. Liu, E. Richard, Y. Yang, *Macromolecules* **2013**, 46, 3384-3390.
- [15] Y. Chen, X. Wan, G. Long, *Acc. Chem. Res.* **2013**, 46, 2645-2655.
- [16] J. Roncali, P. Frère, P. Blanchard, R. de Bettignies, M. Turbiez, S. Roquet, P. Leriche, Y. Nicolas, *Thin Solid Films* **2006**, 511-512, 567-575.
- [17] X. Sun, Y. Zhou, W. Wu, Y. Liu, W. Tian, G. Yu, W. Qiu, S. Chen, D. Zhu, *J. Phys. Chem. B* **2006**, 110, 7702-7707.
- [18] N. Kopidakis, W. J. Mitchell, J. van de Lagemaat, D. S. Ginley, G. Rumbles, S. E. Shaheen, W. L. Rance, *Appl. Phys. Lett.* **2006**, 89, 103524.
- [19] M. T. Lloyd, A. C. Mayer, S. Subramanian, D. A. Mourey, D. J. Herman, A. V. Bapat, J. E. Anthony, G. G. Malliaras, *J. Am. Chem. Soc.* **2007**, 129, 9144-9149.
- [20] P. F. Xia, X. J. Feng, J. Lu, S.-W. Tsang, R. Movileanu, Y. Tao, M. S. Wong, *Adv. Mater.* **2008**, 20, 4810-4815.
- [21] S. Roquet, A. Cravino, P. Leriche, O. Alévêque, P. Frère, J. Roncali, *J. Am. Chem. Soc.* **2006**, 128, 3459-3466.
- [22] F. Silvestri, M. D. Irwin, L. Beverina, A. Facchetti, G. A. Pagani, T. J. Marks, *J. Am. Chem. Soc.* **2008**, 130, 17640-17641.

- [23] N. M. Kronenberg, M. Deppisch, F. Würthner, H. W. A. Lademann, K. Deing, K. Meerholz, *Chem. Commun.* **2008**, 6489-6491.
- [24] T. Rousseau, A. Cravino, T. Bura, G. Ulrich, R. Ziessel, J. Roncali, *Chem. Commun.* **2009**, 1673-1675.
- [25] J. Roncali, *Acc. Chem. Res.* **2009**, *42*, 1719-1730.
- [26] K. Schulze, C. Uhrich, R. Schüppel, K. Leo, M. Pfeiffer, E. Brier, E. Reinold, P. Bäuerle, *Adv. Mater.* **2006**, *18*, 2872-2875.
- [27] R. Fitzner, E. Mena-Osteritz, A. Mishra, G. Schulz, E. Reinold, M. Weil, C. Körner, H. Ziehlke, C. Elschner, K. Leo, M. Riede, M. Pfeiffer, C. Uhrich, P. Bäuerle, *J. Am. Chem. Soc.* **2012**, *134*, 11064-11067.
- [28] A. Mishra, P. Bäuerle, *Angew. Chem.* **2012**, *124*, 2060-2109; *Angew. Chem. Int. Ed.* **2012**, *51*, 2020-2067.
- [29] R. Meerheim, C. Körner, K. Leo, *Appl. Phys. Lett.* **2014**, *105*, 063306.
- [30] http://www.heliatek.com/newscenter/latest_news; press release **2013**. (retrieved on May 7, 2015)
- [31] B. Walker, C. Kim, T.-Q. Nguyen, *Chem. Mater.* **2010**, *23*, 470-482.
- [32] J. Zhou, Y. Zuo, X. Wan, G. Long, Q. Zhang, W. Ni, Y. Liu, Z. Li, G. He, C. Li, B. Kan, M. Li, Y. Chen, *J. Am. Chem. Soc.* **2013**, *135*, 8484-8487.
- [33] A. K. K. Kyaw, D. H. Wang, D. Wynands, J. Zhang, T.-Q. Nguyen, G. C. Bazan, A. J. Heeger, *Nano Lett.* **2013**, *13*, 3796-3801.
- [34] V. Gupta, A. K. K. Kyaw, D. H. Wang, S. Chand, G. C. Bazan, A. J. Heeger, *Sci. Rep.* **2013**, *3*, 1965.
- [35] H.-L. Yip, A. K. Y. Jen, *Energy Environ. Sci.* **2012**, *5*, 5994-6011.
- [36] M. C. Scharber, D. Mühlbacher, M. Koppe, P. Denk, C. Waldauf, A. J. Heeger, C. J. Brabec, *Adv. Mater.* **2006**, *18*, 789-794.
- [37] B. P. Rand, J. Genoe, P. Heremans, J. Poortmans, *Prog. Photovolt: Res. Appl.* **2007**, *15*, 659-676.
- [38] Y. Lin, Y. Li, X. Zhan, *Chem. Soc. Rev.* **2012**, *41*, 4245-4272.
- [39] B. Walker, A. B. Tamayo, X.-D. Dang, P. Zalar, J. H. Seo, A. Garcia, M. Tantiwiwat, T.-Q. Nguyen, *Adv. Funct. Mater.* **2009**, *19*, 3063-3069.
- [40] S. Qu, H. Tian, *Chem. Commun.* **2012**, *48*, 3039-3051.
- [41] J. Liu, B. Walker, A. Tamayo, Y. Zhang, T.-Q. Nguyen, *Adv. Funct. Mater.* **2013**, *23*, 47-56.
- [42] J. Liu, Y. Sun, P. Moonsin, M. Kuik, C. M. Proctor, J. Lin, B. B. Hsu, V. Promarak, A. J. Heeger, T.-Q. Nguyen, *Adv. Mater.* **2013**, *25*, 5898-5903.
- [43] W. Li, M. Kelchtermans, M. M. Wienk, R. A. J. Janssen, *J. Mater. Chem. A* **2013**, *1*, 15150-15157.

- [44] G. D. Sharma, M. A. Reddy, K. Ganesh, S. P. Singh, M. Chandrasekharam, *RSC Adv.* **2014**, *4*, 732-742.
- [45] Y. Lin, L. Ma, Y. Li, Y. Liu, D. Zhu, X. Zhan, *Adv. Energy Mater.* **2013**, *3*, 1166-1170.
- [46] J. Huang, C. Zhan, X. Zhang, Y. Zhao, Z. Lu, H. Jia, B. Jiang, J. Ye, S. Zhang, A. Tang, Y. Liu, Q. Pei, J. Yao, *ACS Appl. Mater. Interfaces* **2013**, *5*, 2033-2039.
- [47] Y. Liu, J. Zhou, X. Wan, Y. Chen, *Tetrahedron* **2009**, *65*, 5209-5215.
- [48] B. Yin, L. Yang, Y. Liu, Y. Chen, Q. Qi, F. Zhang, S. Yin, *Appl. Phys. Lett.* **2010**, *97*, 023303.
- [49] Y. Liu, X. Wan, F. Wang, J. Zhou, G. Long, J. Tian, J. You, Y. Yang, Y. Chen, *Adv. Energy Mater.* **2011**, *1*, 771-775.
- [50] Y. Liu, X. Wan, F. Wang, J. Zhou, G. Long, J. Tian, Y. Chen, *Adv. Mater.* **2011**, *23*, 5387-5391.
- [51] Z. Li, G. He, X. Wan, Y. Liu, J. Zhou, G. Long, Y. Zuo, M. Zhang, Y. Chen, *Adv. Energy Mater.* **2012**, *2*, 74-77.
- [52] H. Jin, M. Tuomikoski, J. Hiltunen, P. Kopola, A. Maaninen, F. Pino, *J. Phys. Chem. C* **2009**, *113*, 16807-16810.
- [53] J. J.-A. Chen, T. L. Chen, B. Kim, D. A. Poulsen, J. L. Mynar, J. M. J. Fréchet, B. Ma, *ACS Appl. Mater. Interfaces* **2010**, *2*, 2679-2686.
- [54] J. Zhou, X. Wan, Y. Liu, Y. Zuo, Z. Li, G. He, G. Long, W. Ni, C. Li, X. Su, Y. Chen, *J. Am. Chem. Soc.* **2012**, *134*, 16345-16351.
- [55] R. S. Kularatne, P. Sista, H. Q. Nguyen, M. P. Bhatt, M. C. Biewer, M. C. Stefan, *Macromolecules* **2012**, *45*, 7855-7862.
- [56] Y. Liang, D. Feng, Y. Wu, S.-T. Tsai, G. Li, C. Ray, L. Yu, *J. Am. Chem. Soc.* **2009**, *131*, 7792-7799.
- [57] Y. Liu, Y. Yang, C.-C. Chen, Q. Chen, L. Dou, Z. Hong, G. Li, Y. Yang, *Adv. Mater.* **2013**, *25*, 4657-4662.
- [58] S. Shen, P. Jiang, C. He, J. Zhang, P. Shen, Y. Zhang, Y. Yi, Z. Zhang, Z. Li, Y. Li, *Chem. Mater.* **2013**, *25*, 2274-2281.
- [59] Y. Lin, Z.-G. Zhang, H. Bai, Y. Li, X. Zhan, *Chem. Commun.* **2012**, *48*, 9655-9657.
- [60] G. C. Welch, L. A. Perez, C. V. Hoven, Y. Zhang, X.-D. Dang, A. Sharenko, M. F. Toney, E. J. Kramer, T.-Q. Nguyen, G. C. Bazan, *J. Mater. Chem.* **2011**, *21*, 12700-12709.
- [61] Y. Sun, G. C. Welch, W. L. Leong, C. J. Takacs, G. C. Bazan, A. J. Heeger, *Nat. Mater.* **2012**, *11*, 44-48.
- [62] C. J. Takacs, Y. Sun, G. C. Welch, L. A. Perez, X. Liu, W. Wen, G. C. Bazan, A. J. Heeger, *J. Am. Chem. Soc.* **2012**, *134*, 16597-16606.
- [63] T. S. van der Poll, J. A. Love, T.-Q. Nguyen, G. C. Bazan, *Adv. Mater.* **2012**, *24*, 3646-3649.
- [64] X. Liu, Y. Sun, L. A. Perez, W. Wen, M. F. Toney, A. J. Heeger, G. C. Bazan, *J. Am. Chem. Soc.* **2012**, *134*, 20609-20612.

- [65] A. Garcia, G. C. Welch, E. L. Ratcliff, D. S. Ginley, G. C. Bazan, D. C. Olson, *Adv. Mater.* **2012**, *24*, 5368-5373.
- [66] D. H. Wang, A. K. K. Kyaw, V. Gupta, G. C. Bazan, A. J. Heeger, *Adv. Energy Mater.* **2013**, *3*, 1161-1165.
- [67] A. Mishra, C.-Q. Ma, P. Bäuerle, *Chem. Rev.* **2009**, *109*, 1141-1276.
- [68] M. Singh, R. Kurchania, J. A. Mikroyannidis, S. S. Sharma, G. D. Sharma, *J. Mater. Chem. A* **2013**, *1*, 2297-2306.
- [69] J. C. Hummelen, B. W. Knight, F. LePeq, F. Wudl, J. Yao, C. L. Wilkins, *J. Org. Chem.* **1995**, *60*, 532-538.
- [70] Y. Liu, X. Wan, B. Yin, J. Zhou, G. Long, S. Yin, Y. Chen, *J. Mater. Chem.* **2010**, *20*, 2464-2468.
- [71] L. Yang, H. Zhou, W. You, *J. Phys. Chem. C* **2010**, *114*, 16793-16800.
- [72] S. Ko, E. T. Hoke, L. Pandey, S. Hong, R. Mondal, C. Risko, Y. Yi, R. Noriega, M. D. McGehee, J.-L. Brédas, A. Salleo, Z. Bao, *J. Am. Chem. Soc.* **2012**, *134*, 5222-5232.
- [73] R. Fitzner, E. Reinold, A. Mishra, E. Mena-Osteritz, H. Ziehlke, C. Körner, K. Leo, M. Riede, M. Weil, O. Tsaryova, A. Weiß, C. Urich, M. Pfeiffer, P. Bäuerle, *Adv. Funct. Mater.* **2011**, *21*, 897-910.
- [74] C. Elschner, M. Schrader, R. Fitzner, A. A. Levin, P. Bäuerle, D. Andrienko, K. Leo, M. Riede, *RSC Adv.* **2013**, *3*, 12117-12123.

Chapter 5

Structurally Defined Co-Oligomers Containing Dithienopyrrole for Solution-Processed Organic Solar Cells

Adapted from M. Weidelener et al., *Chem. Commun.* **2013**, 49, 10865-10867.
with permission from The Royal Society of Chemistry

5.1 Introduction

5.1.1 General introduction

In the previous chapter, an overview was given about highly performing donor oligomers and co-oligomers for solution-processed bulk-heterojunction solar cells (BHJSC). It was shown that the application of the linear acceptor(A)-donor(D)-acceptor(A) concept generates well performing structurally defined oligomers and co-oligomers. One way to further improve the performance of these oligomers and co-oligomers is to red-shift the absorption giving rise to better light-harvesting systems, thus increasing short-circuit current (J_{sc}) and therefore the power conversion efficiency (PCE) of the corresponding solar cells. This can be realized by introducing a very strong electron-donating group D_2 into linear A-D-A systems resulting in a linear A- D_1 - D_2 - D_1 -A assembly as depicted in Figure 1a, where A denotes electron-accepting units and D_1 and D_2 electron-donating moieties. By enhancing the electron density of the molecular backbone the charge-transfer (CT) absorption band should be red-shifted and intensified. Additionally, the use of electron-rich conjugated moieties can further improve hole transport properties.

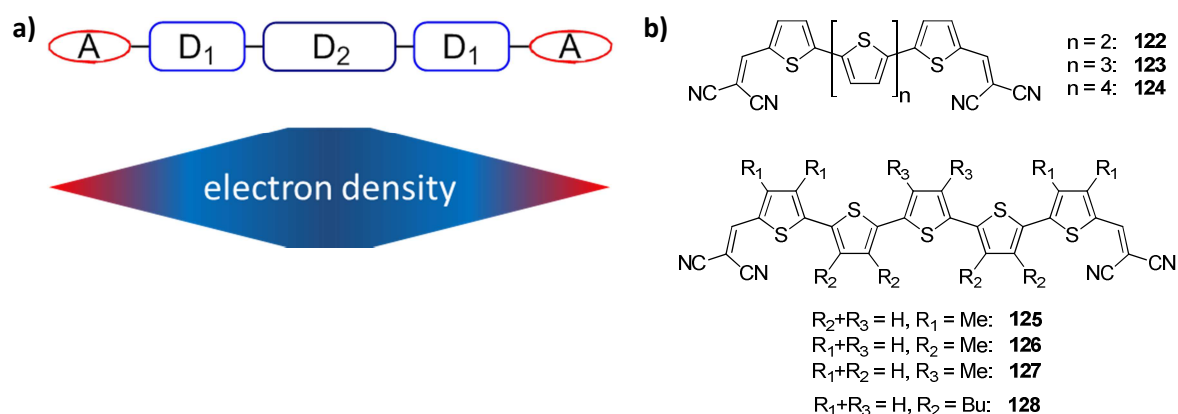


Figure 1. (a) Molecular design of compounds synthesized in this chapter and a schematic illustration of the electron density distribution; blue: high electron density, red: low electron density. (b) DCV-substituted oligothiophenes successfully applied in vacuum-processed OSC.

By the start of this project, dicyanovinylene(DCV)-substituted A-D-A oligothiophenes **122-127** have already been widely investigated by the group of P. Bäuerle and successfully implemented in vacuum-processed organic solar cells (OSCs) achieving PCEs up to 8.3% in single junction solar cells (Figure 1b).^[1-4] They show high thermal stabilities, low solubilities due to missing or only poorly solubilizing substituents, but fine-tunable good electronic and charge transport properties, owing to their oligothiophene backbone.^[5] Oligothiophenes **122**, **123**, and **124** feature absorption maxima in

solution of 518, 530, and 532 nm and reversible first oxidation waves at 0.84, 0.64, and 0.46 V, respectively. Quaterthiophene **122** possesses a blue-shifted absorption in comparison to **123** and **124** which led to a lower J_{SC} , thus reducing the overall photovoltaic performance. Sexithiophene **124** possessed the highest lying HOMO energy level among the series **122-124** resulting in a lower open-circuit voltage (V_{OC}) compared to **122** and **123**. Vacuum-processed bilayer OSCs with C_{60} as acceptor led to PCEs between 1.2% (**122**) and 2.8% (**123**). BHJSCs of **124** and C_{60} yielded up to 5.2% PCE, with a J_{SC} of 11.1 mA cm^{-2} , a V_{OC} 0.97 V, and a fill factor (FF) of 0.49, which was the highest efficiency at that time.^[1] Further structural fine-tuning was realized by adding methyl groups to the oligothiophene backbone.^[2] The methyl substitution pattern along the conjugated backbone was systematically varied to obtain **125**, **126**, and **127** with methyl groups on the outer thiophenes, thiophenes two and four, or the central thiophene, respectively. The three derivatives showed slight blue-shifts in their absorption compared to parental compound **123** due to backbone twisting induced by the methyl groups. Oligomer **127** performed best in OSC, achieving a PCE of 6.9% ($J_{SC} = 11.5 \text{ mA cm}^{-2}$, $V_{OC} = 0.95 \text{ V}$, and $FF = 0.63$) compared to 4.8% for **125** and **126**. The better efficiency is correlated to a better packing and morphology of **127**/ C_{60} blends, pointed out by X-ray diffraction (XRD) measurements of co-evaporated films and single-crystal X-ray structure analysis of **127**.^[2] Recently, Meerheim *et al.* could further improve the PCE of **127** by device optimization to 8.3% for a single junction and up to 9.7% for a triple junction cell.^[4]

In contrast to poorly soluble oligothiophenes **122-127**, well soluble tetrabutyl-quinquethiophene **128**^[3] can be applied in solution- as well as in vacuum-processed OSCs. G. Schulz *et al.* reported solution-processed BHJSCs incorporating **128**: $[6,6]$ -phenyl-C₆₁-butyric acid methyl ester (PC₆₁BM) as active layer reaching PCEs of up to 3.0%,^[6] whereas vacuum-processed OSCs of **128** with C_{60} yielded comparable PCEs of 3.5%.^[7] This rare direct comparison is a very promising result for the use of DCV-substituted oligothiophenes in solution-processed BHJSCs.

Expanding these oligothiophene series by the strong electron donor dithieno[3,2-b:2',3'-d]pyrrole (DTP) led to a first series of DTP-containing structurally co-oligomers **129-131** for solution-processed BHJSCs (Figure 2). Solubilizing alkyl chains had to be implemented to ensure solution processability: D_1 moieties consisting of thiophenes are equipped with regioregular hexyl chains; for DTP the branched alkyl side chain 2-ethylhexyl was chosen to compensate the solubility decreasing effect of the planar and rigid DTP-unit.

The motivation in the variations within series **129-131** layed in the investigation of the effect of different hexyl substitution patterns (**129** vs. **130**) and different conjugation lengths (**129** vs. **131**) on the optoelectronic properties as well as solubility and solar cell characteristics. Changing the hexyl

substitution pattern in **129** (hexyl chains arranged on thiophene β -positions distal to the DTP-unit), so that the hexyl substituents are located at the thiophene β -positions proximal to the DTP-unit, co-oligomer **130** is generated. It is expected that the shift of the alkyl side chains has an effect on the optoelectronic properties, the solubility as well as on the packing in the bulk due to a different π -backbone twisting. Going from co-oligomer **129** to **131** the theoretical conjugation length is reduced by two hexylthiophenes which should lead to differences in the optoelectronic properties and of course on the solubility affecting film forming properties.

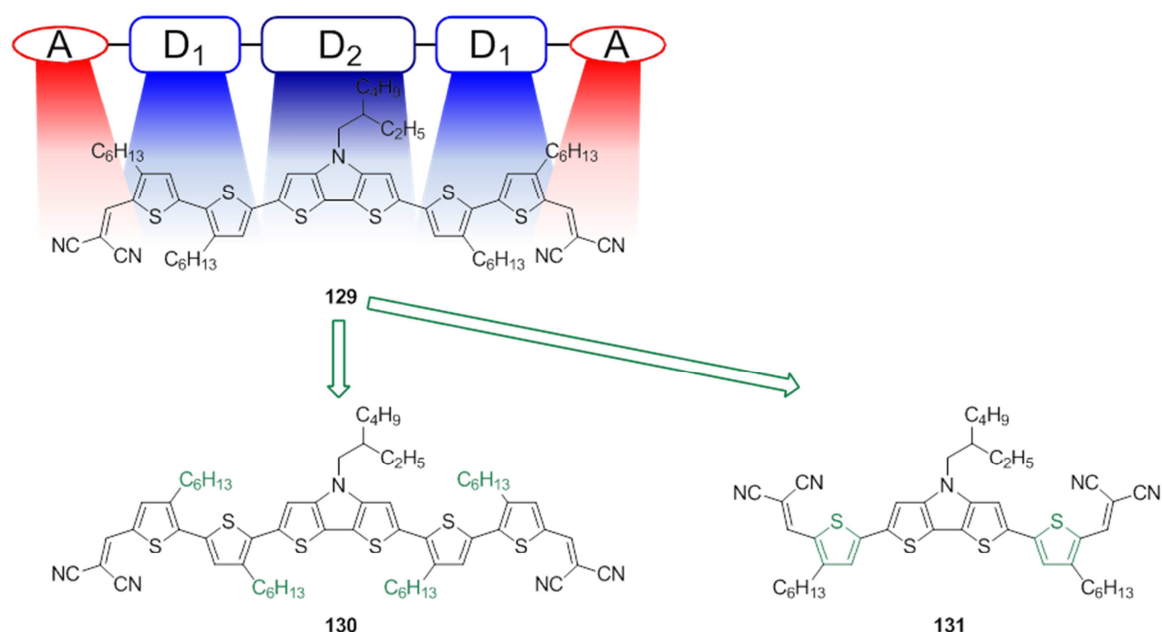


Figure 2. Structurally defined co-oligomer series **129-131** following A-D₁-D₂-D₁-A design concept.

In the following section, the synthesis of the DTP-unit and the advantageous properties of DTP-comprising oligomers and co-oligomers and their use in organic photovoltaics (OPVs) showing that DTP is a promising building block for solution-processed oligomers.^[8]

5.1.2 Dithieno[3,2-b:2',3'-d]pyrrole-based materials

DTP – Synthesis and Properties

DTP **132a** is an annulated system consisting of a bithiophene bridged with a nitrogen atom (Chart 1). Due to the electron-rich bridging unit, DTP is a conjugated system possessing a strong electron-donating character. This can be seen in its electrochemical properties as its HOMO energy level is located at ~ -4.0 eV vs. vacuum compared to the one of 2,2'-bithiophene at ~ -3.5 eV.^[9-11] Electron-

rich moieties are typically used 1) to build D-A oligomers and copolymers in order to achieve panchromatic absorption by CT absorption bands and 2) to generate p-type semiconducting properties. Additionally, the annulation of aromatic rings decreases the torsion along the conjugated backbone leading to an elongated effective conjugation length and thus to improved charge transport properties, also due to the higher possibility to form larger π - π stacks.^[12] A further advantage of the bridging lies in the functionalization of the DTP-nitrogen with solubilizing alkyl chains, which does not result in backbone twisting or desymmetrization of the molecule as in the case of bithiophene.^[8]

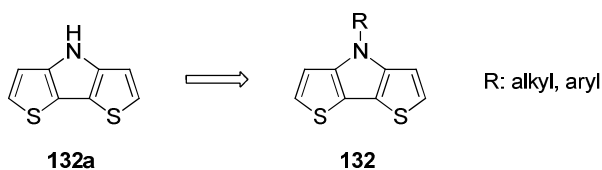
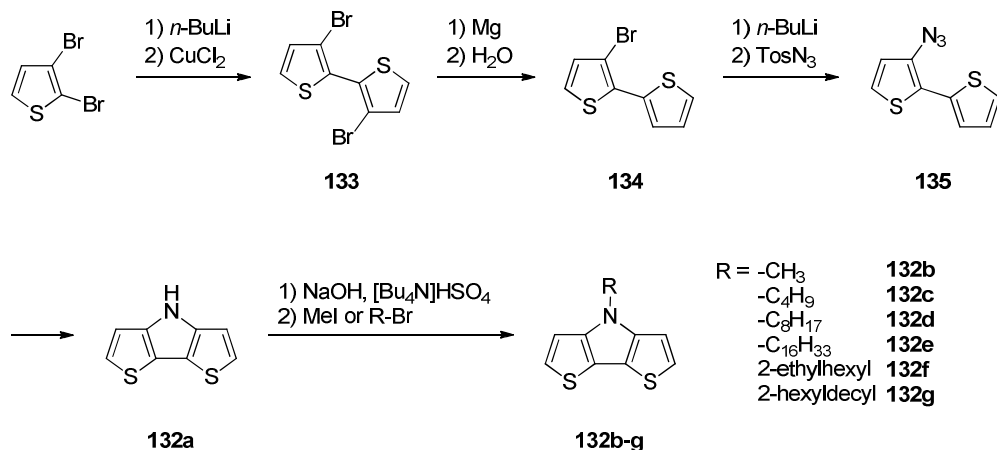


Chart 1. Structure of 4H-dithieno[3,2-b:2',3'-d]pyrrole (**132a**) and more soluble derivatives **132** bearing a side chain R.

DTP **132a** was firstly reported and synthesized by Zanirato *et al.* in 1983 by thermal decomposition of *ortho*-azidobithiophene **135** (Scheme 1).^[13]

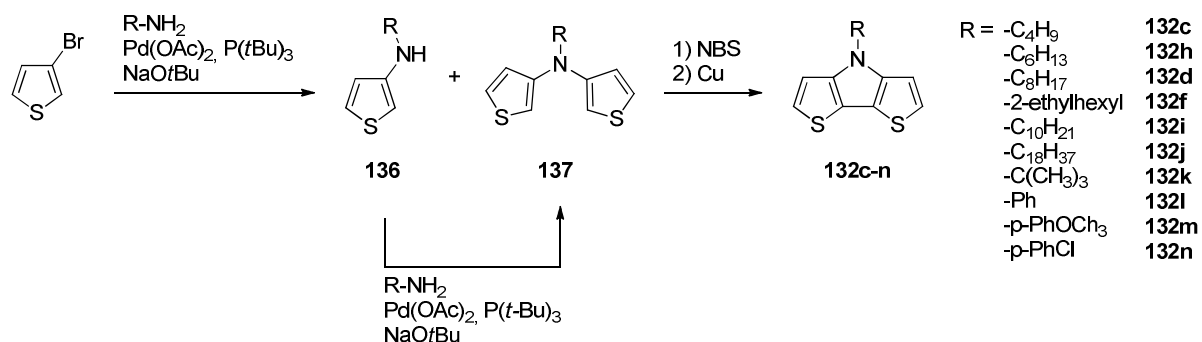


Scheme 1. First synthesis of 4H-dithieno[3,2-b:2',3'-d]pyrrole **132a** and its N-alkylated derivatives **132b-132g**.

For the synthesis of azide **135**, 2,3-dibromothiophene was homo-coupled by lithiation and addition of copper(II) chloride.^[14] The resulting dibromo-bithiophene **133** was partially debrominated to obtain bromobithiophene **134**^[15] which was then lithiated and treated with tosyl azide in order to generate DTP precursor **135**. Via this route, unsubstituted DTP **132a** was obtained in four steps in an overall

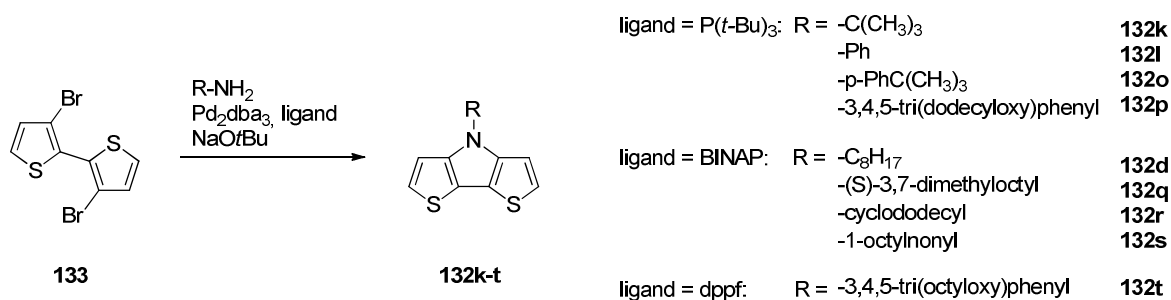
yield of ~19%. Alkylation of the DTP nitrogen in **132a** to increase solubility was reported by Zotti *et al.* using a base and the corresponding alkyl halide (Scheme 1). With this reaction sequence, various DTPs (**132b-132g**) have become available. However, the number of synthetic steps and the moderate overall yields of ~13% limited their use as building block for organic materials.

In 2003, a new route to *N*-substituted DTPs was reported by Ogawa and Rasmussen (Scheme 2).^[10] Starting with different primary amines and commercially available 3-bromothiophene Buchwald-Hartwig amination was applied to obtain a mixture of alkylated aminothiophene **136** and *N*-(thienyl)aminothiophene **137**. Isolation of the mono-reacted **136** and further conversion with 3-bromothiophene led to a total yield of ~60% for *N*-(thienyl)aminothiophenes **137**.^[16] Following copper-mediated Ullmann coupling produced DTPs **132c-132n** in overall yields of >40%. This is a more than three times increased yield compared to the previously reported route of Zanirato *et al.*



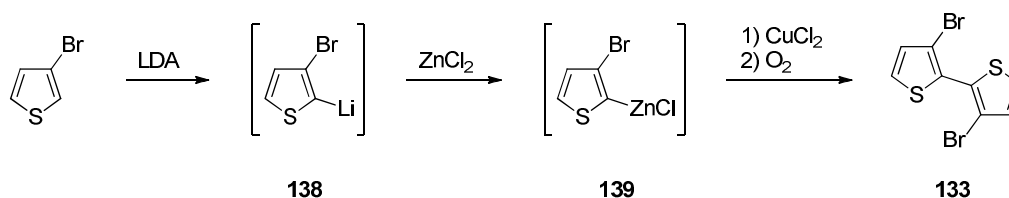
Scheme 2. Synthesis of *N*-functionalized DTPs **132c-132n** via Buchwald-Hartwig amination of 3-bromothiophene and subsequent annulation.

Nozaki *et al.* also used the Buchwald-Hartwig amination to generate *N*-functionalized DTPs **132k-132t** via tandem coupling of aniline with 3,3'-dibromo-2,2'-bithiophene (Scheme 3).^[17] *N*-Phenyl-DTP **132l** was produced in this way with a yield of 35%. Koeckelberghs *et al.* could enhance this yield for various DTPs (**132d**, **132q-132s**) to ~80% by changing the ligand from P(*t*Bu)₃ to BINAP and increasing the temperature from 80 °C to 110 °C.^[18] Taking the synthesis of **133** into account, overall yields of >40% were obtained for different *N*-functionalized DTPs similarly to the synthetic method shown in Scheme 2.



Scheme 3. Tandem Buchwald-Hartwig amination towards *N*-functionalized DTPs **132k-132t** starting from 3,3'-dibromo-2,2'-bithiophene **133**.

Due to the more stable and therefore easier to handle 3,3'-dibromo-2,2'-bithiophene **133** in comparison to aminothiophenes **136** and **137**, the method presented in Scheme 3 was preferred for the synthesis of DTPs. However, a main drawback of this route is the moderate yield in the preparation of 3,3'-dibromo-2,2'-bithiophene (~60%) and the need for the more expensive 2,3-dibromothiophene as starting material (Scheme 1) compared to 3-bromothiophene. Thus, to improve the utility of **133**, Evenson and Rasmussen developed a new procedure for the synthesis of dibromo-bithiophene **133** (Scheme 4).^[19] Selective deprotonation of 3-bromothiophene with lithium diisopropylamide (LDA) at the 2-position and subsequent addition of $ZnCl_2$ to the lithiated intermediate **138** led to thienylzinc chloride **139**, which reacts in a more controlled fashion with $CuCl_2$ than its lithiated analogue **138**.^[20] The $CuCl_2$ -mediated oxidative coupling was assisted by the addition of oxygen whereupon **133** was obtained in high yields (85-90%).^[19] By combination of the procedures given in Scheme 3 and 4, large scale synthesis of different DTPs can be carried out in two steps with overall yields of 70-80% offering a great opportunity to use DTP as building block in organic materials.

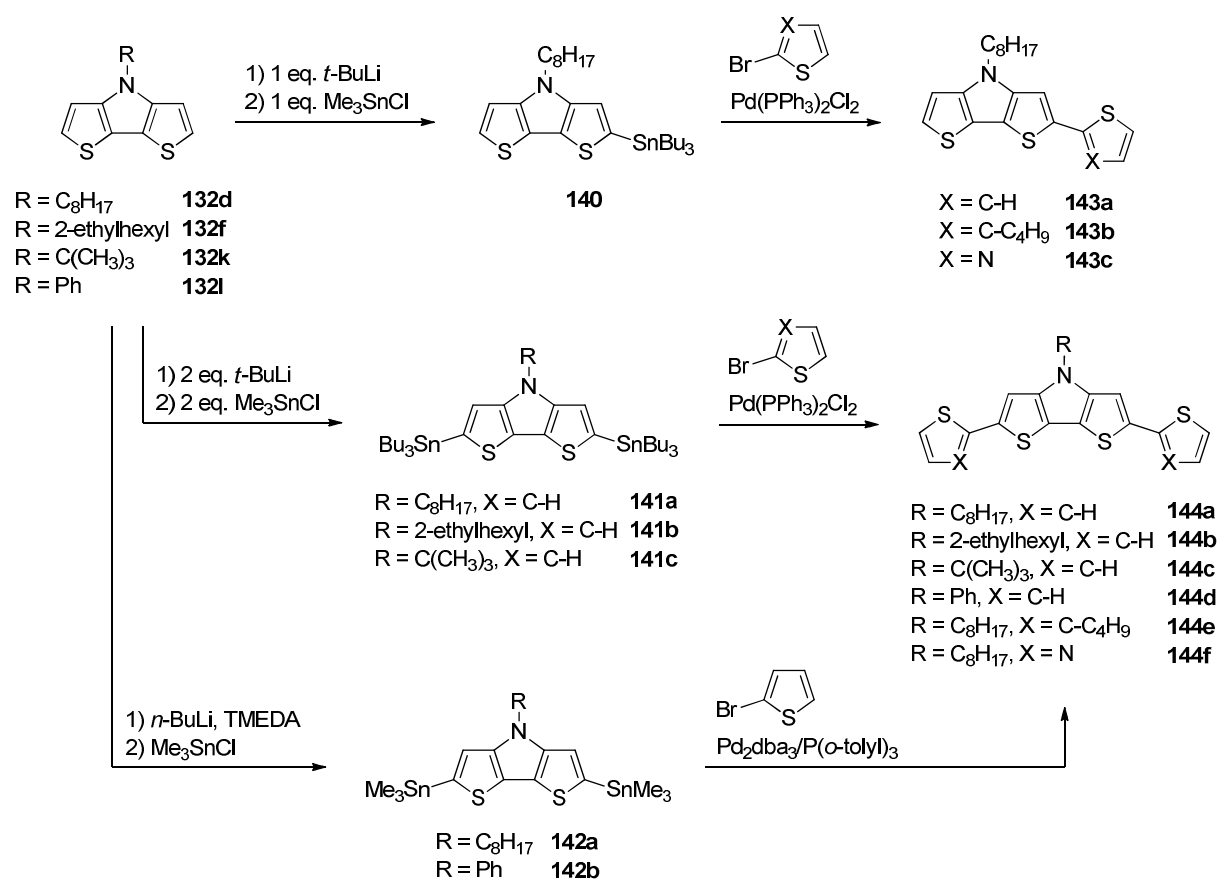


Scheme 4. Synthesis of 3,3'-dibromo-2,2'-bithiophene **133** starting from 3-bromothiophene developed by Evenson and Rasmussen.

Synthesis and properties of DTP-Oligomers

DTP-based homo- and copolymers were implemented as donor material in BHJSCs since 2007 and best polymers nowadays reach up to 5.0% PCE.^[21,22] However, structurally defined oligomers and co-oligomers containing DTP were hardly used and reached only low PCEs of $\leq 1.3\%$ by the start of this project.^[8] Most oligomers synthesized so far were typically analyzed on their optoelectronic properties and can be considered as model compounds, since they were not applied in OPV. In the following, a selection of DTP-based oligomers is presented.

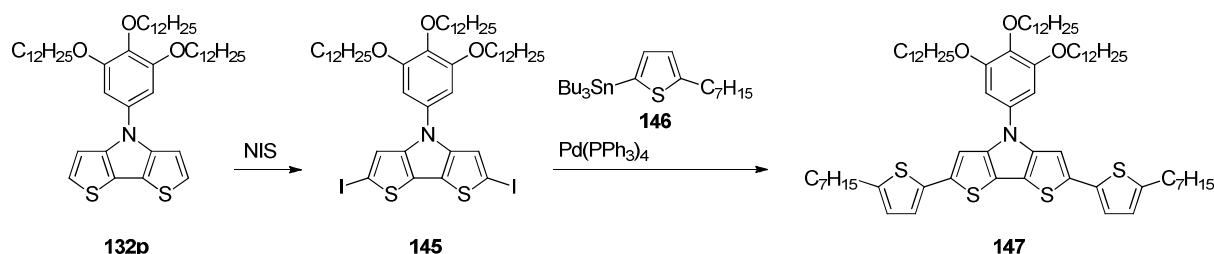
For the synthesis of conjugated oligomers and polymers, C-C cross-coupling is the most frequently used reaction type in order to build up the π -conjugated backbone. Therefore, metallation and halogenation of DTP in the free 2- and 6-position is crucial. Evenson *et al.*^[23,24] and Barlow *et al.*^[25] presented one of the first DTP-based oligothiophene series synthesized by Stille cross-coupling reaction (Scheme 5).



Scheme 5. Synthesis of DTP-containing oligothiophene derivatives **143a-143c** and **144a-144f** via one-pot stannylation and Stille cross-coupling reaction.

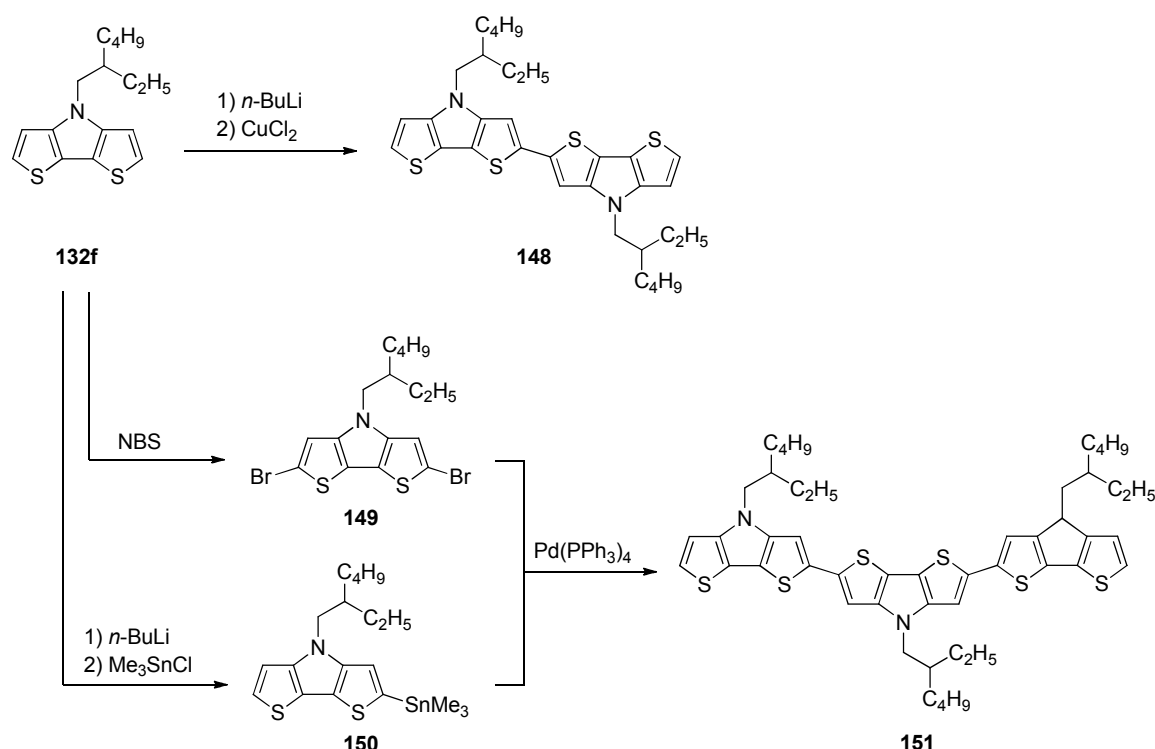
It was found that 2,6-dibromo-DTPs are very reactive and tend to polymerize easily even when stored under argon atmosphere at low temperatures.^[8] Therefore, DTP **132d**, **132f**, **132k**, and **132l** were stannylated and then further coupled with the corresponding halogenated heterocycle, as presented in Scheme 5. The electron-rich character of DTP however complicated deprotonation. Hence, *tert*-butyllithium (*t*-BuLi) or a mixture of *n*-butyllithium (*n*-BuLi) and tetramethylethylenediamine (TMEDA) at higher temperatures had to be used to achieve high conversions, even for monolithiation.^[23-25] Stannylated DTP species **140-142** were further converted in a one-pot reaction sequence due to failure in isolation and purification of the stannyl intermediates. However, it was recently shown that distannylated derivatives of **132d** and **132l** can be purified using triethylamine-deactivated silica to obtain pure distannylated DTPs with yields >95%.^[24,26] Nevertheless, formal ter- and quaterthiophenes **143a-143c** and **144a-144f** were also obtained in good yields applying the one-pot reaction sequence depicted in Scheme 5.^[23-25]

The stability of dihalogenated DTPs can be improved by introducing iodine instead of bromine and possessing an aryl substituent on the DTP-nitrogen. A combination of both effects was used by Barlow *et al.* to create diiodo-DTP **145** in 80% yield by iodination of *N*-aryl DTP **132p** with *N*-iodosuccinimide. Reacting **145** with stannylated thiophene **146** in a Stille cross-coupling reaction led to heptyl-terminated oligomer **147** (Scheme 6).^[25]



Scheme 6. Synthesis of diiodoDTP **145** and subsequent formation of **147** via Stille cross-coupling reaction.

Yassin *et al.* were the first who reported on the synthesis of oligoDTPs shown in Scheme 7.^[27] Dimeric species **148** was obtained in 33% yield by oxidative homo-coupling of DTP **132f** with CuCl_2 . The required monolithiated species was generated by the use of mere *n*-BuLi and warming up to room temperature (r.t.) for several hours. TerDTP **151** was synthesized via Stille cross-coupling reaction of **149** and **150** in 48% yield. Monostannylated DTP **150** was built using the same lithiation procedure as used for the synthesis of biDTP **148** with subsequent quenching with Me_3SnCl .



Scheme 7. Synthesis of oligoDTPs **148** and **151**.

For the synthesis of dibromoDTP **149**, DTP **132f** was reacted with NBS using standard bromination conditions. While other attempts to brominate DTP mainly led to decomposition,^[24,28] Yassin *et al.* reported quantitative conversion, but did not point out any special precautions/treatments.^[27] However, it is stated that dibromoDTP **149** was not further purified due to its high sensitivity to light and silica gel. The oligomeric DTP series consisting of **132f**, **148**, and **151** featured exceptional absorption properties in solution with absorption maxima at 310, 410, and 464 nm, respectively (Figure 3a).^[27] When going from the rigid DTP **132f** to the longer oligomers **148** and **151**, the absorption band broadens due to additional rotational freedom among the DTP moieties. Additionally, the extinction coefficients increased with the number of DTP-units from 28,160 M⁻¹cm⁻¹ for monomer **132f**, to 42,480 M⁻¹cm⁻¹ for dimer **148**, and further to 55,130 M⁻¹cm⁻¹ for trimer **151**.

Cyclic voltammograms of the oligomeric series are depicted in Figure 3b from which several electrochemical properties can be derived: DTP **132f** showed an irreversible oxidation at ~0.95 V vs. saturated calomel electrode (SCE) (~0.55 V vs. Fc/Fc⁺). The irreversibility is due to electropolymerization, which has been reported in literature.^[9,29] More electron-rich dimer **148** featured two reversible oxidation waves with E^o_{ox1} = 0.49 V and E^o_{ox2} = 0.87 V vs. SCE (~0.09/0.47 V vs. Fc/Fc⁺). The elongation of the conjugated system shifted E^o_{ox1} as expected towards lower potentials. Similarly, trimer **151** showed even lower redox potentials for its two reversible oxidation waves (E^o_{ox1} = 0.05 V and E^o_{ox2} = 0.42 V vs. SCE). The reversible cyclovoltammetric behaviour of **148**

and **151** is in contrast to quarter- and sexithiophenes which undergo electrochemical coupling.^[30] This unusual stability of α -unsubstituted oligomers can also be observed with oligomers presented in Scheme 5.^[24,25] This is due to stabilization of the radical cation by the electron-donating effect of the nitrogen leading to a decreased reactivity.^[8,27] By the onset of the first oxidation wave, HOMO level energies of **132f**, **148**, and **151** can be calculated to be -5.8, -5.4 and 5.2 eV vs. vacuum. Especially the HOMO energy levels of dimer **148** and trimer **151** are promising concerning their use as donor moieties for D-A oligomers for BHJSCs.

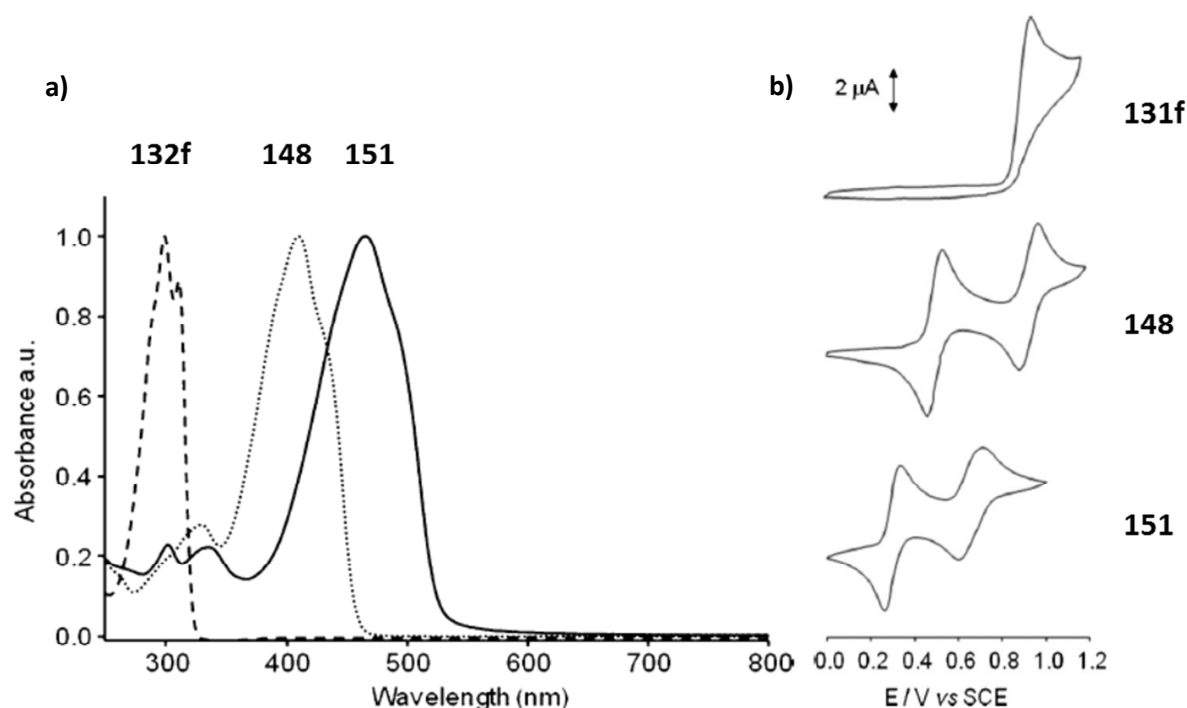


Figure 3. (a) UV-Vis absorption spectra of DTP **132f**, **148**, and **151** (from left to right) in dichloromethane (DCM). (b) Cyclic voltammograms of **132f**, **148**, and **151** measured in DCM using tetra-*n*-butylammonium hexafluorophosphate ($(n\text{-Bu})_4\text{NPF}_6$) (0.1 M) as supporting electrolyte at 100 mV s^{-1} . Copyright © 2010 WILEY-VCH Verlag GmbH & Co. KGaA, Weinheim.

DTP-based D-A systems

Besides copolymeric materials, where DTP has been combined with a variety of electron-accepting moieties,^[8] there are only a few structurally defined oligomers and co-oligomers consisting of DTP as electron donor and different electron acceptors. The group of S. Marder synthesized two series of D-A oligomers comprising DTP (Chart 2).^[31-34] Rylene-containing A-D-A series **152-154** was synthesized in order to investigate their charge transport properties.^[31,32,35] Naphthalenediimide (**152**) and perylenediimide (**153** and **154**) were chosen as acceptors as they feature high electron affinities, high

electron mobilities, and chemical, thermal, and photochemical stabilities and are therefore widely used in the field of organic field effect transistors (OFETs) and OPVs.^[36-41]

The general synthesis of **152-154** is shown in Scheme 8 and was realized by Stille cross-coupling reaction of distannylated DTP **155** and the corresponding brominated rylene **156a-c**. Pd₂dba₃ and P(*o*-tol)₃ was used as catalyst systems leading to yields of 40-70% for **152-154**. The symmetrical A-D-A systems were investigated concerning their optoelectronic properties and charge transport mobilities. UV-vis absorption of **152-154** in solution showed two absorption maxima corresponding to the rylene absorption and an additional weak CT band at 660-680 nm. The reason for the low intensity of the CT band is most likely a large torsion between the DTP-core and the rylene moieties. For naphthalene-containing triad **152** the maxima were located at 385 and 681 nm and shifted in thin films to 400 and 744 nm, respectively. Perylenediimide-DTP-perylenediimide **153** and **154** featured absorption maxima at 530 and 517 nm in solution, respectively. The weak CT band at ~665 nm was slightly blue-shifted and experienced a less prominent red-shift when going to thin films compared to naphthalene derivative **152**. This resulted in an absorption maximum for the CT band in thin film at 703 and 685 nm for **153** and **154**, respectively.^[31,32]

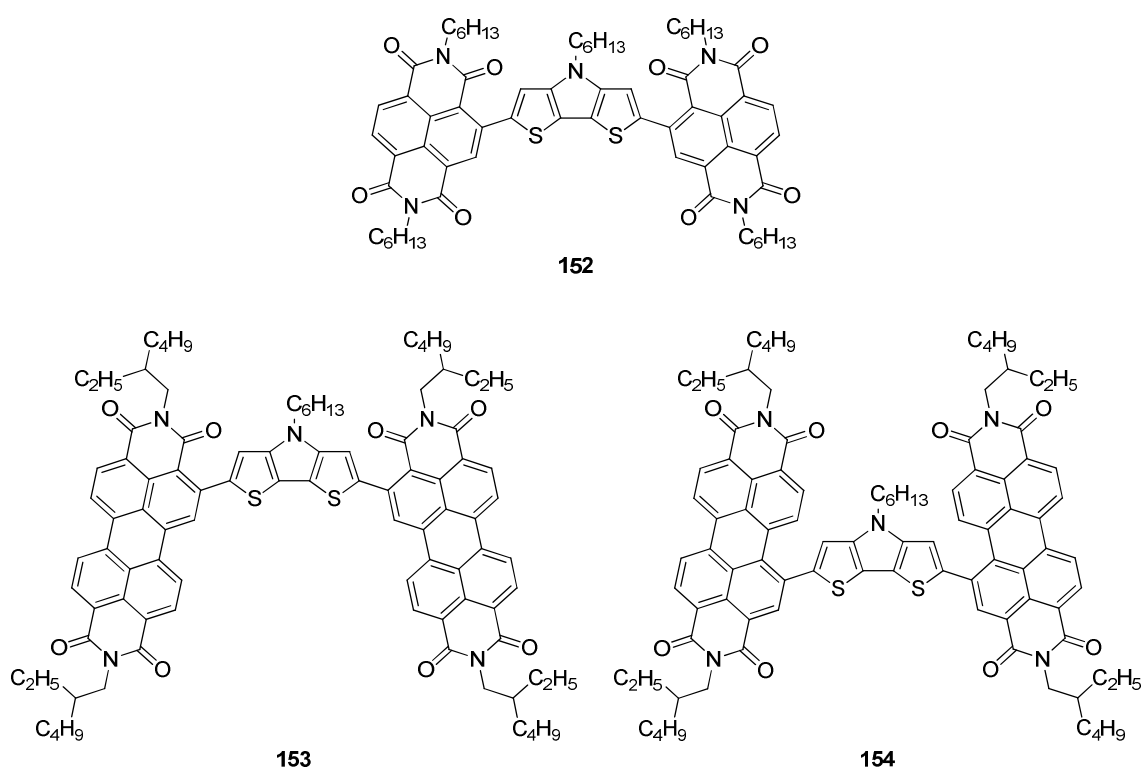
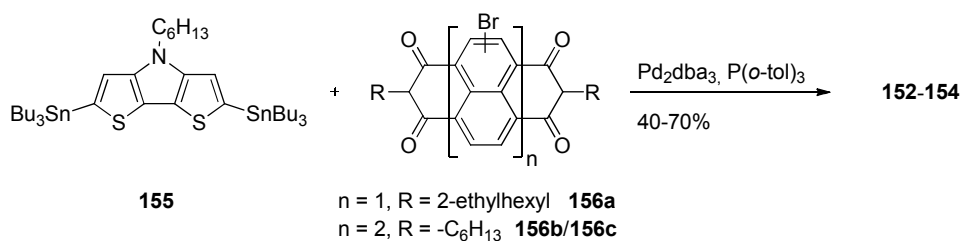


Chart 2. DTP-rylene D-A oligomers **152-154**.

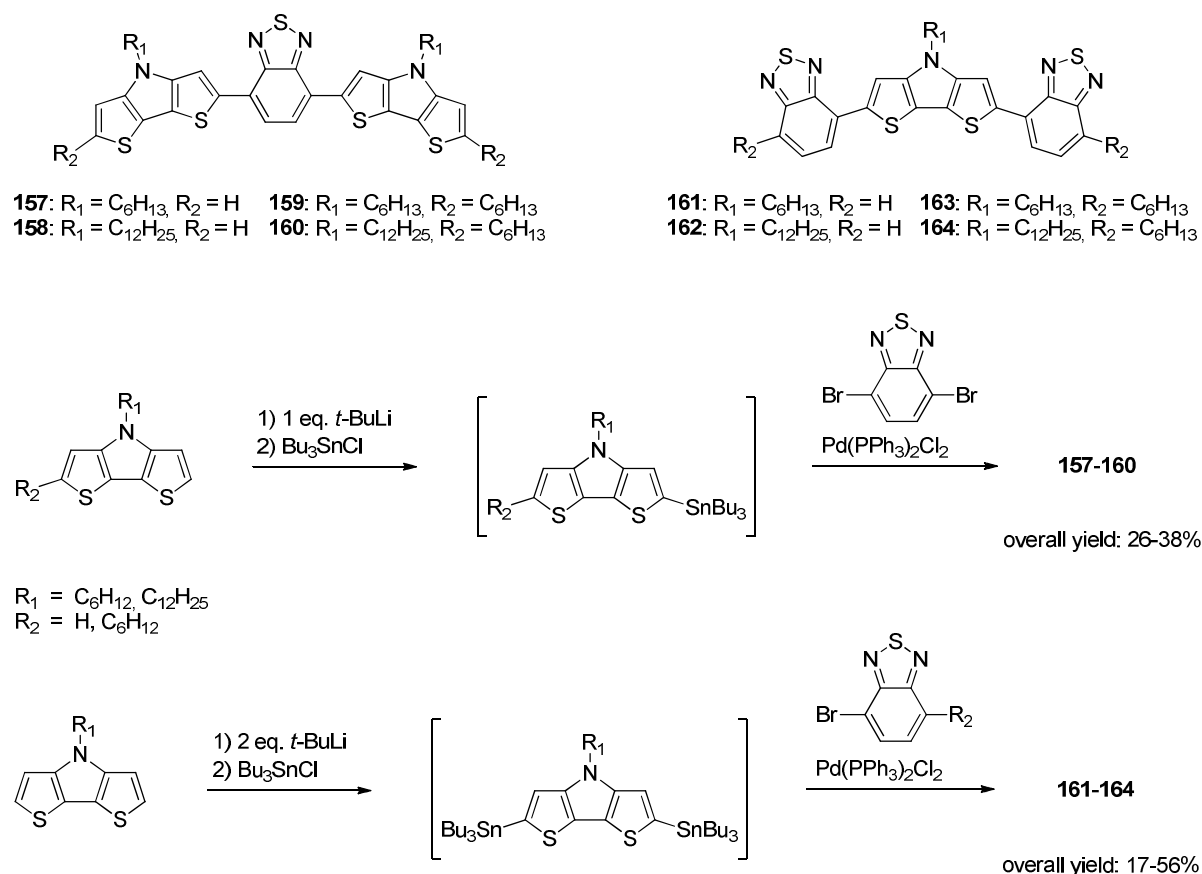


Scheme 8. Synthesis of rylene-substituted DTPs **152-154** by the group of S. Marder.

Triads **152-154** showed similar cyclic voltammograms: two reversible two-electron reduction waves and one reversible one-electron oxidation wave corresponding to the reduction of each terminal acceptor group and the oxidation of the DTP-unit, respectively. The reductions approximately take place at the potentials of the parent compounds naphthalenediimide and perylenediimide. Naphthalene derivative **152** is reduced at -1.09 and -1.50 V vs. Fc/Fc^+ , whereas perylene derivatives **153** and **154** are reduced at ~ -1.05 and -1.25 V vs. Fc/Fc^+ . The oxidation potential of the DTP-moiety in **152-154** is ~ 0.5 V vs. Fc/Fc^+ and therefore reduced by 0.3 V compared to DTP **132f**.^[31,32] OFETs using **152** were fabricated and showed ambipolar electrical characteristics with dominant n-channel transistor behavior. Devices exhibited high electron mobilities of up to $1.5 \text{ cm}^2 \text{ V}^{-1} \text{ s}^{-1}$ and average hole mobilities of $0.01 \text{ cm}^2 \text{ V}^{-1} \text{ s}^{-1}$. The ambipolarity resulting from the good charge transport properties of naphthalene-diimide and DTP means that the transistors are not fully turned off at zero gate bias and that no $I_{\text{on}}/I_{\text{off}}$ could be measured which is problematic for applications.^[31] This could be the reason why **153** and **154** were not further tested in OFETs.

In another D-A series by the group of S. Marder DTP was used as donor and benzothiadiazole as acceptor. D-A-D co-oligomers **157-160** as well as A-D-A co-oligomers **161-164** were synthesized (Scheme 9).^[33,34] Again Stille cross-coupling reactions were performed. This time, $\text{Pd}(\text{PPh}_3)_2\text{Cl}_2$ was used as catalyst to obtain triads **157-164** in 17-52% yield. The moderate yields could be either due to a low yield in Stille cross-coupling or/and due to a low conversion in the preceding stannylation, as the stannyl compounds were used without isolation or purification.

Variation of the alkyl substitution at the DTP-nitrogen and the periphery of the triads had only minor effects on the optical and redox properties. However, thermal properties and solubility of these co-oligomers could be influenced strongly: The longer the alkyl chain on the DTP-nitrogen, the higher the solubility of the respective oligomer; additional improvement in solubility could be obtained by the use of terminal hexyl chains.^[33] Absorption spectra of **157-164** were measured in solution and in thin films. The corresponding data are summarized in Table 1.



Scheme 9. Structure and synthesis of benzothiadiazole-containing A-D-A and D-A-D DTP-based oligomers **157-164**.

The absorption spectra in solution showed two absorption maxima at 377-389 nm and 565-588 nm for **157-160** and at 356-364 nm and 518-521 nm for **161-164**. For D-A-D co-oligomers **157-160**, both absorptions were observed at lower energy than the corresponding absorption of A-D-A co-oligomers **161-164**. Additionally, the extinction coefficients of D-A-D systems **157-160** for the low energy absorption band ($\sim 43,000 \text{ M}^{-1}\text{cm}^{-1}$) were 1.6 times higher in comparison to the A-D-A systems **161-164** ($\sim 27,000 \text{ M}^{-1}\text{cm}^{-1}$).^[33] This shows the strong effect of DTP regarding extinction enhancement and thus improvement of light harvesting. Thin film absorptions of **157-164** are fairly similar to the ones in solution but are 22-53 nm red-shifted. Regarding D-A-D triads **157-160**: **157** and **158** showed a moderate red-shift of the absorption maxima of 23 nm, whereas hexyl-substituted **159** and **160** possessed a red-shift of 53 nm. Comparing D-A-D triads **161-164** among each other, an inverse trend is observed: **161** and **162** bearing no peripheral hexyl chains featured a bigger red-shift when going from solutions to thin films (31-38 nm) than **163** and **164** (22 nm). The authors attribute these differences to the terminal alkylation which can play a significant role in determining intermolecular interactions and thus packing effects.^[33]

Table 1. Optical data of triads **157-164** in chloroform and in thin films. Redox potentials obtained from cyclic voltammetry were measured in DCM/*(n*-Bu)₄NPF₆.

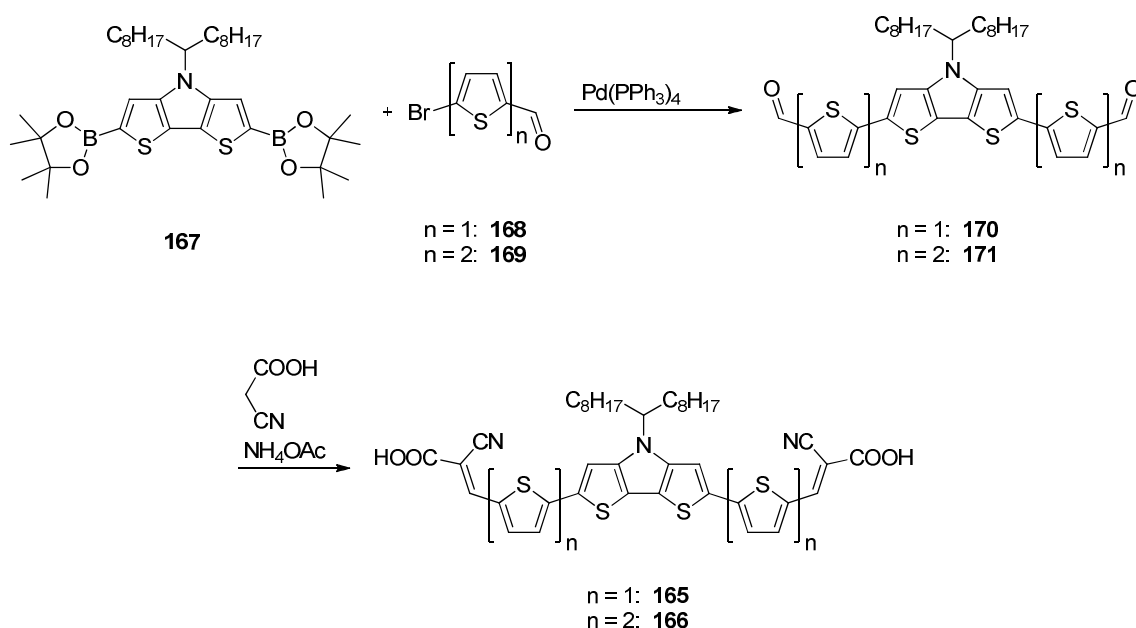
D-A system	λ_{abs} [nm] (ϵ [M ⁻¹ cm ⁻¹])	$\lambda_{\text{max film}}$ [nm]	E°_{ox1} [V] ^[a]	E°_{ox2} [V]	E°_{red1} [V]
157	377 (43,100), 565 (32,100)	588	0.11	0.47	-1.74
158	377 (42,000), 565 (31,300)	588	0.12	0.46	-1.74
159	389 (43,900), 588 (33,200)	641	0.01	0.34	-1.76
160	389 (44,900), 588 (33,900)	641	0.01	0.34	-1.76
161	356 (25,700), 518 (32,800)	549	0.37	-	-1.86 ^[b]
162	358 (26,200), 518 (33,400)	556	0.36	-	-1.88 ^[b]
163	364 (28,200), 521 (32,500)	543	0.28	-	-1.94 ^[b]
164	364 (28,500), 521 (32,600)	543	0.27	-	-1.95 ^[b]

[a] Vs. Fc/Fc⁺. [b] Corresponds to two closely overlapping redox waves.

The electrochemical properties of **157-164** were investigated using cyclic voltammetry in DCM/*(n*-Bu)₄NPF₆. The data are summarized in Table 1. The D-A-D and A-D-A co-oligomers showed reversible oxidation and reduction waves corresponding to their number of D and A blocks. As expected, electron-rich D-A-D systems **157-160** experienced negatively shifted first oxidation potentials of 0.01-0.12 V vs. Fc/Fc⁺ in comparison to A-D-A systems **161-164**, which are oxidized at 0.27-0.37 V. Co-oligomers bearing hexyl chains at the periphery, **159**, **160**, **163**, and **164** were more readily oxidized (~0.1 V) than the non-alkylated derivatives **157**, **158**, **161**, and **162** due to the positive inductive effect of the alkyl chain. D-A-D systems **157-160** can be oxidized a second time at ~0.40 V, the same trend concerning the shift to lower potentials upon terminal alkyl substitution is observed. Remarkably, they showed nearly similar oxidation potentials as biDTP **148** (~0.09/0.47 V vs. Fc/Fc⁺) with apparently no significant effect of the central benzothiadiazole unit on E°_{ox1} and E°_{ox2} .^[27] The reduction potentials of derivatives **157-164** were observed at -1.74 to -1.95 V. Contrary to the expectations, D-A-D derivatives **157-160** were more easily reduced than their A-D-A counterparts **161-164**. The authors attribute this to solvation effects as electron affinities obtained from DFT-calculations predict easier reduction of A-D-A systems **161-164**.^[33] It is noted that the reduction feature of **161-164** consisted of two closely overlapping redox waves corresponding to two one-electron processes.

DTP-containing co-oligomers **157-164** were tested in OFETs to measure hole mobilities. **161**, **163**, and **164** did not show measurable OFET behaviour. **162** featured the lowest measured hole mobility of $6.6 \times 10^{-5} \text{ cm}^2 \text{ V}^{-1} \text{ s}^{-1}$. The reason for the poor hole transport properties of A-D-A co-oligomers **161-164** could be due to the presence of the two strong electron-accepting benzothiadiazoles. D-A-D systems **157-160** possessed mobilities of $2.5 \times 10^{-4} - 5.9 \times 10^{-3} \text{ cm}^2 \text{ V}^{-1} \text{ s}^{-1}$. The variation is ascribed to differences in packing and film morphology which result from different alkyl substitution.^[33] In a later publication, **162** and **164** were mixed with PC₆₁BM to fabricate solution-processed BHJSCs in order to study the effect of terminal alkylation on morphology of the blend layer.^[34] No explanation is given why **157-160** showing red-shifted absorption maxima in comparison to **162** and **164** and therefore better light harvesting as well as better hole mobilities in OFETs were not used as donor materials. A series of solar cells was fabricated with different donor:acceptor (D:A) ratios, spin-coating speeds, solvents, and post-fabrication annealing. For **162** a maximum PCE of 0.5% was reached using chlorobenzene (CB) as solvent. Chloroform led to low PCEs <0.1%. Hexyl-capped **164** yielded PCEs of <0.3% regardless whether chloroform or CB was used as solvent. Reasons for the low PCEs are the poor FF (absolute values were not given in literature)^[34] which is most likely due to a large energy offset of the LUMO of PC₆₁BM and the LUMO of **162/164** of about 1 V leading to a low yield in exciton separation and hence to a big series resistance. Furthermore, atomic force microscopy (AFM) of the blended films indicated a well-mixed, uniform, and amorphous active layer surface for **162**. Together with dynamic secondary ion mass spectrometry (D-SIMS) measurements showing a constant composition profile throughout the active layer, it is supposed that a completely mixed film is formed with missing percolation pathways for the charges to reach the electrodes. Consequently, this led to high recombination rates of the separated charges. In contrast to this, AFM images of **164**:PC₆₁BM films display a high degree of crystalline texture on the surface and with D-SIMS a larger fraction of S-containing ions is observed near the film surface which is increased upon annealing (even at low temperatures). On the basis of these results, it is assumed that **164** exhibits a lower miscibility with PC₆₁BM leading to a formation of a donor-enriched layer on the surface of active layer, which has in fact an insulating effect on the electrons migrating/diffusing to the top electrode.^[34]

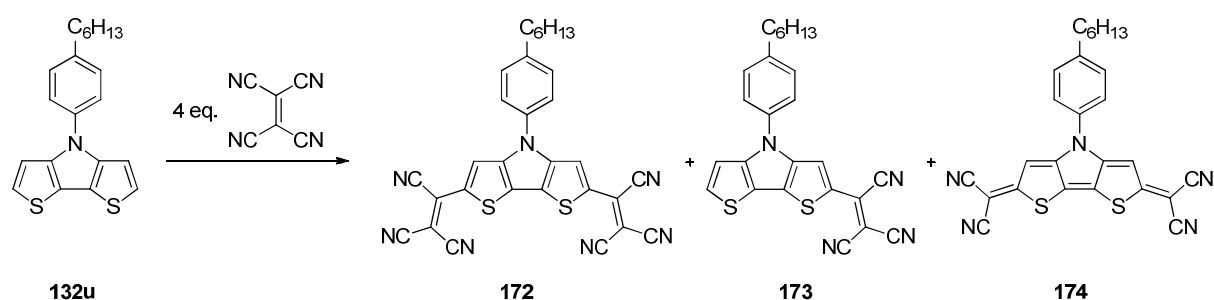
Sahu *et al.* synthesized two DTP-based A-D-A sensitizers for n-type DSSCs (Scheme 10).^[42] Sensitizers **165** and **166** consist of a DTP-based quater- or sexithiophene, respectively, flanked with cyanoacrylic acid groups as electron-accepting anchors and were synthesized via Knoevenagel condensation by reacting cyanoacetic acid with dialdehydes **170** and **171**, respectively. The corresponding aldehydes were obtained via Suzuki cross-coupling reaction of diborylated DTP **167** and brominated thiophenes **168** and **169**.



Scheme 10. Synthesis of A-D-A sensitizers **165** and **166** via Suzuki cross-coupling reaction and Knoevenagel condensation.

Absorption spectroscopy in solution revealed intense absorption bands for **165** and **166** at 557 ($\epsilon = 74,600 \text{ M}^{-1}\text{cm}^{-1}$) and 564 nm ($\epsilon = 79,000 \text{ M}^{-1}\text{cm}^{-1}$), respectively. As expected, longer oligomer **166** possessed a more intense and red-shifted absorption compared to **165** due to the increased conjugation length. HOMO and LUMO energy levels were calculated using cyclic voltammetry to -5.32/-5.14 eV and -3.40/-3.34 eV for **165/166**, respectively.^[42] n-Type DSSCs were fabricated using **165** and **166** as sensitizers achieving PCEs of 3.40 and 1.24%, respectively. The lower PCE of **166** is attributed to ineffective charge regeneration after electron injection, which is most likely due to the relatively high HOMO energy level of -5.14 eV or due to strong aggregation on TiO_2 of **166** compared to **165**. The PCE of **165** could be further improved to 4.31% by the use of the coadsorbent chenodesoxycholic acid, which competes with the sensitizer for adsorption sites at the TiO_2 , thus reducing aggregation of **165**.^[42]

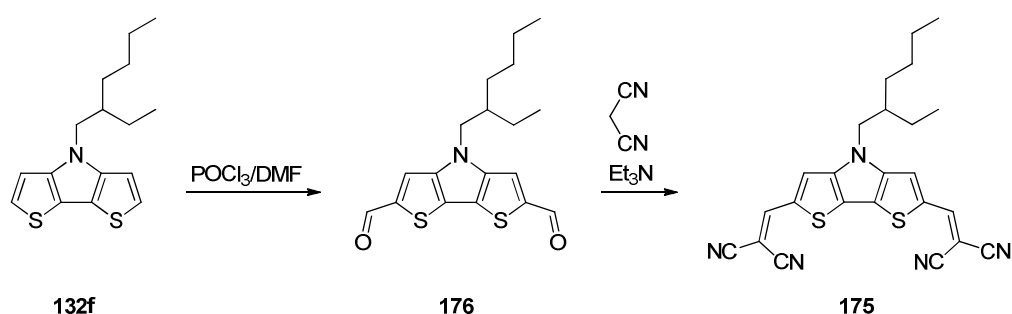
Tricyanovinylene(TCV)-bearing DTP **172** was synthesized by the group of Rasmussen by treatment of DTP **132u** with 4 eq. of tetracyanoethylene (Scheme 11).^[43] This usually affords mono and twice TCV-substituted systems if applied on activated heterocycles.^[44-46] However, an additional side-product emerges besides TCV-substituted DTPs **172** (yield: 7%) and **173** (yield: 55%): quinoid DTP **174** (yield: 10%). The authors propose that a cycloaddition process is responsible for the formation of quinoid system **174** showing n-type semiconducting behaviour. The low yield of **172** compared to **173** is thought to be due to deactivation of the remaining α -position upon introduction of the first TCV substituent.^[43]



Scheme 11. Synthesis of TCV-substituted DTP **172** coming along with the formation of mono-substituted **173** and quinoidal side-product **174**.

Absorption spectroscopy and cyclic voltammetry of **172-174** were recorded in DCM. Compared to unsubstituted DTP **132u** absorbing at 300 nm, **172**, **173**, and **174** featured red-shifted absorption maxima at 577, 538, and 545 nm, respectively. The reduced band gaps for **172-174** are the result of the large stabilization of the LUMO by the electron-withdrawing cyano groups. This can also be seen in the cyclic voltammogram, in which the first reduction wave is shifted to more positive values upon introduction of acceptor groups TCV and dicyanomethylene resulting in LUMO energy values of -4.3 eV (**172**), -3.4 eV (**173**), and -4.1 eV (**174**). HOMO energy levels were also stabilized compared to **132u** (-5.1 eV) and are positioned at -6.7, -6.1, and -6.3 eV for **172**, **173**, and **174**, respectively. The reduced band gaps of **172-174** compared to unsubstituted DTP **132** and the favorable redox properties in conjunction with π -stacking observed from single crystal X-ray analysis render **172-174** suitable candidates for electronic devices.^[43]

DCV-substituted DTP **175** was synthesized by Yassin *et al.* in order to use it as donor material for OSCs.^[47] Scheme 12 depicts the two-step synthesis of **175** starting from DTP **132f**. In the first step, two aldehyde groups were introduced via Vilsmeier-Haack reaction to obtain **176** in 84% yield. In the second step, Knoevenagel condensation was carried out using malononitrile and triethylamine as base to form the terminal DCV groups. Isolation and purification of **175** led to a yield of 51%.



Scheme 12. Synthesis of DCV-substituted DTP **175**.

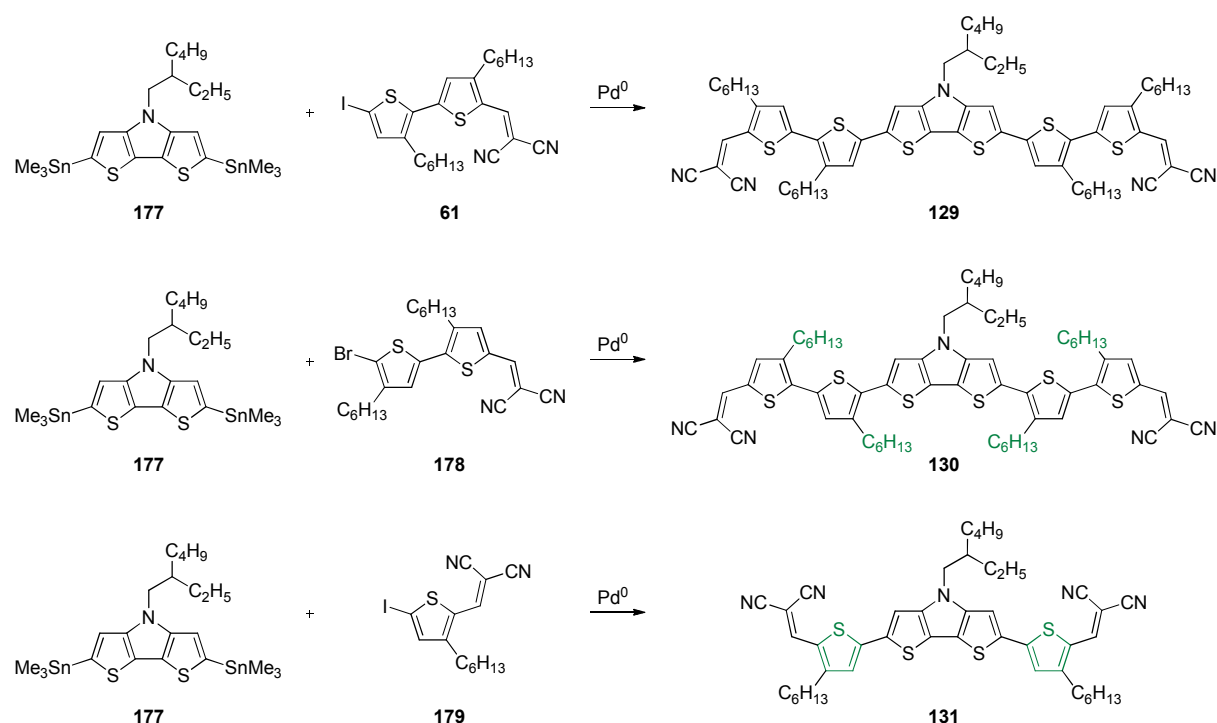
The absorption spectrum of DCV-substituted DTP **175** was recorded in DCM and showed an intense structured absorption band with its maximum at 519 nm. The corresponding thin film spectrum is 40 nm red-shifted and strongly broadened due to aggregation/ π - π stacking. The electrochemical properties were measured in DCM (oxidation) and tetrahydrofuran (THF) (reduction) and revealed a partly reversible oxidation and two reversible reduction waves.^[47] Based on the cyclic voltammograms, HOMO and LUMO energy levels were estimated to be -6.1 and -4.1 eV vs. vacuum, respectively. In order to evaluate the potentiality of **175** as donor material in OSC, bilayer devices were fabricated due to the fact that solution-processing with PC₆₁BM did result in inhomogeneous blend layers. Bilayer solar cells were made by vacuum-processing or spin-casting of **175** followed by vacuum sublimation of C₆₀. In both cases, only low efficiencies were obtained of maximum 0.24% for spin-cast layers of **175** (vacuum-processed: PCE_{max} = 0.09%).^[48] The main reason is the nearly similar HOMO and LUMO energy levels of **175** and C₆₀, thus resulting in an insufficient driving force for charge separation. Regarding the energy levels, DCV-substituted DTP **175** can rather be used as an acceptor than as a donor in BHJSCs.

5.2 Results and discussion

5.2.1 Synthesis of DTP-based co-oligomers 129-131

As reported in the previous section, the Stille cross-coupling reaction is highly compatible with DTP building blocks. Hence, structurally defined DTP-based co-oligomers **129-131** were synthesized via Stille cross-coupling of distannylated DTP **177** and the corresponding halogenated building block **61**, **178** and **179**, respectively (Scheme 13).

The synthesis of building blocks **177** and **178** and the final coupling step to the three co-oligomers **129-131** is described in the following. The synthesis of building block **61** is described in *Chapter 3*. DCV-substituted iodothiophene **179** was synthesized by Dr. G. Götz.^[49]



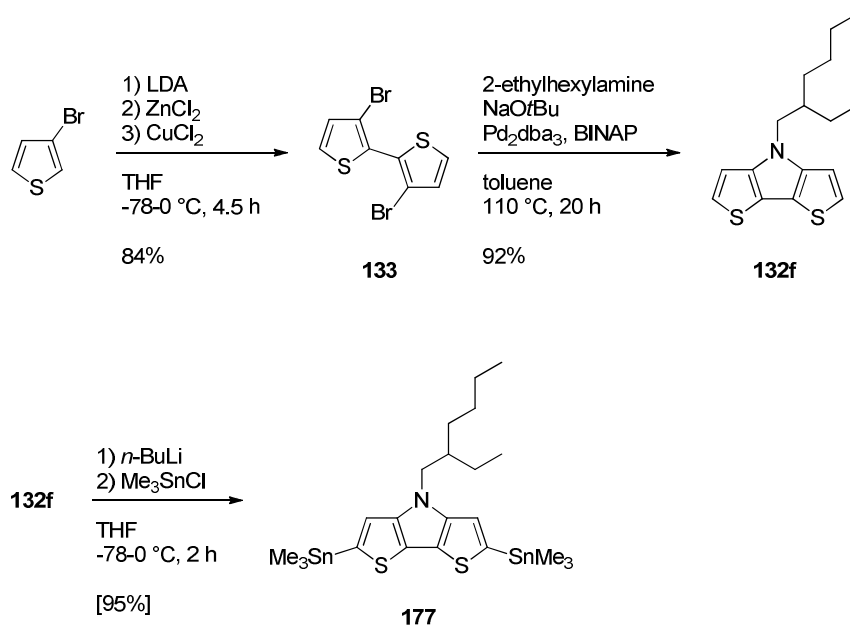
Scheme 13. Synthesis of DTP-containing structurally defined co-oligomers **129-131** via Stille cross-coupling of distannylated DTP **177** and halogenated building blocks **61**, **178** and **179**.

Synthesis of distannylated DTP **177**

Distannylated DTP **177** was synthesized according to the most efficient synthetic pathway presented above (see section 5.1.2) with several modifications.

First, DTP **132f** was synthesized following the reaction sequence shown in Scheme 14. In the first step 3,3'-dibromo-2,2'-bithiophene **133** was formed according to a literature procedure with slight modifications.^[19] After selective deprotonation of the 2-position, ZnCl_2 is added in order to form 3-bromo-2-thienylzinc chloride, which is then oxidatively coupled by the addition of CuCl_2 . In literature, conclusively oxygen is added to reach a higher conversion and the work-up is done by hydrolysis with saturated aqueous NH_4Cl solution and subsequent extraction of the organic compounds with diethyl ether.^[19] The usage of oxygen was skipped and instead of an aqueous work-up, silica gel was added directly to the reaction mixture and the solvent was removed by rotary evaporation. The resulting crude product/silica mixture was then purified via silica gel column chromatography (eluent: *n*-hexane) to obtain bithiophene **133** in 84% yield, which is comparable to the yield achieved in literature (88%) with less effort concerning work-up.^[19] Subsequently, Buchwald-Hartwig amination of **133** with 2-ethylhexylamine afforded DTP **132f**. Reaction conditions which were described by Koeckelberghs *et al.* for the synthesis of *N*-octyl DTP **132d** were applied: Sodium *t*-butoxide was used as base and Pd_2dba_3 in combination with BINAP was used as catalyst system.^[18] The reaction was

carried out in a Schlenk tube in toluene and was heated to 110 °C overnight. Purification via silica gel column chromatography yielded **132f** in 92%, denoting an increase in yield compared to the reported one of Koeckelberghs *et al.* for **132d** (80%).^[18]



Scheme 14. Synthesis of distannylated *N*-2-ethylhexyl DTP **177**.

Formation of distannylated DTP **177** with *t*-BuLi or TMEDA/*n*-BuLi and subsequent addition of trialkyltin chloride is reported in literature.^[23-25] Up to the start of this project, the usage of *n*-BuLi without auxiliary reagent seemed to be not sufficient to dilithiate the DTP moiety in high conversions due to its electron-rich character. However, in a new dilithiation approach, DTP **132f** was reacted with 2.2 eq. *n*-BuLi and trimethyltin chloride to obtain distannylated DTP **177** (Scheme 14). The addition of *n*-BuLi was carried out at -78 °C and the reaction mixture was then stirred for 1 h at -78 °C and 1 h at 0 °C. It has to be pointed out that a high concentration of *n*-BuLi and the long reaction time for the lithiation are necessary to obtain **177** in high conversion. After lithiation, trimethyltin chloride was added at -78 °C and the reaction mixture was stirred at that temperature for further 2.5 h. Shorter reaction times led to a high amount of mono-stannylated side-product. Aqueous work-up was carried out without ceasing and with cold water. Otherwise partial decomposition took place. The obtained oil contained distannylated DTP **177** and the mono-stannylated side-product which was proven by ¹H NMR and mass spectrometry. The ratio of di- to mono-stannylated species was determined by integration of the corresponding signals in the ¹H NMR spectrum and was calculated

to 95:5. Purification and isolation of **177** was neglected since the side-product could be easily separated after the next reaction step.

Coupling partners of **177** for the Stille cross-coupling reactions are DCV-substituted building blocks **61**, **178**, and **179** (Chart 3). Iodobithiophene **61** was already used as building block in *Chapter 3* and its synthesis is described there. Thiophene **179** was obtained from Dr. G. Götz.^[49]

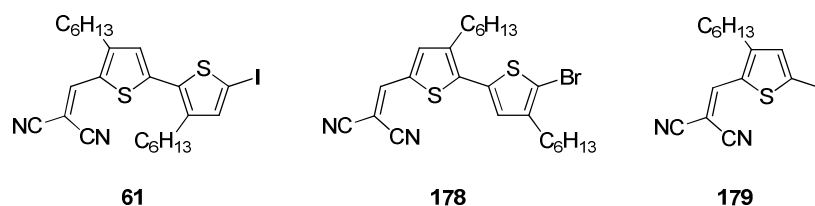
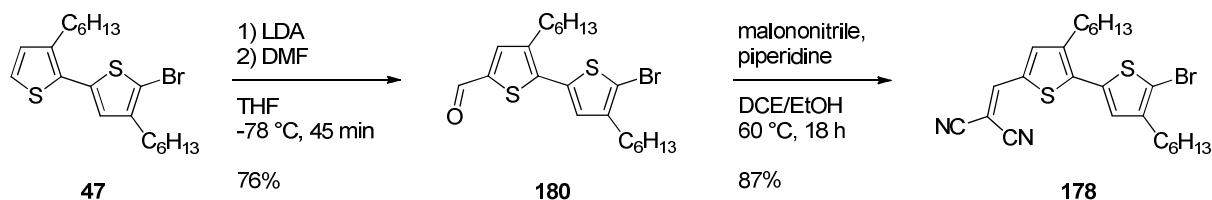


Chart 3. Chemical structure of DCV-functionalized D₁ building blocks **61**, **178**, and **179**.

Synthesis of DCV-substituted building block **178**

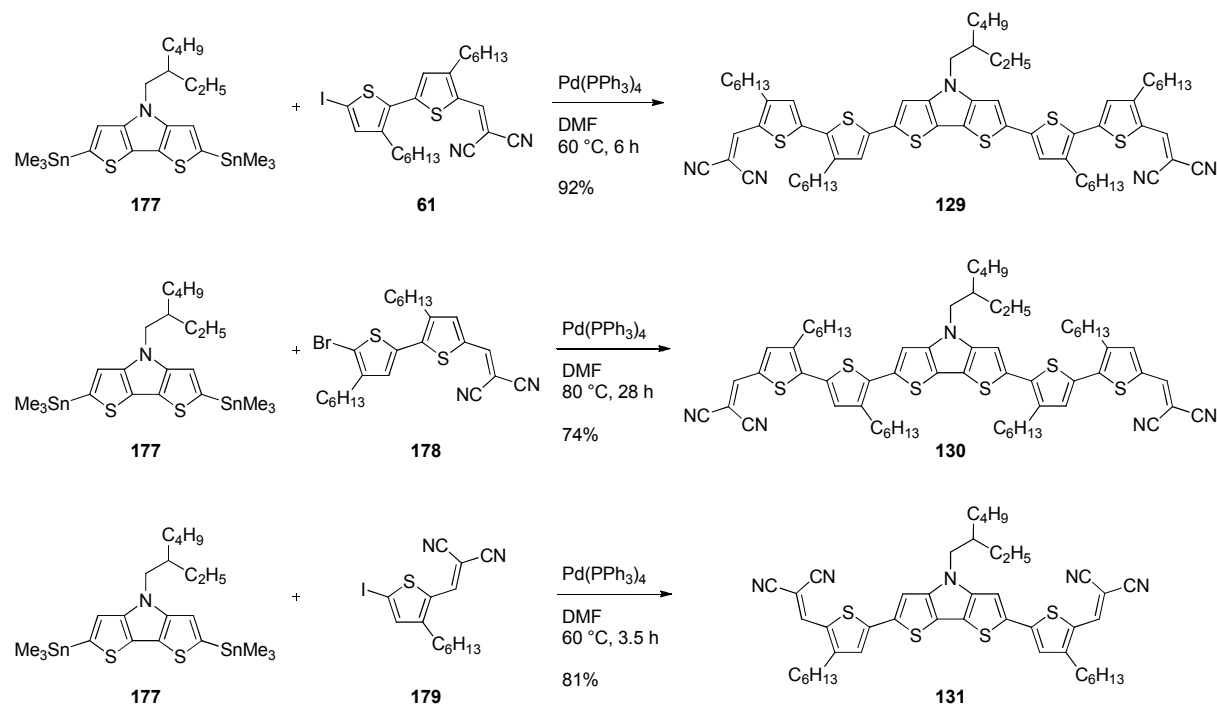
The synthesis of DCV-capped bromobithiophene **178** started with the formylation of 5-bromo-2,2'-bithiophene **47**^[50] (Scheme 15). Vilsmeier-Haack formylation did not selectively lead to the α -substituted product due to the β -directing and positive inductive effect of the hexyl chains. Therefore, lithiation of the free α -position with LDA at -78 °C with subsequent addition of DMF was applied to introduce the carbaldehyde group selectively at the 5'-position. Purification in terms of column chromatography led to bromoaldehyde **180** in a yield of 76%. The obtained aldehyde functionality was then further converted to the DCV group using Knoevenagel condensation. Accordingly, aldehyde **180** was reacted with malononitrile and piperidine as base. Once again, column chromatography afforded pure building block **178** with hexyl chains being positioned at the β -positions proximal to the halogen functionality.



Scheme 15. Synthesis of DCV-capped bromobithiophene **178**.

Synthesis of co-oligomers 129-131 via Stille cross-coupling reaction

Structurally defined co-oligomers **129-131** were synthesized via Stille cross-coupling reactions according to Scheme 16. $\text{Pd}(\text{PPh}_3)_4$ was used as catalyst system as for the synthesis of many DTP-containing oligothiophenes, since $\text{Pd}(\text{PPh}_3)_2\text{Cl}_2$ and $\text{Pd}(\text{PPh}_3)_4$ proved to be good catalysts.^[23-25,27]



Scheme 16. Stille cross-coupling reaction of distannylDTP **177** with DCV-functionalized D₁ building blocks **61**, **178** and **179**.

For reactions with iodinated building blocks **61** and **179** a temperature of 60 °C was sufficient to obtain complete conversion of distannylated DTP **177** within several hours. In the case of brominated bithiophene **178** the temperature and the reaction time had to be increased to 80 °C and 28 h, respectively, to achieve complete conversion of **177**. The higher temperature and longer reaction time needed for the coupling of **177** and **178** can be explained by the lower reactivity of C-Br bonds compared to C-I bonds concerning oxidative addition in the catalytic cycle. Additionally, there is more sterical hindrance concerning oxidative addition in the case of **178** compared to **61** due to the adjacent hexyl chain, which is in **178** directly positioned at the neighboring β -position. A-D-A co-oligomer **129** was formed in high yields of 92%. In the case of **130** a somewhat lower yield of 74% was obtained, whereas for **131** again an increase in yield to 81% could be observed. The decrease in yield for **130** is most likely because of the slightly harsher reaction conditions which led to a higher amount of destannylation and gave rise to homo-coupling of the intermediate mono-coupled

species. The emergence of this homo-coupled side-product containing an additional DTP-unit did not only decrease the theoretical yield, but also extended and complicated purification coming along with loss of yield. It is noted that compared to $\text{Pd}(\text{PPh}_3)_2\text{Cl}_2$ the use of $\text{Pd}(\text{PPh}_3)_4$ as catalyst is highly recommended on such systems. The reason for this is that in the case of $\text{Pd}(\text{PPh}_3)_2\text{Cl}_2$ the catalytically active $\text{Pd}(0)$ species would be formed by homo-coupling of **177** which would then also result in the above mentioned homo-coupling side-product. The somewhat lower yield of **131** compared to **129** is due to the lower solubility of **131** leading to loss of compound upon column chromatography. The chromatographic purification of **129-131** can be eased by extracting most of the side-products (reactants and mono-coupled side-product) with ethyl acetate in a Soxhlett extractor before column chromatography. The mono-coupled side-product is formed because of destannylation of the mono-coupled intermediate and the reaction of one equivalent of aryl-halogenide with mono-stannylated DTP which is a small impurity ($\sim 5\%$) in **177** as mentioned earlier. In the case of **130** which is better soluble in ethyl acetate compared to **129** and **131**, the extracting process has to be carried out carefully to avoid loss of product.

After column chromatography, the presence of **129-131** was confirmed by ^1H -NMR, ^{13}C -NMR, mass analysis, and elemental analysis. In Figure 4a the ^1H -NMR spectrum of **130** is depicted representatively: signals at 7.69, 7.52, 7.24, and 7.08 ppm correspond to the olefinic and aromatic protons, aliphatic protons are detected at 4.15-4.05, 2.87-2.83, 2.02-1.94, and 1.76-0.87 ppm (for more detailed assignment see Figure 4a and the experimental section). Mass spectrometry of **130** (MALDI-TOF) resulted in one signal with $m/z = 1108$ which corresponds to $[\text{M}+\text{H}]^+$ (Figure 4b). Also ^{13}C -NMR and elemental analysis indicated the presence of only one compound as well. Nevertheless analytical HPLC was run routinely to further determine the purity of DTP-based A-D-A co-oligomers **129-131**. In the case of **130** a small amount of an impurity could be detected for which reason HPLC was used to purify dye **130**. Figure 5 shows the HPLC chromatograms of **130** during purification on a nitrophenyl modified silica gel column using a *n*-hexane/DCM eluent mixture and the resulting analytical chromatogram after purification. In Figure 5a, the impurity can be seen as a small bump eluting at a shorter retention time than **130**. The impurity is most likely the above mentioned homo-coupling side-product. In the analytical chromatogram of **129** and **131**, no impurities were detected. Due to this and the lower solubility, making HPLC purification very tedious, HPLC purification was omitted.

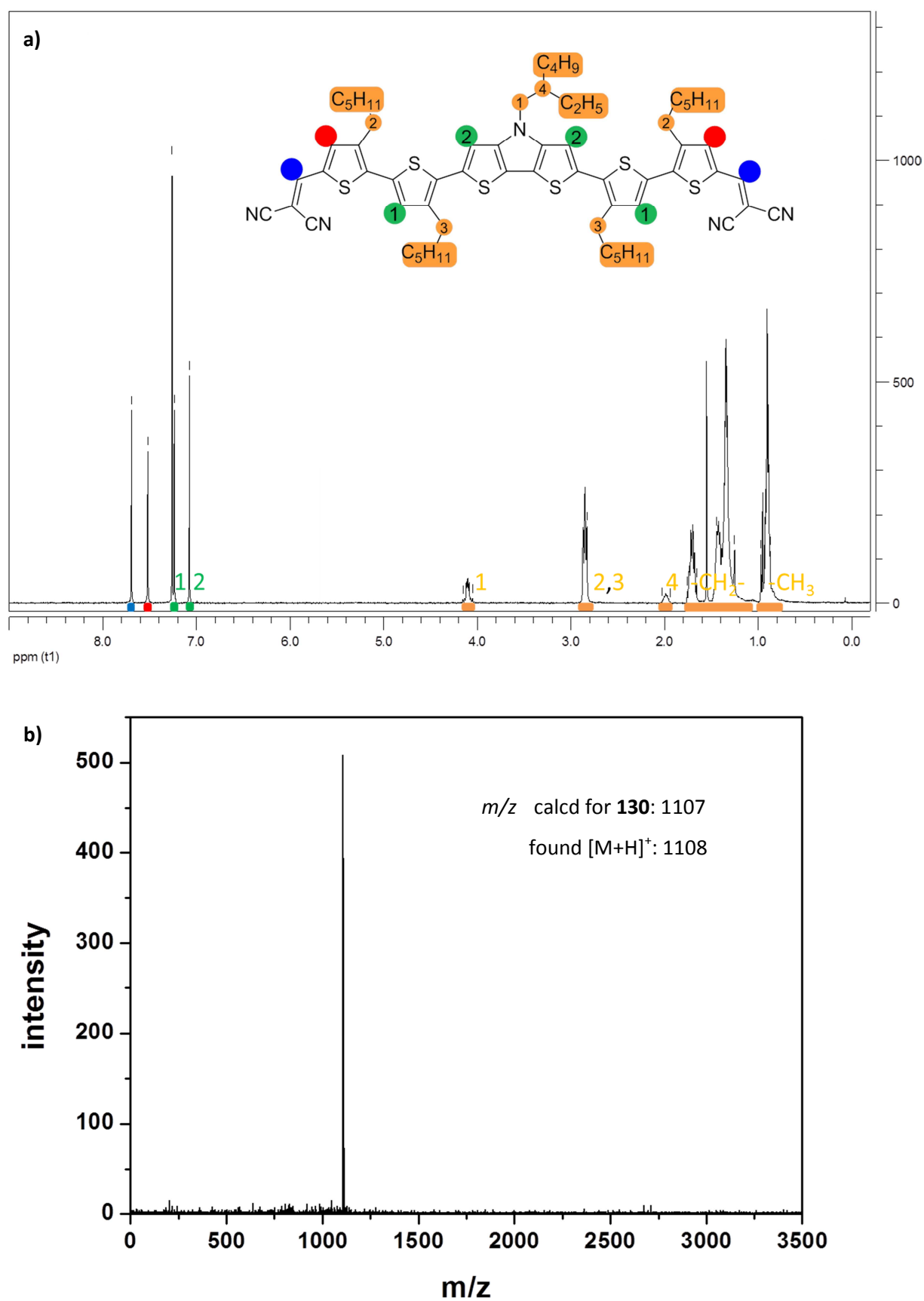


Figure 4. (a) ^1H -NMR spectrum and (b) mass spectrum of **130** after column chromatography.

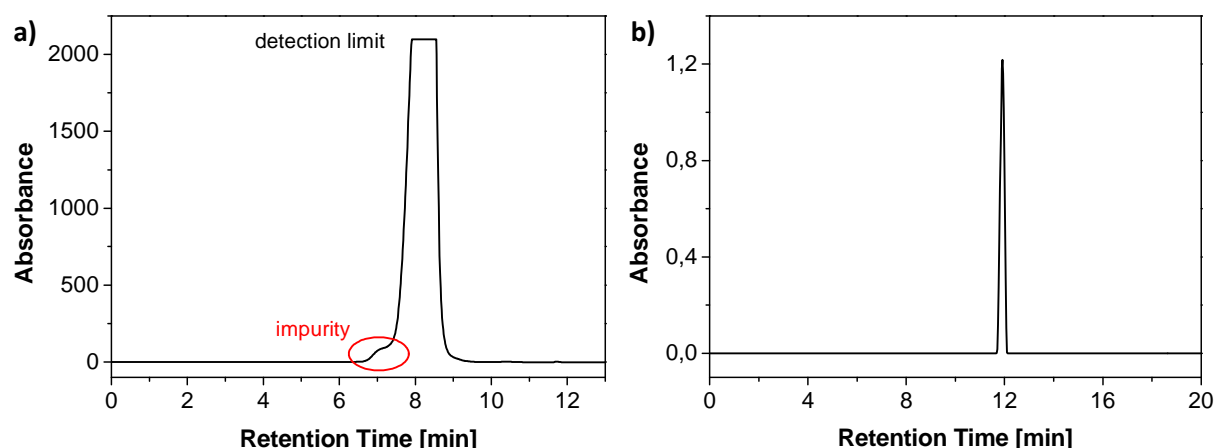


Figure 5. (a) Semi-preparative HPLC chromatogram of **130** with a small impurity shoulder at shorter retention time which could be successfully separated. (b) Pure HPLC chromatogram of **130** recorded on an analytical HPLC setup after purification via semi-preparative HPLC.

5.2.2 Optical properties of co-oligomers 129-131

Absorption spectroscopy of **129-131** was measured in chloroform and in thin films (Figure 6). The corresponding data are summarized in Table 1. In solution, **129** and **130** showed two absorption bands at ~ 400 and ~ 600 nm corresponding to the absorption of the DCV-bithiophene moiety and a CT transfer band, respectively. As can be seen in Figure 6, the different hexyl substitution patterns in **129** and **130** have quite a strong influence on the optical properties. Isomer **129** with hexyl chains pointing outward featured a maximum absorption at 601 nm with an extinction coefficient of $72,800 \text{ M}^{-1}\text{cm}^{-1}$, whereas **130** bearing hexyl chains on the inner β -positions experiences a 32 nm blue-shifted absorption at 569 nm with a decreased extinction coefficient of $57,600 \text{ M}^{-1}\text{cm}^{-1}$ compared to **129**. The reason therefore is most probably a stronger torsion between the DTP and the bithiophene moieties in **130**, induced by sterical hindrance of the adjacent hexyl chains. This leads to a reduced conjugation and thus communication between the DCV acceptor and the DTP donor reducing the CT character and resulting in a blue-shifted absorption and lower extinction coefficient for **130**. This explanation is also consistent with the stronger absorption at 400 nm for **130** in comparison to **129** indicating a more strongly DTP-decoupled DCV-bithiophene part. An additional effect of the stronger torsion in **130** is that the low energy CT band is broadened manifesting a broader distribution of conformers. Isomer **130** showed a full width at half maximum (FWHM) of $5,050 \text{ cm}^{-1}$ being 1.3x broader than the one of **129** ($3,880 \text{ cm}^{-1}$). Nevertheless, the fact that some conformers of **129** and **130** have the same conjugation length can be seen in their similar absorption onsets of around 680 nm leading to optical band gaps of 1.79 and 1.80 eV, respectively.

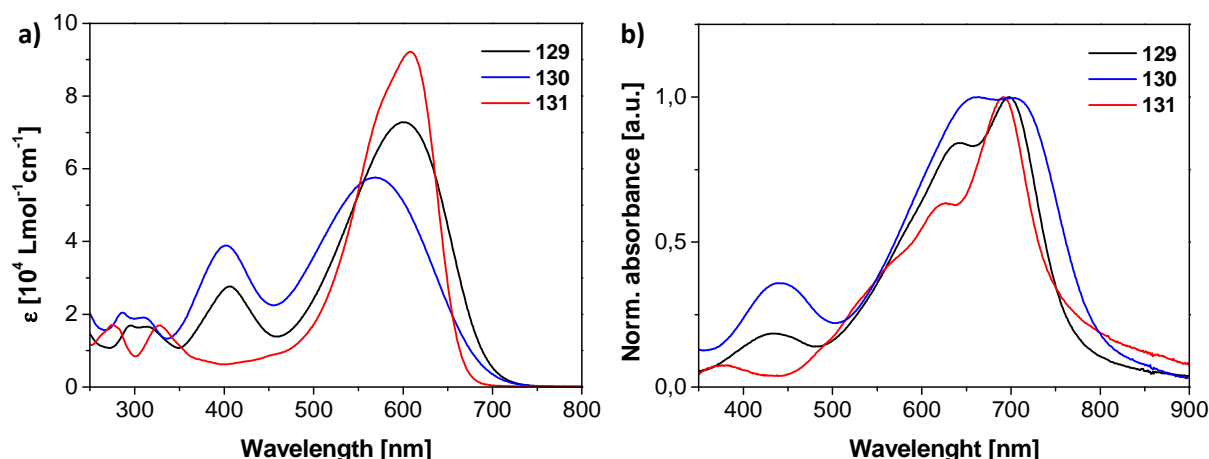


Figure 6. (a) Absorption spectroscopy of **129-131** in chloroform solution. (b) Absorption spectroscopy of **129-131** in thin films spin-coated from chloroform on a glass substrates.

Structurally defined co-oligomer **131** showed its maximum absorption at 609 nm featuring an extinction coefficient of $92,200 \text{ M}^{-1} \text{ cm}^{-1}$. Therefore, it possesses the most red-shifted absorption and the highest extinction among the three dyes, although **131** features the shortest conjugated system. This result is most probably due to smaller torsion angles in **131** between the conjugated parts (DCV, thiophene and DTP) compared to **129** and **130**. A hint for the more planar geometry in solution can be found in the weak shoulder on the high energy side of the absorption band suggesting vibrational splitting and in the narrow absorption with a reduced FWHM of $2,830 \text{ cm}^{-1}$ in comparison to $3,880$ and $5,050 \text{ cm}^{-1}$ for longer homologues **129** and **130**, respectively. Hence, the DCV acceptor and the strong DTP donor part are well conjugated resulting in an intense and red-shifted CT absorption band. Furthermore, in **129** and **130** there is additional torsion within the bithiophene donor part which is not existent in **130**. Therefore the conjugation between DCV and DTP unit in **131** is even better than in **129** leading to the most red-shifted and intense absorption. However, due to the shorter conjugation length of **131** compared to **129** and **130** the absorption onset is blue-shifted to 662 nm resulting in an optical band gap ΔE_{opt} of 1.87 eV.

Thin films of **129-131** were made by spin-coating chloroform solutions of the co-oligomers on glass substrates. The corresponding absorption spectra are depicted in Figure 6b. The absorption maxima of **129-131** in thin films are by 82-97 nm red-shifted compared to the absorption in solution which is on one hand due to planarization of the co-oligomers upon solidification and on the other hand due to π - π stacking. It is assumed that structurally defined co-oligomer **130** shows a completely different morphology and tendency to aggregate in comparison to **129**, since a more intense shoulder at 700 nm is formed. This is presumably also the reason for the bigger red-shift of 113 nm for the absorption onset of **130** when going from solution to thin film compared to **129** which is only shifted

by 74 nm. This results in absorption onsets of 768 and 800 nm for A-D-A co-oligomers **129** and **130**, respectively, leading to optical gaps in thin film $\Delta E_{\text{opt, film}}$ of 1.61 eV (**129**) and 1.55 eV (**130**).

Table 2. Optical data of A-D-A co-oligomers **129-131** in chloroform ($c = 10^{-5}$ M) and in thin films on glass.

dye	λ_{abs} [nm] (ϵ [$\text{M}^{-1}\text{cm}^{-1}$])	FWHM [cm^{-1}]	$\lambda_{\text{abs, onset}}$ [nm]	ΔE_{opt} [eV] ^[a]	$\lambda_{\text{max, film}}$ [nm]	FWHM _{film} [cm^{-1}]	$\lambda_{\text{abs, film, onset}}$ [nm]	$\Delta E_{\text{opt, film}}$ [eV] ^[a]
129	601 (72,800) 406 (27,700)	3,880	694	1.79	(642) ^[b] 698	3,840	768	1.61
130	569 (57,600) 403 (38,900)	5,050	687	1.80	663 (700) ^[b]	4,410	800	1.55
131	609 (92,200)	2,830	662	1.87	(627) ^[b] 691	3,270	759	1.63

[a] Calculated by the low energy onset of λ_{max} . [b] Shoulder.

Shorter homologue **131** exhibited the largest red-shift of the absorption onset by about 140 nm to 759 nm and further development of the vibrational fine structure which is due to its planarity leading to an $\Delta E_{\text{opt, film}}$ of 1.63 eV. The tendency of the FWHM values in thin films remains the same as in solution: **130** featured the highest value of 4,410 cm^{-1} , followed by isomer **129** with a FWHM of 3,840 cm^{-1} , and shortest structurally defined co-oligomer **131** with 3,270 cm^{-1} .

5.2.3 Electrochemical properties of co-oligomers 129-131

Cyclic voltammograms of A-D-A co-oligomers **129-131** were measured in DCM using $(n\text{-Bu})_4\text{NPF}_6$ as supporting electrolyte (Figure 7). Redox potentials, the electrochemically determined band gaps as well as the HOMO and LUMO level energies are listed in Table 3. All three co-oligomers featured one irreversible reduction wave corresponding to the simultaneous one-electron reduction of the two DCV-units and two reversible oxidation waves corresponding to two one-electron oxidations of the central donor block. In general, the cyclic voltammograms of **129** and **130** resemble each other very much compared to the absorption spectra shown in the previous section. The reduction potentials E°_{red1} of **129-131** were determined by differential pulse voltammetry (DPV). In the case of longer triads **129** and **130**, E°_{red1} took place at around -1.50 V. In contrast, the DCV groups of **131** were slightly easier reduced ($E^{\circ}_{\text{red1}} = -1.43$ V) which is most likely due to the smaller donor moiety compared to **129** and **130**. The oxidation potentials E°_{ox1} and E°_{ox2} of **129** and **130** are positioned at ~ 0.25 V and ~ 0.65 V, whereas the ones for **131** are shifted to higher potentials ($E^{\circ}_{\text{ox1}} = 0.45$ V and $E^{\circ}_{\text{ox2}} = 1.03$ V). This is the result of the lower donor strength of the formal quaterthiophene in **131**.

compared to the formal sexithiophene donor moieties in **129** and **130**. It has to be noted that **131** has a much lower solubility in DCM than **129** and **130** resulting in deposition of **131** on the working electrode, which to a small extent influences the reversibility of the cyclic voltammogram in the oxidative regime (see Figure 7).

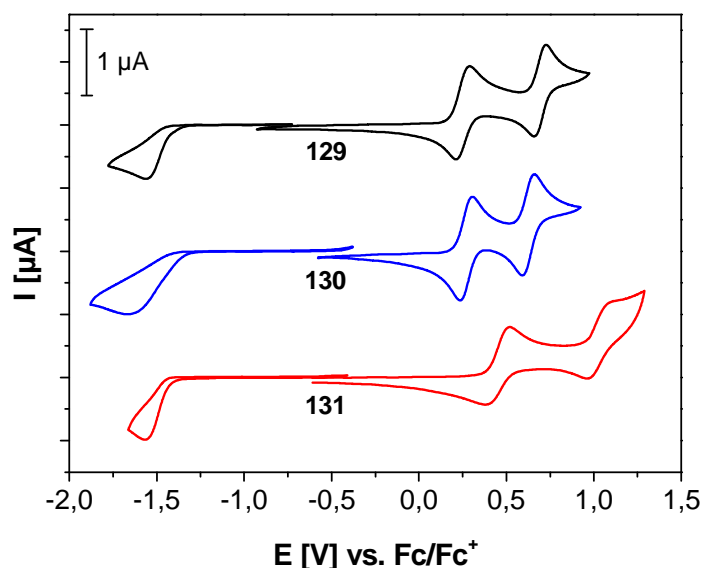


Figure 7. Cyclic voltammograms of **129-131** measured in DCM using $(n\text{-Bu})_4\text{NPF}_6$ (0.1 M) as supporting electrolyte at 100 mV s^{-1} ; $c = 5 \times 10^{-4} \text{ mol/L}$.

Table 3. Electrochemical data of **129-131** in DCM with $(n\text{-Bu})_4\text{NPF}_6$ (0.1 M) as supporting electrolyte measured vs. Fc/Fc^+ at 100 mV s^{-1} .

co-oligomer	E_{ox1}° [V]	E_{ox2}° [V]	E_{red1}° [V]	E_{HOMO} [eV] ^[a]	E_{LUMO} [eV] ^[a]	ΔE_{CV} [eV] ^[b]
129	0.25	0.69	-1.49 ^[c]	-5.28	-3.68	1.60
130	0.27	0.63	-1.50 ^[c]	-5.30	-3.75	1.55
131	0.45	1.03	-1.43 ^[c]	-5.49	-3.67	1.82

[a] E_{HOMO} and E_{LUMO} calculated from the onset of E_{ox1}° and E_{red1}° , respectively; related to the Fc/Fc^+ -couple with a calculated absolute energy of -5.1 eV. [b] Band gap calculated to $\Delta E_{\text{CV}} = E_{\text{HOMO}} - E_{\text{LUMO}}$. [c] Taken from DPV measurement.

The HOMO and LUMO energy levels of the structurally defined co-oligomers were calculated from the onsets of the first oxidation and reduction wave, respectively. The LUMO energy levels are all positioned at around -3.7 eV, due to the similar reduction potentials. The HOMO energy levels of **129**

and **130** lie at ~ -5.3 eV which is 0.2 eV higher than the one of **131** lying at ~ -5.5 eV. The origin thereof is the longer conjugation length of **129** and **130** lifting the HOMO level energy. Thus, the resulting electrochemically determined band gaps ΔE_{CV} s are smaller for **129** and **130** ($\Delta E_{\text{CV}} \approx 1.6$ eV) than for **131** ($\Delta E_{\text{CV}} \approx 1.8$ eV). The HOMO and LUMO energy levels obtained by cyclic voltammetry point out that **129-131** possess suitable energy levels for being used as donor in BHJSCs. When PC₆₁BM is used as acceptor possessing a LUMO energy level of -4.0 eV and a HOMO energy level of -6.0 eV,^[48] the offset between the LUMO energy levels of the donor and the acceptor amounts to ~ 0.3 eV, thus favoring exciton separation. Additionally, there is no energy waste, since the LUMO energy levels of **129-131** lie not much higher than the required offset. The theoretical V_{OC} values can be calculated corresponding to Scharber *et al.*: $V_{\text{OC}} = (1/e)(|E_{\text{HOMO,donor}}| - |E_{\text{LUMO,acceptor}}|) - 0.3$ V (e : elementary charge)^[51] and are ~ 1.0 V for **129** and **130** and ~ 1.2 V for **131**, respectively. The subtracted value of 0.3 V in the equation is an empirical factor which was elaborated on the basis of polymer-based BHJSCs. This result and the fact that the HOMO energy level is not measured of the bulk material can lead to lower V_{OC} values than predicted by the equation above.

5.2.4 Photovoltaic performance of co-oligomers 129-131

Photovoltaic performances of structurally defined co-oligomers **129-131** in BHSJs were tested and optimized. In order to assess their potential application in solution-processed OSCs, the maximum solubility was determined and the absorption of the active layer (co-oligomer:PC₆₁BM blend) was measured prior to solar cell fabrication. Furthermore, since pyridine-containing co-oligomer **115** was not inert against protonation by the hole transport layer (see *Chapter 4*),^[52-54] the stability of the structurally defined co-oligomers towards protonation was investigated.

Solubilities of **129-131** in chloroform at r.t. were determined using absorption spectroscopy. Longer co-oligomers **129** and **130** showed higher solubilities of 11 and 19 mg/mL, respectively. Shorter homologue **131** featured a lower solubility of only 2 mg/mL in chloroform due to less solubilizing alkyl side chains present in the molecule. This lower solubility restricts parameters for the spin-coating process, such as concentration and temperature complicating the optimization process of the active layer. Thin film absorption spectroscopy of **129-131** blended with PC₆₁BM (D:A = 1:2) were recorded in order to roughly evaluate film formation (Figure 8a). The absorbances of the blend layers resembled those of the neat films of **129-131** for wavelengths >500 nm (Figure 6b). Below 500 nm PC₆₁BM also contributes to the absorbance. The absolute absorbance decreases from **131**:PC₆₁BM to **129**:PC₆₁BM and to **130**:PC₆₁BM which is on one hand due to the differences in solubility and on the other because of the higher required processing temperature (60 °C vs. r.t. for **129** and **130**) in order

to obtain homogenous films of **131**:PC₆₁BM. The lower the processing temperature is the less material is deposited during spin-coating leading to a lower absorbance. Owing to the low solubility of **131** and the higher spin-coating temperature used to deposit the blend layer, films with a higher thickness of ~110 nm were obtained in comparison to the films of **129**:PC₆₁BM and **130**:PC₆₁BM of 95-100 nm. Film thicknesses were determined by a profilometer. A roughness of ±10 nm was observed for the **131**:PC₆₁BM blend layer, whereas mixtures of **129** and **130** with PCBM formed smoother films (±2 nm). Additionally, there is stronger light scattering for **131**:PC₆₁BM for wavelengths >700 nm, which can be seen by the heightened baseline pointing towards small crystallites or aggregates within the blend layer.

The stability of the DTP-unit within the series **129-131** against acidic conditions was investigated using absorption spectroscopy, since protonation of the donor, for example by the hole transport layer (HTL), can lead to significant decreases in photovoltaic performance (see *Chapter 4*).^[54] Upon addition of 1000 and 2000 eq. of trifluoroacetic acid (TFA) to a 10⁻⁵ M solution of **129** in chloroform no changes in the absorption spectra were detected (Figure 8b) emphasizing the stability and rather low basicity of conjugated DTP-containing structurally defined co-oligomers towards acids, which is ascribed to the participation of the DTP N-atom lone pair in the conjugation. Hence, no chemical interaction between the oligomer and the acidic HTL poly(3,4-ethylenedioxythiophene):poly(styrene-sulfonate) (PEDOT:PSS) are expected.

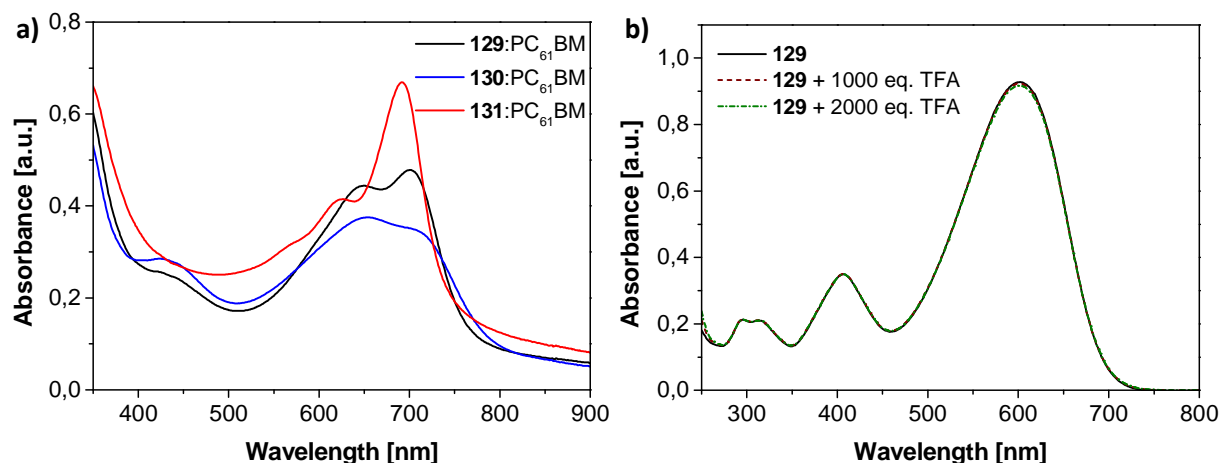


Figure 8. (a) Absorption spectroscopy of the blend layers co-oligomer:PC₆₁BM [1:2], 12.5 mg/mL, spin-coated from chloroform at r.t. (**129** and **130**) and at 60 °C (**131**) at a spin-coating velocity (v_{spin}) of 1000 rpm on PEDOT:PSS-covered ITO glass. (b) Absorption spectroscopy of **129** in chloroform solution and upon addition of 1000 and 2000 eq. TFA (the three spectra superimpose).

Solar cells with a standard device structure: ITO|PEDOT:PSS(35 nm)|D:A|LiF(0.7 nm)|Al(100 nm) were fabricated with the use of **129-131** as donor (D) and PC₆₁BM as acceptor (A). First devices were built using sexithiophene analogue **129** as electron donor. The corresponding photovoltaic parameters are summarized in Table 4. Due to the moderate solubility of **129** in chloroform at r.t., 60 °C was chosen as processing temperature for the solution and the substrate which should prevent dye aggregation and lead to homogenous films. Upon variation of the D:A ratio, it was found that ratios with equivalent or excess acceptor, such as 1:1 and 1:2 mixtures, gave better efficiencies of up to 2.8% with a J_{SC} of 8.7 mA cm⁻², a V_{OC} of 0.81 V, and a FF of 0.42. This stands in contrast to the observations made in literature for structurally defined co-oligomers, where usually higher donor contents yielded the best performing solar cells.^[55,56]

Table 4. Photovoltaic parameters for BHJSCs using structurally defined co-oligomer **129** as donor material with different D:A ratios and spin-coating conditions. Device structure: ITO|PEDOT:PSS|**129**:PC₆₁BM|LiF|Al; solvent: chloroform. For each entry, three solar cells were fabricated using three different spin-coating velocities (750/1000/1250 rpm, if not otherwise stated), whereas only the best one is tabulated.

D:A	conc. [mg/mL]	T [°C] ^[a]	v_{spin} [rpm]	J_{SC} [mA cm ⁻²]	V_{OC} [V]	FF	PCE [%]
1:1	12.5	60 °C	1250	7.80	0.81	0.43	2.69
1:2	12.5	60 °C	1250	8.73	0.80	0.42	2.80
1:1	15.0	60 °C	5000 ^[b]	6.42	0.80	0.52	2.65
2:1	15.0	60 °C	5000 ^[b]	4.27	0.81	0.46	1.61
3:2	12.5	r.t.	1250	2.02	0.80	0.27	0.44
1:1	12.5	r.t.	1250	6.13	0.81	0.49	2.40
1:2	12.5	r.t.	1000	7.93	0.82	0.58	3.74
1:3	12.5	r.t.	750	6.89	0.79	0.49	2.67

[a] Temperature of the spin-coating solution and the substrate. [b] 3000, 4000, and 5000 rpm were used.

By changing to higher spin-coating velocities (v_{spin}), the kinetics of the film formation of the active layer was influenced. In order to maintain a similar active layer thickness of ~100 nm, the concentration was slightly increased from 12.5 to 15.0 mg/mL. Using v_{spin} of 3000, 4000, and 5000 rpm and different D:A ratios solar cells were obtained with similar maximum PCEs when slower v_{spin} were applied (see Table 4, upper four rows). Higher FFs were reached, but these were compensated by lower J_{SC} values. Next, the active layer was spin-coated at r.t. since absorption spectroscopy of active

layers spin-coated on ITO|PEDOT:PSS at r.t. proved uniform film formation (*vide infra*). Four different D:A ratios were screened (3:2, 1:1, 1:2, and 1:3) confirming that still 1:2 yielded the best BHJSCs with a PCE of 3.7%. The improved PCE compared to devices which were prepared at 60 °C is due to an increased FF of 0.58 pointing towards a more favorable morphology of the active layer with good charge separation and transport. A similar trend concerning the D:A ratio could be observed: devices with acceptor contents lower than 50% led to a decline in FF and J_{SC} resulting in considerably lower PCEs, whereas solar cells with D:A ratios of 1:1 and 1:3 still performed quite well (PCE \approx 2.5%). It is noteworthy that devices with D:A ratios of 1:2 or 1:3 fabricated at r.t. gave best PCEs when spin-coated at a v_{spin} of 1000 and 750 rpm, respectively. Higher v_{spin} led to a decrease in PCE, which is caused by thinner films and hence less light harvesting. This result proved a good morphology of the thicker active layers, since too thick layers usually lead to high recombination rates which is not the restrictive factor in this case. Interestingly, no matter how the devices were constructed V_{OC} always reached 0.8 V approaching the theoretically calculated V_{OC} of 1.0 V. Further optimization regarding the use of additives (1,8-diiodooctane (DIO), chloronaphthalene (CN), and polydimethylsiloxane (PDMS)) or thermal annealing did not lead to any further improvement, also the use of other solvents or PC₇₁BM as acceptor yielded lower performing solar cells.

The insights obtained from the optimization of co-oligomer **129** were then adopted for the device fabrication using isomer **130** as donor. An excerpt of the numerous experiments is tabulated in Table 5. Conditions leading to PCEs of up to 3.7% for **129** did not result in well performing BHJSCs using **130** together with PC₆₁BM or PC₇₁BM. In fact, all solar cell parameters decreased compared to devices using **129** as donor.

Table 5. Photovoltaic parameters for BHJSCs using structurally defined co-oligomer **130** as donor material. Device structure: ITO|PEDOT:PSS|**130**:PC₆₁BM|LiF|Al; D:A ratio = 1:2, solvent: chloroform. For each entry, three solar cells were fabricated using three different spin-coating velocities (750/1000/1250 rpm), whereas only the best one is tabulated.

solvent	conc. [mg/mL]	T [°C] ^[a]	v_{spin} [rpm]	J_{SC} [mA cm ⁻²]	V_{OC} [V]	FF	PCE [%]
CHCl₃	12.5	r.t.	750	1.45	0.44	0.24	0.15
CHCl ₃	12.5	40 °C	750	0.61	0.30	0.15	0.03
CB	25.0	r.t.	750	0.04	0.71	0.20	0.01
TCE	20.0	r.t.	1250	1.09	0.52	0.25	0.14

[a] Temperature of the spin-coating solution and the substrate.

The change of the spin-coating solvent, D:A ratio, temperature, concentration, or v_{spin} as well as solvent additives or thermal annealing did not lead to any improvements. Devices containing a **130**:PC₆₁BM blend layer mostly produced poor V_{OC} values pointing towards insufficient diodic quality of the solar cells. The reason for this is due to an unfavorable morphology of the active layer as shown in the next section. The best device reached a PCE of 0.15%, with a J_{SC} of 1.45 mA cm⁻², a V_{OC} of 0.44 V, and a FF of 0.24.

The best performing solar cell which was spin-coated at 60 °C and contained co-oligomer **129** reached a PCE of 2.8%. The conditions used to prepare this cell (Table 4, second entry) were transferred to device fabrication of BHJSCs incorporating **131**:PC₆₁BM as active layer and resulted in a PCE of 1.25%, with a moderate J_{SC} of 3.0 mA cm⁻², a high V_{OC} of 1.0 V, and a FF of 0.40 (Table 6). Due to the lower solubility of **131** in chloroform compared to the other two longer co-oligomers **129** and **130**, solar cells being spin-coated from solutions with a D:A ratio ≥ 1 or at r.t. did not form uniform films of the blend layer producing poorly performing devices.

Table 6. Photovoltaic parameters for BHJSCs using structurally defined co-oligomer **131** as donor. Device structure: ITO|HTL|**131**:PC₆₁BM|LiF|Al; D:A ratio = 1:2, solvent: chloroform; T = 60 °C. For each entry, three solar cells were fabricated using three different v_{spin} 750/1000/1250 rpm or 4000/5000/6000 rpm, whereas only the best one is tabulated.

HTL	conc. [mg/mL]	v_{spin} [rpm]	J_{SC} [mA cm ⁻²]	V_{OC} [V]	FF	PCE [%]
PEDOT:PSS	12.5	1250	3.03	1.04	0.40	1.25
PEDOT:PSS	15.0	6000	5.20	1.07	0.55	3.06
VO_x ^[a]	15.0	6000	5.08	1.10	0.62	3.46

[a] Experiments performed by Dr. G. Schulz [b] Conc. = 0.2 mg/mL.

Device optimization using higher v_{spin} has been performed in our institute where PCEs of up to 3.1% were achieved for BHJSCs using PEDOT:PSS as HTL and v_{spin} of up to 6000 rpm (Table 6, experiments were partly performed by Dr. G. Schulz). The improvement is due to the increased J_{SC} of 5.2 mA cm⁻² and FF of 0.55 compared to cells with active layers fabricated at lower v_{spin} . A possible explanation could be that film formation takes less time when higher v_{spin} is applied. Therefore, **131** cannot aggregate unfavorably, thus building smaller domain sizes. This could then result in a more favorable morphology. Upon the exchange of the HTL PEDOT:PSS by non-stoichiometric VO_x, the FF further increased to 0.62, which did result in an improved PCE of 3.5% despite a slightly lower J_{SC} of 5.1 mA

cm^{-2} . The reason therefore is most probably a better charge extraction by VO_x in comparison to PEDOT:PSS indicated by the higher FF. VO_x was also implemented in BHJSCs using **129** and **130** as donor, however, no significant changes were observed concerning solar cell parameters. This outcome proved that the DTP-moiety is not negatively affected by the acidity of the HTL as it is the case for **115** (see Chapter 4).^[54]

In Figure 9a J - V curves of the best performing BHJSCs of **129-131** (see Table 4-6) are depicted clearly visualizing the different photovoltaic performances of the three structurally defined co-oligomers. For **129** and **131** high FFs of about 0.6 and stable V_{OC} values of 0.8 and 1.0 V, respectively give rise to the assumption of little charge recombination in the cells. This is supported by the low saturation factors (defined as $J_{-1\text{V}}/J_{\text{SC}}$) of about 1.08. Hence, PCEs of BHJSC using **129** and **131** as donor reached 3.5-3.7%.

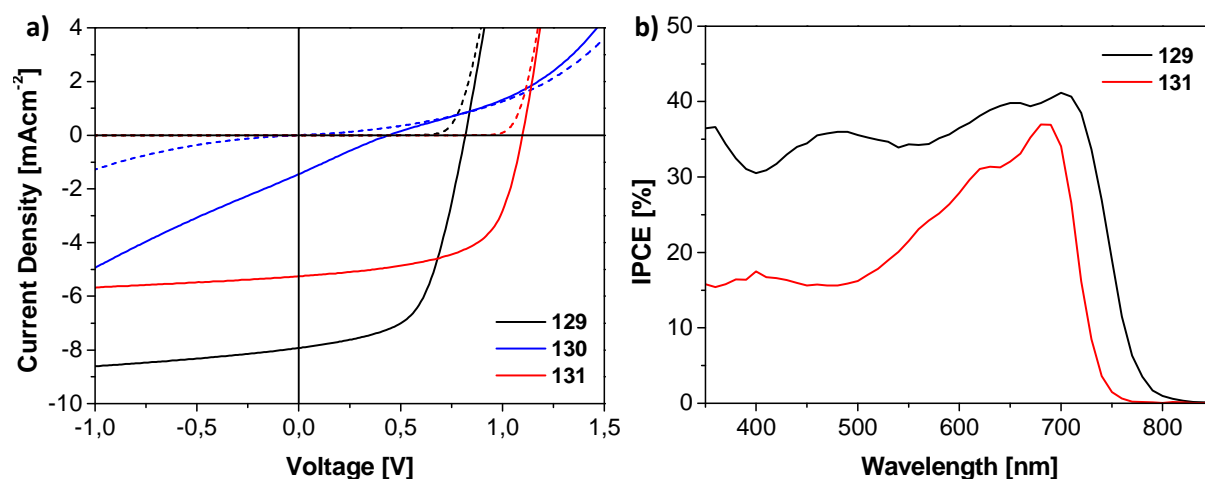


Figure 9. (a) J - V curves of best performing BHJSCs of **129-131**; device architecture and spin-coating conditions are tabulated in Table 4-6 (bold entries), respectively. Solid line: measurement under illumination; dashed line: measurement in the dark (b) IPCE spectra of the corresponding devices, the IPCE spectra of **130** is not depicted due to low informative value.

On the other hand, **130** with hexyl side-chains pointing towards the DCV groups possesses the same potential to achieve high PCEs regarding its optoelectronic properties (*vide supra*), but solar cells containing **130** as donor material did not show real diodic behaviour, as can be seen by its J - V curve under illumination and in the dark (Figure 9a). The poor saturation factor of 3.41 and its low V_{OC} and FF values point to a high portion of recombination being responsible for the low PCE. The main reason therefore is the bad morphology of the active layer as proven in the next section.

IPCE spectra of **129** and **131** are shown in Figure 9b. The spectrum of **130** is not depicted due to its low IPCE responses. Longer homologue **129** showed a nearly rectangular spectrum from 350-750 nm with an onset at 777 nm and a maximum of 41% at 700 nm. Shorter homologue **131** featured an onset at 734 nm and a maximum of 37% at 680-690 nm. The IPCE spectrum of **131** resembles more to its absorption spectra of the thin film compared to **129** (Figure 6b) showing a decrease in IPCE to ~17% at shorter wavelengths (350-525 nm). The stronger IPCE response of **129** in this region can be attributed to a contribution of the bithiophene moiety and/or to a stronger contribution of PC₆₁BM. In general, the IPCE response of **129** and **131** could be higher as well as their J_{SC} values regarding the coverage of the solar spectrum. An even more favorable morphology or a better charge extraction at the interfaces might increase these two values.

5.2.5 Photoactive layer characterization and external device optimization

In collaboration with the Center for Solar Energy and Hydrogen Research (ZSW) Baden-Württemberg in Stuttgart and the Institute of Inorganic Chemistry II, Ulm University further optimization of BHJSCs containing **129** and **130** and investigation of the corresponding photoactive layers were carried out.^[57,58] Device optimization was performed concerning active layer thicknesses at ZSW in Stuttgart. Best results were obtained for active layer thicknesses of ~75 nm for **129** and ~60 nm for **130**, respectively. Table 7 summarizes the photovoltaic data as well as the average PCE over 12-14 devices. The data clearly shows that for structurally defined co-oligomer **129** all solar cell parameters are still by far better. A higher J_{SC} (8.8 vs. 3.4 mA cm⁻²), V_{OC} (0.83 vs. 0.72 V), and FF (0.66 vs. 0.33) resulted in a significantly larger PCE of 4.8% for DTP-derivative **129** compared to 0.8% for **130**.

Table 7. Photovoltaic parameters of fabricated BHJSCs using the following device structure: ITO|PEDOT:PSS|D:PC₆₁BM|LiF|Al; D:A = 1:2 ratio, solvent: chloroform; T = r.t.. Active layer thicknesses of the cells were ~75 nm for **129** and ~60 nm ± 10 nm for **130**.

co-oligomer	J_{SC} [mA cm ⁻²]	V_{OC} [V]	FF	PCE [%]	average PCE (± std. dev.) [%]
129	8.8	0.83	0.66	4.8	4.39 (± 0.22) ^[a]
130	3.4	0.72	0.33	0.8	0.51 (± 0.19) ^[b]

[a] Average over 12 devices. [b] Average over 14 devices.

Thinner and thicker devices led to lower PCEs as illustrated in Figure 10 due to a less favorable compromise between light-harvesting and charge transport. The optimum active layer film thickness

for BHJSCs containing donor **129** is at ~ 75 nm. This is most probably the reason for the lower performance of BHJSCs fabricated in-house (Table 4 and 5), which possessed layer thicknesses of 90–110 nm.

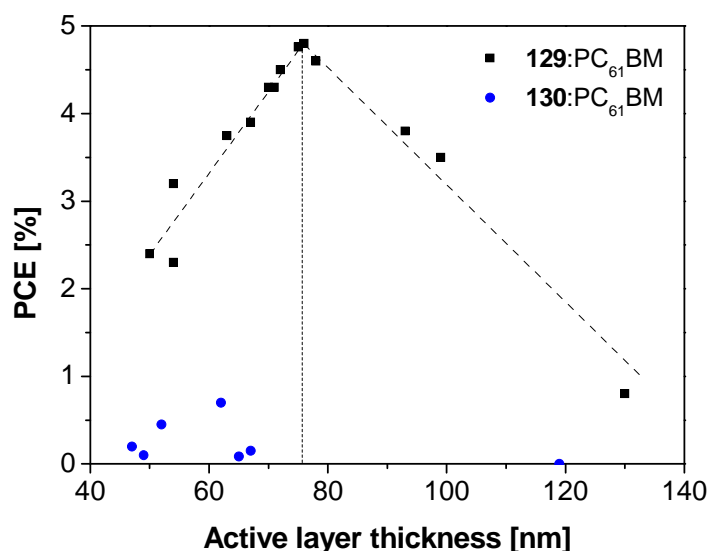


Figure 10. PCE dependence on active layer thickness for **129** and **130** blended with PC₆₁BM (D:A ratio = 1:2).

Subsequently, the morphology of the best performing devices containing structurally defined co-oligomer **129** and **130** were investigated with respect to the active layer surface (via AFM) and crystallinity/packing of the structurally defined co-oligomers (via XRD) to evaluate the differences in photovoltaic performance.

In-house AFM measurements were performed by Dr. E. Mena-Osteritz. The samples were prepared in the same way as the photoactive layers for the solar cell devices. Figure 11 depicts the characteristic long range topography images for both blend films. **129**:PC₆₁BM (Figure 11a) showed a regular grain-structured surface. However, **130**:PC₆₁BM (Figure 11d and inset) showed a flatter topography with few crystallites on top. The short range images in Figure 11b and c and Figure 11e and f underline the differences in film characteristics: the surface of **129**:PC₆₁BM (Figure 11b) is composed of fine aligned fibers (~ 20 nm \pm 2 nm) with a 32 nm \pm 1 nm height profile. In contrast, the **130**:PC₆₁BM blend (Figure 11e) showed an almost flat surface (2.0 nm \pm 0.2 nm). Crystallites of a size of 40–250 nm could be identified on top of the surface. The corresponding phase image (Figure 11f) showed almost no contrast ($4^\circ \pm 0.2^\circ$) demonstrating a completely mixed film. The borders of the crystallites on top show a higher phase contrast compared with their center and the mixed phase ($25^\circ \pm 1^\circ$, inset Figure 11f). In the phase images of **129**:PC₆₁BM (Figure 11c), fiber domains with an

averaged contrast of 18° can be identified. It is possible to assign the lighter regions (higher phase shift) to areas with mostly donor **129**, whereas the darker regions (lower phase shift) contain mostly acceptor PC₆₁BM.^[59] The analysis of the phase images reveals domains of ~ 20 nm in size for the higher phase shift. It can be concluded that the photoactive blends containing structurally defined co-oligomer **129** phase-separate into domains of approximately 20 nm in size. Whereas on the surface of isomer **130**-based blends no phase separation of the two components can be observed. In case of the very finely mixed blend, recombination of the generated charges during solar cell operation should occur as a result of the lack of percolation pathways. A significant amount of recombination in **130**:PC₆₁BM devices is consistent with the rather low fill factor (0.33) and J_{SC} (3.4 mA cm^{-2}) as well as the reduced V_{OC} (0.72 V, see Table 7).

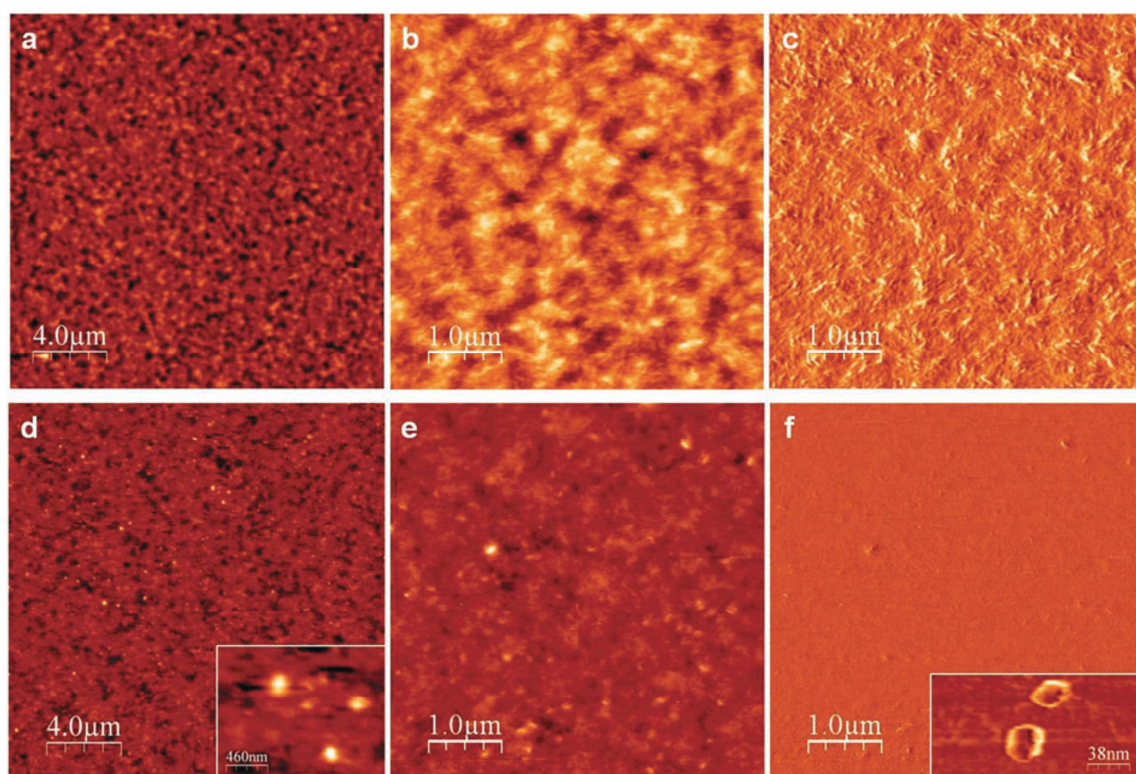


Figure 11. AFM images of **129**:PC₆₁BM (**a,b**: topography **c**: phase) and **130**:PC₆₁BM (**d,e**: topography **f**: phase) thin films on PEDOT:PSS-coated ITO substrates.

XRD patterns were measured for thin films of **129**:PC₆₁BM and **130**:PC₆₁BM on PEDOT:PSS-coated ITO substrates in the Institute of Inorganic Chemistry II, Ulm University. In case of **130**, the low-angle reflection can be ascribed to the presence of some crystallites of the structurally defined co-oligomer (Figure 12). The d-spacing correlates to the separation of the thiophene backbones and depends on the length and orientation of the side chains and was determined to 15.6 \AA ($2\theta = 5.6^\circ$) for **130**. This is

lower than typically observed for regioregular poly(3-hexylthiophene) (~ 16 Å)^[60] indicating a somewhat denser packing through a better interdigitation of the hexyl chains. The intense reflection of the **130**:PC₆₁BM system shows larger crystallites than in the case of the **129**:PC₆₁BM blend, where no significant reflection was found. This is in agreement with the AFM images (Fig. 11d and inset), where some aggregates can be observed on the surface.

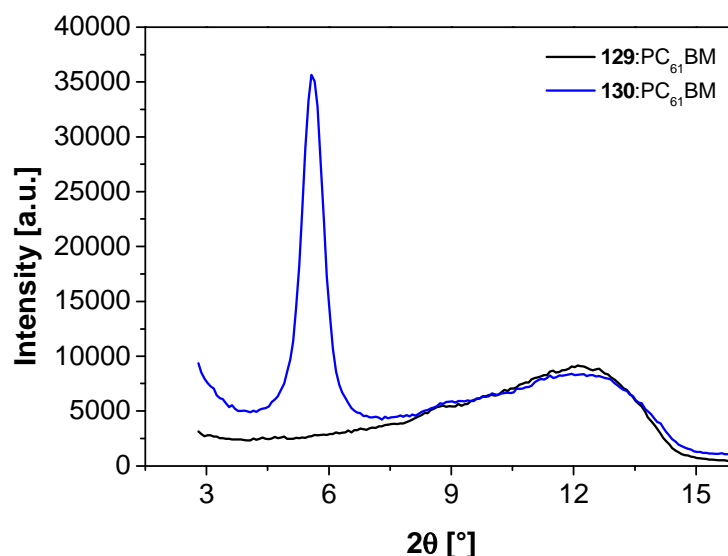


Figure 12. XRD diffraction patterns measured for **129**:PC₆₁BM and **130**:PC₆₁BM thin films on PEDOT:PSS-coated ITO substrates; D:A ratio = 1:2. The broad reflection at $2\theta = 12.5^\circ$ corresponds to the substrate.

These results let assume that **130** forms some bigger crystallites within a very well and fine mixed **130**:PC₆₁BM matrix which probably does not lead to an interpenetrating network, contrary to **129**:PC₆₁BM blends. Thus, a better phase separation and ordering in the active layer should improve charge transport and hence the PCE. As described in the previous section several attempts to influence the phase separation of **130**:PC₆₁BM blends have been carried out without significant improvements in solar cell parameters. However, by using solvent vapor annealing (SVA) the photovoltaic performance of **130** in BHJSCs could be drastically increased from 0.8% (no SVA, Table 7) to up to 4.4% (90s exposure to chloroform, Table 8).^[58] BHJSCs of **130**:PC₆₁M where the active layer was solvent-annealed with chloroform for 90 s showed doubled J_{sc} and FF values of 8.2 mA cm^{-2} and 0.65, respectively, compared to devices fabricated without SVA. This clearly indicates an improvement in morphology of the active layer upon SVA. Less recombination also leads to a higher V_{oc} of 0.83 V, which is comparable to the one of **129**:PC₆₁BM blends. SVA of BHJSCs using **129** as donor material did not improve PCE. Slight decreases in FF and V_{oc} rather suggest unfavorable

further phase separation compared to as-cast films, where domain sizes of ~ 20 nm have been shown by AFM measurements (*vide supra*). Longer SVA times for **129**:PC₆₁BM blends resulted in even lower PCEs.

Table 8. Photovoltaic parameters of fabricated BHJSCs with SVA using the following device structure: ITO|PEDOT:PSS|co-oligomer:PC₆₁BM|LiF|Al; D:A ratio = 1:2, solvent: chloroform. Active layer thicknesses of the cells were ~ 75 nm for **129** or ~ 60 nm for **130**. The averaged values consist of 10 cells.

co-oligomer	SVA [s]	J_{sc} [mA cm ⁻²]	V_{oc} [V]	FF	PCE [%]	average PCE (\pm std. dev.) [%]
129	30	8.9	0.82	0.63	4.6	3.97 (\pm 0.30)
130 ^[a]	90	8.2	0.83	0.65	4.4	3.23 (\pm 0.70)

[a] solution-processed at 50 °C.

These results suggest that exposure to chloroform vapor allows for a re-organization of the blend, which leads to an increase of the crystallinity of the donor. Hence, SVA improves phase separation in the D:A blend layer.^[58] Therefore, it is crucial to know that SVA can also promote phase separation to the degree of damaging the interpenetrating network coming along with lower performing BHJSCs.

5.3 Summary

In summary, three novel DTP-containing structurally defined co-oligomers **129-131** have been synthesized and characterized. Solubilizing side chains were introduced at the central nitrogen (2-ethylhexyl) and at each residual thiophene ring (*n*-hexyl). For co-oligomer **129** containing four thiophene rings, the hexyl chains point towards the DCV end groups, whereas **130**, representing a constitutional isomer of **129**, bears hexyl chains pointing towards the central DTP-unit. **131** represents a shorter homologue of **129** comprising only two thiophenes and one DTP-unit as donor moiety. Absorption spectroscopy revealed high potential as light harvesting donor material in organic solar cells with extinction coefficients of 57,600-92,200 M⁻¹cm⁻¹ and absorption maxima between 570-610 nm in solution, which shift by about 100 nm when measured in thin films suggesting flattening and ordering of the co-oligomers in the bulk. Cyclic voltammetry measurements of **129-131** showed HOMO and LUMO energy levels which match well to those required for efficient PC₆₁BM-based BHJSCs. As-cast **129**:PC₆₁BM and **130**:PC₆₁BM blends in BHJSCs yielded PCEs of 4.8 and

0.8%, respectively. The big discrepancy in PCE is attributed to the very different blend morphology and phase separation probed by AFM and XRD-techniques and probably induced by the different solubilities of **129** (10 mg/mL) and **130** (19 mg/mL) in chloroform. However, SVA of **130**:PC₆₁BM films could presumably induce a better phase separation and ordering, thus leading to solar cells with PCEs as high as 4.4%. Shorter structurally defined co-oligomer **130** gave rise to 3.5% PCE when used as donor material in BHJSCs. In order to create a favorable morphology in the active layer completely different spin-coating parameters compared to **129** and **130** had to be chosen, because of the low solubility of 2 mg/mL in chloroform. For all three structurally defined co-oligomers **129-131** excellent V_{oc} values of 0.8-1.0 V and high FF values of about 0.65 were obtained.

5.4 Experimental section

5.4.1 General procedures

¹H NMR spectra were recorded in CDCl₃ on a Bruker AMX 400 at 400 MHz. ¹³C NMR spectra were recorded in CDCl₃ on a Bruker AMX 400 at 100 MHz. Chemical shifts are denoted by a δ unit (ppm) and are referenced to the residual solvent peak (CDCl₃: ¹H δ = 7.26 ppm and ¹³C δ = 77.0 ppm). The splitting patterns are designated as follows: s (singlet), d (doublet), t (triplet), and m (multiplet). Mass spectra were recorded with a Varian Saturn 2000 GC-MS and with a MALDI-TOF MS Bruker Reflex 2 (*trans*-2-[3-(4-*tert*-butylphenyl)-2-methyl-2-propenylidene]malono-nitrile (DCTB) as matrix). Melting points of the intermediates were determined with a Büchi B-545 melting point apparatus and are not corrected. Melting points of **129-131** were determined using a Mettler Toledo DSC 823. Gas chromatography was carried out using a Varian CP-3800 gas chromatograph. HPLC analyses were performed on a Merck Hitachi L7000 equipped with a L7455 photodiode array detector, a L7200 autosampler and a L7100 solvent delivery system using a LiChrospher column (Nucleosil 100-5 NO₂). Preparative HPLC was performed on a Merck Hitachi 7000/Shimadzu CBM-20A equipped with a L7420/SPD-20A UV-vis detector and a L7150/LC-8A solvent delivery system using LiChrospher columns (Nucleosil 100-5 NO₂). Thin-layer chromatography was carried out on Silica Gel 60 F254 aluminium plates (Merck). Solvents and reagents were purified and dried by usual methods prior to use and used under inert gas atmosphere. The following starting materials were purchased and used without further purification: diisopropylamine (Merck), sodium *t*-butoxide (Merck), zinc(II) chloride (Merck), copper(II) chloride (Merck), piperidine (Merck), 2-ethylhexylamine (Merck), β -alanine (Merck), malononitrile (Aldrich), *n*-butyllithium (Aldrich), trimethyltin chloride (Aldrich), (\pm)-BINAP

(Aldrich), tris(dibenzylideneacetone)dipalladium(0) (Aldrich), 3-bromothiophene (fluorochem). Tetrakis(triphenylphosphine)palladium(0) was synthesized according to literature.^[61]

Optical and cyclic voltammetry measurements

UV-Vis spectra in chloroform solution and thin film were taken on a Perkin-Elmer Lambda 19 spectrometer. Cyclic voltammetry experiments were performed with a computer-controlled Autolab PGSTAT30 potentiostat in a three-electrode single compartment cell (3 mL). The platinum working electrode consisted of a platinum wire sealed in a soft glass tube with a surface of $A = 0.785 \text{ mm}^2$, which was polished down to $0.25 \text{ }\mu\text{m}$ with Buehler polishing paste prior to use in order to obtain reproducible surfaces. The counter electrode consisted of a platinum wire and the reference electrode was an Ag/AgCl reference electrode. All potentials were internally referenced to the ferrocene/ferrocenium couple. For the measurements, concentrations of $5 \times 10^{-4} \text{ M}$ of the electro-active species were used in freshly distilled and deaerated DCM (Lichrosolv, Merck) purified with an MB-SPS-800 and 0.1 M (*n*-Bu)₄NPF₆ (Fluka; recrystallized twice from ethanol).

Device fabrication

In-house fabrication: PEDOT:PSS (Clevios P, VP.AI 4083 solution from Heraeus) was spin-coated onto pre-cleaned, patterned ITO-coated glass from Kintec ($15 \text{ }\Omega \text{ cm}^{-2}$) upon which $\sim 35 \text{ nm}$ thick layers were obtained. Afterwards the photoactive layer was spin-coated from a mixed solution loaded with donor and PC₆₁BM (Solenne BV). Thin layers of LiF ($\sim 0.7 \text{ nm}$) and Al ($\sim 100 \text{ nm}$) were then deposited by vacuum evaporation at $2 \times 10^{-6} \text{ Torr}$ (Nano 36, Kurt J. Lesker Co.). The photoactive areas of the cells were 0.25 cm^2 .

External fabrication; ZSW (Stuttgart): ITO-coated glass from VisionTec ($14 \text{ }\Omega \text{ cm}^{-2}$) was structured and plasma etched (Diener electronic, Pico) with Argon for 120 s at 30W and a base pressure of 0.38 mbar. Then PEDOT:PSS (Clevios P VP.AI 4083 solution from Heraeus) which was diluted with deionized water in a 1:1 ratio was doctor-bladed and $\sim 10 \text{ nm}$ thick layers were obtained. Afterwards, the substrates were spin-coated (Laurell CZ-650 series) from chloroform solutions loaded with structurally defined co-oligomer **129** or **130** and PC₆₁BM (Solenne BV) leading to the photoactive layers. Thin layers of LiF ($\sim 0.7 \text{ nm}$) and Al ($\sim 100 \text{ nm}$) were then deposited by vacuum evaporation at $2 \times 10^{-6} \text{ mbar}$ (Univex 450, Leybold). The photoactive areas of the cells were between 0.07 and 0.25 cm^2 and no size dependence was found.

Current-voltage characterization

Characterization of in-house fabricated devices: *J-V* characteristics were measured with a Oriel Instruments solar simulator (class AAA, AM 1.5G, 100 mWcm^{-2}) and a Keithley 2400 source meter. IPCE was measured under monochromatic light from a 300 W Xenon lamp in combination with a

monochromator (Oriel, Cornerstone 260), modulated with a mechanical chopper. The response was recorded as the voltage over a 220 Ω resistance, using a lock-in amplifier (Merlin 70104). A calibrated Si cell was used as reference.

Characterization of externally fabricated devices; ZSW (Stuttgart): *J-V* analysis was carried out with a WACOM 2-lamp solar simulator (class AAA, AM 1.5G, 100 mWcm⁻²) and a Keithley 2400 current source measure unit. IPCE measurements were performed using equipment from Optosolar. As light source a 100 W xenon lamp was used and the filtered monochromatic light was monitored with a Si cell. A bias light with 0.1-0.2 sun was used.

Thin layer thickness

Film thicknesses were measured using a Dektak profilometer and also by using high resolution field emission scanning electron microscopy (Sirion XL30) from FEI.

Atomic force microscopy

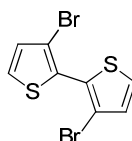
Topography and phase shift images of the photoactive layers were recorded with the help of a Bruker Nanoscope V AFM at ambient conditions in tapping mode.

XRD

Diffraction patterns were measured using a Bruker D8 diffractometer with a fixed incoming angle of 0.2° and a Cu K α source.

5.4.2 Synthesis

3,3'-Dibromo-2,2'-bithiophene (133)^[19]



n-BuLi (1.6 M, 31.5 mL, 78.7 mmol) was added to a solution of diisopropylamine (11.1 mL, 78.7 mmol) in 600 mL THF, cooled to 0 °C. The mixture was stirred for 30 min at 0 °C. Then 3-bromothiophene (11.7 g, 71.6 mmol) was added in one portion and the reaction mixture was stirred for 2 h at 0 °C. Afterwards ZnCl₂ (10.7 g, 78.7 mmol) was added and it was stirred for further 45 min at 0 °C. Upon cooling with a dry ice/acetone cooling bath CuCl₂ (11.5 g, 85.9 mmol) was added in one portion and the mixture was stirred for 1.5 h at -60 to -78 °C. Subsequently, the mixture was allowed to warm up to r.t. overnight. Silica was added and the solvents were removed by rotary

evaporation. The residue was filtrated over a thick silica column with petroleum ether as eluent to obtain 3,3'-dibromo-2,2'-bithiophene **133** (9.70 g, 29.9 mmol, 84%) as a colorless solid.

M.p.: 98-99 °C.

¹H NMR (400 MHz, CDCl₃): δ = 7.41 (d, ³J = 5.4 Hz, 2 H, 5-H, 5'-H), 7.08 (d, ³J = 5.4 Hz, 2 H, 4-H, 4'-H).

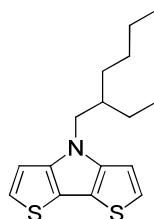
¹³C NMR (100 MHz, CDCl₃): δ = 130.78, 128.85, 127.50, 112.61.

MS (EI) *m/z*: calcd for C₈H₄Br₂S₂: 322; found [M]⁺: 322.

Elemental analysis: calcd (%) for C₈H₄Br₂S₂: C 29.65, H 1.24, S 19.79; found (%): C 29.89, H 1.50, S 19.55.

Analyses match with Ref. ^[19].

4-(2-Ethylhexyl)-4H-dithieno[3,2-b:2',3'-d]pyrrole (**132f**)



3,3'-Dibromo-2,2'-bithiophene **133** (9.00 g, 27.8 mmol), sodium *t*-butoxide (6.27 g, 65.2 mmol), Pd₂dba₃*CHCl₃ (431 mg, 0.42 mmol) and BINAP (1.04 g, 1.67 mmol) were added in a flame-dried Schlenk-tube and evacuated for several minutes. Then 80 mL toluene were added and the mixture was degassed several times. 2-Ethylhexylamine (4.55 mL, 27.8 mmol) was added and the mixture was degassed once more. The reaction mixture was heated to 110 °C for 20 h. After that the mixture was poured into water. The organic layer was separated and the aqueous phase was extracted with diethyl ether. The combined organic phases were dried over sodium sulfate and the solvents were removed by rotary evaporation. The crude product was purified via column chromatography (silica/*n*-hexane) to obtain 4-(2-ethylhexyl)-4H-dithieno[3,2-b:2',3'-d]pyrrole **132f** (7.41 g, 25.4 mmol, 92%) as a colorless oil.

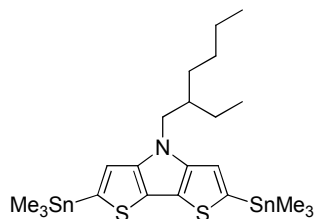
¹H NMR (400 MHz, CDCl₃): δ = 7.12 (d, ³J = 5.2 Hz, 2 H, 5-H,5'-H), 6.98 (d, ³J = 5.2 Hz, 2 H, 4-H,4'-H), 4.11-4.01 (m, 2 H, N-CH₂), 1.98-1.89 (m, 1 H, -CH-), 1.39-1.20 (m, 8 H, -CH₂-), 0.92-0.85 (m, 6 H, -CH₃).

¹³C NMR (100 MHz, CDCl₃): δ = 145.25, 122.67, 114.48, 111.06, 51.30, 40.44, 30.62, 28.65, 24.00, 22.97, 14.03, 10.67.

MS (EI) *m/z*: calcd for C₁₆H₂₁NS₂: 291; found [M]⁺: 291.

Elemental analysis: calcd (%) for $C_{16}H_{21}NS_2$: C 65.93, H 7.26, N 4.81; found (%): C 66.14, H 7.36, N 4.57.

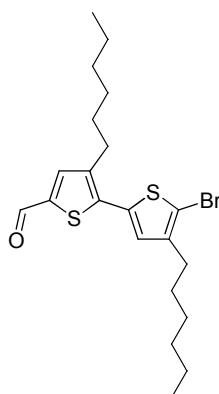
4-(2-Ethylhexyl)-2,6-bis(trimethylstannyl)-4H-dithieno[3,2-b:2',3'-d]pyrrole (177**)**



n-BuLi (1.6 M, 1.16 mL, 1.85 mmol) was added dropwise to a solution of 4-(2-ethylhexyl)-4H-dithieno[3,2-b:2',3'-d]pyrrole **132f** (245 mg, 0.84 mmol) in 3.3 mL THF at -78 °C. After the addition the solution was stirred at -78 °C for 1 h and then at 0 °C for 1 h. Subsequently, the reaction mixture was cooled down again to -78 °C and trimethyltin chloride (377 mg, 1.89 mmol) dissolved in 0.55 mL THF was added in one portion. Then after stirring at -78 °C for 2.5 h the reaction mixture was poured into water. *n*-Hexane was added and the organic layer was washed three times with cold water. The organic phase was dried over sodium sulfate and the solvent was removed by rotary evaporation. 4-(2-Ethylhexyl)-2,6-bis(trimethylstannyl)-4H-dithieno[3,2-b:2',3'-d]pyrrole **177** was obtained as a slightly greyish to brownish oil (550 mg) with a conversion of 95% (calculated by 1H -NMR). It was used without further purification.

1H NMR (400 MHz, $CDCl_3$): δ = 6.96 (s, 2 H, 3-H,3'-H), 4.10-3.99 (m, 2 H, N-CH₂), 2.01-1.94 (m, 1 H, -CH-), 1.43-1.30 (m, 8 H, -CH₂-), 0.92 (t, 3J = 7.4 Hz, 3 H, -CH₃), 0.88 (m, 3J = 7.2 Hz, 3 H, -CH₃).

MS (MALDI-TOF) *m/z*: calcd for $C_{22}H_{37}NS_2Sn_2$: 619; found $[M]^+$: 619.

5'-Bromo-3,4'-dihexyl-2,2'-bithiophene-5-carbaldehyde (180)

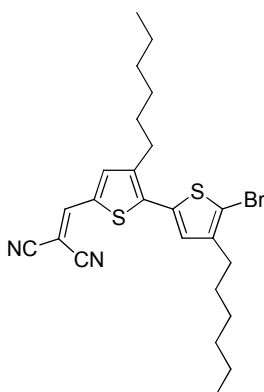
Diisopropylamine (245 mg, 2.42 mmol) was added dropwise to a solution of *n*-BuLi (1.6 M, 1.51 mL, 2.42 mmol) in 20 mL THF at -78 °C. The mixture was stirred for 30 min and warmed to 0 °C and stirred for another 30 min. 5'-Bromo-3,4'-dihexyl-2,2'-bithiophene **47** (1.00 g, 2.42 mmol) dissolved in 5 mL THF was added to the LDA mixture dropwise. The reaction mixture was stirred for 1 h before it was quenched with DMF and stirred overnight. The solvent was removed and the crude product was purified via column chromatography (silica/petrol ether:DCM (3:2)) to yield 5'-bromo-bithiophene-5-carbaldehyde **180** (812 mg, 1.84 mmol, 76%) as a bright yellow oil.

¹H NMR (400 MHz, CDCl₃): δ = 9.82 (s, 1 H, CHO), 7.57 (s, 1 H, 4-H), 6.96 (s, 1 H, 3'-H), 2.74 (t, ³*J* = 7.9 Hz, 2 H, α-CH₂), 2.57 (t, ³*J* = 7.8 Hz, 2 H, α'-CH₂), 1.70-1.56 (m, 4 H, β-CH₂, β'-CH₂), 1.44-1.26 (m, 12 H, -CH₂-), 0.89 (t, ³*J* = 6.7 Hz, 6 H, -CH₃).

¹³C NMR (100 MHz, CDCl₃) 182.6, 143.0, 140.5, 140.4, 138.8, 134.3, 128.3, 111.2, 31.6, 30.3, 29.6, 29.5, 29.2, 29.1, 28.9, 22.6, 14.1, 14.1.

MS (CI) *m/z*: calcd for C₂₁H₂₉BrOS₂: 440; found [M]⁺: 440.

Elemental analysis: calcd (%) for C₂₁H₂₉BrOS₂ (%): C 57.13, H 6.62, S 14.53; found (%): C 57.25, H 6.67, S 14.45.

2-(5'-Bromo-3,4'-dihexyl-[2,2'-bithien-5-yl]methylene)malononitrile (178)

5'-Bromo-bithiophene-5-carbaldehyde **180** (800 mg, 1.81 mmol), malononitrile (0.360 g, 5.45 mmol) and 2 drops of piperidine were dissolved in 15 mL DCE:ethanol (3:1) and heated to 60 °C for 18 h. Then, the solvent was evaporated and the crude product was purified via column chromatography (silica/*n*-hexane:DCM [1:1]) followed by recrystallization from ethanol to obtain DCV bromo-bithiophene **178** (771 mg, 1.57 mmol, 87%) as orange solid.

M.p.: 71 °C.

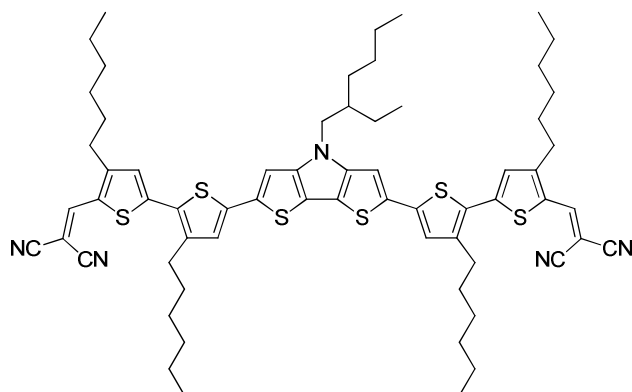
¹H NMR (400 MHz, CDCl₃): δ = 7.69 (s, 1 H, CH), 7.50 (s, 1 H, 4-H), 7.05 (s, 1 H, 3'-H), 2.75 (t, ³*J* = 7.9 Hz, 2 H, α-CH₂), 2.57 (t, ³*J* = 7.7 Hz, 2 H, α'-CH₂), 1.63-1.58 (m, 4 H, β-CH₂, β'-CH₂), 1.37-1.28 (m, 12 H, -CH₂-), 0.89 (t, ³*J* = 6.7 Hz, 6 H, -CH₃).

¹³C NMR (100 MHz, CDCl₃): δ = 150.1, 143.1, 141.6, 140.8, 133.4, 132.2, 129.1, 31.5, 30.1, 29.6, 29.5, 29.1, 28.9, 22.6, 22.5, 14.1, 14.0.

MS (MALDI-TOF) *m/z*: calcd for C₂₄H₂₉BrN₂S₂: 488; found [M]⁺: 488.

Elemental analysis: calcd for C₂₄H₂₉BrN₂S₂ (%): C 58.88, H 5.97, N 5.72, S 13.10; found (%): C 58.99, H 6.09, N 5.60, S 13.15.

2,2'-(5,5'-[N-{2-Ethylhexyl}-dithieno[3,2-b:2',3'-d]pyrrole-2,6-diyl]-bis[3',4-diethyl-2,2'-bithien-5,5'-diyl])-bis(methane-1-yl-1-ylidene)dimalononitrile (129)



Bis(trimethylstannyl)-DTP **177** (227 mg, 400 μmol), DCV iodo-bithiophene **61** (515 mg, 960 μmol) and $\text{Pd}(\text{PPh}_3)_4$ (18.5 mg, 16.0 μmol) were added in a Schlenk-tube and evacuated for several minutes. After adding 23 mL DMF the reaction mixture was carefully degassed and heated to 60 $^\circ\text{C}$ for 6 h. Then the reaction mixture was poured into saturated aqueous ammonium chloride solution. The organic compounds were extracted with DCM. The combined organic phases were dried with sodium sulfate and the solvents were removed by rotary evaporation. The crude product was purified via digesting with ethyl acetate and subsequent column chromatography (silica/DCM) to obtain structurally defined co-oligomer **129** (410 mg, 370 μmol , 92%) as a black solid.

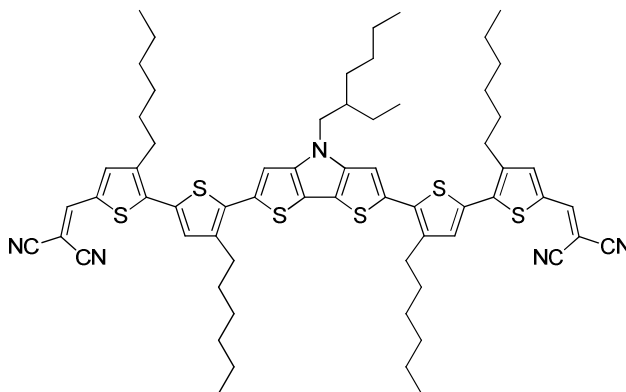
M.p.: 264 $^\circ\text{C}$.

^1H NMR (400 MHz, CDCl_3): δ = 7.78 (s, 2 H, C=CH), 7.08 (s, 2 H, DTP-H), 7.05 (s, 4 H, 3-H,4'-H), 4.08-3.98 (m, 2 H, N-CH₂), 2.83 (t, 3J = 7.9 Hz, 4 H, α' -CH₂), 2.74 (t, 3J = 7.8 Hz, 4 H, α -CH₂), 1.99-1.93 (m, 1 H, N-CH), 1.74-1.60 (m, 4 H, β' -CH₂), 1.48-1.42 (m, 4 H, β -CH₂), 1.40-1.27 (m, 28 H, -CH₂-), 0.96-0.88 (m, 18 H, -CH₃).

^{13}C NMR (100 MHz, CDCl_3): δ = 156.42, 147.09, 147.00, 145.71, 144.93, 139.89, 134.39, 128.92, 127.57, 126.79, 126.67, 115.32, 115.06, 114.05, 108.12, 73.15, 51.51, 40.30, 31.64, 31.52, 31.28, 30.51, 30.37, 30.08, 29.23, 29.12, 29.06, 28.48, 23.95, 23.04, 22.58, 22.54, 14.09, 14.06, 10.72.

MS (MALDI-TOF) m/z : calcd for $\text{C}_{64}\text{H}_{77}\text{N}_5\text{S}_6$: 1107; found $[\text{M}+\text{H}]^+$: 1108.

Elemental analysis: calcd (%) for $\text{C}_{64}\text{H}_{77}\text{N}_5\text{S}_6$: C 69.33, H 7.00, N 6.32, S 17.35; found (%): C 69.35, H 6.96, N 6.25, S 17.49.

2,2'-(5,5'-[N-{2-Ethylhexyl}-4H-dithieno[3,2-b:2',3'-d]pyrrole-2,6-diyl]-bis[3,4'-diethyl-2,2'-bithien-5,5'-diyl])-bis(methane-1-yl-1-ylidene)dimalononitrile (130)

Bis(trimethylstannyl)-DTP **177** (86.4 mg, 140 μmol), DCV bromo-bithiophene **178** (167 mg, 340 μmol) and $\text{Pd}(\text{PPh}_3)_4$ (9.4 mg, 8.1 μmol) were added in a Schlenk-tube and evacuated for several minutes. After adding 6.7 mL DMF the reaction mixture was carefully degassed and heated to 80 $^\circ\text{C}$ for 28 h. Then the reaction mixture was poured into saturated aqueous ammonium chloride solution. The organic compounds were extracted with DCM. The combined organic phases were dried with sodium sulfate and the solvents were removed by rotary evaporation. The crude product was purified via digesting with ethyl acetate and subsequent column chromatography (silica/DCM) to obtain structurally defined co-oligomer **130** (114 mg, 104 μmol , 74%) as a black solid.

M.p.: 214 $^\circ\text{C}$.

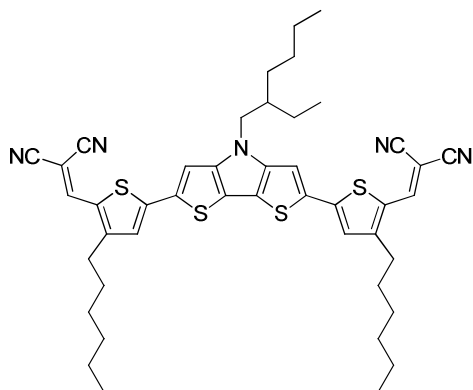
^1H NMR (400 MHz, CDCl_3): δ = 7.68 (s, 2H, C=CH), 7.51 (s, 2 H, 4-H), 7.23 (s, 2 H, 3'-H), 7.07 (s, 2 H, DTP-H), 4.14-4.04 (m, 2 H, N-CH₂), 2.87-2.72 (m, 8H, α -CH₂), 2.01-1.94 (m, 1 H, -CH-), 1.75-1.65 (m, 8 H, β -CH₂), 1.47-1.30 (m, 28 H, -CH₂-), 0.97-0.87 (m, 18 H, -CH₃).

^{13}C NMR (100 MHz, CDCl_3): δ = 149.83, 145.14, 144.05, 141.97, 140.50, 140.34, 135.86, 132.99, 131.91, 131.57, 115.65, 114.48, 113.57, 109.97, 75.50, 51.41, 40.50, 31.65, 31.56, 30.64, 30.61, 29.98, 29.52, 29.35, 29.30, 29.14, 28.63, 24.04, 22.99, 22.65, 22.58, 14.08, 14.05, 10.72.

MS (MALDI-TOF) m/z : calcd for $\text{C}_{64}\text{H}_{77}\text{N}_5\text{S}_6$: 1107; found $[\text{M}+\text{H}]^+$: 1108.

Elemental analysis: calcd (%) for $\text{C}_{64}\text{H}_{77}\text{N}_5\text{S}_6$: C 69.33, H 7.00, N 6.32, S 17.35; found (%): C 69.54, H 6.87, N 6.27, S 17.29.

2,2'-(5,5'-[N-{2-Ethylhexyl}-4H-dithieno[3,2-b:2',3'-d]pyrrole-2,6-diyl]-bis[3-hexylthien-5,2-diyl])-bis(methane-1-yl-1-ylidene)dimalononitrile (131)



Bis(trimethylstannyl)-DTP **177** (59.2 mg, 96.0 μmol), DCV iodo-thiophene **179** (89.8 mg, 243 μmol) and $\text{Pd}(\text{PPh}_3)_4$ (6.8 mg, 5.91 μmol) were added in a Schlenk-tube and evacuated for several minutes. After adding 5 mL DMF the reaction mixture was carefully degassed and heated to 60 $^\circ\text{C}$ for 3.5 h. Then the reaction mixture was poured into saturated aqueous ammonium chloride solution. The organic compounds were extracted with DCM. The combined organic phases were dried with sodium sulfate and the solvents were removed by rotary evaporation. The crude product was purified via digesting with ethyl acetate and subsequent column chromatography (silica/DCM) to obtain structurally defined co-oligomer **131** (60.0 mg, 77.3 μmol , 81%) as a black solid.

M.p.: 308.

^1H NMR (400 MHz, CDCl_3): δ = 7.80 (s, 2 H, C=CH), 7.28 (s, 2 H, 4-H), 7.13 (s, 2 H, DTP-H), 4.13-4.03 (m, 2 H, N-CH₂), 2.74 (t, 3J = 7.8 Hz, 4 H, α -CH₂), 2.04-1.95 (m, 1 H, -CH-), 1.69-1.61 (m, 4 H, β -CH₂), 1.44-1.27 (m, 20 H, -CH₂-), 0.94-0.89 (m, 12 H, -CH₃).

^{13}C NMR (100 MHz, CDCl_3): δ = 157.06, 148.74, 147.22, 146.91, 134.78, 128.74, 125.46, 117.51, 115.06, 114.03, 110.53, 73.99, 52.13, 40.35, 31.54, 31.21, 30.75, 29.32, 29.06, 28.59, 24.26, 23.02, 22.51, 13.92, 13.89, 10.74.

High-Resolution MS (MALDI-TOF) m/z : calcd for $\text{C}_{44}\text{H}_{49}\text{N}_5\text{S}_4$: 775.28708; found $[\text{M}]^+$: 775.28628, $\delta m/m$ = 1.0 ppm.

5.5 References

- [1] R. Fitzner, E. Reinold, A. Mishra, E. Mena-Osteritz, H. Ziehlke, C. Körner, K. Leo, M. Riede, M. Weil, O. Tsaryova, A. Weiß, C. Urich, M. Pfeiffer, P. Bäuerle, *Adv. Funct. Mater.* **2011**, *21*, 897-910.
- [2] R. Fitzner, E. Mena-Osteritz, A. Mishra, G. Schulz, E. Reinold, M. Weil, C. Körner, H. Ziehlke, C. Elschner, K. Leo, M. Riede, M. Pfeiffer, C. Urich, P. Bäuerle, *J. Am. Chem. Soc.* **2012**, *134*, 11064-11067.
- [3] K. Schulze, C. Urich, R. Schüppel, K. Leo, M. Pfeiffer, E. Brier, E. Reinold, P. Bäuerle, *Adv. Mater.* **2006**, *18*, 2872-2875.
- [4] R. Meerheim, C. Körner, K. Leo, *Appl. Phys. Lett.* **2014**, *105*, 063306.
- [5] A. Mishra, C.-Q. Ma, P. Bäuerle, *Chem. Rev.* **2009**, *109*, 1141-1276.
- [6] G. L. Schulz, M. Urdanpilleta, R. Fitzner, E. Brier, E. Mena-Osteritz, E. Reinold, P. Bäuerle, *Beilstein J. Nanotechnol.* **2013**, *4*, 680-689.
- [7] S. Haid, A. Mishra, C. Urich, M. Pfeiffer, P. Bäuerle, *Chem. Mater.* **2011**, *23*, 4435-4444.
- [8] S. C. Rasmussen, S. J. Evenson, *Prog. Polym. Sci.* **2013**, *38*, 1773-1804.
- [9] A. Berlin, G. Pagani, G. Zotti, G. Schiavon, *Makromol. Chem.* **1992**, *193*, 399-409.
- [10] K. Ogawa, S. C. Rasmussen, *J. Org. Chem.* **2003**, *68*, 2921-2928.
- [11] M. Fujitsuka, T. Sato, F. Sezaki, K. Tanaka, A. Watanabe, O. Ito, *J. Chem. Soc., Faraday Trans.* **1998**, *94*, 3331-3337.
- [12] L. Zhang, N. S. Colella, B. P. Cherniawski, S. C. B. Mannsfeld, A. L. Briseno, *ACS Appl. Mater. Interfaces* **2014**, *6*, 5327-5343.
- [13] P. Zanirato, P. Spagnolo, G. Zanardi, *J. Chem. Soc., Perkin Trans. 1* **1983**, 2551-2554.
- [14] S. Gronowitz, *Acta Chem. Scand.* **1961**, *15*, 1393-1395.
- [15] S. Gronowitz, J. E. Skramstad, B. Eriksson, *Arkiv Kemi* **1967**, *28*, 99-107.
- [16] K. Ogawa, K. R. Radke, S. D. Rothstein, S. C. Rasmussen, *J. Org. Chem.* **2001**, *66*, 9067-9070.
- [17] K. Nozaki, K. Takahashi, K. Nakano, T. Hiyama, H.-Z. Tang, M. Fujiki, S. Yamaguchi, K. Tamao, *Angew. Chem.* **2003**, *115*, 2097-2099; *Angew. Chem. Int. Ed.* **2003**, *42*, 2051-2053.
- [18] G. Koeckelberghs, L. De Cremer, W. Vanormelingen, W. Dehaen, T. Verbiest, A. Persoons, C. Samyn, *Tetrahedron* **2005**, *61*, 687-691.
- [19] S. J. Evenson, S. C. Rasmussen, *Org. Lett.* **2010**, *12*, 4054-4057.
- [20] S. M. H. Kabir, M. Miura, S. Sasaki, G. Harada, Y. Kuwatani, M. Yoshida, M. Iyoda, *Heterocycles* **2000**, *52*, 761-774.
- [21] E. Zhou, J. Cong, K. Hashimoto, K. Tajima, *Energy Environ. Sci.* **2012**, *5*, 9756-9759.
- [22] D. Hong, M. Lv, M. Lei, Y. Chen, P. Lu, Y. Wang, J. Zhu, H. Wang, M. Gao, S. E. Watkins, X. Chen, *ACS Appl. Mater. Interfaces* **2013**, *5*, 10995-11003.

- [23] H. Mo, K. R. Radke, K. Ogawa, C. L. Heth, B. T. Erpelding, S. C. Rasmussen, *Phys. Chem. Chem. Phys.* **2010**, *12*, 14585-14595.
- [24] S. J. Evenson, T. M. Pappenfus, M. C. R. Delgado, K. R. Radke-Wohlers, J. T. L. Navarrete, S. C. Rasmussen, *Phys. Chem. Chem. Phys.* **2012**, *14*, 6101-6111.
- [25] S. Barlow, S. A. Odom, K. Lancaster, Y. A. Getmanenko, R. Mason, V. Coropceanu, J.-L. Brédas, S. R. Marder, *J. Phys. Chem. B* **2010**, *114*, 14397-14407.
- [26] S. J. Evenson, M. J. Mumm, K. I. Pokhodnya, S. C. Rasmussen, *Macromolecules* **2011**, *44*, 835-841.
- [27] A. Yassin, P. Leriche, J. Roncali, *Macromol. Rapid Commun.* **2010**, *31*, 1467-1472.
- [28] S. A. Odom, K. Lancaster, L. Beverina, K. M. Lefler, N. J. Thompson, V. Coropceanu, J.-L. Brédas, S. R. Marder, S. Barlow, *Chem. Eur. J.* **2007**, *13*, 9637-9646.
- [29] K. Ogawa, S. C. Rasmussen, *Macromolecules* **2006**, *39*, 1771-1778.
- [30] D. Delabouglise, M. Hmyene, G. Horowitz, A. Yassar, F. Garnier, *Adv. Mater.* **1992**, *4*, 107-110.
- [31] L. E. Polander, S. P. Tiwari, L. Pandey, B. M. Seifried, Q. Zhang, S. Barlow, C. Risko, J.-L. Brédas, B. Kippelen, S. R. Marder, *Chem. Mater.* **2011**, *23*, 3408-3410.
- [32] J. Zhang, S. Singh, D. K. Hwang, S. Barlow, B. Kippelen, S. R. Marder, *J. Mater. Chem. C* **2013**, *1*, 5093-5100.
- [33] L. E. Polander, L. Pandey, S. Barlow, S. P. Tiwari, C. Risko, B. Kippelen, J.-L. Brédas, S. R. Marder, *J. Phys. Chem. C* **2011**, *115*, 23149-23163.
- [34] B. H. Wunsch, M. Rumi, N. R. Tummala, C. Risko, D.-Y. Kang, K. X. Steirer, J. Gantz, M. Said, N. R. Armstrong, J.-L. Bredas, D. Bucknall, S. R. Marder, *J. Mater. Chem. C* **2013**, *1*, 5250-5260.
- [35] Y. Zhou, J. W. Shim, C. Fuentes-Hernandez, A. Sharma, K. A. Knauer, A. J. Giordano, S. R. Marder, B. Kippelen, *Phys. Chem. Chem. Phys.* **2012**, *14*, 12014-12021.
- [36] F. S. Kim, G. Ren, S. A. Jenekhe, *Chem. Mater.* **2010**, *23*, 682-732.
- [37] H. Usta, A. Facchetti, T. J. Marks, *Acc. Chem. Res.* **2011**, *44*, 501-510.
- [38] C. Wang, H. Dong, W. Hu, Y. Liu, D. Zhu, *Chem. Rev.* **2011**, *112*, 2208-2267.
- [39] E. Zhou, J. Cong, Q. Wei, K. Tajima, C. Yang, K. Hashimoto, *Angew. Chem.* **2011**, *123*, 2851-2855; *Angew. Chem. Int. Ed.* **2011**, *50*, 2799-2803.
- [40] X. Zhan, A. Facchetti, S. Barlow, T. J. Marks, M. A. Ratner, M. R. Wasielewski, S. R. Marder, *Adv. Mater.* **2011**, *23*, 268-284.
- [41] F. Würthner, M. Stolte, *Chem. Commun.* **2011**, *47*, 5109-5115.
- [42] D. Sahu, H. Padhy, D. Patra, J.-F. Yin, Y.-C. Hsu, J.-T. S. Lin, K.-L. Lu, K.-H. Wei, H.-C. Lin, *Tetrahedron* **2011**, *67*, 303-311.
- [43] T. M. Pappenfus, B. J. Hermanson, T. J. Helland, G. G. W. Lee, S. M. Drew, K. R. Mann, K. A. McGee, S. C. Rasmussen, *Org. Lett.* **2008**, *10*, 1553-1556.
- [44] M. M. M. Raposo, G. Kirsch, *Tetrahedron* **2003**, *59*, 4891-4899.

- [45] J. Ohshita, K.-H. Lee, M. Hashimoto, Y. Kunugi, Y. Harima, K. Yamashita, A. Kunai, *Org. Lett.* **2002**, *4*, 1891-1894.
- [46] K. Ogura, R. Zhao, M. Jiang, M. Akazome, S. Matsumoto, K. Yamaguchi, *Tetrahedron Lett.* **2003**, *44*, 3595-3598.
- [47] A. Yassin, T. Rousseau, P. Leriche, A. Cravino, J. Roncali, *Sol. Energy Mater. Sol. Cells* **2011**, *95*, 462-468.
- [48] J. C. Hummelen, B. W. Knight, F. LePeq, F. Wudl, J. Yao, C. L. Wilkins, *J. Org. Chem.* **1995**, *60*, 532-538.
- [49] unpublished results.
- [50] J. Cremer, E. Mena-Osteritz, N. G. Pschierer, K. Müllen, P. Bäuerle, *Org. Biomol. Chem.* **2005**, *3*, 985-995.
- [51] M. C. Scharber, D. Mühlbacher, M. Koppe, P. Denk, C. Waldauf, A. J. Heeger, C. J. Brabec, *Adv. Mater.* **2006**, *18*, 789-794.
- [52] G. C. Welch, L. A. Perez, C. V. Hoven, Y. Zhang, X.-D. Dang, A. Sharenko, M. F. Toney, E. J. Kramer, T.-Q. Nguyen, G. C. Bazan, *J. Mater. Chem.* **2011**, *21*, 12700-12709.
- [53] C. J. Takacs, Y. Sun, G. C. Welch, L. A. Perez, X. Liu, W. Wen, G. C. Bazan, A. J. Heeger, *J. Am. Chem. Soc.* **2012**, *134*, 16597-16606.
- [54] A. Garcia, G. C. Welch, E. L. Ratcliff, D. S. Ginley, G. C. Bazan, D. C. Olson, *Adv. Mater.* **2012**, *24*, 5368-5373.
- [55] Y. Chen, X. Wan, G. Long, *Acc. Chem. Res.* **2013**, *46*, 2645-2655.
- [56] J. E. Coughlin, Z. B. Henson, G. C. Welch, G. C. Bazan, *Acc. Chem. Res.* **2014**, *47*, 257-270.
- [57] M. Weidelener, C. D. Wessendorf, J. Hanisch, E. Ahlswede, G. Götz, M. Linden, G. Schulz, E. Mena-Osteritz, A. Mishra, P. Bäuerle, *Chem. Commun.* **2013**, *49*, 10865-10867.
- [58] C. D. Wessendorf, G. L. Schulz, A. Mishra, P. Kar, I. Ata, M. Weidelener, M. Urdanpilleta, J. Hanisch, E. Mena-Osteritz, M. Lindén, E. Ahlswede, P. Bäuerle, *Adv. Energy Mater.* **2014**, *4*, 1400266.
- [59] V. Shrotriya, Y. Yao, G. Li, Y. Yang, *Appl. Phys. Lett.* **2006**, *89*, 063505.
- [60] X. Xiao, Z. Wang, Z. Hu, T. He, *J. Phys. Chem. B* **2010**, *114*, 7452-7460.
- [61] L. Malatesia, M. Angoletta, *J. Chem. Soc.* **1957**, 1186-1188.

Chapter 6

Acceptor-Substituted Bi(dithienopyrrole) Derivatives

6.1 Introduction

6.1.1 General introduction

In *Chapter 5*, novel dithienopyrrole(DTP)-based structurally defined co-oligomers were synthesized on the basis of dicyanovinylene(DCV)-substituted quaterthiophene **122** and sexithiophene **124** (Chart 1). Substitution of the central bithiophene-unit by DTP led to **131** and **129**, respectively, possessing improved light-harvesting properties compared to their thiophenic counterparts **122** and **124**.^[1] DTP-containing co-oligomer **129** showed an absorption maximum in solution at 601 nm with an extinction coefficient of $72,800 \text{ M}^{-1}\text{cm}^{-1}$. Shorter co-oligomer **131** featured a slightly red-shifted absorption maximum at 609 nm with an increased extinction coefficient of $92,200 \text{ M}^{-1}\text{cm}^{-1}$. The reason for that is a more intense conjugation between the electron-donating DTP-unit and the electron-accepting DCV-groups due to smaller torsion angles within the conjugated backbone.

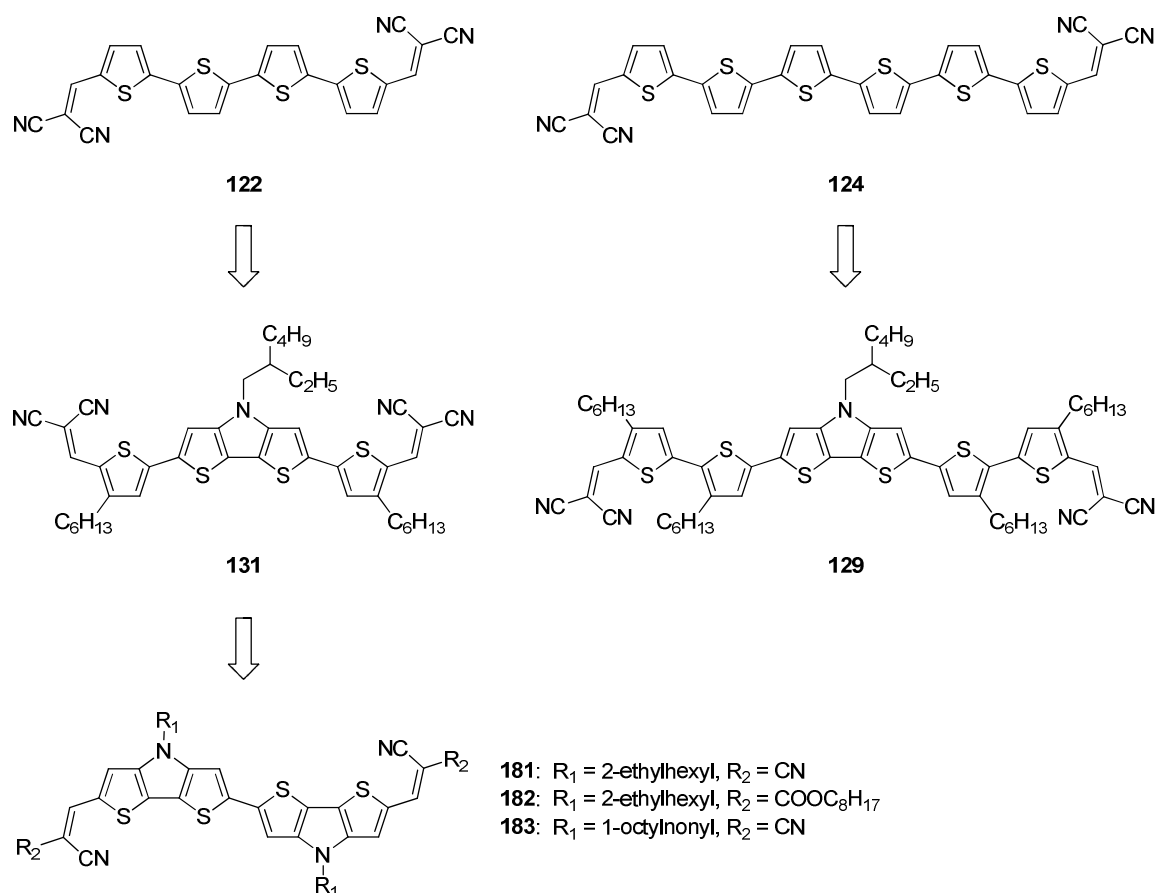


Chart 1. Structural development of structurally defined oligomers and co-oligomers starting from vacuum-processed DCV-oligothiophenes **122** and **124**^[1] via DTP-based analogues **131** and **129**, respectively (*Chapter 5*) to bi(DTP)s **181-183** presented in this chapter.

In comparison to their respective parental compounds **122** and **124** which absorb at 518 and 532 nm in solution, respectively **129** and **131** possess 70-90 nm red-shifted absorptions. Furthermore, **131** has a nearly 1.4 times higher extinction coefficient than **122** ($66,800 \text{ M}^{-1}\text{cm}^{-1}$; the extinction coefficient of **124** was not determined due to low solubility for which reason no comparison with **129** can be made). These improvements in light-harvesting properties are attributed to the DTP-unit being a stronger electron-donating unit than bithiophene. Solution-processed bulk-heterojunction solar cells (BHJSCs) were fabricated using **129** and **131** as donor materials reaching power conversion efficiencies (PCEs) of up to 4.8%. Fill factors (FFs) of optimized devices were as high as ~ 0.65 for both co-oligomers indicating high and balanced charge mobilities. Therefore, the DTP-unit represents a valuable building block for oligomeric donor materials in BHJSCs.

Modification of the conjugated backbone of dye **131** is now performed by substituting the remaining two thiophenes by another DTP-unit to obtain bi(dithienopyrrole)s (bi(DTP)s) **181-183** (Chart 1). The presence of an additional DTP-unit should further increase the donor strength and enhance light-harvesting as well as hole transport properties. Bi(DTP) **181** is constituted of two DTP-units being *N*-alkylated with 2-ethylhexyl chains and two terminal DCV groups as electron acceptors. In order to increase the solubility, bi(DTP) **182** and **183** are equipped with solubilizing groups. In **182** the DCV acceptor groups are substituted with *n*-octyl cyanoacrylates which probably leads to a blue-shifted absorption due to the lower electron-accepting capability of cyanoacrylate compared to DCV, but should provide a better solubility.^[2] For derivative **183**, the longer branched alkyl group 1-octylnonyl is chosen instead of 2-ethylhexyl. An advantage of 1-octylnonyl being used as alkyl chain is its non-chirality compared to 2-ethylhexyl which prevents the formation of stereoisomers during synthesis. Recently, it was shown that the stereochemistry of the solubilizing alkyl chain can have a significant effect on the morphology, hence absorption in the bulk, and processing conditions of thin films.^[3]

In this chapter, the synthesis of A-D-A bi(DTP)s **181-183** is presented. Their different alkyl substitution patterns are investigated concerning their optoelectronic properties and their potential use as donor material in solution-processed BHJSCs. In the following section literature-known synthesis and properties of bi(DTP)-based compounds are summarized.

6.1.2 Bi(dithienopyrroles)

Only a few examples of bi(DTP)-based compounds are described in literature so far. Heliathek GmbH and LMS Co. Ltd. published patents containing bi(DTP)s **184-186** for the use in organic solar cells (OSCs) and organic light emitting diodes (OLEDs) (Chart 2).^[4,5]

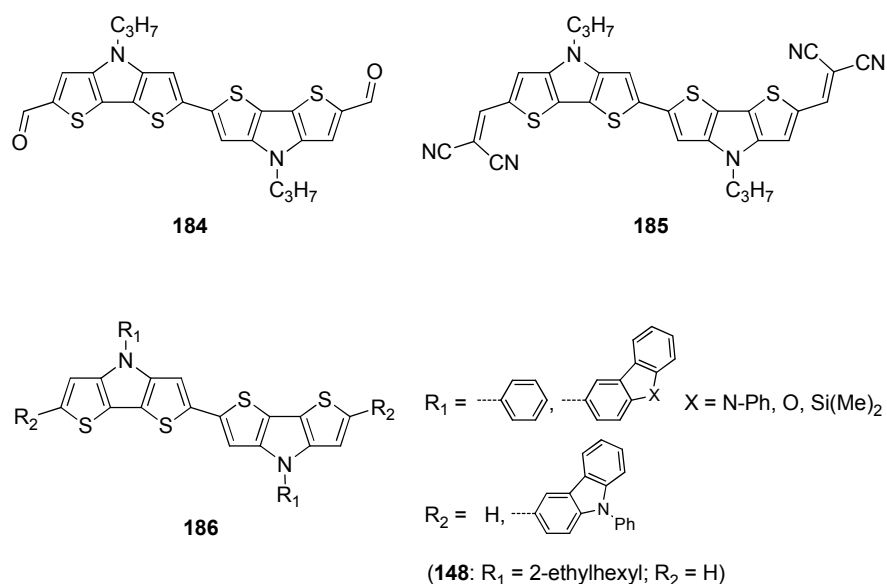
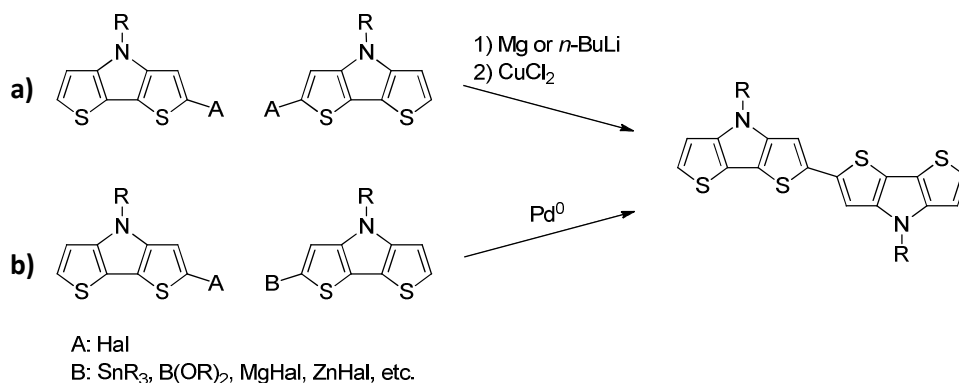


Chart 2. General structures of bi(DTP)-based compounds **184–186**.

An exact description of the preparation of **184** and **185** was not given. However, it is mentioned that bi(DTP)s can be built by oxidative homo- or transition metal catalyzed cross-coupling reactions as shown in Scheme 1.^[6] Unfortunately, the authors did not comment which route they chose or preferred for their synthesis.^[4]

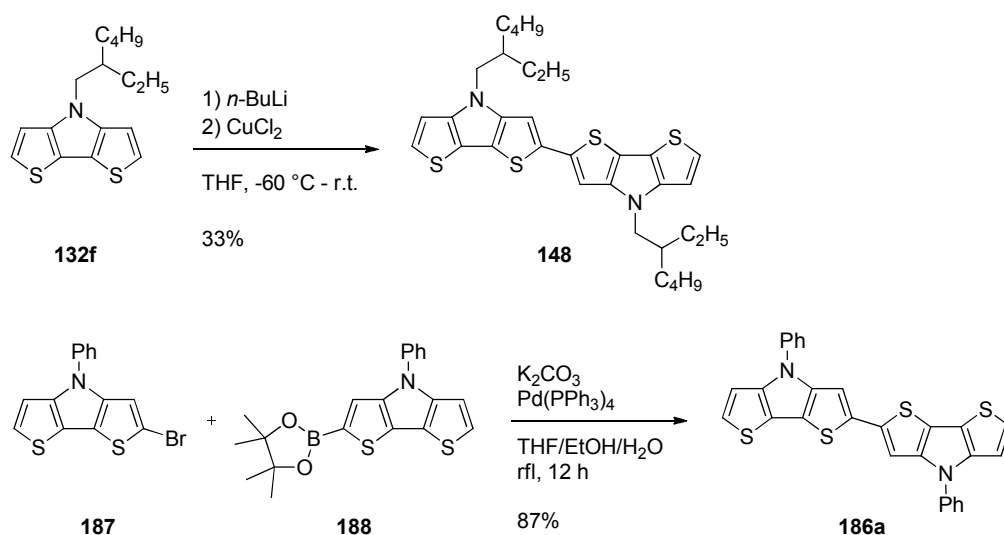


Scheme 1. Schematic synthesis of bi(DTP)s using **(a)** homo- or **(b)** cross-coupling reaction.

The subsequent introduction of the acceptor groups was realized by formylation to obtain dialdehyde **184** and Knoevenagel condensation to gain the target product **185**. DCV-endcapped bi(DTP) **185** possessed a low solubility, therefore no $^1\text{H-NMR}$ spectra could be recorded. Vacuum-deposited thin films of **185** featured an absorption maximum at 616 nm.^[4] This means a blue-shift of

about 80 nm compared to the absorption maximum of the thin film of DTP-based co-oligomer **131** (spin-coated from chloroform).

Yassin *et al.* reported about the synthesis and optoelectronic properties of bi(DTP) **148**, as presented in *Chapter 5*. The synthesis of dimer **148** was accomplished via a homo-coupling reaction of DTP **132f** using *n*-butyllithium (*n*-BuLi) and CuCl₂ in a yield of 33% (Scheme 2) being the first procedure described in detail in literature.^[7] Absorption spectroscopy of bi(DTP) **148** showed an absorption maximum at 410 nm with an extinction coefficient of 42,480 M⁻¹cm⁻¹. Cyclic voltammetry revealed that **148** can be oxidized reversibly twice ($E^{\circ}_{\text{ox1}} = 0.1$ V; $E^{\circ}_{\text{ox2}} = 0.5$ V vs. Fc/Fc⁺). Stable charged states are a prerequisite for the materials used within OSCs.

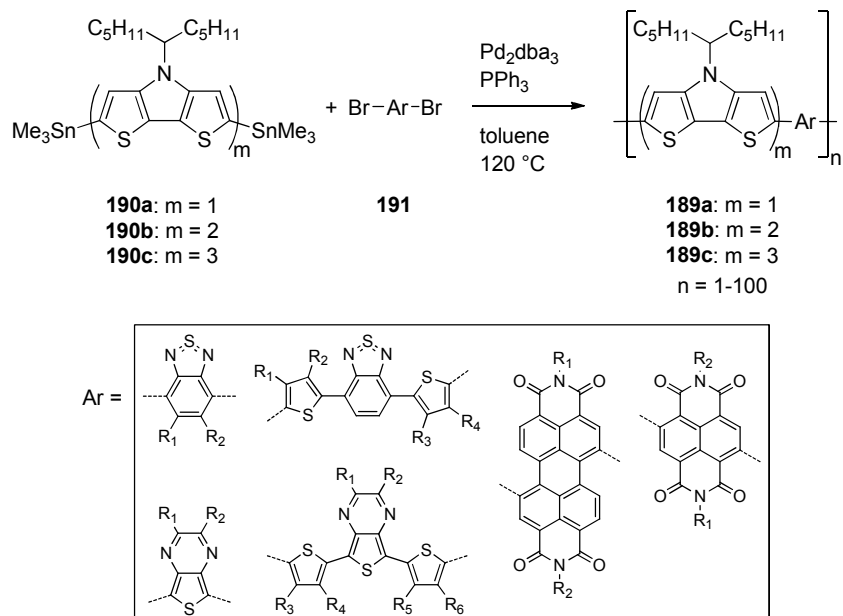


Scheme 2. Synthesis of bi(DTP) **148** and **186** according to Ref. [5,7].

Recently, in a patent of LMS Co. Ltd., the synthesis of aryl-substituted bi(DTP)s **186** (see Chart 2) via Suzuki cross-coupling reaction was reported (Scheme 3).^[5] BromoDTP **187** was reacted with boronic acid ester **188** in the presence of K₂CO₃ and Pd(PPh₃)₄ to obtain phenyl-substituted bi(DTP) **186a** in 87% yield. Aryl-substituted bi(DTP)s **186** were applied as hole transporting material in organic light emitting diodes and could improve hole injection and transport performance.^[5]

Copolymers **189a-c**, published in a patent by the Changchun Institute of Applied Chemistry (Chinese Academy of Sciences), were synthesized by Stille cross-coupling reaction of distannylated mono-, bi-, and terDTP **190a-c** ($m = 1, 2, 3$) with various electron-deficient dibrominated arenes **191** (Scheme 3).^[8] The synthesis of distannylated species **190a-c** is only described in detail for monoDTP **190a**. Distannylated bi(DTP) **190b** and ter(DTP) **190c** are not further discussed by the authors. DTP-based

polymers **189a-c** absorb in the range of 300-1000 nm. BHJSCs were fabricated using copolymers **189a-c** as donor in combination with PC₆₁BM as acceptor resulting in moderate PCEs between 1 and 3%.^[8]

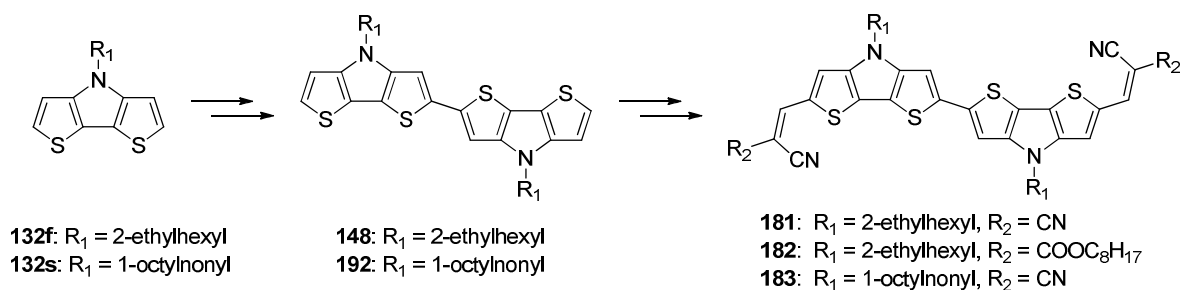


Scheme 3. Synthesis of copolymers **189a-c** via Stille cross-coupling reaction of distannylated oligo(DTP)s **190a-c** with dibrominated arenes **191**.

6.2 Results and discussion

6.2.1 Synthesis of bi(DTP)s **181-183**

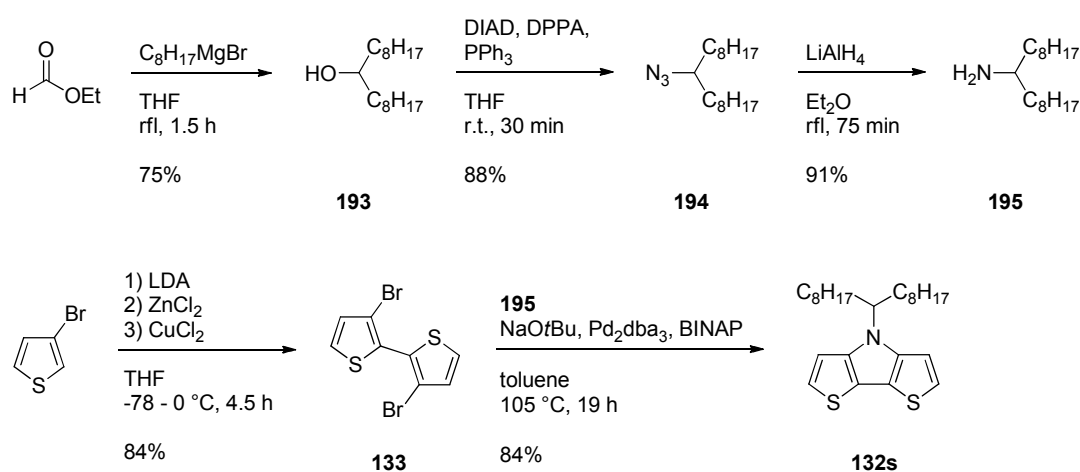
For the synthesis of bi(DTP)-based A-D-A donors **181-183**, donor moieties bi(DTP) **148** and **192** are synthesized starting from the corresponding DTP monomers **132f** and **132s** prior to the introduction of the acceptor groups (Scheme 4).



Scheme 4. Synthesis of **181-183** via *N*-alkylated bi(DTP)s **148** and **192**.

Synthesis of bi(DTP)s **148** and **192**

In order to form bi(DTP)s **148** and **192**, the corresponding DTPs, *N*-2-ethylhexyl-DTP **132f** and *N*-1-octylnonyl-DTP **132s** had to be synthesized first. Since DTP **132f** was obtained in good yields following the described procedures of the group of Rasmussen^[9] and Verbiest,^[10] the same synthetic route was chosen for the preparation of DTP **132s**. In contrast to **132f**, for which the required 2-ethylhexylamine is commercially available, for the synthesis of **132s** branched alkylamine **195** had to be prepared in advance (Scheme 5). This was realized according to a reaction sequence used by Ashraf *et al.* which was used in order to synthesize the longer homologue pentacosan-13-amine.^[11]

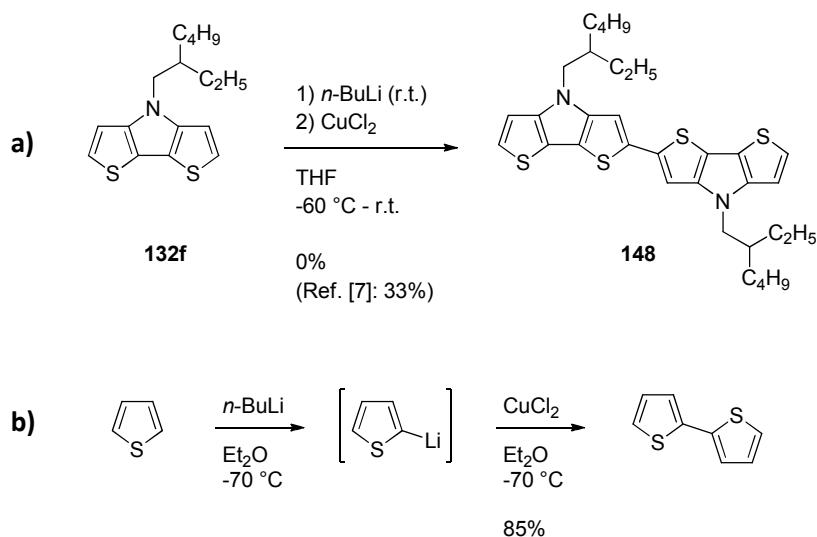


Scheme 5. Synthesis of alkyl amine **195** and *N*-1-octylnonyl DTP **132s**.

In the first step, ethyl formate was added to 2.1 eq. octylmagnesium bromide which was formed by the reaction of magnesium turnings with *n*-octyl bromide. Upon acidic work-up secondary alcohol **193** was obtained after recrystallization from acetonitrile in 75% yield which is a slight increase compared to the yield of Ashraf *et al.* for their longer homologue (65%).^[11] In the following step, the hydroxyl group of **193** was converted into an azido group via a Mitsunobu reaction to obtain azide **194**. Triphenylphosphine (PPh₃) and diisopropylazodicarboxylate (DIAD) convert the hydroxyl group into a better leaving group, whereas diphenylphosphoryl azide (DPPA) is used as azide source.^[12,13] The yield of 88% after column chromatography was similar to the one obtained by Ashraf *et al.* for their branched system.^[11] Azide **194** was subsequently reduced with lithium aluminium hydride to the desired amine **195** in a yield of 91% (pentacosan-13-amine: 81%^[11]). Tandem Buchwald-Hartwig reaction was then carried out with amine **195** and dibromobithiophene **133** (*Chapter 5*) using sodium *tert*-butoxide (NaOtBu) as base and tris(dibenzylideneacetone)dipalladium (Pd₂dba₃) and 2,2'-bis(diphenylphosphino)-1,1'-binaphthyl (BINAP) as catalyst system.^[14,15] Column chromatography afforded

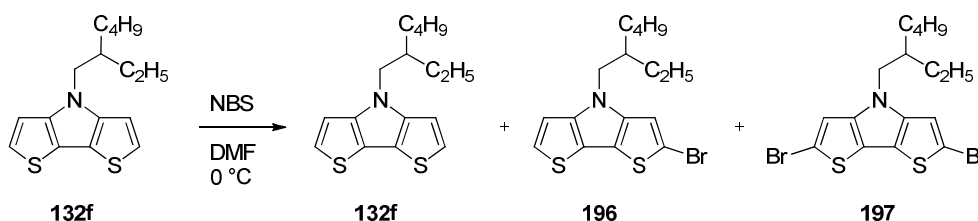
DTP **132s** in 84% yield, which represents an improvement compared to the previously reported one by Koeckelberghs *et al.* (71% yield).^[15]

By the start of this project, the synthesis of bi(DTP)s (Scheme 1) was described in detail by the group of Roncali (**148**, Scheme 6a). However, adopting the procedure of Yassin *et al.*^[7] did not lead to bi(DTP) **148** in my case. Instead a black highly viscous oil was formed which probably consisted of polymeric DTP and various longer DTP oligomers. An explanation is that DTP **132f** was only deprotonated to a small extend which is due to the substoichiometric use of *n*-BuLi. Yassin *et al.* used only 0.33 eq. *n*-BuLi for deprotonation and 0.53 eq. copper(II) chloride (CuCl₂) for the oxidative coupling.^[7] Taking the widely assumed mechanism into account (two lithiated species dimerize under the assistance of equimolar amounts of CuCl₂) a maximum yield of 33% with respect to DTP **132f** is given. For the synthesis of 2,2'-bithiophene, Gronowitz and Karlsson reacted 2-thienyllithium with more than one eq. of CuCl₂ (Scheme 6b) and yielded 2,2'-bithiophene in 85% yield.^[16] In analogy to the conditions used by Gronowitz and Karlsson, dimerization of DTP **132f** was carried out using one eq. of *n*-BuLi and a slight excess of CuCl₂. However, again a black tar-like material was obtained probably consisting of polymerized DTP. A possible explanation is that slight excesses of the oxidizing agent CuCl₂ induce oligomerization or polymerization of product **148** or remaining reactant **132f**. This might also be the reason for the substoichiometric use of CuCl₂ by Yassin *et al.*^[7] Due to the sensitivity of the DTP moiety towards oxidation, further experiments concerning the formation of **148** and **192** via oxidative homo-coupling were spared.



Scheme 6. Synthesis of (a) bi(DTP) **148** as reported by Yassin *et al.*^[7] and (b) 2,2'-bithiophene as reported by Gronowitz and Karlsson.^[16]

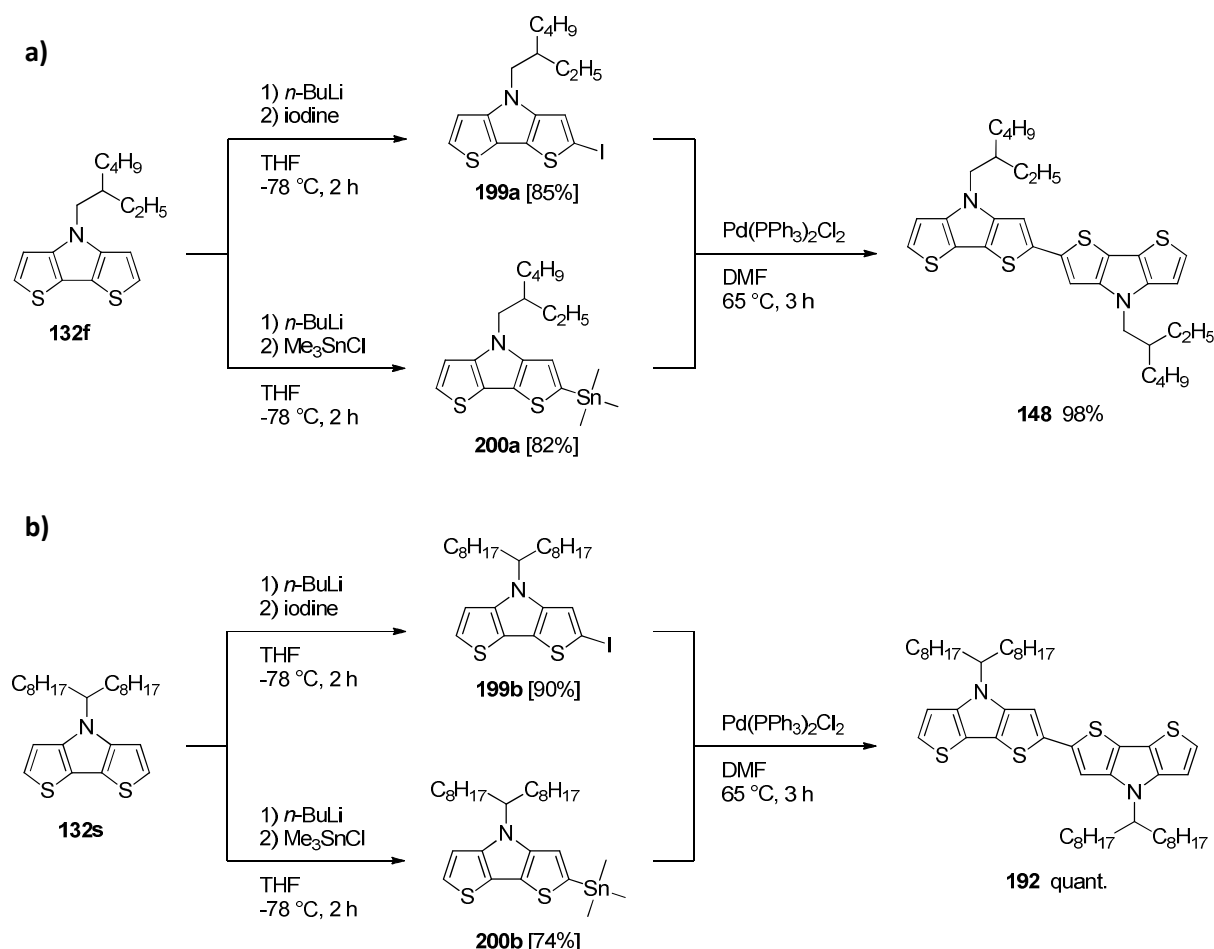
Because of the unsuccessful preparation of **148** via homo-coupling it was decided to change the focus to the cross-coupling approach (Scheme 1b). In this respect, Stille cross-coupling reaction was chosen as various DTP-containing oligomers were successfully built up with this reaction type (see Chapter 5). Firstly, a monohalogenated species was synthesized. Electrophilic aromatic substitution is widely applied to from halogenated arenes. Upon addition of *N*-bromosuccinimide (NBS) to **132f** in *N,N*-dimethylformamide (DMF) at 0 °C a mixture of reactant and mono- and di-brominated species in a ratio of 1:3:1 was formed (Scheme 7).



Scheme 7. Bromination of **132f** with NBS

Purification of the obtained oil on silica gel was not possible due to decomposition of the product. By performing the reaction at -40 °C or -78 °C, respectively, no significant changes in the ratio of the obtained mixture could be observed. The reason for that is the high reactivity of the electron-rich DTP species concerning electrophilic aromatic substitution. The reaction outcome could not be controlled thermodynamically by the reduction of the temperature to -78 °C. Hence, a kinetically driven, statistical product mixture with a ratio of 1:3:1 (**132f**:**196**:**197**) was formed. Since monohalogenation of DTP via electrophilic aromatic substitution is highly unselective, mono-iodo DTPs **198a** and **198b** were synthesized in a different way (Scheme 7). By using *n*-BuLi and elemental iodine difunctionalization of the DTP moiety could be avoided. DTP **132f**/**132s** were lithiated with 1 eq. *n*-BuLi within 2 h at -78 °C. Subsequently, iodine was added as solid to generate iodo-DTPs **199a**/**199b**. The crude products were not further purified and the conversions were calculated by ¹H NMR spectroscopy to 85% and 90%, respectively. There are several advantages in using iodine instead of bromine. Firstly, iodine is easier to handle since it is a solid at ambient conditions and easier to keep free of moisture than bromine. Secondly, diiodo-DTPs have proven to be more stable than dibromoDTPs.^[17] Hence, it is assumed that the monohalogenated species show the same trend concerning their stability. Additionally, iodoarenes are more reactive towards Stille cross-coupling reactions. Monostannyl DTPs **200a** and **200b** were formed by lithiation and subsequent addition of trimethyltin chloride. Again, the crude products were not purified and conversions of around 80%

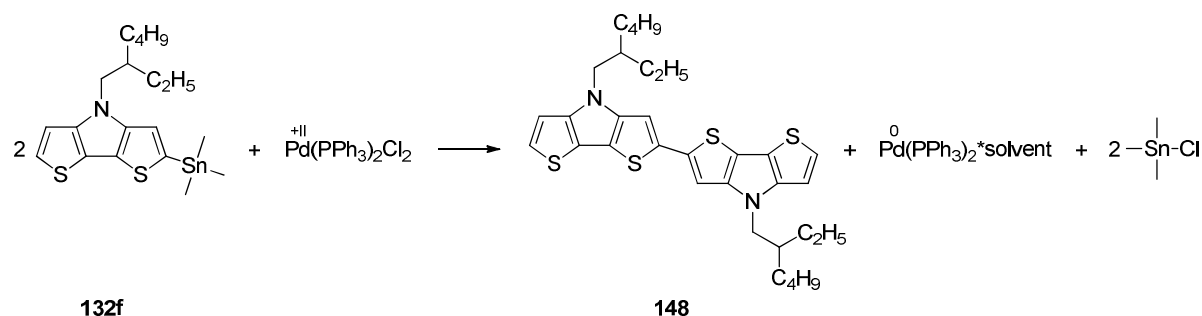
(determined by $^1\text{H-NMR}$ spectroscopy) were obtained. In both cases, the only remaining impurity was reactant **132f** or **132s**, respectively which can be easily separated after the next reaction step.



Scheme 8. Synthesis of bi(DTP) (**a**) **148** and (**b**) **192** via Stille cross-coupling reaction.

Stille cross-coupling reactions of 2-ethylhexyl-substituted iodo-DTP **199a** with stannyl-DTP **200a** and 1-octynonyl-substituted iodo-DTP **199b** with stannyl-DTP **200b** were performed at 65 °C within 3 h using 3 mol% $\text{Pd}(\text{PPh}_3)_2\text{Cl}_2$ as catalyst and DMF as solvent (Scheme 8). After aqueous work-up, the crude products were purified via column chromatography. By using silica gel as stationary phase,^[7] partial decomposition is observed during column chromatography and product fractions of bi(DTP)s **148** and **192** still contained impurities, probably by-products from decomposition. With the replacement of silica gel by alumina no decomposition was observed and bi(DTP)s **148** and **192** could be isolated pure in 98% and quantitative yield, respectively. Stannyl-DTPs **6.16a** and **6.16b** were used in slight excess. Therefore, the yields were calculated based on the amount of iodo-DTP (conversion

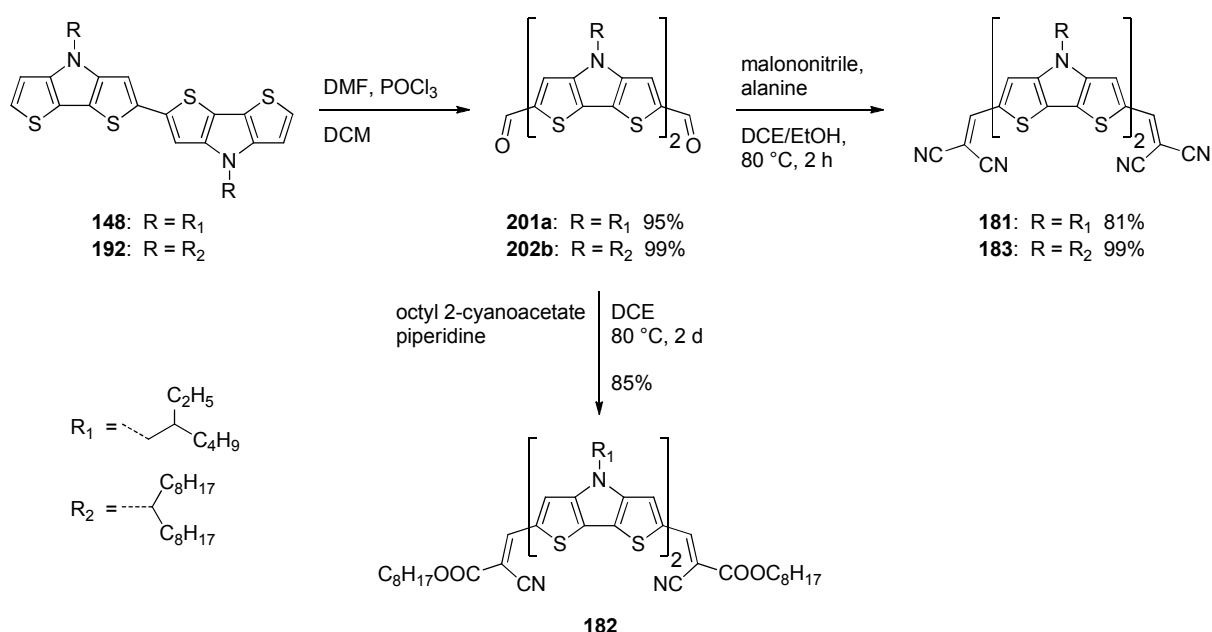
calculated by integration of the $^1\text{H-NMR}$ spectrum) plus the amount of bi(DTP) being formed by in situ preparation of the active catalyst species (Scheme 9).



Scheme 9. In situ preparation of the active catalyst species during Stille cross-coupling (Scheme 8) coming along with the formation of an equimolar amount of bi(DTP).

Synthesis of acceptor-substituted bi(DTP)s **181-183**

The attachment of the acceptor groups to bi(DTP) donor cores **148** and **192** was accomplished via Vilsmeier-Haack formylation and subsequent Knoevenagel condensation (Scheme 10). Introduction of the aldehyde groups took place in dichloromethane (DCM) by addition of a high excess of Vilsmeier-Haack reagent to the corresponding bi(DTP). After full conversion, hydrolysis was carried out using saturated aqueous NaHCO_3 solution and solid K_2CO_3 .



Scheme 10. Introduction of the acceptor groups via Vilsmeier-Haack formylation and subsequent Knoevenagel condensation to obtain acceptor-substituted bi(DTP)s **181-183**.

In the case of 2-ethylhexyl-substituted bi(DTP) **148**, the resulting crude product was hardly soluble. However, washing with *n*-hexane and DCM led to pure dialdehyde **201a** in 95% yield. For the conversion of 1-octylnonyl-substituted bi(DTP) **192** to dialdehyde **201b** the yield could be even increased to 99%. The reason lies in the much higher solubility of **201b** for which reason column chromatography was used to isolate **201b**. For **201a** small losses in yield can be explained by washing the crude product with DCM in order to remove traces of mono-aldehyde.

Dialdehydes **201a** and **201b** were then further functionalized via Knoevenagel condensation. In order to obtain **181** and **183**, the corresponding dialdehyde was reacted with 3 eq. of malononitrile and 6 mol% β -alanine as catalyst. The increased solubility of DCV-substituted derivative **181** in comparison to formyl-substituted bi(DTP) **201a** now allowed column chromatography for purification. However, a small loss of product could not be avoided due to solubility issues. Thus, DCV-substituted bi(DTP) **181** was obtained in a yield of 81%. In the case of better soluble 1-octylnonyl-substituted derivative **183** a yield of 99% after column chromatography could be achieved. The higher yield of **183** in comparison to **181** is on hand due to less losses during column chromatography and on the other due to a higher conversion because of the better solubility of reactant **201b** compared to **201a**. For the synthesis of *n*-octyl cyanoacrylate-substituted bi(DTP) **182**, 2-ethylhexyl-substituted dialdehyde **201a** was converted with 6 eq. of *n*-octyl cyanoacetate in the presence of piperidine as base. In order to obtain full conversion of dialdehyde **201a** it is crucial to add piperidine several times. The reason for this might be consumption of piperidine by excessive *n*-octyl 2-cyanoacetate operating as proton donor. Removal of the solvent, remaining volatile reactant, and piperidine by vacuum led to the crude product. By TLC, traces of various by-products were detected with similar r_f values than the suspected product. Hence, several column chromatographies were necessary to afford pure diester **182** in 85% yield. The by-products might be formed upon partial decomposition of the acceptor group in presence of piperidine. This was supported by the formation of more by-products with longer reaction times, observed by thin layer chromatography. However, the amounts of these by-products were quite low, thus characterization was not possible.

The purity of structurally defined donor molecules **182** and **183** was checked via high performance liquid chromatography (HPLC), nuclear resonance spectroscopy (NMR), mass spectrometry (MS), and elemental analysis (EA), whereupon no impurities were found. Due to the low solubility of **181** HPLC was not feasible. **182** and **183** were HPLC pure, as depicted in Figure 1 for donor **182**.

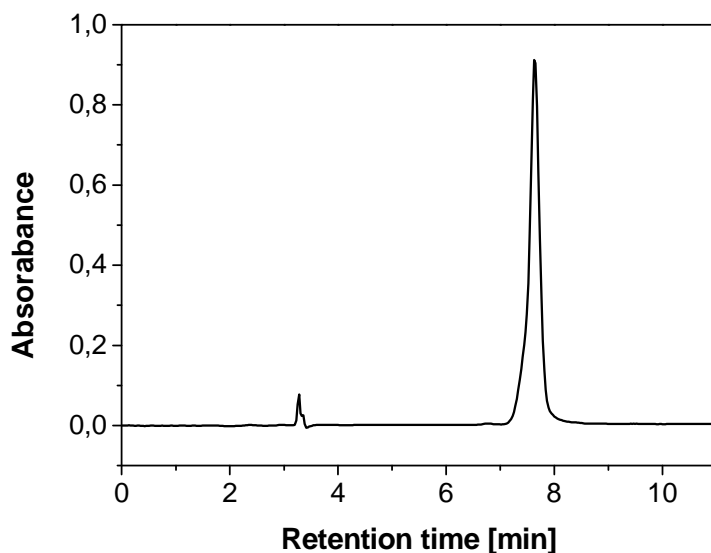


Figure 1. Pure HPLC chromatogram of **182**, the small peak at a retention time of 3,28 min corresponds to the injection peak.

6.2.2 Optical properties of bi(DTP)s **181-183**

Absorption spectroscopy of acceptor-substituted bi(DTP)s **181-183** was measured in chloroform and in thin films (Figure 2). The corresponding data are summarized in Table 1.

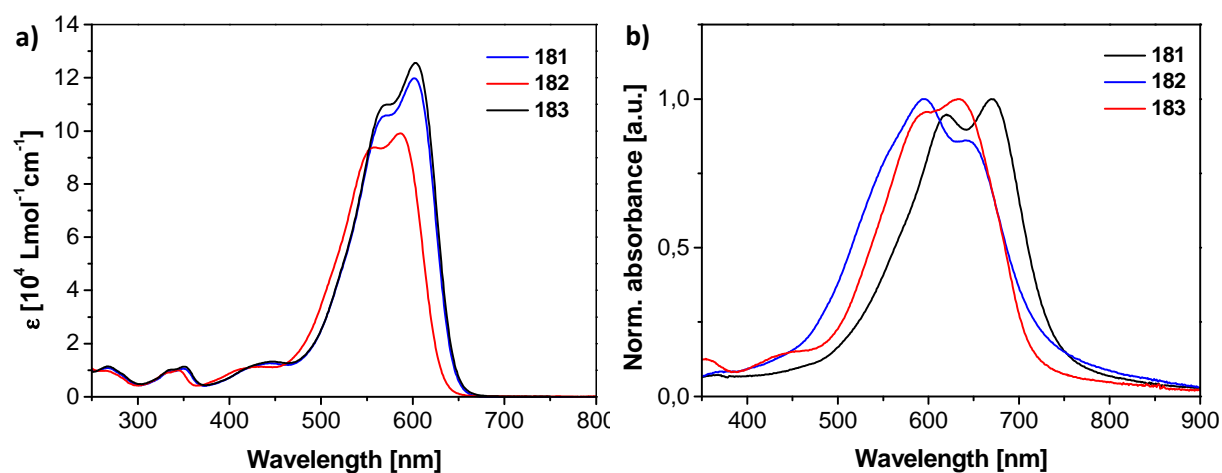


Figure 2. (a) Absorption spectroscopy of **181-183** in chloroform solution. (b) Absorption spectroscopy of **181-183** in thin films spin-coated from TCE (**181**) or chloroform (**182** and **183**) on a glass substrates.

In solution, DCV-substituted bi(DTP)s **181** and **183** showed nearly identical absorption spectra. As can be seen in Figure 2a, the absorption curves of **181** and **183** are very similar. Both donors featured an absorption band at 602 nm with extinction coefficients of 120,000-126,000 $\text{M}^{-1}\text{cm}^{-1}$ and absorption

onsets at 643 nm. Hence, they possessed optical band gaps (ΔE_{opt}) of 1.93 eV. The only difference is the slightly higher extinction of **183** compared to **181**. The reason therefore is that in **183** the DTP-nitrogen atoms are connected to a secondary carbon atom (1-octylnonyl chains) having a stronger inductive effect in comparison to the primary carbon atoms (2-ethylhexyl chains) being attached to the DTP nitrogen atoms of **181**. Thus the electron density of the donor moiety is slightly increased in **183** compared to **181** leading to a more intense CT-band. These results reveal that the nature of the alkyl side chain attached to the DTP-nitrogen can slightly affect the optical properties in solution. Octyl 2-cyanoacrylate end-capped bi(DTP) **182** showed a similar absorption curve in solution as **181** and **183**. However, the absorption maximum is blue-shifted by 15 nm to 587 nm compared to DCV-substituted derivatives **181** and **183** which is due to the weaker electron-accepting capability of the 2-cyanoacrylate groups in comparison to DCV. Hence, the absorption onset is shifted hypsochromically to 630 nm resulting in a larger ΔE_{opt} of 1.97 eV. The incorporation of the weaker 2-cyanoacrylate acceptor in **182** also decreases the extinction of the CT-band to $99,100 \text{ M}^{-1}\text{cm}^{-1}$ in comparison to $\sim 120,000 \text{ M}^{-1}\text{cm}^{-1}$ for **181** and **183**. The full width at half maximum (FWHM) values of bi(DTP)s **181** and **183** lie around $2,800 \text{ cm}^{-1}$ and is slightly larger for **182** with $\sim 3,100 \text{ cm}^{-1}$ emphasizing the better light harvesting properties of DCV-capped bi(DTP)s **181** and **183** compared to 2-cyanoacrylate-substituted derivative **182**.

Table 1. Optical data of bi(DTP)s **181-183** in chloroform ($c = 10^{-5} \text{ M}$) and in thin films on glass in comparison to DTP-based co-oligomer **131**.

dye	λ_{max} [nm] ($\epsilon [\text{M}^{-1}\text{cm}^{-1}]$)	FWHM [cm^{-1}]	λ_{onset} [nm]	ΔE_{opt} [eV] ^[a]	$\lambda_{\text{max, film}}$ [nm]	FWHM _{film} [cm^{-1}]	$\lambda_{\text{film, onset}}$ [nm]	$\Delta E_{\text{opt, film}}$ [eV] ^[a]
181	602 (119800)	2812	643	1.93	(622) ^[b] , 670	3677	737	1.68
182	587 (99100)	3104	630	1.97	598 (644) ^[b]	4840	732	1.69
183	603 (125600)	2803	643	1.93	(600) ^[b] 633	4048	718	1.73
131	609 (92200)	2830	662	1.87	(627) ^[b] 691	3270	759	1.63

[a] Calculated by the low energy onset of λ_{max} . [b] Shoulder.

Comparing the absorption data of **131** featuring an electron density gradient within the donor part of the molecule (A-D₁-D₂-D₁-A; D₂ denotes a stronger donor moiety than D₁) to the data of A-D₂-D₂-A-based bi(DTP)s **181** and **183**, advantages of the corresponding designs can be extracted. For **131** slight red-shifts of 7 and 19 nm are observed for λ_{max} and λ_{onset} , respectively in comparison to **181** and **183**. Whereas bi(DTP)s **181** and **183** showed increased extinction coefficient of 120,000-

126,000 M⁻¹cm⁻¹, which emphasize the extinction increasing effect of the DTP-unit. Regarding the low FWHM values of ~2,800 cm⁻¹, the torsion within the molecules seems to be low for all three structurally defined bi(DTP)s, whereas a more structured absorption is observed for **181-183** compared to **131**. An explanation for that is the smaller number of rotatable bonds within the donor backbone for **181-183** compared to **131**.

Thin films of **182** and **183** were made by spin-coating from chloroform. Due to the low solubility of 2-ethylhexyl-substituted DCV-capped bi(DTP) **181** in chloroform, tetrachloroethane (TCE) was used to prepare thin films of **181**. The corresponding absorption spectra are depicted in Figure 2b. The absorption curves of **181**, **182**, and **183** were quite different and showed absorption maxima at 670, 598, and 630 nm, respectively, and $\lambda_{\text{film,onset}}$ values of 737, 732, and 718 nm, respectively. The differently structured absorption curves and red-shifts of the maxima of 68, 11, and 30 nm for **181**, **182**, and **183**, respectively, compared to the corresponding absorption in solution are probably based on different alignments of the molecules in the bulk. Linear conjugated systems with terminal alkyl chains can have quite a different morphology in the bulk than their counterparts without terminal side chains (see Chapter 5).^[18,19] This could be an explanation why the absorption band of **182** possessed a low energy shoulder, whereas the absorption band of **181** and **183** featured a high energy shoulder. The differences of **181** and **183** can be explained on one hand by the different solution-processing solvent and on the other by differently formed morphology due to longer alkyl chains in the case of **183**. The longer alkyl chains might hamper effective π - π stacking leading to the blue-shifted and less structured absorption band of 1-octylnonyl-substituted bi(DTP) **183** in comparison to 2-ethylhexyl-substituted derivative **181**. Parental DTP-based co-oligomer **131** had the most red-shifted absorption (691 nm) and $\lambda_{\text{film,onset}}$ (759 nm) among the four formal quaterthiophenes **131** and **181-183**. In summary, it is hard to compare thin film absorptions of **131** and **181-183** due to their assumed different ordering in the bulk. However, based on the FWHM values and the fine structure of the absorption spectra, **131** most probably accomplishes to form larger π - π stacks compared to **181-183** which might be due to less alkyl side-chains.

6.2.3 Electrochemical properties of bi(DTP)s 181-183

Cyclic voltammetry of acceptor-capped bi(DTP)s **181-183** was measured in dichloromethane (DCM) using tetra-*n*-butylammonium hexafluorophosphate ((*n*-Bu)₄NPF₆) as supporting electrolyte (Figure 3). Redox potentials, the electrochemically determined band gaps (ΔE_{CV}) as well as the highest occupied molecular orbital (HOMO) and lowest unoccupied molecular orbital (LUMO) level energies are listed in Table 2.

DCV-endcapped donors **181** and **183** differ solely in their solubilizing alkyl chains and therefore feature almost identical cyclic voltammograms. For both DCV-substituted bi(DTP)s two reversible oxidation waves at $E^{\circ}_{\text{ox1}} = 0.5$ V and $E^{\circ}_{\text{ox2}} = 0.9$ V and one irreversible reduction wave at -1.6 V were observed. Similar as for the absorption in solution, cyclic voltammetry is practically independent of the nature of the alkyl side chains. Hence, the same HOMO and LUMO energy levels of -5.53 eV and -3.68 eV, respectively were found for **181** and **183** resulting in $\Delta E_{\text{CV}} = \sim 1.85$ eV. Interestingly, **131** possessed a lower E°_{ox1} of 0.45 V and a higher E°_{ox2} of 1.03 V in comparison to **181** and **183**. The former one is attributed to the spatial separation of the single DTP-unit from the DCV acceptor groups in **131** resulting in a negatively shifted first oxidation. This also led to slightly lowered HOMO energy levels for **181** and **183** of -5.53 eV in comparison to the one of **131** (-5.49 eV). Smaller E°_{ox2} values of **181** and **183** compared to the one of **131** are explained by the electron-rich donor moieties present in **181** and **183** due to the presence of two DTP-units vs. only one DTP in the donor backbone of **131**.

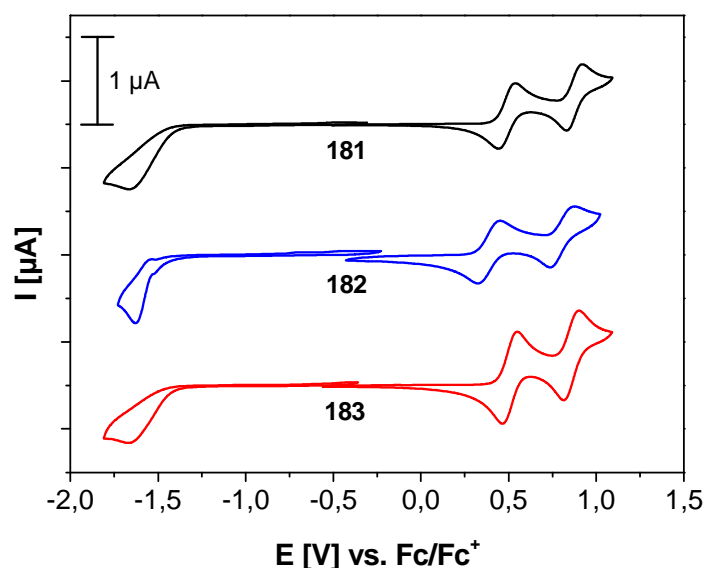


Figure 3. Cyclic voltammograms of **181-183** measured in DCM using $(n\text{-Bu})_4\text{NPF}_6$ (0.1 M) as supporting electrolyte at 100 mV s^{-1} ; $c = 5 \times 10^{-4} \text{ mol/L}$.

The reduction potentials of **181** and **183** are nearly identical ($E^{\circ}_{\text{red1}} = -1.57$ V and $E^{\circ}_{\text{red1}} = -1.58$ V, respectively). Thus, for both bi(DTP)s a LUMO energy level of -3.68 eV is calculated. Structurally defined molecule **182** bearing a different acceptor group showed slightly different electrochemical properties. 2-Cyanoacrylate-substituted bi(DTP) **182** featured two reversible oxidation waves and one irreversible reduction wave comparable to DCV-substituted derivatives **181** and **183**. However,

the oxidation potentials of **182**, $E^{\circ}_{\text{ox1}} = 0.4 \text{ V}$ and $E^{\circ}_{\text{ox2}} = 0.8 \text{ V}$, are $\sim 0.1 \text{ V}$ shifted to lower potentials with respect to E°_{ox1} and E°_{ox2} of **181** and **183**. The reason for that is the less electron-withdrawing capability of the 2-cyanoacrylate acceptor groups in **182**. This also explains the slightly lower reduction potential at -1.61 V of **182** compared to the one of **181** and **183** ($E^{\circ}_{\text{red1}} = -1.57/-1.59 \text{ V}$). HOMO and LUMO energy levels of **182** were extracted from its cyclic voltammogram as well and were with values of -5.42 and -3.58 eV , respectively, about 0.1 eV higher in energy compared to the corresponding energy levels of DCV-endcapped **181** and **183**. Similar as for DTP-based donor **131**, bi(DTP)-based donors **181-183** possess suitable energy levels for the use as donor materials in PC₆₁BM-based BHJSCs. Due to the slightly higher HOMO level energy for **182** in comparison to **181** and **183** a $\sim 0.1 \text{ V}$ smaller open-circuit voltage (V_{OC}) is expected for devices containing **182** as donor material.

Table 2. Electrochemical data of bio(DTP)s **181-183** in DCM with $(n\text{-Bu})_4\text{NPF}_6$ (0.1 M) as supporting electrolyte measured vs. Fc/Fc^+ at 100 mV s^{-1} in comparison to DTP-based co-oligomer **131**.

dye	$E^{\circ}_{\text{ox1}} [\text{V}]$	$E^{\circ}_{\text{ox2}} [\text{V}]$	$E^{\circ}_{\text{red1}} [\text{V}]$	$E_{\text{HOMO}} [\text{eV}]^{[a]}$	$E_{\text{LUMO}} [\text{eV}]^{[a]}$	$\Delta E_{\text{CV}} [\text{eV}]^{[b]}$
181	0.49	0.87	$-1.57^{[c]}$	-5.53	-3.68	1.85
182	0.39	0.81	$-1.61^{[c]}$	-5.42	-3.58	1.86
183	0.51	0.86	$-1.58^{[c]}$	-5.54	-3.68	1.86
131	0.45	1.03	$-1.43^{[c]}$	-5.49	-3.67	1.82

[a] E_{HOMO} and E_{LUMO} calculated from the onset of E°_{ox1} and E°_{red1} , respectively; related to the Fc/Fc^+ -couple with an absolute energy of -5.1 eV . [b] Electrochemical band gap calculated to $\Delta E_{\text{CV}} = E_{\text{HOMO}} - E_{\text{LUMO}}$. [c] Taken from DPV measurement.

6.2.4 Photovoltaic performance of bi(DTP)s **181-183**

Photovoltaic performances of acceptor end-capped bi(DTP)s **181-183** were tested and optimized in BHSJC. In order to assess their potential application in solution-processed OSCs the maximum solubility was determined and the absorption of the active layer (D:PC₆₁BM blend) was measured prior to solar cell fabrication.

Solubilities of bi(DTP)s **181-183** in chloroform at ambient temperature were determined using absorption spectroscopy. DCV-substituted bi(DTP) **181** with 2-ethylhexyl chains attached to the DTP-nitrogen atoms showed a rather moderate solubility of only 1.0 mg/mL which is not sufficient to spin-coat well-performing active layers for BHJSCs. Therefore, other (high boiling) solvents had to be used

for active layer deposition. For **183**, where longer branched alkyl chains are attached to the DTP-units, the solubility was increased to 34.5 mg/mL enabling a variety of possibilities for active layer deposition. By replacing the DCV groups in **181** by *n*-octyl 2-cyanoacetate moieties in **182**, the highest solubility of 42.5 mg/mL in chloroform was obtained within this series. Thin film absorption spectroscopy of **181-183** blended with PC₆₁BM (D:A = 1:2) was performed in order to roughly evaluate film formation (Figure 4). In the case of **181**, blend layers spin-coated from chloroform at 60 °C showed strong scattering above 750 nm (Figure 4a) and small particles were visible by eye within the film which can be ascribed to the poor solubility of **181** in chloroform. Using 1,1,2,2-tetrachloroethane (TCE), chlorobenzene (CB), or *o*-dichlorobenzene (ODCB) heated to ≥100 °C the solubility was noticeably higher than in chloroform at 60 °C. However, only spin-coating from TCE led to complete substrate coverage. Blends deposited from TCE at 100 °C featured a nearly doubled absorbance at the CT-band absorption than blends spin-coated from chloroform at 60 °C (Figure 4a). The higher absorbance is due to the higher solubility of **181** in hot TCE. This can also be observed by the lower scattering in higher wavelength region proving less aggregates and crystallites in blend films of **181**:PC₆₁BM when processed from TCE at 100 °C. Thus, spin-coating from TCE at 100 °C seems to be the best solution to produce well-absorbing blend layers, although only thicknesses of about 70 nm were obtained.

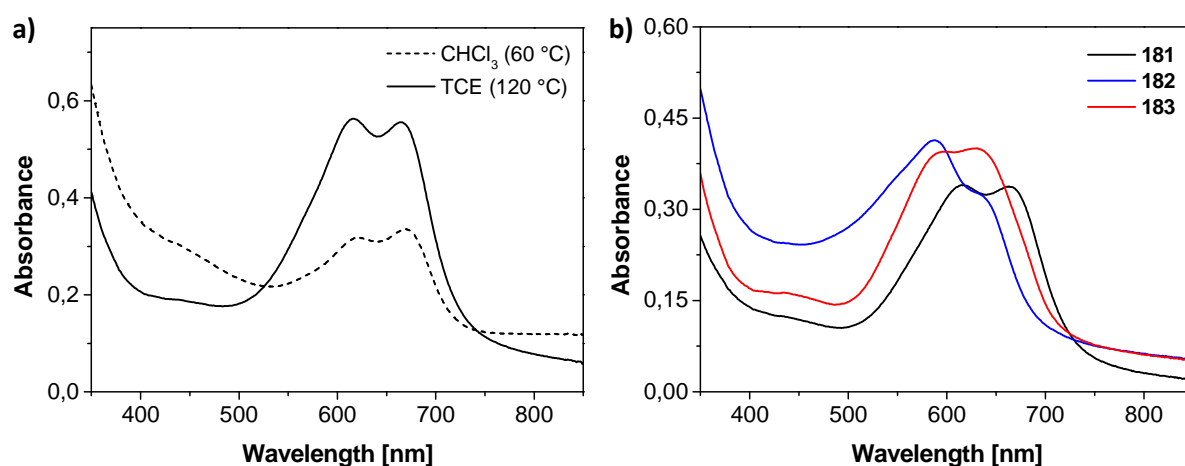


Figure 4. (a) Absorption spectra of **181**:PC₆₁BM [1:2] blends spin-coated from chloroform at 60 °C (dashed line) and TCE at 100 °C (solid line) at $v_{\text{spin}} = 1000$ rpm on PEDOT:PSS covered ITO glass. (b) Absorption spectroscopy of the blend layers bi(DTP):PC₆₁BM [1:2]; spin-coated from TCE at 100 °C (**181**, $c = 16.5$ mg/mL, black line) and chloroform at r.t. (**182** and **183**; $c = 12.5$ mg/mL, blue and red line, respectively) at $v_{\text{spin}} = 1000$ rpm on PEDOT:PSS covered ITO glass.

For **182** and **183**, which do not have this solubility issue, spin-coating PC₆₁BM blends from chloroform at room temperature (r.t.) generated smooth films with layer thicknesses around 105 nm (± 5) (Figure

4b). The absorption profile between 500 and 800 nm of **182**:PC₆₁BM and **183**:PC₆₁BM blends resemble those of the corresponding neat films with somewhat less structured absorption bands which can be explained by the presence of PC₆₁BM molecules, which alter the ordering of the donor molecules.

Solar cells with a standard device structure consisting of ITO|PEDOT:PSS(35 nm)|D:A|LiF (0.7 nm) |Al(100 nm) were fabricated with the use of **181-183** as donor (D) and PC₆₁BM as acceptor (A). First, devices were built using structurally defined molecule **181** as electron donor. The processing conditions were very limited due to the low solubility of **181**. BHJSCs with a D:A ratio of > 0.5 were not possible due to precipitation of **181** from the spin-coating solution. In all cases, hot TCE (>100 °C) was used as solvent and substrates were preheated (>100 °C). The concentration of the spin-coating solution was only 17.5 mg/mL which is quite low for such a high boiling solvent. Though, higher concentrations were not possible without reducing the D:A ratio to smaller donor contents. Despite these solubility issues, a maximum PCE of 2.08% was achieved. A moderate short-circuit current density (J_{sc}) of 4.70 mA cm⁻² and FF of 0.43 were obtained. However, a high V_{oc} of 1.03 V seemed promising for this series. Optimization regarding J_{sc} and FF values is very complicated due to solubility limitation as mentioned before. For instance, J_{sc} could be improved by producing thicker films owing to increased absorption. However, higher concentrations were not possible and significantly lower spin-coating velocities (v_{spin}) led to incomplete coverage and rough films. In this case, another processing method might lead to a better photovoltaic performance. On the basis of these results solar cell testing and optimization was focused on donor materials **182** and **183** which possess higher solubilities.

Because of the solubilizing octyl chains on the acceptor groups of bi(DTP) **182** spin-coating is considerably facilitated. In order to investigate the influence of the D:A ratio, BHJSCs with three different ratios were fabricated (Table 3, entry 1-3). Among 2:1, 1:1, and 1:2 being spin-coated with 750, 1000, and 1250 rpm, the highest PCE of 1.27% and FF of 0.53 was reached for BHJSCs with a D:A ratio of 1:1 (entry 2). V_{oc} values of around 0.94 V are ~0.1 V lower than the ones of solar cells incorporating **181** as donor which fits well to the ~0.1 V higher lying HOMO energy level of **182** compared to DCV-substituted bi(DTP)s **181** and **183**. Both values, V_{oc} and FF are very promising for the use of soluble bi(DTP)-based donors in BHJSCs. However, the relatively low J_{sc} of 2.56 mA cm⁻² needs improvement.

Using a D:A ratio of 2:1, a lower J_{sc} of 1.71 mA cm⁻² in comparison to cells with a D:A ratio of 1:1 is obtained. Additionally, FF is reduced to 0.39 in comparison to entry 2, thus resulting in a much lower PCE of 0.60%. For solar cells with a D:A ratio of 1:2, a higher J_{sc} of 2.68 mA cm⁻² is produced.

Compared to devices of entry 1 and 2 a lower amount of **182** is present within the active layer, thus the increase in J_{SC} is attributed to a different morphology resulting in a better charge transport or charge generation. Nonetheless, the lower FF of 0.44 for devices with a D:A ratio of 1:1 compared to devices of entry 2 predominates over the beneficial higher J_{SC} leading to a drop in PCE to 1.06%. Improving the absorbance by increasing the active layer thickness should result in higher J_{SC} values assuming a consistently good morphology. Indeed, for devices listed in Table 3, entry 4 a 5% higher J_{SC} of 2.70 mA cm^{-2} compared to the J_{SC} of BHJSC of entry 2 was achieved, while V_{OC} and FF values remained constant. This resulted in a higher PCE of 1.37% most probably due to better light harvesting based on an increase in active layer thickness from $111 \pm 3 \text{ nm}$ to $120 \pm 4 \text{ nm}$.

Table 3. Photovoltaic parameters for BHJSCs using bi(DTP) **182** as donor, with different D:A ratios. Device structure: ITO|PEDOT:PSS|**182**:PC₆₁BM|LiF|Al; solvent: chloroform. For each entry, three solar cells were fabricated using three different spin-coating velocities (750/1000/1250 rpm), whereas only the best is tabulated.

entry	D:A	conc. [mg/mL]	v_{spin} [rpm]	J_{SC} [mA cm^{-2}]	V_{OC} [V]	FF	PCE [%]
1	2:1	12.5	750	1.71	0.94	0.39	0.60
2	1:1	12.5	1250	2.56	0.94	0.53	1.27
3	1:2	12.5	1000	2.68	0.91	0.44	1.06
4	1:1	15.0	1250	2.70	0.94	0.53	1.37

Further improvement concerning J_{SC} aimed at morphology optimization due to the fact that increasing active layer thickness at one point will definitely lead to a drop in FF. A common method concerning morphology optimization is thermal annealing. By heating the blend layer, the donor and acceptor molecules can reorder to a certain extent. Usually a solid-solid phase separation is induced leading to larger domain sizes. Based on this, the solar cells summarized in Table 3 were thermally annealed. No significant change of any photovoltaic parameter was observed upon thermal annealing at $80 \text{ }^{\circ}\text{C}$ for 1 min. Continuing thermal annealing led to a steady decrease of all solar cell characteristics pointing to the formation of too large domain sizes. Fabrication of BHJSCs using PC₇₁BM as acceptor did not lead to better performing solar cells, as well as changing the solvent from chloroform to CB. Both attempts aimed at gaining a completely different morphology.

In order to influence phase separation and hence to modify film morphology, solvent additives were employed. Solvent additives change mainly two properties in the film morphology, the crystallinity

and the degree of phase-separation.^[20] The origin of this effect is based on the high boiling points of solvent additives and the different solubility of donor and acceptor in the solvent additive. The combination of these two points allows the additive to remain longer in the blend film during film formation compared to the actual solvent keeping either the donor or the acceptor longer in solution and hence leading to a better phase-separation. In the following experiments, 1,8-diiodooctane (DIO), ODCB, polydimethylsiloxane (PDMS), and CN (chloronaphthalene) were tested as solvent additives. The corresponding photovoltaic data are summarized in Table 4.

Table 4. Photovoltaic parameters for BHJSCs using bi(DTP) **182** as donor, with different solvent additives. Device structure: ITO|PEDOT:PSS|**182**:PC₆₁BM|LiF|Al; D:A ratio = 1:1, c = 15.0 mg/mL, solvent: chloroform. For each entry, three solar cells were fabricated using three different spin-coating velocities v_{spin} (1000/1250/1500 rpm), whereas only the best one is tabulated.

entry	additive	c_{additive} [mg/mL]	v_{spin} [rpm]	J_{SC} [mA cm ⁻²]	V_{OC} [V]	FF	PCE [%]
1	DIO	5.0	1250	3.30	0.96	0.42	1.34
2	ODCB	5.0	1500	3.50	0.95	0.38	1.27
3	PDMS	0.2	1250	2.70	0.93	0.54	1.36
4	CN	5.0	1250	7.10	0.95	0.53	3.55
5	CN	3.0	1500	4.30	0.95	0.42	1.74
6	CN	4.0	1500	6.00	0.95	0.51	2.91
7	CN	6.0	1000	7.40	0.95	0.47	3.30

For DIO, ODCB, and CN an additive concentration in the spin-coating solution of 5.0 mg/mL was used. In the case of PDMS, which is not volatile and remains in the active layer a lower concentration is recommended. Therefore, a PDMS concentration of 0.2 mg/mL was applied.^[21] The effect on the active layer of such a high molecular weight and insulating polymer is described by Huang *et al.*^[22] For active layers prepared with DIO, ODCB, and PDMS additives (Table 4, entry 1-3) BHJSCs yielded similar PCEs as solar cells which were prepared without the use of additives (Table 3, entry 4). When DIO or ODCB was used as solvent additive, J_{SC} improved to about 3.4 mA cm⁻² which means an increase of 25% compared to cells fabricated without solvent additives. However, the FF declined from ~0.5 to ~0.4, thus a comparable PCE of 1.3% was obtained. Solar cells with PDMS showed no significant changes in the photovoltaic characteristics. BHJSCs with active layers prepared by the use

of CN as additive featured greatly improved J_{SC} of 7.1 mA cm^{-2} , whereas V_{OC} and FF values of 0.95 V and 0.53, respectively, could be sustained. In order to investigate the effect of the CN concentration three further concentrations were tested: 3.0, 4.0, and 6.0 mg/mL (Table 4, entry 5-7). The V_{OC} values were unaffected by increasing the additive concentration. Photocurrent generation reached a maximum at 7.4 mA cm^{-2} , when films were prepared with an additive concentration of 6.0 mg/mL. However, a lower PCE of 3.3% was obtained due to the lower FF of 0.47 in comparison to cells with 5.0 mg/mL additive concentration which reach 3.55% PCE with a FF of 0.53. Solar cells from entry 5 and 6 with lower additive concentrations produced lower J_{SC} and FF values leading to inferior PCEs. Further morphology optimization was carried out using D:A ratios of 2:3 and 3:2 with a concentration of 5.0 mg/mL CN as additive. However, no improvement was found, similarly to thermal annealing experiments. Thus, the best performing **182**-based BHJSC was prepared from a 1:1-solution of **182**:PC₆₁BM containing 5.0 mg/mL CN in chloroform yielding a PCE of 3.55% (Table 4, entry 4).

Since it is known that even subtle changes in molecular structure can strongly influence photovoltaic properties (*Chapter 4*), solar cell testing with 1-octylnonyl-substituted bi(DTP) **183** was started from the beginning. In first experiments, BHJSCs with D:A ratios of 1:2, 1:1, and 2:1 were tested. The corresponding data is summarized in Table 5. Among the three different active layers, as-cast solar cells with a D:A ratio of 1:2 performed best with a PCE of 1.54% in comparison to as cast 1:1- and 2:1-cells with PCEs of 1.01 and 0.30%, respectively. It can be clearly seen that the J_{SC} and FF values decrease with increasing content of **183** from 4.59 mA cm^{-2} and 0.34 for cells with a D:A ratio of 1:1 to 1.23 mA cm^{-2} and 0.23 for cells with a D:A ratio of 1:2. In contrast to this, V_{OC} values were slightly higher for cells containing a higher amount of **183**. However, changes in J_{SC} and FF predominate. After the photovoltaic characterization of BHJSCs with D:A ratios of 1:2, 1:1, and 2:1, these solar cells were thermally annealed at 80 °C under inert atmosphere and changes in the performance were recorded (Table 5). Again a clear trend concerning the donor content can be observed: the higher the D:A ratio in thermally annealed BHJSCs, the higher the improvement in PCE upon thermal annealing. Solar cells with an active layer composition of a D:A ratio of 1:2 deteriorated upon thermal treatment. In fact, the FF improved within 5 min from 0.34 to 0.41. However, even more significantly was the reduction of J_{SC} from 4.59 to 3.64 mA cm^{-2} and V_{OC} from 0.99 to 0.83 V. Thus, the PCE was reduced within 5 min of annealing by about 20% from 1.54 to 1.23%, longer annealing times even further decreased the PCE. In the case of BHJSCs with a D:A ratio of 1:1, the PCE was increased when the devices were thermally annealed. In the first few minutes, the rise in PCE can clearly be noticed. After 5 min, J_{SC} and FF were increased by about 30% resulting in a PCE of 1.58%. In the following, further annealing led to a slow, but steady increase of the photovoltaic performance. A total thermal annealing time of 60 min finally brought up a PCE of 1.80%, with a J_{SC} of 4.23 mA cm^{-2} , a V_{OC} of 1.01 V,

and a FF of 0.42. Additional annealing for 40 min then resulted in a drop of the J_{SC} . For BHJSCs with a D:A ratio of 1:2, annealing showed to be even more effective. As-cast solar cells showed poor performance of 0.30% due to low J_{SC} and FF values of 1.23 mA cm^{-2} and 0.23, respectively. Thermal annealing for 5 min boosted the J_{SC} and FF to 5.34 mA cm^{-2} and 0.43, respectively, leading to a PCE of 2.28%. After 40 min of thermal annealing a maximum PCE of 2.51% was reached due to further improvement of J_{SC} and FF representing an 8-fold PCE compared to the as-cast cell. It has to be noted that the V_{OC} values decrease slightly upon annealing. They experience their strongest drop within the first 5 min and stabilize at 1.0 V for D:A ratios of 1:1 and 2:1. An explanation for this behavior is given in the next paragraph.

Table 5. Photovoltaic parameters for BHJSCs using bi(DTP) **183** as donor, with different D:A ratios. Device structure: ITO|PEDOT:PSS|**183**:PC₆₁BM|LiF|Al; c = 12.5 mg/mL, solvent: chloroform, $T_{\text{annealing}} = 80 \text{ }^{\circ}\text{C}$. For each entry, three solar cells were fabricated using three different spin-coating velocities (750/1000/1250 rpm), whereas only the best one is tabulated.

D:A	annealing [min]	v_{spin} [rpm]	J_{SC} [mA cm^{-2}]	V_{OC} [V]	FF	PCE [%]
1:2	-	1250	4.59	0.99	0.34	1.54
	0.5	-	4.16	0.99	0.34	1.39
	5	-	3.64	0.83	0.41	1.23
1:1	-	1250	3.07	1.06	0.31	1.01
	5	-	3.98	1.01	0.39	1.58
	60	-	4.23	1.01	0.42	1.80
	100	-	4.12	1.01	0.42	1.73
2:1	-	1250	1.23	1.05	0.23	0.30
	5	-	5.34	0.99	0.43	2.28
	40	-	5.57	1.00	0.45	2.51
	60	-	5.36	1.00	0.44	2.38

The use of other solvents such as CB, another acceptor (PC₇₁BM) or higher processing temperatures did not lead to better performing solar cells. Hence, further optimization focused on thermal annealing and solvent additives. In order to investigate the effects of thermal annealing absorption

spectra of as-cast and at 80 °C annealed thin films of neat **183** and **183**:PC₆₁BM blends were recorded (Figure 5). Thin film absorption spectroscopy of neat films of **183** and the effect of thermal annealing is shown in Figure 5a. Independent of the annealing time (>1 min), the absorption band became more structured and the maximum was red-shifted to 678 nm compared to the as-cast film which has its maximum at 633 nm. This could be due to a rearrangement of the long branched alkyl chains of **183** enabling the bi(DTP) core to π -stack more efficiently. The stronger π - π -stacking would then lead to a broadening of the energy bands. Thus, the absorption onset experienced a red-shift of ~10 nm and the optical band gap is decreased accordingly. Another explanation might be that most of the donor molecules are arranged in an edge-on configuration relative to the substrate. If thermal annealing leads to a reordering of the donor molecules to a face-on configuration, a larger absorption cross-section area for photons entering the blend perpendicularly would be the result, improving light-harvesting. Absorption spectra of blend films of **183**:PC₆₁BM in a D:A ratio of 2:1 showed the same behavior upon thermal annealing (Figure 5b). The rather unstructured absorption band becomes well-structured with an absorption maximum at 680 nm. In comparison to the neat film of **183**, the absorption between 350 and 500 nm does not really change in the case of the PC₆₁BM-blended film since PC₆₁BM is the main absorbing component in this region. The more effective π - π -stacking and the closely related band broadening is reflected in the V_{OC} of as-cast and annealed BHJSCs (*vide supra*). For solar cells with D:A ratios of 1:1 and 2:1, the V_{OC} of as-cast devices is about 1.05 V, whereas annealed devices showed a slightly decreased V_{OC} of ~1.0 V (Table 5).

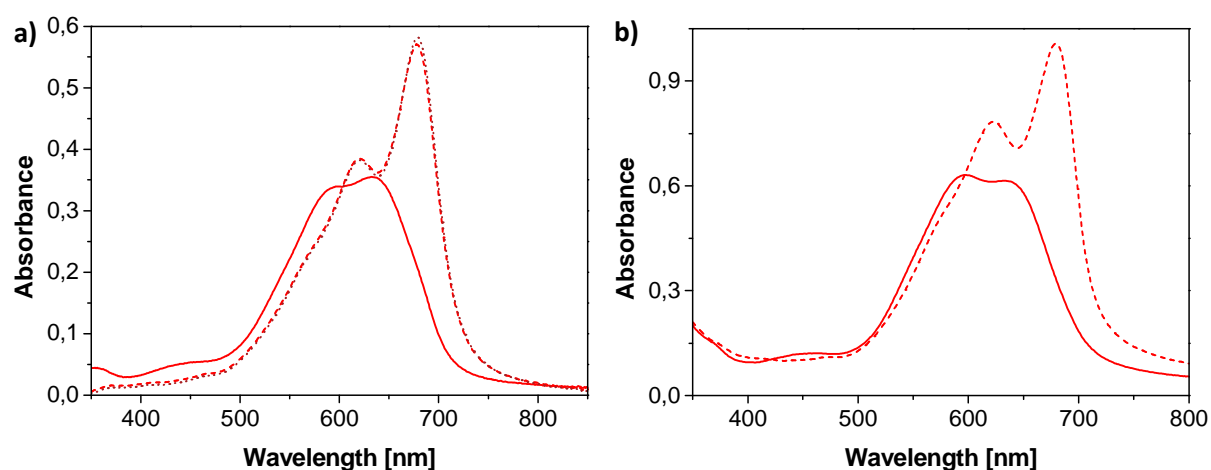


Figure 5. (a) Absorption spectra of as-cast (solid red line), for 1 min (dashed red line) and 40 min (dotted dark red line) at 80 °C thermally annealed thin films of **183**, spin-coated from chloroform on glass. (b) Absorption spectra of as-cast (solid red line) and for 1 min at 80 °C thermally annealed (dashed red line) blend films **183**:PC₆₁BM (D:A ratio = 2:1), spin-coated from chloroform on PEDOT:PSS covered ITO glass at $v_{spin} = 1500$ rpm.

It has to be noted that after the annealing process film thicknesses between 95 and 135 nm were measured across the substrate. The reason for this fluctuation is unclear. Longer annealing times did not lead to further changes in the absorption spectra. However, the photovoltaic performance of the BHJSCs declined. An explanation for that is that not only the alkyl chains are rearranged upon thermal treatment, but also that the photoactive **183**:PC₆₁BM blend phase-separates, which is also hypothesized for other structurally defined molecule:PC₆₁BM systems.^[23] In particular for poly(3-alkylthiophene):PC₆₁BM blends it was proven that diffusion of the PC₆₁BM molecules within the blend layer play a major role in improving the photovoltaic performance.^[24] Hence, this finding suggests that in the case of solar cells with a D:A ratio of 2:1 an optimal domain size is reached after 40 min of thermal annealing at 80 °C. Further annealing could then result in even larger domain sizes, which amplify the exciton recombination rate which would be confirmed by a drop in J_{SC} and constant V_{OC} and FF values for longer annealing times (Table 5).

In the following experiments, different annealing temperatures were applied aiming at the reduction of the long annealing times. Additionally, solar cells were annealed before evaporation of the top electrode (LiF|Al) and BHJSCs without LiF were fabricated in order to clarify if the improvement in PCE of annealed devices containing bi(DTP) donor **183** are solely due to changes in bulk morphology or if post-annealing induce modification of the interface morphology plays a role as well. The corresponding photovoltaic data are tabulated in Table 6. Entry 1 serves as a reference and yields a PCE of 2.76% after 40 min thermal annealing which is an improvement of ~10% compared to the data given in Table 5. The reason for that lies in the slightly higher concentration used for BHJSCs of Table 6 ($c = 15.0$ mg/mL) leading to thicker active layer and thus to a 0.5 mA cm^{-2} higher photocurrent.

Entry 3 and 5 represent the photovoltaic data of devices being thermally annealed at 110 and 140 °C, respectively. These two temperatures were chosen since 110 °C showed to be a beneficial annealing temperature for BHJSCs based on structurally defined oligomers and co-oligomers^[23,25] and 140 °C is often used for poly(3-hexylthiophene):PC₆₁BM blends.^[26,27] As expected, solar cells which were annealed at 110 and 140 °C reached their maximum PCE in a shorter annealing time (approximately 1 min) compared to the ones annealed at 80 °C (40 min). However, the higher the annealing temperature was, the lower were the photovoltaic performance. In the case of annealing the photoactive layer at 140 °C for 5 min, complete deterioration concerning the photovoltaic performance was observed. BHJSCs listed in entries 2, 4, and 6 correspond to the devices in entries 1, 3, and 5 with the difference that for 2, 4, and 6 the active layer was thermally annealed before LiF|Al deposition. It can be clearly seen, that for each annealing temperature post-fabrication annealing led to a better PCE. The reasons for that are higher J_{SC} and FF values implying that annealing is also

beneficial for the interface morphology, thus leading most probably to a better charge extraction. It seems that LiF is an important interlayer for **183**-containing BHJSCs since devices fabricated without LiF (Table 6, entries 7, 8, and 9) yielded only half the PCE as cells with a LiF interlayer (Table 6, entry 1) which is mostly owed to a reduced V_{oc} of ~ 0.8 V and FF of ~ 0.3 .

Table 6. Photovoltaic parameters for BHJSCs using bi(DTP) **183** as donor with different annealing times. Device structure: ITO|PEDOT:PSS|**183**:PC₆₁BM(|LiF)|Al; D:A ratio = 2:1, c = 15.0 mg/mL, solvent: chloroform, v_{spin} = 1500 rpm.

entry	annealing [min]	$T_{annealing}$ [°C]	J_{sc} [mA cm ⁻²]	V_{oc} [V]	FF	PCE [%]
1	-	-	1.50	1.07	0.23	0.37
	40	80	6.02	1.00	0.46	2.76
2 ^[a]	40	80	4.87	1.01	0.39	1.93
3	-	-	1.57	1.07	0.23	0.39
	1	110	3.51	0.96	0.47	1.58
	5	110	3.24	0.93	0.46	1.38
4 ^[a]	1	110	3.78	1.00	0.37	1.38
5	-	-	1.52	1.08	0.23	0.38
	1	140	2.45	0.96	0.43	1.01
6 ^[a]	1	140	1.95	1.00	0.38	0.75
7 ^[b]	-	-	0.96	0.97	0.22	0.20
	30	80	5.35	0.78	0.31	1.34
8 ^[b]	-	-	0.81	0.99	0.23	0.18
	40	80	5.23	0.81	0.32	1.34
9 ^[b]	-	-	0.92	0.98	0.23	0.20
	50	80	4.80	0.79	0.31	1.16

[a] Thermal annealing before LiF|Al deposition. [b] Without LiF.

For BHJSCs incorporating structurally defined oligomers and co-oligomers as donor only a few examples of simultaneous application of solvent additives and thermal annealing are reported.^[21,28,29]

For **183**-based BHJSCs DIO, CN, and PDMS were tested as solvent additives in combination with thermal annealing at 80 °C to further improve the morphology. Based on the conditions used for solution processing listed in Table 6, entry 1, BHJSCs were fabricated with additional use of solvent additives (Table 7).

Table 7. Photovoltaic parameters for BHJSCs using bi(DTP) **183** as donor with different solvent additives. Device structure: ITO|PEDOT:PSS|**183**:PC₆₁BM|LiF|Al; D:A ratio = 2:1, c = 15.0 mg/mL, solvent: chloroform, T_{annealing} = 80 °C. For each entry, three solar cells were fabricated using three different spin-coating velocities (1000/1250/1500 rpm), whereas only the best one is tabulated.

additive	C _{additive} [mg/mL]	annealing [min]	v _{spin} [rpm]	J _{sc} [mA cm ⁻²]	V _{oc} [V]	FF	PCE [%]
DIO	5.0	-	1250	0.77	0.99	0.23	0.18
		30	-	4.58	0.97	0.40	1.76
CN	5.0	-	1500	1.08	1.07	0.23	0.26
		12	-	6.10	1.01	0.44	2.69
PDMS	0.2	-	1250	1.23	1.07	0.23	0.30
		10	-	6.79	1.01	0.46	3.13

Comparing the as-cast devices with DIO, CN, and PDMS as solvent additives with the as-cast device without a solvent additive, it can be clearly seen that the former ones feature lower PCEs due to decreased photocurrents. Especially cells with DIO showed an additional lack in V_{oc}. When devices fabricated with solvent additives were annealed they reached their maximum PCE in a shorter time than the reference cell without additive. For solar cells using DIO as additive the annealing time is reduced to 30 min, for CN to 12 min, and for PDMS to 10 min. In the case of DIO, annealed BHJSCs with a PCE of 1.76 perform considerably lower than those without solvent additive (2.76%, Table 6, entry 1). This is due to a much lower J_{sc}, whereas V_{oc} and FF are in the same range as the additive-free device. Too large domain sizes are typically seen with low J_{sc} and high FF values. Using CN as solvent additive resulted in the same photovoltaic parameters as if no solvent additive would have been used. However, the advantage is the shorter annealing time of 12 min, still reaching a PCE of 2.7%. For solar cells prepared with PDMS as solvent additive the maximum PCE is on one hand reached in a shorter annealing time of only 10 min and on the other improved to 3.13% compared to

40 min annealing time and a PCE of 2.76% for additive-free devices. The improvement is caused by an increase in J_{SC} to 6.79 mA cm^{-2} . It seems that the PDMS helps to create a better morphology in combination with thermal annealing, than for solar cells which were fabricated without the use of solvent additives. Interestingly, the PCE before annealing is even poorer than the one of additive-free as-cast devices, which stands in contrast to a study by Graham *et al.*^[21] Measuring film thicknesses of the active layer across the substrate the most conspicuous feature is that the film is more uniform ($125 \pm 4 \text{ nm}$) than annealed active layers fabricated without PDMS. The PDMS polymer chains, which are distributed in the film, might function as shape stabilizer for **183**:PC₆₁BM blends during thermal annealing and hence lead to a more uniform film and thus an improved PCE.

In Figure 6, the J - V characteristics and IPCE of the best performing BHJSCs containing bi(DTP)s **181-183** together with PC₆₁BM as acceptor are visualized. The corresponding data are summarized in Table 8. For lowest soluble donor **181** there was only limited scope in varying the processing conditions for device fabrication. Only a D:A ratio of 1:2 spin-coated from hot TCE formed functioning solar cells. Nevertheless, a high V_{OC} of 1.03 V was obtained, partly compensating the moderate J_{SC} of 4.70 mA cm^{-2} and a FF of 0.43 and thus leading to a maximum PCE of 2.08%.

Table 8. Photovoltaic parameters for best BHJSCs using bi(DTP)s **181-183** as donor. Device structure: ITO|PEDOT:PSS|bi(DTP):PC₆₁BM|LiF|Al. D:A solutions were spin-coated at r.t. with a concentration of 15.0 mg/mL if not stated otherwise.

bi(DTP)	D:A ratio	solvent	additive	annealing [min]	J_{SC} [mA cm^{-2}]	V_{OC} [V]	FF	PCE [%]
181	1:2	TCE ^[c]	-	-	4.70	1.03	0.43	2.08
182	1:1	CHCl ₃	CN ^[b]	-	7.10	0.95	0.53	3.55
183	2:1	CHCl ₃	PDMS ^[c]	10 ^[d]	6.79	1.01	0.46	3.13

[a] Spin-coated at 100 °C on 100 °C preheated substrates with a concentration of 17.5 mg/mL. [b] $c_{\text{additive}} = 5.0 \text{ mg/mL}$. [c] $c_{\text{additive}} = 0.2 \text{ mg/mL}$. [d] Annealing at 80 °C under argon atmosphere.

1-Octylnonyl-substituted bi(DTP) **183** features a much higher solubility than **181** because of the longer 1-octylnonyl branched alkyl chains on the DTP-units compared to the 2-ethylhexyl substituents of **181**. This allowed a more elaborate optimization process. However, it seems that the long alkyl chains also face difficulties in forming well ordered π -stacks which is a disadvantage concerning absorption (Figure 5) and most probably transport due to the long alkyl chains residing between the π -systems. This is most probably why BHJSCs with as-cast films containing **183** perform so poorly (PCE < 0.4%). Despite this, thermal annealing provided well-performing devices with PCEs

of up to 2.76% due to a boost in J_{SC} and FF (Figure 6a, red dotted line). Similar high V_{OC} values of 1.0 V as for **181**, but better J_{SC} and FF values than for **181** were reached. However, very long annealing times for **183**:PC₆₁BM blends of ~40 min were required to reach the maximum PCE. The annealing time could be reduced to 10 min by using PDMS as solvent additive. Furthermore, it seems that PDMS has an additional beneficial effect to the photovoltaic performance since the efficiency is improved to 3.13% because of a higher J_{SC} of 6.79 mA cm⁻² (Figure 6a, red solid line) compared to 6.02 mA cm⁻² for cells without PDMS.

Similar to **183**, the optimization process of diester **182** was also not restricted by its solubility. The *n*-octyl-substituted 2-cyanoacrylate groups in **182** provided a solubility of 42.5 mg/mL, which is the highest within this series. As-cast solar cells showed PCEs of 1.37% (Figure 6a, dashed blue line) with already good FF and V_{OC} values of 0.53 and 0.94 V, respectively. The usage of the solvent additive CN enhanced the photocurrent while V_{OC} and FF were maintained at the same level. Thus, the best BHJSCs containing **182** as donor reached a PCE of 3.55%. The corresponding J_{SC} value of 7.10 mA cm⁻² represents the highest value among structurally defined oligomers **181-183**. However, the V_{OC} values of **182**-based solar cells are ~0.1 V smaller than the ones for devices containing DCV-substituted bi(DTP)s **181** and **183**, which can be clearly seen in Figure 6a. This is due to a higher HOMO energy level of **182** (*vide supra*).

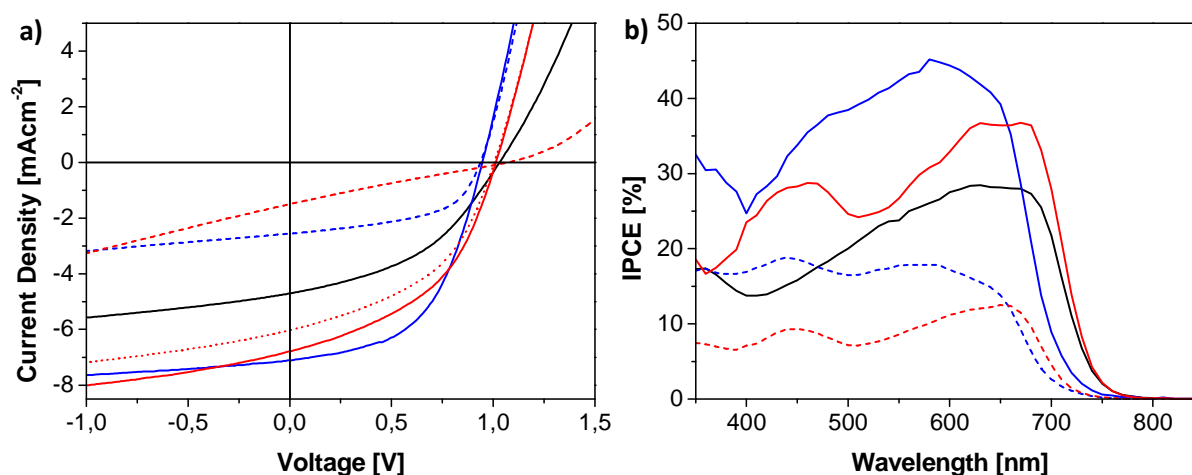


Figure 6. (a) *J*-*V* curves of the best performing BHJSCs containing **181** (solid black line), **182** (solid blue line) or **183** (solid red line) as donor, for processing conditions see Table 8. Dashed lines: corresponding non-optimized (as-cast) devices (blue: **182**, red: **183**). (b) IPCE spectra of the corresponding BHJSCs.

The IPCE spectra in Figure 6b again illustrate the important optimization process. As-cast devices of **182** and **183** showed not only lower efficiencies, but also a smaller coverage of the spectral light. Best

performing solar cells of **181** and **183** converted light from 350-740 nm into current with a maximum IPCE between 630-680 nm of 28 and 37%, respectively. The IPCE spectrum of **182**, possessing a slightly smaller band gap, covers 350-710 nm and features a maximum of 45% at 580 nm. The integration of the IPCE spectra fits the measured J_{sc} and follows the trend of the amount of produced photocurrent: $J_{sc}(\mathbf{182}) > J_{sc}(\mathbf{183}) > J_{sc}(\mathbf{181})$.

6.3 Summary

In summary, three acceptor-substituted bi(DTP)s **181-183** have been synthesized and characterized. In order to improve the moderate solubility of DCV-endcapped **181** bearing two 2-ethylhexyl side chains two approaches were taken: (1) Substitution of a cyano group in each DCV acceptor group by an octyl ester functionality which resulted in **182**; (2) Elongation of the existing side chains in **181** to 1-octylnonyl substituents which led to **183**. Both approaches delivered satisfying solubility in chloroform for solution-processing. Absorption spectroscopy proved the high light-harvesting potential of D-A systems incorporating DTP-units, especially bi(DTP)s. High extinction coefficients of over 120,000 M⁻¹cm⁻¹ and absorption onsets of up to 643 nm in solution were reached, which red-shift by about 100 nm when measured in thin films. Cyclic voltammetry measurements of **181-183** showed two reversible oxidations and one irreversible reduction for each system. HOMO and LUMO energy levels were calculated and fit well to those of PC₆₁BM concerning successful electron transfer in BHJSCs. As-cast PC₆₁BM-based BHJSCs of **181-183** yielded a maximum PCE of 2.08% using **181** as donor. Solar cells containing more soluble bi(DTP)s **182** and **183** reached only efficiencies of ~1.4 and ~0.4%, respectively. However, device optimization using solvent additives and thermal annealing led to great improvements resulting in PCEs of 3.55% and 3.13% for **182** and **183**, respectively. The high V_{oc} values of around 1 V achieved within this series and the good absorption properties render bi(DTP)s to promising donor building blocks in OPV-materials.

6.4 Experimental section

6.4.1 General procedures

¹H NMR spectra were recorded in CDCl₃, THF-d₈, and TCE-d₂ on a Bruker AMX 400 at 400 MHz.

¹³CNMR spectra were recorded in CDCl₃, THF-d₈, and TCE-d₂ on a Bruker AMX 400 at 100 MHz.

Chemical shifts are denoted by a δ unit (ppm) and are referenced to the residual solvent peak (CDCl_3 : ^1H δ = 7.26 ppm and ^{13}C δ = 77.0 ppm; THF-d_8 : ^1H δ = 3.57 ppm and ^{13}C δ = 67.20 ppm; TCE-d_2 : ^1H δ = 6.00 ppm and ^{13}C δ = 73.24 ppm). The splitting patterns are designated as follows: s (singlet), d (doublet), t (triplet), and m (multiplet). Mass spectra were recorded with a Varian Saturn 2000 GC-MS and with a MALDI-TOF MS Bruker Reflex 2 (*trans*-2-[3-(4-*tert*-butylphenyl)-2-methyl-2-propenylidene]malono-nitrile (DCTB) as matrix). Melting points of the intermediates were determined with a Büchi B-545 melting point apparatus and are not corrected. Melting points of **181-183** were determined using a Mettler Toledo DSC 823. Gas chromatography was carried out using a Varian CP-3800 gas chromatograph. HPLC analyses were performed on a Merck Hitachi L7000 equipped with a L7455 photodiode array detector, a L7200 autosampler and a L7100 solvent delivery system using a LiChrospher column (Nucleosil 100-5 NO_2). Thin-layer chromatography was carried out on Silica Gel 60 F254 aluminium plates (Merck). Solvents and reagents were purified and dried by usual methods prior to use and used under inert gas atmosphere. The following starting materials were purchased and used without further purification: ethyl formate (Merck), magnesium (Merck), triphenylphosphine (Merck), diisopropyl azodicarboxylate (Merck), lithium aluminium hydride (Merck), sodium *t*-butoxide (Merck), octyl bromide (Merck), phosphoryl chloride (Merck), piperidine (Merck), iodine (Merck), β -alanine (Merck), diphenyl phosphoryl azide (Aldrich), octyl 2-cyanoacetate (Aldrich), malononitrile (Aldrich), *n*-butyllithium (Aldrich), trimethyltin chloride (Aldrich), (\pm)-BINAP (Aldrich), tris(dibenzylideneacetone)dipalladium(0) (Aldrich). Tetrakis(triphenylphosphine)palladium(0) was synthesized according to literature.^[30]

Optical and cyclic voltammetric measurements

UV-Vis spectra in chloroform solution and thin film were taken on a Perkin-Elmer Lambda 19 spectrometer. Cyclic voltammetry experiments were performed with a computer-controlled Autolab PGSTAT30 potentiostat in a three-electrode single compartment cell (3 mL). The platinum working electrode consisted of a platinum wire sealed in a soft glass tube with a surface of $A = 0.785 \text{ mm}^2$, which was polished down to $0.25 \text{ }\mu\text{m}$ with Buehler polishing paste prior to use in order to obtain reproducible surfaces. The counter electrode consisted of a platinum wire and the reference electrode was an Ag/AgCl reference electrode. All potentials were internally referenced to the ferrocene/ferrocenium couple. For the measurements, concentrations of $5 \times 10^{-4} \text{ M}$ of the electroactive species were used in freshly distilled and deaerated DCM (Lichrosolv, Merck) purified with an MB-SPS-800 and 0.1 M (*n*-Bu) $_4\text{NPF}_6$ (Fluka; recrystallized twice from ethanol).

Device fabrication

PEDOT:PSS (Clevios P, VP.AI 4083 solution from Heraeus) was spin-coated onto pre-cleaned, patterned ITO-coated glass from Kintec ($15 \Omega \text{ cm}^{-2}$) upon which $\sim 35 \text{ nm}$ thick layers were obtained. Afterwards the photoactive layer was spin-coated from a mixed solution loaded with donor and PC₆₁BM (Solenne BV). Thin layers of LiF ($\sim 0.7 \text{ nm}$) and Al ($\sim 100 \text{ nm}$) were then deposited by vacuum evaporation at $2 \times 10^{-6} \text{ Torr}$ (Nano 36, Kurt J. Lesker Co.). The photoactive areas of the cells were 0.25 cm^2 .

Current-voltage characterization

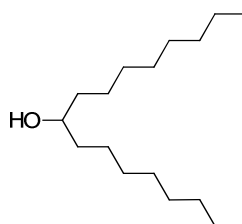
J-V characteristics were measured with a Oriel Instruments solar simulator (class AAA, AM 1.5G, 100 mWcm^{-2}) and a Keithley 2400 source meter. IPCE was measured under monochromatic light from a 300 W Xenon lamp in combination with a monochromator (Oriel, Cornerstone 260), modulated with a mechanical chopper. The response was recorded as the voltage over a 220Ω resistance, using a lock-in amplifier (Merlin 70104). A calibrated Si cell was used as reference.

Thin layer thickness

Film thicknesses were measured using a Dektak profilometer and also by using high resolution field emission scanning electron microscopy (Sirion XL30) from FEI.

6.4.2 Synthesis

Heptadecan-9-ol (193)



A solution of ethyl formate (7.41 g, 100 mmol) in 15 mL diethyl ether was added dropwise to a freshly prepared solution of octylmagnesium bromide (obtained by adding a solution of octyl bromide (84.3 g, 210 mmol) in 90 mL diethyl ether to a suspension of magnesium turnings (6.08 g, 210 mmol) in 15 mL diethyl ether and refluxing the mixture for 2 h). Subsequently, the reaction mixture was stirred for further 10 min before 14 mL water were slowly added. Then 50 mL of 1.5 N hydrochloric acid were added and the solids were filtered off and washed with diethyl ether. The organic layer was thoroughly washed with saturated aqueous NaHCO_3 solution and brine and dried

over sodium sulfate. The solvent was removed by rotary evaporation. Finally, the crude product was recrystallized from acetonitrile to give heptadecan-9-ol **193** (19.2 g, 74.9 mmol, 75%) as a white solid.

M.p.: 57-58 °C.

¹H NMR (400 MHz, CDCl₃): δ = 3.63-3.55 (m, 1 H, HO-CH), 1.43-1.28 (m, 28 H, -CH₂-), 0.88 (t, *J*³ = 6.5 Hz, 6 H, -CH₃).

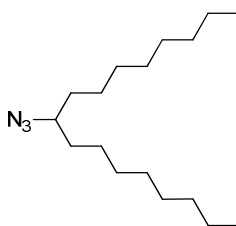
¹³C NMR (100 MHz, CDCl₃): δ = 65.74, 35.16, 31.61, 29.44, 29.23, 29.11, 26.56, 22.59, 15.34, 14.12.

MS (CI) *m/z*: calcd for C₁₇H₃₆O: 256; found [M-H]⁺: 255.

Elemental analysis: calcd (%) for C₁₇H₃₆O: C 79.61, H 14.15; found (%): C 79.83, H 14.11.

Analyses match with Ref. [31].

9-Azidoheptadecane (**194**)

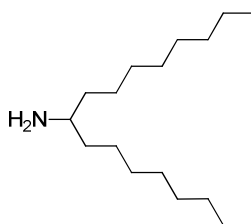


Heptadecan-9-ol **193** (4.11 g, 14.6 mmol), DIAD (4.02 g, 19.0 mmol), PPh₃ (4.98 g, 19.0 mmol), and DPPA (5.23 g, 19.0 mmol) were dissolved in 250 mL tetrahydrofuran (THF). The mixture was then sonicated for 30 min at r.t. Subsequently, the solvent was removed by rotary evaporation and the residue was extracted thoroughly with *n*-hexane. The organic phase was concentrated and subjected to column chromatography (silica/*n*-hexane) to obtain 9-azidoheptadecane **194** (3.61 g, 12.8 mmol, 88%) as a colorless oil.

¹H NMR (400 MHz, CDCl₃): δ = 3.25-3.17 (m, 1 H, N₃-CH), 1.47-1.26 (m, 28 H, -CH₂-), 0.88 (t, *J*³ = 6.6 Hz, 6 H, -CH₃).

¹³C NMR (100 MHz, CDCl₃): δ = 63.24, 34.42, 31.83, 29.54, 29.46, 29.41, 26.14, 21.99, 14.09.

MS (CI) *m/z*: calcd for C₁₇H₃₅N₃: 281; found [M-N₃]⁺: 239.

Heptadecan-9-amine (195)

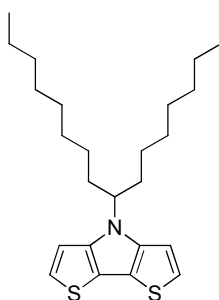
9-Azidoheptadecane **194** (2.77 g, 9.84 mmol) was dissolved in 270 mL diethyl ether. A suspension of lithium aluminum hydride (0.45 g, 11.8 mmol) in 12 mL diethyl ether was added and the mixture was refluxed for 1 h. Then 50 mL moist diethyl ether were added, followed by the addition of 15% aqueous NaOH solution. The aqueous layer was removed and the organic layer was washed thoroughly with water. After drying the organic phase over sodium sulfate, the solvent was removed by rotary evaporation, whereupon heptadecan-9-amine **195** (2.28 g, 8.92 mmol, 81%) was obtained as a colorless oil. The product was used without further purification.

^1H NMR (400 MHz, CDCl_3): δ = 2.72-2.65 (m, 1 H, N-CH), 1.38-1.19 (m, 28 H, $-\text{CH}_2-$), 0.88 (t, J^3 = 6.6 Hz, 6 H, $-\text{CH}_3$).

^{13}C NMR (100 MHz, CDCl_3): δ = 51.29, 38.24, 31.21, 30.10, 30.04, 29.71, 26.44, 23.09, 14.28.

MS (CI) m/z : calcd for $\text{C}_{17}\text{H}_{37}\text{N}$: 255; found $[\text{M}+\text{H}]^+$: 256.

Elemental analysis: calcd (%) for $\text{C}_{17}\text{H}_{37}\text{N}$: C 79.92, H 14.60, N 5.48; found (%): C 79.93, H 14.51, N 5.48.

4-(Heptadecan-9-yl)-4H-dithieno[3,2-b:2',3'-d]pyrrole (132s)

3,3'-Dibromo-2,2'-bithiophene **133** (2.00 g, 6.17 mmol), sodium *t*-butoxide (1.33 g, 13.8 mmol), $\text{Pd}_2\text{dba}_3 \cdot \text{CHCl}_3$ (100 mg, 96.6 μmol) and BINAP (240 mg, 386 μmol) were added in a flame-dried Schlenk-tube and evacuated for several minutes. Then 15 mL toluene were added and the mixture was degassed several times. Heptadecan-9-amine **195** (1.58 g, 6.17 mmol) was added and the

mixture was degassed once more. The reaction mixture was heated to 110 °C for 18 h. After that, the mixture was poured into water. The organic layer was separated and the aqueous phase was extracted with DCM. The combined organic phases were dried over sodium sulfate and the solvents were removed by rotary evaporation. The crude product was purified via column chromatography (silica/petrol ether) to obtain 4-(heptadecan-9-yl)-4H-dithieno[3,2-b:2',3'-d]pyrrole **132s** (1.65 g, 5.08 mmol, 82%) as a colorless oil.

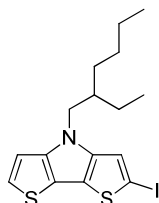
¹H NMR (400 MHz, CDCl₃): δ = 7.11 (d, ³J = 5.2 Hz, 2 H, 2-H,6-H), 7.02 (d, ³J = 5.2 Hz, 2 H, 3-H,5-H), 4.26-4.19 (m, 1 H, N-CH), 2.08-1.98 (m, 2 H, N-CH-CH₂), 1.87-1.78 (m, 2 H, N-CH-CH₂), 1.27-1.03 (m, 8 H, -CH₂-), 0.86 (t, ³J = 7.0 Hz, 6 H, -CH₃).

¹³C NMR (100 MHz, CDCl₃): δ = 130.12, 122.16, 111.47, 111.40, 59.41, 34.98, 31.74, 31.67, 29.87, 29.56, 29.12, 26.13, 22.73, 14.01.

MS (CI) *m/z*: calcd for C₂₅H₃₉NS₂: 417; found [M]⁺: 417.

Elemental analysis: calcd (%) for C₂₅H₃₉NS₂: C 71.88, H 9.41, N 3.35; found (%): C 72.13, H 9.69, N 3.57.

4-(2-Ethylhexyl)-2-iodo-4H-dithieno[3,2-b:2',3'-d]pyrrole (**199a**)

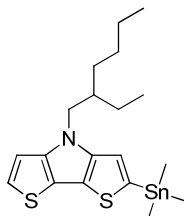


n-BuLi (1.6 M, 0.85 mL, 1.36 mmol) was added dropwise to a solution of 4-(2-ethylhexyl)-4H-dithieno[3,2-b:2',3'-d]pyrrole **132f** (386 mg, 1.32 mmol) in 4.5 mL THF at -78 °C. After the addition, the solution was stirred at -78 °C for 2 h and subsequently iodine (390 mg, 1.54 mmol) was added in one portion. After stirring at -78 °C for 1.5 h the reaction mixture was poured into 1 N sodium metabisulfite solution. The organic compounds were extracted with DCM, the combined organic phases were dried over sodium sulfate and the solvent was removed by rotary evaporation. 2-Iodo-DTP **199a** was obtained as a slightly greenish oil (470 mg) with a conversion of 85% (calculated by GC). It was used without further purification.

¹H NMR (400 MHz, CDCl₃): δ = 7.15 (s, 1 H, 3-H), 7.11 (d, ³J = 5.3 Hz, 1 H, 6-H), 6.95 (d, ³J = 5.3 Hz, 1 H, 5-H), 4.10-3.91 (m, 2 H, N-CH₂), 1.97-1.85 (m, 1 H, CH), 1.38-1.21 (m, 8 H, -CH₂-), 0.91-0.85 (m, 6 H, -CH₃);

MS (EI) m/z : calcd for $C_{16}H_{20}INS_2$: 417; found $[M]^+$: 417.

4-(2-Ethylhexyl)-2-trimethylstannyl-4H-dithieno[3,2-b:2',3'-d]pyrrole (200a)

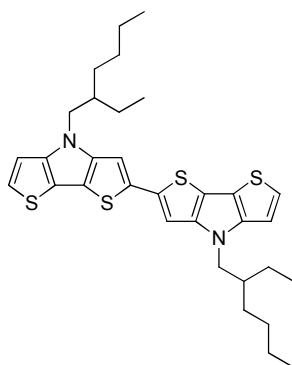


n-BuLi (1.6 M, 0.93 mL, 1.48 mmol) was added dropwise to a solution of 4-(2-ethylhexyl)-4H-dithieno[3,2-b:2',3'-d]pyrrole **132f** (432 mg, 1.48 mmol) in 5 mL THF at -78 °C. After the addition, the solution was stirred at -78 °C for 2 h and subsequently trimethyltin chloride (295 mg, 1.48 mmol) dissolved in 0.5 mL dry THF was added in one portion. After stirring at -78 °C for 2 h the reaction mixture was poured into water. *n*-Hexane was added and the organic layer was washed three times with water. The organic phase was dried over sodium sulfate and the solvent was removed by rotary evaporation. 2-Trimethylstannyl-DTP **200a** was obtained as a slightly greyish oil (620 mg) with a conversion of 82% (calculated by GC). It was used without further purification.

1H NMR (400 MHz, $CDCl_3$): δ = 7.09 (d, 3J = 5.4 Hz, 1 H, 6-H), 6.98 (s, 1 H, 3-H), 6.97 (d, 3J = 5.4 Hz, 1 H, 5-H), 4.12-4.00 (m, 2 H, N-CH₂), 2.01-1.91 (m, 1 H, CH), 1.41-1.25 (m, 8 H, -CH₂-), 0.92-0.84 (m, 6 H, -CH₃), 0.41 (s, 9 H, Sn-CH₃).

MS (EI) m/z : calcd for $C_{19}H_{29}NS_2Sn$: 455; found $[M]^+$: 455.

4,4'-Di(2-ethylhexyl)-4H,4'H-2,2'-bidithieno[3,2-b:2',3'-d]pyrrole (148)



2-Iodo-DTP **199a** (1.54 g, 3.69 mmol), 2-trimethylstannyl-DTP **200a** (2.00 g, 4.40 mmol) and $Pd(PPh_3)_2Cl_2$ (77.7 mg, 111 μ mol) were added in a flame-dried Schlenk-tube and evacuated for several minutes. After adding 22 mL DMF the reaction mixture was carefully degassed and heated to

65 °C for 3 h. Then DCM was added and the organic phase was washed with water and brine, dried over sodium sulfate and the solvents were removed by rotary evaporation. The crude product was purified via column chromatography (alumina/*n*-hexane:DCM [95:5] to [90:10]) to obtain 2-ethylhexyl-substituted bi(DTP) **148** (2.10 g, 3.61 mmol, 98%) as a yellow solid.

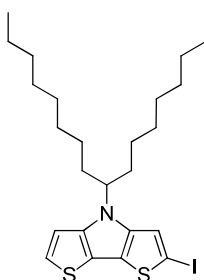
M.p.: 127-128 °C.

¹H NMR (400 MHz, THF-*d*₈): δ = 7.23 (s, 2 H, 3-H,3'-H), 7.18 (d, ³*J* = 5.3 Hz, 2 H, 6-H,6'-H), 7.05 (d, ³*J* = 5.3 Hz, 2 H, 5-H,5'-H), 4.18-4.09 (m, 4 H, N-CH₂), 2.03-1.97 (m, 2 H, -CH-), 1.42-1.26 (m, 16 H, -CH₂-), 0.93-0.86 (m, 12 H, -CH₃).

¹³C NMR (100 MHz, THF-*d*₈): δ = 135.31, 123.51, 116.32, 115.99, 112.41, 112.10, 108.05, 62.78, 36.75, 32.45, 29.98, 26.48, 23.72, 14.37, 11.12.

High-Resolution MS (MALDI-TOF) *m/z*: calcd for C₃₂H₄₀N₂S₄: 580.20704; found [M]⁺: 580.20714, δ*m/m* = 0.2 ppm.

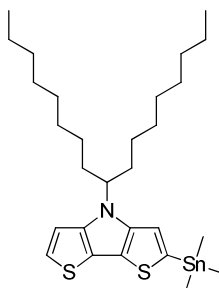
4-(Heptadecan-9-yl)-2-iodo-4H-dithieno[3,2-b:2',3'-d]pyrrole (199b)



n-BuLi (1.6 M, 0.21 mL, 0.34 mmol) was added dropwise to a solution of 4-(2-ethylhexyl)-4H-dithieno[3,2-b:2',3'-d]pyrrole **132s** (141 mg, 0.34 mmol) in 3.5 mL THF at -78 °C. After the addition, the solution was stirred at -78 °C for 2 h and subsequently iodine (85.7 mg, 0.34 mmol) was added in one portion. After stirring at -78 °C for 1.5 h the reaction mixture was poured into 1 N sodium metabisulfite solution. The organic compounds were extracted with DCM, the combined organic phases were dried over sodium sulfate and the solvent was removed by rotary evaporation. 2-Iodo-DTP **199a** was obtained as a slightly greenish oil (170 mg) with a conversion of 90% (calculated by ¹H-NMR). It was used without further purification.

¹H NMR (400 MHz, CDCl₃): δ = 7.19 (s, 1 H, 3-H), 7.10 (d, ³*J* = 5.4 Hz, 1 H, 6-H), 6.98 (d, ³*J* = 5.4 Hz, 1 H, 5-H), 4.17-4.10 (m, 1H, N-CH), 2.01-1.92 (m, 2 H, N-CH-CH₂), 1.84-1.76 (m, 2 H, N-CH-CH₂), 1.25-1.09 (m, 20 H, -CH₂-), 1.08-0.98 (m, 4 H, CH₂-CH₃), 0.85 (t, ³*J* = 7.0 Hz, 6 H, -CH₃).

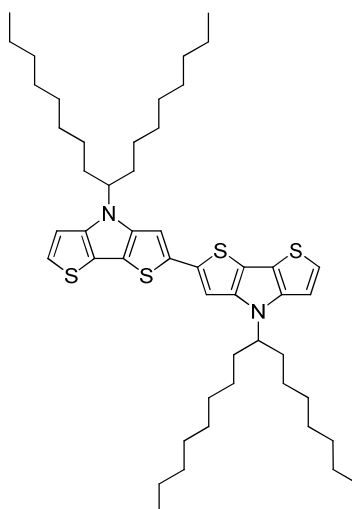
MS (MALDI-TOF) *m/z*: calcd for C₂₅H₃₈INS₂: 543; found [M]⁺: 543.

4-(Heptadecan-9-yl)-2-(trimethylstannyl)-4H-dithieno[3,2-b:2',3'-d]pyrrole (200b)

n-BuLi (1.6 M, 0.28 mL, 0.45 mmol) was added dropwise to a solution of 4-(2-ethylhexyl)-4H-dithieno[3,2-b:2',3'-d]pyrrole **132s** (186 mg, 0.45 mmol) in 5.5 mL THF at -78 °C. After the addition, the solution was stirred at -78 °C for 2 h and subsequently trimethyltin chloride (91.4 mg, 0.45 mmol) dissolved in 0.15 mL THF was added in one portion. After stirring at -78 °C for 2 h the reaction mixture was poured into water. *n*-Hexane was added and the organic layer was washed three times with water. The organic phase was dried over sodium sulfate and the solvent was removed by rotary evaporation. 2-Trimethylstannyl-DTP **200b** was obtained as a slightly yellowish oil (240 mg) with a conversion of 74% (calculated by ¹H-NMR). It was used without further purification.

¹H NMR (400 MHz, CDCl₃): δ = 7.07 (d, ³J = 5.2 Hz, 1 H, 6-H), 7.03-6.99 (m, 2 H, 3-H, 5-H), 4.25-4.18 (m, 1 H, N-CH), 2.05-1.97 (m, 2 H, N-CH-CH₂), 1.85-1.78 (m, 2 H, N-CH-CH₂), 1.25-1.05 (m, 24 H, -CH₂-), 0.84 (t, ³J = 7.0 Hz, 6 H, -CH₃), 0.40 (s, 9 H, Sn-CH₃).

MS (MALDI-TOF) *m/z*: calcd for C₂₈H₄₇NS₂Sn: 581 found [M]⁺: 581.

4,4'-Di(heptadecan-9-yl)-4H,4'H-2,2'-bidithieno[3,2-b:2',3'-d]pyrrole (192)

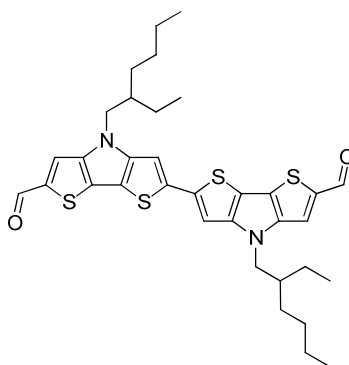
2-Iodo-DTP **199b** (145 mg, 0.27 mmol), 2-trimethylstannyl-DTP **200b** (194 mg, 0.33 mmol) and $\text{Pd}(\text{PPh}_3)_2\text{Cl}_2$ (5.6 mg, 8.00 μmol) were added in a flame-dried Schlenk-tube and evacuated for several minutes. After adding 2 mL DMF the reaction mixture was carefully degassed and heated to 60 °C for 3 h. Then DCM was added and the organic phase was washed with water and brine, dried over sodium sulfate and the solvents were removed by rotary evaporation. The crude product was purified via column chromatography (alumina/*n*-hexane:DCM [100:0] to [95:5]) to obtain 1-octylnonyl-substituted-bi(DTP) **192** (224 mg, 0.27 mmol, quantitative) as a yellow amorphous solid.

^1H NMR (400 MHz, THF-d_8): δ = 7.29 (s, 2 H, 3-H,3'-H), 7.17 (d, 3J = 5.2 Hz, 2 H, 6-H,6'-H), 7.12 (d, 3J = 5.2 Hz, 2 H, 5-H,5'-H), 4.41-4.33 (m, 2 H, N-CH), 2.15-2.06 (m, 4 H, N-CH-CH₂), 1.91-1.83 (m, 4 H, N-CH-CH₂), 1.30-1.19 (m, 40 H, -CH₂-), 1.13-1.05 (m, 8 H, CH₂-CH₃), 0.83 (t, 3J = 6.9 Hz, 12 H, -CH₃).

^{13}C NMR (100 MHz, THF-d_8): δ = 136.44, 123.43, 115.69, 113.91, 112.54, 108.29, 60.31, 35.74, 32.58, 30.12, 30.10, 29.98, 27.25, 23.32, 14.23.

High-Resolution MS (MALDI-TOF) m/z : calcd for $\text{C}_{32}\text{H}_{40}\text{N}_2\text{S}_4$: 832.48913; found $[\text{M}]^+$: 832.48814, $\delta m/m$ = 1.2 ppm.

4,4'-Bis(2-ethylhexyl)-4H,4'H-(2,2'-bidithieno[3,2-b:2',3'-d]pyrrole)-6,6'-dicarbaldehyde (**201a**)



DMF (0.40 mL, 5.21 mmol) and phosphoryl chloride (0.48 mL, 5.21 mmol) were dissolved in 12 mL DCM and stirred at room temperature for 45 min. Then, this solution was added dropwise to a solution of 4,4'-bis(2-ethylhexyl)-4H,4'H-2,2'-bidithieno[3,2-b:2',3'-d]pyrrole **148** (60.5 mg, 104 μmol) in 6 mL DCM, which was cooled to 0 °C with an ice bath. After the addition, the reaction mixture was stirred at room temperature for 2 d. Subsequently, saturated sodium bicarbonate solution and sodium carbonate were added carefully and the two-phase system was stirred at room temperature for 17 h. The organic compounds were then extracted with DCM, the combined organic phases dried over sodium sulfate and the solvent was removed by rotary evaporation. The crude product was

purified by washing the solid with a lot of *n*-hexane and a little DCM to obtain bi(DTP)-6,6'-dicarbaldehyde **201a** (63.0 mg, 98.9 μ mol, 95%) as a lilac solid.

M.p.: 229 °C.

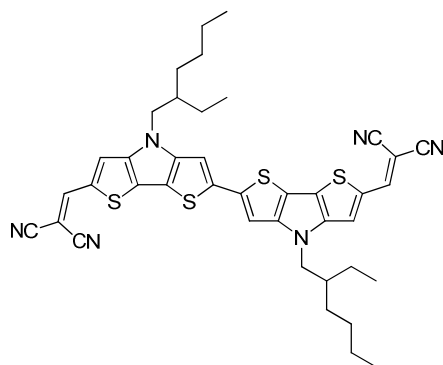
^1H NMR (500 MHz, TCE- d_2): δ = 9.90 (s, 2 H, CHO), 7.64 (s, 2 H, 5-H,5'-H), 7.18 (s, 2H, 3-H,3'-H), 4.18-4.11 (m, 4 H, N- CH_2), 2.07-2.00 (m, 2 H, -CH-), 1.47-1.31 (m, 16 H, - CH_2 -), 1.00 (t, 3J = 7.4 Hz, 6 H, - CH_3), 0.94 (t, 3J = 7.0 Hz, 6 H, - CH_3).

^{13}C NMR (125 MHz, TCE- d_2): δ = 181.88, 148.59, 144.27, 140.20, 139.58, 122.40, 118.22, 113.76, 106.87, 51.02, 39.81, 30.16, 27.96, 23.62, 22.21, 13.20, 10.03.

MS (MALDI-TOF) m/z : calcd for $\text{C}_{34}\text{H}_{40}\text{N}_2\text{O}_2\text{S}_4$: 636; found $[\text{M}]^+$: 636.

Elemental analysis: calcd (%) for $\text{C}_{34}\text{H}_{40}\text{N}_2\text{O}_2\text{S}_4$: C 64.11, H 6.33, N 4.40, S 20.14; found (%): C 64.13, H 6.28, N 4.34, S 19.94.

2,2'-([4,4'-Bis{2-ethylhexyl}-4H,4'H-{2,2'-bidithieno[3,2-b:2',3'-d]pyrrole}-6,6'-diyl]bis[methanylylidene])dimalononitrile (181**)**



2-Ethylhexyl-substituted bi(DTP)-dicarbaldehyde **201a** (30.0 mg, 47.1 μ mol), malononitrile (9.33 mg, 141 μ mol) and β -alanine (0.30 mg, 2.83 μ mol) were dissolved in 5 mL dichloroethane(DCE):ethanol [1:1] in a Schlenk-tube. The reaction mixture was stirred at 80 °C for 19 h. After that, the solvent was removed by rotary evaporation. The crude product was purified via column chromatography (silica/DCM) to obtain DCV-substituted bi(DTP) **181** (28.0 mg, 38.2 μ mol, 81%) as a dark metallic green solid.

M.p.: 301 °C.

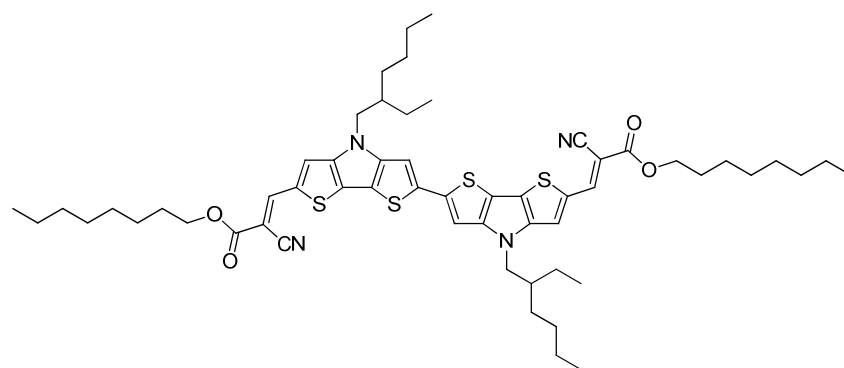
^1H NMR (400 MHz, CDCl_3): δ = 7.70 (s, 2 H, 5-H,5'-H), 7.65 (s, 2 H, C=CH), 7.18 (s, 2 H, 3-H,3'-H), 4.15-4.07 (m, 4 H, N- CH_2), 2.00-1.95 (m, 2 H, -CH-), 1.43-1.28 (m, 16 H, - CH_2 -), 0.96 (t, 3J = 7.4 Hz, 6 H, - CH_3), 0.90 (t, 3J = 7.1 Hz, 6 H, - CH_3).

^{13}C NMR (100 MHz, CDCl_3): δ = 150.92, 150.35, 142.24, 133.20, 127.23, 118.71, 114.92, 114.46, 107.68, 51.84, 40.59, 30.83, 28.70, 24.30, 22.95, 13.92, 10.74.

MS (MALDI-TOF) m/z : calcd for $\text{C}_{40}\text{H}_{40}\text{N}_6\text{S}_4$: 732; found $[\text{M}]^+$: 732.

Elemental analysis: calcd (%) for $\text{C}_{40}\text{H}_{40}\text{N}_6\text{S}_4$: C 65.54, H 5.50, N 11.46; found (%): C 65.32, H 5.40, N 11.39.

(2E,2'E)-Dioctyl 3,3'-(4,4'-bis[2-ethylhexyl]-4H,4'H-[2,2'-bidithieno[3,2-b:2',3'-d]pyrrole]-6,6'-diyl)-bis(2-cyanoacrylate) (182)



2-Ethylhexyl-substituted bi(DTP)-dicarbaldehyde **201a** (50.0 mg, 78.5 μmol), 2-cyanoacrylic octyl ester (100 μL , 473 μmol) and 2 drops of piperidine were dissolved in 4 mL DCE in a Schlenk-tube. The reaction mixture was stirred at 80 $^{\circ}\text{C}$ for 2 d. After 1 d, another 100 μL 2-cyanoacrylic octyl ester and 2 drops of piperidine were added. After the completion of the reaction the solvent was removed by rotary evaporation and most of the excessive reactant was removed in vacuo. The crude product was purified via column chromatography (silica/DCM) to obtain octyl cyanoacrylate-substituted bi(DTP) **182** (66. mg, 66.3 μmol , 85%) as a dark green solid.

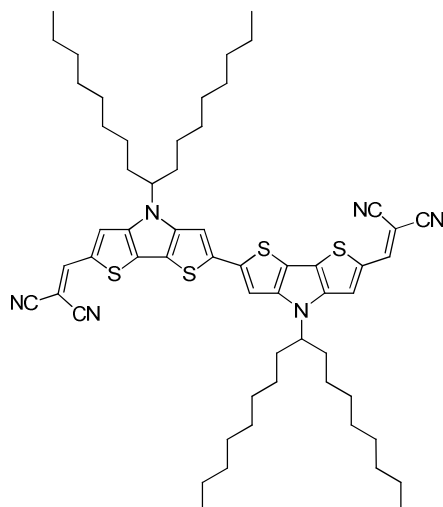
M.p.: 216 $^{\circ}\text{C}$.

^1H NMR (400 MHz, CDCl_3): δ = 8.24 (s, 2 H, C=CH), 7.61 (s, 2 H, 5-H,5'-H), 7.18 (s, 2 H, 3-H,3'-H), 4.27 (t, 3J = 6.8 Hz, 4 H, O-CH₂), 4.14-4.03 (m, 4 H, N-CH₂), 2.00-1.90 (m, 2 H, -CH-), 1.78-1.71 (m, 4H, O-CH₂-CH₂), 1.43-1.29 (m, 36H, -CH₂-), 0.96-0.87 (m, 18H, -CH₃).

^{13}C NMR (100 MHz, CDCl_3): δ = 163.62, 149.81, 147.14, 145.50, 141.11, 133.66, 124.45, 117.08, 114.33, 107.17, 94.55, 66.31, 51.51, 40.40, 31.79, 30.57, 29.21, 29.17, 28.61, 28.57, 25.83, 24.06, 22.98, 22.65, 14.10, 14.04, 10.72.

High-Resolution MS (MALDI-TOF) m/z : calcd for $\text{C}_{56}\text{H}_{74}\text{N}_4\text{O}_4\text{S}_4$: 994.45929; found $[\text{M}]^+$: 994.45864, $\delta m/m$ = 0.7 ppm.

2,2'-([4,4'-Di{heptadecan-9-yl}-4H,4'H-{2,2'-bidithieno[3,2-b:2',3'-d]pyrrole}-6,6'-diyl]bis[methanylylidene])dimalononitrile (183)



1-Octylnonyl-substituted bi(DTP)-dicarbaldehyde **6.17b** (112 mg, 0.13 mmol), malononitrile (25.0 mg, 0.38 mmol) and β -alanine (0.7 mg, 7.56 μ mol) were dissolved in 10 mL DCE:ethanol [1:1] in a Schlenk-tube. The reaction mixture was stirred at 80 °C for 2 d. After that the solvent was removed by rotary evaporation. The residual solid was purified via column chromatography (silica/DCM) and subsequently washed with methanol to obtain DCV-substituted bi(DTP) **183** (122 mg, 0.12 mmol, 98%) as a dark metallic green solid.

M.p.: 224 °C.

^1H NMR (400 MHz, CDCl_3): δ = 7.75 (s, 2 H, 5-H,5'-H), 7.63 (s, 2 H, C=CH), 7.18 (s, 2 H, 3-H,3'-H), 4.29-4.23 (m, 2 H, N-CH), 2.07-1.88 (m, 8 H, N-CH-CH₂), 1.33-1.03 (m, 24 H, -CH₂-), 0.82 (t, 3J = 7.9 Hz, 12 H, -CH₃).

^{13}C NMR (100 MHz, CDCl_3): δ = 150.63, 142.16, 133.04, 126.13, 115.16, 114.84, 114.59, 108.15, 72.32, 60.78, 34.98, 31.72, 29.25, 29.16, 29.09, 26.55, 22.58, 14.05.

MS (MALDI-TOF) m/z : calcd for $\text{C}_{58}\text{H}_{76}\text{N}_6\text{S}_4$: 985; found $[\text{M}]^+$: 985.

Elemental analysis: calcd (%) for $\text{C}_{58}\text{H}_{76}\text{N}_6\text{S}_4$: C 70.69, H 7.77, N 8.53, S 13.01; found (%): C 70.89, H 7.61, N 8.49, S 12.91.

6.5 References

- [1] R. Fitzner, E. Reinold, A. Mishra, E. Mena-Osteritz, H. Ziehlke, C. Körner, K. Leo, M. Riede, M. Weil, O. Tsaryova, A. Weiß, C. Urich, M. Pfeiffer, P. Bäuerle, *Adv. Funct. Mater.* **2011**, *21*, 897-910.
- [2] Y. Liu, X. Wan, F. Wang, J. Zhou, G. Long, J. Tian, J. You, Y. Yang, Y. Chen, *Adv. Energy Mater.* **2011**, *1*, 771-775.
- [3] R. B. Zerdan, N. T. Shewmon, Y. Zhu, J. P. Mudrick, K. J. Chesney, J. Xue, R. K. Castellano, *Adv. Funct. Mater.* **2014**, n/a-n/a.
- [4] D. Hildebrandt, G. Mattersteig, O. Tsaryova, S. Vetter, A. Weiss, *DE102010030500 A1*, Heliathek, **2011**.
- [5] J. O. Choi, O. K. Kwon, J. H. Jung, *WO2014025231 A3*, Lms Co., Ltd, **2014**.
- [6] A.-B. Britta-Hörnfeldt, S. Gronowitz, *Thiophenes, Vol. 1. Auflage*, Elsevier Academic Press, Oxford, **2004**.
- [7] A. Yassin, P. Leriche, J. Roncali, *Macromol. Rapid Commun.* **2010**, *31*, 1467-1472.
- [8] Y. Geng, W. Yue, *CN101407574 B*, Changchun Applied Chemistry, **2011**.
- [9] S. J. Evenson, S. C. Rasmussen, *Org. Lett.* **2010**, *12*, 4054-4057.
- [10] G. Koeckelberghs, L. De Cremer, W. Vanormelingen, W. Dehaen, T. Verbiest, A. Persoons, C. Samyn, *Tetrahedron* **2005**, *61*, 687-691.
- [11] R. S. Ashraf, J. Gilot, R. A. J. Janssen, *Sol. Energy Mater. Sol. Cells* **2010**, *94*, 1759-1766.
- [12] O. Mitsunobu, *Synthesis* **1981**, *1981*, 1-28.
- [13] D. L. Hughes, *Organic Reactions*, John Wiley & Sons, **1992**.
- [14] G. Koeckelberghs, L. De Cremer, W. Vanormelingen, W. Dehaen, T. Verbiest, A. Persoons, C. Samyn, *Tetrahedron* **2005**, *61*, 687-691.
- [15] G. Koeckelberghs, L. De Cremer, A. Persoons, T. Verbiest, *Macromolecules* **2007**, *40*, 4173-4181.
- [16] S. Gronowitz, H.-O. Karlsson, *Arkiv Kemi* **1961**, *17*, 89.
- [17] S. Barlow, S. A. Odom, K. Lancaster, Y. A. Getmanenko, R. Mason, V. Coropceanu, J.-L. Brédas, S. R. Marder, *J. Phys. Chem. B* **2010**, *114*, 14397-14407.
- [18] L. E. Polander, L. Pandey, S. Barlow, S. P. Tiwari, C. Risko, B. Kippelen, J.-L. Brédas, S. R. Marder, *J. Phys. Chem. C* **2011**, *115*, 23149-23163.
- [19] B. H. Wunsch, M. Rumi, N. R. Tummala, C. Risko, D.-Y. Kang, K. X. Steirer, J. Gantz, M. Said, N. R. Armstrong, J.-L. Bredas, D. Bucknall, S. R. Marder, *J. Mater. Chem. C* **2013**, *1*, 5250-5260.
- [20] H.-C. Liao, C.-C. Ho, C.-Y. Chang, M.-H. Jao, S. B. Darling, W.-F. Su, *Mater. Today* **2013**, *16*, 326-336.
- [21] K. R. Graham, J. Mei, R. Stalder, J. W. Shim, H. Cheun, F. Steffy, F. So, B. Kippelen, J. R. Reynolds, *ACS Appl. Mater. Interfaces* **2011**, *3*, 1210-1215.

- [22] Y. Huang, W. Wen, S. Mukherjee, H. Ade, E. J. Kramer, G. C. Bazan, *Adv. Mater.* **2014**, *26*, 4168-4172.
- [23] A. Sharenko, M. Kuik, M. F. Toney, T.-Q. Nguyen, *Adv. Funct. Mater.* **2014**, *24*, 3543-3550.
- [24] L. H. Nguyen, H. Hoppe, T. Erb, S. Günes, G. Gobsch, N. S. Sariciftci, *Adv. Funct. Mater.* **2007**, *17*, 1071-1078.
- [25] G. D. Sharma, M. A. Reddy, K. Ganesh, S. P. Singh, M. Chandrasekharam, *RSC Adv.* **2014**, *4*, 732-742.
- [26] A. J. Pearson, T. Wang, R. A. L. Jones, D. G. Lidzey, P. A. Staniec, P. E. Hopkinson, A. M. Donald, *Macromolecules* **2012**, *45*, 1499-1508.
- [27] X. Yang, A. Uddin, *Renew. Sust. Energy Rev.* **2014**, *30*, 324-336.
- [28] T. S. van der Poll, J. A. Love, T.-Q. Nguyen, G. C. Bazan, *Adv. Mater.* **2012**, *24*, 3646-3649.
- [29] J. A. Love, C. M. Proctor, J. Liu, C. J. Takacs, A. Sharenko, T. S. van der Poll, A. J. Heeger, G. C. Bazan, T.-Q. Nguyen, *Adv. Funct. Mater.* **2013**, *23*, 5019-5026.
- [30] L. Malatesia, M. Angoletta, *J. Chem. Soc.* **1957**, 1186-1188.
- [31] G.-y. Chen, S.-c. Lan, P.-y. Lin, C.-w. Chu, K.-h. Wei, *J. Polym. Sci., Part A: Polym. Chem.* **2010**, *48*, 4456-4464.

Chapter 7

Dicyanovinylene-Substituted Oligo(dithienopyrrole)s

7.1 Introduction

In *Chapter 6*, promising results were obtained for acceptor-substituted bidithienopyrrole (bi(DTP)) **183** (in this chapter referred to as “**203**”) concerning its light-harvesting and electrochemical properties as well as its photovoltaic performance in bulk-heterojunction solar cells (BHJSCs). In this chapter, DCV-substituted oligo(DTP)s **202**, **204**, and **205** containing one, three, and four DTP-units, respectively, are synthesized in order to build a homologous series (Chart 1). Furthermore, the optoelectronic and photovoltaic properties of this series are investigated. This aims at the extraction of structure-property relationships of DTP-based A-D-A systems. 1-Octylnonyl-substituted dithienopyrrole (DTP) was chosen as monomer-unit since it gave a satisfying solubility for bi(DTP) **203**. DCV was chosen over 2-cyanoacrylate as acceptor unit due to its high thermal and chemical stability and its stronger electron-accepting capability leading to a larger red-shift in absorption.^[1-3]

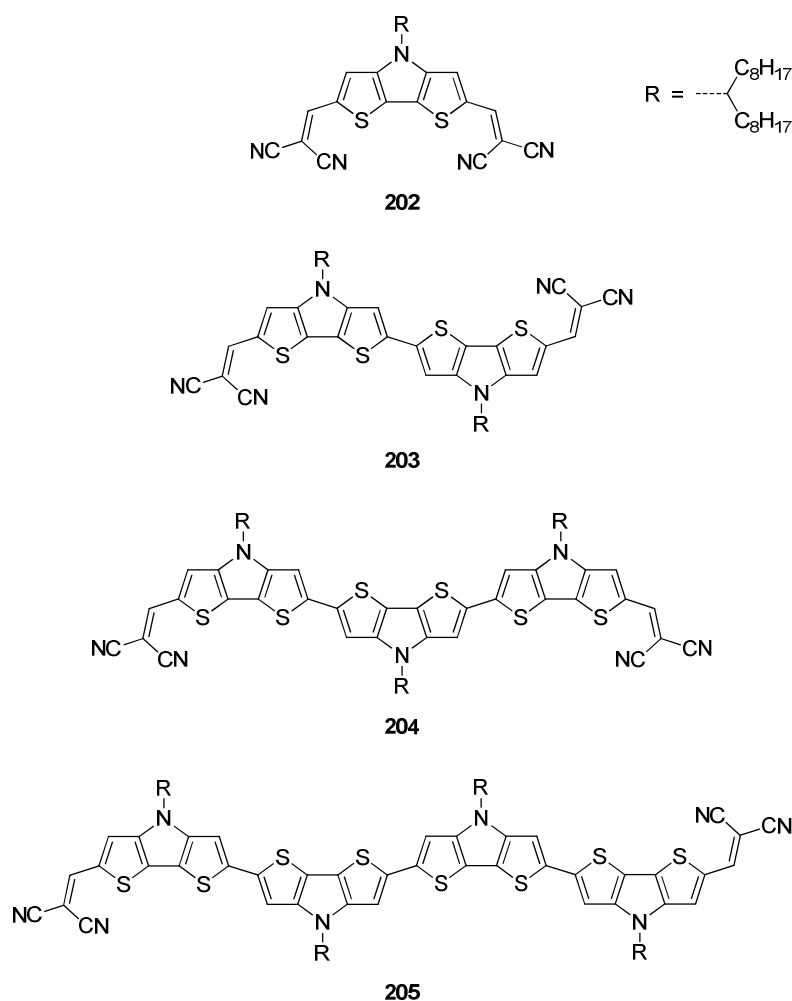


Chart 1. Chemical structure of DCV-substituted oligo(DTP) series **202-205**.

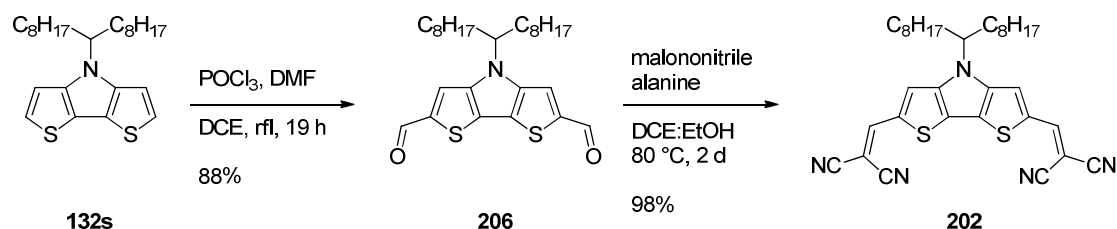
Good light-harvesting properties are expected with absorption bands approaching the near-infrared region and high extinction coefficients due to the usage of the strong electron-donating DTP-unit being known for increasing the extinction and the usage of strong electron-acceptor DCV. Additionally, numerous stabilized oxidation states are anticipated for longer homologues due to the electron-rich nature of DTP.^[4] Finally, an evaluation for the use of the structurally defined oligomers in OSCs is given.

7.2 Results and discussion

7.2.1 Synthesis of DCV-substituted oligo(DTP)s **202**, **204**, and **205**

Synthesis of DCV-substituted DTP **202**

DTP **202** was synthesized starting from DTP **132s** in two steps (Scheme 2). In the first step, **132s** (preparation described in *Chapter 6*) was converted in a Vilsmeier-Haack formylation to dialdehyde **206**. Therefore, DTP **132s** was reacted with 20 eq. of *N,N*-dimethylformamide (DMF) and phosphoryl chloride. Basic work-up then led to DTP dialdehyde **206** which was purified with column chromatography reaching a yield of 88%.

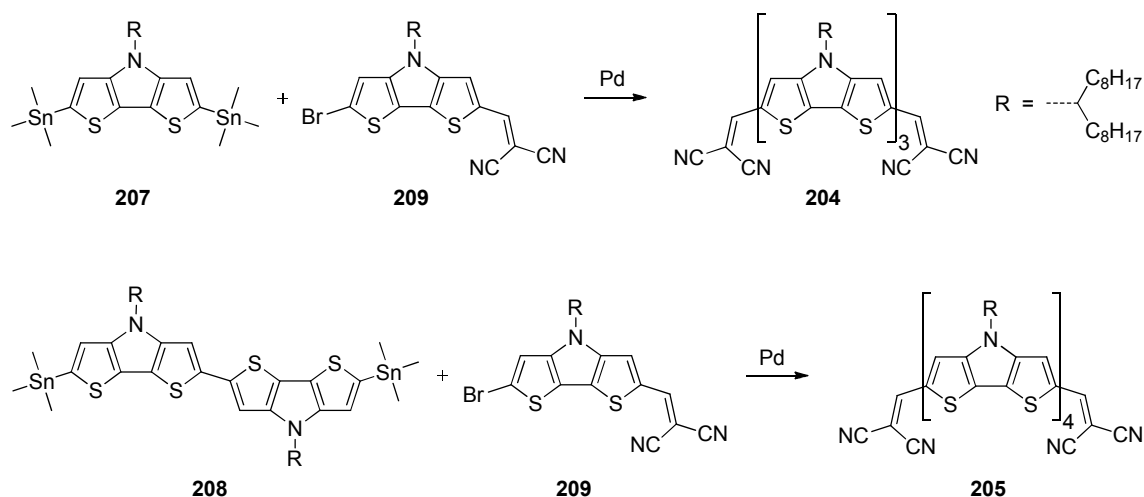


Scheme 1. Synthetic pathway to DCV-substituted DTP **202** starting from DTP **132s**.

The next step, the Knoevenagel condensation, was carried out under the same conditions used for the synthesis of DCV-substituted bi(DTP) **203** (see *Chapter 6*, there referred to as **183**). β -Alanine was used as catalyst and a dichloroethane (DCE):EtOH mixture served as solvent system. A nearly quantitative yield of 98% was reached for DCV-substituted DTP **203** after column chromatography.

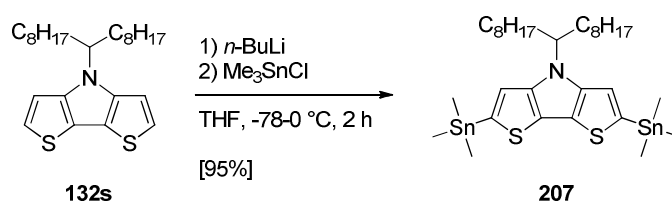
Synthesis of stannylated building blocks **207** and **208** as well as bromo-DTP **209**

In order to synthesize oligo(DTP)s **204** and **205** via Stille cross-coupling reaction distannylated building blocks **207** and **208** as well as halogenated DTP **209** had to be prepared (Scheme 2).



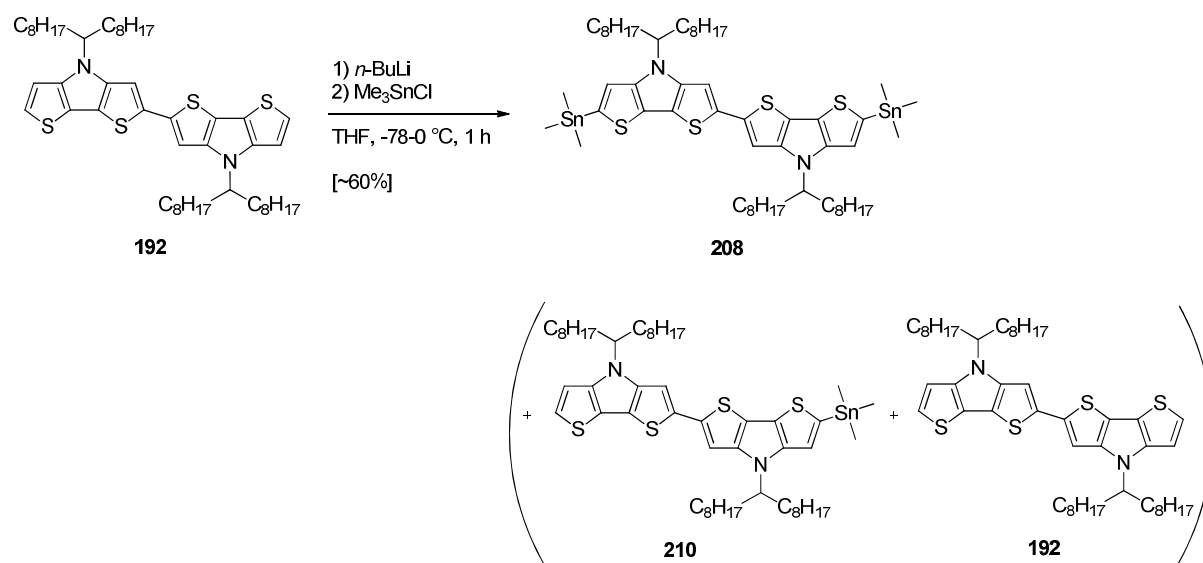
Scheme 2. Synthesis of oligo(DTP)s **204** and **205** via Stille cross-coupling reaction by reacting stannylated building blocks **207** and **208** with DCV-substituted bromoDTP **209**.

The synthesis of the precursors for stannylated building blocks DTP **207** and bi(DTP) **208** are described in *Chapter 6*. Stannylation of **132s** and **192**, shown in Scheme 3 and 4, respectively, was carried out with an 1.1-1.2 fold excess of *n*-butyllithium (*n*-BuLi) and lithiation temperatures of up to 0 °C to ensure high conversions to the metallated intermediates. Subsequent addition of the stannylation reagent (Me₃SnCl) was carried out at -78 °C. In doing so, it is important that Me₃SnCl is dissolved in as less solvent as possible since diluted solutions of Me₃SnCl led to lower conversions. In the case of distannyl-DTP **207** (Scheme 3), a high conversion of 95% was obtained which was determined by ¹H NMR spectroscopy. The crude product contained still some monostannylated side-product (~5%). Further purification was omitted because of presumable losses due to possible decomposition and the fact that the side-products can be more easily separated after the next reaction step.



Scheme 3. Synthesis of distannylated DTP **207**.

For distannyl-bi(DTP) **208**, the stannylation was carried out with the same reaction conditions as for the synthesis of stannylated DTP **207** (Scheme 4). Unfortunately, the excellent conversion obtained for DTP **207** could not be reproduced for bi(DTP) **208**. The reason for that is the higher electron density present at the unsubstituted α -positions of bi(DTP) **192** compared to those of DTP **132s** impeding lithiation. MALDI-TOF mass spectrometry and ^1H NMR spectroscopy of the crude product showed the presence of desired distannylated product **208** as well as monostannylated side-product **210** and remaining reactant **192**.



Scheme 4. Synthesis of distannylated bi(DTP) **208**.

The ratio of these three components can be extracted from the ^1H NMR spectrum of the crude product of **208** which is depicted in Figure 1. The aromatic peaks of the three components are superimposed in the region of 7.3–7.1 ppm. The inset is an magnification of the aromatic region of the spectrum. It shows two singlets: the one located at 7.28 ppm corresponds to the inner aromatic protons and the other with a chemical shift of 7.14 ppm and tin-satellites corresponds to the outer aromatic protons. The two hydrogens of the two carbons attaching the alkyl chains to the DTP experiences a chemical shift to 4.40–4.33 ppm; the affiliated methylene groups show two different chemical shifts: one at 2.16–2.08 ppm and the other one at 1.90–1.83 ppm; the residual methylene groups superimpose at 1.38–1.07 ppm; the methyl groups of the alkyl chains can be observed at 0.83 ppm as a well resolved triplet. Finally, the trimethylstannyl groups are located at 0.39 ppm manifesting in a singlet with Sn-satellites.

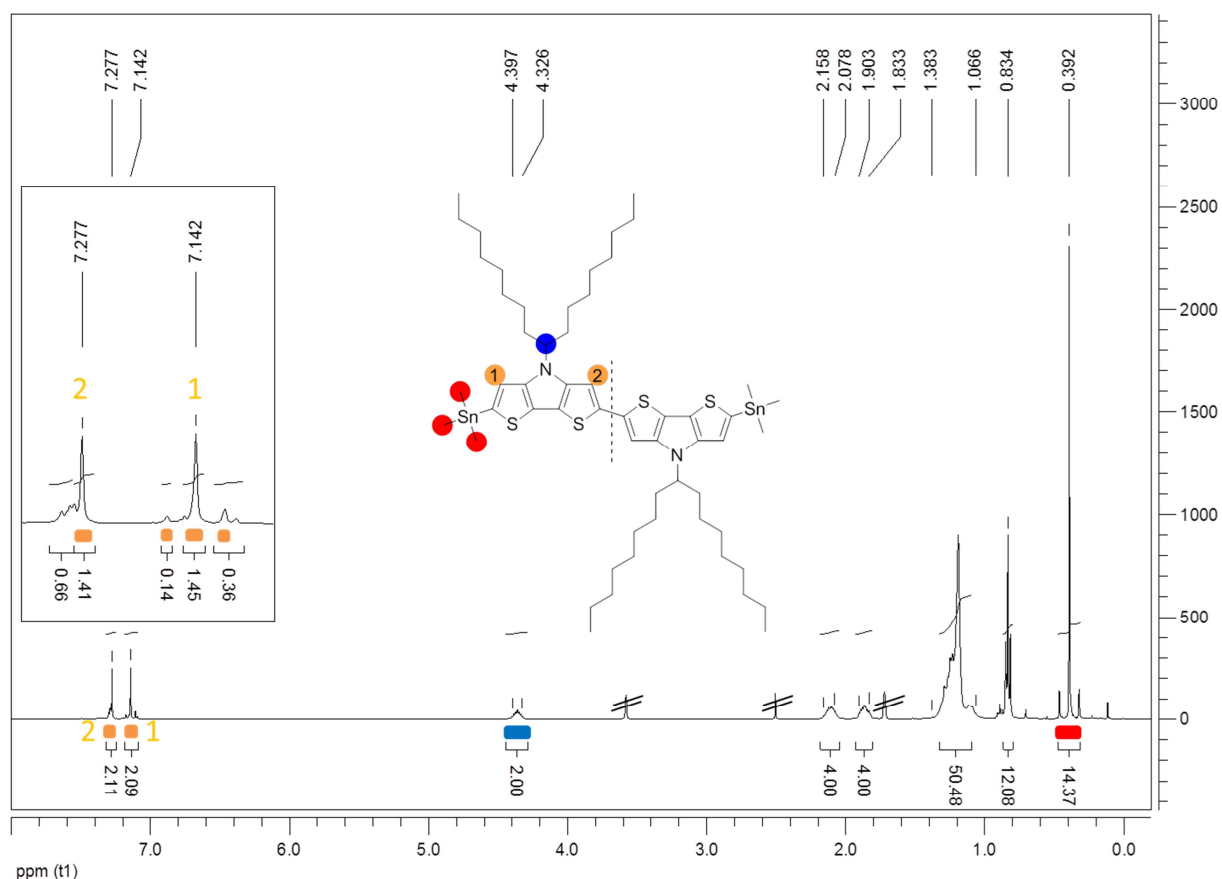
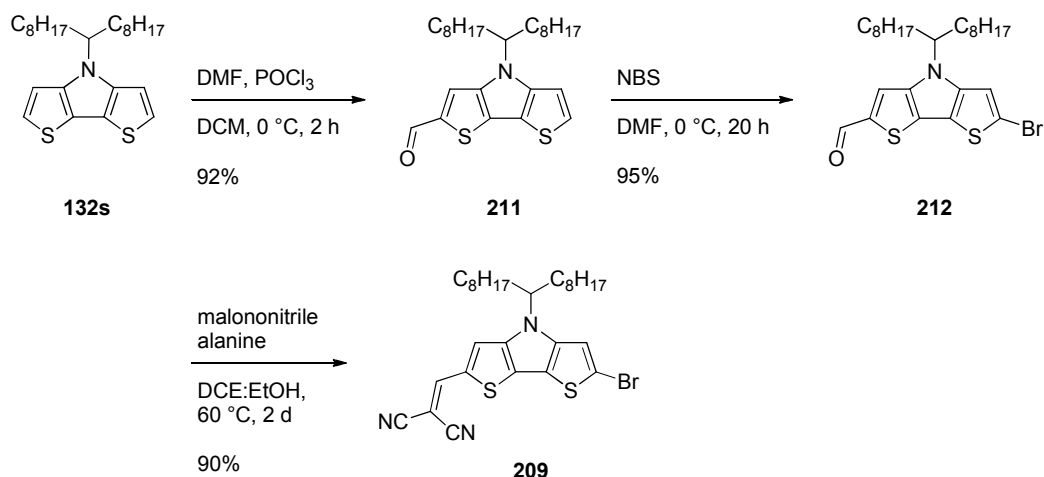


Figure 1. ^1H NMR spectrum of the crude product of bi(DTP) **208** in THF-d_8 . Inset: Magnification of the aromatic region. Blue and red marked groups are relevant for the calculation of the converted α -positions. THF-d_8 solvent residual peaks are located at 3.58 and 1.79 ppm. The peak at 2.46 ppm corresponds to water.

In order to determine the conversion of the free α -positions to stannyl groups, the integral of the blue marked protons were set to two, since **192**, **210**, and **208** have these in common. By dividing the integral of the stannyl groups by 18 (an integral of 18 would correspond to 100% conversion), integration analysis revealed that about 80% of the α -positions were bearing stannyl groups. The quite high conversion concerning insertion of stannyl groups proves that distannylated bi(DTP) **208** is the main product whereupon the peaks at 7.28 and 7.14 ppm were assigned to the DTP protons of product **208**. From these results a conversion of at least 60% concerning distannyl-bi(DTP) **208** is given. Similar to distannylated DTP **207**, further purification of the crude product was skipped for **208** as well.

DCV-substituted bromo-DTP **209** was synthesized according to the reaction sequence elaborated in the Institute of Organic Chemistry II and Advanced Materials, Ulm University which is illustrated in Scheme 5.^[7] Selective Vilsmeier-Haack monoformylation of DTP **132s** towards aldehyde **211** is obtained, when milder reaction conditions were applied as for synthesis of dialdehyde **206** (*vide supra*). 5 Eq. of Vilsmeier reagent and stirring at 0 °C was sufficient to reach complete consumption

of the reactant within 2 h. TLC proved selective monoformylation since no dialdehyde was detected. This is due to a strong deactivation of the monoreacted intermediate with respect to a second substitution.^[7] Silica column chromatography afforded DTP monoaldehyde **211** in 92% yield.



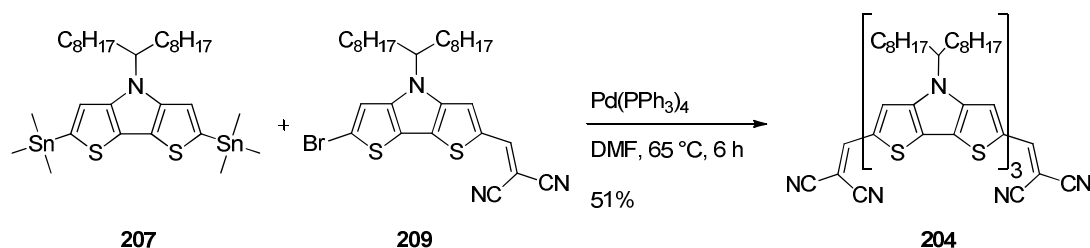
Scheme 5. Synthesis of brominated building block **209**.

In the following reaction, DTP **211** was subjected to a bromination using *N*-bromosuccinimide (NBS). The presence of the aldehyde group in **211** reduced the reactivity of the DTP-unit towards aromatic electrophilic substitutions. However, reacting **211** with one eq. NBS at 0 °C was sufficient to obtain full conversion which is due to the electron-rich character of the DTP-unit. Subsequent column chromatography yielded 95% bromo-DTP aldehyde **212**.^[7] In the last step, Knoevenagel condensation with conditions already used for the synthesis of DCV-substituted DTP **202** and DCV-substituted bi(DTP) **203** was carried out. For DCV-DTP **209** a yield of 90% was reached which is somewhat lower than for the synthesis of **202** and **203**. The reason for that was residual malononitrile and an additional unidentified impurity which could not be separated by silica chromatography. Thus, recrystallization from ethanol was necessary which led to slight losses in yield. However, pure brominated building block **209** was afforded in an overall yield of 79% within three steps starting from DTP **132s**.

Synthesis of DCV-substituted ter(DTP) **204** and quater(DTP) **205**

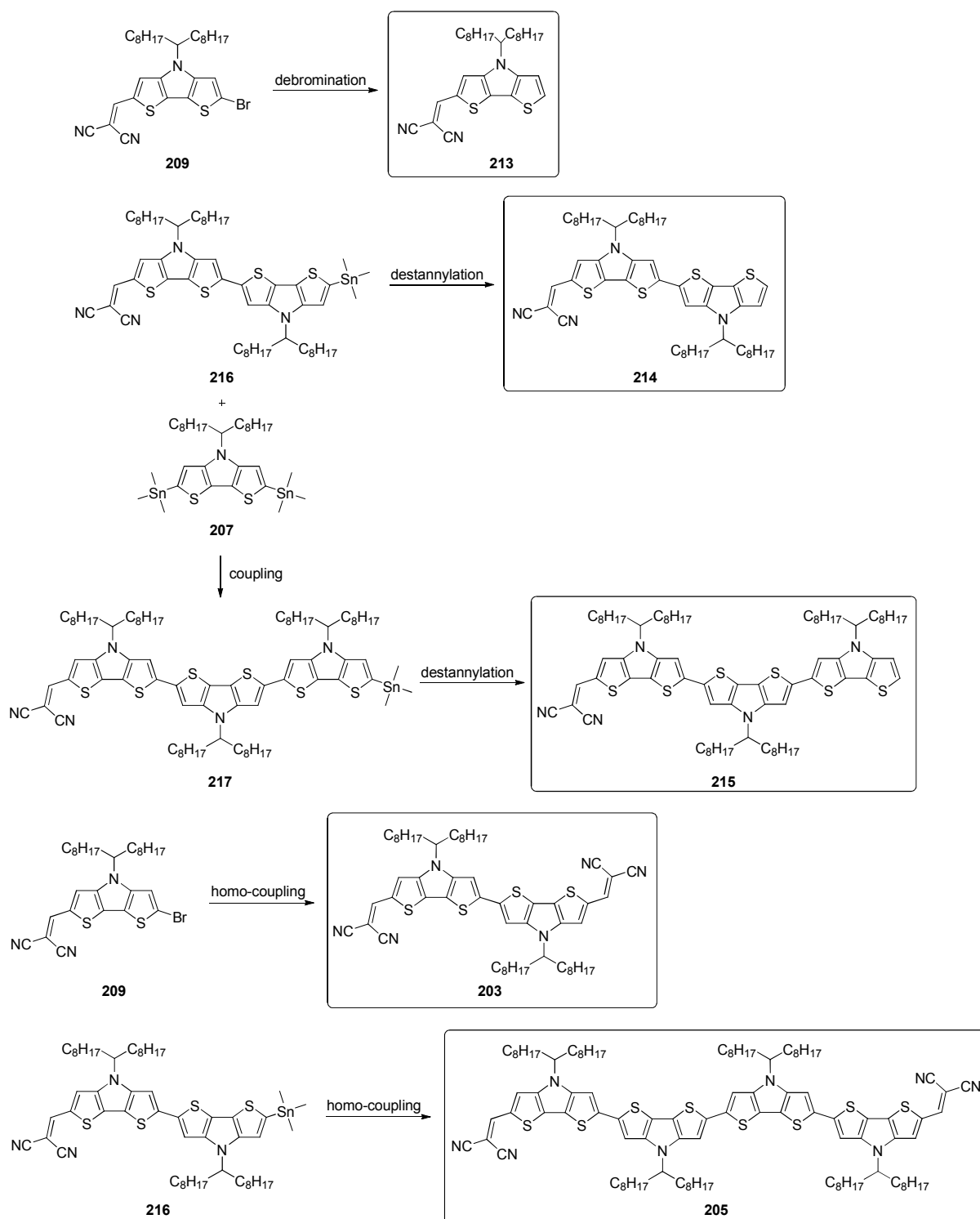
Stille cross-coupling reaction of distannylated building blocks **207** and **208** with brominated DTP **209** was carried out using Pd(PPh₃)₄ as catalyst, since it proved to be suitable for the synthesis of DTP-containing structurally defined co-oligomers in *Chapter 5*.

Regarding the synthesis of ter(DTP) **204** (Scheme 6), bromo-DTP **209** was reacted with distannylated DTP **207**. In order to ensure full conversion of stannylated building block **207**, the reaction was performed with an excess of bromo-DTP **209**.



Scheme 6. Stille cross-coupling reaction towards DCV-substituted ter(DTP) **204**.

Reaction control by TLC showed several spots besides one main product, pointing to the formation of various side-products. Firstly, column chromatography on silica gel was used to separate the main product band. In doing so, monoDCV *n*-meric DTP ($n = 1, 2, 3$) **213-215** could be separated (proven by MALDI-TOF mass spectrometry). These side-products (Scheme 7) arose by debromination of reactant **209**, destannylation of the mono-coupling intermediate **216**, and for monoDCV ter(DTP) **215** when another distannyl DTP **207** is coupled with **216** and then destannylated. It has to be taken into account that **207** also contained around 5% monostannylated DTP promoting the formation of **214**. In the next purification step, the main band from silica gel column chromatography was subjected to size exclusion chromatography (SEC) since MALDI-TOF mass spectrometry showed beside product **204** and some minor impurities the presence of shorter and longer homologue **203** and **205**, respectively (Scheme 7). Those two were formed due to homo-coupling reaction of reactant **209** and mono-coupling intermediate **216**. After SEC, $^1\text{H-NMR}$ spectroscopy and MALDI-TOF spectrometry showed mainly product **204** with small amounts of **205** and some unassigned minor impurities. DCV-substituted bi(DTP) **203** was more readily separated from **204** by SEC than quater(DTP) **205**. This is due to the fact that elongation by one 1-octyl-1H-indole-3-yl-DTP unit has a bigger influence on the molecular size when going from bi(DTP) **203** to ter(DTP) **204** than going from ter(DTP) **204** to quater(DTP) **205**. Final purification was realized via HPLC affording pure DCV-substituted ter(DTP) **204** in 51% yield. The moderate yield is due to the excessive purification which was necessary to isolate trimer **204**. The major reasons for that are homo-coupling and destannylation.



Scheme 7. Formation of side-products **213-215** and **203** and **205** during Stille cross-coupling reaction towards DCV-substituted ter(DTP) **204**.

In Figure 2, the ^1H NMR spectrum of pure product **204** is depicted. The chemical shift for the vinyl protons is shifted downfield to 7.71 ppm. The DTP-protons adjacent to the DCV-groups are located at 7.61 ppm due to the strong electron-withdrawing effect of the DCV group. The aromatic protons in

the center of the molecule are positioned at 7.21 and 7.09 ppm, whereas the protons being more remote from the acceptor groups are observed at higher chemical shifts. The peaks for the protons in the branched alkyl chains show up in a similar pattern as the ones in the ^1H NMR spectrum of stannylated bi(DTP) **208** (*vide supra* or see section 7.4.2).

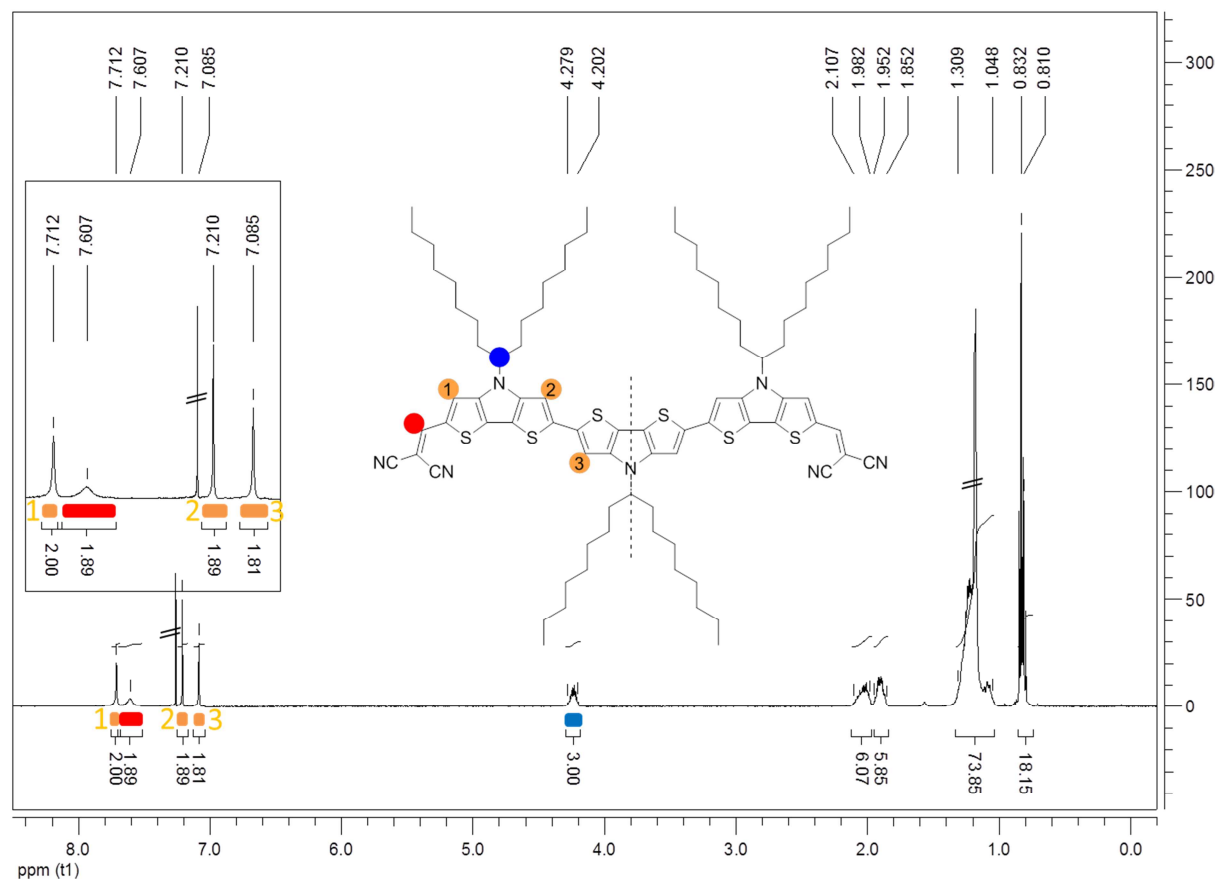


Figure 2. ^1H NMR spectrum of DCV-substituted ter(DTP) **204** in CDCl_3 after purification via HPLC. Inset: Magnification of the aromatic region. CDCl_3 solvent residual peak is located at 7.26 ppm. The peak at 1.56 ppm corresponds to water.

Figure 3 shows the MALDI-TOF mass spectrum of DCV-substituted ter(DTP) **204** possessing a calculated mass of $m/z = 1399$. Two masses were found: $m/z = 1400$ corresponding to $[\text{M}+\text{H}]^+$ and $m/z = 1415$ corresponding to the oxidized species $[\text{M}+\text{O}]^+$. The emergence of the oxidized species hints to a high lying highest occupied molecular orbital (HOMO) energy level which leads probably to oxidation during the ionization process.

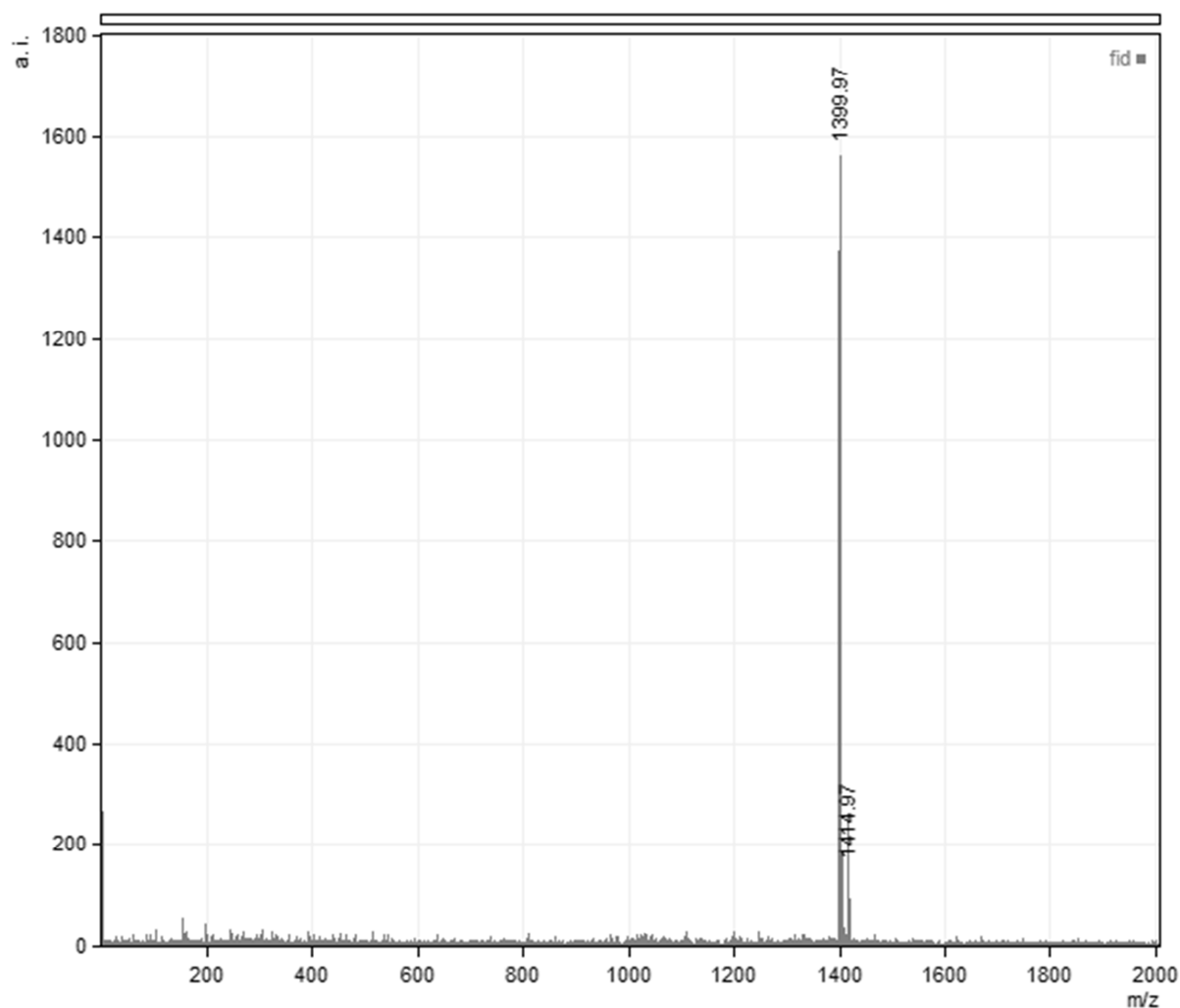
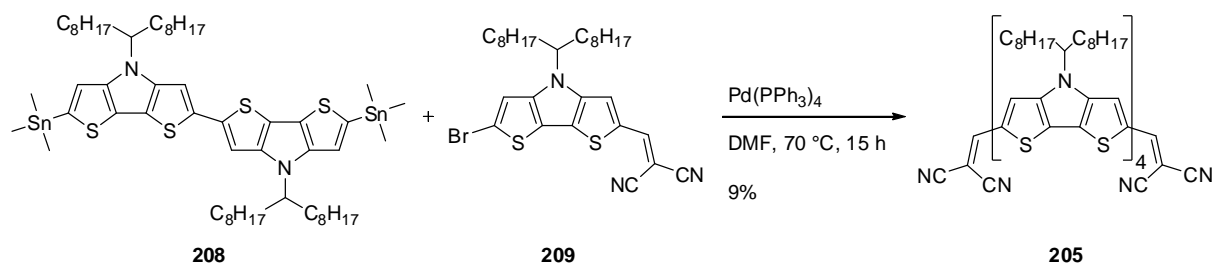


Figure 3. MALDI-TOF mass spectrum of DCV-substituted ter(DTP) **204** after purification via HPLC.

DCV-substituted quater(DTP) **205** was synthesized with the same Stille cross-coupling conditions used for the synthesis of shorter homologue **204** by reacting distannyl-bi(DTP) **208** with brominated DTP **209** (Scheme 8).



Scheme 8. Stille cross-coupling reaction towards DCV-substituted quater(DTP) **205**.

The reaction time for the synthesis of quater(DTP) **205** was elongated to 15 h compared to 6 h in the case of ter(DTP) **204** in order to ensure complete conversion of distannylated bi(DTP) **208**. After the reaction was stopped, the crude product was subjected to silica gel column chromatography. However, the separation was not very good which is due to the similar chemical structure of the product and most of the side-products. Nevertheless, short DTP oligomers, for example the mono-coupling side-product **215** or homo-coupling product of **209**, namely bi(DTP) **203**, could be removed. Repetitive SEC was more suitable to further purify **205** since most of the impurities were oligo(DTP) derivatives consisting of two DCV groups and three or five DTP-units. Due to the assumed high lying HOMO energy level of quater(DTP) **205**, decomposition may take place during SEC. Hence, for the final purification, once again column chromatography was applied. In the end, DCV-substituted quater(DTP) **205** could be isolated in a yield of 9% (the purity based on ^1H -NMR spectroscopy was determined to be >95%). Reasons for the low yield are the formation of many side-products impeding efficient isolation and purification of product **205**. Identified side-products were mono- and diDCV-substituted oligo(DTP)s with two to eight DTP-units (**203**, **215**, **218**, **219**, **220**, and **221**, Chart 2; proven by MALDI-TOF mass spectrometry) with yields <2% each.

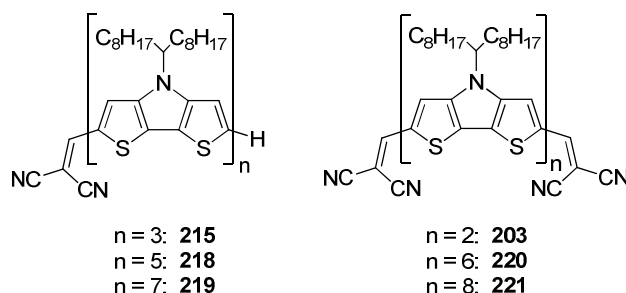


Chart 2. Side-products being formed during the Stille cross-coupling reaction towards quater(DTP) **205**.

This result implies a quite high amount of homo-coupling which was also observed during the synthesis of shorter homologue **204**. Furthermore, an estimated high lying HOMO energy level might decrease the stability and lead to oxidation/decomposition during the reaction and the purification process. It has to be noted that **204** showed limited stability in solution and when stored as solid under ambient conditions as well. Figure 4 and 5 show the ^1H NMR and MALDI-TOF mass spectrum of purified quater(DTP) **205**. The ^1H NMR spectrum resembles the one of **204**, except of course an additional aromatic peak due to the increased oligo(DTP) length. The chemical shifts for the aromatic protons of quater(DTP) **205** are shifted to low field compared to those of ter(DTP) **204** which is ascribed to the use of different solvents (THF-d_8 and CDCl_3 , respectively). THF-d_8 was used as solvent

since decomposition initiated faster in CDCl_3 -solutions which is most probably due to the presence of acidic impurities within CDCl_3 resulting from solvent decomposition.

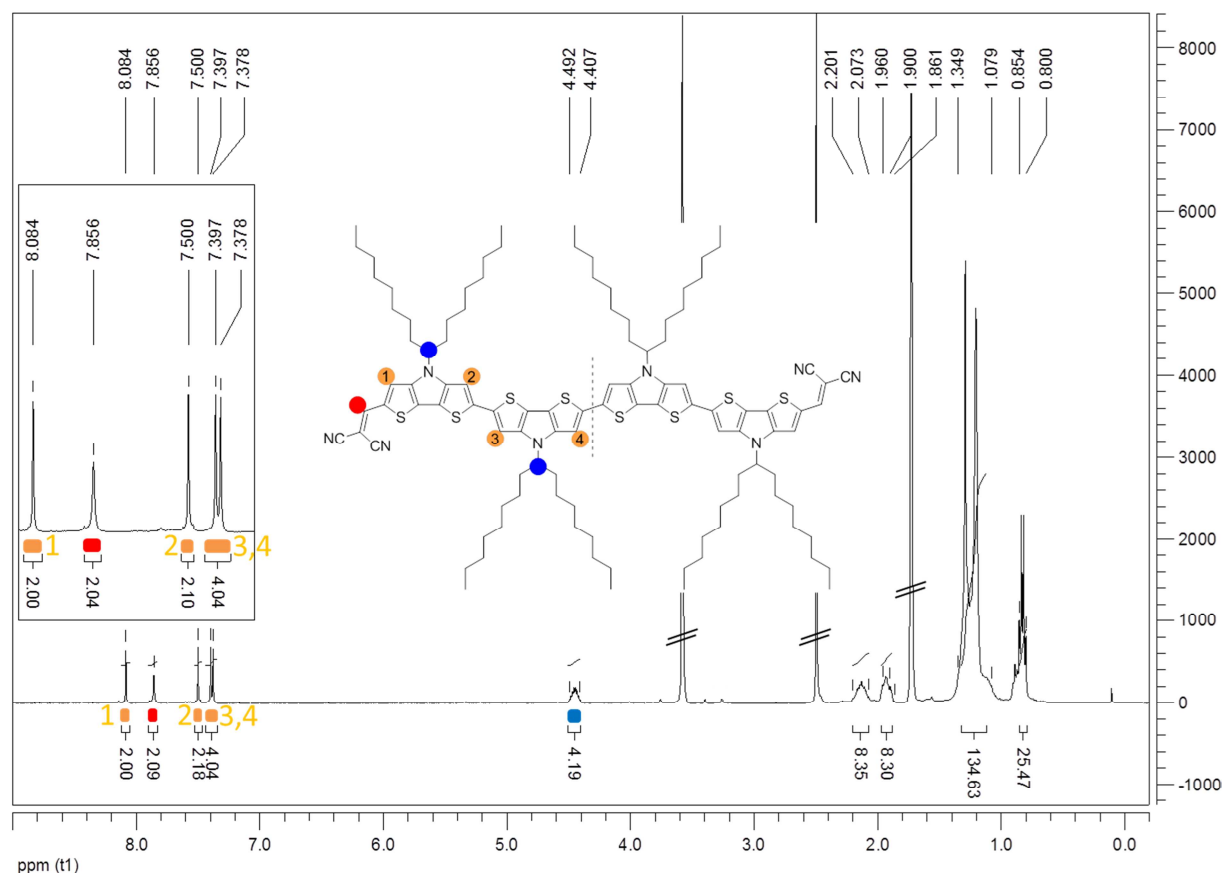


Figure 4. ^1H NMR spectrum of DCV-substituted quater(DTP) **205** in THF-d_8 after repetitive SEC and column chromatography. Inset: Magnification of the aromatic region. THF-d_8 solvent residual peaks are located at 3.58 and 1.79 ppm. The peak at 2.46 ppm corresponds to water.

The vinylic proton of the DCV groups of quater(DTP) **205** possesses a chemical shift of 7.86 ppm and is better resolved than the corresponding one of ter(DTP) **204** (Figure 2). The adjacent aromatic DTP-proton is located at 8.08 ppm. The following three aromatic peaks at 7.50, 7.40, and 7.38 ppm correspond to the residual protons at the DTP-units, whereas the protons being more remote from the acceptor groups are observed at higher chemical shifts. The assignment of the alkyl protons is the same as in other 1-octylnonyl DTP-based compounds (for a more detailed assignment see section 7.4.2).

MALDI-TOF mass spectrometry of DCV-substituted quater(DTP) **205** showed a mass peak at $m/z = 1816$ matching well to $[\text{M}+\text{H}]^+$ (calculated mass of **205**: $m/z = 1815$). Similar to the mass spectrum of ter(DTP) **204** (*vide supra*), an additional peak with weaker intensity was observed with $m/z = 1831$

corresponding to $[M+O]^+$. This result points out the sensitivity of **205** towards oxidation. Whether the addition of oxygen happened before or during ionization is unclear since NMR spectroscopy in fact revealed the presence of only one compound but traces of the oxidized species of **205** might lie below the detection limit.

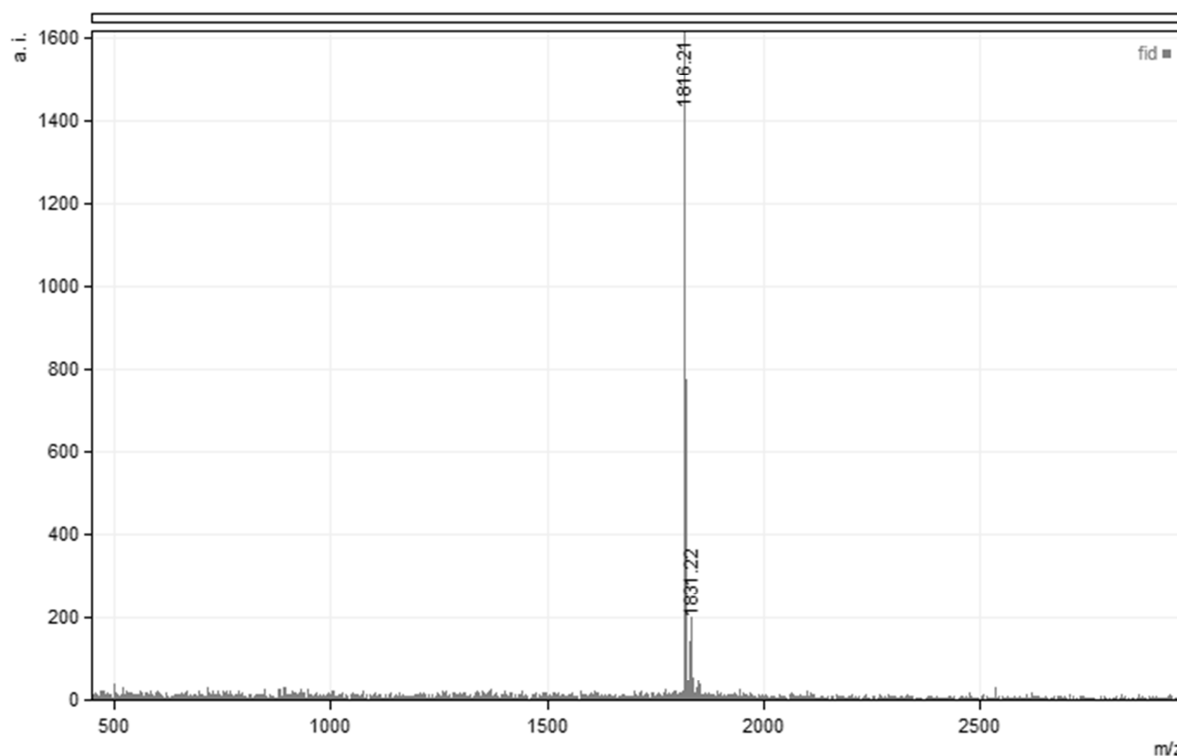


Figure 5. MALDI-TOF mass spectrum of DCV-substituted quater(DTP) **205** after repetitive SEC and column chromatography.

7.2.2 Optical properties of DCV-substituted oligo(DTP)s **202-205**

Absorption spectroscopy of A-D-A oligo(DTP)-based series **202-205** was measured in chloroform and in thin films (Figure 6). The corresponding data are summarized in Table 1. The oligo(DTP) series showed absorption maxima from 521 nm for DTP **202** to 642 nm for quater(DTP) **205** in solution. Three trends can be observed upon elongation of the donor moiety of A-D-A DTP-based oligomers **202-205**: 1) Red-shift of the absorption maximum. 2) Loss of the vibrational fine-structure. 3) Increase in extinction coefficient. 4) Broadening of the absorption band from $2,151\text{ cm}^{-1}$ for **202** to $3,489\text{ cm}^{-1}$ for **205**. However, the more DTP-units are introduced the less intense the red-shift, the band broadening and the increase in extinction coefficient in comparison to the preceding homologue.

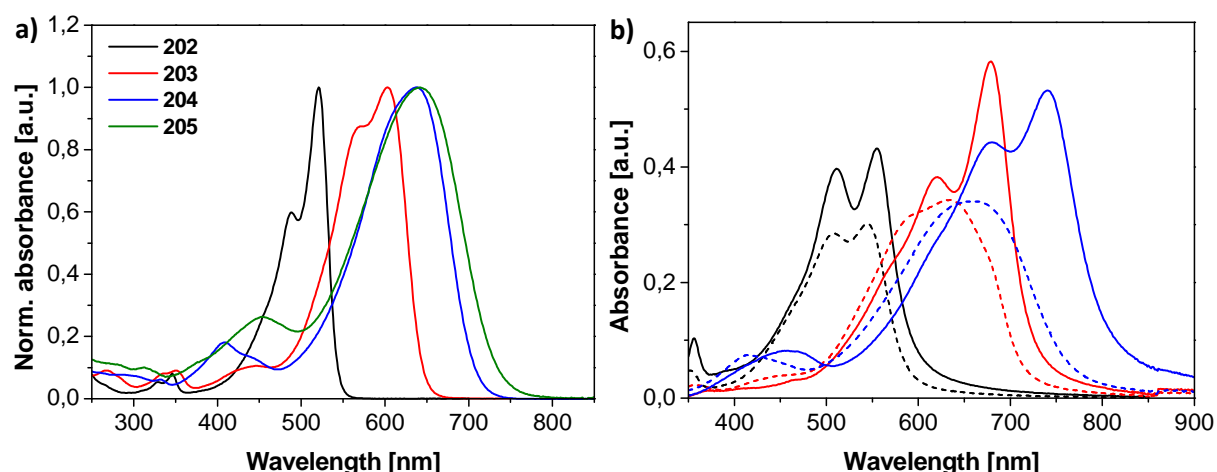


Figure 6. (a) Absorption spectra of **202-205** in chloroform solution. (b) Absorption spectra of **202** (black), **203** (red), and **204** (blue) in thin films on glass substrates: as-cast from chloroform (dashed line) and annealed at 80 °C (solid line).

As a result of the red-shifted absorption maxima and broadened absorption bands for longer homologues compared to the shorter ones, the absorption onset was similarly shifted to longer wavelengths from 541 nm for DTP **202** to 726 nm for quater(DTP) **205**. This led to an optical band gap (ΔE_{opt}) of 2.29 eV to 1.70 eV for this series. The red-shift of the absorption maxima for longer homologues can be explained by the increased donor strength in longer oligo(DTP)s. In the case of **202**, two DCV groups are directly attached to one DTP-unit. Hence, it experienced the most blue-shifted absorption maximum and onset as well as the lowest extinction coefficient which is still considerably high with $104,700 \text{ M}^{-1}\text{cm}^{-1}$. Additionally, due to the rigid and planar DTP π -system a well resolved fine structure can be observed with a vibrational shoulder-type peak at 488 nm. Going to bi(DTP)-based oligomer **203**, absorbing at 603 nm, the fine structure is less distinct which is due to the C-C rotation between the two DTP-units. Additionally, the absorption band broadens possessing a FWHM of 2803 cm^{-1} . Despite that, the extinction coefficient increased to $125,600 \text{ M}^{-1}\text{cm}^{-1}$ compared to **202** ($104,700 \text{ M}^{-1}\text{cm}^{-1}$). Ter(DTP) **204** and quater(DTP) **205** do not show a vibrational fine structure anymore. However, additional weaker absorption bands at 408 and 453 nm are observed. These absorptions correspond quite well with the absorption maxima of unsubstituted bi(DTP) **148** (410 nm) and ter(DTP) **151** (464 nm), for which reason they are ascribed to π - π^* absorptions within the donor backbone. For **202** and **203**, weak absorptions with vibrational splitting at $\sim 350 \text{ nm}$ are detected which might correspond to the π - π^* absorption of the DTP moiety, as seen in **132f**.^[5]

Table 1. Optical data of A-D-A oligoDTPs **202-205** in chloroform ($c = 10^{-5}$ M) and **202-204** in thin films on glass.

oligomer	λ_{abs} [nm] (ϵ [$\text{M}^{-1}\text{cm}^{-1}$])	FWHM [cm^{-1}]	$\lambda_{\text{abs,onset}}$ [nm]	ΔE_{opt} [eV] ^[a]	$\lambda_{\text{max,film}}$ [nm]	FWHM _{film} [cm^{-1}]	$\lambda_{\text{abs,film,onset}}$ [nm]	$\Delta E_{\text{opt,film}}$ [eV] ^[a]
202	521 (104700)	2151	541	2.29	555 (544) ^[b]	3634 (4086) ^[b]	595 (587) ^[b]	2.08 (2.11) ^[b]
203	603 (125600)	2803	643	1.93	679 (633) ^[b]	2688 (4048) ^[b]	723 (718) ^[b]	1.72 (1.73) ^[b]
204	638 (138900)	3019	706	1.76	741 (661) ^[b]	3354 (4010) ^[b]	806 (768) ^[b]	1.54 (1.61) ^[b]
205	642 (- ^[c])	3489	726	1.70	-	-	-	-

[a] Calculated by the low energy onset of λ_{max} . [b] As-cast thin film. [c] Not determined due to decomposition of **205** when dissolved for longer times.

The changes in absorption maximum, absorption onset and ΔE_{opt} between **204** and **205** became rather small in comparison to those of **202** and **203** or **203** and **204**. In Figure 7a-f these three optical characteristics are plotted vs. the number (Figure 7a-c) or the inverse number (Figure 7d-f) of DTP-units n in DCV-substituted oligo(DTP)s **202-205**.

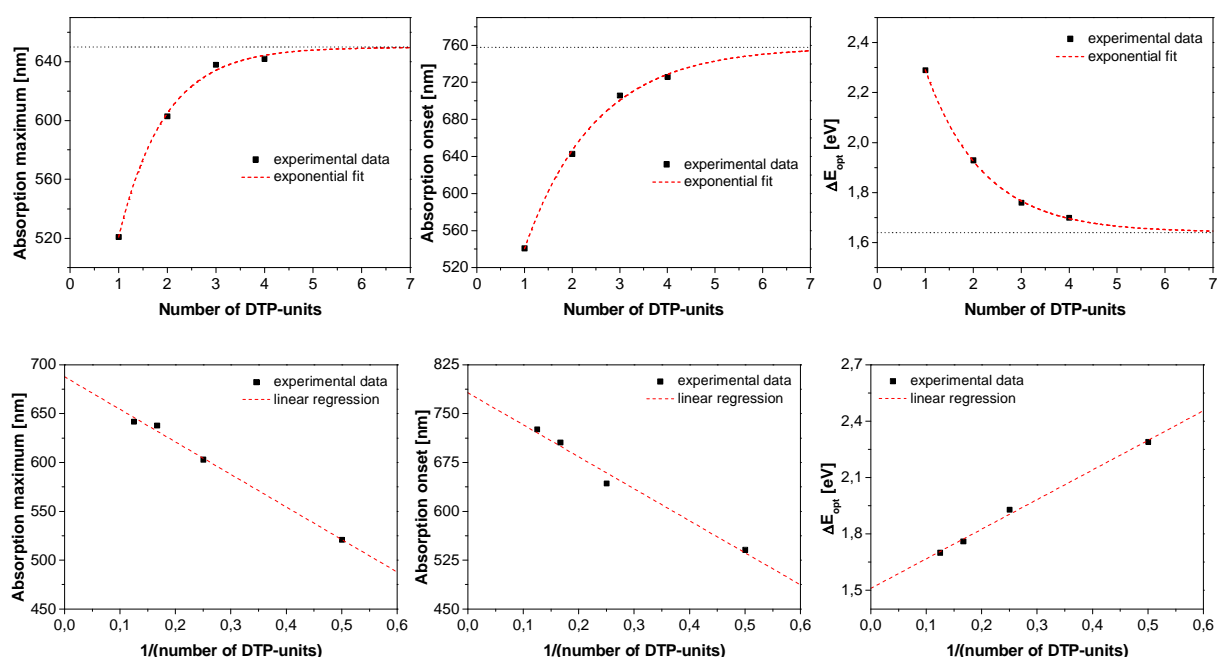


Figure 7. (a) / (d) Absorption maximum, (b) / (e) absorption onset, and (c) / (f) optical band gap in dependence of the number of DTP-units within A-D-A oligothiophenes **202-205**. Logarithmic fits in order to extrapolate the data for longer (DTP)_n ($n > 4$) are shown in (a), (b), and (c). The corresponding linear fits are shown in (d), (e), and (f).

It can be clearly seen that all three characteristics reach thresholds for $n \rightarrow \infty$. Hence, logarithmic and linear fits were used to estimate the properties of even longer homologues. The thresholds obtained from the two different fittings differ slightly. Using the logarithmic fitting the thresholds were calculated to be 650 nm for the absorption maximum, 758 nm for the absorption onset, and 1.64 eV for the optical band gap. In case of the linear fitting, the ordinate intercepts equal to the thresholds: 688 nm for the absorption maximum, 782 nm for the absorption onset, and 1.51 eV for the optical band gap. However, the thresholds might be slightly overestimated since **202** is a special case due to the two DCV-units being attached to the same DTP-unit which is not the case for longer homologues. Disregarding **202** for the fitting would lead to steeper slopes and hence to lower thresholds for the absorption maximum and onset and to a higher threshold for the band gap.

Thin film absorption spectroscopy was measured for oligo(DTP)s **202-204**. In *Chapter 5*, the sensitivity of **203** towards thermal annealing was shown. Hence, absorption spectra of as-cast and thermally annealed thin films were measured and are depicted in Figure 6b. As-cast thin films of **202-204** possessed absorption maxima located at 544, 600, and 661 nm, respectively being red-shifted 23-30 nm compared to their absorption maxima in solution. The absorption onset values were shifted by 46-75 nm to higher wavelengths as well. Hence, **202-204** showed optical band gaps of 2.11, 1.73, and 1.61 eV, respectively in as-cast thin films. Upon annealing at 80 °C under argon atmosphere the absorption bands of the structurally defined oligomers are red-shifted and increased. This effect is more pronounced for longer homologues **203** and **204** than for **202** due to the emergence of an intense low energy absorption which could be due to π - π stacking. Another reason could be that the randomly disordered molecules rearrange in a face-on orientation relative to the substrate increasing the absorption cross-section area and hence its absorptivity. As a result of this, the absorption maxima are further red-shifted to 595, 723 and 806 nm for DTP **202**, bi(DTP) **203**, and ter(DTP) **204**, respectively. It has to be noted that the thin film of DCV-substituted ter(DTP) **204** had to be annealed for 15 min at 80 °C until it showed its final absorption curve as depicted in Figure 6b, whereas for thin films of shorter homologues **202** and **203** 1 min was sufficient. The reason might be the increased number of alkyl chains in **204** and the more flexible π -conjugated backbone compared to **202** and **203** requiring higher activation energy and hence a longer time to reorder.

7.2.3 Electrochemical properties of DCV-substituted oligo(DTP)s **202-205**

Cyclic voltammetry of structurally defined oligomers **202-205** was measured in dichloromethane (DCM) using tetra-*n*-butylammonium hexafluorophosphate ($n\text{-Bu}$)₄NPF₆ as supporting electrolyte

(Figure 8). Redox potentials, the electrochemically determined bandgaps as well as the HOMO and lowest unoccupied molecular orbital (LUMO) energy levels are listed in Table 2.

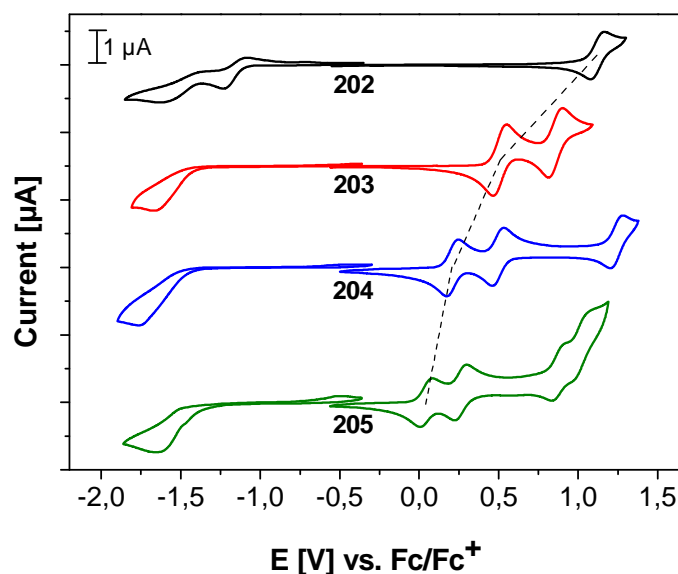


Figure 8. Cyclic voltammograms of **202-205** measured in DCM using $(n\text{-Bu})_4\text{NPF}_6$ (0.1 M) as supporting electrolyte at 100 mV s^{-1} ; $c = 5 \times 10^{-4} \text{ mol/L}$; dashed line: highlighted shift of E°_{ox1} towards lower potentials upon backbone elongation.

A-D-A Oligo(DTP)s **202-205** showed n reversible one-electron oxidation waves where n is the number of DTP-units within the corresponding structurally defined oligomer. In the reductive regime, DCV-substituted DTP **202** showed one quasi-reversible and one irreversible one-electron reduction wave in contrast to one irreversible two-electron reduction wave for **203-205**. The difference can be explained by the spatial separation of the DCV groups. In DTP-based A-D-A system **202**, both DCV groups are attached to the same DTP-unit equally withdrawing electron density from the DTP-moiety as well as from each other. Thus, the first reduction of **202** takes place at -1.17 V which is positively shifted in comparison to the one of longer homologues **203-205** ($E^\circ_{\text{red1}} = \sim -1.55 \text{ V}$), where the DCV groups do not affect each other noticeably. After the first reduction, **202** is charged with an additional electron, hence the second reduction occurs at more negative potentials ($E^\circ_{\text{red2}} = -1.52 \text{ V}$). In **203-205**, the reduction of both DCV groups happens simultaneously at $\sim -1.55 \text{ V}$. The reason for that is that the DCV groups are spatially separated by the donor moiety to such an extent that they do not influence each other's electron density anymore (at least regarding cyclic voltammetry measurements). Concerning the oxidative regime, E°_{ox1} of the A-D-A oligo(DTP)s **202-205** shifts to lower potentials with increasing conjugation length/number of DTP-units. Similar to the saturation effects in the optical data also E°_{ox1} seems to converge a threshold (see Figure 8, dashed line). DTP

202 experienced the highest E°_{ox1} with 1.12 V. Elongation by one, two, and three DTP-units led to E°_{ox1} of 0.51 V (**203**), 0.21 V (**204**), and -0.03 V (**205**), respectively. Bi(DTP) **203** exhibited two oxidations at 0.51 and 0.86 V, respectively. For ter(DTP) **204**, the first two oxidation potentials were shifted by 0.3 V to 0.21 and 0.50 V, respectively, compared to bi(DTP) **203**. E°_{ox3} of **204** takes place at 1.24 V. Interestingly, quater(DTP) **205** featuring four oxidation waves possesses a E°_{ox4} of 1.01 V meaning a lower potential than E°_{ox3} of **204**.

Table 2. Electrochemical data of **202-205** in DCM with (*n*-Bu)₄NPF₆ (0.1 M) as supporting electrolyte measured vs. Fc/Fc⁺ at 100 mV s⁻¹.

oligomer	E°_{ox1} [V]	E°_{ox2} [V]	E°_{ox3} [V]	E°_{ox4} [V]	E°_{red1} [V]	E°_{red2} [V]	E_{HOMO} [eV] ^[a]	E_{LUMO} [eV] ^[a]	ΔE_{CV} [eV] ^[b]
202	1.12	-	-	-	-1.17 ^[c]	-1.52 ^[c]	-6.15	-4.00	2.15
203	0.51	0.86	-	-	-1.58 ^[c]	-	-5.54	-3.68	1.86
204	0.21	0.50	1.24	-	1.53 ^[c]	-	-5.24	-3.64	1.60
205	-0.03	0.26	0.88	1.01	-1.55 ^[c]	-	-5.08	-3.69	1.39

[a] E_{HOMO} and E_{LUMO} calculated from the onset of E°_{ox1} and E°_{red1} , respectively; related to the Fc/Fc⁺-couple with an absolute energy of -5.1 eV. [b] Electrochemical band gap calculated to $\Delta E_{\text{CV}} = E_{\text{HOMO}} - E_{\text{LUMO}}$. [c] Taken from DPV measurement.

According to the decrease of E°_{ox1} within the oligo(DTP) series upon elongation of the conjugated backbone, HOMO energy levels are raised to higher values resulting in HOMO energy levels of -6.15, -5.54, -5.24, and -5.08 eV for **202-205**, respectively. This goes along with a reduction of the theoretical V_{OC} for the longer homologues when used as donor material in BHJSC. In *Chapter 6*, spin-coated BHJSCs of **203** (in *Chapter 6* referred to as “**183**”) yielded V_{OC} values of ~1.0 V. Hence, BHJSC of **204** and **205** should produce a V_{OC} of around 0.7 and 0.5 V, respectively. LUMO energy values of **203**, **204**, and **205** did not differ very much lying between -3.64 and -3.69 eV which would allow exciton separation in PC₆₁BM-based OSCs. DCV-substituted DTP **202** showed a higher lying LUMO energy level of -6.15 eV. Thus, **202** possesses nearly similar HOMO and LUMO energy levels as PC₆₁BM. Hence, BHJSCs with PC₆₁BM as acceptor and **202** as donor would result in low efficiencies due to insufficient exciton separation. However, **202** might be used as soluble acceptor material in OSCs. Corresponding to the optical band gap in solution, the electrochemical band gap is decreasing from 2.15 eV for DTP **202** to 1.86 eV and 1.60 eV for bi(DTP) **203** and ter(DTP) **204**, respectively, and finally to 1.39 eV for quater(DTP) **205**.

7.2.4 Photovoltaic performance of DCV-substituted ter(DTP) **204**

Photovoltaic performance of DCV-substituted ter(DTP) **204** was tested in PC₆₁BM-based BHJSCs and compared to that of DCV-substituted bi(DTP) **203**. Shortest homologue DTP **202** has unsuitable HOMO and LUMO energy levels concerning usage as donor in PC₆₁BM-based OSCs. This is proven by the low photovoltaic performance of 2-ethylhexyl derivative **175** in OSCs.^[6] In contrast to this, **202** could be used as acceptor substituting fullerene derivatives such as PC₆₁BM since it shows a stabilized negatively charged species in solution being a prerequisite for acceptor materials. Additionally, **202** possesses superior light-harvesting properties compared to soluble fullerenes which are commonly used in BHJSCs. However, other factors have to be considered as well when comparing acceptors such as miscibility with the donor, good electron transport mobility, or the availability of electron accepting states.^[8,9] In the case of DCV-substituted DTP **202**, the miscibility with donor materials synthesized in this thesis (**129-131**, **181-183**, and **203-205**) would be very high due to their structural similarities. Thus, a very homogeneously mixed blend layer would most probably not lead to an interpenetrating network of donor and acceptor resulting to low photovoltaic performance. Due to the sensitivity of DCV-substituted quater(DTP) **205** to oxygen, BHJSCs were not fabricated since the setup only allowed spin-coating under air exposure leading then to partial oxidation of the donor/blend layer. Consequentially, trap states would be present reducing photovoltaic performance to an unknown extent making evaluation of solar cell results impossible. Therefore, BHJSC fabrication was concentrated on DCV-substituted ter(DTP) **204** as donor blended with PC₆₁BM as acceptor. For **204**, a solubility of >100 mg/mL in chloroform was measured by absorption spectroscopy. In comparison to bi(DTP) **203**, this means a more than 2.5 fold increase and can be explained by the diminishing solubility decreasing effect of the polar DCV end groups upon elongation of the π -conjugated backbone with 1-octylnonyl-functionalized DTP-units. Absorption spectroscopy of thin films blended with PC₆₁BM are shown in Figure 9 and are compared to **203**:PC₆₁BM films (see *Chapter 6*). Similar to the thin film absorption spectrum of DCV-substituted ter(DTP) **204** (Figure 6b), **204**:PC₆₁BM (2:1) blend layers responded to thermal annealing as well leading to a more intense and red-shifted absorbance (Figure 9). The absorption maximum of annealed **204**:PC₆₁BM blend layers was red-shifted to 736 nm compared to the as-cast thin film absorbing at 647 nm. The same effect is observed for **203**:PC₆₁BM (2:1) blend layers and can be explained by a reordering of the donor molecules. It is assumed that the donor molecules are in a random disorder within the as-cast blend layer. By annealing, the majority of the donor molecules rearranges, so that the π -systems are oriented face-on relative to the substrate increasing the absorption cross-section area and hence improve light-harvesting of photons entering the substrate

perpendicularly. Another explanation could be the rearrangement of the long alkyl chains leading to an improved packing of the π -conjugated backbones.

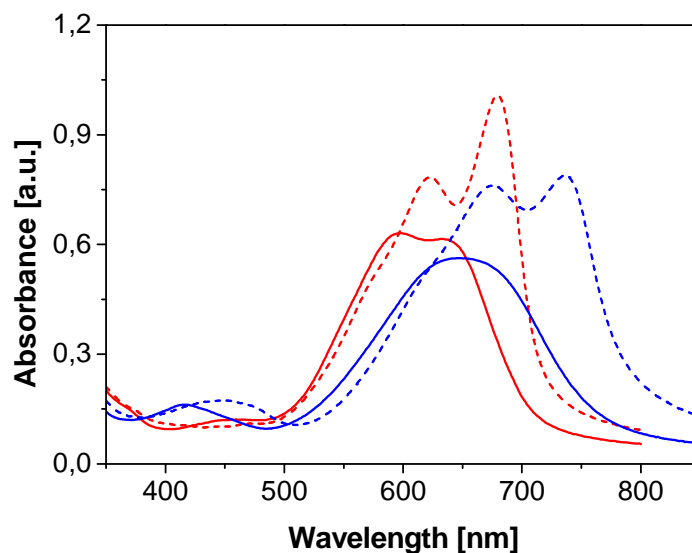


Figure 9. Absorption spectroscopy of as-cast (solid lines) and thermally annealed (dashed lines) thin films of **204**:PC₆₁BM (blue) and **203**:PC₆₁BM blends (red) with a D:A ratio of 2:1, spin-coated from chloroform on PEDOT:PSS covered ITO glass with a spin-coating velocity of 1000 rpm.

Firstly, BHJSC with a standard device structure: ITO|PEDOT:PSS(~35 nm)|**204**:PC₆₁BM|LiF(~0.7 nm)|Al(~100 nm) were fabricated using different D:A ratios (Table 3). BHJSCs with high donor contents showed inferior PCEs of around 0.5% (D:A ratio = 2:1) compared to cells with D:A ratios of 1:1 or 1:2 yielding PCEs of 1.1-1.2%. As-cast cells of shorter homologue bi(DTP) **203** showed the same trend concerning D:A ratio and photovoltaic performance (see *Chapter 6*, Table 5). Thermal annealing had massive impact on the PCE of devices using **203** as donor material, especially for a D:A ratio of 2:1. Hence, devices listed in Table 3 were thermally annealed at 80 °C under argon atmosphere to improve their photovoltaic parameters. However, a lower sensitivity to thermal annealing was found for devices containing donor ter(DTP) **204** in comparison to **203**. For DCV-substituted bi(DTP) **203**, the PCE of cells with a D:A ratio of 2:1 could be raised by a factor of ~8 by 40 min of thermal annealing at 80 °C under argon atmosphere (longer annealing times led to deterioration). In the case of ter(DTP) **204**, the PCE of equally prepared devices experienced a rather moderate improvement from 0.46 to 0.53% by 2 min of thermal annealing at 80 °C under argon atmosphere. Despite the fact that both blend layers experienced better light-harvesting properties upon annealing (Figure 9) but only the PCE of bi(DTP) **203**-based devices was raised significantly proves that not only the spatial arrangement of the molecules but also changes of the morphology play a major role during thermal

annealing. The difference can be explained by the larger molecular size of ter(DTP) **204** compared to bi(DTP) **203** which probably limits the thermal induced phase separation. Larger oligomers such as DCV-substituted ter(DTP) **204** do not phase-separate from PC₆₁BM as easily as DCV-substituted bi(DTP) **203**. Applying higher temperatures (100 °C) or longer annealing times to overcome the potentially higher activation barrier led to deterioration of the devices. Ter(DTP) **204**-based BHJSCs incorporating blend layers with larger PC₆₁BM amounts responded negatively upon thermal annealing concerning their photovoltaic parameters, within 1 min PCEs decreased from 1.18 to 1.08% and from 1.11 to 0.99% for D:A ratios of 1:2 and 1:1, respectively. Generally, V_{OC} and FF values of 0.84 V and up to 0.38, respectively, were obtained. The 0.2-0.3 V lower V_{OC} values of devices containing **204** compared to the V_{OC} values of bi(DTP) **203** reflects the 0.3 eV higher HOMO energy level of longer conjugated ter(DTP) **204** very well.

Table 3. Photovoltaic parameters for BHJSCs using structurally defined oligomer **204** as donor, with different D:A ratios. Device structure: ITO|PEDOT:PSS|**204**:PC₆₁BM|LiF|Al; c = 12.5 mg/mL, solvent: chloroform, $T_{\text{annealing}}$ = 80 °C. For each entry, three solar cells were fabricated using three different spin-coating velocities v_{spin} (750/1000/1250 rpm), whereas only the best is tabulated.

D:A	annealing [min]	v_{spin} [rpm]	J_{SC} [mA cm ⁻²]	V_{OC} [V]	FF	PCE [%]
1:2	-	1000	3.74	0.83	0.38	1.18
	1	-	3.47	0.82	0.38	1.08
1:1	-	1250	3.64	0.81	0.37	1.11
	1	-	3.30	0.82	0.36	0.99
2:1	-	1250	2.00	0.83	0.27	0.46
	1	-	2.29	0.83	0.28	0.53
	2	-	2.40	0.84	0.36	0.58
	6	-	1.74	0.65	0.27	0.30

In comparison to **203**-based BHJSCs where FF values of up to 0.47 were reached, the morphology of devices using **204** as donor showed only moderate FF values of up to 0.38. Additionally, photocurrents below 4 mA cm⁻² lag far behind the possibilities of the good absorption properties of **204**. Hence, further experiments concerning optimization of solution-processed BHJSCs based on ter(DTP) **204** were carried out involving the use of solvent additives and solvent vapor annealing

(Table 4). Three different solvent additives were tested: 1,8-diiodooctane (DIO), chloronaphthalene (CN), and polydimethylsiloxane (PDMS). For cells fabricated with DIO, FF values improved to 0.40, however a reduced J_{SC} of 2.70 mA cm^{-2} and V_{OC} of 0.79 V led to a decrease in PCE to 0.87% compared to devices prepared with similar conditions but without the use of solvent additive. In entry 2 and 3 in Table 4, the photovoltaic parameters of BHJSCs using CN and PDMS as solvent additives are listed. In both cases, the data resemble to the ones of additive-free solar cells reaching PCEs of around 1.1%. A possible explanation might be that the already high solubility of **204** in the spin-coating solvent is only influenced to a very small extend not leading to dramatic changes in the morphology formation during spin-coating. Solvent vapor annealing of spin-coated blend layers of **204**:PC₆₁BM for 30, 60, or 90 s led to lower PCEs of <0.7% in comparison to as-cast devices (Table 4, entry 4). Combined use of thermal treatment and solvent additives did not lead to better performing OSC as well in contrast to of **203**-based devices.

Table 4. Photovoltaic parameters for BHJSCs using structurally defined oligomer **204** as donor, with different solvent additives or solvent vapor annealing. Device structure: ITO|PEDOT:PSS|**204**:PC₆₁BM|LiF|Al; D:A ratio = 1:1, solvent: chloroform, c = 15.0 mg/mL. For entry 1-3, three solar cells were fabricated using three different spin-coating velocities v_{spin} (1000/1250/1500 rpm), whereas only the best is tabulated.

entry	additive	$c_{additive}$ [mg/mL]	v_{spin} [rpm]	J_{SC} [mA cm^{-2}]	V_{OC} [V]	FF	PCE [%]
1	DIO	5.0	1500	2.70	0.79	0.40	0.87
2	CN	5.0	1500	3.80	0.80	0.34	1.06
3	PDMS	0.2	1500	3.70	0.82	0.38	1.14
4 ^[a]	-	-	1500	2.20	0.83	0.37	0.68

[a] 60 s solvent vapor annealing (chloroform); 30 and 90 s led to even lower photovoltaic performance.

Several additional optimization experiments concerning the morphology of the **204**:PC₆₁BM blend layer were performed. A D:A ratio of 1:3, a higher spin-coating temperature (60 °C), and a higher concentration of the spin-coated solution were tested (Table 5, entry 1-3, respectively). Similar changes in processing conditions were also tested for shorter homologue **203** and led to lower efficiencies. Nevertheless, these conditions were tested since film forming properties of **204**:PC₆₁BM mixtures seemed to be quite different than the ones of **203**:PC₆₁BM mixtures. This finding can be ascribed to the much higher solubility and the linear extension in size of ter(DTP) **204** compared to bi(DTP) **203** leading to a different miscibility with PC₆₁BM and smaller tendency to crystallize.

Increasing the PC₆₁BM content in **204**:PC₆₁BM blends to 1:3 led to a slight decrease in photovoltaic performance to 1.02% due to a reduction of the J_{sc} to 3.4 mA cm⁻² compared to solar cells with a D:A ratio of 1:2 or 1:1 (Table 3). The lower photocurrent production is ascribed to less absorbed photons in the spectral area from 550-750 nm due to the lower amount DCV-substituted ter(DTP) **204** present in the blend layer. Entry 2 and 3 in Table 5 represent the data of BHJSCs with active layers spin-coated at 60 °C and with a higher concentration of the spin-coated solution, respectively. In both cases, similar photovoltaic properties were obtained, with J_{sc} values of 3.70-3.80 mA cm⁻², V_{oc} values of 0.81 V, FF values of ~0.4, and PCEs of ~1.2%. BHJSC performance and thin layer thicknesses (~100 nm) equaled those of devices constructed as described in Table 3 leading to the assumption that a very similar morphology is obtained despite fairly different processing conditions.

Table 5. Photovoltaic parameters for BHJSCs using structurally defined oligomer **204** as donor, with varying D:A ratio, concentrations, and spin-coating velocities v_{spin} . Device structure: ITO|PEDOT:PSS|**204**:PC₆₁BM|LiF|Al; solvent: chloroform.

entry	D:A	c [mg/mL]	T [°C]	v_{spin} [rpm]	J_{sc} [mA cm ⁻²]	V_{oc} [V]	FF	PCE [%]
1	1:3	15.0	r.t.	1500 ^[a]	3.40	0.81	0.37	1.02
2	1:1	15.0	60 °C	6000	3.70	0.81	0.39	1.16
3	1:1	20.0	r.t.	6000^[b]	3.80	0.81	0.40	1.23

[a] 1000 and 1250 rpm led to lower efficiencies; [b] 1000 and 2000 rpm led to lower efficiencies.

Despite the promising optoelectronic properties of DCV-substituted ter(DTP) **204**, solar cell testing and optimization using ter(DTP) **204** as donor led only to a moderate maximum PCE of 1.2% which is about a third of the PCE of the best cell of bi(DTP) **203** (PCE = 3.13%, Chapter 6). The difference in photovoltaic properties can be clearly seen in Figure 10a showing the J - V curves of the best performing BHJSCs based on bi(DTP) **203** and ter(DTP) **204**. In Figure 10b the corresponding IPCE spectra are depicted, clearly showing a lacking contribution of ter(DTP) **204** to the photocurrent generation. The IPCE spectrum of **204**-based devices featured a global IPCE maximum of 24% at 420 nm and a local one of 22% at 680 nm clearly reflecting the higher acceptor amount compared to **203** based devices (37% at 630-680 nm). However, the lacking contribution of **204** cannot be solely ascribed to the smaller D:A ratio of 1:1 compared to 2:1 for the displayed **203**-based device. Furthermore, the onset of the IPCE spectra of **203**:PC₆₁BM and **204**:PC₆₁BM are at 740 and 777 nm, respectively, which does not match the shift of the absorption onset of the neat thin films of **203** and

204 from 723 to 806 nm. Various changes of the processing conditions were undertaken without significant changes in the photovoltaic performance of devices containing ter(DTP) **204**. The experienced insensitivity of the PCE concerning active layer optimization is an exception among the structurally defined oligomer and co-oligomers synthesized and tested in this thesis (*Chapter 5-7*). The limiting factor of the PCE are mainly the low J_{sc} and FF of $<4 \text{ mA cm}^{-2}$ and <0.4 , respectively, pointing to a suboptimal morphology leading to charge transport and extraction issues which can also be seen by the higher saturation for the J - V curve of **204** compared to **203** (Figure 10a). A possible performance restricting factor in **204**-based active layers might be the presence of many bulky, insulating alkyl moieties which could not be forced to align in a beneficial ordering as it is assumed to be for **203**-containing active layers.

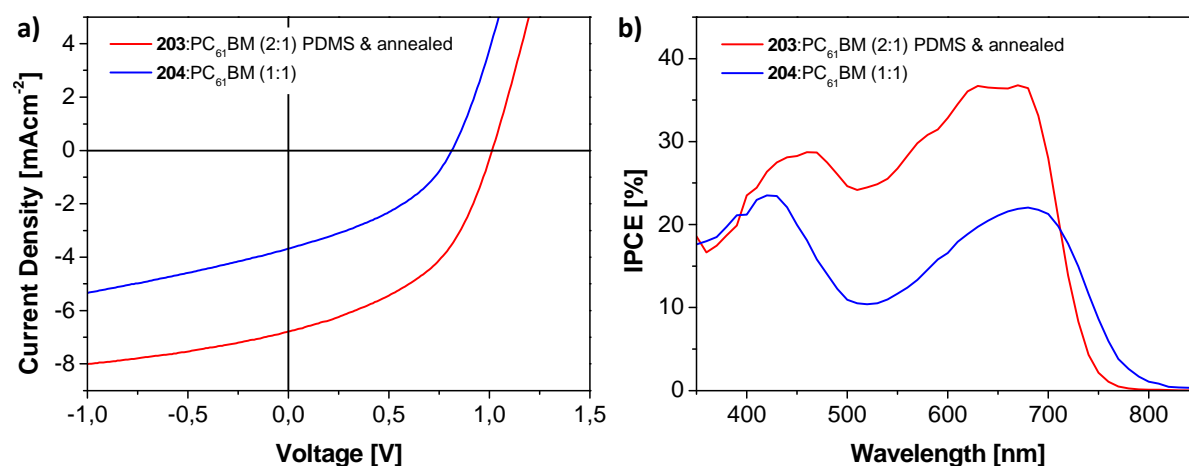


Figure 10. (a) J - V curves of best-performing BHJSCs containing **203** and **204** as donor. (b) IPCE spectra of the corresponding BHJSCs.

7.3 Summary

In summary, the synthesis of linear A-D-A structurally defined oligomers **202**, **204**, and **205** granted access to an interesting series of DCV-substituted oligo(DTP)s. DCV-substituted DTP **202** was synthesized in two steps starting from DTP **132s**, whereas DCV-substituted ter- and quater(DTP) **204** and **205** were prepared using Stille cross-coupling reaction. However, isolation and purification became more complex for longer homologues. Including DCV-substituted bi(DTP) **203** from the previous chapter (there referred to as “**183**”), structure-property relationships were established concerning optical and electrochemical properties. Improvement of the light-harvesting properties,

namely a more intense and red-shifted absorptio, was found upon elongation of the series reaching absorption maxima of up to 642 nm. Furthermore, the band gap is reduced and approaches a theoretical threshold of ~ 1.6 eV for infinitely long oligomers. Absorption spectroscopy of the oligomers in thin films revealed an annealing sensitive behaviour of the absorption properties. Upon cyclic voltammetry n reversible oxidation waves were found for each oligoDTP whereas n denotes the number of DTP-units. Elongation of the oligomer series led to a decrease in the first oxidation potential to -0.03 V for DCV-substituted quater(DTP) **205** explaining its limited stability at ambient conditions. DTP **202** stands out from the series not only due to its high first oxidation potential of 1.12 V but also concerning reduction properties showing two reduction waves compared to one reduction wave for longer homologues **203-205**. The HOMO and LUMO energy levels of **202** are not suitable concerning its use as donor in PC₆₁BM-based OSCs. In contrast to this, it might be used as PC₆₁BM substitute but with a higher light-harvesting ability. Longer homologues **203-205** showed suitable HOMO and LUMO energy levels concerning their use as donor in BHJSCs. Due to a very low HOMO energy level of -5.1 eV for quater(DTP) **205**, it is sensitive to air-oxidation and was not tested in BHJSCs. In contrast to this, **204**-based BHJSCs were fabricated and optimized reaching PCEs of up to 1.23% being limited due to moderate J_{sc} and FF values of <4 mA cm⁻² and <0.4 , respectively.

7.4 Experimental section

7.4.1 General procedures

¹H NMR spectra were recorded in CDCl₃ and THF-d₈ on a Bruker AMX 400 at 400 MHz. ¹³CNMR spectra were recorded in CDCl₃ and THF-d₈ on a Bruker AMX 400 at 100 MHz. Chemical shifts are denoted by a δ unit (ppm) and are referenced to the residual solvent peak (CDCl₃: ¹H δ = 7.26 ppm and ¹³C δ = 77.0 ppm; THF-d₈: ¹H δ = 3.57 ppm and ¹³C δ = 67.20 ppm). The splitting patterns are designated as follows: s (singlet), d (doublet), t (triplet), and m (multiplet). Mass spectra were recorded with a Varian Saturn 2000 GC-MS and with a MALDI-TOF MS Bruker Reflex 2 (*trans*-2-[3-(4-tert-butylphenyl)-2-methyl-2-propenylidene]malononitrile (DCTB) as matrix). Melting points of the intermediates were determined with a Büchi B-545 melting point apparatus and are not corrected. Melting points of **202** and **204** were determined using a Mettler Toledo DSC 823. Gas chromatography was carried out using a Varian CP-3800 gas chromatograph. HPLC analyses were performed on a Merck Hitachi L7000 equipped with a L7455 photodiode array detector, a L7200 autosampler and a L7100 solvent delivery system using a LiChrospher column (Nucleosil 100-5 NO₂). Thin-layer chromatography was carried out on Silica Gel 60 F254 aluminium plates (Merck). Solvents

and reagents were purified and dried by usual methods prior to use and used under inert gas atmosphere. The following starting materials were purchased and used without further purification: phosphoryl chloride (Merck), β -alanine (Merck), malononitrile (Aldrich), *N*-bromosuccinimide (Merck), *n*-butyllithium (Aldrich), trimethyltin chloride (Aldrich). Tetrakis(triphenylphosphine)palladium(0) was synthesized according to literature.^[10]

Optical and cyclic voltammetric measurements

UV-Vis spectra in chloroform solution and thin film were taken on a Perkin-Elmer Lambda 19 spectrometer. Cyclic voltammetry experiments were performed with a computer-controlled Autolab PGSTAT30 potentiostat in a three-electrode single compartment cell (3 mL). The platinum working electrode consisted of a platinum wire sealed in a soft glass tube with a surface of $A = 0.785 \text{ mm}^2$, which was polished down to $0.25 \text{ }\mu\text{m}$ with Buehler polishing paste prior to use in order to obtain reproducible surfaces. The counter electrode consisted of a platinum wire and the reference electrode was an Ag/AgCl reference electrode. All potentials were internally referenced to the ferrocene/ferrocenium couple. For the measurements, concentrations of $5 \times 10^{-4} \text{ M}$ of the electroactive species were used in freshly distilled and deaerated DCM (Lichrosolv, Merck) purified with an MB-SPS-800 and 0.1 M (*n*-Bu)₄NPF₆ (Fluka; recrystallized twice from ethanol).

Device fabrication

PEDOT:PSS (Clevios P, VP.AI 4083 solution from Heraeus) was spin-coated onto pre-cleaned, patterned ITO-coated glass from Kintec ($15 \text{ }\Omega \text{ cm}^{-2}$) upon which $\sim 35 \text{ nm}$ thick layers were obtained. Afterwards the photoactive layer was spin-coated from a mixed solution loaded with donor and PC₆₁BM (Solenne BV). Thin layers of LiF ($\sim 0.7 \text{ nm}$) and Al ($\sim 100 \text{ nm}$) were then deposited by vacuum evaporation at $2 \times 10^{-6} \text{ Torr}$ (Nano 36, Kurt J. Lesker Co.). The photoactive areas of the cells were 0.25 cm^2 .

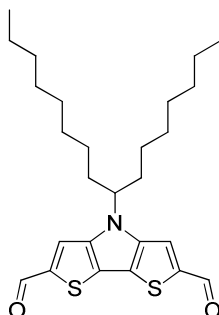
Current-voltage characterization

J-*V* characteristics were measured with a Oriel Instruments solar simulator (class AAA, AM 1.5G, 100 mWcm^{-2}) and a Keithley 2400 source meter. IPCE was measured under monochromatic light from a 300 W Xenon lamp in combination with a monochromator (Oriel, Cornerstone 260), modulated with a mechanical chopper. The response was recorded as the voltage over a $220 \text{ }\Omega$ resistance, using a lock-in amplifier (Merlin 70104). A calibrated Si cell was used as reference.

Thin layer thickness

Film thicknesses were measured using a Dektak profilometer and also by using high resolution field emission scanning electron microscopy (Sirion XL30) from FEI.

7.4.2 Synthesis

4-(Heptadecan-9-yl)-4H-dithieno[3,2-b:2',3'-d]pyrrole-2,6-dicarbaldehyde (**206**)

DMF (0.35 mL, 4.50 mmol) and phosphoryl chloride (0.41 mL, 4.50 mmol) were dissolved in 20 mL DCE and stirred at room temperature for 1 h. The resulting solution was then added dropwise to a solution of 4-(heptadecan-9-yl)-4H-dithieno[3,2-b:2',3'-d]pyrrole **132s** (94 mg, 0.23 mmol) in 3 mL DCE, which was cooled with an ice bath. After the addition the reaction mixture was refluxed overnight. Subsequently saturated sodium bicarbonate solution and sodium carbonate was added carefully and the two-phase system was stirred at room temperature for 4 h. The organic compounds were then extracted with DCM, the combined organic phases were dried over sodium sulfate and the solvent was removed by rotary evaporation. The crude product was purified via column chromatography (silica/DCM) to obtain DTP dicarbaldehyde **206** (93.7 mg, 0.20 μ mol, 88%) as a red solid.

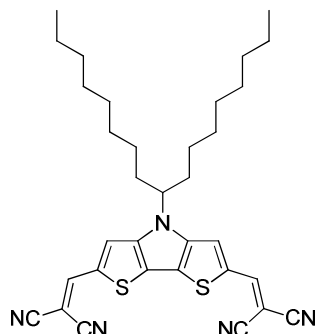
M.p.: 104-105 °C.

^1H NMR (400 MHz, CDCl_3): δ = 9.95 (s, 2 H, CHO), 7.70 (s, 2 H, 5-H,3-H), 4.32-4.25 (m, 2 H, N-CH), 2.08-1.89 (m, 4 H, N-CH-CH₂), 1.32-0.98 (m, 24 H, -CH₂-), 0.83 (t, 3J = 7.0 Hz, 12 H, -CH₃).

^{13}C NMR (100 MHz, CDCl_3): δ = 183.24, 146.38, 143.95, 121.99, 119.59, 60.58, 35.02, 31.64, 29.18, 29.09, 29.02, 26.51, 22.51, 13.99.

High-Resolution MS (MALDI-TOF) m/z : calcd for $\text{C}_{27}\text{H}_{39}\text{NO}_2\text{S}_2$: 473.24222, found $[\text{M}]^+$: 473.24984, $\delta m/m$ = 16.1 ppm.

2,2'-([4-{Heptadecan-9-yl}-4H-dithieno[3,2-b:2',3'-d]pyrrole-2,6-diyl]bis[methanylylidene])dimalononitrile (202)



DTP dicarbaldehyde **206** (44.0 mg, 92.9 μmol), malononitrile (18.4 mg, 279 μmol) and β -alanine (0.5 mg, 5.57 μmol) were dissolved in 1 mL DCE:ethanol [1:1] in a Schlenk-tube. The reaction mixture was stirred at 80 $^{\circ}\text{C}$ for 2 d. After that the solvent was removed by rotary evaporation. The crude product was purified via column chromatography (silica/DCM:*n*-hexane [3:1]) to obtain DCV-substituted DTP **202** (52.0 mg, 91.3 μmol , 98%) as a dark red solid.

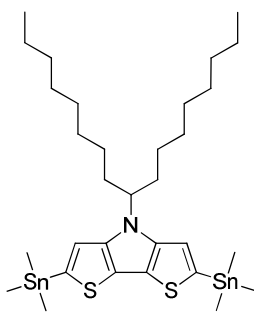
M.p.: 144 $^{\circ}\text{C}$.

^1H NMR (400 MHz, CDCl_3): δ = 7.80 (s, 2 H, 3-H,5-H), 7.76 (s, 2 H, C=C-H), 4.31-4.23 (m, 1 H, N-CH), 2.03-1.88 (m, 4 H, N-CH-CH₂), 1.25-1.16 (m, 24 H, -CH₂-), 0.84 (t, 3J = 7.0 Hz, 6 H, -CH₃).

^{13}C NMR (100 MHz, CDCl_3): δ = 150.64, 137.17, 119.19, 114.00, 113.46, 61.17, 34.94, 31.70, 29.21, 29.09, 29.06, 26.52, 22.58, 14.06.

MS (MALDI-TOF) m/z : calcd for $\text{C}_{33}\text{H}_{39}\text{N}_5\text{S}_2$: 569; found $[\text{M}]^+$: 569.

Elemental analysis: calcd (%) for $\text{C}_{33}\text{H}_{39}\text{N}_5\text{S}_2$: C 69.56, H 6.90, N 12.29; found (%): C 69.66, H 6.85, N 12.23.

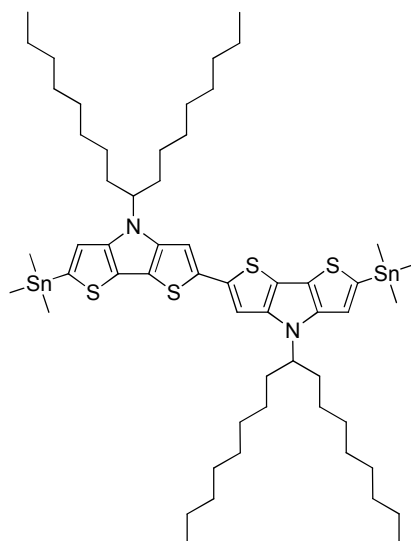
4-(Heptadecan-9-yl)-2,6-bis(trimethylstannyl)-4H-dithieno[3,2-b:2',3'-d]pyrrole (207)

n-BuLi (1.6 M, 0.63 mL, 1.01 mmol) was added dropwise to a solution of 4-(heptadecan-9-yl)-4H-dithieno[3,2-b:2',3'-d]pyrrole **132s** (183 mg, 0.44 mmol) in 1.7 ml tetrahydrofuran (THF) at -78 °C. After the addition the solution was stirred at -78 °C for 1 h and then at 0 °C for 1 h. Subsequently, the reaction mixture was cooled down again to -78 °C and trimethyltin chloride (210 mg, 1.05 mmol) dissolved in 0.25 mL THF was added in one portion. Then, after stirring at -78 °C for 2 h and at -50 °C for 30 min the reaction mixture was poured into water. *n*-Hexane was added and the organic layer was washed three times with water. The organic phase was dried over sodium sulfate and the solvent was removed by rotary evaporation. Distannylated DTP **207** was obtained as a slightly yellow-brown oil (320 mg) with a conversion of >95% (calculated by ¹H-NMR). It was used without further purification.

¹H NMR (400 MHz, CDCl₃): δ = 6.99 (s, 2 H, 3-H,3'-H), 4.25-4.18 (m, 1 H, N-CH), 2.07-1.99 (m, 2 H, N-CH-CH₂), 1.86-1.79 (m, 2 H, N-CH-CH₂), 1.30-1.06 (m, 24 H, -CH₂-), 0.84 (t, ³J = 7.0 Hz, 6 H, -CH₃), 0.40 (s, 18 H, -CH₃).

MS (MALDI-TOF) *m/z*: calcd for C₃₁H₅₅NS₂Sn₂: 745; found [M]⁺: 745.

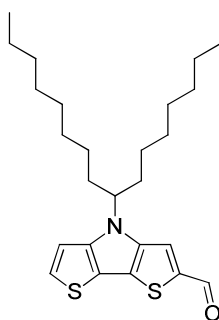
4,4'-Di(heptadecan-9-yl)-6,6'-bis(trimethylstannyl)-4H,4'H-2,2'-bidithieno[3,2-b:2',3'-d]pyrrole (208)



n-BuLi (1.6 M, 0.33 mL, 0.531 mmol) was added dropwise to a solution of di(heptadecan-9-yl)-bi(DTP) **192** (201 mg, 0.24 mmol) in 1 mL THF at -78 °C. After the addition, the solution was stirred at -78 °C for 45 min, at 0 °C for 15 min and additional 30 min between -70 and -60 °C. Subsequently, the reaction mixture was cooled down again to -78 °C and trimethyltin chloride (111 mg, 0.55 mmol) dissolved in 0.1 mL THF was added in one portion. Then, the reaction was warmed up until stirring was possible again. After that, the mixture was cooled down again and was stirred at -78 °C for 1.5 h. Afterwards, the reaction mixture was poured into water and the organic compounds were extracted with *n*-hexane. The organic phase was dried over sodium sulfate and the solvent was removed by rotary evaporation. Distannylated bi(DTP) **208** was obtained as a yellow-brown oil (265 mg) with a conversion of 60% (calculated by ¹H-NMR). It was used without further purification.

¹H NMR (400 MHz, THF-*d*₈): δ = 7.28 (s, 2 H, 5-H,5'-H), 7.14 (s, 2 H, 3-H,3'-H), 4.39-4.33 (m, 2 H, N-CH), 2.16-2.08 (m, 4 H, N-CH-CH₂), 1.90-1.83 (m, 4 H, N-CH-CH₂), 1.34-1.07 (m, 48 H, -CH₂-), 0.83 (t, ³*J* = 6.9 Hz, 12 H, CH₃), 0.39 (s, 18 H, Sn-CH₃).

MS (MALDI-TOF) *m/z*: calcd for C₅₆H₉₂N₂S₄Sn₂: 1158; found [M]⁺: 1158.

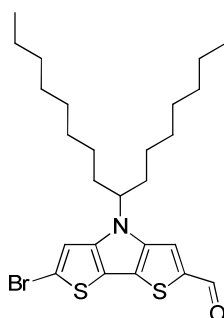
4-(Heptadecan-9-yl)-4H-dithieno[3,2-b:2',3'-d]pyrrole-2-carbaldehyde (211)

DMF (0.90 mL, 9.65 mmol) and phosphoryl chloride (0.73 mL, 9.55 mmol) were dissolved in 10 mL DCE and stirred at room temperature for 1 h. The resulting solution was then added dropwise to a solution of 4-(heptadecan-9-yl)-4H-dithieno[3,2-b:2',3'-d]pyrrole **132s** (1.00 g, 1.91 mmol) in 15 mL DCE, which was cooled with an ice bath. After the addition, the reaction was stirred for further 2 h at 0 °C. Subsequently, saturated sodium bicarbonate solution and sodium carbonate was added carefully and the two-phase system was stirred at room temperature for 4 h. The organic compounds were then extracted with DCM, the combined organic phases were dried over sodium sulfate and the solvent was removed by rotary evaporation. The crude product was purified via column chromatography (silica/DCM:*n*-hexane [1:1]) to obtain DTP-2-carbaldehyde **211** (93.7 mg, 0.20 μ mol, 92%) as a yellow solid.

^1H NMR (400 MHz, CDCl_3): δ = 9.90 (s, 1 H, CHO), 7.68 (s, 1 H, 3-H), 7.35 (d, $J^3 = 5,4$ Hz, 1 H, 5-H), 7.03 (d, $J^3 = 5,4$ Hz, 1 H, 6-H), 4.30-4.19 (m, 1 H, N-CH), 2.06-1.92 (m, 2 H, N-CH-CH₂), 1.90-1.75 (m, 2 H, N-CH-CH₂), 1.29-1.15 (m, 24 H, -CH₂-), 0.83 (t, $J^3 = 6.7$ Hz, 6 H, CH₃).

MS (CI) m/z : calcd for $\text{C}_{26}\text{H}_{39}\text{NOS}_2$: 446; found $[\text{M}]^+$: 446.

Analyses match with Ref. [7].

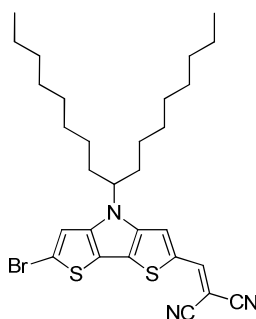
6-Bromo-4-(heptadecan-9-yl)-4H-dithieno[3,2-b:2',3'-d]pyrrole-2-carbaldehyde (212)

DTP-2-carbaldehyde **211** (750 mg, 1.68 mmol) was dissolved in 20 mL DMF and cooled to 0 °C. Subsequently, NBS (299 mg, 1.68 mmol) dissolved in 6 mL DMF was added dropwise. After keeping the reaction mixture at 0 °C for 20 h, it was poured into ice water. The precipitate was washed and filtered off. The aqueous phase was extracted with DCM, the combined organic layers were dried over sodium sulphate and the solvent was removed. The crude product was combined with the precipitate and passed through a short silica column (DCM:*n*-hexane [1:1]) to obtain 6-bromo-DTP-2-carbaldehyde **212** (839 mg, 1.60 mmol, 95%) as a yellow solid.

¹H NMR (400 MHz, CDCl₃): δ = 9.87 (s, 1 H, CHO), 7.65 (s, 1 H, 3-H), 7.09 (s, 1 H, 5-H), 4.21-4.13 (m, 1 H, N-CH), 2.02-1.81 (m, 4 H, CH-CH₂), 1.31-1.16 (m, 22 H, -CH₂-), 1.06-0.97 (m, 2 H, -CH₂-), 0.84 (t, ³J = 7.0 Hz, 6 H, -CH₃).

MS (MALDI-TOF) *m/z*: calcd for C₂₆H₃₈BrNOS₂: 523; found [M]⁺: 523.

Analyses match with Ref. [7].

2-([6-Bromo-4-{heptadecan-9-yl}-4H-dithieno[3,2-b:2',3'-d]pyrrol-2-yl]methylene)malononitrile (209)

6-Bromo-DTP-2-carbaldehyde **212** (1.13 g, 2.15 mmol), malononitrile (427 mg, 6.46 mmol) and β-alanine (9.60 mg, 0.11 mmol) were dissolved in 20 mL DCE:ethanol [1:1] in a Schlenk-tube. The reaction mixture was stirred at 60 °C for 2 d. After that, the solvent was removed by rotary

evaporation. The crude product was purified via column chromatography (silica/DCM:*n*-hexane [4:3], silica/*n*-hexane:ethyl acetate [15:1]) and recrystallization from ethanol to obtain brominated DCV-DTP **209** (1.11 g, 1.94 mmol, 90%) as a dark red solid.

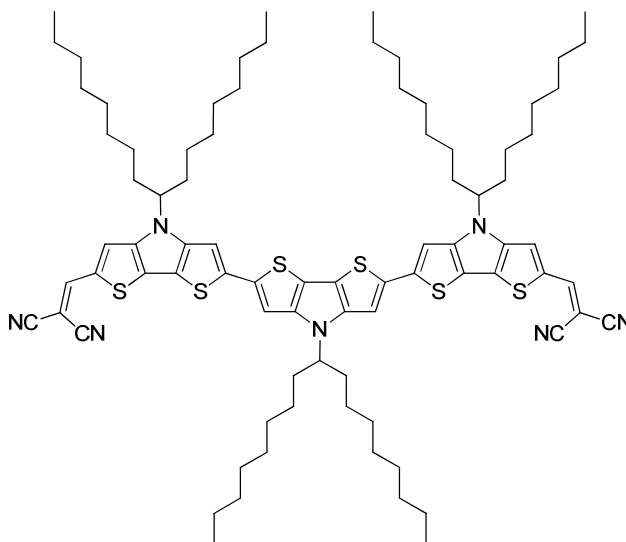
M.p.: 71 °C.

¹H NMR (400 MHz, CDCl₃): δ = 7.73 (s, 1 H, 3-H), 7.66 (s, 1 H, C=CH), 7.09 (s, 1 H, 5-H), 4.20-4.13 (m, 1 H, N-CH), 1.99-1.81 (m, 4 H, CH-CH₂), 1.24-1.16 (m, 22 H, -CH₂-), 1.07-0.95 (m, 2 H, -CH₂-), 0.845 (t, ³*J* = 7.0 Hz, 6 H, -CH₃).

MS (CI) *m/z*: calcd for C₂₉H₃₈BrN₃S₂: 571; found [*M*]⁺: 571.

Analyses match with Ref. [7].

2,2'-([4,4',4''-Tri{heptadecan-9-yl}-4H,4'H,4''H-{2,2':6',2''-terdithieno[3,2-b:2',3'-d]pyrrole}-6,6''-diyl]bis[methanylylidene])dimalononitrile (204)



Distannylated DTP **207** (72.0 mg, 96.9 μmol), brominated DCV-DTP **209** (128 mg, 224 μmol) and Pd(PPh₃)₄ (4.5 mg, 3.89 μmol) were added in a Schlenk-tube and evacuated for several minutes. After adding 8 mL DMF, the reaction mixture was carefully degassed and heated to 65 °C for 6 h. Then, the solvent was removed by rotary evaporation and the residue was purified via column chromatography (silica/DCM:*n*-hexane from [1:1] to [5:1]). The crude product was then further purified by size exclusion chromatography (BioBeads/DCM) and HPLC (nucleosil/DCM:*n*-hexane [55:45]) to obtain DCV-substituted ter(DTP) **204** (69.0 mg, 49.2 μmol, 51%) as a black solid.

M.p.: 227 °C.

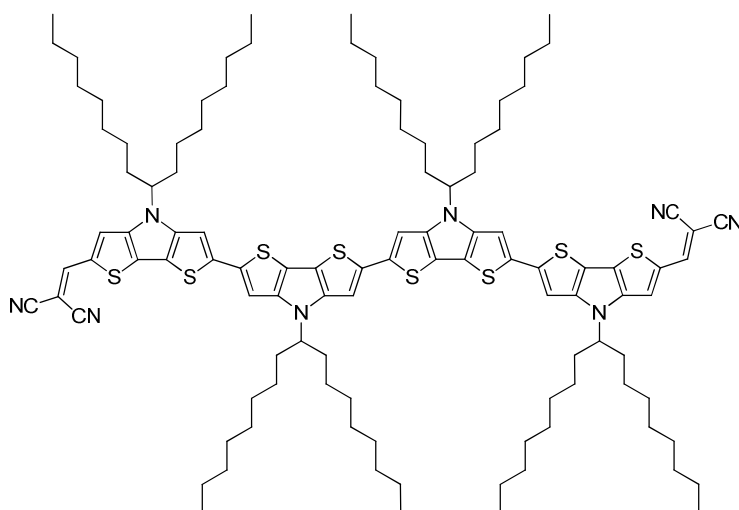
^1H NMR (500 MHz, CDCl_3): δ = 7.71 (s, 2 H, 5-H,5''-H), 7.61 (s, 2 H, C=CH), 7.21 (s, 2 H, 3-H,3''-H), 7.08 (s, 2 H, 3'-H,5'-H), 4.28-4.20 (m, 3 H, N-CH), 2.11-1.98 (m, 6 H, N-CH- CH_2), 1.95-1.85 (m, 6 H, N-CH- CH_2), 1.31-1.05 (m, 36 H, $-\text{CH}_2-$), 0.83 (t, 3J = 7.0 Hz, 9 H, $-\text{CH}_3$), 0.81 (t, 3J = 6.9 Hz, 9 H, $-\text{CH}_3$).

^{13}C NMR (100 MHz, CDCl_3): δ = 150.40, 144.14, 135.70, 132.29, 132.28, 126.81, 115.57, 115.48, 114.98, 113.83, 109.00, 106.47, 71.04, 60.69, 60.43, 35.17, 35.02, 31.80, 29.34, 29.33, 29.25, 29.21, 29.18, 26.68, 26.62, 22.66, 14.12.

MS (MALDI-TOF) m/z : calcd for $\text{C}_{83}\text{H}_{113}\text{N}_7\text{S}_6$: 1399; found $[\text{M}+\text{H}]^+$: 1400.

Elemental analysis: calcd (%) for $\text{C}_{83}\text{H}_{113}\text{N}_7\text{S}_6$: C 71.14, H 8.13, N 7.00, S 13.73; found (%): C 71.36, H 7.94, N 6.92, S 13.61.

2,2'-([4,4',4'',4'''-tetra{heptadecan-9-yl}-4H,4'H,4''H,4'''H-{2,2':6',2'':6'',2'''-quaterdithieno[3,2-b:2',3'-d]pyrrole}-6,6'''-diyl]bis[methanylylidene])dimalononitrile (205)



Distannylated biDTP **208** (63.1 mg, 54.4 μmol), brominated DCV-DTP **209** (74.8 mg, 131 μmol) and $\text{Pd}(\text{PPh}_3)_4$ (2.4 mg, 2.1 μmol) were added in a Schlenk-tube and evacuated for several minutes. After adding 5 mL DMF, the reaction mixture was carefully degassed and heated to 70 $^\circ\text{C}$ for 15 h. Then, the solvent was removed by rotary evaporation and the residue was purified via column chromatography (silica/DCM:*n*-hexane from [1:2] to [1:0]). The crude product was then further purified by size exclusion chromatography (BioBeads/DCM) and column chromatography (silica/DCM:*n*-hexane [2:1]) to obtain DCV-substituted quater(DTP) **205** (9.3 mg, 5.1 μmol , 9%) as a black solid.

¹H NMR (400 MHz, THF-d₈): δ = 8.08 (s, 2 H, 5-H,5'''-H), 7.86 (s, 2 H, C=CH), 7.50 (s, 2 H, 3-H,3'''-H), 7.40 (s, 2 H, 3'-H,5''-H), 7.38 (s, 2 H, 5'-H,3''-H), 4.49-4.41 (m, 4 H, N-CH), 2.20-2.07 (m, 8 H, N-CH-CH₂), 1.96-1.88 (m, 8 H, N-CH-CH₂), 1.35-1.08 (m, 48 H, -CH₂-), 0.85-0.80 (m, 24 H, -CH₃).

¹³C NMR could not be measured due to decomposition of the analyte within the time scale of the experiment.

High-Resolution MS (MALDI-TOF) *m/z*: calcd for C₁₀₈H₁₅₀N₈S₈: 1815.97827; found [M]⁺: 1815.97614, $\delta m/m = 1.2$ ppm.

7.5 References

- [1] K. Schulze, C. Uhrich, R. Schüppel, K. Leo, M. Pfeiffer, E. Brier, E. Reinold, P. Bäuerle, *Adv. Mater.* **2006**, *18*, 2872-2875.
- [2] R. Fitzner, E. Reinold, A. Mishra, E. Mena-Osteritz, H. Ziehlke, C. Körner, K. Leo, M. Riede, M. Weil, O. Tsaryova, A. Weiß, C. Uhrich, M. Pfeiffer, P. Bäuerle, *Adv. Funct. Mater.* **2011**, *21*, 897-910.
- [3] Y. Liu, X. Wan, F. Wang, J. Zhou, G. Long, J. Tian, J. You, Y. Yang, Y. Chen, *Adv. Energy Mater.* **2011**, *1*, 771-775.
- [4] S. C. Rasmussen, S. J. Evenson, *Prog. Polym. Sci.* **2013**, *38*, 1773-1804.
- [5] A. Yassin, P. Leriche, J. Roncali, *Macromol. Rapid Commun.* **2010**, *31*, 1467-1472.
- [6] A. Yassin, T. Rousseau, P. Leriche, A. Cravino, J. Roncali, *Sol. Energy Mater. Sol. Cells* **2011**, *95*, 462-468.
- [7] D. Zauner, bachelor thesis, Ulm University, **2012**.
- [8] D. T. Duong, B. Walker, J. Lin, C. Kim, J. Love, B. Purushothaman, J. E. Anthony, T.-Q. Nguyen, *J. Polym. Sci., Part B: Polym. Phys.* **2012**, *50*, 1405-1413.
- [9] T. Liu, A. Troisi, *Adv. Mater.* **2013**, *25*, 1038-1041.
- [10] L. Malatesia, M. Angoletta, *J. Chem. Soc.* **1957**, 1186-1188.

Summary

The aim of this thesis has been the synthesis and the optoelectronic characterization of organic donor(D)-acceptor(A)-type dyes. The main focus was directed at the development of dye series with subtle structural changes in order to obtain structure-property relationships. In the first part, unsymmetrical D-A-substituted bithiophenes were synthesized and characterized and can be used as sensitizers in p-type dye-sensitized solar cells (p-type DSSCs). The second part concentrates on the synthesis and characterization of acceptor-substituted oligomers and co-oligomers containing dithieno[3,2-b:2',3'-d]pyrrole (DTP) which can be implemented as donor materials in bulk heterojunction solar cells (BHJSCs) by solution-processing. Corresponding introductions into the two topics are given in *Chapter 1* and *4*.

In *Chapter 2*, the influence of the hexyl substitution pattern in perylenemonoimide(PMI)-bithiophene-triphenylamine(TPA) triads **14** and **44-46** (Chart 1) on the optoelectronic and photovoltaic properties is investigated.

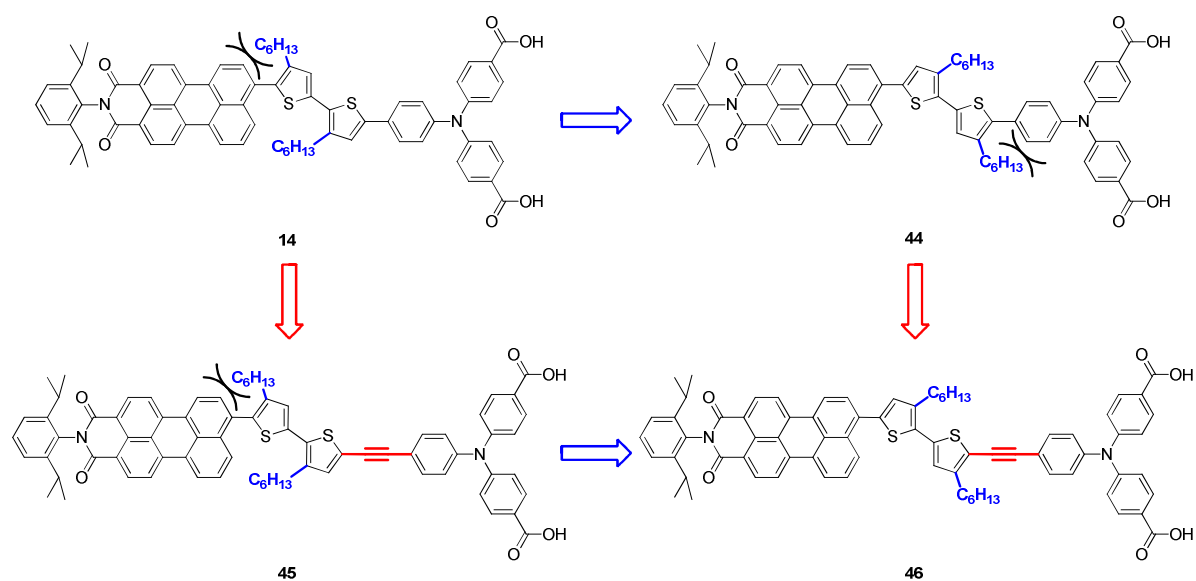


Chart 1. D-A-substituted bithiophenes with different hexyl substitution pattern. Red arrows indicate ethynylene insertion between bithiophene and TPA. Blue arrows denote change of the hexyl substitution pattern. \diagup symbolizes sterical hindrance.

Therefore, triad **46** was synthesized and the whole series fully characterized. The different hexyl chain substitution within the series causes varying torsions along the π -conjugated backbone, in particular between the PMI acceptor and the bithiophene or the TPA donor and the bithiophene. This was supported by quantum-chemical density functional theory calculations showing a planarization of the PMI-thiophene linkage for **44** and **46** compared to **14** and **45**. Hence, slight differences in the optoelectronic properties were observed. The lower torsion between the PMI-acceptor and the bithiophene-TPA donor moiety in **44** and **46** led to advantageous light-harvesting properties. Nevertheless, triads **14** and **45** outperformed **44** and **46** concerning their photovoltaic performance when applied as sensitizers in p-type DSSCs. Power conversion efficiencies (PCEs) of up to 0.1% were achieved for **14** and **45** compared to 0.05% for **44** and **46**. Transient absorption spectroscopy experiments revealed a reduced hole injection yield and/or a fast component of the recombination kinetics for triads **44** and **46**. The better results for **14** and **45** are attributed to the stronger torsion of the PMI-bithiophene linkage and hence to a stronger decoupling of the PMI-acceptor and the bithiophene-TPA donor moiety which seems to be crucial for efficient device performance of D-A-substituted bithiophenes.

In *Chapter 3*, D-A dye series **57-60** was synthesized incorporating the beneficial hexyl substitution pattern of sensitizer **14**. Different electron-accepting moieties were implemented in order to investigate the effect of the acceptor moiety within D-A-substituted bithiophenes concerning optoelectronic and photovoltaic properties (Chart 2).

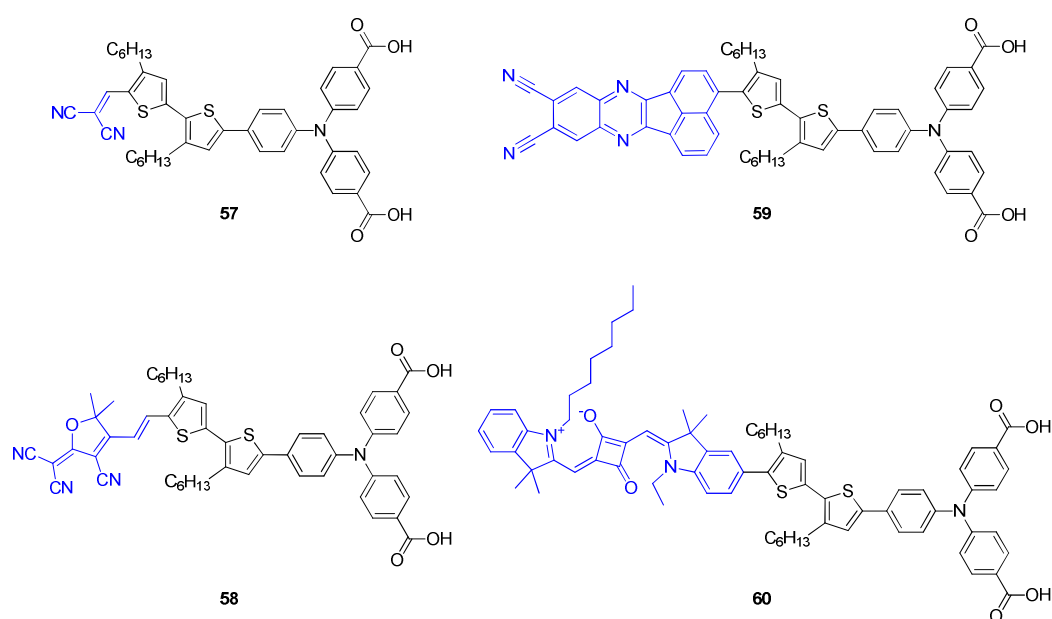


Chart 2. D-A-substituted bithiophenes with varying electron-accepting moieties.

Two different synthetic approaches were used to synthesize **57-60**. In the case of triads **57** and **58**, the acceptors were introduced in an early stage of the synthesis, whereas for **59** and **60**, the acceptor moiety was inserted in the penultimate reaction step. It was shown that the absorption properties as well as the highest occupied molecular orbital (HOMO) and lowest unoccupied molecular orbital (LUMO) energy levels could be easily fine-tuned by the use of different electron-accepting moieties. p-Type DSSCs using **57-60** as sensitizers and iodide-triiodide as redox mediator yielded PCEs in the range of 0.01 to 0.08%. Triad **59** containing a bulky annulated acceptor unit, similarly to PMI-derivative **14**, showed the highest PCE emphasizing that the torsion between the acceptor and donor moieties plays a crucial role to hinder back electron transfer and retard charge recombination processes in the device. Furthermore, impedance spectroscopy measurements points to a low recombination rate of injected hole and dye anions in devices containing **59**.

In the second part of this thesis, structurally defined oligomers and co-oligomers containing dithieno[3,2-b:2',3'-d]pyrrole (DTP) were developed for the use as donor materials in solution-processed BHJSCs. In *Chapter 5*, linear A-D-A dyes **129-131** were synthesized consisting of dicyanovinylene (DCV) acceptors and an oligothiophene backbone with a central DTP-unit as donor (Chart 3). The introduction of DTP into the donor backbone aimed in the amplification of the light-harvesting properties compared to regular DCV-endcapped oligothiophenes.

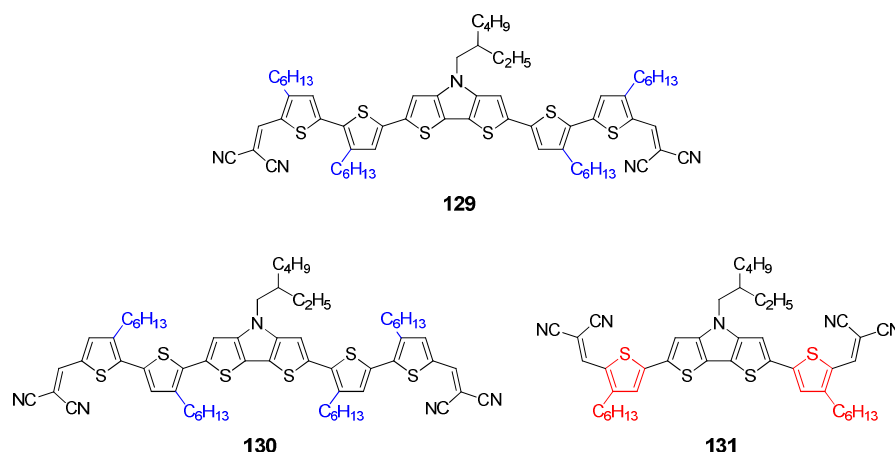


Chart 3. Structurally defined co-oligomers containing DTP as central unit.

Absorption spectroscopy of series **129-131** revealed great potential as light-harvesting donor material for organic solar cells. High extinction coefficients in solution and absorption bands up to 700 nm in thin films were ascribed to the presence of the DTP-unit. All three co-oligomers showed HOMO and LUMO energy levels which fit well to the energy level alignment in BHJSCs with [6,6]-

phenyl-C61-butyric acid methyl ester (PC₆₁BM) as acceptor material. As-cast **129**- and **130**-based BHJSCs yielded PCEs of 4.8 and 0.8%, respectively. The big discrepancy in PCE is contributed to the very different blend morphology and phase separation, probed by atomic force microscopy and X-ray diffraction-techniques. However, solvent vapor annealing of **130**-based active layers could presumably induce a better phase separation and ordering, thus leading to solar cells with PCEs as high as 4.4%. Shorter co-oligomer **131** gave rise to a PCE of 3.5% when used as donor material in BHJSCs. These results show that DTP is a promising building block for light-harvesting donor materials in BHJSCs. Additionally, subtle fine-tuning of the solubilizing alkyl chains and careful optimization of the processing conditions is found to be necessary to obtain highly efficient BHJSCs.

In *Chapter 6*, A-D-A series **181-183** consisting of acceptor-substituted bi(dithienopyrrole)s (bi(DTP)s) (Chart 4) was synthesized by formation of the bi(DTP) core-unit and subsequent functionalization with the corresponding acceptor groups.

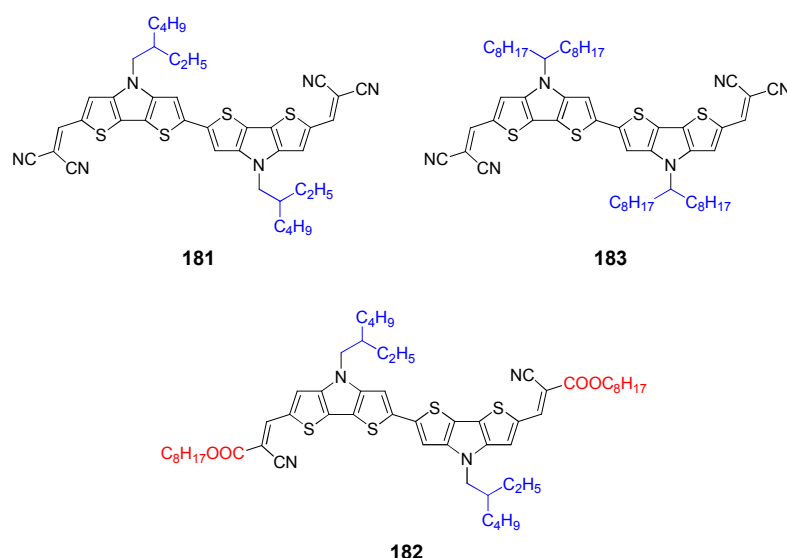


Chart 4. Acceptor-endcapped bi(DTP)s bearing different solubilizing alkyl chains.

The bi(DTP)-unit improved the light-harvesting properties of **181-183** compared to the previous series **129-131** containing only one DTP-unit. The solubility of **181** is rather low for solution-processing but the ones of **182** and **183** could be greatly increased by inserting branched alkyl chains or octyl cyanoacrylate groups, respectively. HOMO and LUMO energy levels were in the optimum range for BHJSCs using PC₆₁BM as acceptor. As-cast **181-183**-based BHJSCs yielded a maximum PCE of 2.08% when **181** was used as donor. Solar cells containing more soluble bi(DTP)s **182** and **183** reached moderate efficiencies of only ~1.4 and ~0.4%, respectively. However, device optimization using solvent additives and thermal annealing led to great improvements resulting in PCEs of 3.6 and

3.1% for **182** and **183**, respectively. The high open-circuit voltage values of around 1 V achieved within this series and the good absorption properties make bi(DTP) a promising donor building block for organic solar cell materials.

In *Chapter 7*, the synthesis of linear A-D-A structurally defined oligomers **202**, **204**, and **205** granted access to a novel DCV-endcapped oligo(DTP) series (Chart 5). By absorption spectroscopy and cyclic voltammetry, structure-property relationships could be gathered with respect to the elongation of the oligo(DTP) donor moiety. Upon increase of the number of DTP-units, a more intense and red-shifted absorption was observed. Furthermore, the optical band gap is reduced and approaches a theoretical threshold of ~ 1.6 eV for infinitely long oligomers. Thin film measurements revealed significant changes in the absorption upon annealing. Due to rearrangement of the oligomers in neat and PC₆₁BM-blended films containing **202-204** a red-shifted and more intense absorption compared to as-cast films was observed. Cyclic voltammetry measurements revealed n reversible oxidation waves for each oligo(DTP) whereas n denotes the number of DTP-units. Elongation of the oligomer series led to a decrease in the first oxidation potential to -0.03 V for quater(DTP) **205** which explains its limited stability at ambient conditions. Besides bi(DTP) **203**, ter(DTP) **204** showed the most promising HOMO and LUMO level energies within the series concerning the use as donor in BHJSCs. Solution-processed solar cells incorporating **204** as donor and using PC₆₁BM as acceptor reached PCEs of up to 1.2%.

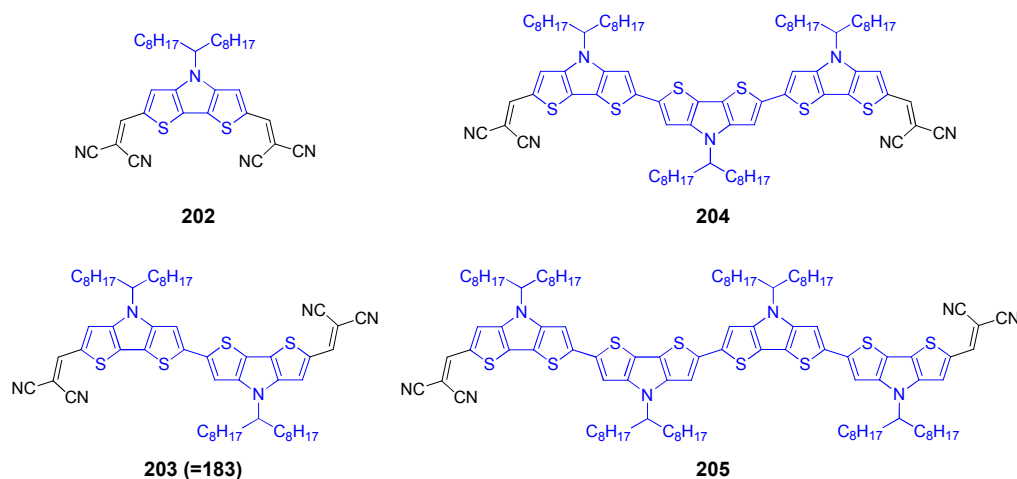


Chart 5. DCV-endcapped oligo(DTP) series.

Zusammenfassung

Das Ziel der vorliegenden Arbeit war die Synthese und Charakterisierung der optoelektronischen Eigenschaften von organischen Donor(D)-Akzeptor(A)-artigen Farbstoffen. Das Hauptaugenmerk lag dabei auf der Entwicklung von Farbstoff-Serien mit feinen strukturellen Unterschieden um Struktur-Eigenschafts-Beziehungen zu erhalten. Im ersten Teil der Arbeit wurden unsymmetrische D-A-substituierte Bithiophene synthetisiert und charakterisiert und können als Sensibilisatoren in p-Typ farbstoffsensibilisierten Solarzellen (p-Typ DSSC) verwendet werden. Der zweite Teil konzentriert sich auf die Synthese und Charakterisierung von akzeptorsubstituierten Oligomeren und Cooligomeren, die Dithieno[3,2-b:2',3'-d]pyrrol (DTP) enthalten und mittels Lösungsprozessierung als Donor-material in Bulk-Heteroübergang Solarzellen (BHJSC) implementiert werden können. Entsprechende Einleitungen zu den zwei Themengebieten befinden sich in *Kapitel 1* und *4*.

In *Kapitel 2* wurde der Einfluss des Hexyl-Substitutionsmusters in Perylenmonoimid(PMI)-Bithiophen-Triphenylamin(TPA) Triaden **14** und **44-46** (Abbildung 1) untersucht.

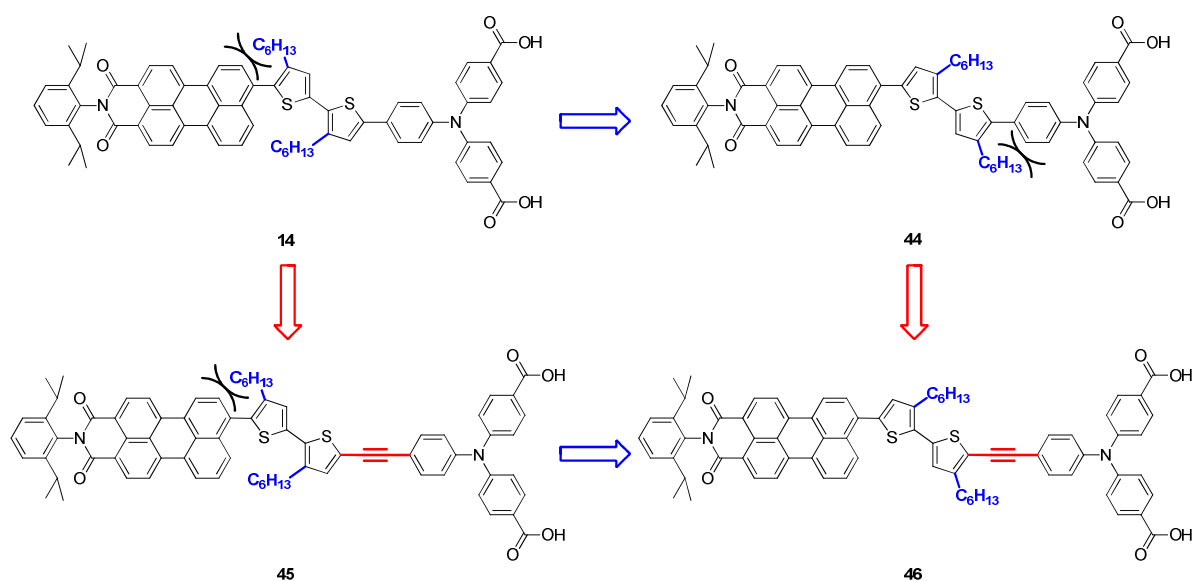


Abbildung 1. D-A-substituierte Bithiophene mit unterschiedlichem Hexyl-Substitutionsmuster. Rote Pfeile: Einführung einer Acetylen-Einheit zwischen Bithiophen und TPA. Blaue Pfeile: Änderung des Hexyl-Substitutionsmusters. symbolisiert sterische Hinderung.

Hierzu wurde Triade **46** synthetisiert und die ganze Serie vollständig charakterisiert. Die variierende Hexylketten Substitution in der Serie verursacht unterschiedliche Torsionen entlang des π -konjugierten Rückgrats, im Speziellen zwischen dem PMI Akzeptor und Bithiophen oder dem TPA und Bithiophen. Dies wurde durch Dichtefunktionaltheorieberechnungen unterstützt, die eine Planarisierung der PMI-Bithiophene Bindung für **44** und **46** im Vergleich zu **14** und **45**. Aufgrund dessen wurden geringe Unterschiede in den optoelektronischen Eigenschaften beobachtet. Die geringere Torsion zwischen dem PMI Akzeptor und der Bithiophen-TPA Donoreinheit in **44** und **46** führte zu vorteilhaften Lichtsammeleigenschaften. Trotzdem übertrafen Triaden **14** und **45** Isomere **44** und **46** bezüglich ihrer photovoltaischen Eigenschaften als Sensibilisator in p-Typ DSSCs. Umwandlungseffizienzen (PCEs) von bis zu 0.1% wurden für **14** und **45** erreicht im Vergleich zu 0.05% für **44** und **46**. Transiente Absorptionsspektroskopie zeigten eine verringerte Lochinjektionsausbeute und/oder eine schnelle Komponente der Rekombinationskinetik für **44** und **46** auf. Das bessere Ergebnis für **14** und **45** wurde der stärkeren Torsion zwischen der PMI-Bithiophen Bindung und damit der stärkeren Entkopplung des PMI Akzeptors und des Bithiophen-TPA Donors zugeschrieben. Diese Entkopplung scheint entscheidend für eine effiziente Solarzellenleistung von D-A-substituierten Bithiophenen.

In *Kapitel 3* wurde D-A-Farbstoffserie **57-60**, die das vorteilhafte Hexyl-Substitutionsmuster von Sensibilisator **14** enthalten, synthetisiert. Unterschiedliche Akzeptorgruppen wurden implementiert um den Effekt dieser in D-A-substituierten Bithiophenen bezüglich ihrer optoelektronischen und photovoltaischen Eigenschaften zu untersuchen (Abbildung 2).

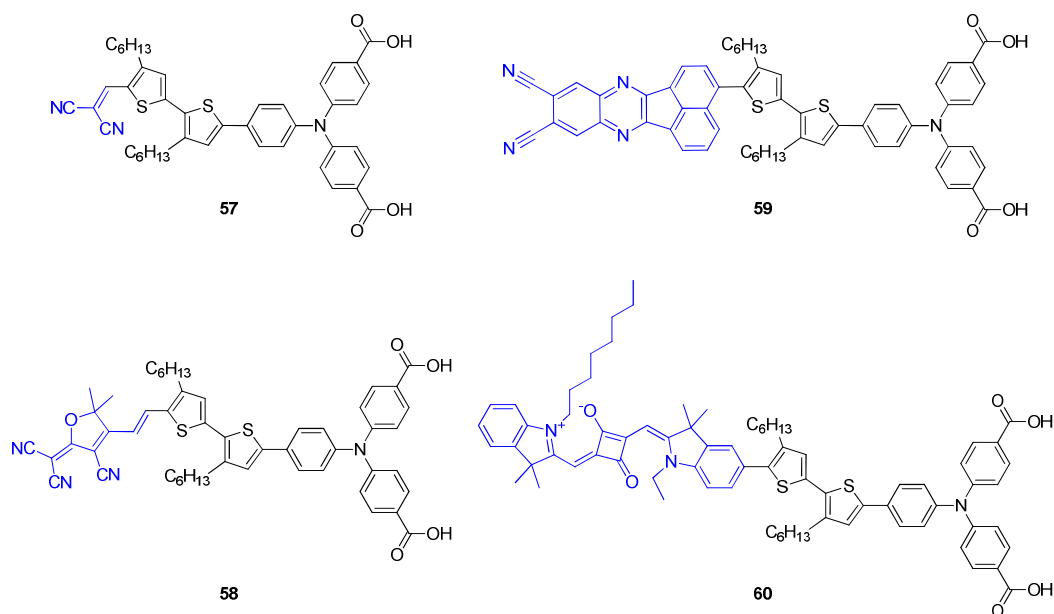


Abbildung 2. D-A-substituierte Bithiophene mit variierenden Akzeptorgruppen.

Zwei unterschiedliche synthetische Ansätze wurden angewandt um **57-60** zu synthetisieren. Im Fall von Triaden **57** und **58** wurden die Akzeptoren in einem frühen Stadium der Synthese eingeführt, wohingegen für **59** und **60** der Akzeptorteil erst im vorletzten Reaktionsschritt eingefügt wurde. Es konnte gezeigt werden, dass die Absorptionseigenschaften, sowie die Energieniveaus des höchsten besetzten Molekülorbitals (HOMO) und des niedrigsten unbesetzten Molekülorbitals (LUMO) leicht durch den Einsatz von unterschiedlichen Akzeptorgruppen reguliert werden können. p-Typ DSSC mit **57-60** als Sensibilisatoren und I^-/I_3^- als Redox Mediator ergaben PCEs von 0.01 bis 0.08%. Triade **59** die einen sterisch anspruchsvollen, annulierten Akzeptor enthält, zeigte die höchste PCE, was hervorhebt, dass die Torsion zwischen dem Akzeptor- und Donorteil eine wichtige Rolle bei der Verzögerung des Rückelektronentransfers und bei Ladungsträgerrekombinationsprozessen spielt. Zudem wurden impedanzspektroskopische Messungen durchgeführt, diese deuten auf eine geringere Rekombinationsrate von injiziertem Loch und Farbstoffanionen in Zellen mit **59** hin.

Im zweiten Teil dieser Arbeit wurden strukturell definierte Oligo- und Cooligomere, die Dithieno[3,2-b:2',3'-d]pyrrol (DTP) enthalten, entwickelt um als Donormaterial in lösungsprozessierten BHJSCs Anwendung zu finden. In *Kapitel 5* wurden lineare A-D-A Farbstoffe **129-131** synthetisiert, welche aus Dicyanovinylen(DCV)-Akzeptoren und einem Oligothiophenrückgrat mit einer zentralen DTP-Einheit bestehen (Abbildung 3). Die Einführung von DTP in das Donorrückgrat zielte auf die Verstärkung der Lichtsammeleigenschaften im Vergleich zu regulären DCV-substituierten Oligothiophenen ab.

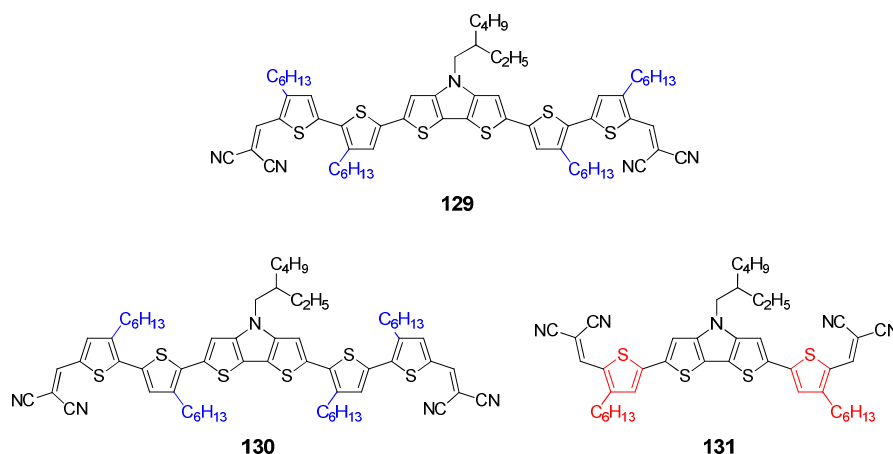


Abbildung 3. Strukturell definierte Cooligomere mit einer zentralen DTP-Einheit.

Absorptionsspektroskopische Untersuchungen von Serie **129-131** legten deren außerordentliches Potential zur Verwendung als lichtsammele Donormaterialien für organische Solarzellen dar. Hohe Extinktionskoeffizienten in Lösung und Absorptionsbanden bis zu 700 nm in dünnen Filmen wurden

der Gegenwart der DTP-Einheit zugeschrieben. Alle drei Cooligomere zeigten HOMO und LUMO Energieniveaus die gut zu den Energieniveaus von BHJSCs mit [6,6]-Phenyl-C₆₁-butylsäuremethylester (PC₆₁BM) als Akzeptormaterial passen. Unbehandelte Aktivschichten in **129**- und **130**-basierten BHJSCs ergaben PCEs von 4.8 bzw. 0.8%. Die große Abweichung im Wirkungsgrad ist der stark unterschiedlichen Mischschicht-Morphologie und Phasenseparation zugeschrieben, welche mittels Atomkraftmikroskopie und Röntgendiffraktionstechniken untersucht wurden. Mittels Lösungsmitteldampfkonditionierung von **130**-basierten Aktivschichten konnte jedoch vermutlich eine bessere Phasenseparation und Anordnung induziert werden, was zu Solarzellen mit PCEs von 4.4% führte. Kürzeres Cooligomer **131** erzielte eine PCE von 3.5% in BHJSCs. Diese Ergebnisse heben DTP als vielversprechenden Baustein für sonnenlichtsammelnde Donormaterialien für BHJSCs hervor. Des Weiteren wurde festgestellt, dass die Feinjustierung der löslichkeitsvermittelnden Alkylketten und eine umsichtige Optimierung der Prozessionsbedingungen notwendig sind um hocheffiziente BHJSC zu erhalten.

In *Kapitel 6* wurde A-D-A Serie **181-183**, bestehend aus Akzeptor-substituierten Bi(DTP)s, durch Bildung des Bi(DTP)-Kerns und anschließender Funktionalisierung mit den entsprechenden Akzeptorgruppen synthetisiert (Abbildung 4).

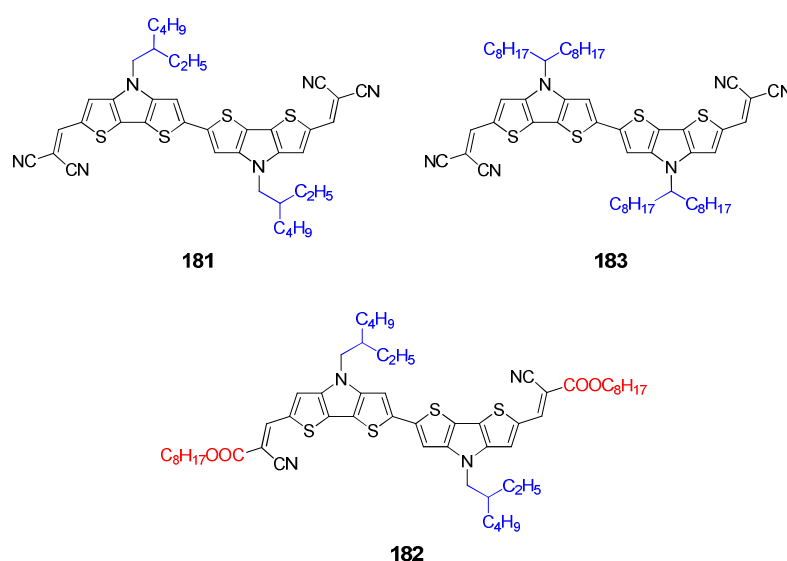


Abbildung 4. Akzeptor-substituierte Bi(DTP)s mit unterschiedlichen löslichkeitsvermittelnden Alkylketten.

Die Bi(DTP)-Einheit verbesserte die lichtsammelnden Eigenschaften von **181-183** im Vergleich zur vorherigen Serie **129-131**, die nur ein DTP enthält. Die Löslichkeit von **181** ist relativ gering für die Lösungsprozessierung, allerdings konnten diese für **182** und **183** enorm verbessert werden, indem verzweigte Alkylketten bzw. Cyanoacrylsäureoktylestergruppen eingeführt wurden. HOMO und LUMO Energieniveaus waren im optimalen Bereich für BHJSCs die PC₆₁BM als Akzeptor verwenden.

Unbe-handelte Aktivschichten in **181-183**-basierten BHJSCs ergaben eine maximale PCE von 2.08% wenn **181** als Donor eingesetzt wurde. Solarzellen, die besser lösliche Cooligomere **182** und **183** enthielten, erzielten moderate Wirkungsgrade von ~ 1.4 bzw. $\sim 0.4\%$. Jedoch führte Zelloptimierung mittels Lösungsmitteladditiven und Tempern zu außerordentlichen Verbesserungen, was in PCEs von 3.55 und 3.13% für **182** bzw. **183** resultierte. Die hohe Leerlaufspannungen von ungefähr 1 V, die mit dieser Serie erreicht wurden und die guten Absorptionseigenschaften machen Bi(DTP) zu einem vielversprechenden Donorbaustein für organische Solarzellenmaterialien.

In Kapitel 7 erlaubte die Synthese von linearen A-D-A Oligomeren **202**, **203** und **205** den Zugang zu einer neuartigen DCV-substituierten Oligo(DTP)-Serie (Abbildung 5). Durch Absorptionsspektroskopie und cyclische Voltammetrie konnten Struktur-Eigenschafts-Beziehungen gesammelt werden bezüglich der Ausdehnung der Oligo(DTP)-Donoreinheit.

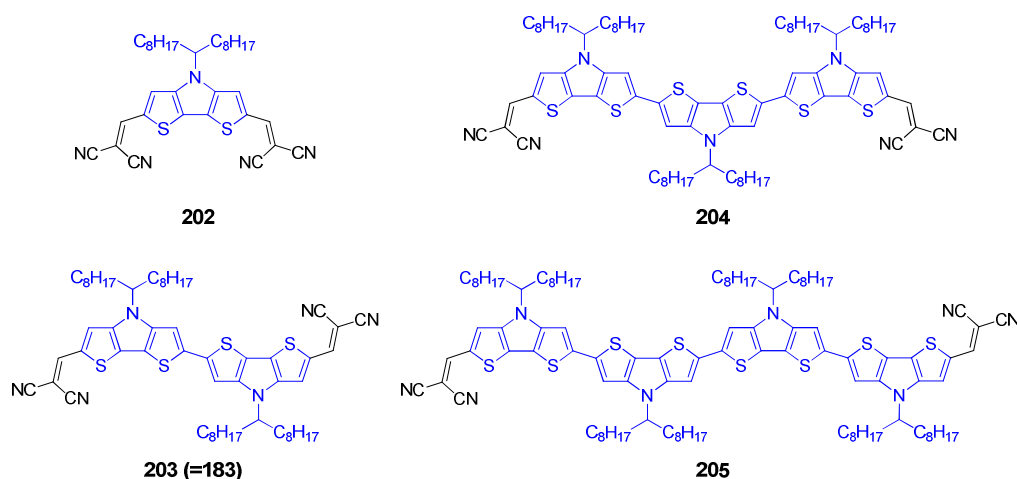


Abbildung 5. DCV-substituierte Oligo(DTP)-Serie.

Durch eine Erhöhung der Anzahl der DTP-Einheiten wurde eine intensivere und rotverschobene Absorption beobachtet. Des Weiteren wird die optische Bandlücke reduziert und erreicht einen theoretischen Grenzwert von ~ 1.6 eV für unendlich lange Oligomere. Dünnschichtabsorptionsmessungen deckten signifikante Absorptionsänderungen durch Tempern auf. Durch Neuordnung der Moleküle in reinen, sowie PC₆₁BM-gemischten Filmen von **202-204** wurde eine rotverschobene und intensivere Absorption im Vergleich zu unbehandelten Filmen beobachtet. Cyclovoltammetrische Messungen ergaben n reversible Oxidationswellen für jedes Oligo(DTP) wobei n der Anzahl an DTP-Einheiten entspricht. Die Ausdehnung der Oligomerserie führte zu einer Verringerung des ersten Oxidationspotentials bis zu -0.03 V für quater(DTP) **205**, was dessen begrenzte Stabilität erklärt.

Neben Bi(DTP) **203** zeigte Ter(DTP) **204** die vielversprechendsten HOMO und LUMO Energieniveaus der Serie bezüglich der Verwendung als Donor in BHJSCs. Lösungsprozessierte Solarzellen, die **204** als Donor einsetzen und PC₆₁BM als Akzeptor verwenden, erreichten PCEs von bis zu 1.2%.

Acknowledgement - Danksagung

Die vorliegende Arbeit wäre ohne die Mithilfe und Unterstützung einer Vielzahl von Personen nicht möglich gewesen und deshalb möchte ich mich hier an dieser Stelle bei diesen ganz herzlich bedanken.

Ein besonderer Dank gilt...

- Prof. Dr. P. Bäuerle, für meine Aufnahme in seinen Arbeitskreis und die damit mir vorliegenden ausgezeichneten Arbeitsbedingungen, die interessante und aktuelle Themenstellung, sowie seine fachliche Unterstützung und Diskussionsbereitschaft.
- Dr. S. Rau, für die freundliche Übernahme des Zweitgutachtens.

Danken möchte ich auch...

- Dr. A. Mishra, für die fachliche Unterstützung als Gruppenleiter, sowie sein stetes Interesse und seine Diskussionsbereitschaft.
- Dr. G. Schulz, für ihre Hilfe rund um das Thema der lösungsprozessierten organischen Solarzellen.
- Dr. E. Mena-Osteritz, für die Durchführung von quantenchemischen Rechnungen und AFM Experimenten, sowie ihr stets offenes Ohr und ihre fachliche Unterstützung.
- Dr. G. Götz, für die Beratung in elektrochemischen und labortechnischen Fragen.
- Dr. S. Powar, Dr. A. Nattestad, Dr. A. Mozer, Prof. Dr. U. Bach, und Dr. T. Geiger, für die hervorragende Kooperation auf dem Gebiet der p-Typ DSSCs.
- Dr. C. W. Wessendorf, Dr. J. Hanisch, Dr. E. Ahlswede und Prof. Dr. M. Lindén, für die hervorragende Kooperation auf dem Gebiet der lösungsprozessierten organischen Solarzellen.
- Dr. M. Wunderlin und E. Brier, für die Aufnahme meiner Massenspektren.
- M. Lang, für die Durchführung der Elementaranalysen.
- Dr. U. Werz, B. Mögenburg und U. Ziegler, für NMR-spektroskopische Dienstleistungen.
- Dr. S. Schmid und Dr. S. Haid, für die Aufnahme vieler NMR-Spektren.
- M. Schwenk, für sein Engagement während seines Praktikums, im Speziellen für das „Nachziehen“ von wichtigen Vorstufen.
- allen Mitarbeitern des Instituts für Organische Chemie II und Neue Materialien, für die tolle Arbeitsatmosphäre, sowie zahlreiche Diskussionen über chemische Themen und darüber hinaus.
- allen Korrekturlesern.

Und zuletzt, aber allen voran...

danke ich meinen Eltern, für die moralische und finanzielle Unterstützung während meines Studiums sowie in vielen anderen Belangen des Lebens.

Curriculum vitae

Der Lebenslauf ist in der Online-Version aus Gründen des Datenschutzes nicht enthalten.

Der Lebenslauf ist in der Online-Version aus Gründen des Datenschutzes nicht enthalten.

Publications and presentations

Publications

M. Weidelener, S. Powar, H. Kast, Z. Yu, P. P. Boix, C. Li, K. Müllen, T. Geiger, S. Kuster, F. Nüesch, U. Bach, A. Mishra, P. Bäuerle, *Chem. Asian J.* **2014**, 9, 3251-3263.

“Synthesis and Characterization of Organic Dyes with Various Electron-Accepting Substituents for p-Type Dye-Sensitized Solar Cells.”

M. Weidelener, C. D. Wessendorf, J. Hanisch, E. Ahlswede, G. Götz, M. Linden, G. Schulz, E. Mena-Osteritz, A. Mishra, P. Bäuerle, *Chem. Commun.* **2013**, 49, 10865-10867.

„Dithienopyrrole-based oligothiophenes for solution-processed organic solar cells.”

M. Weidelener, A. Mishra, A. Nattestad, S. Powar, A. J. Mozer, E. Mena-Osteritz, Y.-B. Cheng, U. Bach, P. Bäuerle, *J. Mater. Chem.* **2012**, 22, 7366-7379.

„Synthesis and characterization of perylene-bithiophene-triphenylamine triads: studies on the effect of alkyl-substitution in p-type NiO based photocathodes.”

C. D. Wessendorf, G. L. Schulz, A. Mishra, P. Kar, I. Ata, M. Weidelener, M. Urdanpilleta, J. Hanisch, E. Mena-Osteritz, M. Lindén, E. Ahlswede, P. Bäuerle, *Adv. Energy Mater.* **2014**, doi: 10.1002/aenm.20140026.

“Efficiency Improvement of Solution-Processed Dithienopyrrole-Based A-D-A Oligothiophene Bulk-Heterojunction Solar Cells by Solvent Vapor Annealing.”

S. Powar, T. Daeneke, M. T. Ma, D. Fu, N. W. Duffy, G. Götz, M. Weidelener, A. Mishra, P. Bäuerle, L. Spiccia, U. Bach, *Angew. Chem.* **2013**, 125, 630-633; *Angew. Chem. Int. Ed.* **2013**, 52, 602-605.

“Highly Efficient p-Type Dye-Sensitized Solar Cells based on Tris(1,2-diaminoethane)Cobalt(II)/(III) Electrolytes.”

S. Powar, Q. Wu, M. Weidelener, A. Nattestad, Z. Hu, A. Mishra, P. Bäuerle, L. Spiccia, Y.-B. Cheng, U. Bach, *Energy Environ. Sci.* **2012**, 5, 8896-8900.

“Improved photocurrents for p-type dye-sensitized solar cells using nano-structured nickel(II) oxide microballs.”

L. Tong, A. Iwase, A. Nattestad, U. Bach, M. Weidelener, G. Götz, A. Mishra, P. Bäuerle, R. Amal, G. G. Wallace, A. J. Mozer, *Energy Environ. Sci.* **2012**, 5, 9472-9475.

“Sustained solar hydrogen generation using a dye-sensitised NiO photocathode/BiVO₄ tandem photo-electrochemical device.”

Presentations

FP11 (11th International Symposium on Functional π -Electron Systems), Arcachon, France, June 2-7, **2013**.

Poster presentation

M. Weidelener, A. Mishra, G. Schulz, P. Bäuerle, *“Oligo(dithienopyrroles) for Solution-Processed Bulk Heterojunction Solar Cells”*.

Integrated Graduate School (SFB 569), seminar weekend, Ulm, Germany, 29th September - 1st October, **2011**.

Oral presentation

M. Weidelener, *“Dyes for NiO-Based p-Type DSSC with Different Acceptor Groups”*.

Integrated Graduate School (SFB 569), PhD student seminar, Ulm, Germany, 1st February, **2011**.

Oral presentation

M. Weidelener, *“Synthesis of Perylenyl-Bithiophene-Triphenylamine-Dyes for p-Type NiO-Based DSSC”*.

FP9 (9th International Symposium on Functional π -Electron Systems), Atlanta, Georgia, USA, May 23-28, **2010**.

Poster presentation

M. Weidelener, A. Nattestad, U. Bach, K. Müllen, A. Mishra, P. Bäuerle, *“Synthesis and Characterization of D-p-A Type Organic Dyes for NiO_x-Based Photocathodes”*.